NEDO-24539
79NED84
CLASS I
AUGUST 1979

MARK I CONTAINMENT PROGRAM

FULL SCALE TEST PROGRAM FINAL REPORT

TASK NUMBER 5.11

G. W. FITZSIMMONS
D. L. GALYARDT
R. B. NIXON
M. J. MANN
K. P. YU

GENERAL ELECTRIC

NEDO-24539
79NED84
Class I
August 1979

MARK I CONTAINMENT PROGRAM

FULL SCALE TEST PROGRAM
FINAL REPORT

TASK NUMBER 5.11

G.W. Fitzsimmons
D.L. Galyardt
R.B. Nixon
M.J. Mann
K.P. Yu

Reviewed: _____
J.E. Torbeck, Technical Leader
Containment Experiments

Approved: _____
A.E. Rogers, Manager
Containment Technology

Reviewed: _____
M. Bein, Test Report Evaluator
Containment Experiments

Approved: _____
E. Kiss, Manager
Applied Mechanics

BOILING WATER REACTOR SYSTEMS DEPARTMENT • GENERAL ELECTRIC COMPANY
SAN JOSE, CALIFORNIA 95125

GENERAL ELECTRIC

DISCLAIMER OF RESPONSIBILITY

Neither the General Electric Company nor any of the contributors to this document makes any warranty or representation (express or implied) with respect to the accuracy, completeness, or usefulness of the information contained in this document or that the use of such information may not infringe privately owned rights; nor do they assume any responsibility for liability or damage of any kind which may result from the use of any of the information contained in this document.

TABLE OF CONTENTS

TABLE OF CONTENTS (Continued)

1157 13

TABLE OF CONTENTS (Continued)

1157 137

TABLE OF CONTENTS (Continued)

APPENDICES

LIST OF ILLUSTRATIONS

1157 139

LIST OF ILLUSTRATIONS (Continued)

LIST OF ILLUSTRATIONS (Continued)

1167

141

LIST OF ILLUSTRATIONS (Continued)

LIST OF ILLUSTRATIONS (Continued)

LIST OF ILLUSTRATIONS (Continued)

LIST OF ILLUSTRATIONS (Continued)

1157 145

LIST OF ILLUSTRATIONS (Continued)

LIST OF ILLUSTRATIONS (Continued)

LIST OF ILLUSTRATIONS (Continued)

1157 148

LIST OF ILLUSTRATIONS (Continued)

LIST OF ILLUSTRATIONS (Continued)

LIST OF ILLUSTRATIONS (Continued)

LIST OF ILLUSTRATIONS (Continued)

1157 152

LIST OF ILLUSTRATIONS (Continued)

LIST OF ILLUSTRATIONS (Continued)

LIST OF ILLUSTRATIONS (Continued)

1157 155

LIST OF TABLES

1157 156

LIST OF TABLES (Continued)

ABSTRACT

Test results are reported for a series of ten tests conducted in a full scale mockup of a 22.5° sector of a Mark I containment torus. The test facility included an appropriately-sized drywell and steam vessel to allow simulation of the torus (wetwell) response to a range of LOCA (loss-of-coolant-accident) conditions. Hydrodynamic loads on the wetwell and the structural response of the wetwell shell, downcomer and support columns resulting from the condensation oscillation and chugging regimes were measured. Tests investigating the effects of LOCA break size and type (liquid or steam), downcomer submergence, wetwell freespace pressure, suppression pool temperature, and vent air content were conducted, covering the range of expected Mark I LOCA conditions. This test report includes a description of the test facility, test operation, and a compilation and analysis of the principal test results.

LIST OF ACRONYMS

CO	Condensation Oscillation
CPSD	Cross Power Spectral Density
DAS	Data Acquisition System
FSI	Fluid Structure Interaction
FSTF	Full Scale Test Facility
LOCA	Loss-of-Coolant Accident
LVDT	Linear Variable Displacement Transducer
NOD	Notice of Deviation
PSD	Power Spectral Density
RPV	Reactor Pressure Vessel

1. INTRODUCTION

1.1 BACKGROUND

As a part of the Mark I Long Term Containment Program, a test program to obtain full scale chugging and condensation oscillation data was defined and implemented. The loads from chugging and condensation oscillation are a result of unsteady steam condensation in the wetwell suppression pool during the low and intermediate steam mass flow rates that are typical of a postulated loss-of-coolant-accident (LOCA).

Preliminary specifications for the test program were established in the fall of 1976. In this same period, C.F. Braun & Co. was selected as the prime contractor to design and construct the facility and Wyle Laboratories was selected as the subcontractor for test operation. The test facility was located on Wyle property near Norco, California. Facility design and construction continued through 1977 and early 1978. Shakedown testing began in March 1978, and the ten-test program was completed in August 1978.

1.2 PROGRAM OBJECTIVE

The overall program objective was to establish a reference data base for chugging and condensation oscillation in a multivent system with representative LOCA conditions in order to define loads caused by these phenomena in a Mark I pressure suppression containment. To meet this objective, a Full Scale Test Facility (FSTF) was designed and erected consisting of a full scale mockup of a 22.5° segment of the Mark I containment torus, including an appropriately sized drywell, reactor pressure vessel and associated auxiliary equipment. A series of tests were performed with the facility to determine:

a. The applied loads on the wetwell walls and downcomers resulting from condensation oscillation and chugging,

b. The structural response of the wetwell walls, downcomers, and support columns resulting from condensation oscillation and chugging.

Parameters were varied to investigate the effects of the following:

a. Blowdown size and type (liquid and steam)

b. Wetwell airspace pressure

c. Downcomer submergence

d. Water temperature

e. Vent air content.

Additional information, such as pool mixing characteristics and the effect of fluid-structure interaction, was also obtained.

1.3 TEST PROGRAM SUMMARY

To ensure that the test objectives were met, the test program included requirements for review of preliminary results following each test. Based on these data reviews, several decisions relating to subsequent tests were made. For reference in discussion of these decisions, a simplified test matrix is presented in Figure 1.3-1. A more detailed test matrix is presented in Section 4 (Figure 4.3-1).

The first three tests were conducted to establish the effect of break size and type on the magnitude of the chugging wall loads. Since it had been anticipated at the onset of the program that the chugging loads would be the most limiting of the condensation loads, the break configuration that gave the largest chugging loads was to be selected after these first three tests to investigate the other parametric effects on condensation loads. The break configuration for these first tests were small steam, medium steam and small liquid for tests M1, M2 and M3, respectively. The large breaks were not included in this front end investigation because it was expected that they would not yield the most limiting chugging data.

Of the first three tests, the only test that exhibited any chugging was M1, the small steam break configuration. Therefore, this break configuration was selected for tests M4, M5, M6, M9 and M10 to investigate the effect of increased freespace pressure, increased pool temperature, decreased submergence, increased submergence and decreased vent air content, respectively. After the first three tests, before starting the parametric studies, two modifications were made to the test facility. A vent header deflector was installed beneath the vent header and prototypical tie-straps were installed between one pair of downcomers. The deflector was installed to reduce pool impact loads on the vent header. The tie-straps were added to assess downcomer response with a prototypical configuration.

After the parametric studies with the small break configuration (tests M4, M5, M6 and M9) were completed, additional facility modifications were made for test M10, which was added to the original nine-test matrix. Because the wetwell-to-drywell vacuum breaker opened during chugging events and may have introduced additional air into the vent system, test M10 was added to determine if reduced air content affected the chugging loads. For this test, several modifications were made to the test facility to provide protection, considering the uncertainty regarding the magnitude of pressure and water level variations in the vent system with the vacuum breaker removed. Two rupture discs and three ring stiffeners were added to the vent header and bracing was added between the three pairs of downcomers without tie-straps. Chugging was observed with the vacuum breaker removed, but the magnitude of the resulting loads was not significantly different from test M1, which had equivalent conditions.

Tests M7 and M8 were conducted with the large steam and large liquid break configurations, respectively, to investigate the effect of large breaks on the condensation loads. Before conducting these tests, perforations were added to the blowdown line discharge standpipe in the drywell to mitigate a facility-related pressure shock wave at test initiation which had been observed during the medium steam break test (Appendix E).

Between tests M7 and M8, the vent header stiffeners and bracing between one pair of downcomers were removed. This was to allow measurement of the unbraced downcomer response with the large liquid break test, M8.

TEST NUMBER*	BREAK CONFIGURATION	PARAMETER INVESTIGATED
M1	Small Steam	Reference test
M2	Medium Steam	Break size increased (steam)
M3	Small Liquid	Break type changed to liquid
M4	Small Steam	Freespace pressure increased
M5	Small Steam	Pool temperature increased
M6	Small Steam	Submergence decreased and pool temperature increased
M9	Small Steam	Submergence increased
M10	Small Steam	Vent air content decreased
M7	Large Steam	Break size increased (steam)
M8	Large Liquid	Break size increased (liquid)

*In order of performance

Figure 1.3-1. Summary Test Matrix

2. SUMMARY OF RESULTS

The FSTF system performance during the ten-test matrix was generally as expected. The system pressure and bulk temperature responses of the steam vessel, drywell, and wetwell agreed well with pretest predictions. This ensured that boundary conditions on the suppression pool, which control the wetwell hydrodynamic loads and structural response, were representative of postulated LOCA conditions in a Mark I containment.

2.1 CHUGGING WALL LOADS

Chugging occurred in only four tests - M1, M4, M9, and M10 - of the ten-test matrix. These four were all small steam break tests with a nominal initial pool temperature of 70°F. During the tests, no chugging was observed when the average downcomer mass flux was greater than 6.5 $lb/sec-ft^2$ or when the pool temperature in the vicinity of the bottom of the downcomers was greater than 135°F. A data base from these tests of nearly 1500 downcomer chugs is available for Mark I load definition.

Two chugging modes or types were observed: one nearly synchronized, with seven or eight downcomers chugging less than 100 msec apart (Type 1); the other type not well synchronized and generally consisting of only single downcomer chugs (Type 2). The more synchronized chugs occurred only in Test M1 at a steam mass flux less than 3.0 $lb/sec-ft^2$ and a pool temperature at the downcomer exit of less than 110°F.

The Type 1 chugging average period varied from 1.6 seconds to 2.4 seconds between pool chugs (defined in Section 6.2.1.4) with a trend to a shorter period as mass flux decreased and pool temperature increased. The average period of Type 2 chugging varied from 0.9 seconds to 2.4 seconds between pool chugs with a tendency toward longer periods as mass flux decreases and pool temperature increases.

Wetwell wall pressure fluctuations tended to have higher local values for Type 1 chugging than for Type 2. The highest peak to peak fluctuation for

a Type 1 chug was a single, isolated spike at the north end of the bottom of the wetwell that went from -3.1 to +6.8 psi. Peak values at other locations were generally in the range of ±2 psi. Spatially averaged wall pressure fluctuations were smaller than the local values and were not significantly different for the two types of chugging. Bounding values of the average wall pressure have been presented as a function of time with the highest values being -1.7 to +1.5 psi seen in data from Test M9. The bounding values support the idea that chugging wall loads increase directly with submergence and decrease with increased free-space pressure.

The frequency content of the wall pressure fluctuations varies greatly with time but three dominant frequencies of approximately 7, 13 and 40 Hz were usually present with the relative magnitudes varying throughout the test.

Pressure distributions for the wetwell wall at times just prior to chug, showed generally higher pressure fluctuations at the bottom of the wetwell and lower fluctuations toward the water surface and were similar to those seen during condensation oscillations. The pressure profiles following a chug were more random with no apparent pattern.

2.2 CONDENSATION OSCILLATION

Condensation oscillations (CO) occurred in all tests. The dynamic portion of the pressure signals for CO are characterized by a continuous waveform at a dominant frequency. This is true for pressure readings located throughout the test facility (drywell, vent system and wetwell). The continuous behavior began early in the tests and extended throughout the test period for six out of ten tests performed. For the other tests this behavior was replaced by chugging after 10 to 30 seconds.

The test data showed that the average wetwell wall pressure amplitudes ranged from 6.3 psi peak-to-peak for the large liquid break test (M8) to 0.20 psi peak-to-peak for small steam break tests. The test with the second highest amplitude wetwell wall pressure oscillations was M7, the large steam break

test. For both large break tests (i.e., M7 and M8), irregularly occurring pressure spikes superimposed on the fundamental waveform were observed. Also for these tests, pressure amplitudes on the wetwell wall were generally higher than downcomer pressure amplitudes. The opposite was true for medium and small break tests. Throughout the entire CO period and for all tests the pressure waveform was observed to be amplitude modulated with a beat frequency ranging from 0.6 Hz for M1 to 1 Hz for M8. This modulation was observed to be present in the pressure signals from the vent system and wetwell. Maximum wetwell wall pressure magnitudes were detected by transducers located at the bottom of the wetwall pool; the magnitudes decreased at wall locations approaching the pool surface.

To investigate the parametric variation effects on the magnitudes of the pressure oscillations, average pressures were calculated using all wetwell wall pressure transducers to characterize the total vertical dynamic load. The maximum positive and maximum negative values of these spatially-averaged pressures were subsequently time averaged over 1.1-sec intervals. The investigation showed the following:

a. Large liquid break wall pressure amplitudes were greater by a factor of two than steam break amplitudes at the same steam flow rates.

b. Variation of wetwell airspace pressure in the range of 30 to 40 psia did not affect pressure magnitudes.

c. No consistent pressure magnitude trends were observed with vent steam air content and local pool temperature variation.

d. Liquid break and steam break pressure magnitudes correlate well with their corresponding total enthalpy rate in the vents.

The dominant CO waveform frequency ranges from 4.8 Hz for the large-break quid test M8 to 7.6 Hz for small break tests. There is a slight increase

1157 166

of the dominant frequency as the total blowdown flow rate is decreased. The downcomer and wetwell wall pressure signals also contain other higher frequencies not present in the vent or the drywell pressure traces.

2.3 STRUCTURAL RESPONSE

2.3.1 Dynamic Response During Condensation Oscillation

The largest dynamic stress levels were measured during the condensation oscillation (CO) phase of the large liquid break test (M8). Peak dynamic stresses for key structural components of the FSTF during CO are summarized below:

a. Wetwell Shell – During CO the peak dynamic surface stress intensity for the wetwell shell was about 3,800 psi. At the wetwell shell/ring girder intersection the peak dynamic surface stress intensity was about 14,800 psi.

b. Wetwell Support Columns – The peak radial and longitudinal column dynamic bending stresses during CO were approximately 1,500 and 500 psi, respectively. For column axial stress (tension/compression) the peak dynamic value during CO was about 1,600 psi.

c. Vent Header Shell – In the downcomer/vent header attachment region of the vent header shell, the peak dynamic surface stress was about 14,000 psi for downcomer pairs with prototypical tie-straps and about 46,000 psi for downcomers pairs without tie-straps or bracing.

2.3.2 Dynamic Responses During Chugging

Dynamic stresses during the small steam break test (M1) were the largest chugging-related stresses observed in the course of testing. Peak dynamic stresses for key structural components of the FSTF during chugging are summarized below:

a. Wetwell Shell — Peak dynamic surface stress intensities during chugging for the wetwell shell and wetwell shell/ring girder intersection were about 2,500 and 2,900 psi, respectively.

b. Wetwell Support Columns — Both the peak dynamic radial and longitudinal column bending stresses were about 300 psi during chugging. The peak dynamic axial column stress was about 500 psi.

c. Vent Header Shell — During chugging the peak dynamic surface stress in the downcomer attachment region of the vent header shell was about 25,000 psi. This peak value occurred at a downcomer pair without tie-straps or bracing (no downcomer pairs were interconnected for the small steam break test (M1)).

2.3.3 Structural Response Simulation

The FSTF was designed to model the structural response of one bay of the Monticello torus. Frequencies corresponding to the calculated structural response for the Monticello torus were observed in FSTF structural response data, indicating that the FSTF accurately modeled Monticello.

2.4 FLUID-STRUCTURE INTERACTION

Fluid-structure interaction (FSI) effects were evident during the condensation oscillation (CO) period of the large liquid break test (M8). FSI effects were also evident following the initiation of a Type I chug (a nearly synchronized light-downcomer chug) observed in the small steam break test (M1).

1157 168

Data indicate that FSI effects relate primarily to the structural response of the wetwell shell. Pool pressure and shell response data for both CO and Type I chugging contain frequencies equivalent to several shell-resonant frequencies as determined from dynamic shake tests. Shell-resonant frequencies of 9.7, 11.0, 15.0 and 19.5 Hz were apparently excited during CO. With the exception of the 9.7 Hz frequency, the same resonant frequencies appear to have been excited during chugging. The relationship between pool pressures and local shell accelerations also suggests that FSI effects were present during CO and Type I chugging. The pool pressure increases at locations where the shell is accelerating toward the pool and decreases at locations where the shell is accelerating away from the pool. This trend is consistent with what would be expected if pool pressures were influenced by local wall motion.

The only FSI effects observed in addition to those resulting from the shell vibrations were caused by wetwell end enclosure vibration during chugging. This effect is similar to the FSI effect associated with shell vibrations; that is, the pressure in the pool region adjacent to the end closures increases as the end closure accelerates into the pool. This data trend implies that end closure motion amplifies the local pool pressure signal. The influence of end closure vibrations on pool pressures during chugging represents an effect unique to the FSTF (not plant prototypical).

3. TEST FACILITY

3.1 SCALING CONSIDERATIONS

This facility was designed to simulate behavior of the Mark I containment system in response to LOCA conditions. The Monticello plant suppression chamber (wetwell) was selected as the reference geometry for the test facility. Appendix A documents the scaling considerations used in specifying the requirements for the facility and the basis for selecting Monticello as the reference plant.

3.2 COMPONENTS

3.2.1 Steam Supply Vessel

The steam supply vessel (V1) is cylindrical in shape, 6-1/2 ft in diameter and uses hemispherical heads, as shown in Figure 3.2-1. Vessel length, tangent to tangent is 36 ft and vessel volume is 1344 ft^3. The vessel is designed for a pressure of 1145 psig and a temperature of 565°F.

A removable 20-in. diameter standpipe located in the center of the vessel is used for the steam breaks in the large blowdown line. The standpipe is removed for the liquid break tests in the large blowdown line. A 6-in. diameter riser pipe located near the wall of the vessel is used for liquid breaks in the small blowdown line. The riser pipe is disconnected and the 8-in. elbow is rotated vertically for steam breaks in the small blowdown line.

3.2.2 Blowdown Line

The blowdown line transfers the fluid (liquid or steam or a mixture of both) at a controlled predetermined rate from the steam supply vessel (V1) to the drywell (V2).

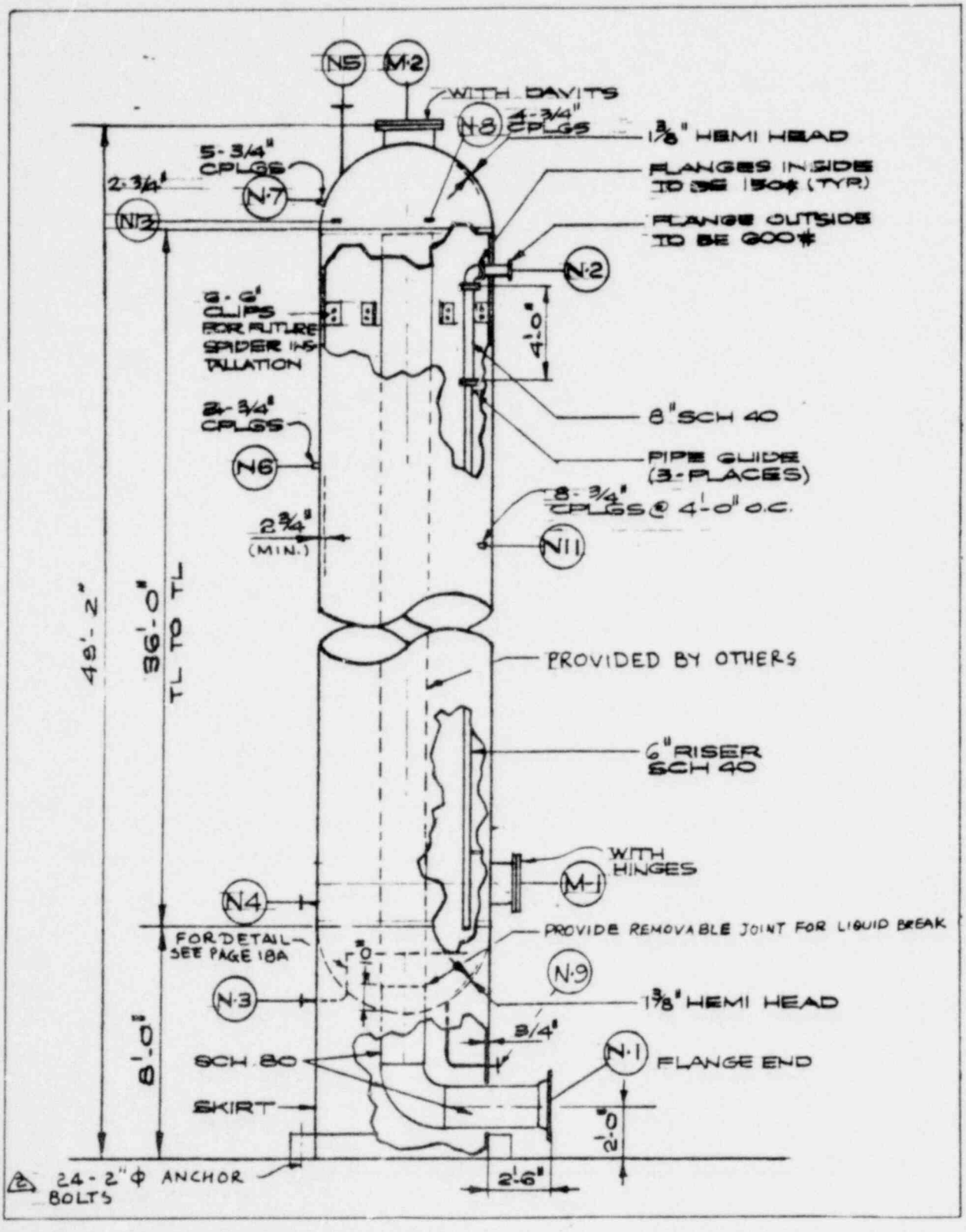

Figure 3.2-1. Mark I FSTF Steam Vessel (V1)

Two blowdown lines (20-in. and 6-in. diameter) were required to prevent fluid stratification and/or slug flow for the range of break areas tested. Both blowdown lines include a motor-operated isolation valve, a double disc rupture disc assembly, a removable standpipe, and a flow control nozzle that simulates the pipe break areas to be tested. Nozzle sizes available to simulate the pipe break areas are listed in Table 3.2-1. Blowdown line lengths and diameters were chosen to minimize line resistance losses. The blowdown lines discharge into the top of the drywell vessel symmetrically with respect to the vent line outlets to minimize mixing in the drywell. The discharge end of the blowdown lines was designed to minimize jet impingement pressures on the drywell wall. For the small line, the end of the pipe was blocked and the flow discharged through three rows of holes near the end of the pipe. For the large line, a deflector plate was positioned above the end of the line with perforations for purging of the top head, as shown in Figure 3.2-2.

3.2.3 Drywell

The drywell vessel (V2) is shown in Figures 3.2-2 and 3.2-3. The vessel is cylindrical with a hemispherical head on the top and a reversed hemispherical head on the bottom to scale the liquid holdup. The vessel is 12-1/2 ft in diameter and 57 ft in length, tangent to tangent. The vessel volume is 6995 ft^3 which includes a 57-ft^3 liquid holdup volume. The two vent line nozzles are located symmetrically relative to the blowdown line discharge, as shown in Figure 3.2-3. The vessel was designed for 70 psig pressure and

Table 3.2-1

BLOWDOWN NOZZLE SIZES

Blowdown Line Size	Nozzle Diameter
6 in. (small)	4 in.
20 in. (large)	6.0, 8.2, 9.0 in.

1157 172

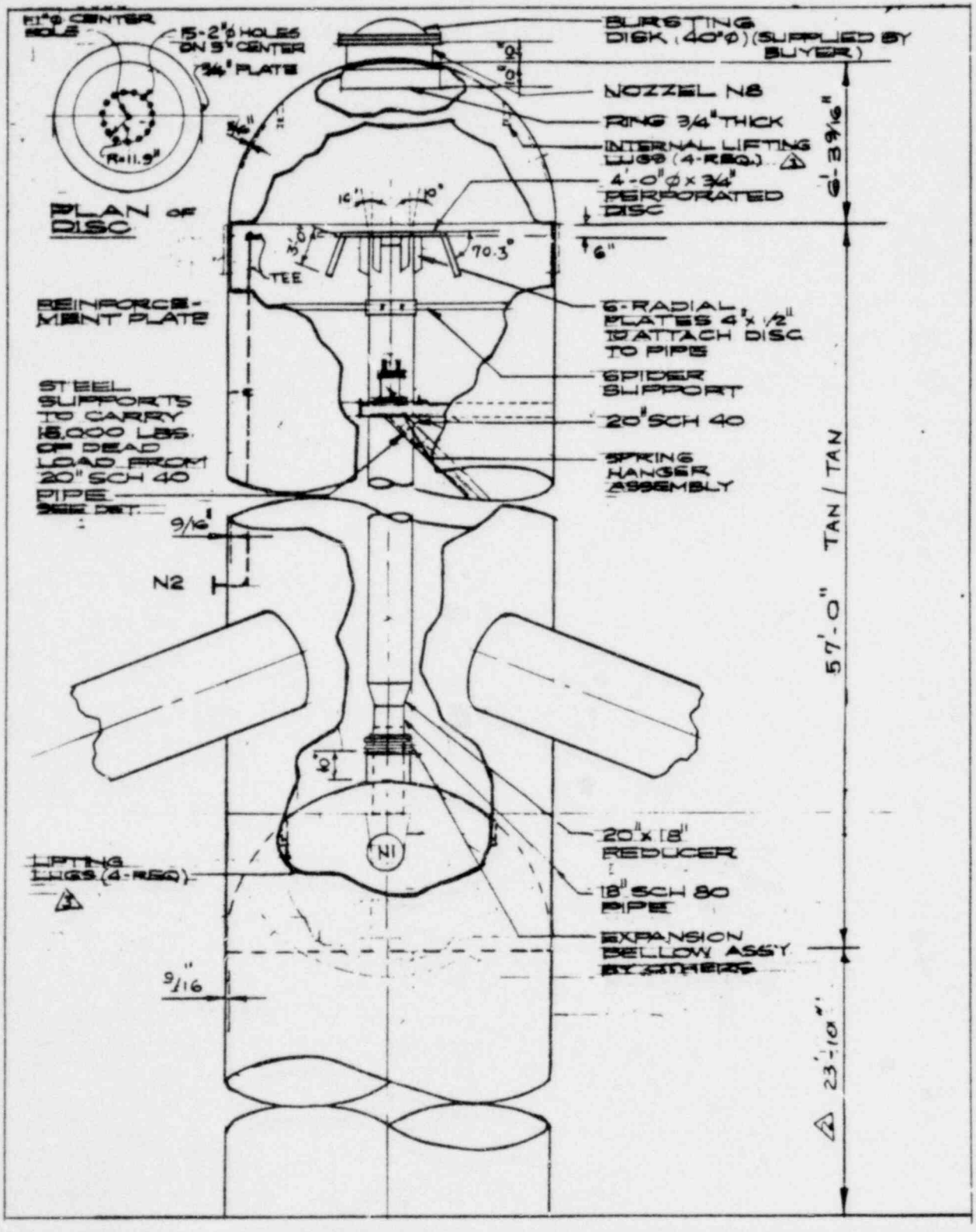

1157 17

Figure 3.2-2. Mark I FSTF Drywell Vessel (V2) View A

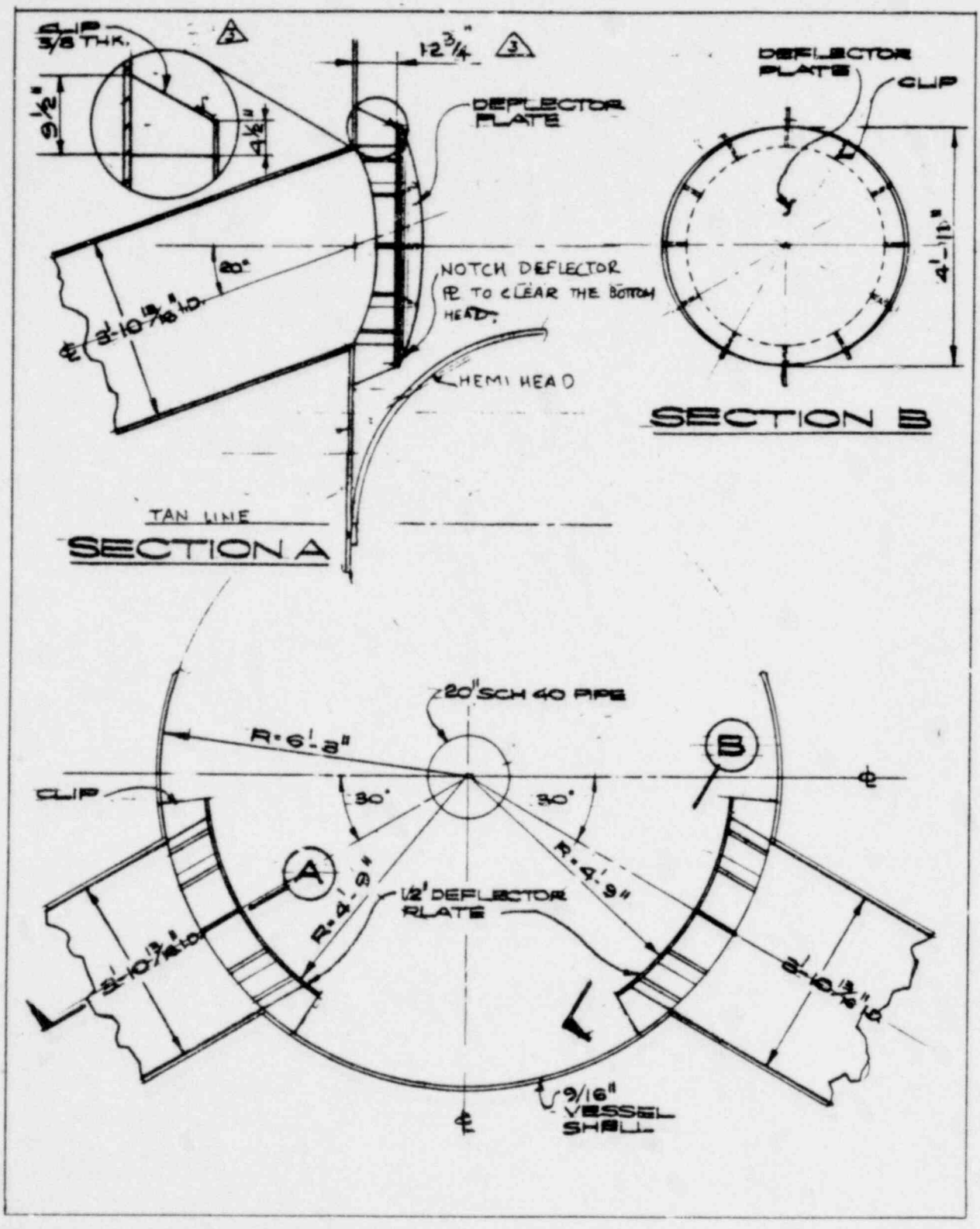

Figure 3.2-3. Mark I FSTF Drywell Vessel (V2) View B

1157 174

650°F temperature. A 40-in. diameter rupture disc was installed in the top head to prevent overpressurization of the drywell (V2) and wetwell (V3) vessels.

3.2.4 Vent Lines

The FSTF south vent line, which is an identical mirror image of the north vent line, is shown in Figure 3.2-4. The vent lines are 46-13/16 in. inside diameter with a 1/4-in. wall thickness. Expansion bellows are located within the vent system to structurally decouple the vent lines and drywell from the wetwell vessel and to allow for thermal expansion during heatup. The relative elevations and distances in the vent system and between the vessels are approximately the same as in the Monticello plant to achieve similar acoustic path lengths, fluid mixing, and flow stratification characteristics. The jet deflectors (shown in Figure 3.2-3) are configured after Monticello. The distance between the deflector and the drywell vessel wall was adjusted to obtain the calculated vent system total flow resistance of Monticello. A comparison of the calculated FSTF and Monticello flow resistances is given in Table 3.2-2.

3.2.5 Wetwell

The wetwell vessel (V3) is shown in Figure 3.2-5. The wetwell is prototypical of one Monticello bay. This particular bay is located between the vent lines and contains eight downcomers. The vessel is rated for an operating pressure of 54 psig and a temperature of 350°F. The vessel is a 22.5° segment of the torus with a 27-ft 8-in. inside diameter and a centerline length of 19-ft 5-15/16-in. The shell thickness is 0.562 in. compared to the 0.533-in. (above water) and 0.584-in. (below water) thickness of the Monticello wetwell. The ring girder at each mitre joint, four-foot diameter manway, vessel column supports, vent header and downcomers are duplications of Monticello.

Four-foot thick rigid end closures are located at each mitre section. The end closures are a composite structure composed of 1-1/4 in. thick steel plates.

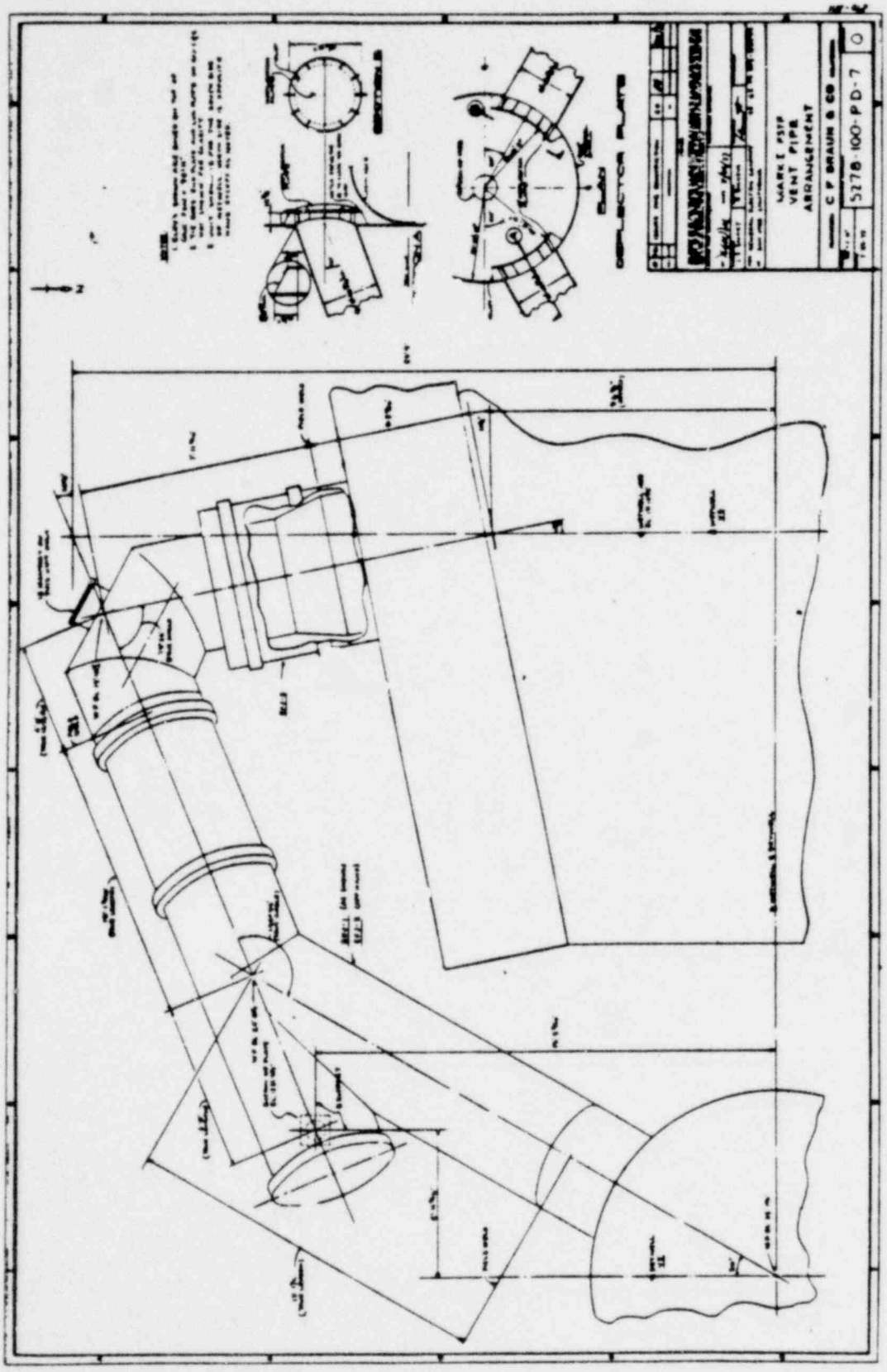

POOR ORIGINAL

Figure 3.2-4. Mark I FSTF Vent Line

1157 17

Table 3.2-2

VENT SYSTEM LOSS COEFFICIENT COMPARISON*

	FSTF	Monticello
Entrance	1.33	0.9
Friction (Vent Line)	0.12	0.1
35° Miter	0.24	-
Elbow/Tee	0.66	1.5
Expansion	0.46	-
11.25° Miter	0.05	-
Downcomer	0.78	1.1
30° Miter	0.16	0.2
Exit	1.0	1.0
Total Resistance	4.8	4.8

*Loss Coefficients are based on downcomer flow area.

POOR ORIGINAL

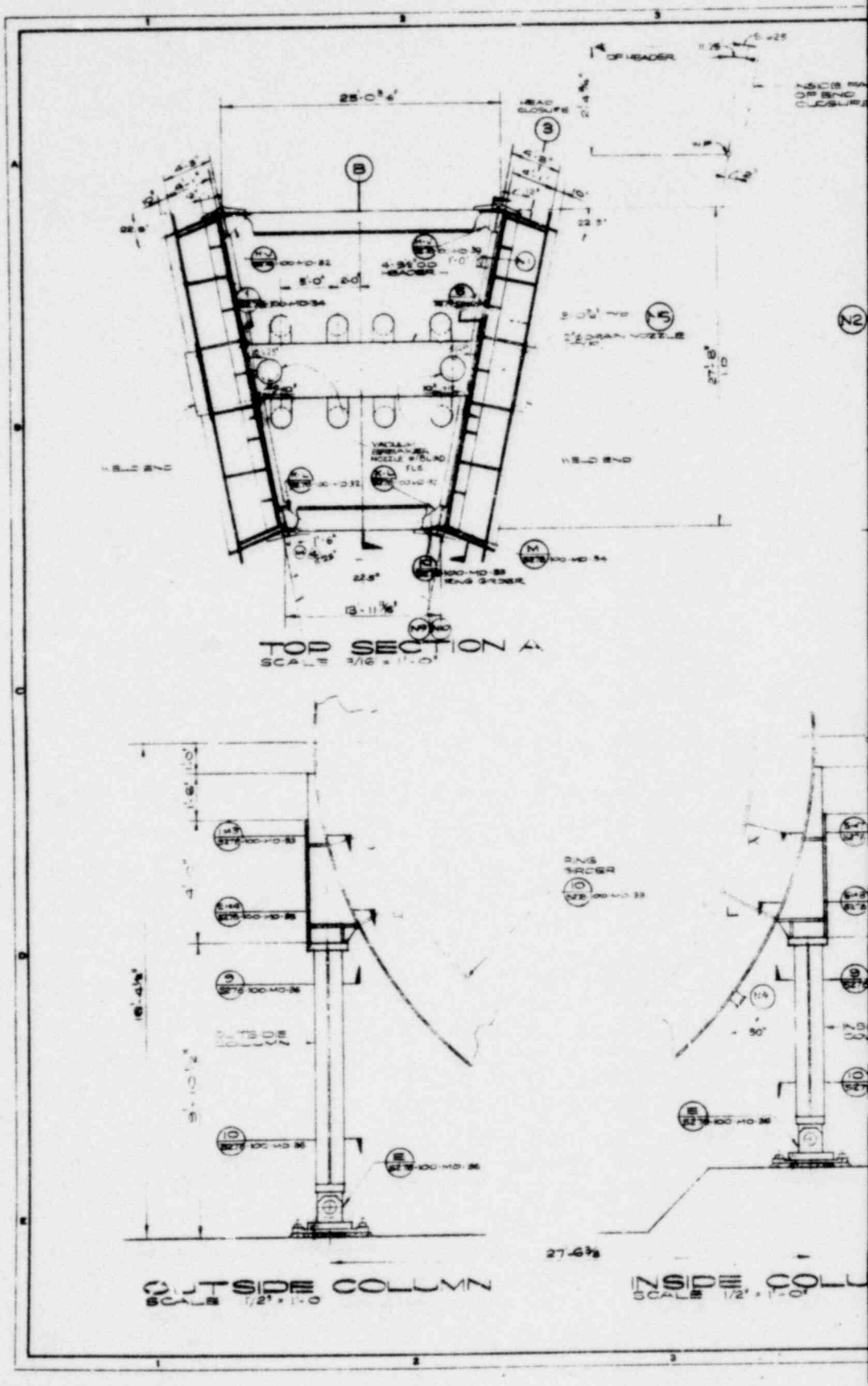

1157 178

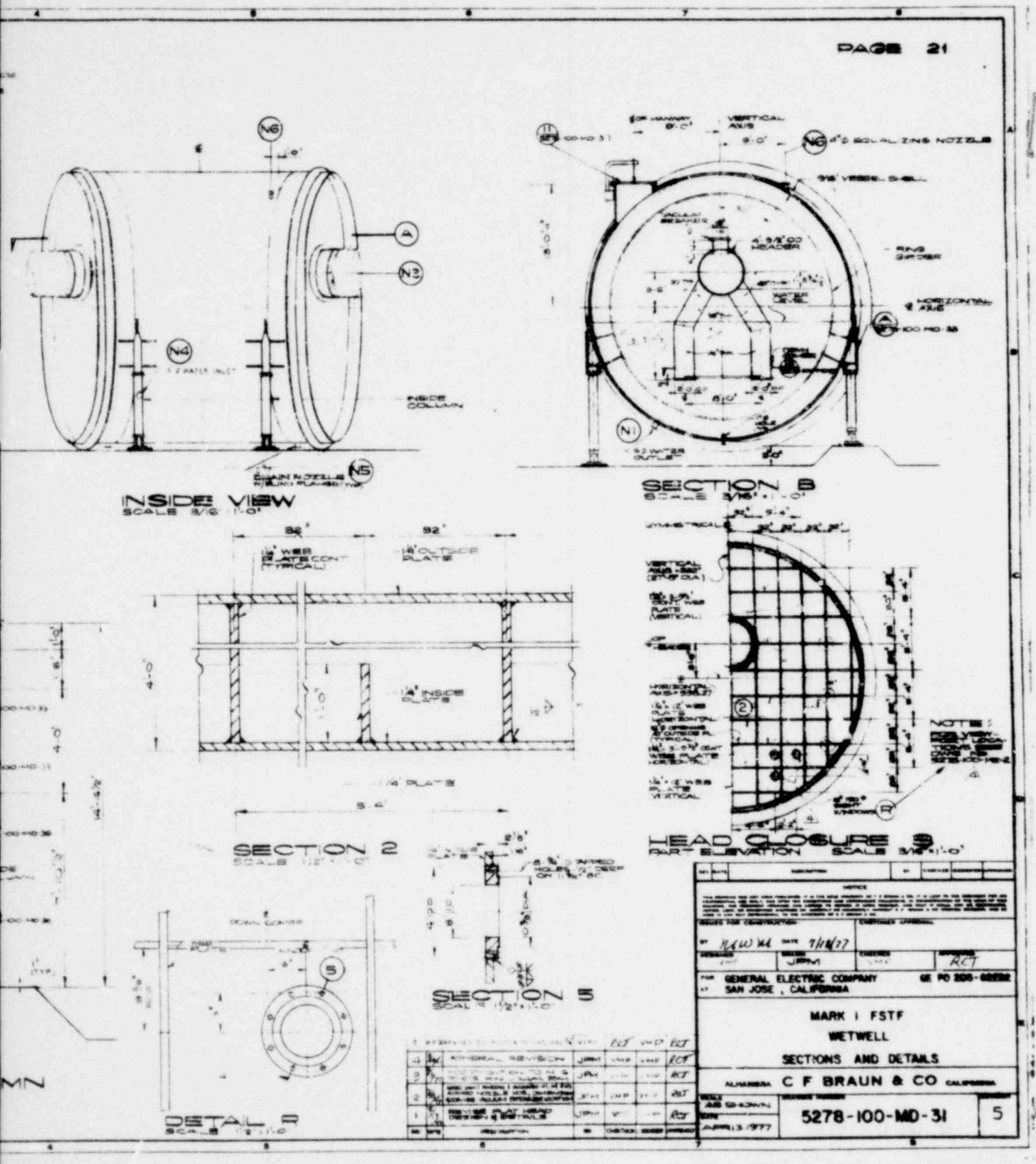

Figure 3.2-5. Mark I FSTF Wetwell-Sections and Details-View 1

The four-foot (48-in.) thickness of the closure was necessary to ensure that the rigid end closures did not significantly influence shell response. Attached to each end closure are 14 12-in. diameter restraint pipes (shown in Figure 3.2-6) 12-ft long with clevises at each end, connected to the "E"-shaped reinforced concrete abutment.

The fourteen restraint pipes attached to each end closure are equally spaced circumferentially around the vessel outer diameter and have varying wall thicknesses to simulate the shell local axial stiffness variation due to differences in axial length. The total cross-sectional area of steel of the pipes is equal to the total cross-sectional area of steel of the adjoining wetwell bay. By having clevises at each end, the restraint pipes allow limited radial movement (between the abutments) of the vessel due to thermal expansion.

The outer ends of the restraint pipes are anchored to the reinforced concrete abutments, which are configured to obtain the maximum practical stiffness with minimum mass. This was necessary to simulate the radial vibration mode of the Monticello wetwell at approximately 13 Hz. Each abutment is integrally tied to a 5-ft thick reinforced concrete basemat, which is in turn tied mechanically to bedrock with 120 anchors to ensure the wetwell loads and responses are not affected by any reaction with the basemat or soil.

At the miter joint at each end of the wetwell, the wetwell is supported by two column supports, shown in Figure 3.2-5. The support columns are prototypical of the modified Monticello column supports and are also attached to the 5-ft thick reinforced concrete basemat. For Monticello, the four columns support the steel and water mass of two bays (a 45° segment). Since the FSTF wetwell is only one bay (22.5° segment) the mass of the end closures was increased to simulate the mass of the adjacent bay (steel and water).

POOR ORIGINAL

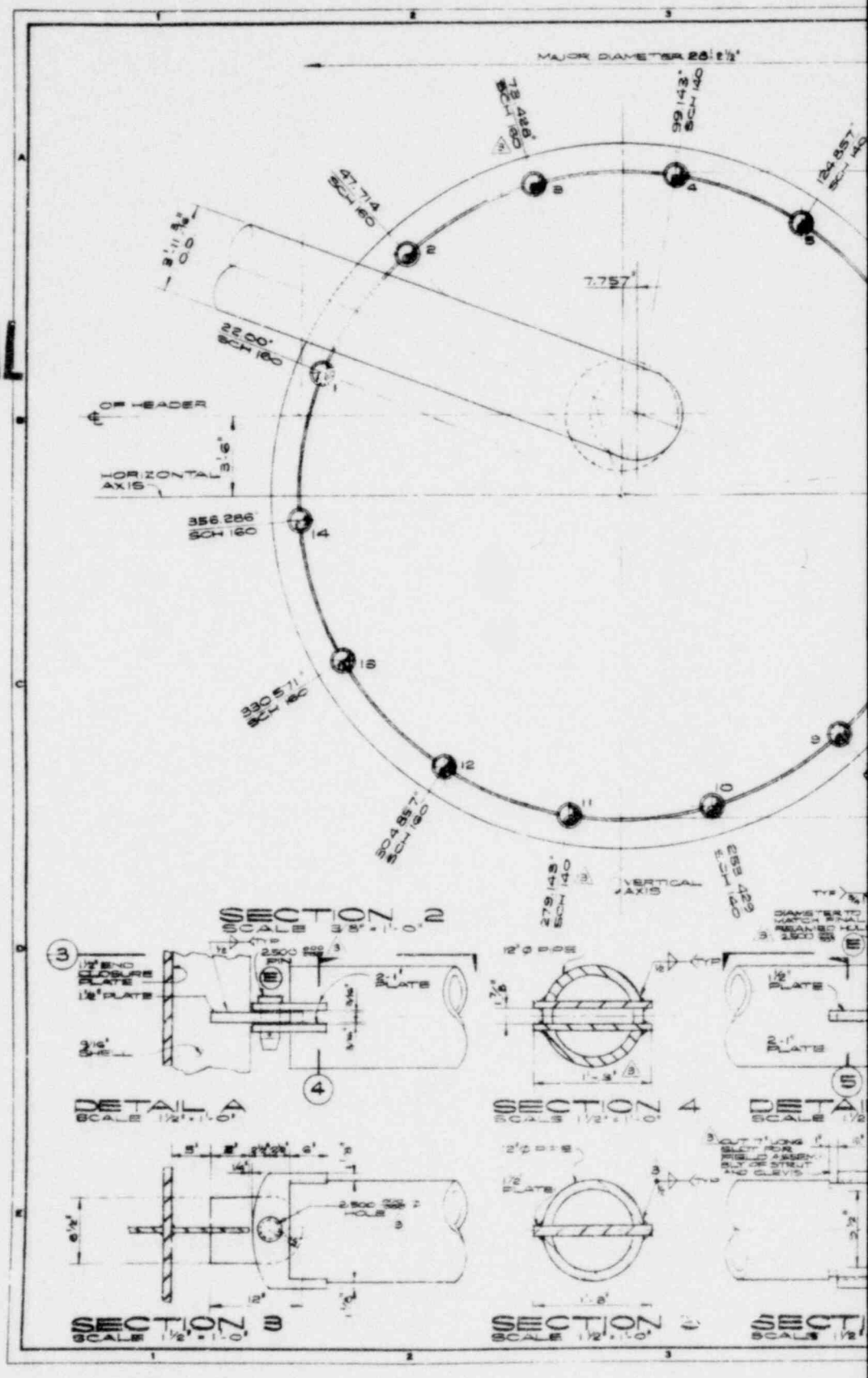

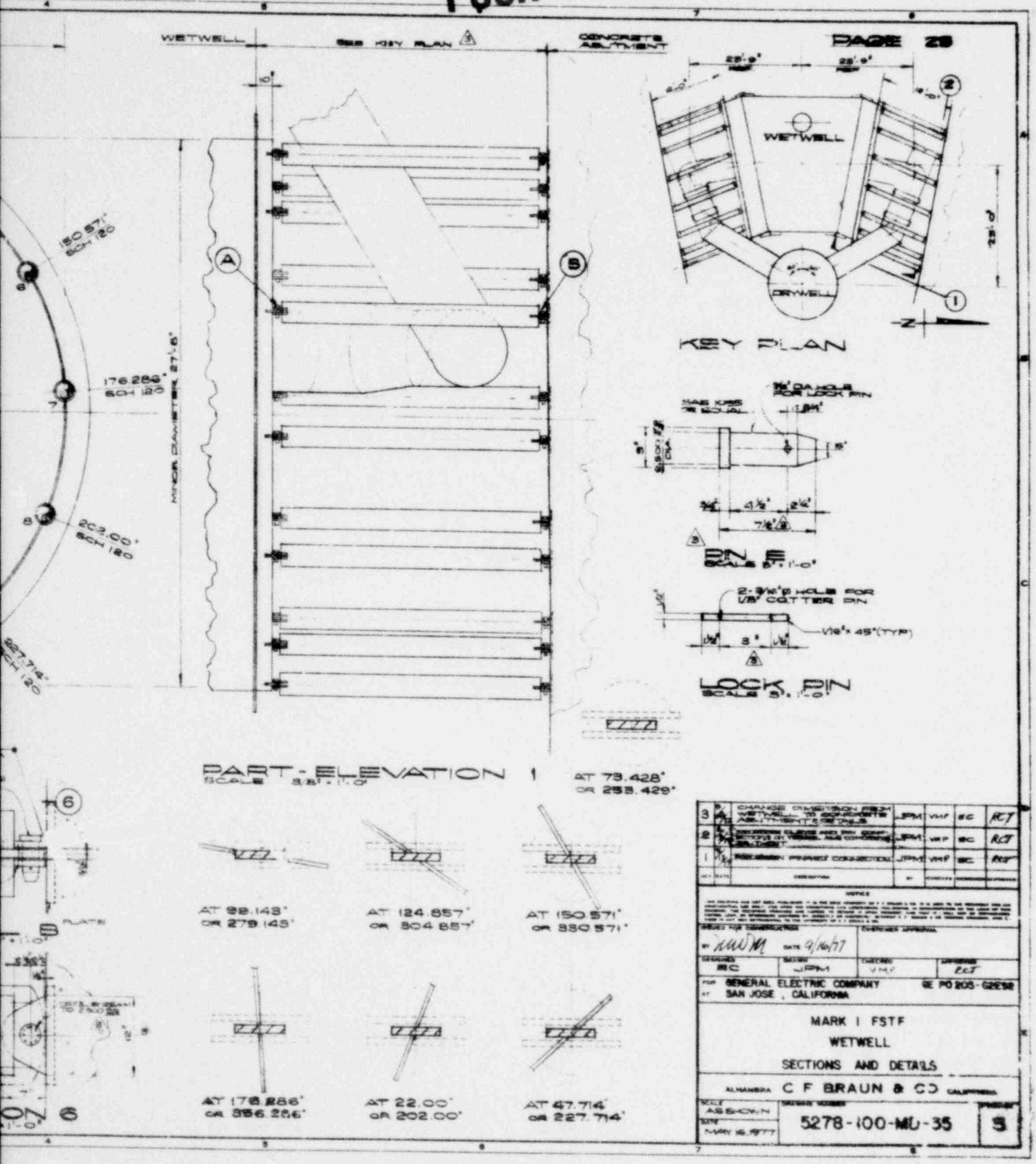

Figure 3.2-6. Mark I FSTF Wetwell Sections and Details-View 2

3.2.6 Vacuum Breakers

The vent header inside the wetwell was designed to accommodate two 18-in. diameter vacuum breakers. For this test series, one 18-in. CPE, Model No. LF 240-331, vacuum breaker valve was installed on the north end of the vent header. The vacuum breaker was installed with instrumentation to continuously monitor the pallet position. This instrumentation failed during the first matrix and was subsequently replaced with limit switches.

To meet the flow scaling requirements in Appendix A, Section 2.7, an orifice plate was installed between the vacuum breaker and the ring header. The orifice plate contained 479 5/8 in. diameter holes for a 58% flow area.

3.3 FACILITY LAYOUT AND PIPING

Figure 3.3-1, a layout of the test facility, shows the relative positions of the three main vessels (V1 - steam supply vessel, V2 - drywell and V3 - wetwell). The figure also shows the position of the reinforced concrete abutment and the restraint pipes relative to the wetwell.

3.3.1 Key System Components

Figure 3.3-2 shows the main components of the FSTF vessels (V1, V2, and V3) and the connecting piping, valves, controls, process instrumentation, and support system connections. The key system components shown on the drawing and their functions are:

a. Recirculation system — provided motive force to circulate water in the blowdown line for liquid breaks to ensure that the fluid in the lines was within 5°F of the steam supply vessel temperature. The system ejector was not needed for steam breaks because the steam traps provided ample circulation.

POOR ORIGINAL

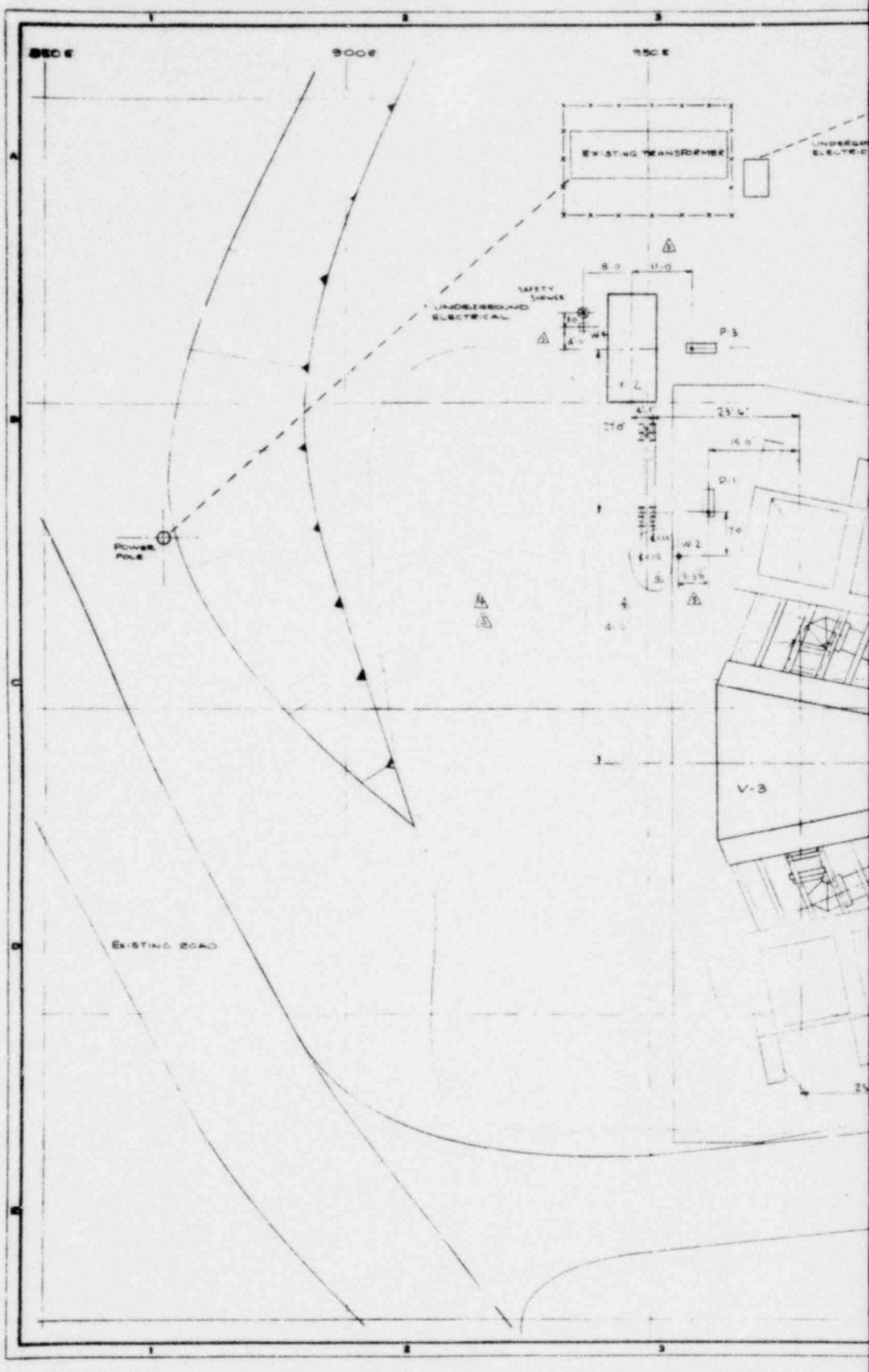

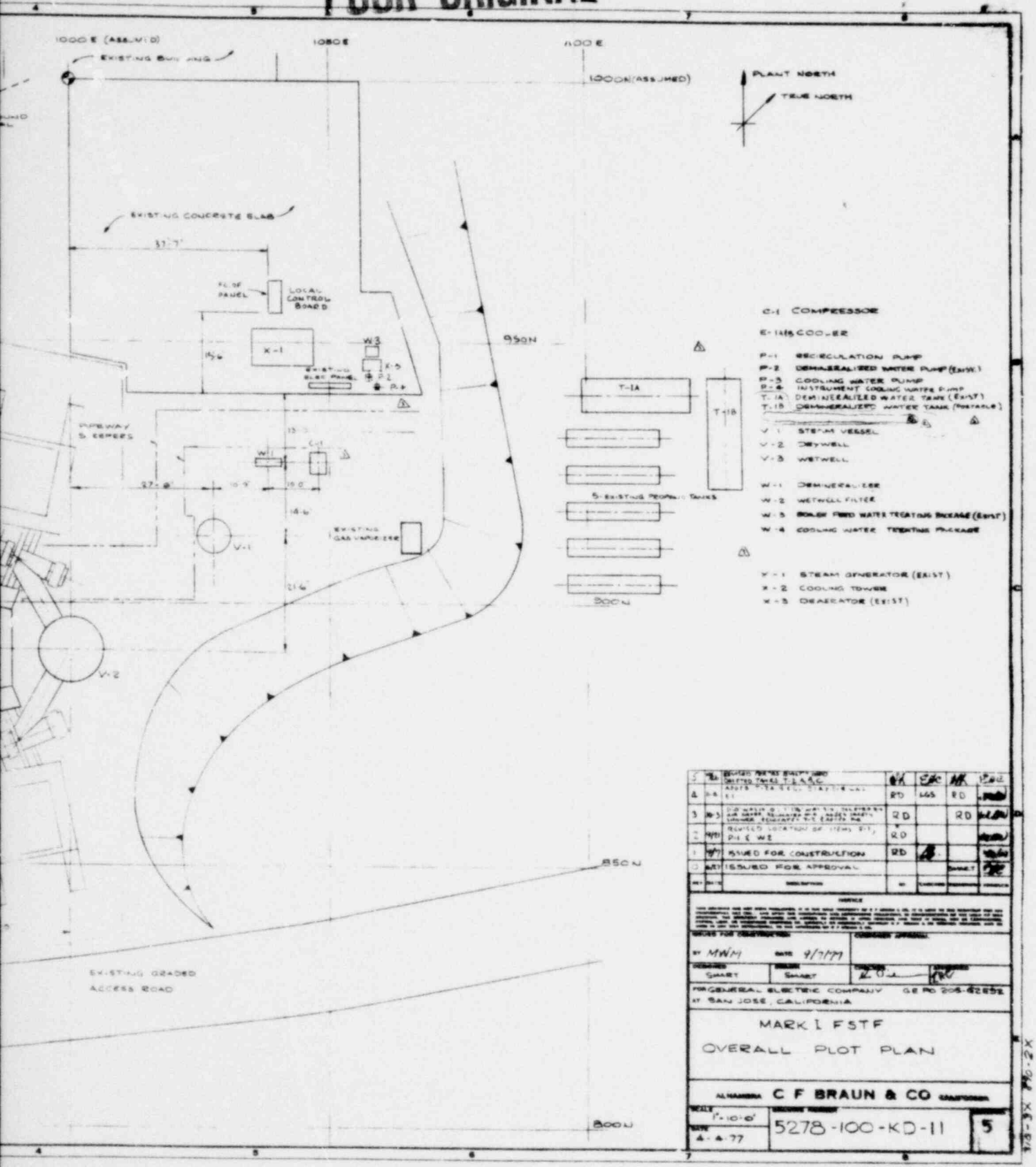

Figure 3.3-1. Mark I FSTF Overall Plot Plan

POOR ORIGINAL

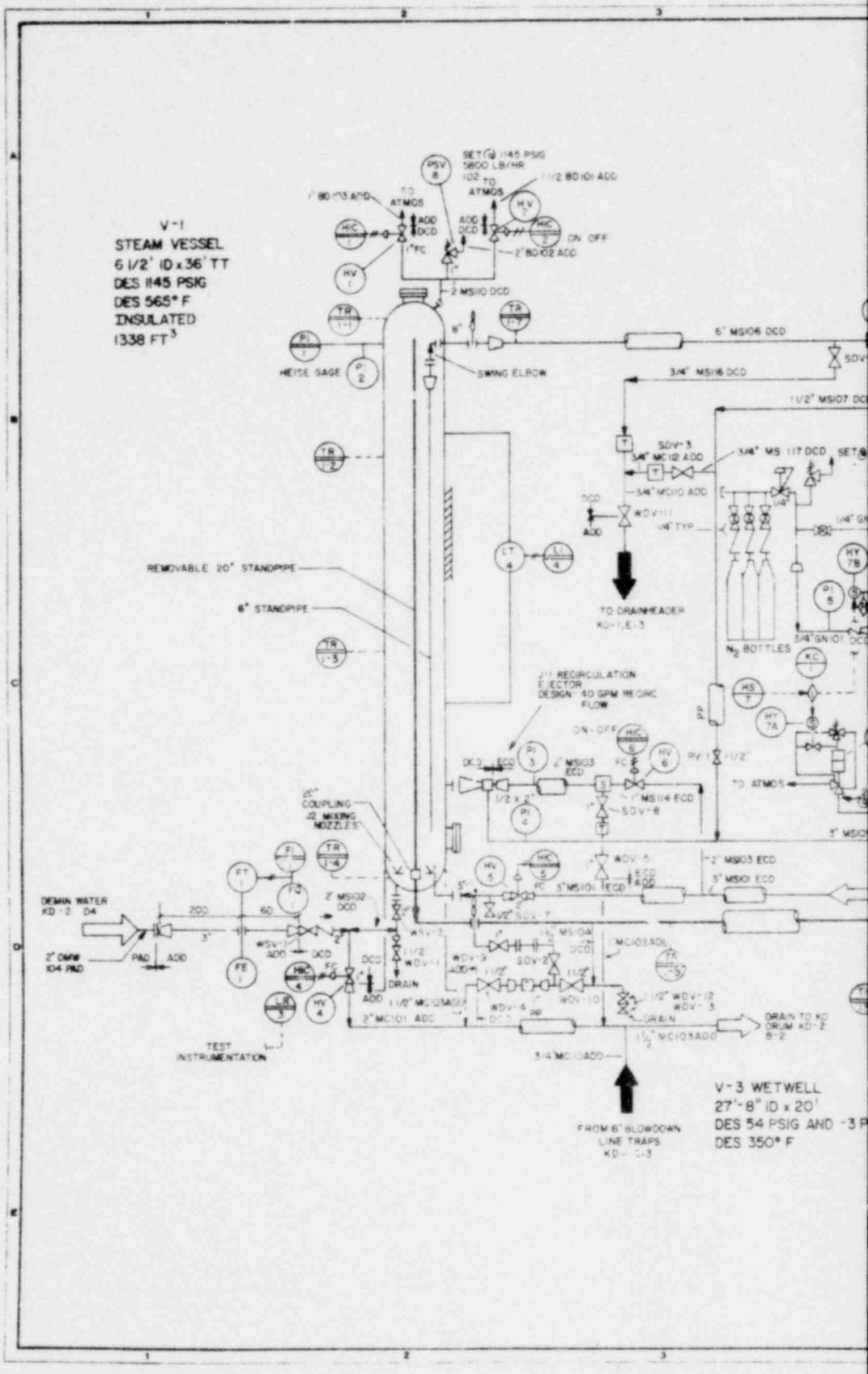

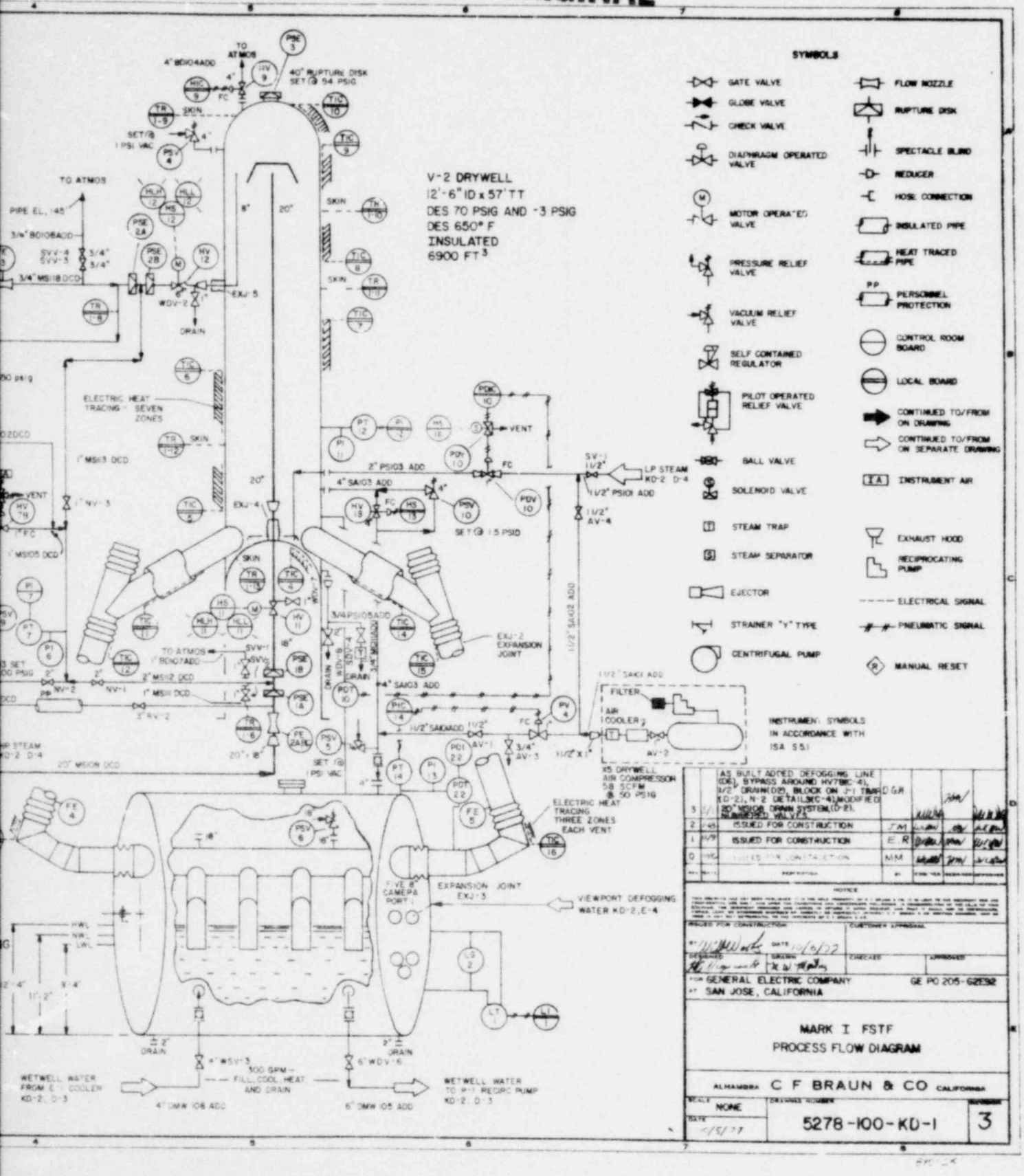

Figure 3.3-2. Mark I FSTF Process Flow Diagram

b. Nitrogen system — provided capability to pressurize the cavity between the double disc rupture discs with N_2 gas and to quickly release the N_2 to initiate the blowdown.

c. Heat tracing — the drywell and the vent lines were provided with an electrical heating grid between the outside surface of the drywell and the insulation. This allowed the drywell and its contents to be heated to a specified temperature before test initiation. The vent lines were heat-traced to minimize the heat loss from the drywell to the vent lines.

d. Air system — provided air to achieve overpressure in the drywell and/or wetwell prior to test initiation.

e. Rupture disc assembly — the double disc rupture disc assembly allowed the steam supply vessel to be pressurized to full operating pressure and the blowdowns to be initiated with a minimum time delay and flow disturbance.

3.3.2 Supporting Components and Systems

The FSTF supporting components/systems are shown in Figure 3.3-3. These systems main functions are:

a. Boiler — to supply the high pressure steam and water to the steam supply vessel.

b. Storage tanks — to feed the boiler and supply makeup water to the wetwell.

c. Recirculation system — to provide recirculation and filtration of the wetwell water during mixing, cleaning and cooling.

d. Cooling tower — used with the recirculation system as the heat sink to cool the wetwell water.

POOR ORIGINAL

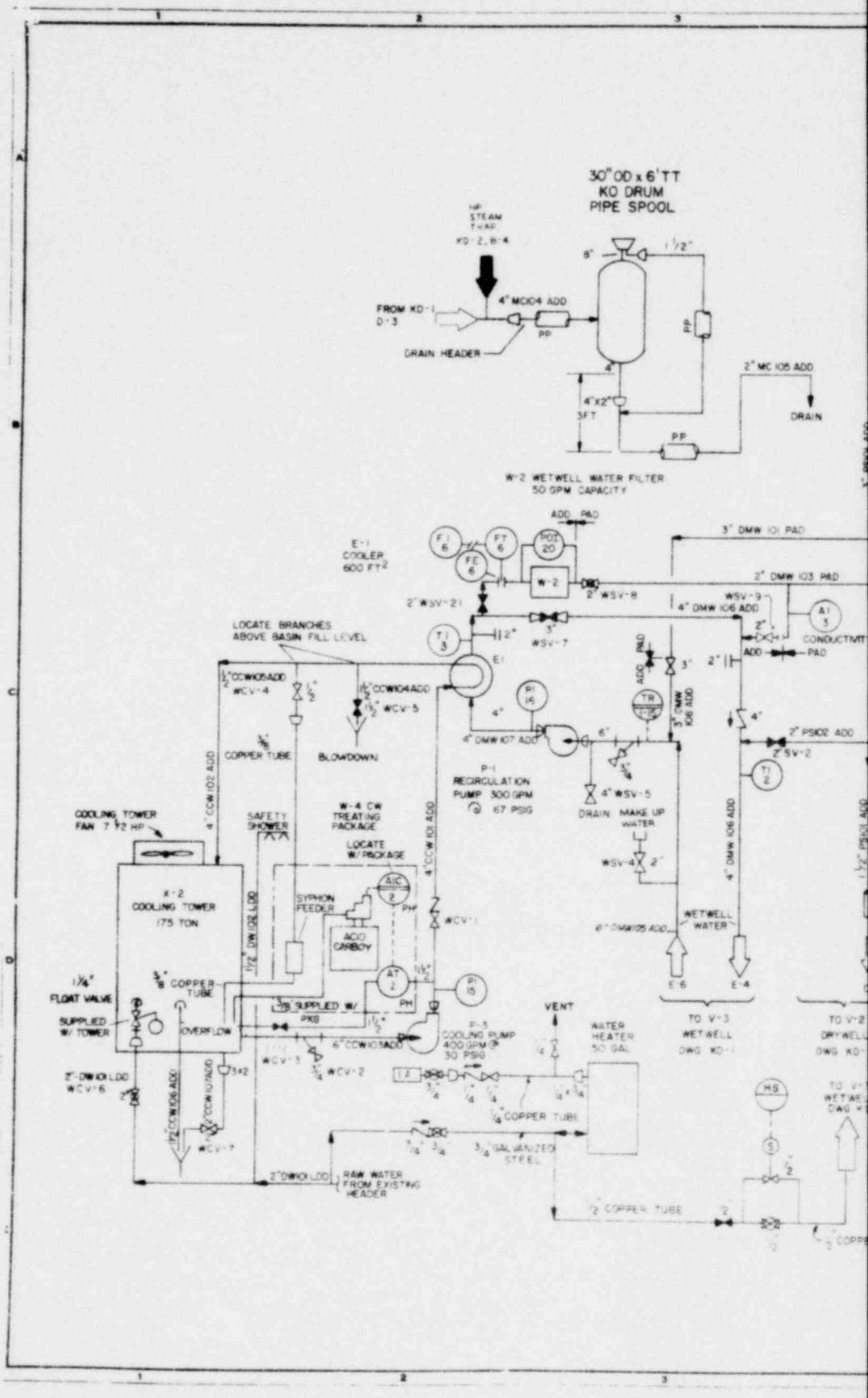

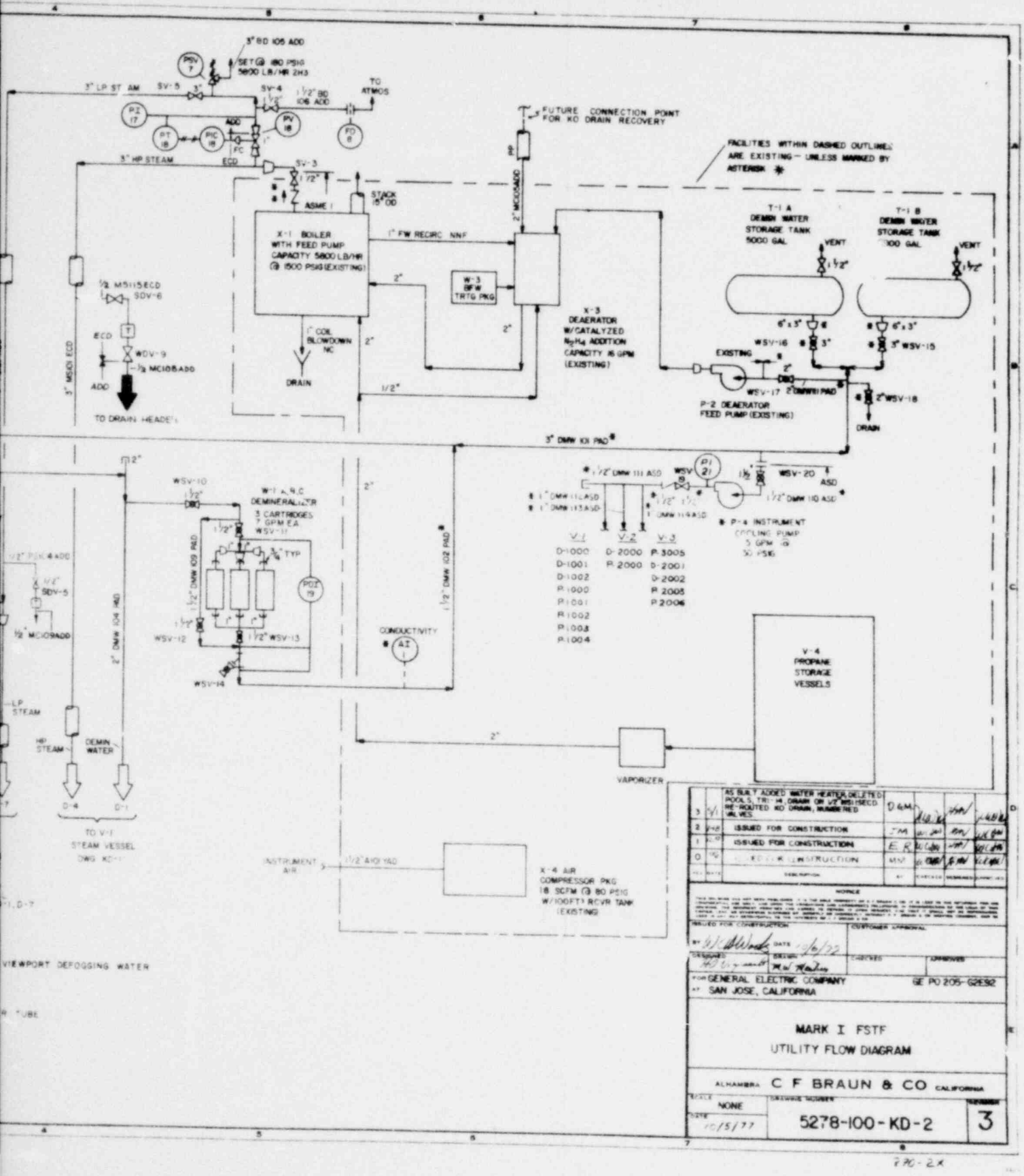

Figure 3.3-3. Mark I Utility Flow Diagram

3.4 INSTRUMENTATION

The Mark I FSTF test instrumentation was designed to provide reliable and accurate measurements of the instantaneous conditions occurring in the FSTF components before, during and following each test blowdown. Each type of sensor is summarized. The following drawings show the test instrumentation locations:

Figure No.	Drawing No.	Instruments Located On
3.4-1	5278-100-ID-1	Wetwell Shell
3.4-2	5278-100-ID-2	Wetwell Section
3.4-3	5278-100-ID-3	Vent Header and Downcomers
3.4-4	5278-100-ID-4	Steam Vessel, Drywell and Misc.
3.4-5	5278-100-ID-12	Vent Header and Support Columns

These drawings show approximately 400 transducer locations. Of the 400 transducer locations, 256 (to match the data recording capability) measurements, considered highest priority, were selected to be recorded. In the course of the test program, several strain gauges and one differential pressure transducer were added to the original instrumentation specified. The strain gages were installed on components added to the facility after it had been constructed (i.e., vent deflector and downcomer bracing). More detailed descriptions of the various transducers are given in the following sections.

The overall system instrument error for each of the transducer types was analyzed. These results for specific conditions are summarized here with the complete analysis presented in Appendix B.

POOR ORIGINAL

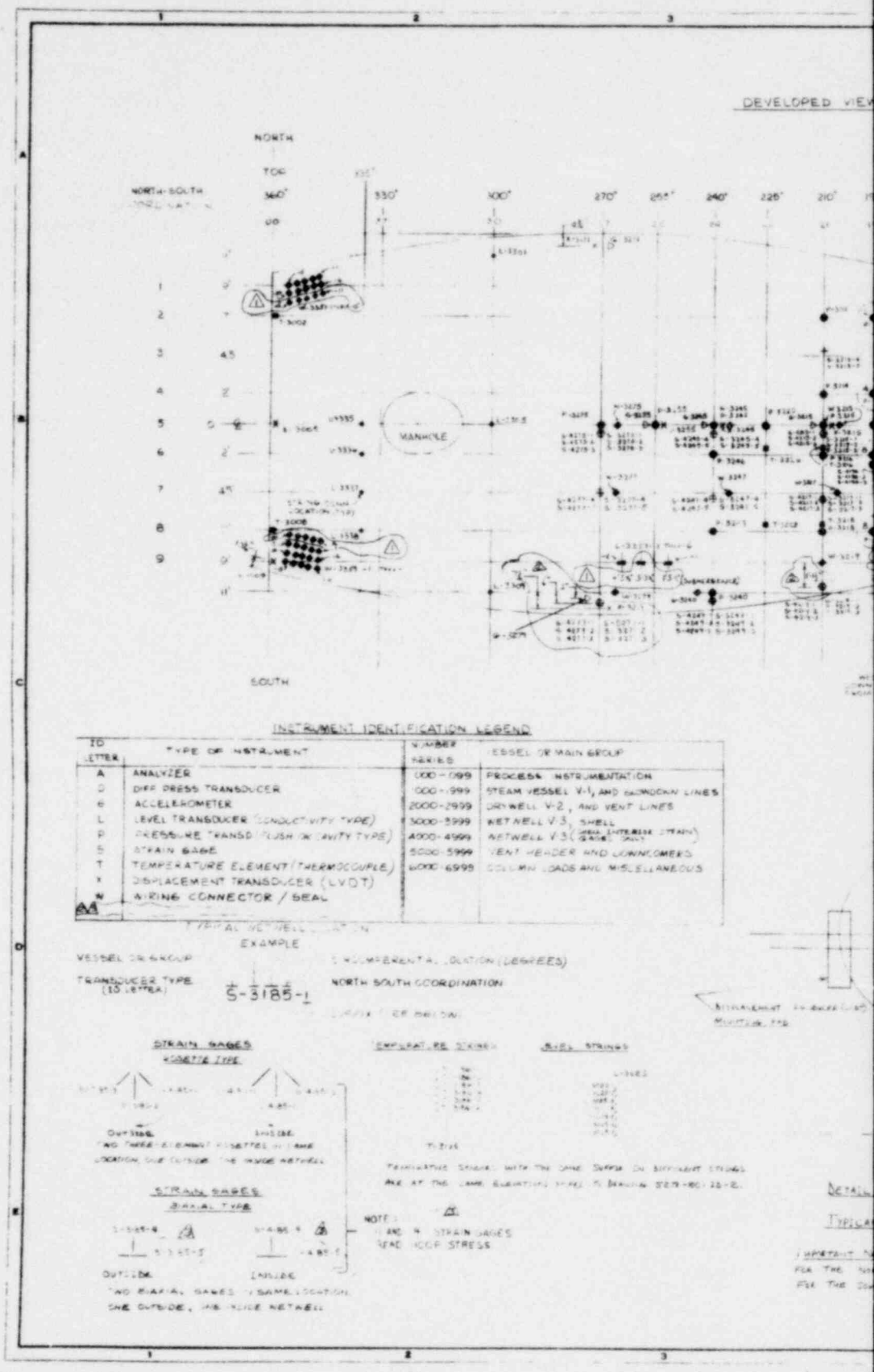

1157 192

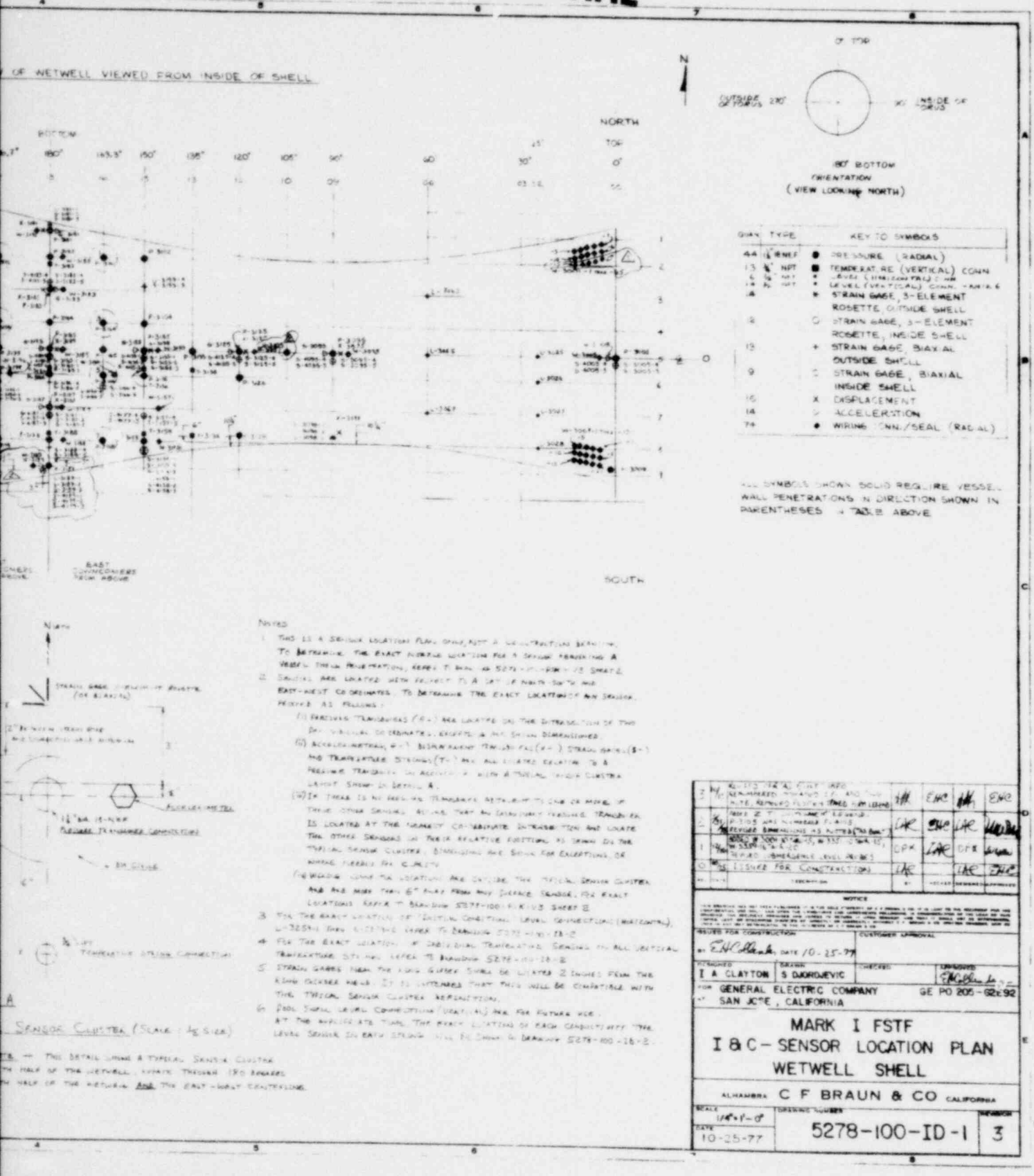

Figure 3.4-1. Mark I FSTF Sensor Location Plan - Wetwell Shell

POOR ORIGINAL

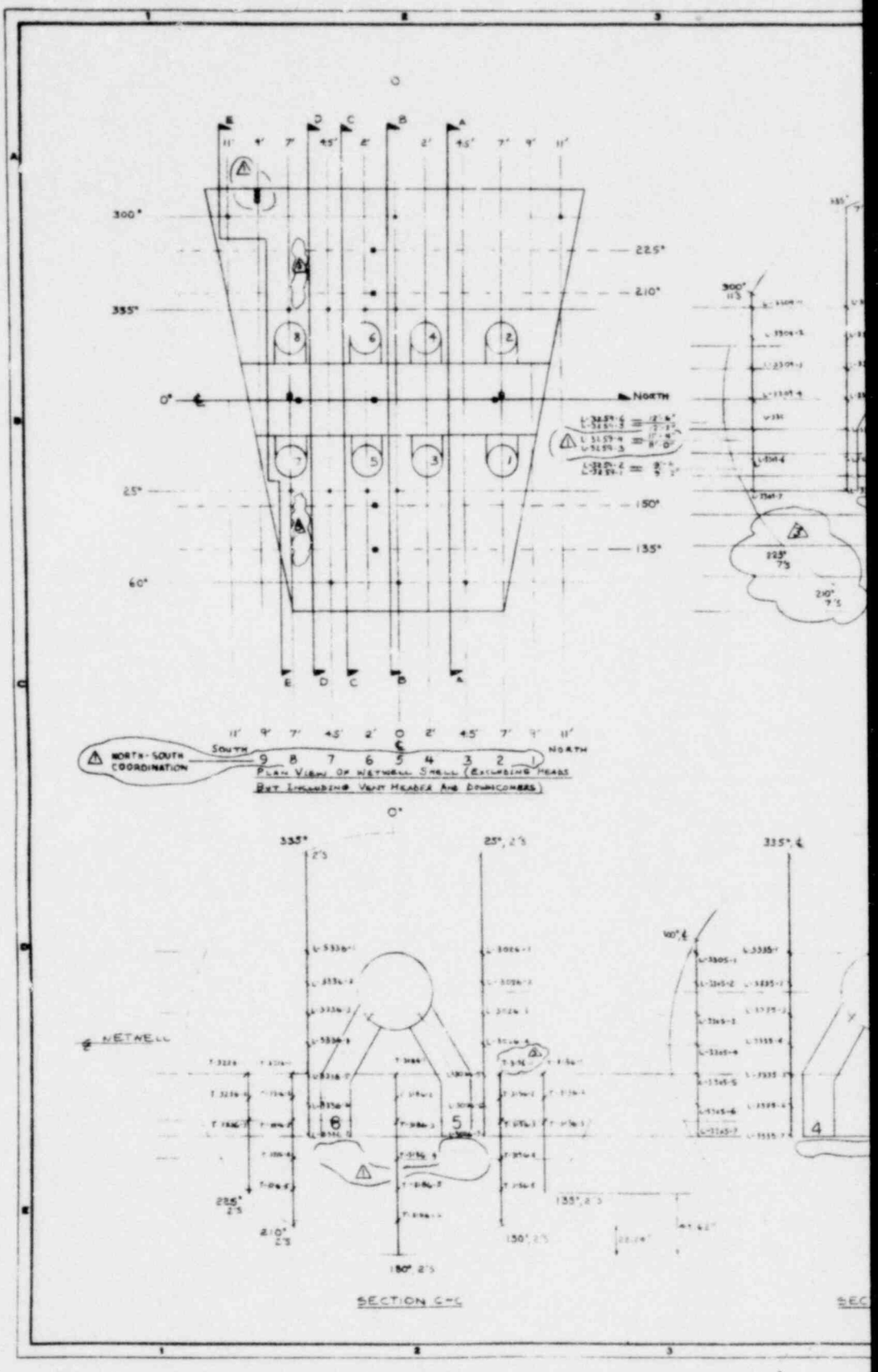

1157 194

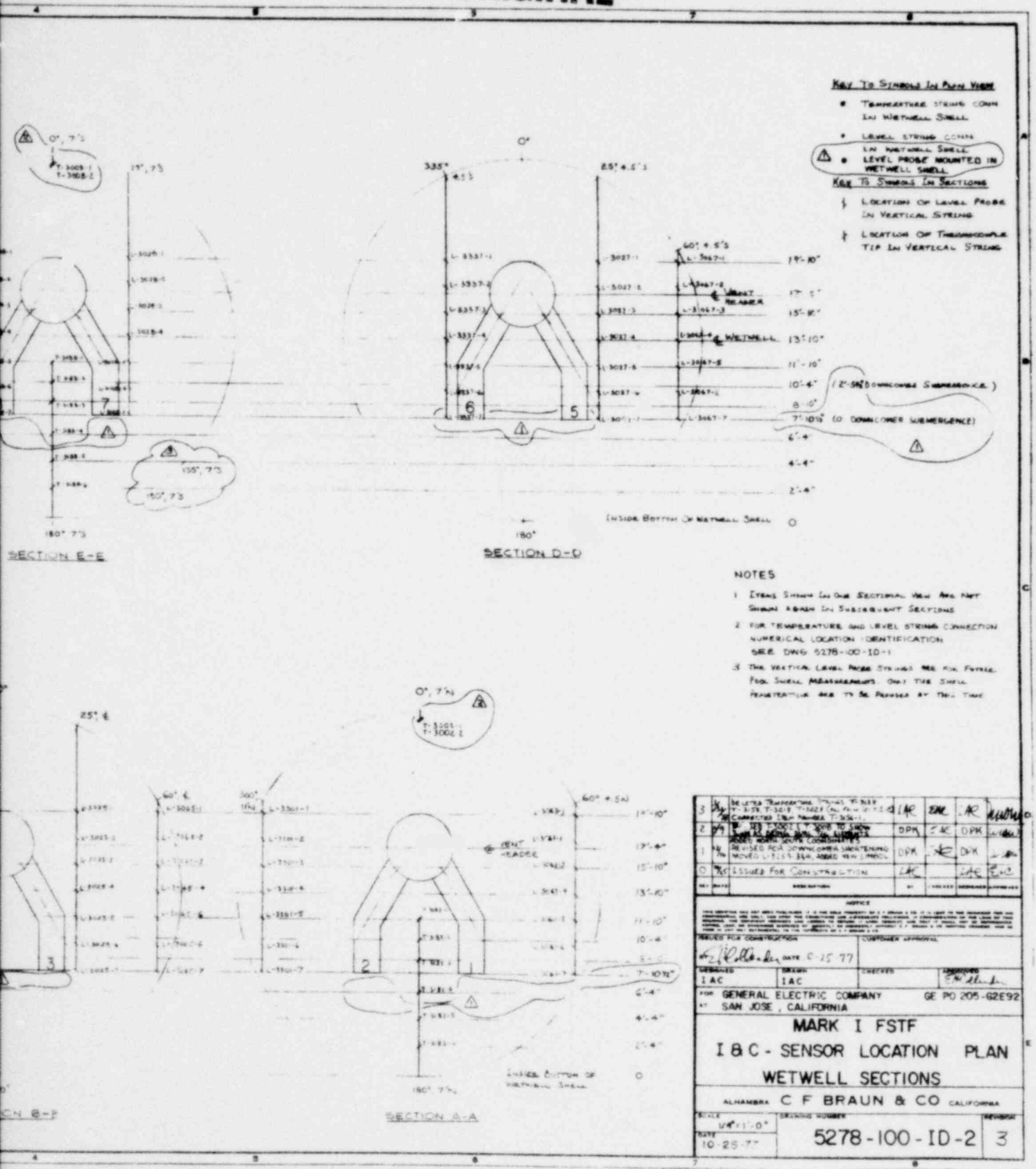

Figure 3.4-2. Mark I FSTF Sensor Location Plan - Wetwell Sections

POOR ORIGINAL

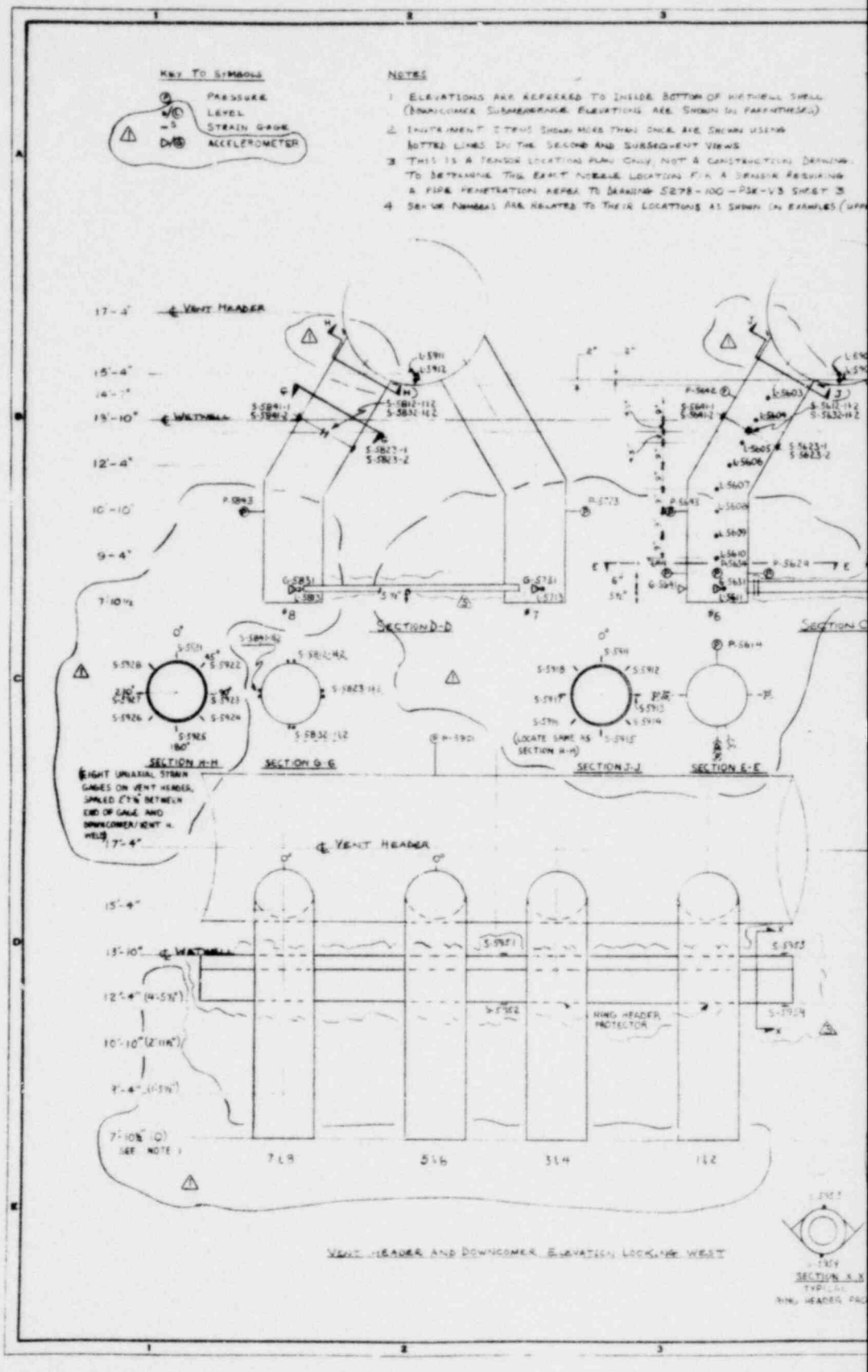

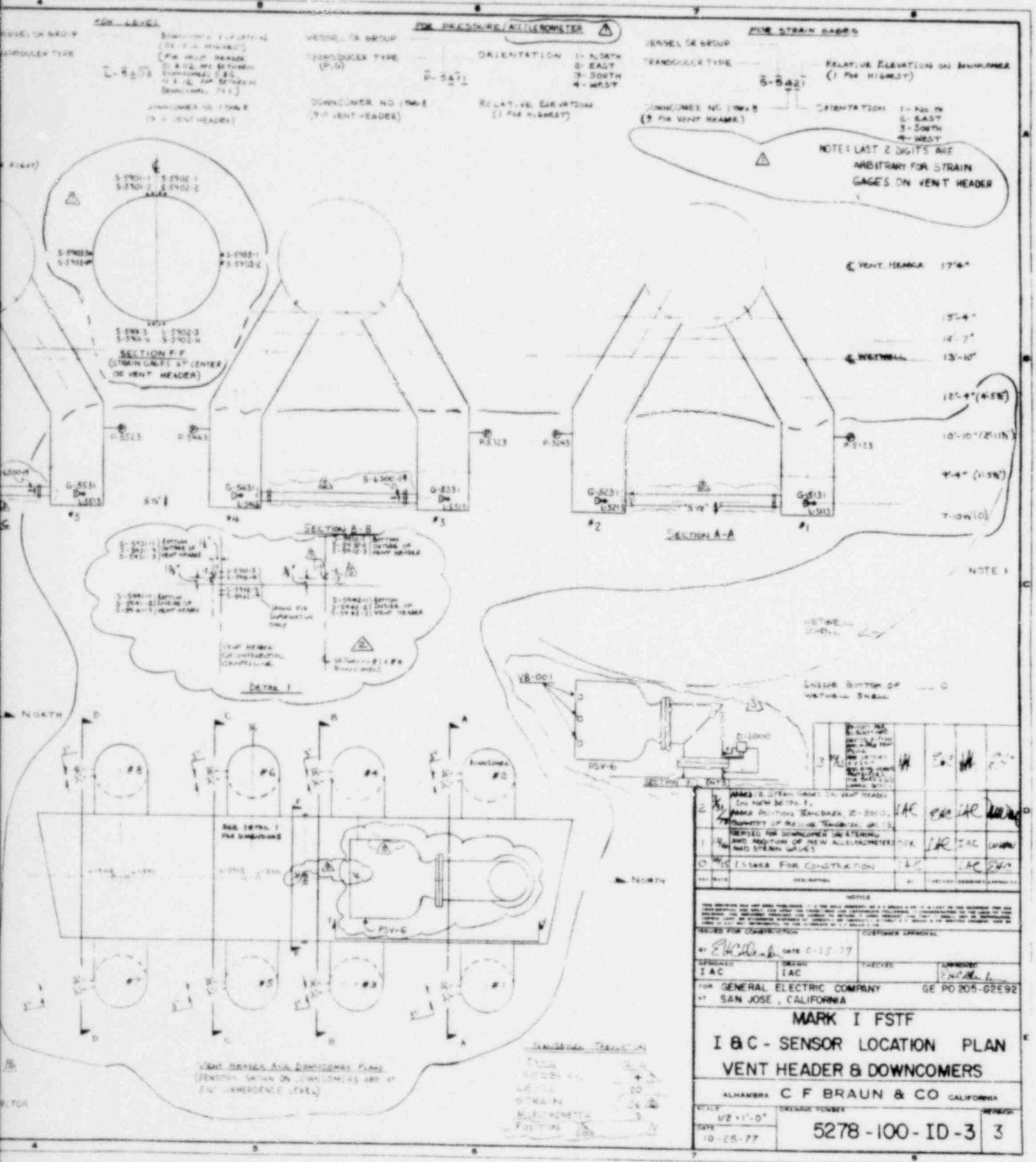

Figure 3.4-3. Mark I FSTF Sensor Location Plan - Vent Header and Downcomers

POOR ORIGINAL

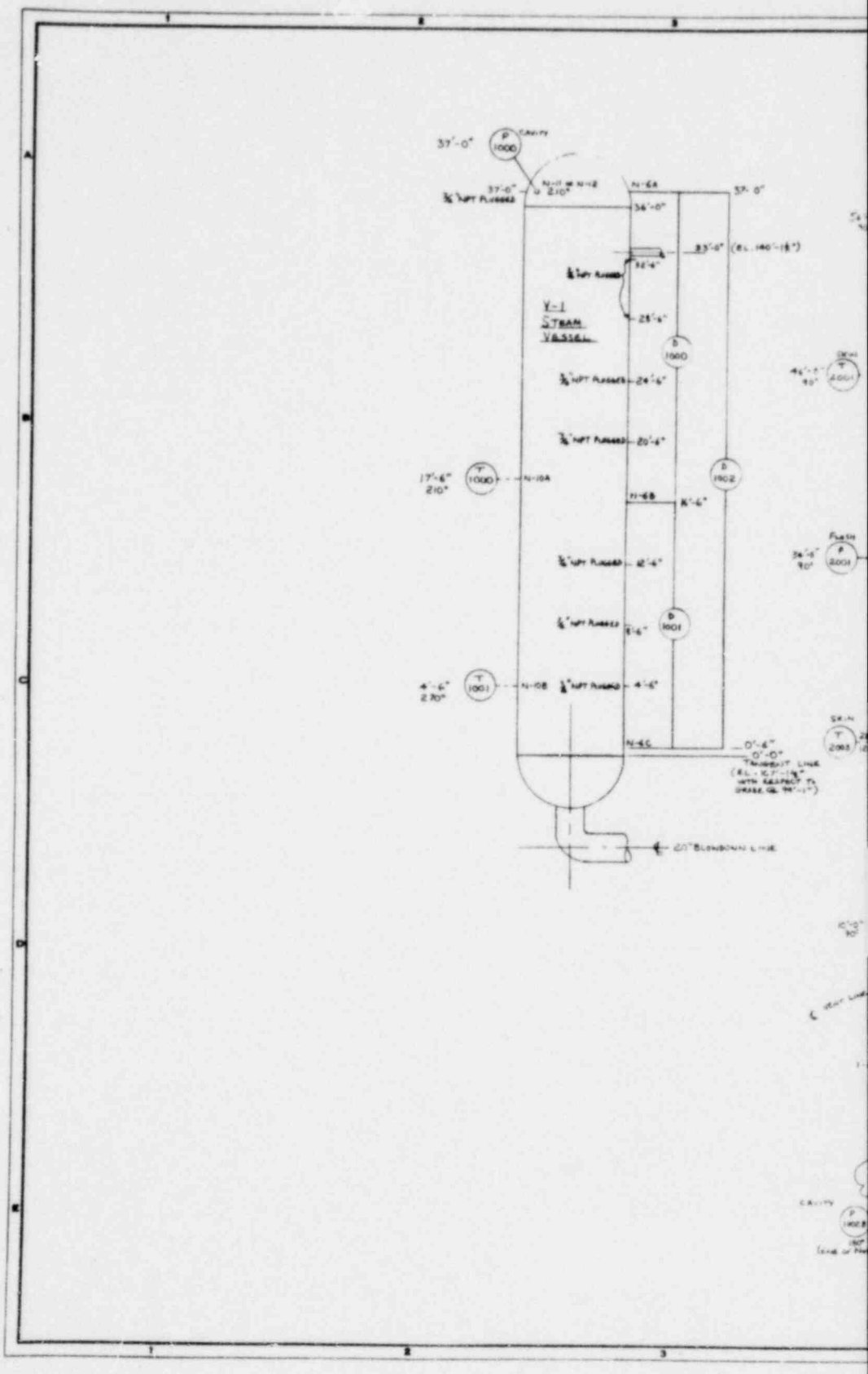

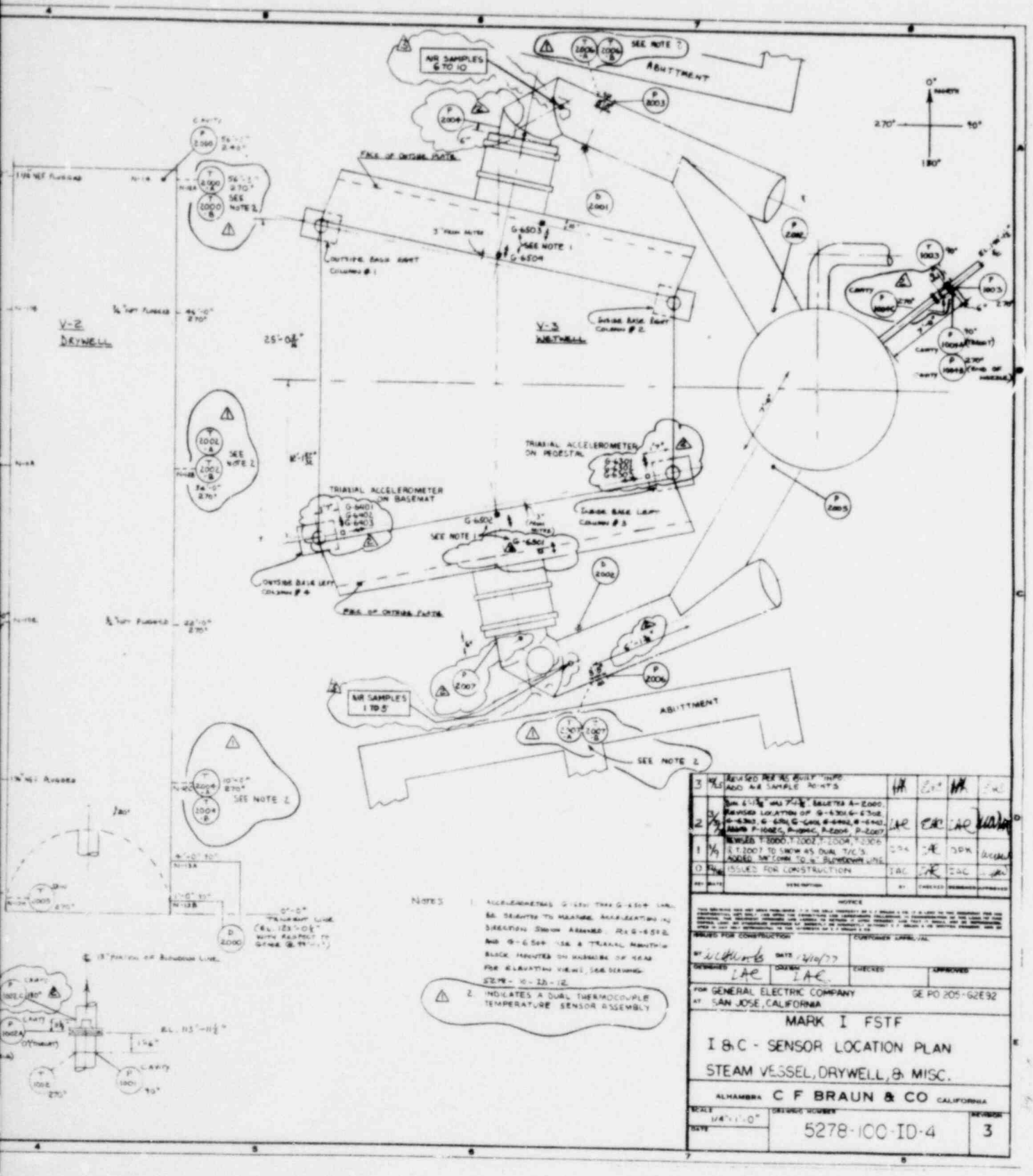

Figure 3.4-4. Mark I FSTF Sensor Location Plan - Steam Vessel, Drywell and Miscellaneous

POOR ORIGINAL

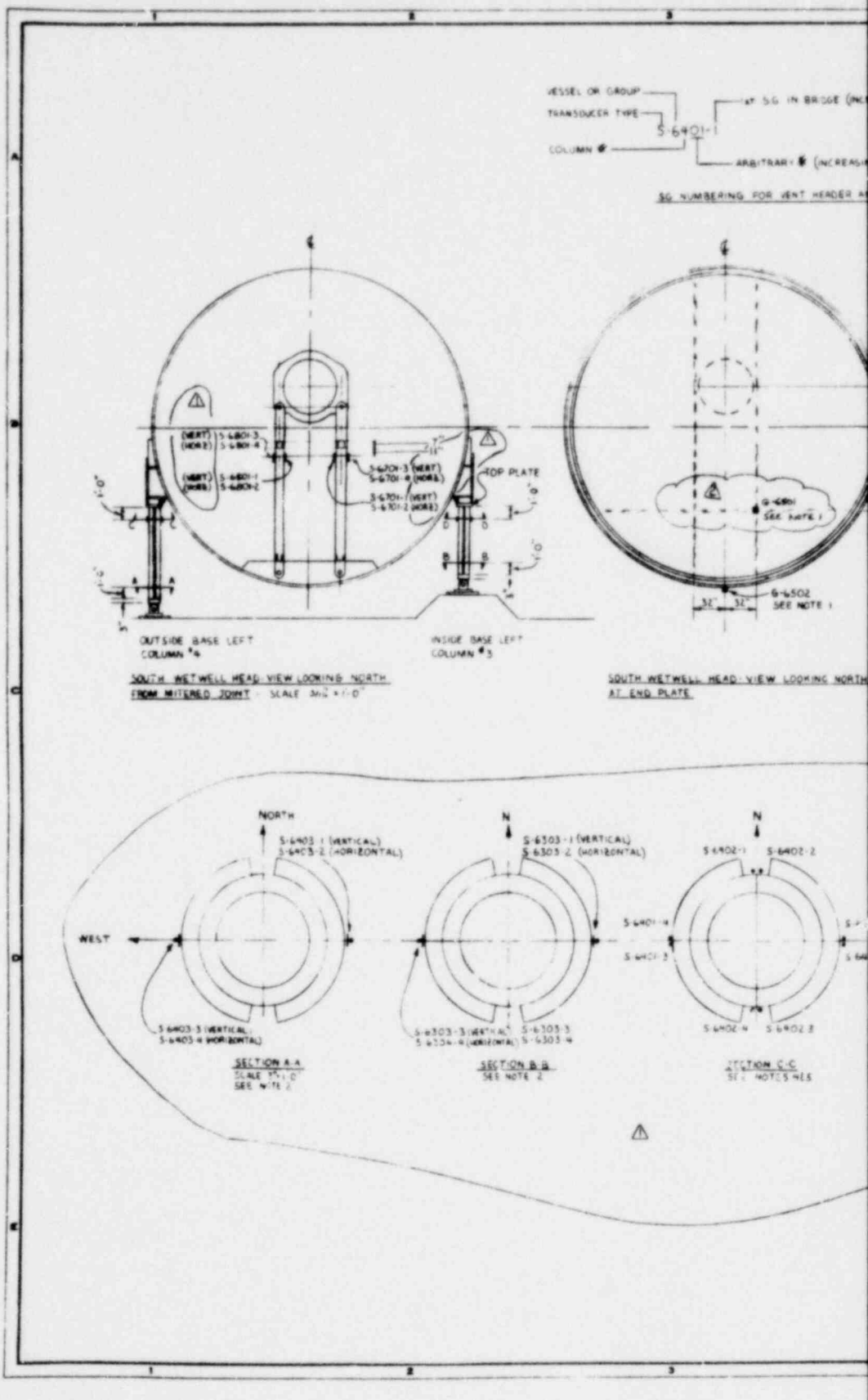

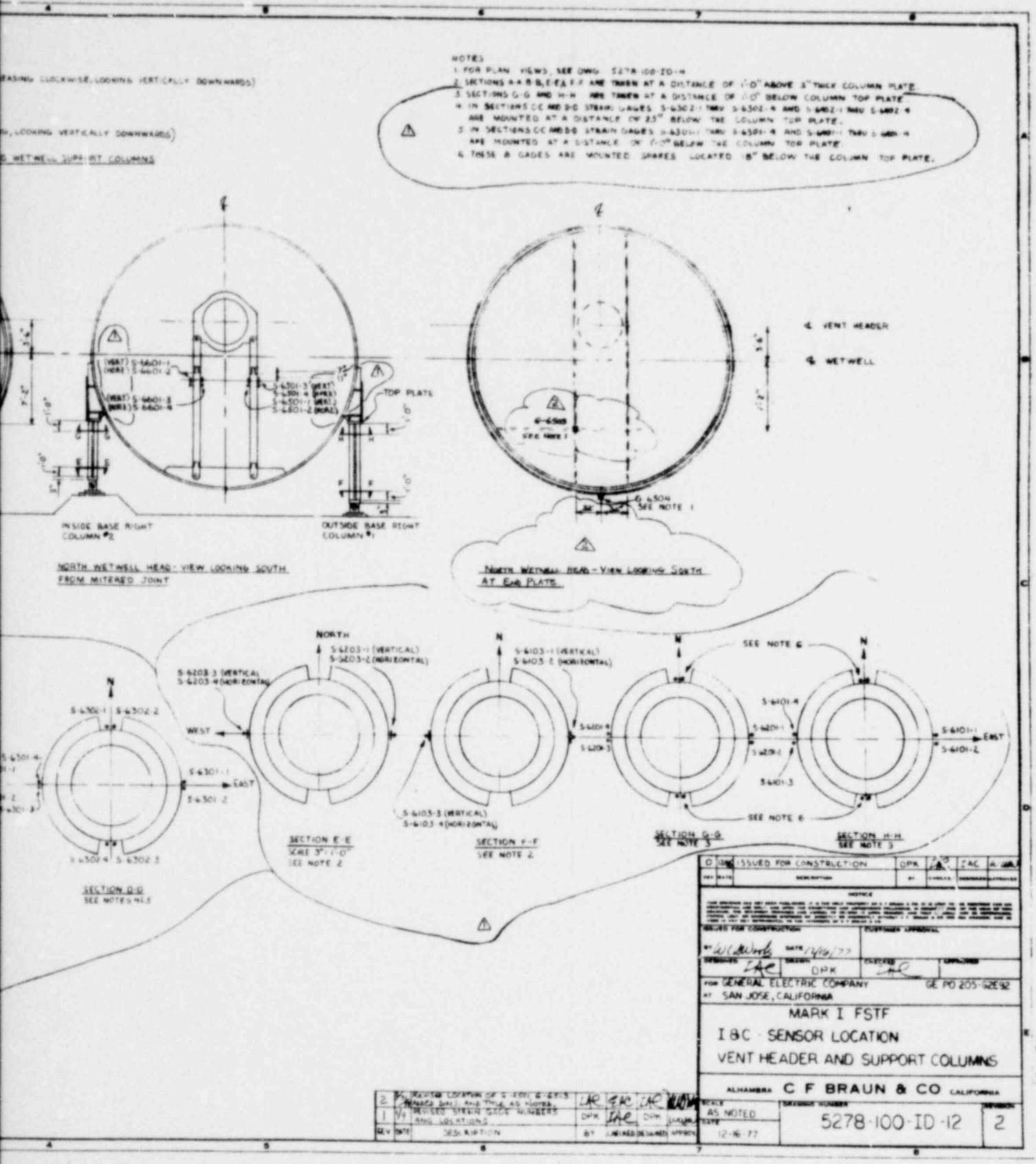

Figure 3.4-5. Mark I FSTF Sensor Location - Vent Header and Support Columns

Transducer Type	Error (%)	ΔT=45°F	ΔT=175°F
Ailtech - Strain	3.4	3.4	12.0
Micro-Measurements - Strain	1.9	3.4	12.0
Endevco - Accelerometer	2.9		
Schaevitz - LVDT	1.5		
Precise Sensor - Pressure	0.8		
Conax - Temperature	0.9		
Rosemount - Differential Pressure	0.6		
Viatran	1.0		

3.4.1 Strain Gauges

Two types of strain gauges were used in the FSTF. All gauges on the interior of the wetwell (V3) were Ailtech, Model No. SG-158-09H-XX-65 1/4 bridge strain gauges. These gauges have hermetically sealed stainless-steel jacketed cables. All gauges on the exterior of the wetwell (V3) were Micro-Measurements, Model No. LWK-06-W250B-350, either 1/4 bridge or 2-element 90° strain gauges. All of the strain gauge locations are shown on Figures 3.4-1, 3.4-3 and 3.4-5.

Three different bridge configurations were used for the strain gauges: one-quarter bridge, bending, and axial. Details of each bridge type are as follows:

a. One-quarter bridge — has only one active arm of the bridge in the field to measure unaxial strain. The rest of the bridge arms were located in the control room. Some of the strain gauges were mounted to form rosettes for determination of principle stresses.

b. Bending — has four active arms in the field and therefore is compensated for local temperature changes. The arms are located two on each side of the member, both in the plane in which bending

is to be measured. The arms are connected in a bridge configuration to add for bending and cancel in tension or compression.

c. Axial – also has four active arms in the field and therefore is temperature compensated. The arms are located two on each side of the component, one parallel and one perpendicular to the plane that has the least expected bending. The arms are connected in a bridge configuration that adds for tension or compression and cancels for bending.

3.4.2 Pressure Transducers

Three types of pressure transducers were used in the FSTF: cavity, flushmount, and differential. The cavity type pressure transducers which were used to measure the system pressure responses of the vessels, the blowdown line and the vent lines were Viatran, Model No. 103, diaphragm, strain gauge type. The pressure ranges of these sensors were: 0 to 1500 psi for the steam supply vessel and blowdown lines; and 0 to 75 psi for the drywell, vent lines and wetwell. The cavity type pressure transducer locations are shown in Figure 3.4-4.

Flushmount pressure transducers were used to measure dynamic pressure within the system. Two types of flushmount sensors with different ranges were used dependent on the location of the measurements. Both flushmount types exhibited temperature sensitivity. Although this did not affect the dynamic response of the instruments, it did prevent a direct comparison to the cavity type instruments. For downcomer and vent header pressures, a Precise Sensor, Model No. 70116-WP-4, pressure transducer was used which had waterproof connections and cables. These sensor locations are shown on Figure 3.4-3. For the wetwell shell, vent lines, and drywell, a Precise Sensor, Model No. 70116-2, pressure transducer was used. These sensor locations are shown on Figures 3.4-1 and 3.4-4.

The differential pressure transducers were used to measure liquid level in the steam supply vessel and the drywell, and fluid flow in the vent lines and

vacuum breaker line. The transducers were all Rosemount, Model No. 1151DP, and were diaphragm capacitance type transducers. Ranges used varied from 0 to 36 in. of water to 0 to 438 in. of water. These sensor locations are shown on Figures 3.4-3 and 3.4-4.

3.4.3 Accelerometers

The accelerometers used were piezoelectric type, Endevco, Model No. 7707-200, located on the wetwell shell as shown on Figure 3.4-1, the endcaps and basemats as shown on Figure 3.4-4, and the downcomers as shown on Figure 3.4-3. The accelerometers mounted on the downcomers and their cables were protected from water damage by installing them in nitrogen pressurized housings and tubing.

3.4.4 LVDTs

Schaevitz Model No. 2000HCD Linear Variable Displacement Transducers (LVDT) was used to measure displacements. They were mounted in specially designed brackets to provide mechanical support for the transducer. LVDTs measure radial displacements of the wetwell shell at the locations shown in Figure 3.4-1. These transducers have positive output for displacements directed radially away from the center of the wetwell.

3.4.5 Thermocouples

The thermocouples used for temperature measurement in the FSTF were manufactured by Conax and were Type E (chromel-constantan) metal sheath with an outside diameter of 0.125 in. Thermocouple tips were reduced to either 0.093 in. or 0.010 in. and were grounded. Thermocouple locations for the steam supply vessel, blowdown line, drywell, and vent lines are shown on Figure 3.4-4. Wetwell thermocouple locations are shown on Figure 3.4-2.

3.4.6 Level Probes

The probes used in the FSTF to monitor water level were developed and manufactured by General Electric. The probes indicated the presence or absence of water by using the difference in conductivity of the water and gas (air or steam). These probes were installed on the wetwell shell as shown on Figure 3.4-1, and in the ring header and downcomers as shown on Figure 3.4-3. The net variation that occurred in the level probe voltage output resulting from changes in temperature and water quality is as follows:

Fluid Monitored	Output (Volts)
Air or steam	6.8 - 7.2
Water	3.5 - 5.5

3.4.7 Miscellaneous

Two additional channels of instrumentation were used during the test program. One channel (CT-001) was used to indicate both test initiation time and high speed camera start time. Test initiation time was shown by a positive 2.5 volt increase, and high speed camera start time by a 0.5 volt decrease. This instrumentation was connected for tests M4 through M10.

The other channel (VB-001) was used to supply vacuum breaker pallet position indication. For test M1, the vacuum breaker pallet position was measured continuously with a potentiometer with the output indicating degrees of rotation directly. Because this position indicator failed during M1, for subsequent tests three position limit switches were used. The limit switches were connected together electrically in order to monitor the pallet position with one data acquisition channel. The angular positions of the pallet corresponding to the switches and the output of the switch circuit are as follows:

Degrees From Closed	VB-001 Output (Volts)
0°	∿0.5
>1°	∿4.6
3°	∿9.0
60°	∿6.8

This measurement was available for all tests except test M10 for which the vacuum breaker was removed from the vent header.

3.4.8 Signal Amplification and Conditioning

The Neff's signal processing system used consists of low pass filters, preamplifiers, and signal conditioning. A Neff Series 100 preamplifier system has a capacity for up to 256 inputs. Accelerometers, differential pressure transducers, LVDTs and level probes used high level preamps (inputs up to 10 volts). Pressure transducers, thermocouples, and strain gauges used low level preamps (inputs up to 1 volt). With each preamp, a low pass filter was installed. The cavity pressure transducers, differential pressure transducers and thermocouples were filtered at 30 Hz. Flushmount pressure transducers, accelerometers, LVDTs, level probes, and strain gauges were filtered at 300 Hz. To configure each channel for a particular transducer type, a Neff Series 300 Signal Conditioner was used. The signal conditioning system provide the excitation supply, shunt calibration circuit (if required), voltage substitution circuit, and a mode card to configure the circuit for operation with a particular type of transducer. Mode cards were available for strain gauge circuits (for one, two or four active arms) and thermocouples.

The Neff system was attached to the transducers by 1000 ft of eight conductor-shielded cable. The cables ran from the control room to junction boxes in the field next to the FSTF. Seven junction boxes were located at the test facility. These junction boxes housed the local signal conditioners and patch panels for the transducer cable connections.

The Neff system was connected to the Data Acquisition System (DAS) through a patchboard, permitting the sequencing of the transducers into the DAS. It also permitted resequencing transducer inputs to maintain transducer groupings (i.e., all strain gauges together) after adding or deleting transducers.

It should be noted that the components of the whole instrumentation system and the techniques used to control the system had noise levels of less than ±2.5 mV which represents one-bit resolution on the DAS.

3.4.9 Air Samplers

The air samplers used in the FSTF were based on a design developed by General Electric. Five samples were taken in each vent line during a test. Timers initiated a time delay relay on a sample chamber on each vent line. The timers were set at predetermined times and the time delay relay energized an isolation valve on each sample chamber for a set time duration. The sample chambers were copper tubing with internal fins and were forced convection cooled to effectively increase the gas sample sampling volume. Before testing, each sample chamber was evacuated to a vacuum of 2 mm Hg with a vacuum pump. After testing, each sample chamber was analyzed to determine the mass of air and steam collected. The location of the sample probe on each vent line is shown on Figure 3.4-4.

A calibration test was performed on the air sample system to determine its operating characteristics when sampling a "zero air" steam environment. These results had a positive 0.015% air offset and a standard deviation of 0.014% air.

3.5 DATA ACQUISITION SYSTEM

The Data Acquisition System (DAS) was housed in a remotely located control room used to initiate testing and record test data. The DAS includes the components required to monitor the test instrumentation, process the signals into the required format, record the signals and provide system control. A simplified block diagram of the DAS is shown in Figure 3.5-1.

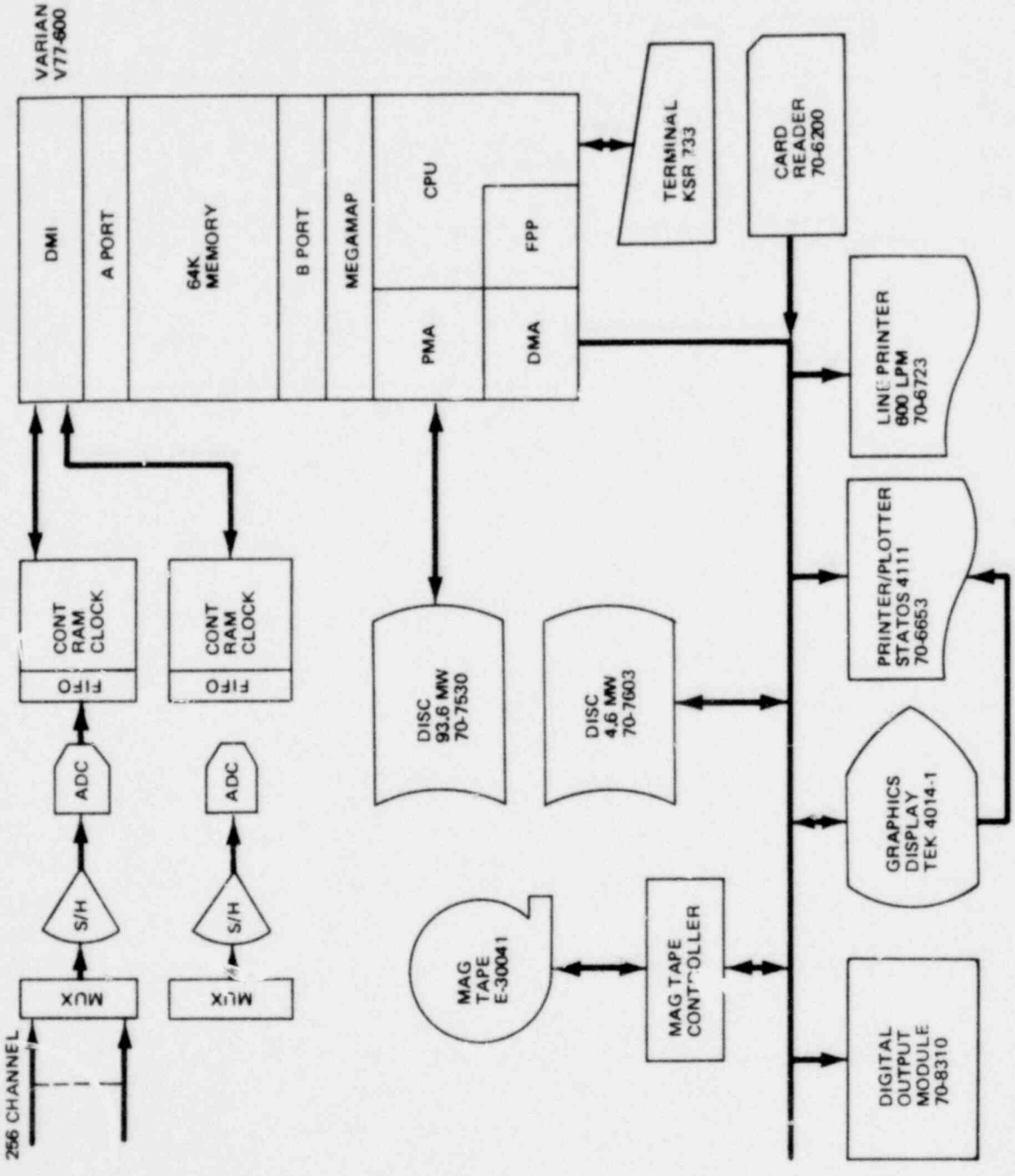

Figure 3.5-1. FSTF DAS System

1157 208

3.5.1 Major Components

Major components of the DAS shown in Figure 3.5-2, include those in the transfer path during high speed acquisition. The Data Acquisition System has the following characteristics:

- Up to 256 inputs
- Plus or minus 10V input
- 250,000 samples/second (977 samples/second/channel) for up to 300 seconds
- 13-bit resolution (12 bits plus sign bit)

A brief description of these major components and their functions follows:

A/D Converter, Phoenix Data, Inc., Model No. 6913 – Two systems were installed although only one system was used at a time. Each A/D converter has three parts: the multiplexer, the sample/hold amplifier, and the analog-to-digital converter. The multiplexer selects an analog signal, and the sample/hold amplifier holds the voltage level of the selected signal while the A/D converter converts the analog signal to a digital representation of the voltage level. During the first three tests of the program, a malfunction occurred in the analog-to-digital signal conversion resulting in data "banding", which was caused by signals overlapping as they were being converted. This problem was minimized by reducing the sample speed for Tests 2 and 3. It was then corrected in the subsequent tests.

Controller, Datacom, Inc., Model No. WRS061310 – The controller provides a high speed, programmable interface between the A/D converter and the computer. Its basic functions are to 1) transfer data from the A/D converter to computer, 2) provide sequencing of the A/D converter channels, 3) control the conversion rate, and 4) provide a buffer to absorb delays in gaining access to the computer.

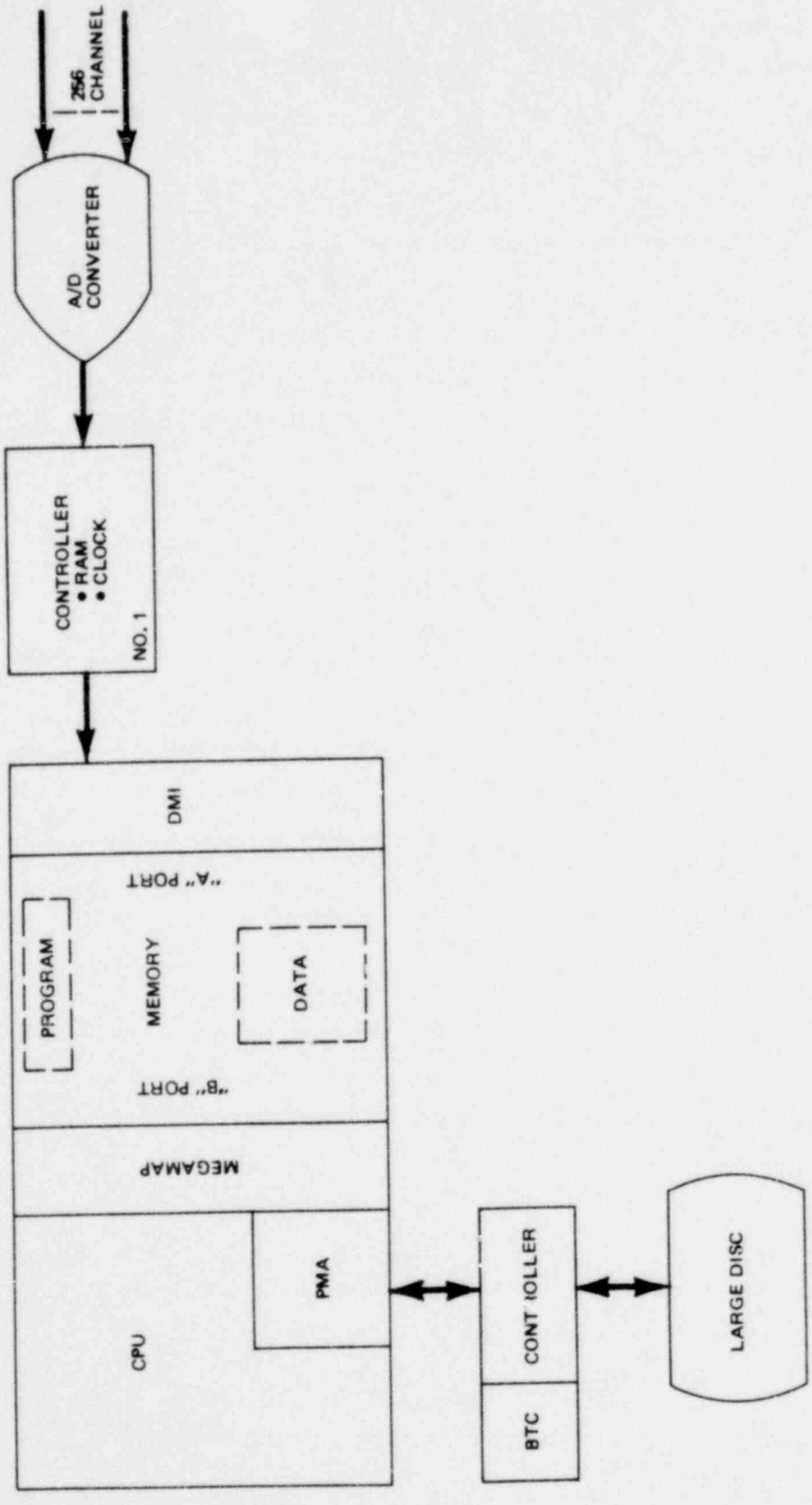

Figure 3.5-2. High Speed Data Path

1157 210

Computer, Varian, Model No. V77-600 – This computer is used to control and interface with the peripherals and data acquisition equipment. The computer also controls the execution of all the software programs and is central to the entire Data Acquisition System. The computer memory is also used as temporary storage during data acquisition. The A/D converter fills one group of memory locations while another group is being read out on the large disc for storage.

Large Disc Unit, Varian, Model No. 70-7530 – The large disc supplies the storage capability for data as it is acquired during the test run. It has a storage capacity of about 100 million words.

3.5.2 Minor Components

The minor components of the DAS and their primary functions are:

Terminal, Texas Instruments, Model No. KSR733 – Is operating system console for instructing computer.

Disc Unit, Varian, Model No. 70-7603 – Stores operating system software for the computer.

Card Reader, Varian, Model No. 70-6200 – Provides program loading and run definition input.

Line Printer, Varian, Model No. 70-6723 – Supplies program listings and data printout.

Magnetic Tape Unit, Varian, Model No. E-3004 – Records data from large disc for long term storage and copies tapes.

Graphics Terminal, Tektronix, Model No. 4104-1 – Is used for test operator communication and for display of data prior to plotting.

Printer/Plotter, Varian, Model No. 4111 – Is used for plotting test results and also serves as a line printer.

3.5.3 DAS Software

The DAS software was designed to permit the operator to perform the functions required to verify the initial conditions, obtain the data and retain the test data. It consists of a series of separate programs that use and/or provide output and input to each other. These programs and their functions are:

SETUP – Provide proper inputs and information before data acquisition.

ACQUIRE – Acquire raw data from the A/D converters and write to the large disc.

QPLOT – Provide plotting capability of multiplexed data stored on large disc.

RELIVE – Copy data from large disc to tape or tape to disc.

DEMUX – Demultiplexer data recorded on large disc (separated by channel identification)

LIST – Provide listing capability for data stored on large disc prior to demultiplexing.

CALIB – Perform instrumentation calibrations and data acquisitions software quality assurance tests.

3.6 MOVIES

The wetwell was constructed with five viewports in the northend plate, two above water and three below water, as shown in Figure 3.6-1. Viewports 2 and 4 were used to observe and photograph the simulated LOCA. The following two sections describe the equipment used to obtain FSTF movies.

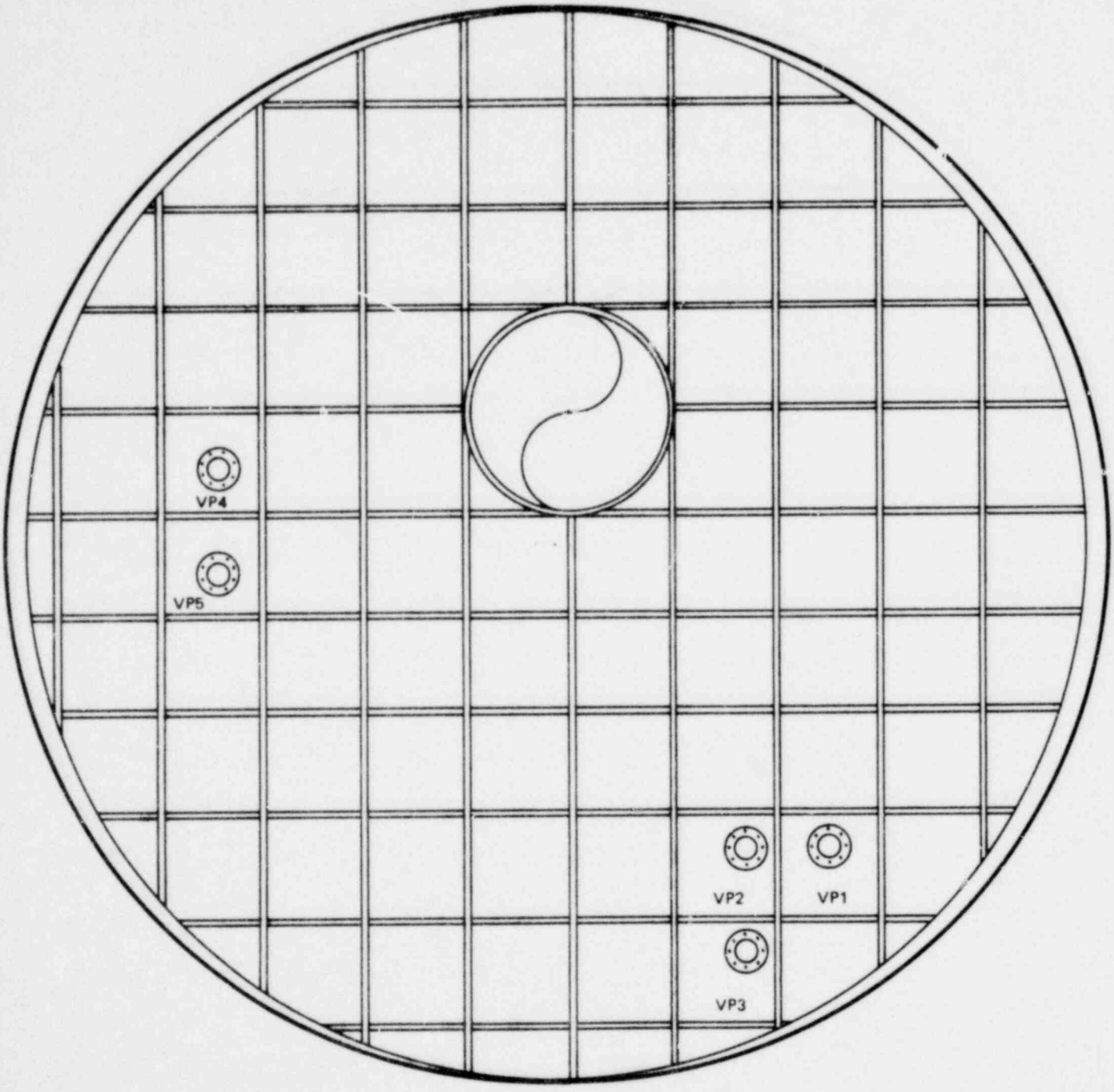

Figure 3.6-1. End Closure Viewports

3.6.1 Above-Water Photography

An Aeroflex Model 50 camera recorded events above the water surface. The camera used Video News Film (ASA 500) and its frame rate was 50 frames/sec. The field of view consisted of downcomers 3, 5 and 7; a portion of the ring header; the south vessel wall and the water surface. Marks were painted at 6-in. vertical intervals on the downcomers and on the south wall to provide references for quantitative measurement of post-LOCA wave motion. Four 200 watt lamps positioned high on the north vessel head provided lighting for the downcomers and south interior wall. The above-water camera was initiated just before the blowdown and operated over the entire test interval (320 sec.)

3.6.2 Below-Water Photography

A Redlake 400-ft Locam camera filmed the below-water events using Video News Film (ASA 500) at 400 frames/sec. The field of view consisted of the bottom of downcomers 2, 4 and possibly 6, if pool water was clear. Ten one-KW lamps located on the north head and below the downcomers provided lighting. The film recorded 40 seconds of test time. Filming was initiated in the control room at a time selected before testing. Timing marks were imprinted on the edge of the film and the DAS recorded camera start time such that film data could be correlated with the DAS recorded data.

4. TEST OPERATIONS

4.1 TEST PROCEDURES

Detailed test procedures were required for the operation of the FSTF test program. The major areas covered were facility preparation, facility operation, data reduction and analysis, instrumentation calibration, and instrumentation installation. All the key operations of the FSTF were accomplished and controlled by using approved procedures. Changes to approved procedures were accomplished by using a Notice of Deviation (NOD) procedure.

4.2 QUALITY ASSURANCE

Quality Assurance procedures were also required for the operation of the FSTF test program. A Quality Assurance program was developed and maintained which was consistent with the requirements of NRC regulations including 10 CFR, Part 50A, Appendix B or American National Standard (ANSI) N45.2 (1971). A brief description of the information exchanges, checks, and controls used to conduct a test in the FSTF is as follows:

a. Complete Inventory Checklist to ensure required materials on hand for conduct of test.

b. Prepare Test Facility Initial Condition List and issue following approval.

c. Complete facility alignment, instrumentation and data acquisition checklists, activities reviewed and approved.

d. Use established procedures to bring test facility to desired initial conditions.

e. Review facility alignment, initial conditions and instrumentation status. When ready to test, complete Test Check List and shut down facility and process systems.

f. Complete Test Check List, review, and when satisfied sign checklist indicating approval to initiate test.

g. Initiate test after or completion of final steps.

h. After test, inspect facility and clear for entry.

i. Complete Post-Test Checklist and start data reduction activities.

j. Initiate post-test procedures for cooldown, etc.

After the first several tests had been completed, a test review was held with the operating personnel to review test performance for identification of potential or actual problem areas. For any problems identified, the appropriate individual component procedure or test procedure was then evaluated and revised as required. Most of the NODs issued during the performance of the FSTF test program concerned updating and streamlining operational procedures for the facility. A total of 22 NODs were issued through the course of the test program.

4.3 TEST MATRIX

The FSTF basic test matrix consisted of nine tests. One test was added to the basic test matrix at the request of the Mark I Owners. Test number 10 was added to investigate the effect of air content in the vents. Figure 4.3-1 shows the test matrix in the order in which the tests were conducted, including the nominal initial conditions for each test.

Changes made to the facility during the course of the test program are summarized below:

a. After test M3 - a) added vent header protector; b) added tie straps between downcomers 7 and 8.

TEST* NUMBER	DATE PERFORMED	BREAK SIZE	BREAK TYPE	WETWELL NOMINAL INITIAL CONDITIONS SUBMERGENCE	TEMPERATURE	PRESSURE
M1	5/5/78	Small	Steam	3 ft 4 in	70°F	0 psig
M2	5/12/78	Medium				
M3	5/25/78	Small	Liquid			
M4	6/17/78		Steam			5 psig
M5	6/26/78				120°F	0 psig
M6	7/6/78			1 ft 6 in		
M9	7/11/78			4 ft 6 in	70°F	
M10**	7/27/78			3 ft 4 in		
M7	8/10/78	Large				
M8	8/22/78		Liquid			

*Shown in order of performance

**Air sensitivity test performed with vacuum breaker replaced with rupture discs

1157 217

Figure 4.3-1. FSTF Test Matrix

b. After test M9 - a) removed vacuum breaker (replaced with rupture discs); b) added vent header stiffeners for the reduced air test; c) added tension and compression tie bars (bracing) between downcomers 1 and 2, 3 and 4, 5 and 6.

c. After test M10 - a) reinstalled vacuum breaker; b) added perforations to large blowdown line standpipe in drywell.

d) After test M7 - removed ring header stiffeners and bracing between downcomers 5 and 6.

5. DATA REDUCTION

5.1 GENERAL DESCRIPTION

The data recorded during each test was processed for analysis using the same computer system provided for data acquisition and described in Section 3.5. The first data reduction activity after each test was to use the limited plotting capability of the data acquisition software to generate a few time-history plots directly from the multiplexed data. This was done usually within two to three hours following the test, to verify as early as possible that the data had been properly recorded, that key instruments had functioned correctly and to get a preliminary assessment of facility response during the test.

The next step was to demultiplex the data. This activity required approximately twelve hours during which the multiplexed data as acquired on the memory disc pack was demultiplexed, recorded on magnetic tape and then re-recorded on a clean disc pack.

The demultiplexed data disc was required for use with the principal data reduction software program, DARS (Data Analysis and Reduction Software). This program was used to generate plots and listing of analyzed data.

As part of the data reduction process, the test data was copied onto a magnetic tape in a format compatible with the General Electric computer system in San Jose. These tapes have been used for analysis of the downcomer lateral loads and for cross-spectral analyses.

5.2 "ON-SITE" DATA REDUCTION SOFTWARE

5.2.1 General Philosophy of Operation

The Data Analysis and Reduction Software (DARS) program was designed to meet the needs of the Mark I FSTF Test Program. The DARS program allows test

engineering personnel to perform a wide variety of analyses on the data acquired during the data acquisition phase. The DARS uses a flexible file building and maintenance capability to efficiently handle the various processing requirements.

The program is designed to use the full capability of the computer hardware and software. This includes an on-line disc storage capacity of about 116 million words. The software includes the full complement of Sperry-Univac software enhanced by programs specially prepared for the FSTF tests.

The DARS provides two basic operational modes to the user: interactive and batch. In the interactive mode a computer operator will converse with DARS via a Tektronix graphic CRT. Batch mode will normally accept input from a card reader. In the interactive mode the emphasis is on flexibility, while in the batch mode the main concern is speed.

The program is designed in a modular fashion. This allows new capabilities to be added at a later date without disrupting present analysis modules. The sections below describe the various operational capabilities of the program.

5.2.2 Overall Operational Flow

The operation of DARS consists basically of performing steps. Specifically it uses a concept known as a Processing Step (PS). Each PS takes data in one form and translates (or processes) it to another form. Each PS requires (as a minimum) the following information:

1. Channel or transducer identifier
2. Time interval of interest
3. Operation(s) to be performed

To assist in this process, tables of modules, functions and parameters are maintained by the DARS.

1157 220

5.2.3 Major Modules

The DARS has a main controlling program and modules (subroutines) for all of the analysis and display functions. The following sections give a short description of each module.

5.2.3.1 Preprocessor (PREP)

This must be the first module called in a PS sequence. PREP converts the data to engineering units by accessing the ADMID file which contains all calibration data. DARS assumes the ADMID file is correct and thus makes no checks on it. Optional capabilities of PREP are:

a. Linear Trend Removal. This is done for data on a piecewise basis. The maximum number of points for one buffer is 1024.

b. Digital Filter. This is a low-pass filter with a selectable cutoff frequency.

c. Decimation. This reduces the number of data points by up to a factor of 1000.

5.2.3.2 Display (DISP)

This module produces all the displays, both plots and printouts. The plot types are:

a. Single plot on single grid/page.

b. Strip chart format with multiple grids/page (up to eight).

c. Single grid with multiple plots/page.

The print format lists a single variable at a time.

5.2.3.3 Stress (STRS)

This module performs the following stress analyses:

a. Computes uniaxial stress and writes strain and stress data to disc.

b. Computes biaxial stress and writes stress and strain components to disc.

c. Computes and writes to disc the following rosette results: maximum principal stress, minimum principal stress, maximum shear, angle of maximum principal axis, and leg 1 and leg 3 component stresses.

5.2.3.4 Maximum/Minimum (MXMN)

This module performs the following analysis:

a. Given a time interval, BEG to END, a given subinterval, Δt, and a string of preprocessed input channels (or a string of up to 10 analysis results, such as RMAX, RMIN, etc.), then for each input channel this routine finds the maximum and minimum over each Δt from BEG to END, and prints a ranked list of the largest and smallest values, together with their associated time and channel ID.

b. If desired, the routine then ranks and prints the 50 largest and 50 smallest of the results of part 1, together with their associated times and channel ID's.

5.2.3.5 Spectrum Analysis (SPEC)

This module computes the power spectral density (PSD) function on an input time series array. The options available include:

a. Windowing — A Hanning window may be applied to reduce effects of discontinuities.

b. Averaging — the PSD results for more than one time interval may be averaged to improve statistical consistency.

SPEC operates on either preprocessor or analysis results data. The only restriction is that the input array be a function of time.

5.2.3.6 Ventline Flow Analysis (VFLO)

This module performs the following:

a. Computes the flow rate in north ventline.

b. Computes the flow rate in south ventline.

Input to VFLO consists of:

a. Pressure measured upstream of the annubar in a ventline.

b. Annubar differential pressure measurement in the ventline.

c. Temperature measured upstream of the annubar in ventline.

The computations are performed twice; once assuming that the fluid flowing in the ventline is air and once assuming the fluid is steam at saturated conditions corresponding to ventline pressure.

5.2.3.7 Blowdown Flow Analysis (BFLO)

This module computes blowdown flowrate from either of the following sets of inputs:

a. Nozzle Pressures (Isentropic nozzle flow)

(1) Static pressure measured in the pipe upstream of the flow nozzle.

(2) Static pressure measured at the flow nozzle throat.

b. Differential Pressures (Rate of change of vessel inventory)

(1) Differential pressure measured between the top and bottom of the steam vessel.

(2) Differential pressure measured between the top and the middle of the steam vessel.

(3) Differential pressure measured between the middle and the bottom of the steam vessel.

5.2.3.8 Bending and Membrane Stress Analysis (BEND)

This module performs the following:

a. Compute bending stress component of wetwell shell.

b. Compute membrane stress component of wetwell shell.

Input data to BEND consists of one of the following:

a. Strain gage data from a uniaxial bending bridge circuit.

b. Strain gage data from biaxial gage.

c. Strain gage data from leg A and leg C components of a Rosette gage.

d. Stress data obtained from prior stress analysis on biaxial or Rosette gages.

Strain gage data is needed from both the outside and inside surfaces of the wetwell.

The bending and membrane stresses are computed in terms of the x (axial) and y (circumferential) components.

5.2.3.9 Statistical Analysis (STAT)

This module performs the following statistical functions for a given input file:

a. Computes and writes to line printer the average, standard deviation, skewness and kurtosis.

b. Plot magnitude histograms over the range of values. The x-axis of the histogram may be scaled by the user, default is automatic scaling.

c. Plot a cumulative probability distribution function complimentary to the histogram.

5.2.3.10 Load Analysis (LOAD)

The LOAD analysis module performs the following calculations:

a. "Four hydrodynamic properties" from wall pressure measurements. The calculation is of a general form $F_n = \frac{1}{C_n} \sum_i P_i A_{in}$. Up to four values of F_n can be calculated using different values of constants C_n, up to 30 transducer outputs, P_i, and corresponding multipliers, A_{in}. The hydrodynamic properties are calculated using wall pressure transducer output for P_i and an appropriate area for A_{in}, however the module will accept any transducer and any values for the constants.

b. A downcomer equivalent static load from strain gage outputs and appropriate calibration coefficients.

c. Resultant and angle of resultant for downcomer lateral force and/or acceleration.

1157 225

5.2.3.11 Find Downcomer Chugs (FIND)

This module's function consists of finding the times at which chugs begin in the downcomers and producing listings and files of the chug start times.

a. Given a time interval of BEG to END and the files of downcomer acceleration, pressure and conductivity probe data from PREP, FIND uses a selected decision logic option (Section 6.2.1.3) and various criteria to determine the chug start times.

b. The chug start times are output to eight files which are then merged to form the files containing the downcomer numbers and the associated chug times.

c. Optionally, FIND will produce one of three reports. To obtain the other reports, FIND can be re-run after the chugs have already been found. The three reports are, a chronological listing of chugs by downcomer number, a chronological listing of all chugs and a multipage plot indicating chug times with an "X".

5.2.3.12 Determine Pool Chugs (POOL)

POOL determines pool chugs (defined in par. 6.2.1.4) by grouping individual chugs received from the FIND Analysis Module. Each individual chug's time is compared with the previous chug time. When this time difference exceeds the user input value DTC, POOL has determined that one pool chug has finished, and another has begun. In this way, POOL allows as few as one downcomer chug per pool chug. POOL uses the downcomer chug time as the pool chug start time. The pool chug mean time is an average of the individual downcomer chug times. The time increment between the downcomer chug times and the associated mean pool chug time can be positive or negative. Negative values correspond to chugs which occur before the mean pool chug time.

The POOL analysis module performs the following function:

a. Determines pool chugs from FIND data.

b. Prints "Pool Chug Chronological Report".

c. Outputs time between pool chugs to disc.

d. Outputs number of downcomers for each pool chug to disc.

e. Outputs time increments from pool chug mean time to each downcomer chug to disc.

5.2.3.13 SPAN Operation

The SPAN Analysis Module provides an interface between the DARS Chug Functions (FIND, POOL) and the maximum/minimum function (MXMN). SPAN sends a series of time intervals to MXMN, which are used as MAX/MIN time intervals. There are three different criteria for determining the time windows:

a. Pool Chug Start Time Method — the start times of the pool-chugs determined by POOL are used as the basis for the time windows. If t1, t2 --- tn are the pool-chug start times, the following windows are used: t1 - CIN to t2 - CIN, t2 - CIN to t3 - CIN, - - -, tn-1 - CIN to tn - CIN. CIN is a constant supplied by the user for this method.

b. Downcomer Chug Times Method — this method is the same as above, except the start time for the downcomer n is used instead of pool-chug start times. The user selects the downcomer number by setting a parameter NDC.

c. Arbritrary Time Input Values. When a parameter, MSP, is set to a value of 3 SPAN inputs a card deck containing one time value per card. If t1, t2 --- tn are the time values, then the windows are t1 to t2, t2 to t3, --- tn-1 to tn.

1157 227

5.2.3.14 GE Compatible Magnetic Tapes (BTAPE)

BTAPE produces magnetic tapes from the raw multiplexed data obtained from Mark I FSTF data acquisition system. Data includes instrument calibration and Engineering Unit conversion information and header data describing the test.

5.3 "ON-SITE" DATA REDUCTION PROCEDURE

The following general types of plots and analyses were done for each test:

a. Time history plots covering the entire test period on a single page

b. Time history plots covering the condensation oscillation and chugging periods at a scale of five sec per page

c. Time history plots covering a single chug or a few cycles of condensation oscillation at a scale of approximately one sec per page

d. A chugging analysis (for tests in which chugging occurred) including finding and listing downcomer-chug start times, organizing into "pool-chugs" and plotting histograms to show degree of synchronization

e. Power spectral density (PSDs) plots and listings over selected 0.5-to 1.5 sec periods

f. Tables and histograms of maximum positive and maximum negative wetwell wall pressures and hydrodynamic property peaks during chugging and condensation oscillation periods

g. Plots and tables of wetwell pool temperature data throughout the test

h. Time history plots of key strain and stess data at various scales for analysis of facility structural response

i. Time histories and PSDs of wetwell pressure, acceleration, displacement and stress during the same time periods for evaluation of fluid structure interaction effects

j. Time histories and PSDs for evaluation of downcomer lateral loads.

5.4 "IN-HOUSE" DATA REDUCTION

General capabilities and procedures for "in-house" (at General Electric in San Jose) processing of FSTF data, will be discussed in this subsection. Primarily, "in-house" data reduction capability was developed to (1) perform cross-power spectral analyses and (2) analyze downcomer lateral loads.

The procedure used in processing FSTF data "in house" is identified in Figure 5-1. The basic elements of this procedure are:

a. Conversion of Varian-formatted raw data tapes to tapes formatted to be compatible with the Honeywell – 6000 computer system

b. Conversion of raw data tapes to engineering units (E.U.) tapes

c. Generation of Engineering Units tapes in a format compatible with spectral analysis and downcomer lateral load analysis routines.

Specifics of the computer programs used in this data processing procedure will be given in the paragraphs that follow.

"In-house" data reduction begins with the generation of Varian-formatted multiplexed raw data tapes at the FSTF site. To generate these tapes, data was read from the computer discs used for data acquisition (data in multiplexed form).

Generally, five tapes were required to store all of the data acquired for each test. Each tape was generated with a header identifying the test (and other pertinent information such as sample rate, test date, etc.) and engineering units conversion factors followed by multiplexed data in computer count form.

An exact duplicate of the Varian-formatted raw data tape was made at GE. The purpose of this step was to have a raw data tape generated on the Honewell — 6000 system available for further processing. These copy tapes are stored in a controlled environment area and are used for saving data over an extended period of time.

A data conversion program processes an input non-standard (relative to the Honeywell — 6000 system) Varian-formatted raw data tape and generates a standard engineering units (E.U.) tapes (two E.U. tapes are required for one raw data tape — a total of ten E.U. tapes are required for each test). The specific purposes of this program are to:

a. Convert Varian words to Honeywell — 6000 words

b. Convert data from computer counts to engineering units. This program also has the capability to list and modify the ADMID file (channel map, transducer names, E.U. conversion factors and gain).

A general data reduction program is then used to generate engineering units tapes formatted for the spectral analysis. In addition, this program has numerous capabilities for data processing and data calculations and can list and plot raw processed and calculational values as well.

Some of the processing and calculational capabilities are identified below:

a. Data Processing

- o Constant trend removal
- o Low pass digital filter
- o Decimation of the data

b. Data Calculations

- o Maximum and minimum values
- o Difference between any two transducers
- o Stress calculations for uniaxial strain gages and rectangular rosette strain gage groups
- o Integration of accelerometers to get velocity and displacement

The spectral analysis program performs digital spectral analysis of constant sampled time signals. The method employed is one of Fourier signal decomposition utilizing the fast Fourier transform. Power spectral density, cross power spectral density, phase, transfer and coherence functions are calculated by this software. Program outputs are plots and tabular printout of results.

Another program is used to merge one or more formatted data tapes to produce one continuous sequential data tape. The purpose of this program is to put a few channels of one complete test on a tape such that the downcomer lateral ' . program can access any time segment without concern for tape boundaries within a test.

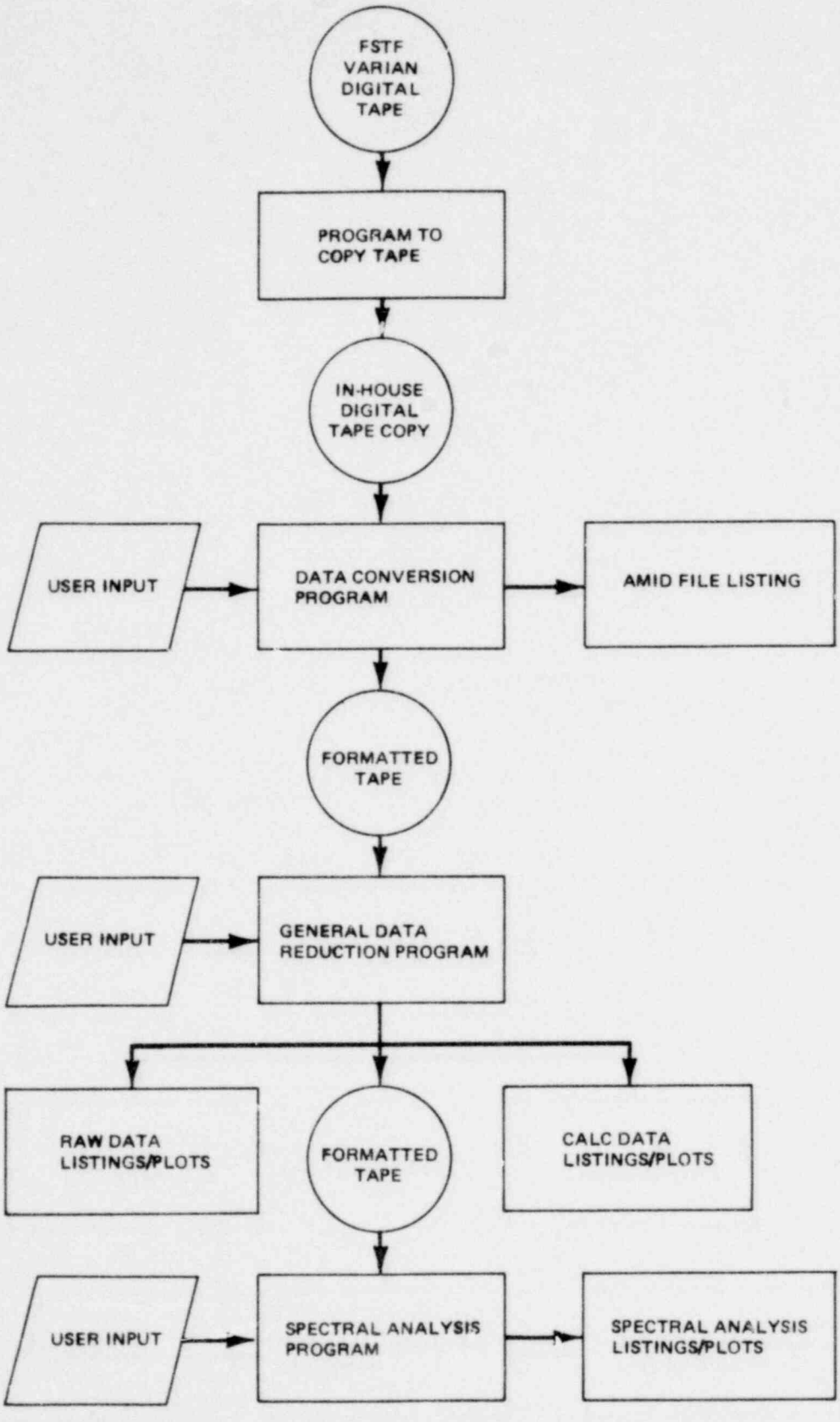

Figure 5-1. Flow Diagram of FSTF In-House Data Processing (1 of 2)

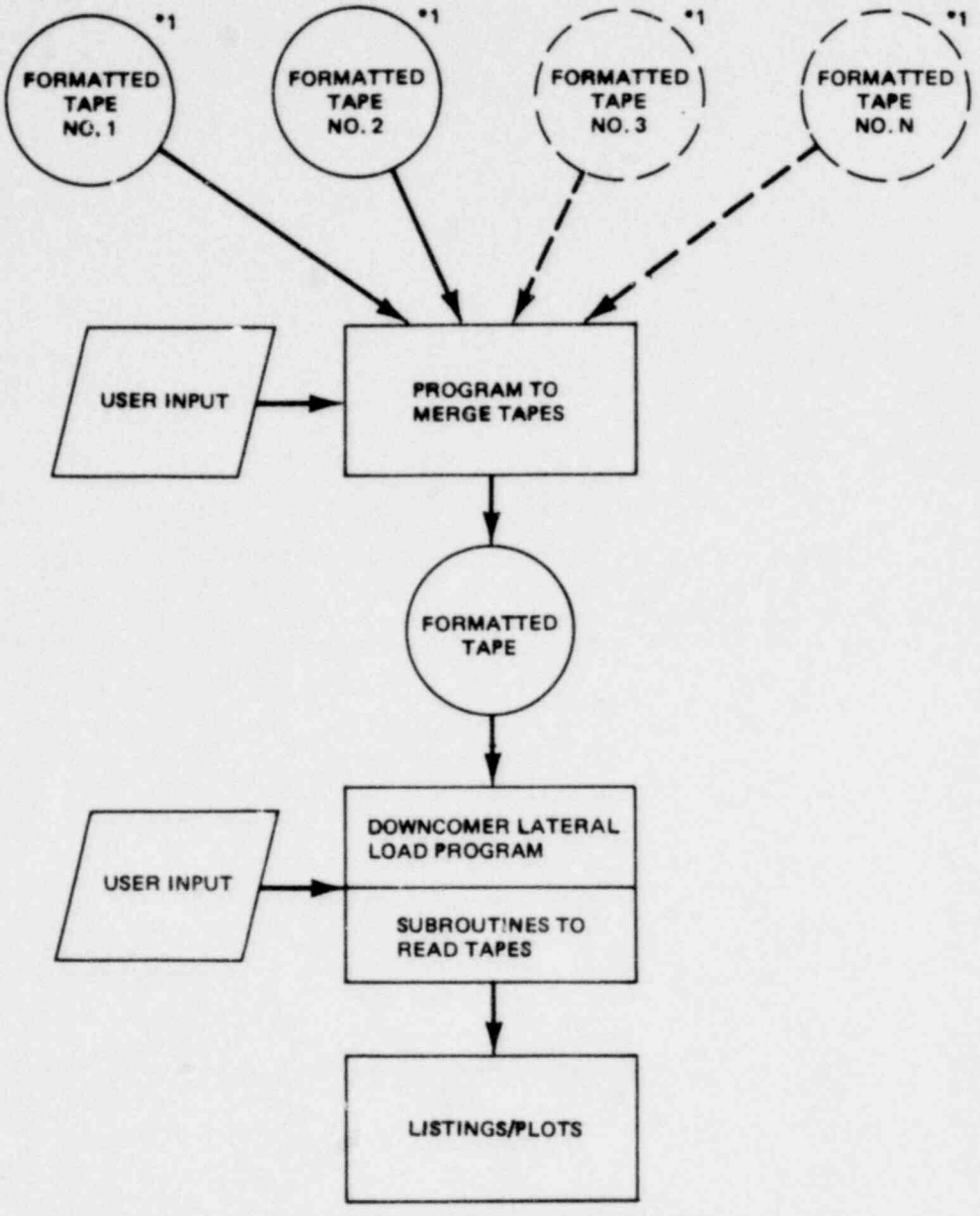

*1 ONE OR MORE SEQUENTIAL TAPES. GENERALLY A SEQUENCE OF TAPES REPRESENTING ONE RUN

Figure 5-1. Flow Diagram of FSTF In-House Data Processing (2 of 2)

6. TEST RESULTS

6.1 SYSTEM PERFORMANCE

FSTF system performance during the ten-test matrix was generally as expected. System pressure and bulk temperature responses of the steam vessel, drywell and wetwell agreed well with pretest predictions. This ensured that the boundary conditions on the suppression pool which control the wetwell hydrodynamic loads and structural response were representative of postulated LOCA conditions in a Mark I containment.

The steam supply vessel serves as the energy source for the tests by supplying high pressure saturated liquid and steam through the blowdown line to the drywell. Saturated liquid and steam drive air from the drywell into the wetwell airspace, increasing the wetwell pressure. Steam then condenses in the wetwell suppression pool, elevating its temperature. This sequence of events was repeated using two types of blowdowns from the steam supply vessel. Steam blowdowns (which simulate main steam line breaks) and liquid blowdowns (which simulate recirculation line breaks) were performed. A range of break areas was covered for each type of steam vessel blowdown. Figure 6.1-1 presents the steam vessel pressure for liquid blowdowns. As shown, the steam supply vessel pressure decreases slowly (for a small break) as liquid is being discharged until the liquid level in the steam vessel reaches the break elevation, then the pressure decreases rapidly as steam is being discharged. Figure 6.1-2 shows the steam supply vessel pressure for steam blowdowns. As shown, the vessel pressure decreases rapidly as steam is being discharged from the vessel for the duration of the blowdown.

Containment loads and responses resulting from these blowdowns are presented and discussed in the following sections. For a detailed discussion of the system performance parameters resulting from these blowdowns, see Appendix C.

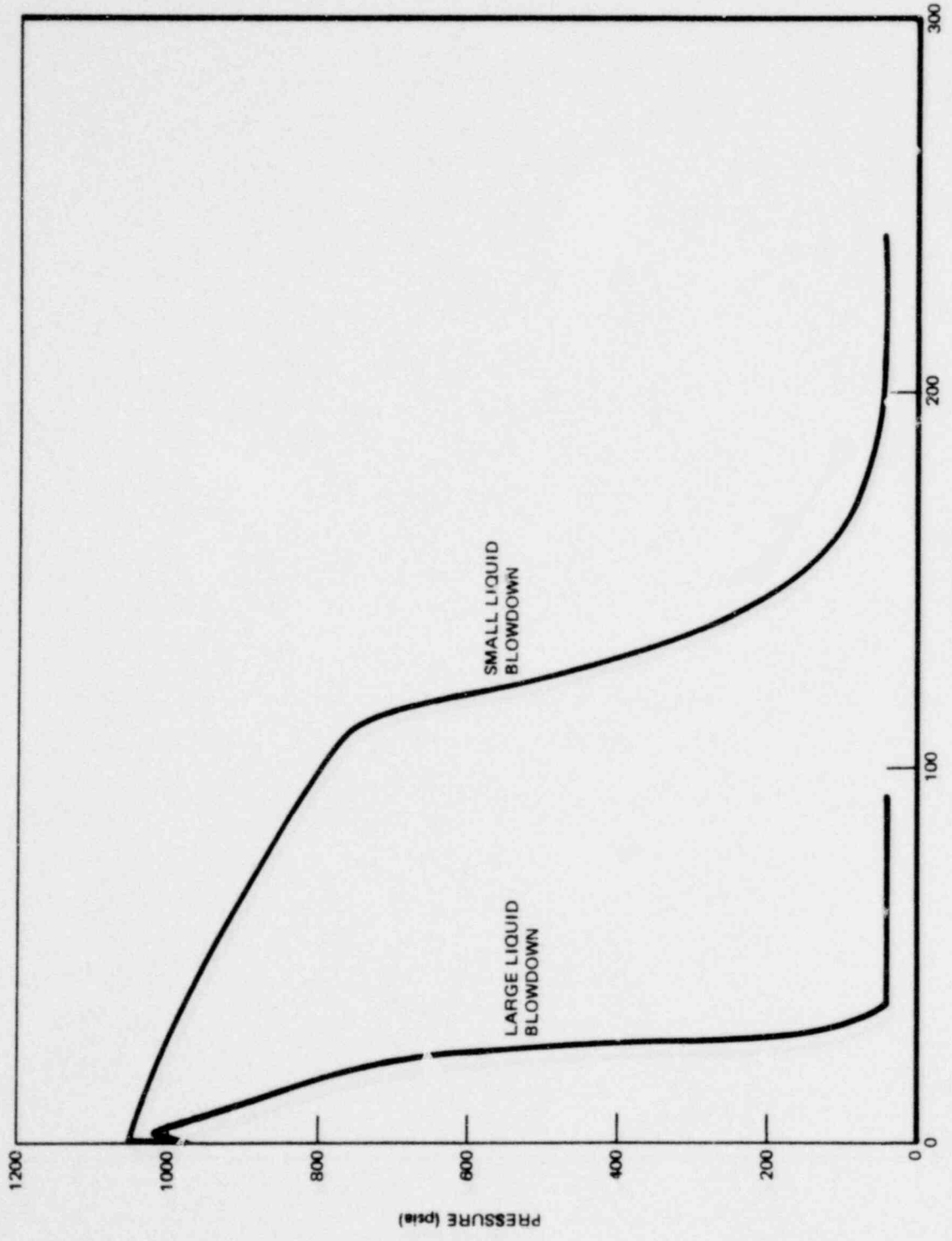

Figure 6.1-1. Comparison of Steam Vessel Pressure for Large and Small Liquid Blowdowns

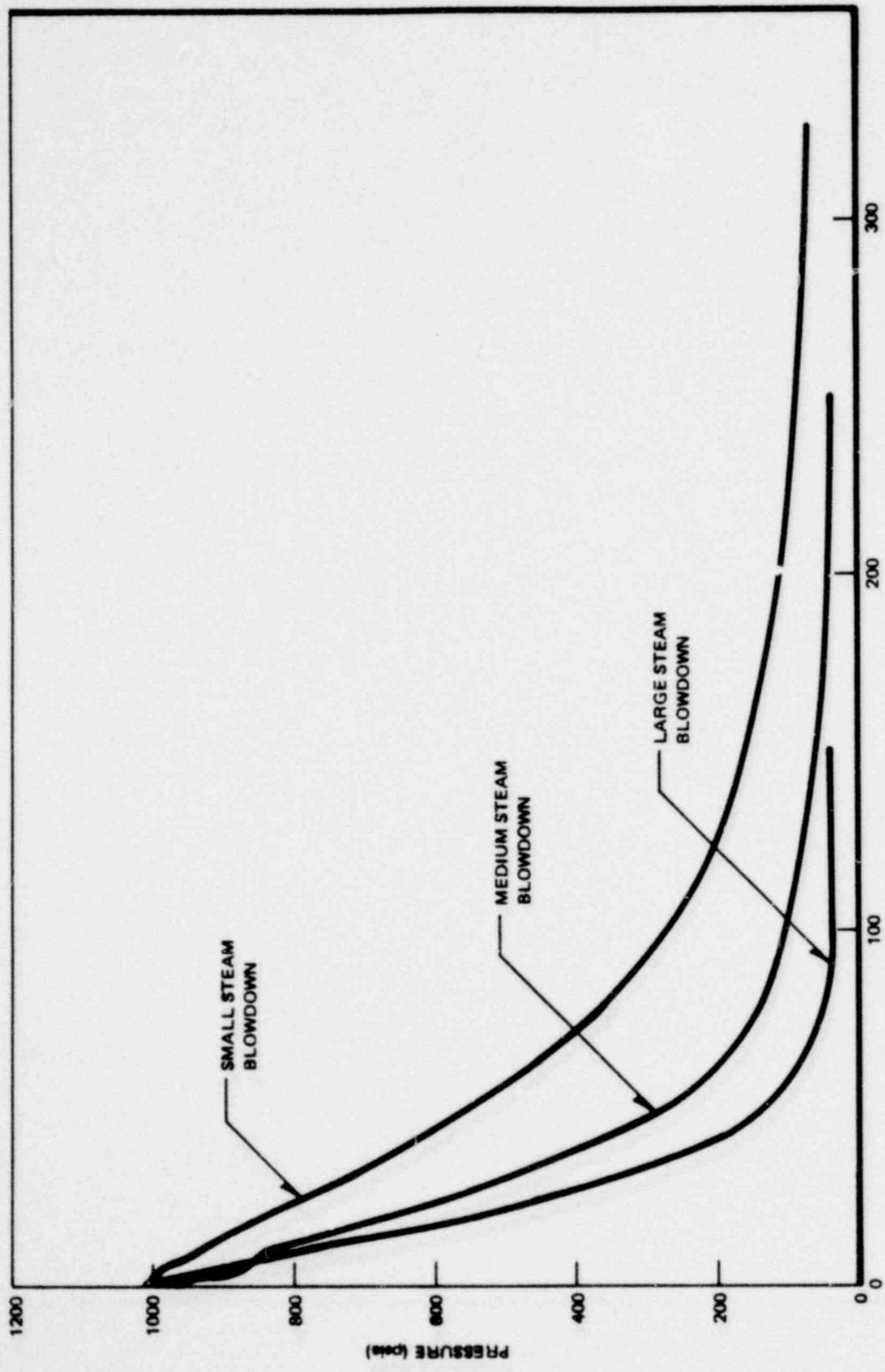

Figure 6.1-2. Comparison of Steam Vessel Pressure for Small, Medium and Large Steam Blowdowns

6.2 WETWELL HYDRODYNAMICS

6.2.1 Chugging

6.2.1.1 Chugging Data Base. The occurrence of chugging during a blowdown was determined by a review of the data from conductivity probes located on the inside of each downcomer, six inches above the bottom. Since one of the characteristics ascribed to chugging is the periodic rise of the steam-water interface into the downcomer, it was assumed that chugging had occurred when the conductivity probes indicated periods of being alternately wet and dry. If such periods were found in a test, the chug detection software described in Section 5.1.2 was then used to determine the start times and synchronization relationships of each downcomer chug.

Substantial chugging was present during four of the ten tests in the series. The four tests were M1, M4, M9 and M10, all of which were small steam break tests with a nominal initial pool temperature of 70°F. Test M1 was run with the nominal initial conditions of 3.33 feet of downcomer submergence, atmospheric free-space pressure and prototypical vacuum breaker installation. The initial free-space pressure was increased to 5 psig for test M4, the submergence was increased to 4.5 feet for M9 and the vacuum breaker was removed for M10. Two small steam break tests, M5 and M6, did not produce chugging. The initial pool temperature in both of these was 120°F. The liquid break tests, M3 and M8, and the large and medium steam breaks, M7 and M2, also did not produce chugging. A discussion of possible reasons for chugging occurrence or non-occurrence is provided in Section 6.2.1.2.

The data recorded during the chugging periods of the four tests M1, M4, M9 and M10 represent the data base from this test series which is available for analyzing Mark I containment chugging loads. The chugging periods and the number of chugs for each test are summarized in Table 6.2.1-1.

Comparison of Test M-1 chugging data with the chugging data of Tests M4, M9 and M10, indicates two distinct types of chugging, or two chugging

regimes. Test M1 contains three time intervals during which the chugging characteristics, particularly wall and vent system pressure time histories, were not duplicated in succeeding tests. The distinction between these two types of chugging is primarily the degree of synchronization between the individual downcomer chugs. During the three unique periods in Test M1, the chugs are closely synchronized into "pool chugs" (as defined in 6.2.1.4) with all eight downcomers chugging, often within a span of 100 msec. Other characteristics are the large, low frequency decreases in the drywell and vent system pressure, the well mixed wetwell pool (uniform temperature) and the damped sinusoidal form of the wall pressure signal with a fairly quiescent period between chugs. A "typical" wall pressure time history for one of these periods during Test M1 is shown in Figure 6.2.1-1. This type of chugging will be referred to as "Type 1". The time intervals during Test M1 in which Type 1 chugging occurred are shown in Table 6.2.1-2.

The remaining chugging intervals in Test M1 show data characteristics that are typical of those seen in Tests M4, M9 and M10. There is a lack of synchronization in these time intervals and many "pool chugs" consist only of a single downcomer chug. The vent system and drywell do not show the large, low frequency pressure decreases indicating lower condensation rates at the interface. The pool tends toward more temperature stratification caused by poor mixing. The wall pressure time history typically has alternate periods of low frequency oscillations similar to condensation oscillation (CO) as well as higher frequency, lower amplitude oscillations. A typical wall pressure trace from an earlier period in M1 is also shown in Figure 6.2.1-1. This behavior will be referred to as "Type 2" chugging. Characteristics of these two types will be discussed in the following paragraphs.

6.2.1.2 Chugging Conditions. Chugging conditions were reviewed to understand why chugging did not occur in some tests. Two variables appear to have the most influence on chugging: some form of the vent system flow rate (mass, momentum, or energy), and the temperature or temperature distribution in the wetwell pool. On this basis, the observed FSTF chugging conditions were mapped using average downcomer steam mass flux to represent flow rate and mean pool temperature at the exit of the downcomers to represent the pool temperature.

The average downcomer steam mass flux was calculated by dividing the steam mass flow rate from the flow nozzle measurement (see Section C.1) by the total cross-sectional area of eight downcomers. For the small steam break tests, the average of the six steam flow-versus-time curves was used to determine the mass flux. For the small liquid-break test, it was assumed that the water undergoes isenthalpic expansion from steam vessel pressure to a steam-water mixture at drywell pressure. The quality of the resulting mixture was used to calculate the steam mass flux from the nozzle flow rate measurement.

The mean pool temperature at the bottom of the downcomers is defined as the average value of the temperatures from eight thermocouples located near the bottom of downcomers 5 and 6, as shown in Figure 6.2.1-2. These are all of the available thermocouples close in elevation to the bottom of the downcomers.

The "map" was made by plotting the mass flux as a function of temperature for each test. On each curve, the periods of non-chugging, Type 1 chugging, and Type 2 chugging were indicated. The result is shown in Figure 6.2.1-3. The large liquid break, Test M8, was omitted because chugging did not occur and the mass flux was outside the range of the figure.

Figure 6.2.1-3 shows that the mass flux and pool temperature conditions during all observed chugging periods are in the area of the map below 6.5 lb/sec ft^2 mass flux and less than 135°F pool temperature. This suggests the existence of a chugging boundary (see Figure 6.2.1-3) that defines temperature and mass flux conditions necessary for the tested geometry to produce chugging. Conditions above and to the right of the boundary line do not result in chugging, while conditions to the left and below do produce chugging. The location of the postulated line is fairly well established by the present data above a steam mass flux of 6 lb/sec-ft^2 and below 1.8 lb/sec-ft^2, but is speculative in the region between the curves for Tests M3, M2, and M10.

Another observation from Figure 6.2.1-3 is that the more active, Type 1 chugging occurred at the test conditions furthest below the postulated boundary line. All Type 1 chugging was observed below 3.0 lb/sec ft^2 mass flux and about 110°F pool temperature.

One apparent inconsistency is the start of chugging for Test M1 which, according to the computer results, occurred at 5 lbs/sec-ft^2. A review of the data has shown that the water level probes near the bottom end of the downcomers indicate alternate wet and dry periods beginning at about 6.3 lb/sec ft^2. Therefore, it is probable that chugging did start at the higher mass flux, but was not indicated by the computer analysis because the downcomer accelerations were less than the 7-g criteria used for M1 (see Section 6.2.1.3). If the chug detection analysis were redone using the 3-g downcomer acceleration criteria, as in tests M4 and M9, the apparent inconsistency in Figure 6.2.1-3 would be removed.

The air content of the steam flow in the vent system is known to have an influence on the thermodynamic conditions that result in chugging. In this test series, since all of the chugging occurred during small steam break tests which began with the same thermodynamic conditions in the steam vessel and drywell, the air content in the steam during chugging is always the same (or nearly so) for a given mass flux. Therefore, since the steam mass flux and air content are changing simultaneously, there is no way to separate the effect of air content from the effect of steam mass flux on chugging for the data reported here. To provide an indication of the air content during chugging, the lines representing tests MI, M4, M9 and M10 on Figure 6.2.1-3 have been marked to show an average percent air in the centline determined from Figure C-34. These values also apply to Tests M5 and M6.

6.2.1.3 Chug Initiation Times. Much of the analysis used to develop a description of the FSTF chugging pressure loads depends upon the chug initiation times determined by the chug detection software module, "FIND". Application of the module requires parameter input that represents criteria for deciding whether or not a chug has occurred. The "FIND" module is described in Section 5.2.3.11.

Based on a review of some time history plots of downcomer level probe, pressure and accelerometer data from test M1, the best indication of the occurrence of a chug was concluded to be a sudden increase in the downcomer accelerometer output and a nearly simultaneous change in the conductivity probe output from the "dry" value to the "wet" value. Downcomer pressure data was not used because the form of the pressure time history plot did not clearly indicate the beginning of a chug. A sample plot of acceleration, pressure and level for downcomer number 5 is shown in Figure 6.2.1-4.

The test performed by the "FIND" module was applied to the accelerometer and level probe data from one downcomer at a time. Beginning at some time t, at the start of a possible chugging period, the accelerometer output at time t + DT2 was compared with the average acceleration in the DT1 seconds preceding time t. If the acceleration at t + DT2 exceeded the average value by a selected amount, DA, then a possible chug was indicated and the level probe data was then tested. If the acceleration criterion was not exceeded, the data at the next time step was similarly tested.

The level probe data was tested by examining the voltage output in the period t + DT3 to t + DT4 to see if a change from "dry" to "wet" was indicated in this period (a voltage decrease to less than a value L1). If this occurred, the time, t, was recorded as a chug start time; if not, the time was advanced to the next data point and the process repeated beginning with the accelerometer data.

For Test M1, the criteria values (DT1, DT2, DT3, DT4, DA and L1) were selected on the basis of the accelerometer and conductivity probe data from a period of Type 1 chugging with downcomer acceleration changes large enough to clearly indicate a chug. For succeeding tests, the acceleration criterion was relaxed because Type 2 chugging and tie straps added between downcomers 7 and 8 reduced downcomer acceleration levels. Other criteria were changed to establish t chug start times more precisely. The values selected for each test are shown in Table 6.2.1-3.

1157 241

6.2.1.4 Chug Synchronization and Period. The "POOL" software module, described in Section 5.2.3.12, was used to organize the chug initiation times from the "FIND" software module, for analysis of the degree of synchronization between chugs occurring in different downcomers. The principal input parameter for "POOL" is a time increment, Δt_c, used to define a pool chug. A pool chug can be defined a number of ways, but the meaning of the term as used here is that downcomer chugs which begin within Δt_c seconds of each other belong to the same pool chug. This definition allows pool chugs to contain one or more downcomer chugs. The output of "POOL" is the Pool Chug Chronological Report which displays pool chug start times, number of downcomer chugs, identification of which downcomers chugged, downcomer chug start time, and other useful information related to synchronization. A sample of this tabulation from Test M1 is shown in Figure 6.2.1-5.

The modules "FIND" and "POOL" were run in 90- to 100-sec intervals during the chugging periods of Tests M1, M4 and M9. The time increment, Δt_c, used for "POOL" was 0.100 seconds. For Test M4, "POOL" was also run once with a Δt_c of 0.300 seconds to check the sensitivity of the results to this parameter. The results of this analysis are summarized in Table 6.2.1-4. This shows that for the not-well-synchronized Type 2 chugging, the pool chug approach to synchronization analysis is relatively sensitive to the selected time increment.

Type 1 and Type 2 chugging, introduced in Section 6.2.1.1, were differentiated by their apparent degrees of synchronization. It is, therefore, appropriate to divide the data from the M1 Pool Chug Chronological Report into Type 1 and Type 2 data and review the synchronization separately.

The number of downcomer chugs per pool chug for the three periods of Type 1 chugging in Test M1 has been separated from Type 2 data and composite histograms drawn for both types. Similar histograms have been prepared for the Type 2 chugging data from tests M4 and M9, and are shown in Figures 6.2.1-6 through -9. The histogram data is summarized in Table 6.2.1-5, clearly showing the higher degree of synchronization during the Type 1 chugging

periods. The histogram shows that about 91% of the Type 1 pool chugs consist of five or more downcomer chugs, with the average about 6.9 downcomer chugs per pool chug.

These histograms were developed from the Pool Chug Chronological Reports, with some editing, particularly for the time period 169 to 228 seconds of Test M1. The "POOL" output indicated a number of single downcomer pool chugs, which upon close examination of the downcomer acceleration and level data, were concluded to be either not real chugs or part of another pool chug. The causes of these false chug indications in the data were in general: (1) saturation of the accelerometer charge amplifier (corrected prior to Test M4), (2) wild data points in the accelerometer output, (also corrected) or (3) a momentary reduction in the conductivity probe output probably indicating splashing out not full submergence of the probe. It is likely that if the accelerometer output had been "cleaner", the histograms would indicate an even higher percentage of seven- and eight-downcomer pool chugs.

The mean period between pool chugs was calculated and is summarized in Table 6.2.1-6. In general, Type 1 chugging has a longer period than Type 2, and Type 1 chugging periods get shorter as time increases (mass flux decreases and temperature increases) while Type 2 periods get longer.

6.2.1.5 Wetwell Wall Pressures. The pressure on the wall of the wetwell was measured throughout each test with flushmount transducers at 26 locations. The positions of these instruments are described in Section 3.4

The general characteristics of the local wall pressure response during the small steam break tests are illustrated by Figures 6.2.1-10, 11, 12 and 13. These figures show the time history of the output of one flushmount pressure transducer, P3181, during the entire data recording periods of Tests M1, M4, M9 and M10. The transducer, P3181 is located on the bottom of the shell near the North end. All of the pressures below the water level exhibit generally similar time histories, although the magnitude and phasing of the fluctuations vary with location.

For all of the tests, the pressure rises rapidly during the first 10 to 12 sec following test initiation as the drywell air is transferred to the wetwell freespace. The pressure then levels off and rises only slightly more during the remainder of the test as the air temperature increases. Just before leveling off, pressure oscillations build up, rapidly reach a maximum value of approximately ±2 psi and then, except for occasional larger swings, slowly decay in magnitude throughout the recording period. Figure 6.2.1-10, from Test M1, is somewhat different that the other three in that there are three periods in which the pressure fluctuations appear to be larger and more irregular. These three periods correspond to the intervals of highly synchronozed, Type 1 chugging, which was described in Section 6.2.1.1 and Table 6.2.1-2. The large pressure spike at 98 seconds is, in fact, the largest fluctuation seen on any wall pressure transducer during any chugging in the test series. The pressure signal during the time periods marked "Type 2", looks similar to that for the other tests.

Figures 6.2.1-14 through-17 provide a closer look at the pressure on an expanded time scale. The first two of these are typical of the Type 2 chugging early in the tests. The signal shows a "beating" characteristic with alternate periods of low frequency, high amplitude and high frequency, low amplitude. The chug detection software indicates that a chug starts* just at the end of the low frequency part of the signal. The amplitude of the pressure following the start of the chug is much reduced. (See chug start times indicated on Figure 6.2.1-15.) The low frequency pressure oscillations appear very similar to those seen during the brief condensation oscillation period just prior to the chugging period.

Wall pressures during a Type 1 chugging period are shown in Figure 6.2.1-16 on the same time scale. This figure shows a distinct difference from the previous two. There is a low frequency oscillation present with a period of 1.5 to 2 sec which represent significant reductions in the pool pressure.

*Note that this "chug start" is determined by a larger acceleration at the vent exit rather than by the bubble collapse under pressure. Triggering the chug finder by acceleration and water level was found more reliable than triggering by the bubble collapse underpressure.

Corresponding low frequency changes are also present in the free-space, ring header, vent line and drywell. The beginnings of the chugs are marked on the figure. As in the Type 2 chugging period, there is a low frequency oscillation just preceding the chug and a higher frequency one following the chug. The difference is that the pressure fluctuation following the start of the Type 1 chug is sometimes as large or larger than those preceding the chug and the amplitude of the higher frequency signal is attenuated to a very low magnitude before the system chugs again.

Pressure signals from the same transducers are shown in Figure 6.2.1-17 for a later period of Type 2 chugging in Test M1. Again chug start times from the "FIND" output are indicated on the figure. The fluctuations at this time are of very much lower amplitude and the dominant frequency is higher ($\sim$40 Hz from the power spectral density analysis) than the 7-8 Hz seen in Figures 6.2.1-14 and 6.2.1-15. During this period there does not seem to be any identifiable form to the chugging signal and chug start times cannot be clearly distinguished on the basis of the wall pressure signal only.

To specify the wall pressures during chugging, the magnitude, the frequency content and the distrubution on the shell must be quantified. The tests were conducted to investigate the effects of the system parameters such as mass flux, pool temperature, air content in the steam, submergence of the downcomers, free-space pressure, etc. Magnitude, frequency content and wall pressure distribution are presented in the paragraphs that follow. The significant effects of the system parameters, which have been varied over the range for Mark I plants, are also included.

Wall Pressure Amplitudes

The magnitude of the wall pressure fluctuations can be represented by a spatial average which has been calculated using all of the pressure transducers below the water level in the wetwell. The calculation included weighting each pressure by a normalized area representing the horizontal projection of the wetwell shell area surrounding the transducer location relative to the total projected area. The resulting average is then proportional to the vertical component of the pressure force on the shell and can be related to the load on the wetwell support columns.

The average pressure calculations were performed using the "LOAD" software module (see Section 5.2.3.10). Trend removal was used on the pressure data prior to the calculation so that only the dynamic part of the signal is averaged. For Test M1 only, P3188 was omitted because of a large number of apparently bad data points. The spatially averaged pressure was calculated for all of the chugging data in Tests M1, M4 and M9, in periods of about 90 to 100 seconds at a time. Following the calculation, the results were then scanned to find and tabulate the maximum positive and maximum negative values of the average pressure in each pool chug. For comparison of average and local pressure fluctuations, representative time-history plots of the output of transducer P3181 and the calculated average pressure are shown in Figures 6.2.1-18 through -29.

Five of the six time periods in these figures include Type 2 chugs. The sixth, 98 to 99.2 seconds in Test M1, includes a Type 1 chug. This is the previously mentioned chug, which results in the highest local wall pressure fluctuation seen in any of the chugging periods. Three observations concerning the comparison of the average pressure and the local pressure plots are:

1. The peak values of the average pressure time history are considerably lower than the peak values of most of the local pressure time histories.

2. For the Type 1 chug, the peak values of the average pressure following the chug are about the same magnitude as the peak average pressures just prior to the chug. This is in contrast to the local pressure which are sometimes much higher just following a chug.

3. A frequency component of about 40 Hz, which is very prominent in the local wall pressures, is greatly attenuated in the average pressure. This is apparently the result of this frequency component not being in phase at all locations on the wetwell wall.

A "bounding-value" approach was selected to quantify the magnitude of the fluctuations in average wall pressure during chugging. A table of maximum positive and maximum negative fluctuations provided the bounding values, plotting in Figures 6.2.1-30 through 32 as a function of the time after test initiation. The figures shown are for Tests M1, M4 and M9 respectively.

The magnitude of the fluctuations in average wall pressure at any time during the test were less than or equal to the bounding value shown on the figure. The curves show that for each of the tests, the bounding values decrease with time (decreasing mass flux, increasing temperature). The highest values are in Test M9 and the lowest in Test M4, which supports the idea that chugging wall loads increase with submergence and decrease with free-space pressure.

Wall Pressure Frequencies

The frequency content of the wetwell wall pressures during chugging was examined through power spectral density analysis (PSDs) for the average and the various local pressures during tests M1, M4, M9 and M10.

A large number of time periods during chugging were selected to calculate PSDs. A representative sample of these for the average pressure and for one local pressure is shown in Figures 6.2.1-33 through -55. The software module used for these calculations requires a block of data with the number of points equal to an integer power of two with a maximum of 1024. This covers a time period of a little more than one sec, and all of the PSDs shown except Figures 6.2.1-42 and -45 (512 points) were done using this time period. This results in a frequency resolution of about one Hz. The pressure signal from which the PSD was calculated is presented with the PSDs for reference.

The wall pressure PSDs can be divided into three frequency bands into which most of the signal falls. The bands, selected somewhat arbitrarily, are 5 to 10 Hz, 10 to 25 Hz and 25 to 50 Hz. Many of the PSDs have one or more major components in each of these bands. To illustrate the frequencies which appear often in the data, a few PSDs from each of the four tests M1, M4, M9 and M10 were divided into these frequency bands, and the frequency with the highest magnitude on

1157 247

the PSD was tabulated for each band, and is shown in Table 6.2.1-7 for the local pressure P3185 and Table 6.2.1-8 for the average pressure. The dominant frequency for each PSD is marked with an asterisk. Referring to this table, it can be seen that for most of the PSDs, the dominant frequency is in the low frequency band and is usually 6.7 or 7.6 Hz. Examples are shown also of time periods in which either the middle band frequency or the high band frequency is dominant. The middle band frequency also has a relatively narrow range from 11.4 to 18.1 Hz for the examples shown. The high band frequencies show more variation but most are in the range of 35 to 50 Hz for the local pressure and 30 to 45 Hz for the average pressure.

The sample PSDs in Figures 6.2.1-33 to -55 were selected to be representative of the PSDs used for the Tables. Figures 6.2.1-33 to 36 show a pressure signal and its PSD from a Type 1 chug which occurred in Test M1. This is an example of a PSD in which the dominant frequency is in the low band. From the signal time history, it is obvious that the frequency content changes greatly throughout the time period, and if the PSD interval had started at 81 seconds the relative magnitudes of the frequency components would not necessarily be the same.

Another pressure signal from a Type 1 chug and its PSD are shown in Figures 6.2.1-37 through -40. This is an example in which the middle band frequency of 13.6 Hz has the greatest magnitude on the local pressure PSD. However, the low frequency band may still contain most of the "power" of the signal as represented by the area under the PSD. The PSD of the average pressure for the same time period is dominated by the low frequency, showing that importance of the middle-band frequency is localized.

An example of the frequency content for a Type 2 chug is shown by Figures 6.2.1-41 through -47. For this case, the time period was divided to show the change in the frequency content before and after the chug. Figures 6.2.1-42 and -45 are the PSDs just prior to the chug and are obviously dominated by the 7.6 Hz part of the signal. Following the chug, the most significant value on the local pressure PSD of Figure 6.2.1-43 is 40.1 Hz,

although there is still a significant amount of signal at 7.6 Hz. For the average pressure, Figure 6.2.1-47 shows the 7.6 Hz to be dominant and thus the high band frequency of P3185 is also only locally significant.

An example of a Type 2 chug from Test M9 is shown in Figures 6.2.1-48 through -51. Here the PSD is taken over a period which includes the time before and after the chug. The low frequency band, particularly 7.6 Hz, dominates, but the PSDs are a good example of how the frequencies tend to be in three bands.

The last example is a Type 2 chug from M10 in which the highest values on both the local pressure and average pressure PSDs are in the middle frequency band from 10 to 25 Hz. Figure 6.2.1-53, for the local pressure, shows two significant frequencies in this range, 13.4 Hz and 15.3 Hz, whereas Figure 6.2.1-55 for the average pressure shows only 13.4 Hz to be significant.

The source of the 7-8 Hz is probably the fundamental acoustic frequency in the vent line (1/4 standing wave). The PSDs of vent and vent header pressures during these tests, contain essentially no other frequencies than the 7-8 Hz. The frequencies seen in the high frequency band may be the acoustic frequency of the downcomer itself. This would explain the variety of signals seen in the band since the resonant frequency in the downcomer would be changing as the level rises and falls. Another factor which points to the downcomers as the source is that these frequencies are seen in the downcomer pressures but not in the vent header or the vent line. The middle band frequencies are not seen in vent line, ring header, or downcomer pressures and are likely a result of a shell structural frequency and fluid structure interaction (see Section 6.4).

Wall Pressure Distribution

A complete description of the wall pressure fluctuations requires a knowledge of the spatial distribution around the wetwell shell. This distribution has been investigated for the chugging periods of the Tests M1, M4 and M9.

Table 6.2.1-9 is a list of ten pressure transducers on the circumferential centerline of the wetwell and their angular locations, and a list of seven pressure transducers on the bottom of the wetwell and their distance from the circumferential centerline. Two time periods from each of the three tests were chosen for review of the pressure profiles as shown below:

Test M1	41-42.2 secs,	98-99.2 secs
Test M4	42.0-43.2 secs,	66.8-68.0 secs
Test M9	49.0-50.2 secs,	73.4-74.6 secs

The wall pressures listed in Table 6.2.1-9 and the spatially averaged wall pressure were tabulated and plotted for the above time periods. Each period contains a chug and the times selected for looking at the pressure distribution were those corresponding to the maximum positive and maximum negative values of the average pressure before and after the beginning of the chug. Two additional times were selected corresponding to the highest observed wall pressure fluctuation in the entire chugging data base. Circumferential and axial pressure distributions were plotted from the tabulated data. The pressure in the free-space has been assumed to be spatially constant and represented by P3005.

The distributions are shown in Figures 6.2.1-56 through 81. The spatially averaged pressure for these times was presented in Figures 6.2.1-18 through 29. The distribution prior to the chug looks very much like those for condensation oscillations shown in Section 6.2.2. Circumferentially, the pressure fluctuations are higher near 180° and approach zero at 90° and 270° (actually the water surface). Axially, the pressure is usually higher on one end than the other, but generally the fluctuations are all positive for a positive peak and all negative for a negative peak. Following a chug, the distributions are much more irregular both axially and circumferentially, and many profiles contain both positive and negative fluctuations.

No particular differences were observed between the spatial distributions which could be attributed to the parameter changes between Tests M1, M4 and M9, or between those for the Type 1 chug and the Type 2 chugs.

6.2.1.6 Effect of Vacuum Breaker on Wall Pressures. Matrix Test Number 10 (M10) was run with conditions matching those for M1 except for the vacuum breaker configuration. The vacuum breaker, oriented between the wetwell free space and the vent header for M1, was removed to assess the effect on chugging of eliminating introduction of air into the vent header.

The scope of the analysis of the hydrodynamic data for this test was limited to a comparison of the magnitude of the wall pressure fluctuations during chugging to those measured in Test M1.

The chug detection software, i.e., the "FIND" module, was not applied to the M10 data because of the influence of the downcomer tie braces on the downcomer accelerometer output. The reduced acceleration at the downcomer ends and the possibility of a chug on one downcomer causing an acceleration on the other one in the pair, make a comparison of chug start times and synchronization data between tests M1 and M10 nearly impossible. Chugging in M10 was judged to occur when the level probes at the bottom of the downcomers exhibited alternate wet and dry periods.

A visual comparison of the M1 and M10 short-time plots (5 sec/page) of wetwell wall pressures revealed that for the time period between 30-70 sec, the amplitude and frequency content were similar. Starting between 70 and 75 sec, the form of the M1 wall pressure signal changed noticeably. The M10 wall pressure did not show this change but continued to be similar in form to that seen during Type 2 chugging in other tests particularly M4 and M9 (see Figures 6.2.1-14 and 15). Because of the similarity in signal form in the period 30-70 sec between M1 and M10, this period was chosen for a more detailed statistical comparison of the magnitude of the peak wall pressure fluctuations.

After defining the time period of comparison, histograms of wall pressure peaks for P3181 (wetwell bottom transducer) were generated for both M1 and M10. A statistical method was used to determine whether the probability

distributions of the wall pressure peaks, from M1 and M10, were significantly different. They would be declared significantly different if one or more of the following terms exceeded specified critical values: mean, mean + 1 standard deviation, mean + 2 standard deviations, or mean + 3 standard deviations.

The means and standard deviations of the peak wall pressure fluctuations calculated for M10 and are shown in Table 6.2.1-10. Using the values from Table 6.2.1-10 in the statistical method described previously, it was concluded that the probability distributions from M10 and M1 were not significantly different in the period from 30-70 sec, i.e., from a statistical standpoint, the fluctuations for M10 could be the same as for M1.

In the period from 70-105 sec during the M1 test, there were a large number of eight downcomer pool chugs, and the highest peak wall pressures for the test occurred during this period. (See Figure 6.2.1-10) In contrast, the wall pressure peaks for M10 are steadily decreasing during this same time (See Figure 6.2.1-13) and are smaller than those seen in M1. From 105 sec to the end of the test, the peak wall pressures in M1 are decreasing with time except for occasional large fluctuations, which are probably the result of some highly synchronized downcomer chugs. For the M10 Test, in this period, the wall pressure peaks continue to decrease regularly with time and no large fluctuations are seen. The highest peaks are less than th in Test M1.

In summary, the peak wall pressures comparison between M10 shows that for the period 30-70 sec, there is no significant statistical difference between the tests and for the period from 70 sec to the end of the test, the wall pressure peaks are lower for M10. These lower peak pressure values for M10 after 70 sec are likely a result of the slightly higher temperatures near the downcomer exit for M10 when compared with M1 temperatures at equivalent downcomer steam mass fluxes (Figure 6.2.1-3).

6.2.1.7 Vent System Pressures. The vent system pressure response was recorded throughout each test using two flushmount pressure transducers in each vent line and one in the vent header, as shown on Figures 3.4-3 and 3.4-4. Typical time history traces of two of these pressures during chugging are shown in Figures 6.2.1-82 to 6.2.1-85. Transducer P2004 is located in the North vent line near the wetwell and transducer P5901 is in the top of the vent header between downcomers 5 and 6.

Figures 6.2.1-82 and -83 show these two pressures during a Type 2 chugging period early in Test M1. They are nearly identical and are essentially a modulated seven to eight-Hz sinusoidal signal.

During a Type 1 chugging period, as shown in Figures 6.2.1-84 and -85, the pressures are again nearly identical, but there is an additional oscillation present corresponding to the chugging frequency. These oscillations are the result of rapid condensation in the downcomers which quickly reduces the pressure throughout the vent system and into the drywell. The five psi decrease shown in these figures was the largest seen during any chugging period in the test series.

Table 6.2.1-1

SUMMARY OF CHUGGING DATA BASE

Test Number	M1	M4	M9	M10
Initial Conditions	nominal	5 psig free space press.	4.5 feet submergence	no vacuum breaker
*Approximate Chugging Periods, Seconds	30-330	26-116	25-305	20-120 250-305
Seconds of Chugging Data Recorded	300	90	280	155
Approximate Number of Downcomer Chugs	670	110	480	200

*Time = 0 is the start of data recording

1157 254

Table 6.2.1-2

CHUGGING PERIODS OF TEST M1

Time Period secs	Elapsed Time sec	Chugging Type	No. of Downcomer Chugs	Average Downcomer Chugs per Sec.
40.0 - 74.9	34.9	2	100	2.9
74.9 - 109.2	34.3	1	95	2.8
109.2 - 144.9	35.7	2	66	1.8
144.9 - 159.6	14.7	1	52	3.5
159.6 - 169.0	9.4	2	11	1.2
169.0 - 228.0	59	1	229	4.1
228.0 - 330.0	102	2	104	1.0
Totals - Type 1	108	-	396	3.5
Totals - Type 2	182	-	281	1.5

Table 6.2.1-3

PARAMETERS USED FOR CHUG IDENTIFICATION

Test Number	M1	M8	M9
DT1, (Interval for Calculation of Acceleration Mean, Sec)	0.100	0.100	0.100
DT2, (Time Search Increment, Sec)	+0.010	+0.001	+0.001
DA, (Acceleration Change Criterion, g's)	7.0	3.0	3.0
DT3 DT4, (Level Probe Wetting Search Increment, Sec)	-0.07 to +0.10	-0.02 to +0.04	-0.02 to +0.04
L1, (Level Probe Wetting Criterion, Volts)	<6.0	<6.0	<6.0

Table 6.2.1-4

SUMMARY OF CHUG SYNCHRONIZATION ANALYSIS FOR TEST M4

	5 g Criteria *DTC - 100 msec	3 g Criteria DTC = 100 msec	3 g Criteria DTC = 300 msec
No. of Pool Chugs	33	55	45
Mean Time Between Pool Chugs	2.38	1.63	1.99
% of Pool Chugs with 5 or More Dowcomer Chugs	6	13	18
Duration** of Pool Chugs with 5 or More Downcomer Chugs	79 to 118 msec	82 to 232 msec	99 to 232 msec

*DTC = Max. time between downcomer chugs.
**Duration - time between the start of the first downcomer chug and the start of the last downcomer chug.

Table 6.2.1-5

SUMMARY OF POOL CHUG SYNCHRONIZATION DATA

Test	Chugging Type	Mean Downcomer Chugs per Pool Chug	% of Pool Chugs with 5 of more Downcomer Chugs
M1	1	6.9	91
M1	2	2.7	20
M4	2	2.0	12
M9	2	2.1	12

Table 6.2.1-6

AVERAGE PERIOD BETWEEN POOL CHUGS

Test	Chug Type	Time Interval Seconds	Chug Period, Seconds
M1	1	74.9 - 109.2	2.4
	1	144.9 - 159.6	2.1
	1	169.0 - 228	1.6
M1	2	40.0 - 74.9	1.1
	2	109.2 - 144.9	1.1
	2	159.6 - 169.0	0.9
	2	228 - 330	2.4
M4	2	26.3 - 116.0	1.7
M9	2	32.2 - 124.7	1.1
	2	125.4 - 211.7	1.3
	2	217.8 - 303.9	1.8

1157 257

Table 6.2.1-7

SUMMARY OF CHUGGING FREQUENCIES - LOCAL WALL PRESSURE (P3185)

Test	PSD Time Interval (seconds)	f_1	f_2	f_3
M1	55.8 - 57	8.5*	13.6	36.5
	82.5 - 83.7	6.0*	11.9	42.5
	137 - 138.2	6.8*	13.6	29.7
	147 - 148.2	7.6	13.6*	36.5
	173 - 174.2	6.8*	15.3	29.7
	272.4 - 273.6	6.8	13.6	39.1*
M4	36.8 - 37.4	7.6*	13.3	45.8
	37.4 - 38.5	7.6	15.3	40.1*
	66.8 - 67.4	7.6*	11.4	45.8
	67.4 - 68.5	7.6*	16.2	45.8
	88.3 - 88.9	7.6*	11.4	45.8
	88.9 - 90.0	7.6	13.4	46.7*
M9	47.5 - 48.6	7.6*	13.4	40.1
	73.4 - 74.5	7.6*	13.4	42.0
	191.5 - 192.6	6.7*	12.4	37.2
	209.1 - 210.2	6.7*	12.4	42.9
	251.4 - 252.5	7.6*	13.4	50.5
	303.5 - 304.6	7.6*	13.4	37.2
M10	28.4 - 29.5	6.7*	15.3	37.2
	44.1 - 45.2	7.6	13.4*	36.2
	76.1 - 77.2	7.6*	13.4	40.0
	101.9 - 103.0	7.6*	14.3	46.7

*indicates dominant frequency

f_1 - frequency with the highest PSD value between 5 and 10 Hz
f_2 - frequency with the highest PSD value between 10 and 25 Hz
f_3 - frequency with the highest PSD value between 25 and 50 Hz

1157 258

Table 6.2.1-8

SUMMARY OF CHUGGING FREQUENCIES - AVERAGE WALL PRESSURE

Test	PSD Time Interval (seconds)	f_1	f_2	f_3
M1	55.8 - 57.0	8.5*	11.9	46.7
	82.5 - 83.7	6.0*	11.9	42.5
	137 - 138.2	6.8*	12.7	29.7
	147 - 148.2	6.0*	13.6	34.0
	173 - 174.2	6.8*	17.0	34.0
	272.4 - 273.6	6.8*	13.6	39.1
M4	36.8 - 37.4	7.6*	13.3	34.3
	37.4 - 38.5	7.6*	13.4	32.4
	66.8 - 67.4	7.6*	13.3	45.8
	67.4 - 68.5	7.6*	13.4	32.4
	88.3 - 88.9	7.6*	11.4	45.8
	88.9 - 90.0	7.6*	13.4	47.7
M9	47.5 - 48.6	7.6*	13.4	35.3
	73.4 - 74.5	7.6*	13.4	46.7
	191.5 - 192.6	6.7*	12.4	37.2
	209.1 - 210.2	6.7*	12.4	37.2
	251.4 - 252.5	7.6*	13.4	51.5
	303.5 - 304.6	7.6*	13.4	41.0
M10	28.4 - 29.5	6.7*	18.1	36.2
	44.1 - 45.2	7.6	13.4*	34.3
	76.1 - 77.2	7.6*	12.4	37.2
	101.9 - 103.0	7.6*	13.4	35.3

*indicates dominant frequency

f_1 - frequency with the highest PSD value between 5 and 10 Hz
f_2 - frequency with the highest PSD value between 10 and 25 Hz
f_3 - frequency with the highest PSD value between 25 and 50 Hz

1157 259

Table 6.2.1-9

TRANSDUCERS FOR CHUGGING WALL PRESSURE DISTRIBUTIONS

Circumferential Centerline		Bottom Centerline	
Transducer	Angle, Degrees	Transducer	Distance from Bottom Centerline, Feet
3095	90	P3189	-9.0
P3106	105	P3188	-7.0
P3125	120	P3187	-4.5
P3155	150	P3186	-2.0
P3185	180	P3185	0
P3195	196.7	P3183	+4.5
P3215	210	P3181	+9.0
P3245	240		
P3255	255		
P3005	270		

Edge of Wetwell = ±9.75 Feet

South = (-), North = (+)

Bottom of Downcomers at 115.5°, 244.5°

Nominal Water Level at 101.0° 259.0°

Vertical Upward = 0°

East = 90°

1157 260

Table 6.2.1-10

COMPARISON OF MEAN AND STANDARD DEVIATION OF PEAK WALL PRESSURE VALUES FROM TESTS M1 AND M10 (30 to 70 Sec)

	M1	M10
Mean Positive Peak, psi	1.18	1.36
Standard Deviation, psi	0.28	0.31
Mean Negative Peak, psi	-1.24	-1.43
Standard Deviation, psi	0.31	0.33
Number of Data Points	40	40

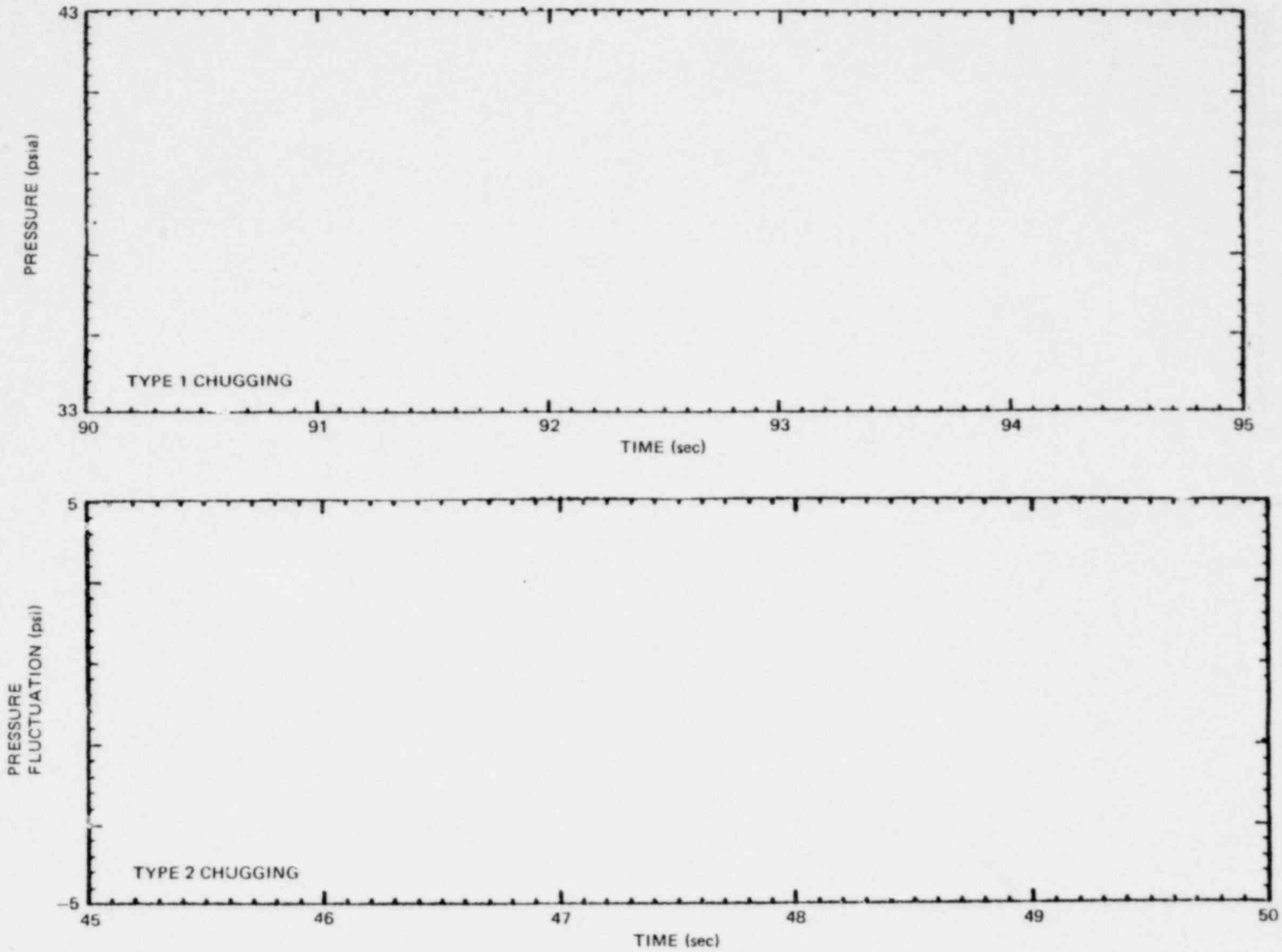

Figure 6.2.1-1. Comparison of Typical Wall Pressure Traces for Type 1 and Type 2 Chugging

*Proprietary information deleted

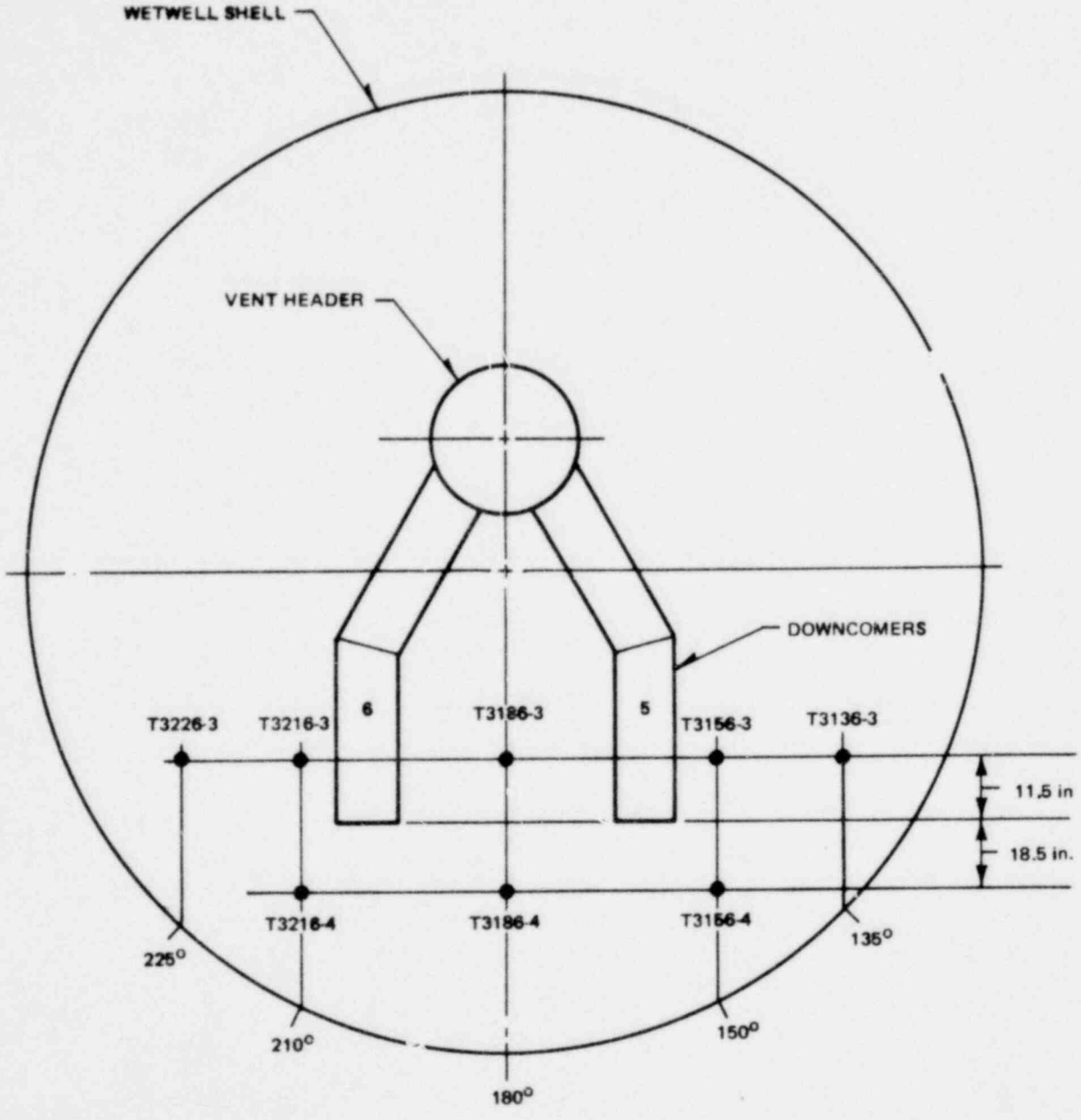

1157 263

Figure 6.2.1-2. Location of Thermocouples for Calculation of Pool Temperature at the Bottom of the Downcomer

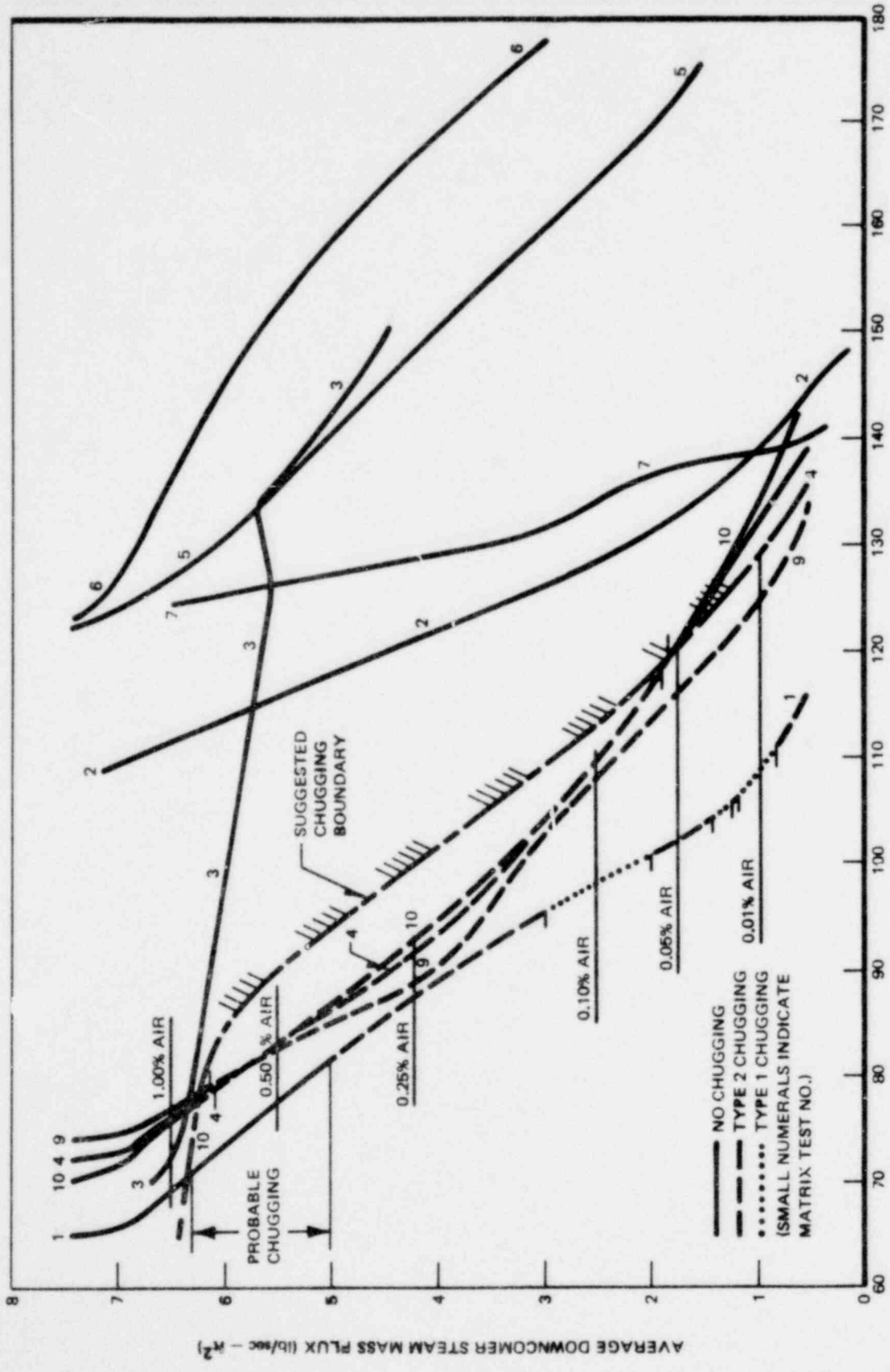

Figure 6.2.1-3. Mass Flux and Pool Temperature Conditions for Chugging

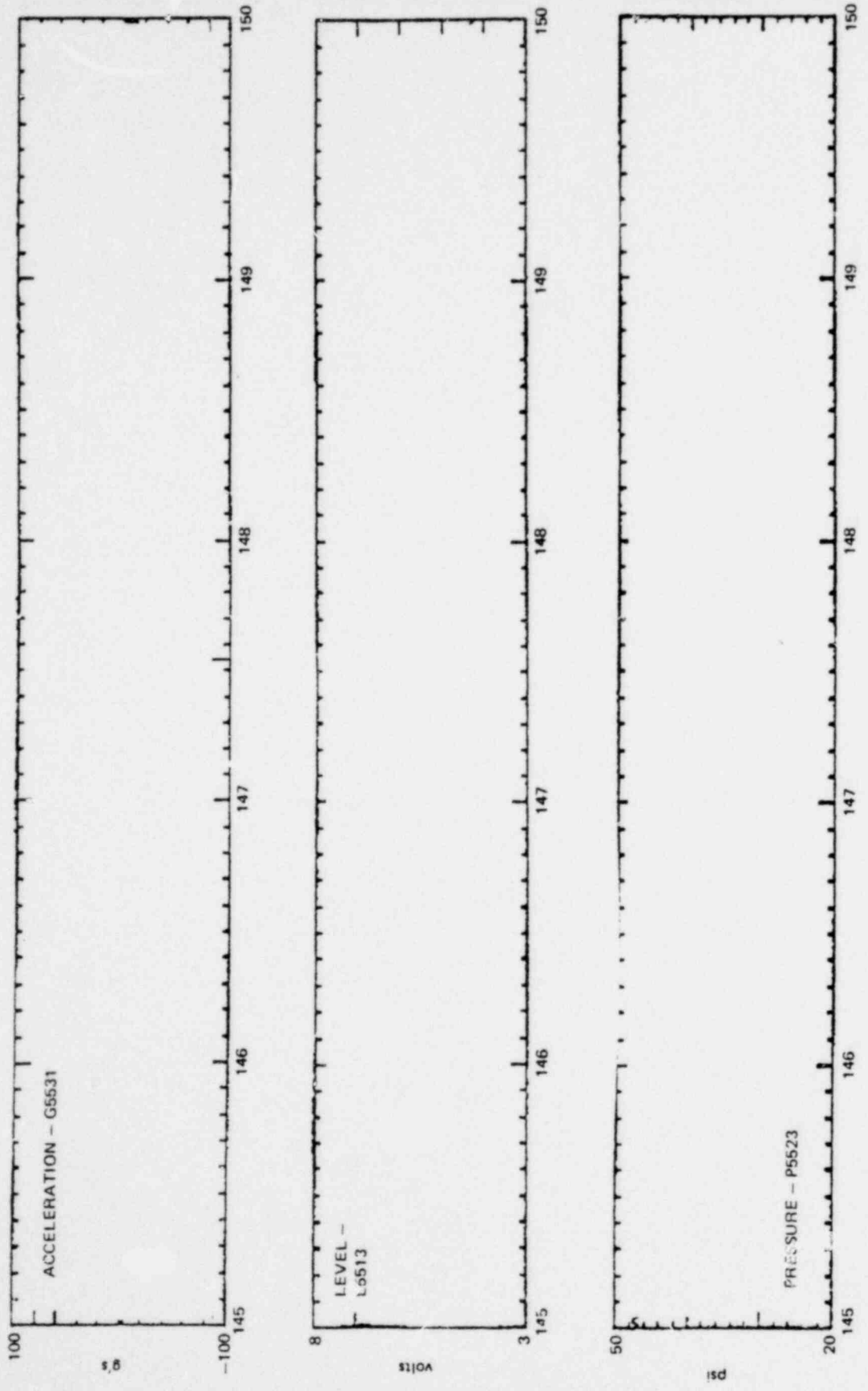

Figure 6.2.1-4. Downcomer Acceleration, Water Level and Pressure During Chugging

*Proprietary information deleted

POOL CHUG CHRONOLOGICAL REPORT

	START TIME (SEC)	MEAN TIME (SEC)	NUMBER DC'S THIS POOL	TIME SINCE LAST POOL MEAN SEC	DOWNCOMER NUMBERS	DOWNCOMER CHUG INIT TIMES (SEC)	TIME INCR DC CHUG VS MEAN POOL (SEC)
16.	144.9165	144.9932	8	.8546	7	144.9165	-.076721
					8	144.9464	-.046814
					2	144.9820	-.011230
					6	145.0073	.014038
					3	145.0130	.019775
					4	145.0176	.024414
					5	145.0222	.028992
					1	145.0406	.047363
17.	146.0942	146.1744	7	1.1812	8	146.0942	-.080139
					6	146.1471	-.027283
					4	146.1563	-.018066
					5	146.1896	.015198
					2	146.1954	.020996
					7	146.2045	.030151
					1	146.2333	.058899
18.	147.3375	147.4719	8	1.2975	3	147.3375	-.134460
					5	147.4087	-.063232
					6	147.4432	-.028748
					2	147.4868	.014893
					4	147.4926	.020630
					7	147.5236	.051697
					8	147.5270	.055115
					1	147.5558	.083862
19.	149.4194	149.4586	8	1.9866	7	149.4194	-.039124
					6	149.4424	-.016113
					8	149.4447	-.013855
					5	149.4482	-.010376
					4	149.4620	.003418
					2	149.4700	.011414
					1	149.4849	.026367
					3	149.4964	.037842
20.	151.2682	151.2991	7	1.8406	8	151.2682	-.030945
					4	151.2716	-.027527
					1	151.2946	-.004517
					2	151.2980	-.001099
					6	151.3027	.003540
					5	151.3256	.026489
					7	151.3325	.033386

Figure 6.2.1-5. Sample Pool Chug Chronological Report From Test M1

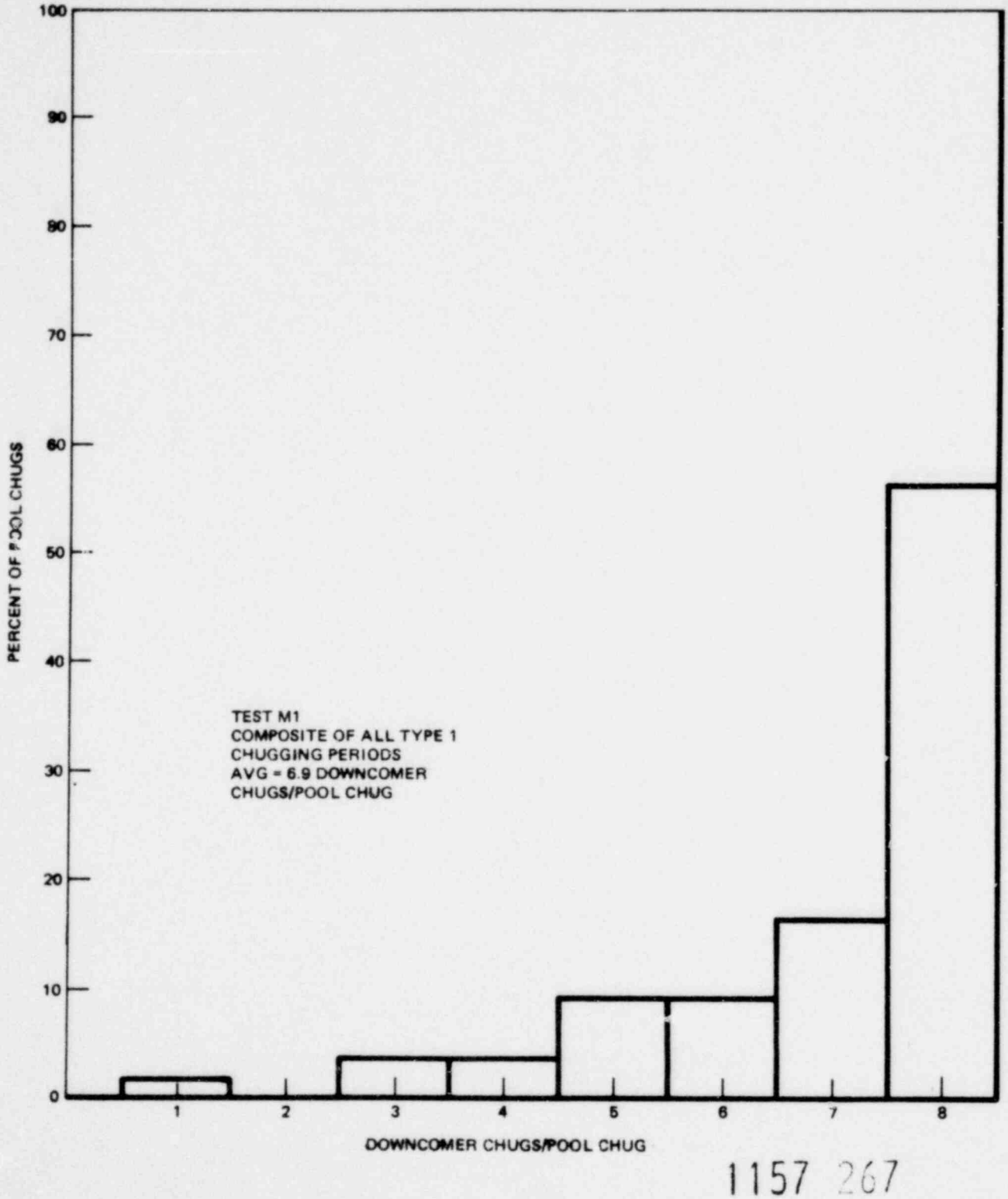

1157 267

Figure 6.2.1-6. Histogram of the No. of Downcomers-Chugs/Pool-Chug for Type 1 Chugging in Test M1

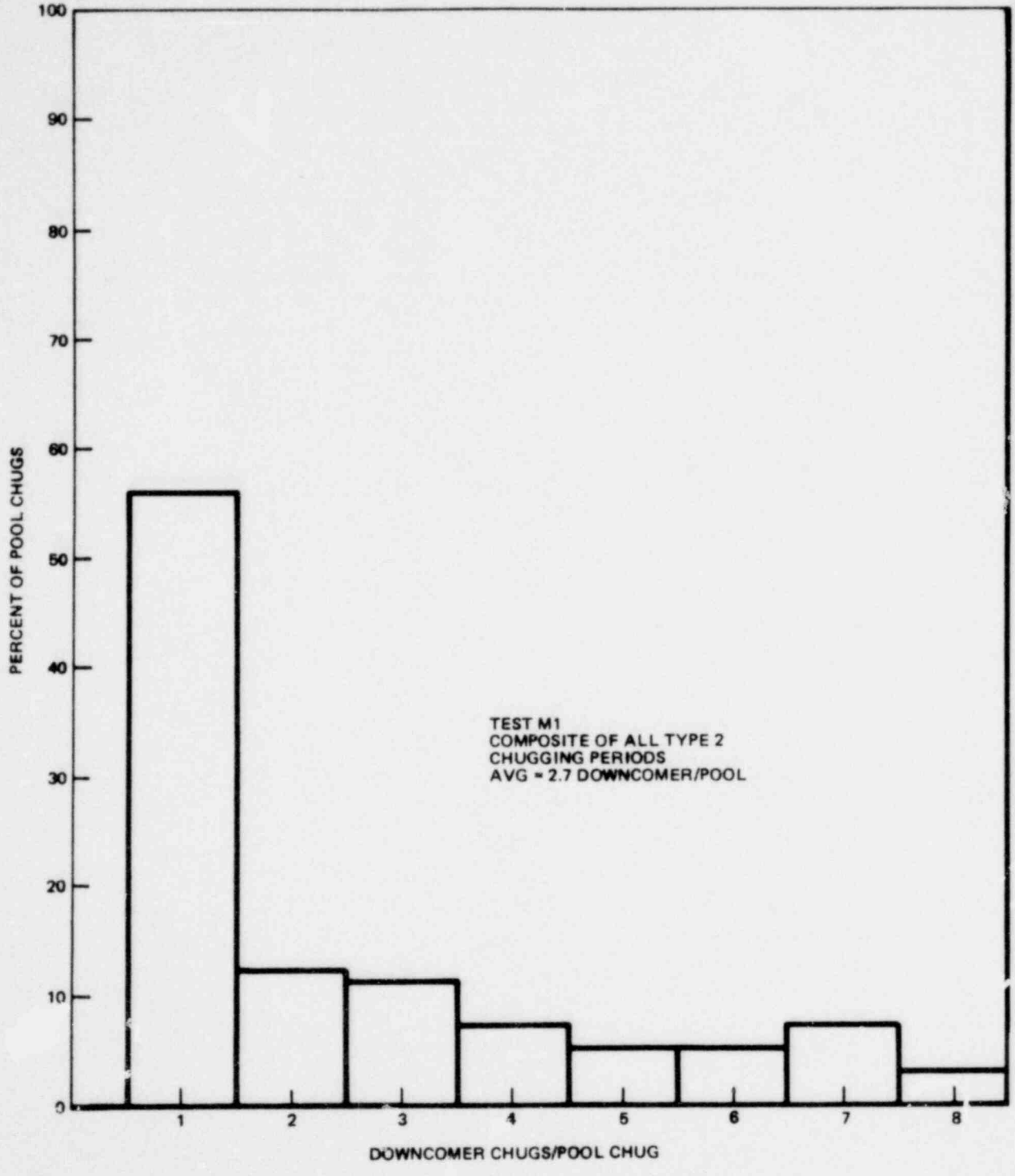

Figure 6.2.1-7. Histogram of the No. of Downcomer Chugs/Pool Chug for Type 2 Chugging in Test M1.

1157 268

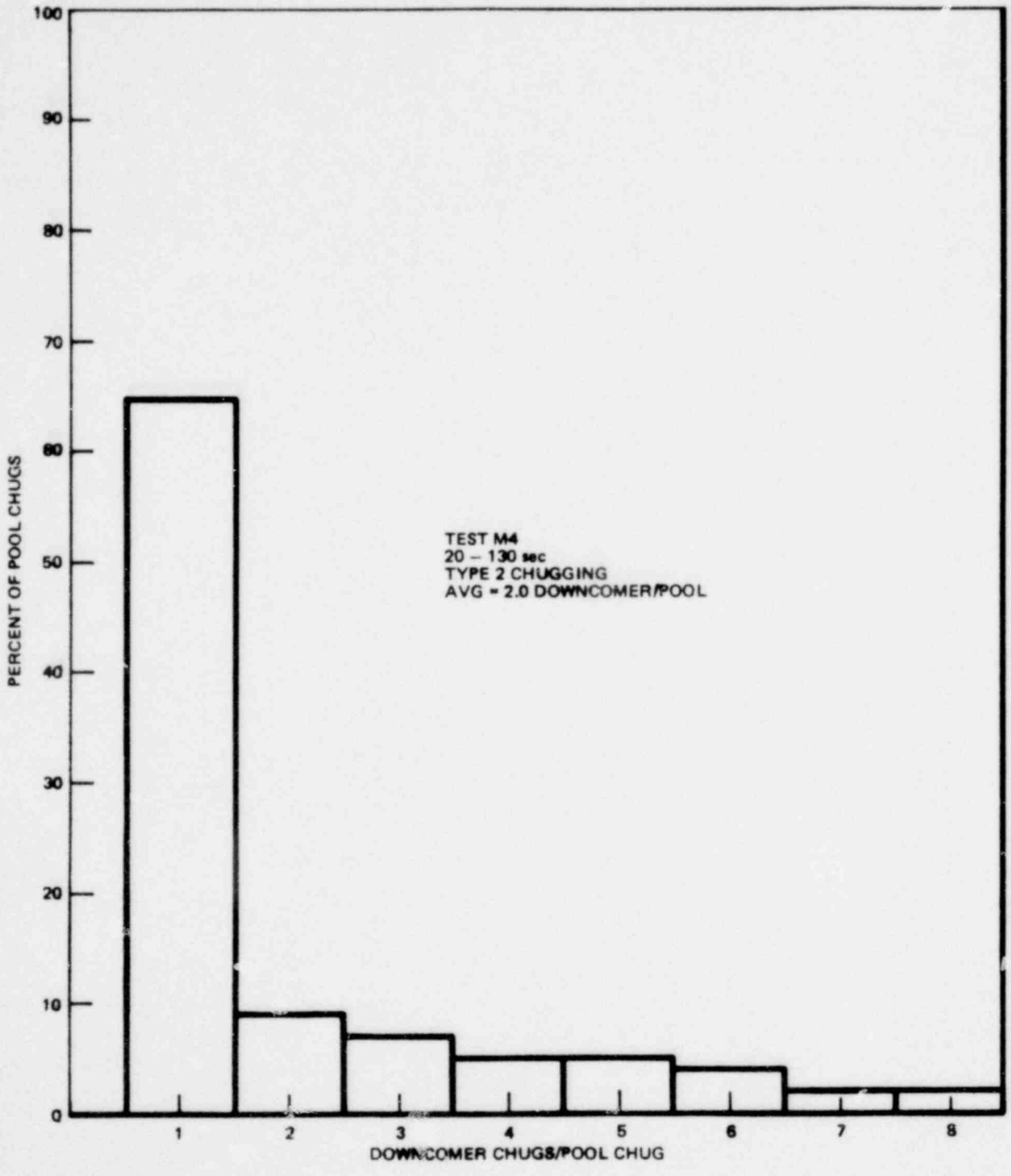

Figure 6.2.1-8. Histogram of the No. of Downcomers-Chugs/Pool-Chug for Type 2 Chugging in Test M4

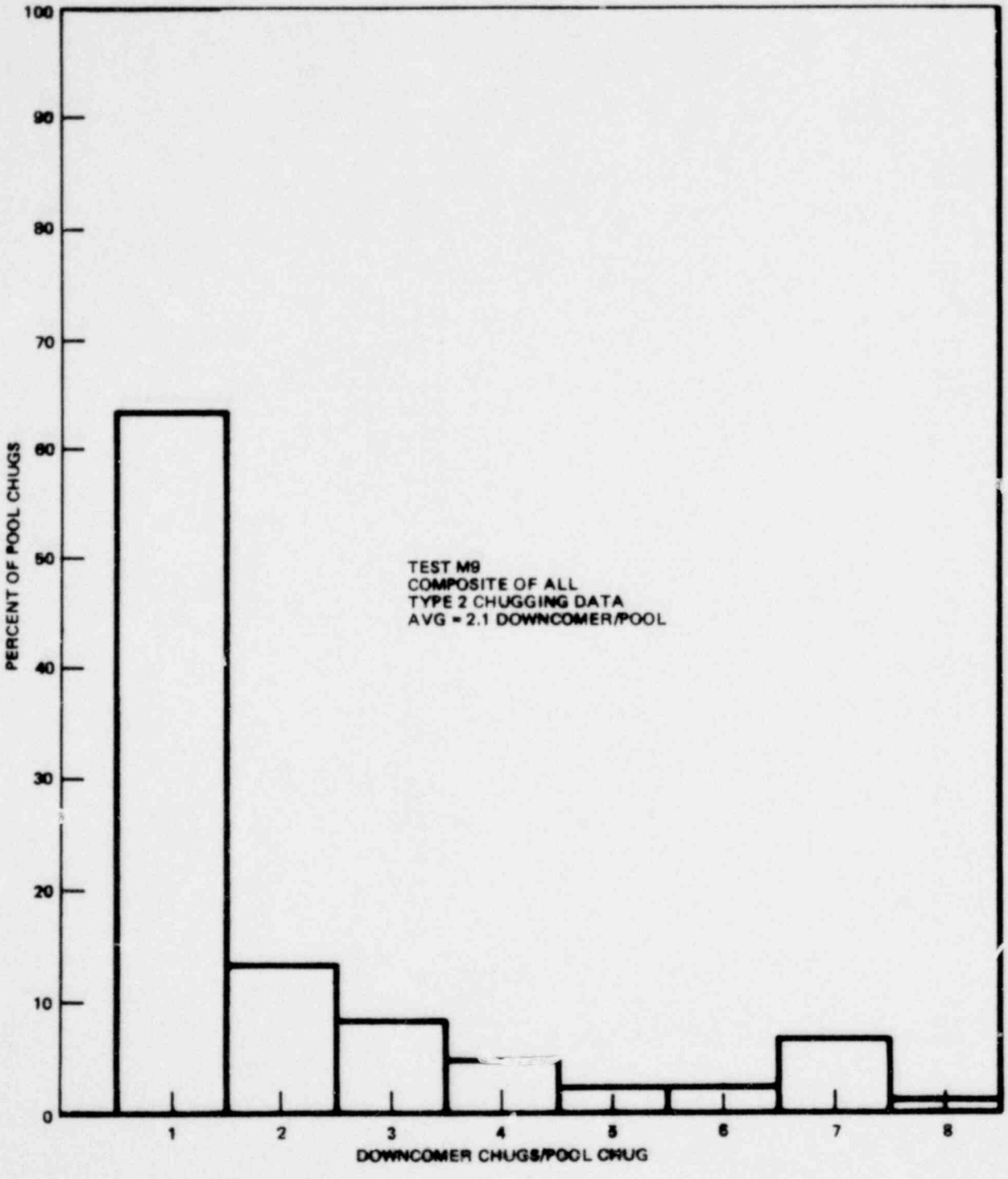

Figure 6.2.1-9. Histogram of the No. of Downcomer Chugs/Pool Chug for Type 2 Chugging in Test M9

1157 270

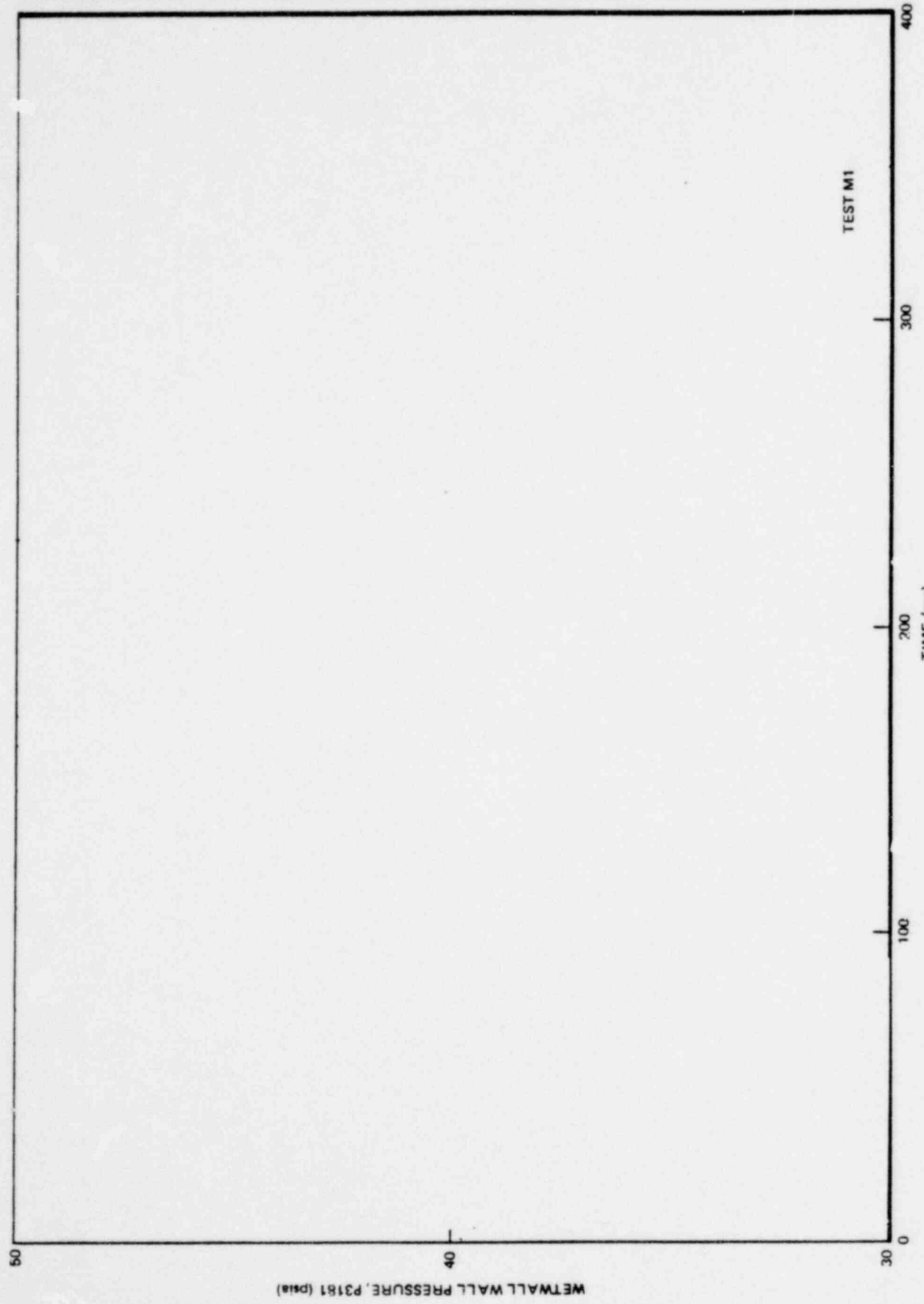

Figure 6.2.1-10. Wall Pressure Time History Throughout Test M1

*Proprietary information deleted

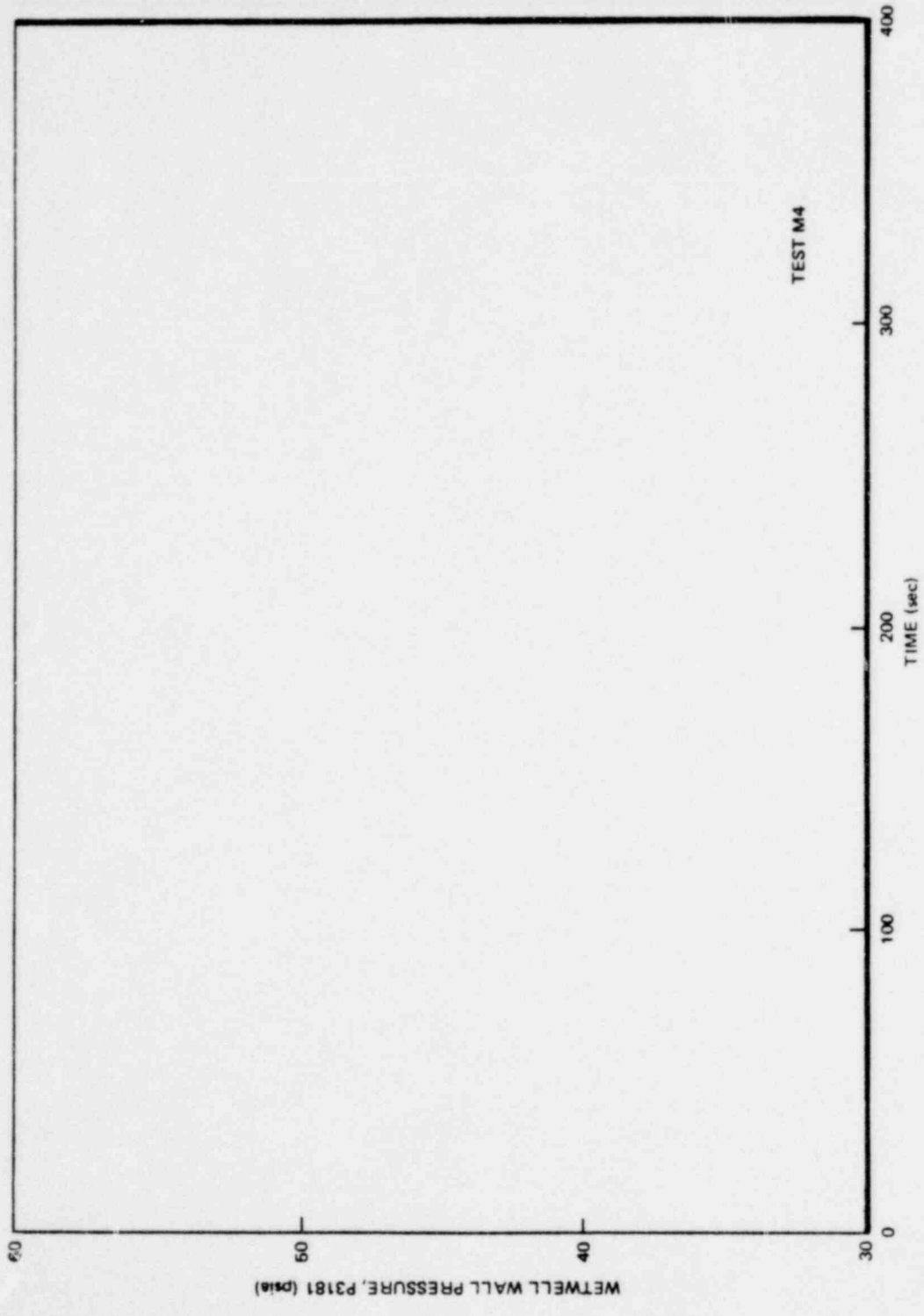

Figure 6.2.1-11. Wall Pressure Time History Throughout Test M4

*Proprietary information deleted

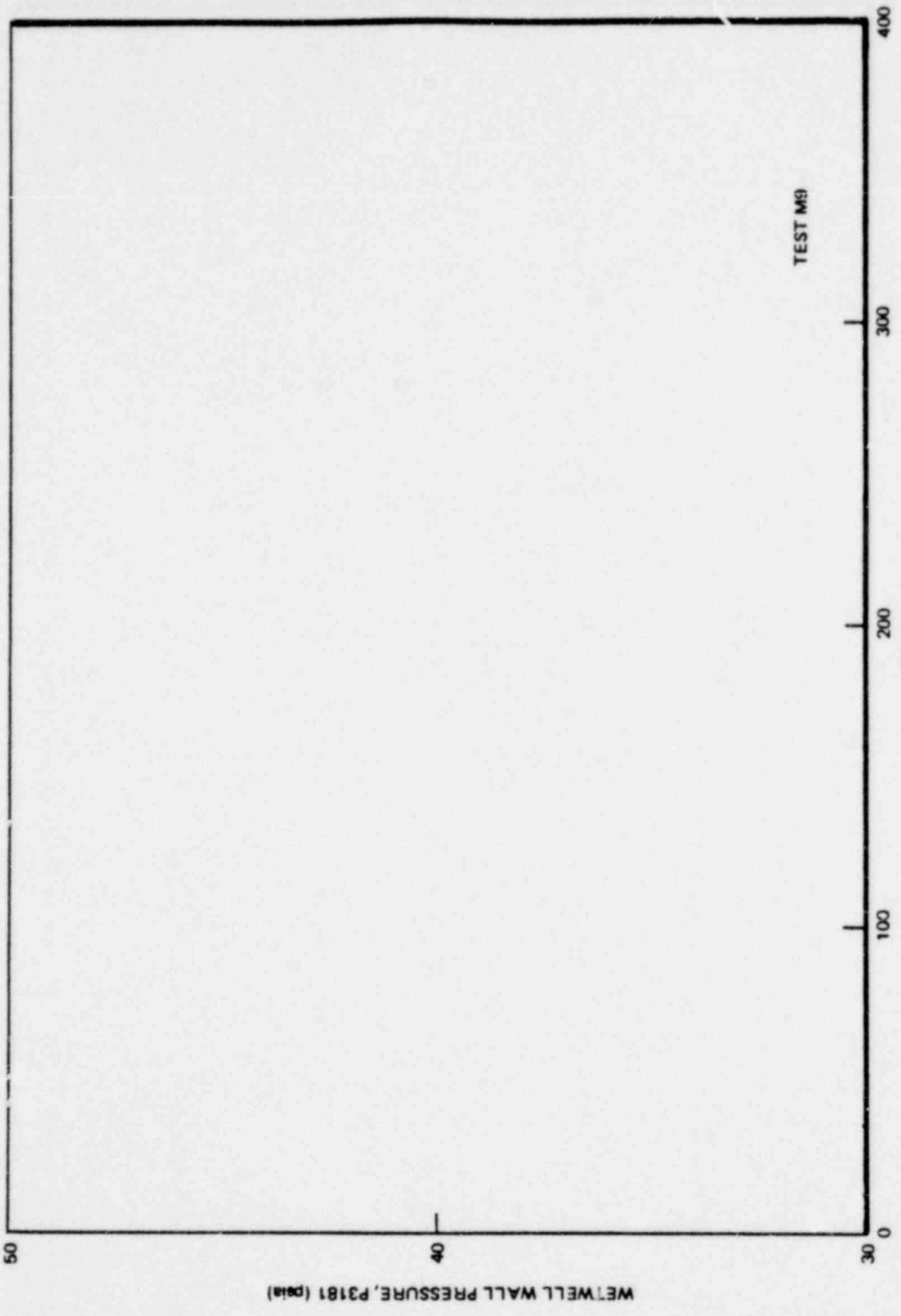

Figure 6.2.1-12. Wall Pressure Time History Throughout Test M9

*Proprietary information deleted

1157 273

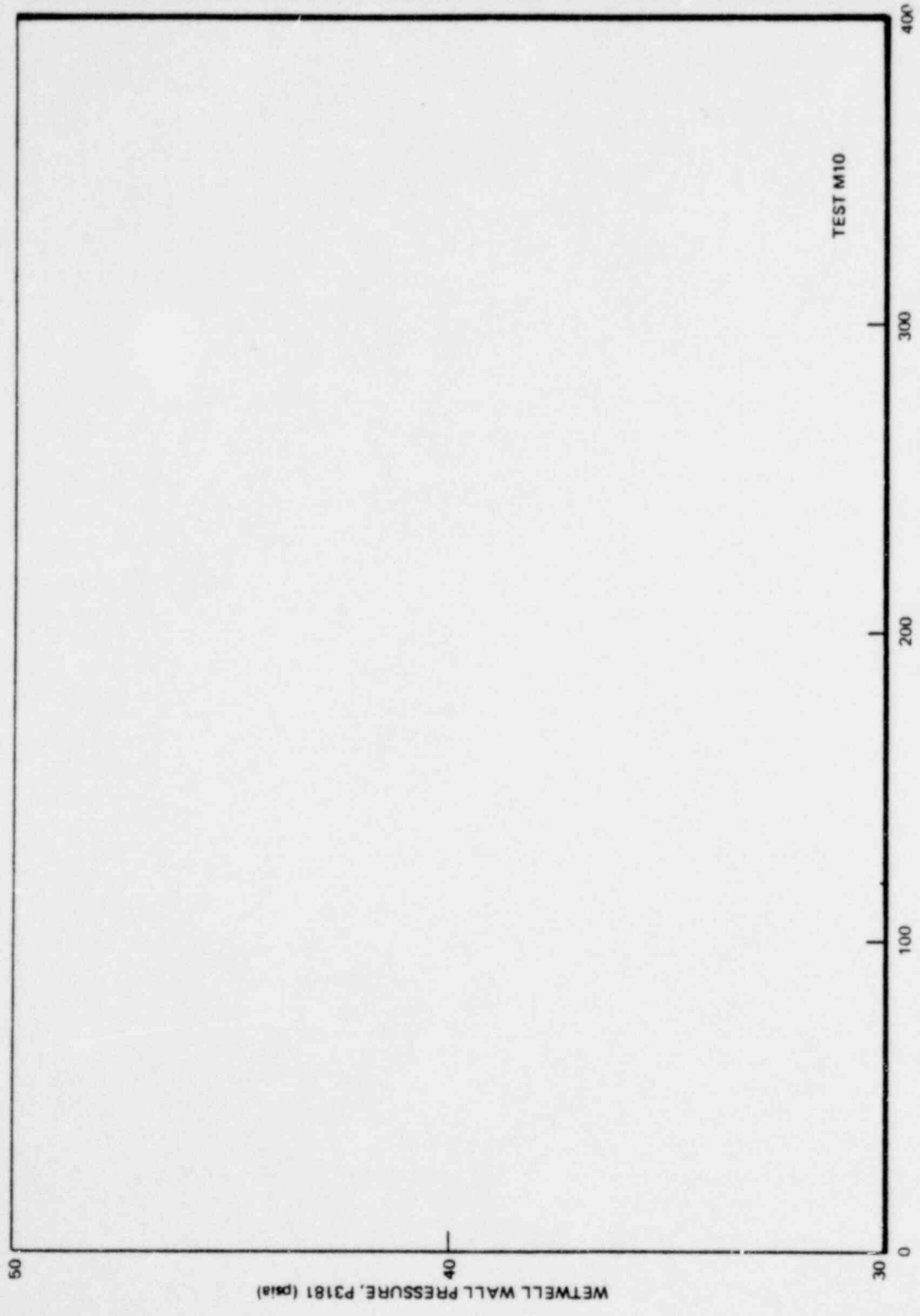

Figure 6.2.1-13. Wall Pressure Time History Throughout Test M10

*Proprietary information deleted

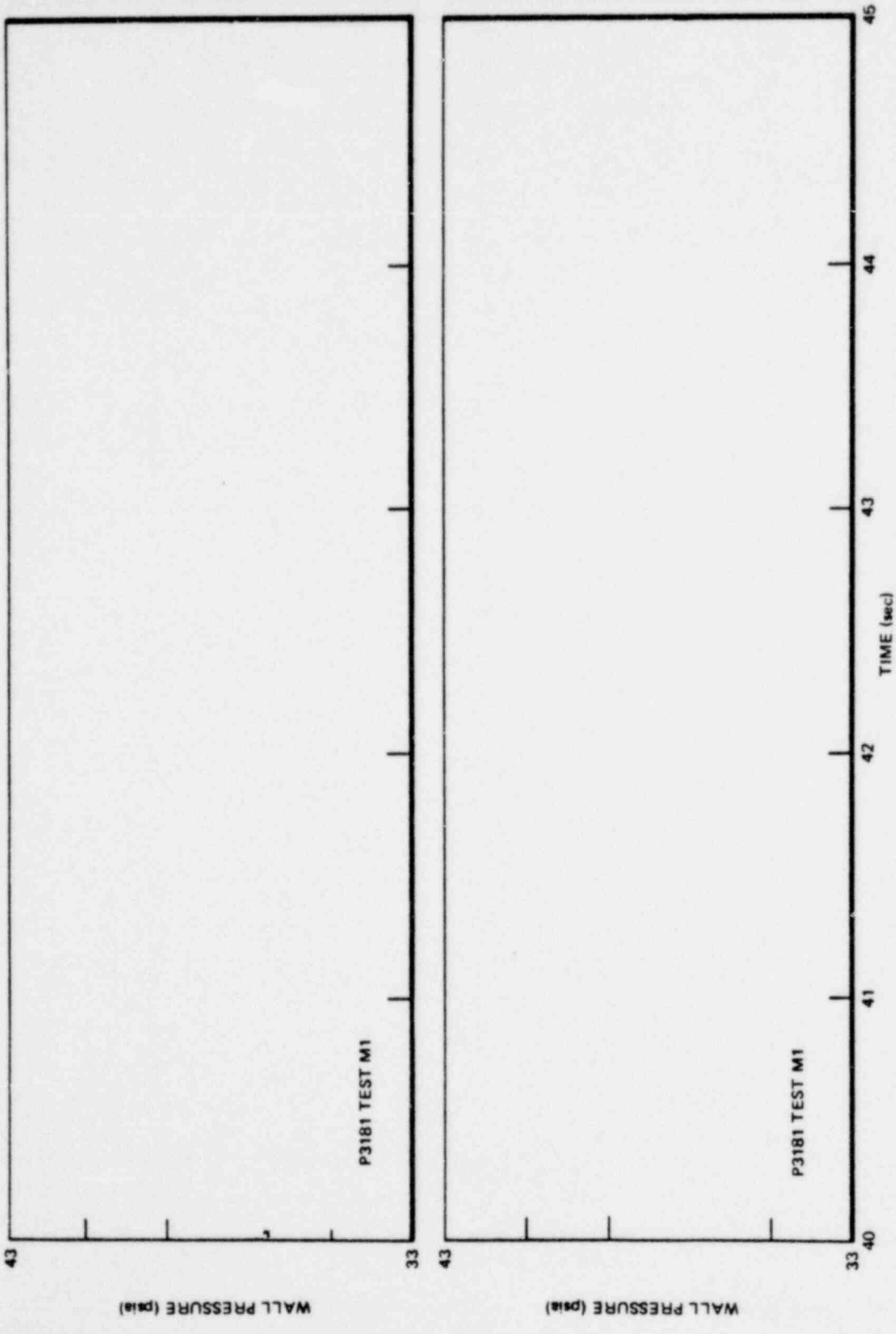

Figure 6.2.1-14. Typical Type 2 Chugging Wall Pressure Signals Early in Test M1

*Proprietary information deleted

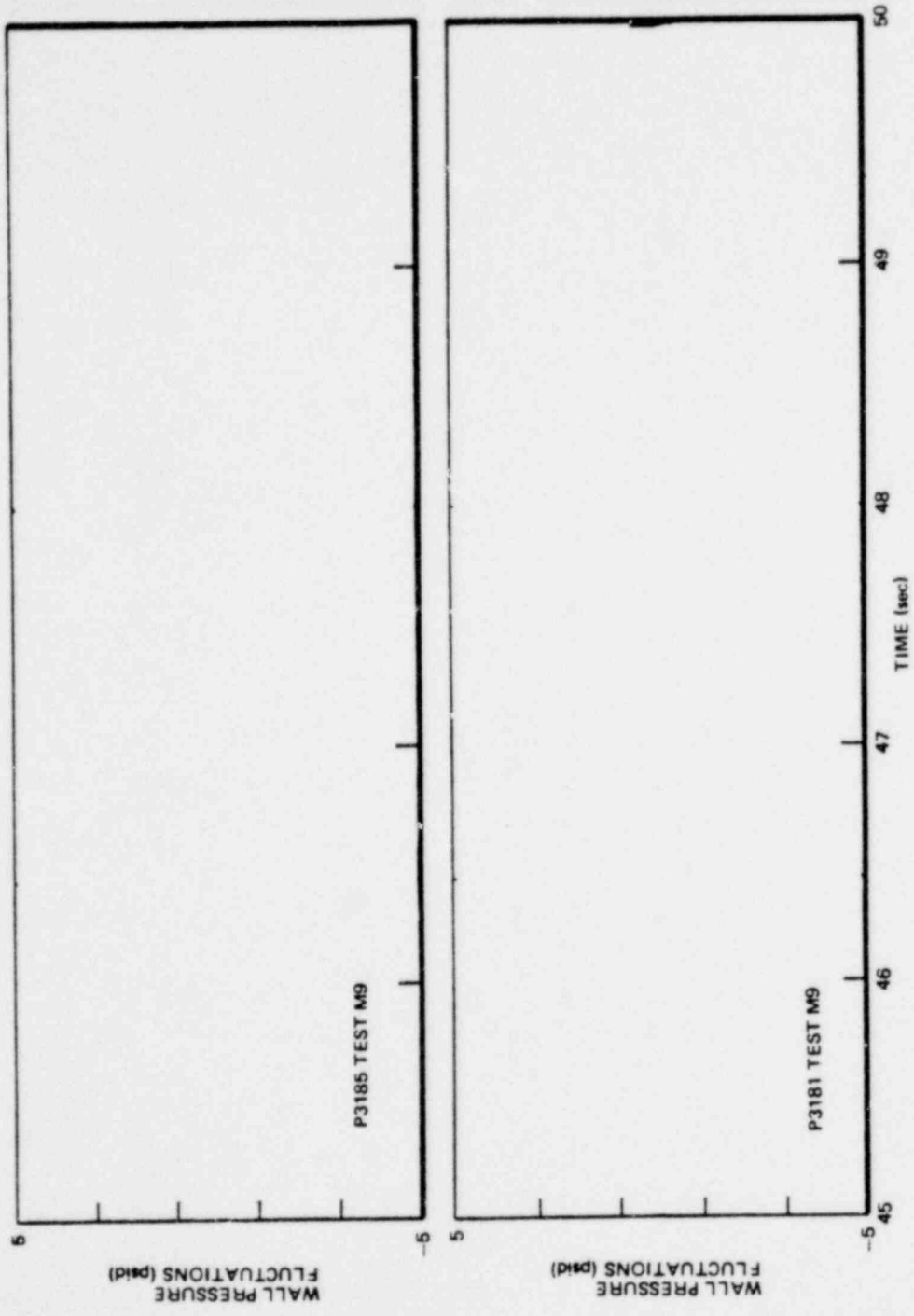

Figure 6.2.1-15. Typical Type 2 Chugging Wall Pressure Signals Early in Test M9

*Proprietary information deleted

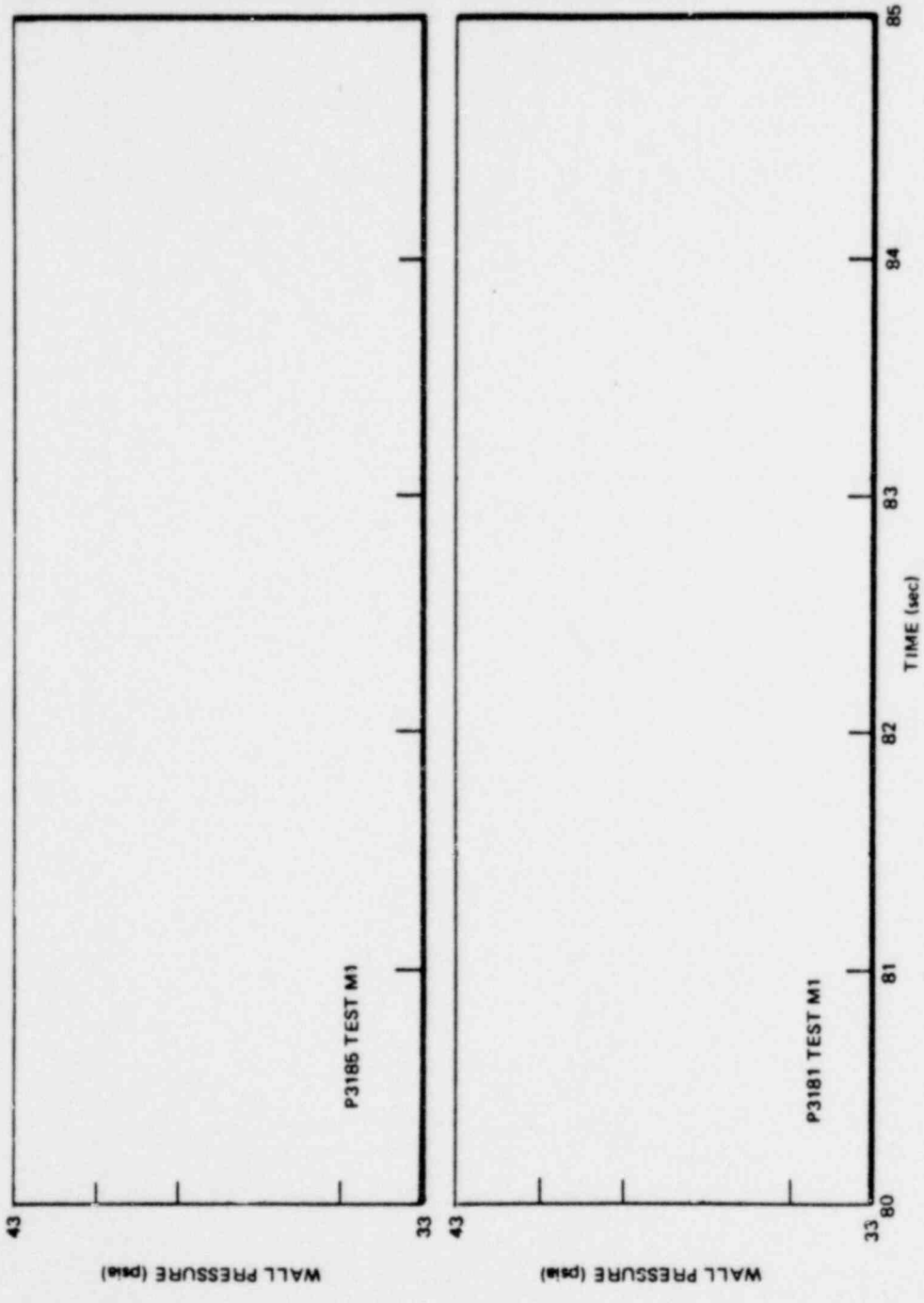

Figure 6.2.1-16. Typical Type 1 Chugging Wall Pressure Signals From Test M1

*Proprietary information deleted

1157 277

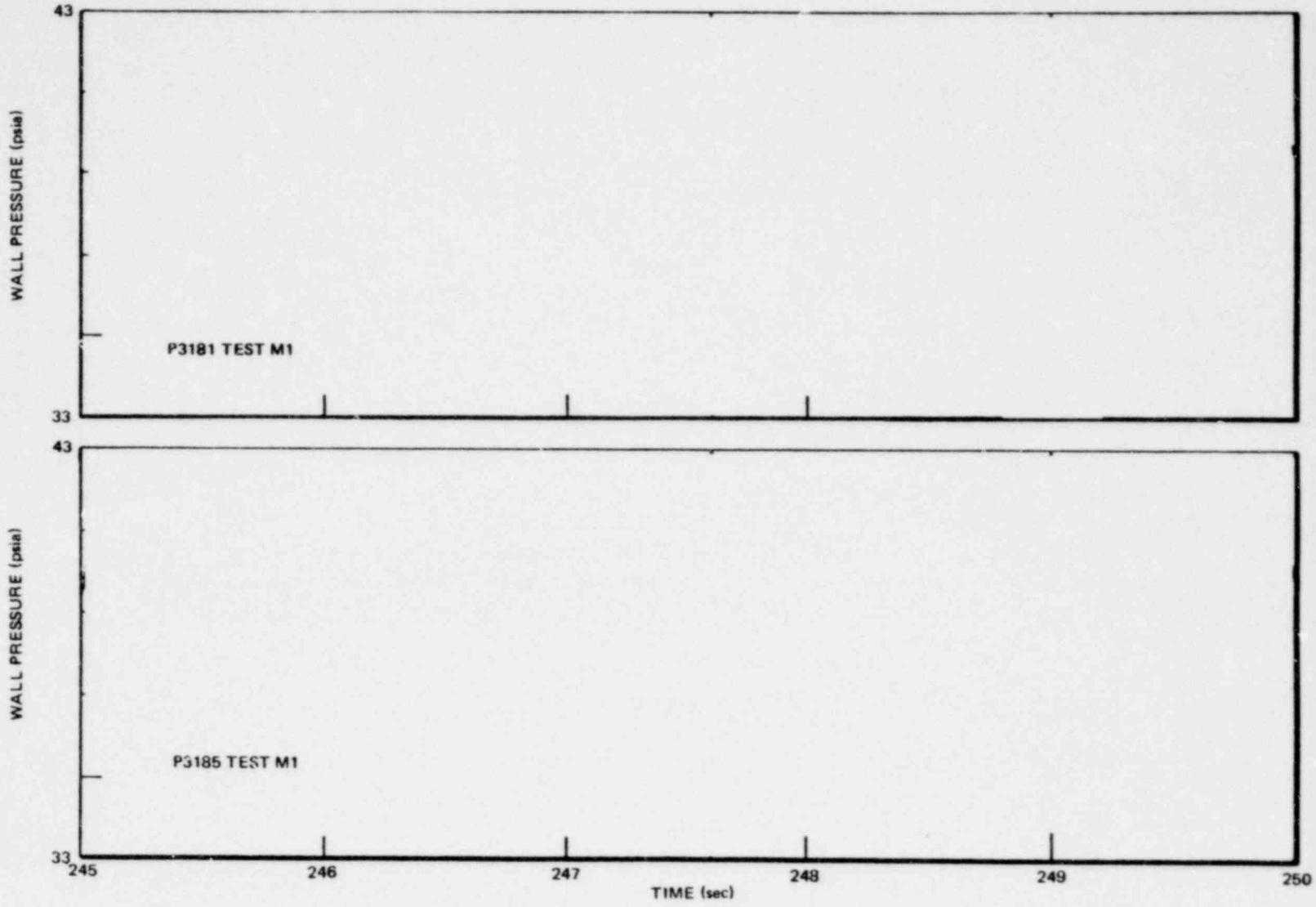

Figure 6.2.1-17. Typical Type 2 Chugging Wall Pressure Signals Late in Test M1

*Proprietary information deleted

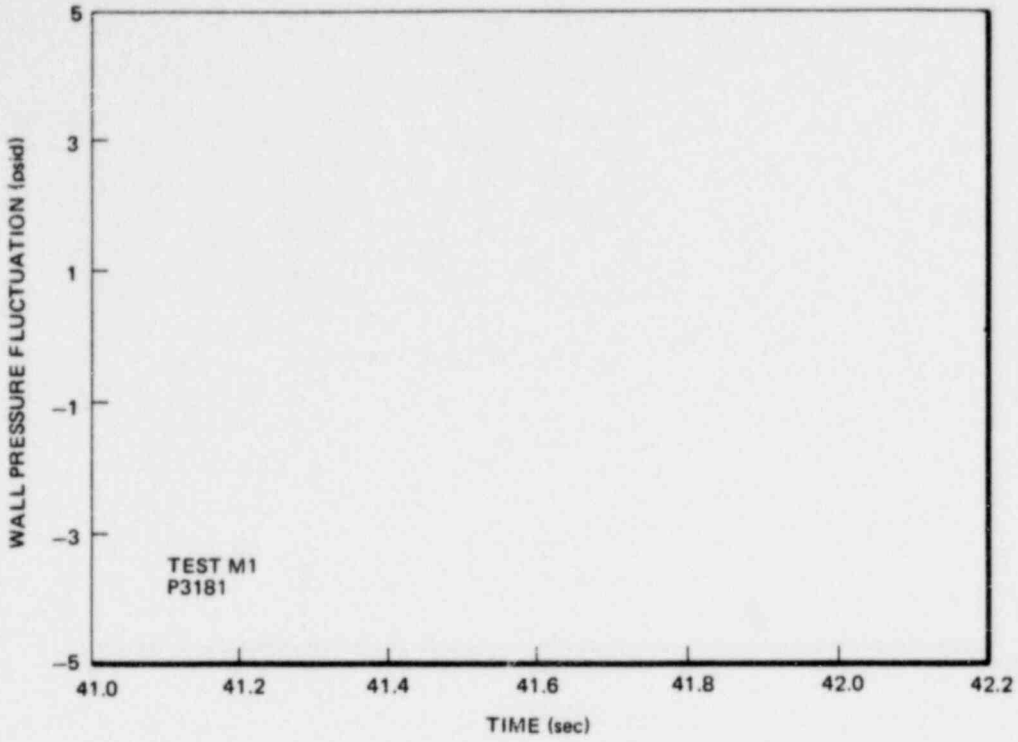

Figure 6.2.1-18. Wall Pressure P3181 During Type 2 Chugging in Test M1, 41.0 to 42.2 Seconds

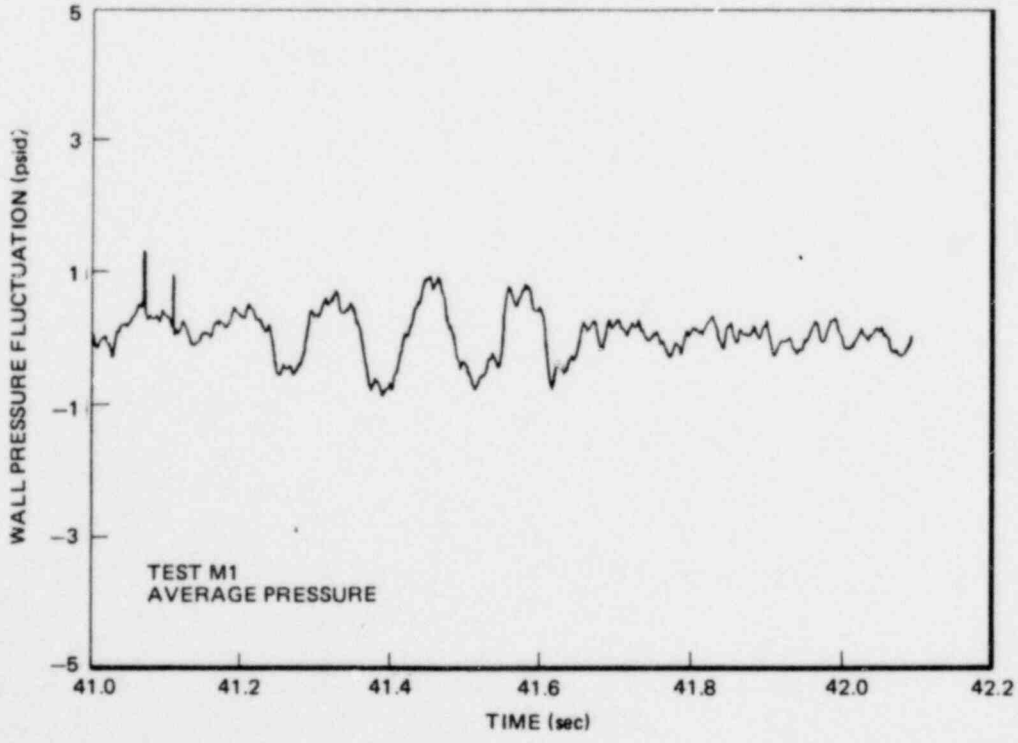

Figure 6.2.1-19. Average Wall Pressure During Type 2 Chugging in Test M1, 41.0 to 42.1 Seconds

*Proprietary information deleted

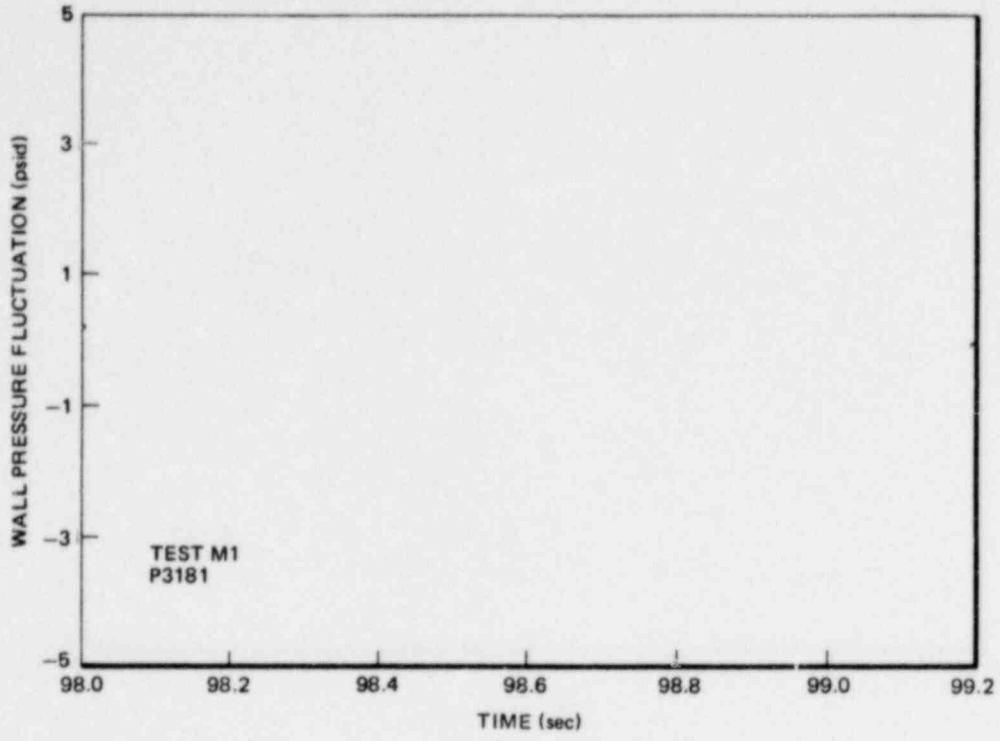

Figure 6.2.1-20. Wall Pressure P3181 During Type 1 Chugging in Test M1, 98.0 to 99.2 Seconds

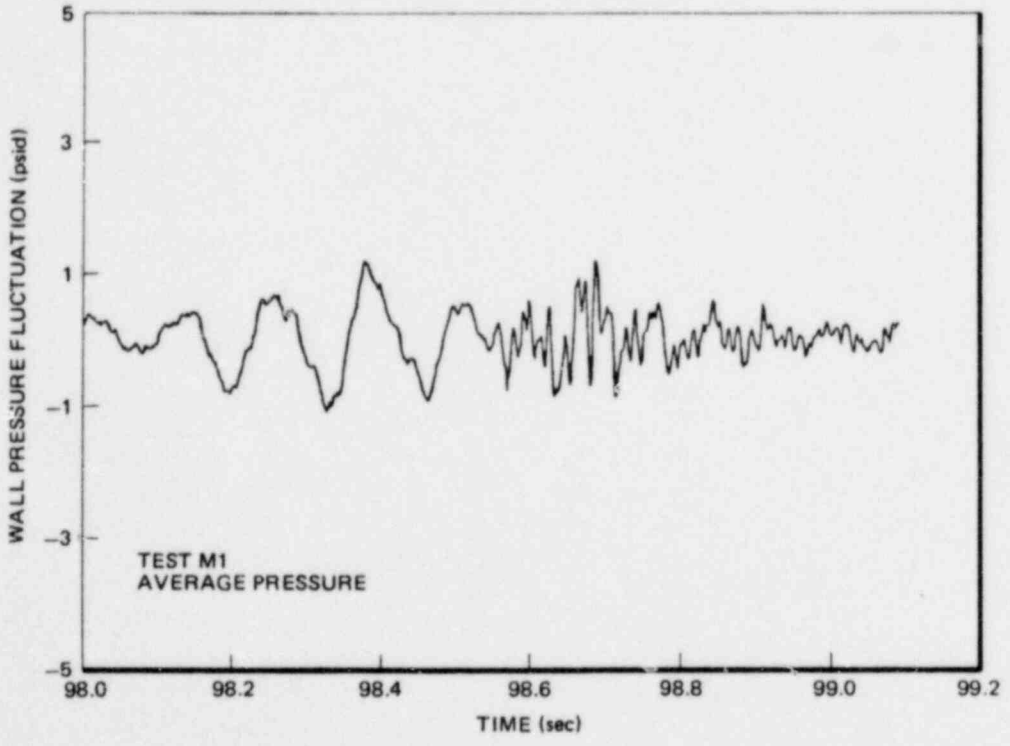

Figure 6.2.1-21. Average Wall Pressure During Type 1 Chugging in Test M1, 98.0 to 99.1 Seconds

1157 280

*Proprietary information deleted

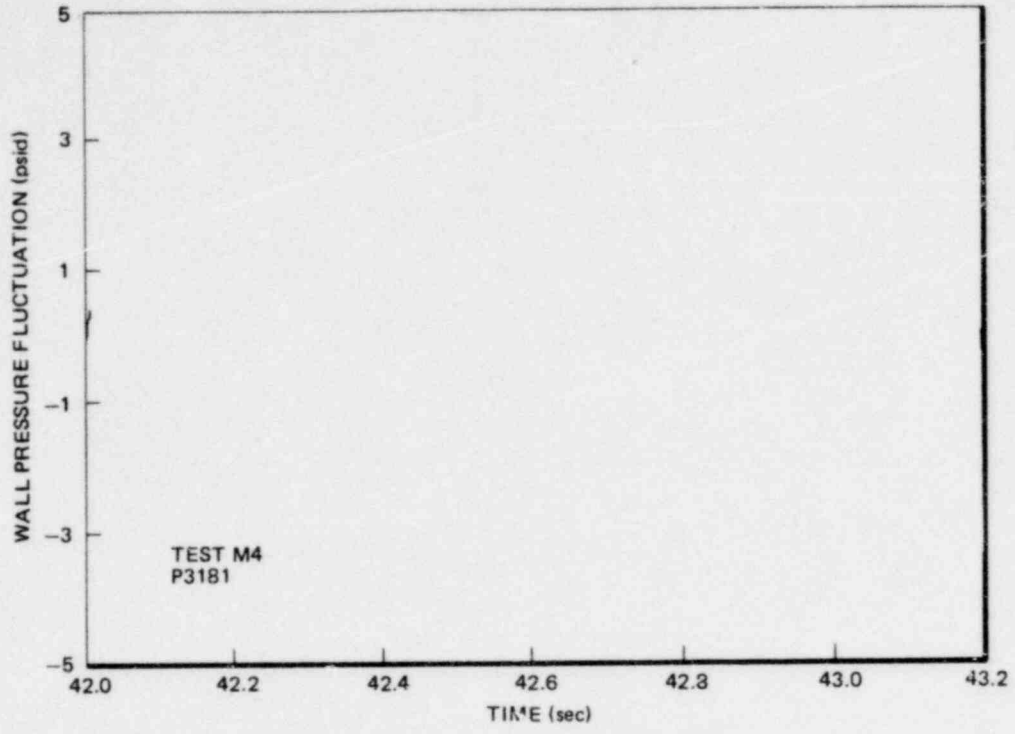

Figure 6.2.1-22. Wall Pressure P3181 During Type 2 Chugging in Test M4, 42.0 to 43.2 Seconds

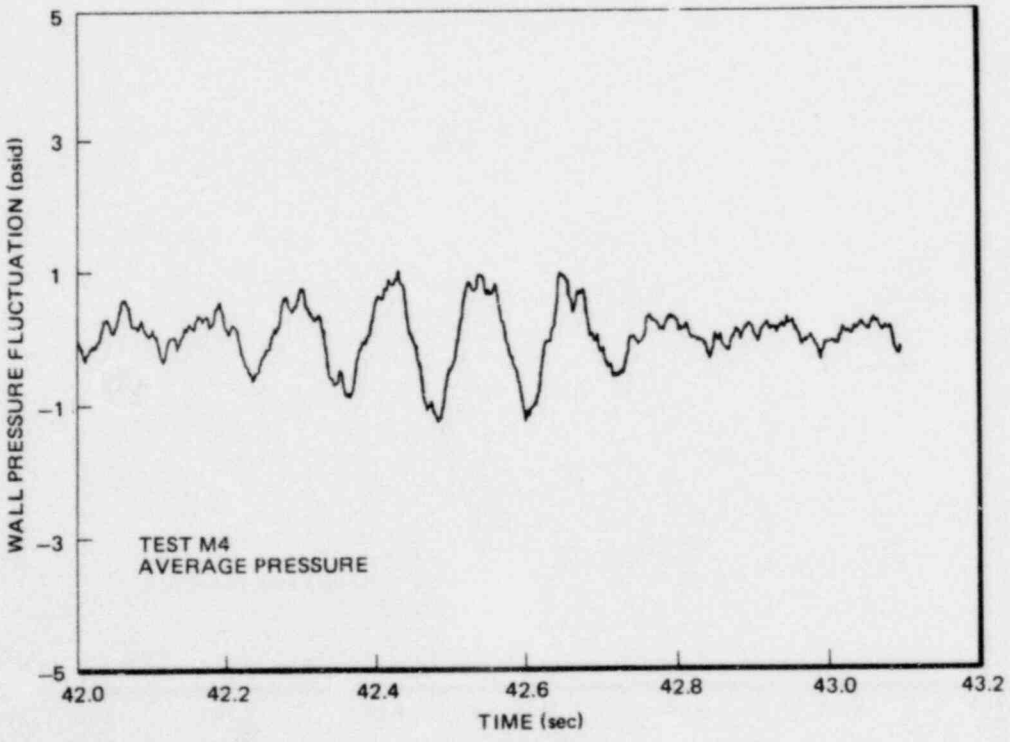

Figure 6.2.1-23. Average Wall Pressure During Type 2 Chugging in Test M4, 42.0 to 43.1 Seconds

*Proprietary information deleted

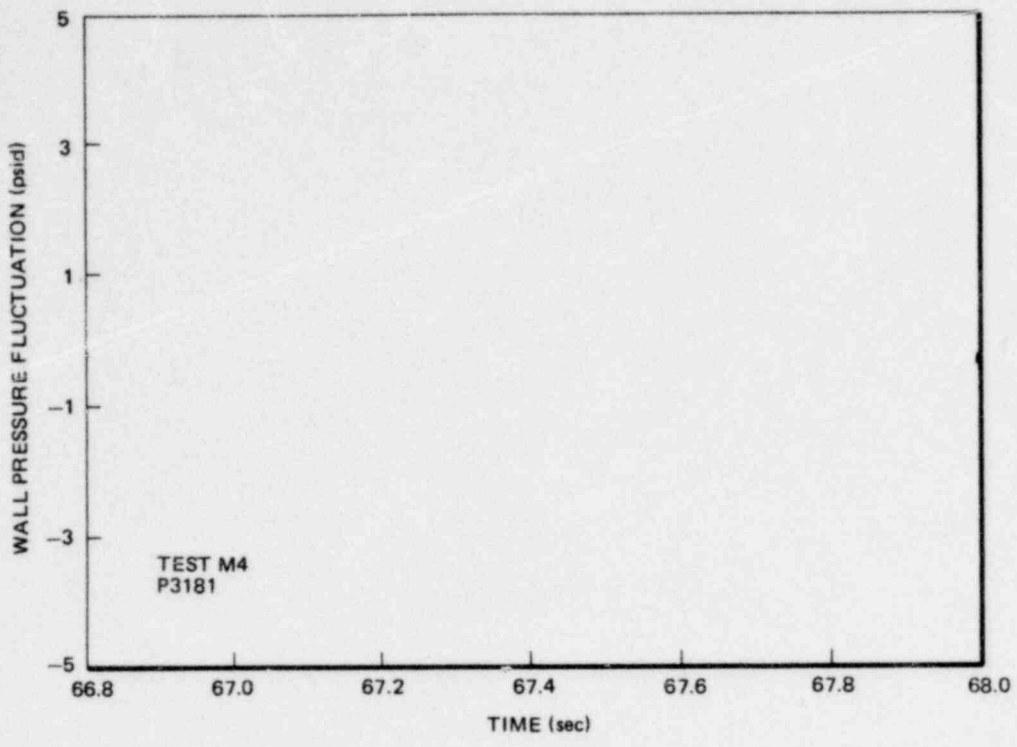

Figure 6.2.1-24. Wall Pressure P3181 During Type 2 Chugging in Test M4, 66.8 to 68.0 Seconds

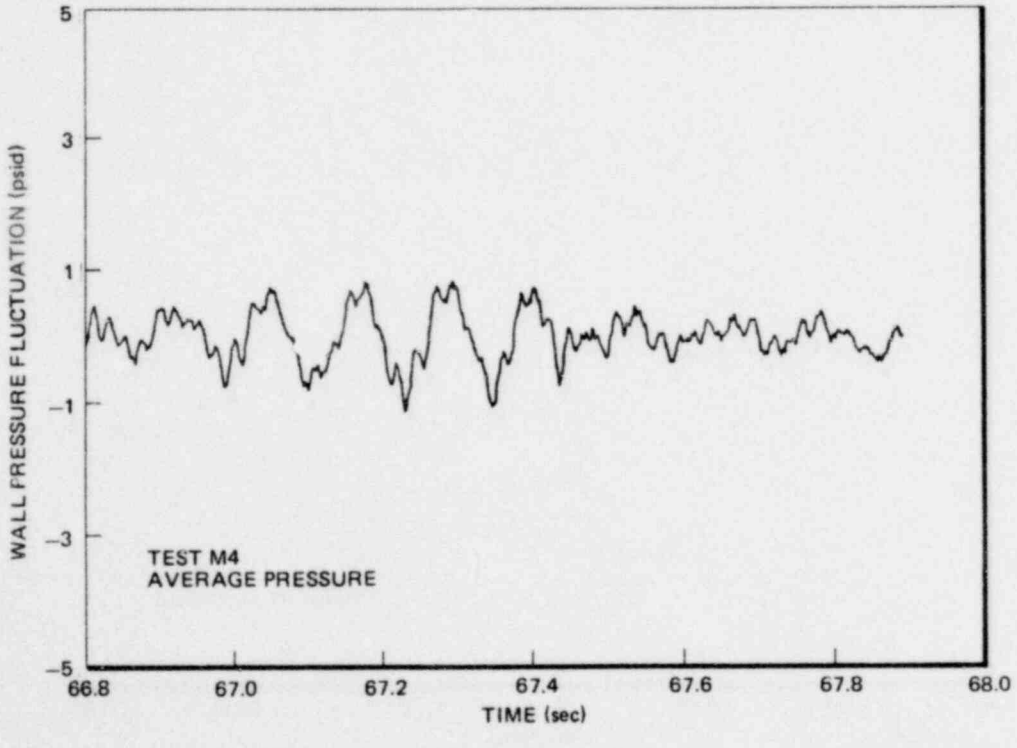

Figure 6.2.1-25. Average Wall Pressure During Type 2 Chugging in Test M4, 66.8 to 67.9 Seconds

*Proprietary information deleted

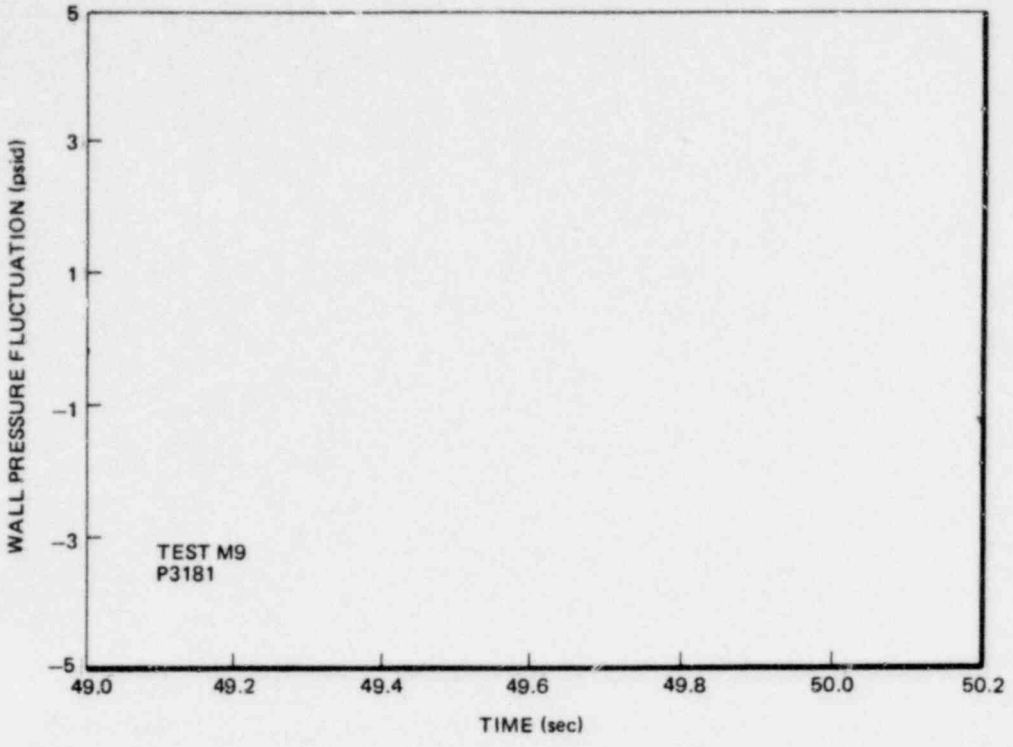

Figure 6.2.1-26. Wall Pressure P3181 During Type 2 Chugging in Test M9, 49.0 to 50.2 Seconds

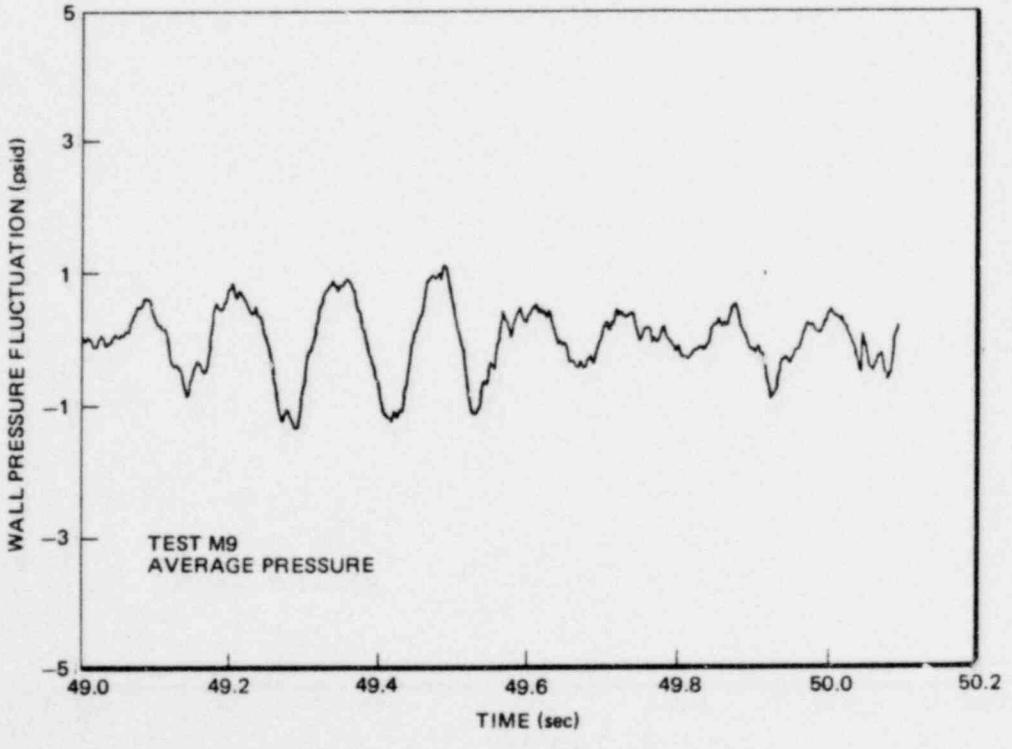

Figure 6.2.1-27. Average Wall Pressure During Type 2 Chugging in Test M9, 49.0 to 50.1 Seconds

1157 283

*Proprietary information deleted

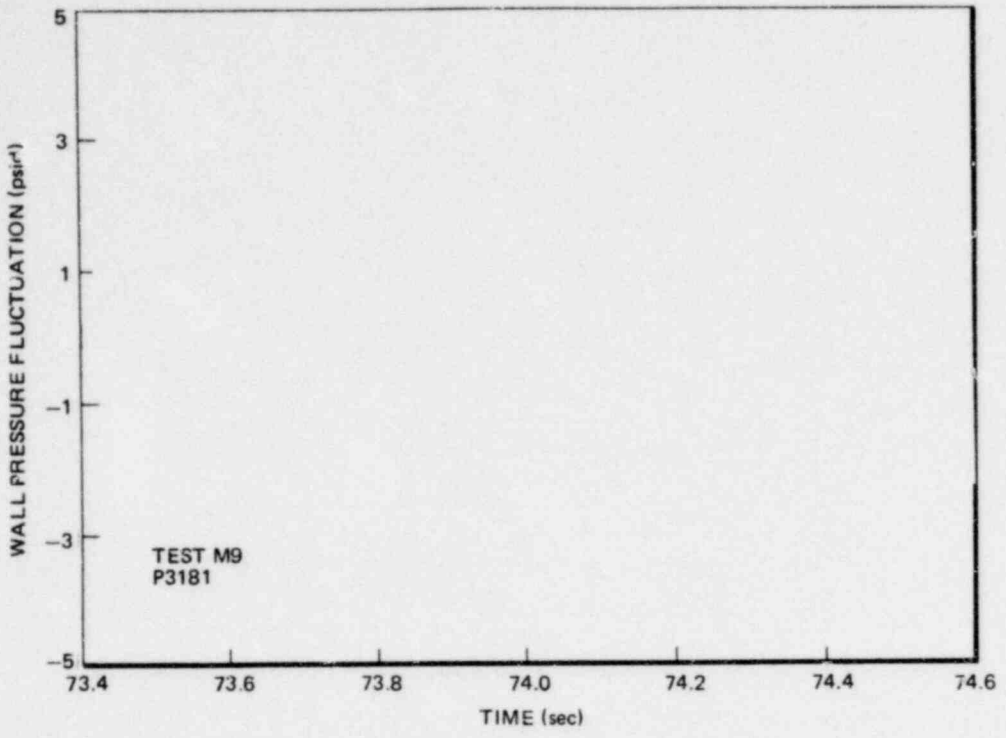

Figure 6.2.1-28. Wall Pressure P3181 During Type 2 Chugging in Test M9, 70.4 to 74.6 Seconds

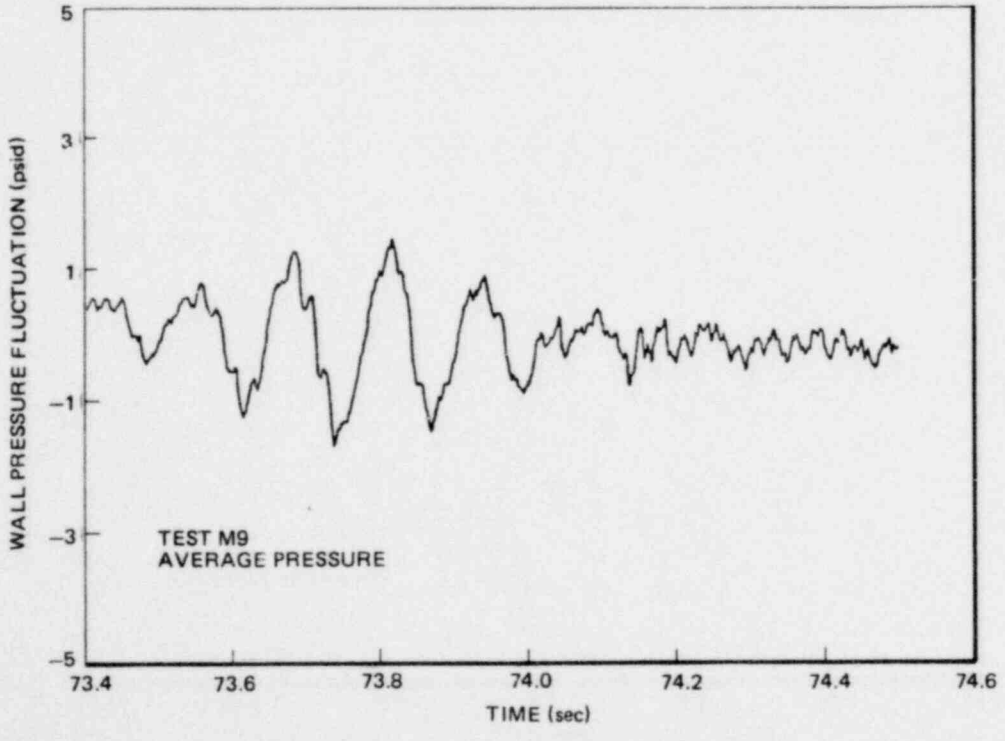

Figure 6.2.1-29. Average Wall Pressure During Type 2 Chugging in Test M9, 73.4 to 94.5 Seconds

*Proprietary information deleted

Figure 6.2.1-30. Bounding Values of Fluctuations in the Average Wall Pressure During Chugging, Test M1

Figure 6.2.1-31. Bounding Values of Fluctuations in the Average Wall Pressure During Chugging, Test M4

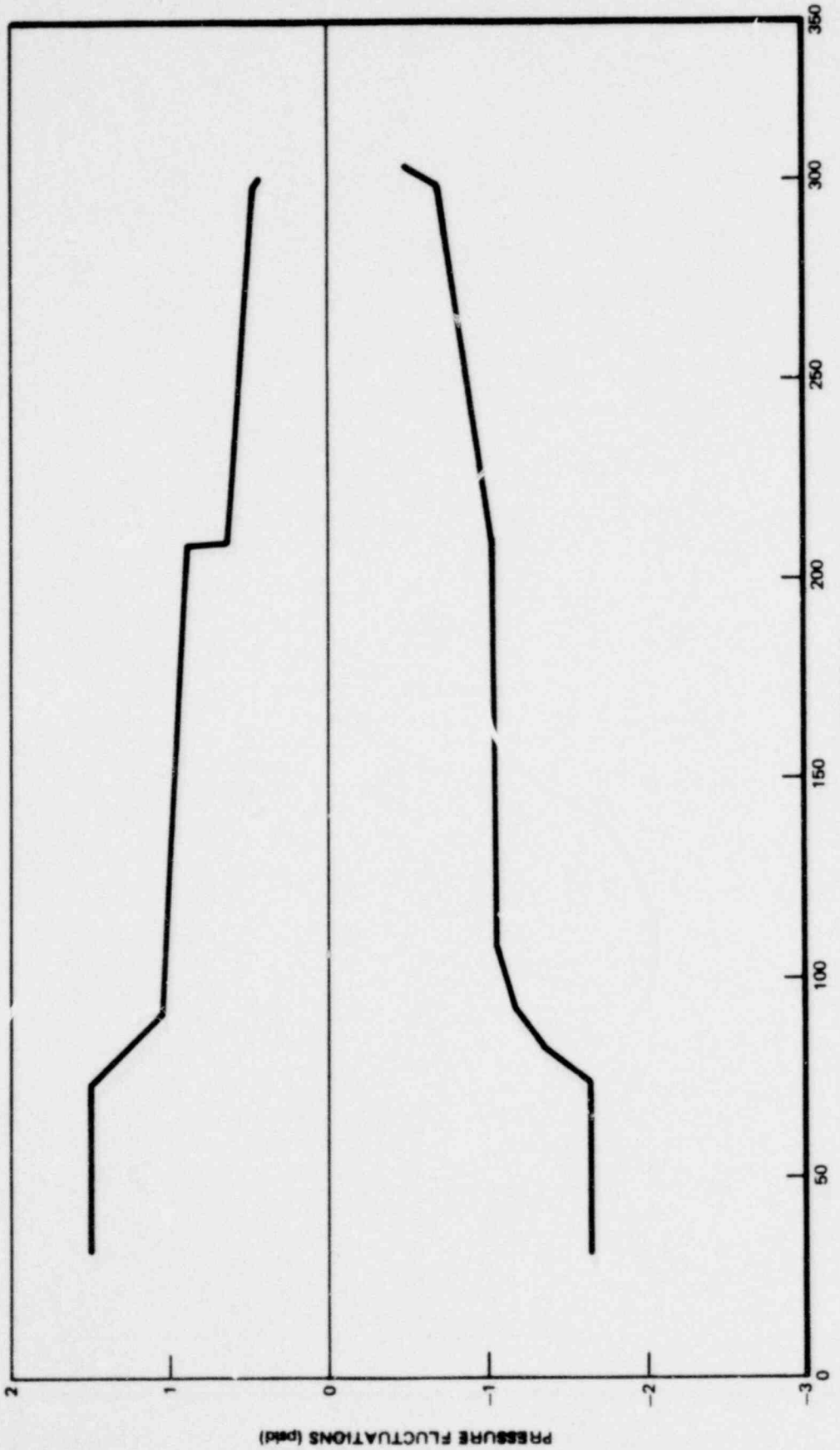

Figure 6.2.1-32. Bounding Values of Fluctuations in the Average Wall Pressure During Chugging, Test M9

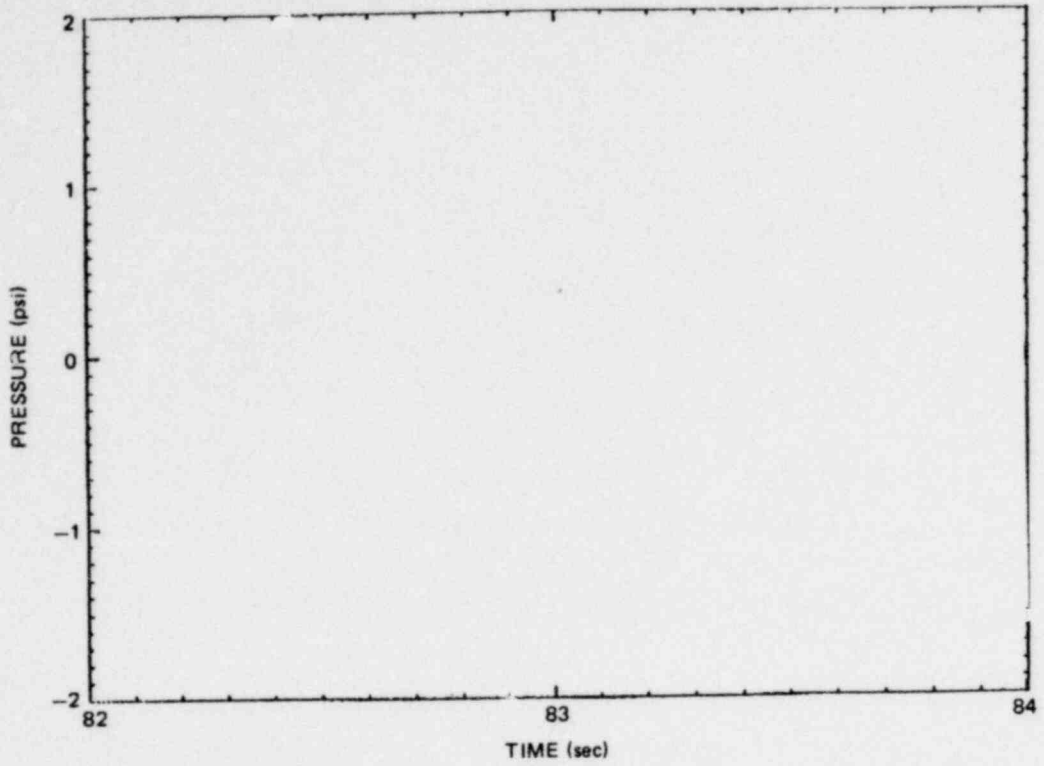

Figure 6.2.1-33. Wall Pressure P3185 During Type 1 Chugging in Test M1, 82.5 to 84.0 Secs.

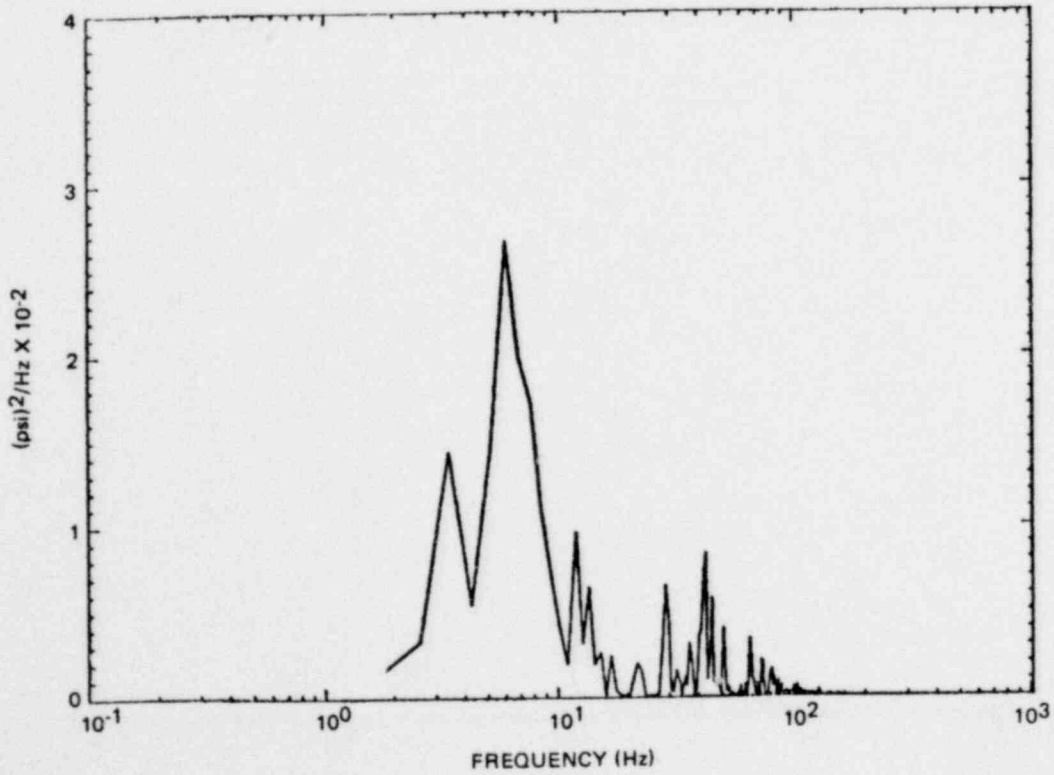

Figure 6.2.1-34. PSD of Wall Pressure P3185 During Type 1 Chugging in Test M1 82.5 to 83.7 Secs.

1157 288

•Proprietary information deleted

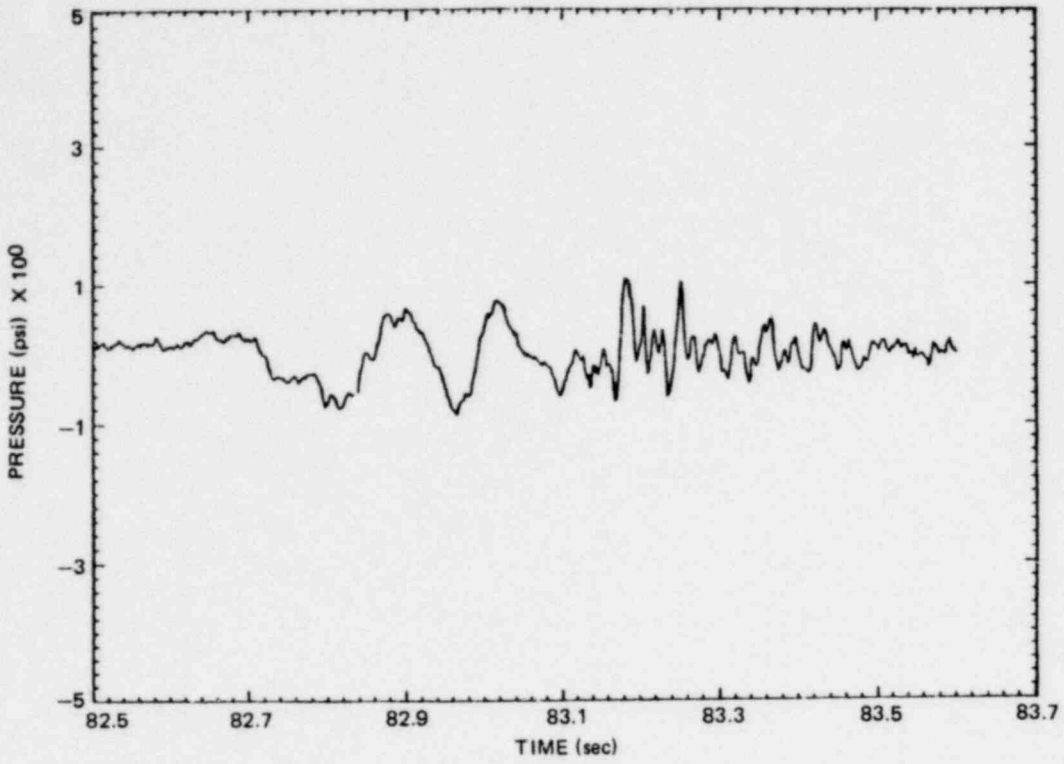

Figure 6.2.1-35. Average Wall Pressure During Type 1 Chugging in Test M1, 82.5 to 83.6 Secs.

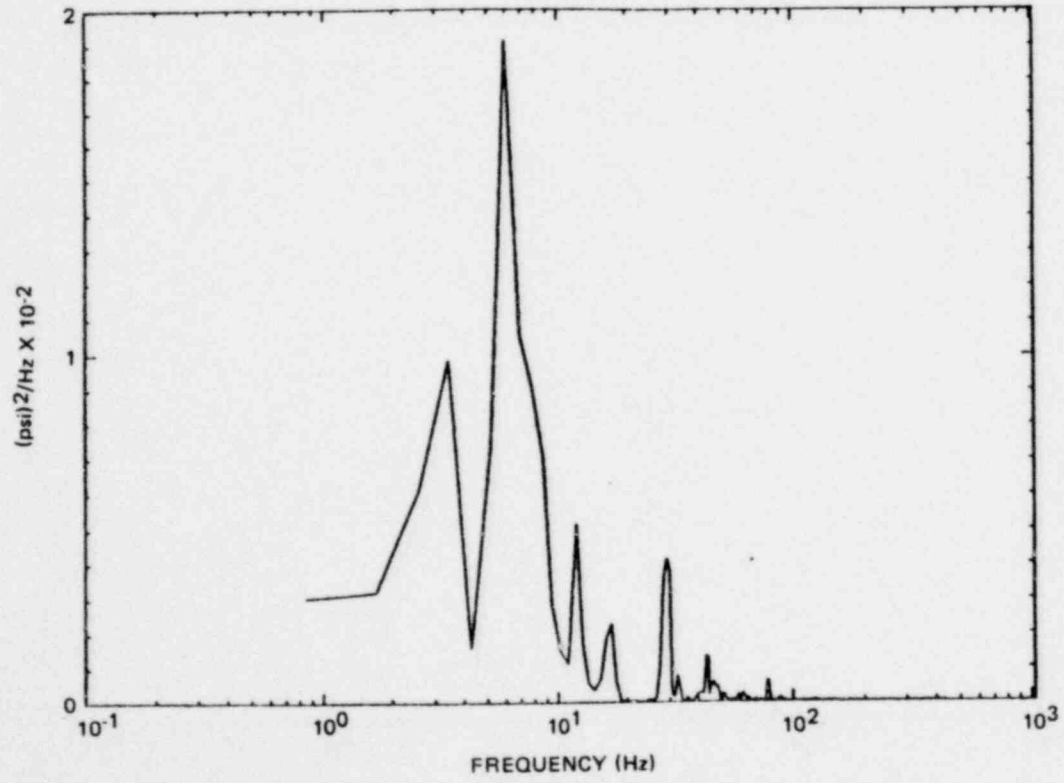

Figure 6.2.1-36. PSD of Average Wall Pressure During Type 1 Chugging in Test M1, 82.5 to 83.6 Secs.

1157 287

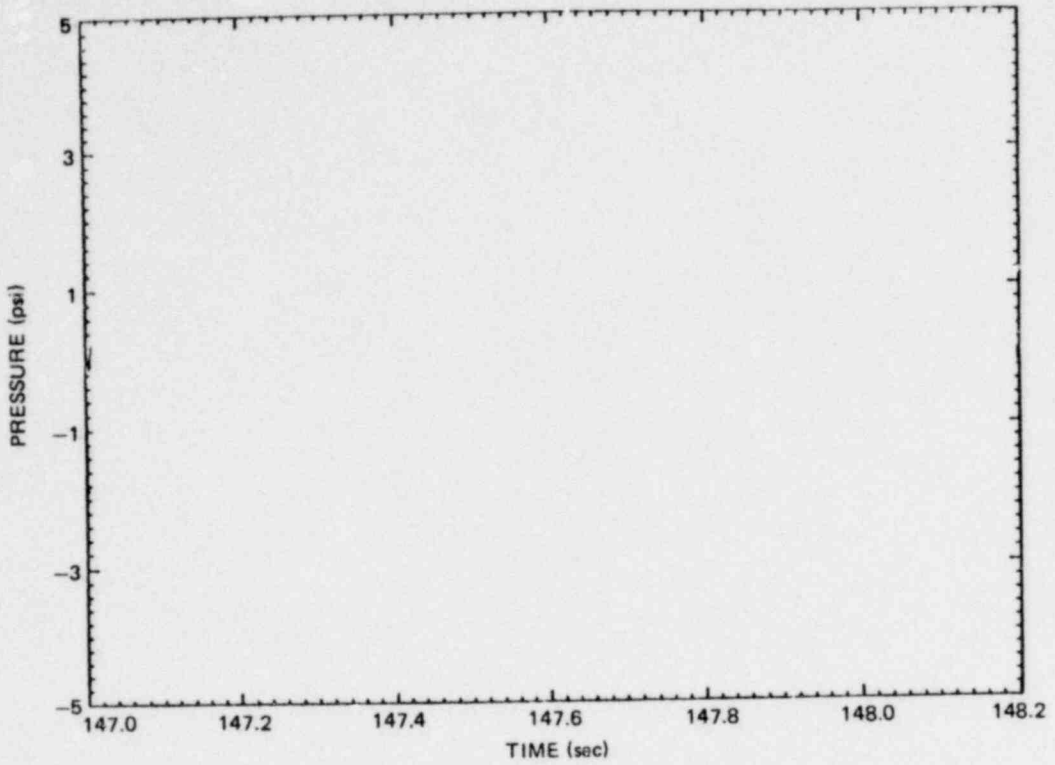

Figure 6.2.1-37. Wall Pressure P3185 During Type 1 Chugging in Test M1, 147.0 to 148.2 Secs.

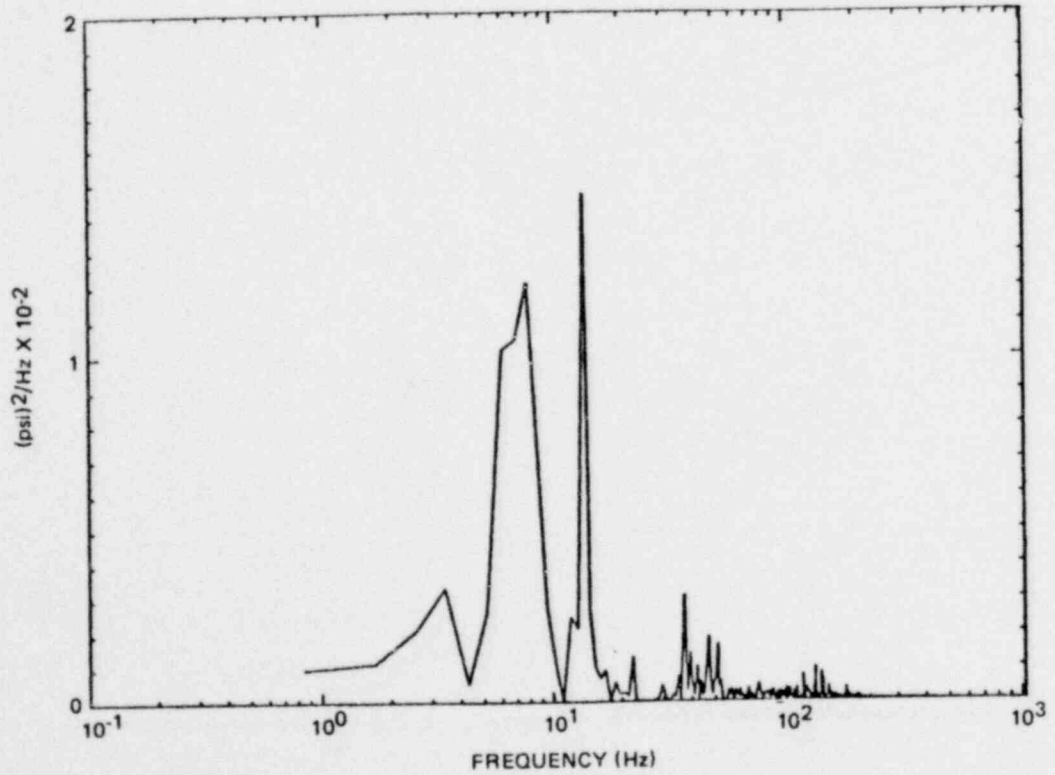

Figure 6.2.1-38. PSD of Wall Pressure P3185 During Type 1 Chugging in Test M1, 147.0 to 148.2 Secs.

*Proprietary information deleted

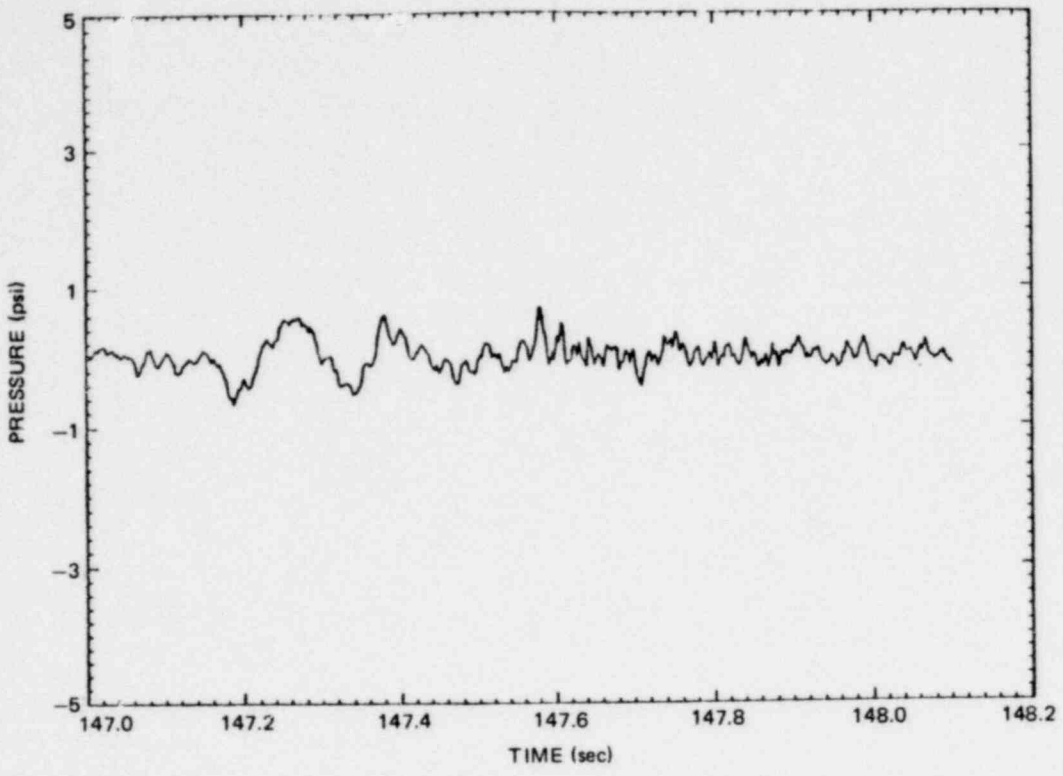

Figure 6.2.1-39. Average Wall Pressure During Type 1 Chugging in Test M1, 147.0 to 148.1 Secs.

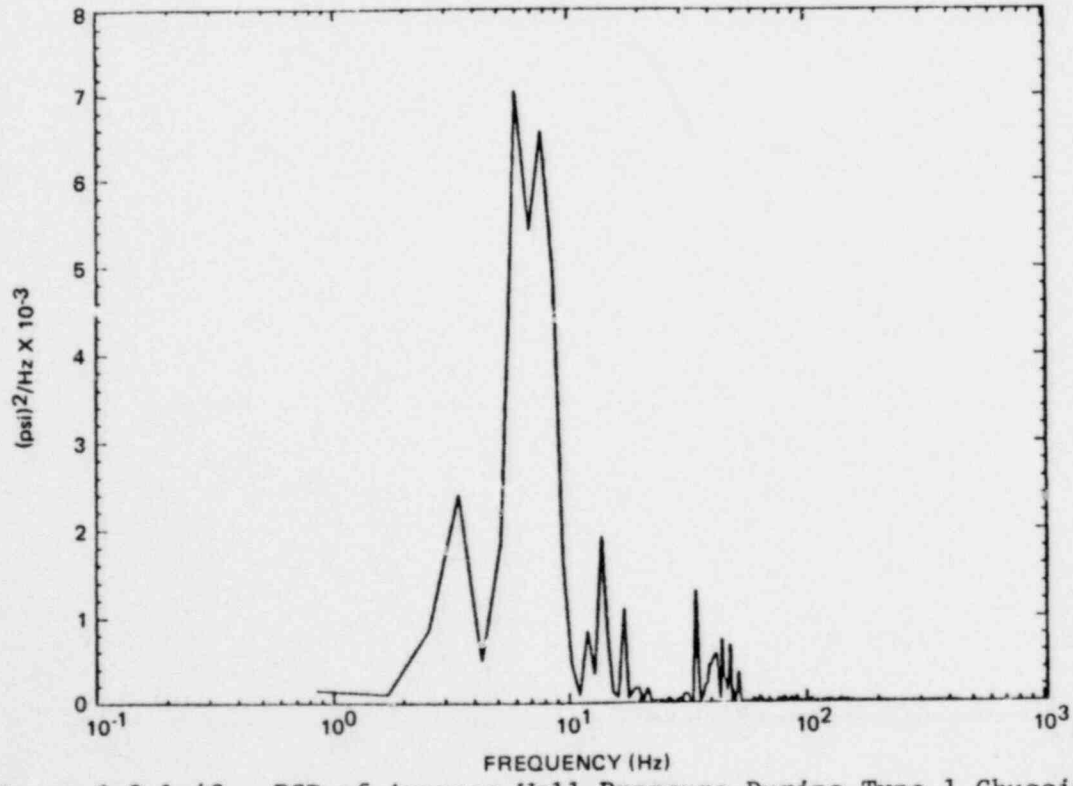

Figure 6.2.1-40. PSD of Average Wall Pressure During Type 1 Chugging in Test M1, 147.0 to 148.1 Secs.

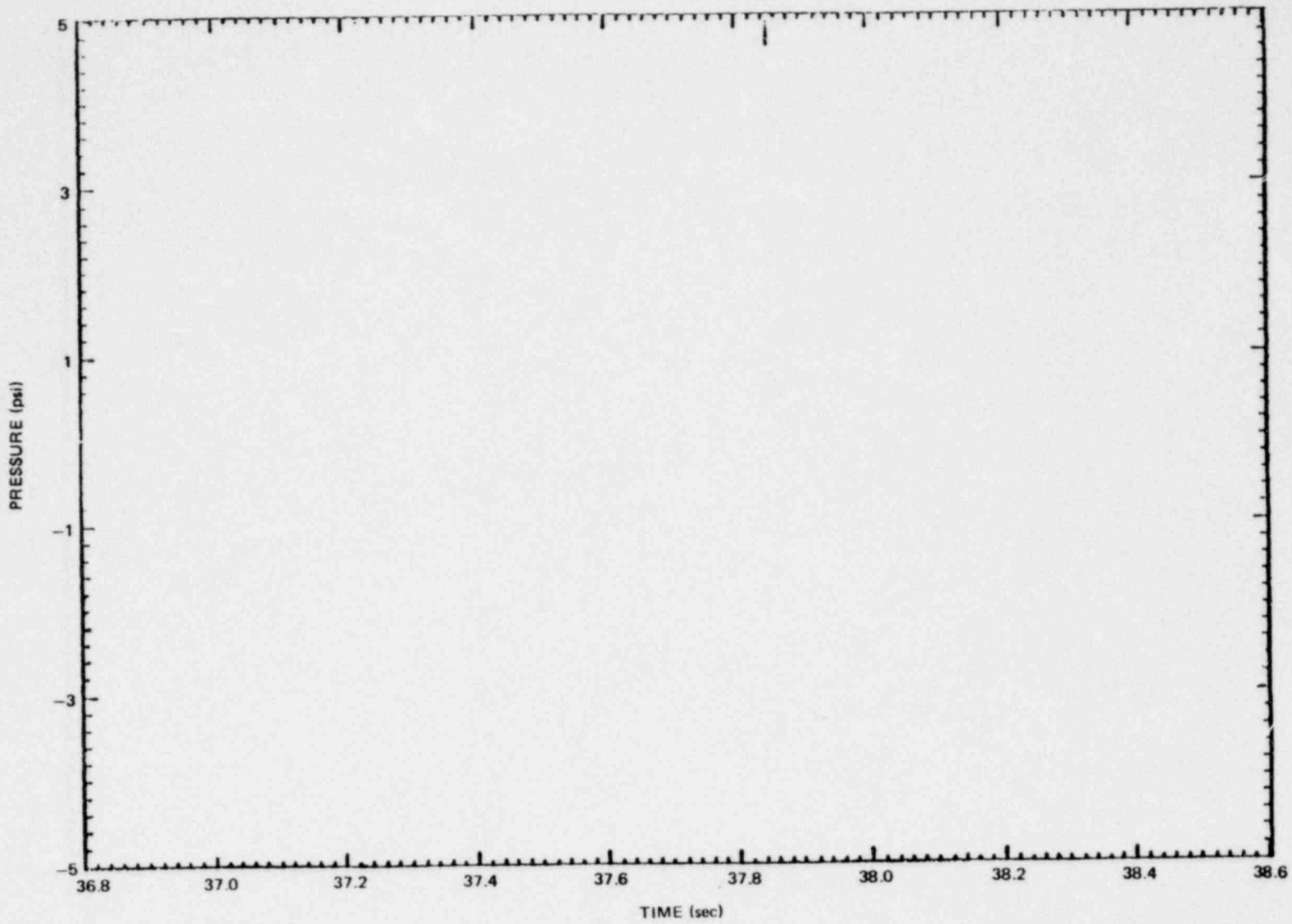

Figure 6.2.1-41. Wall Pressure P3185 During Type 2 Chugging in Test M4, 36.8 to 38.5 Secs.

*Proprietary information deleted

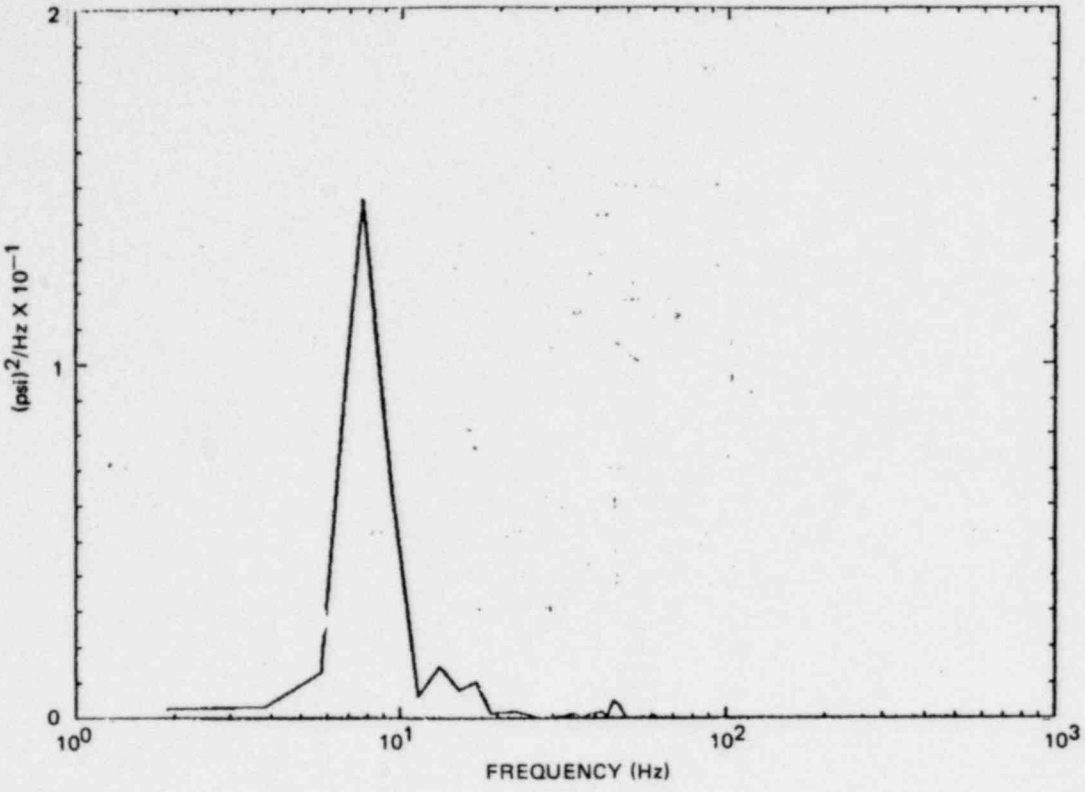

Figure 6.2.1-42. PSD of Wall Pressure P3185 During Type 2 Chugging in Test M4, 36.8 to 37.3 Secs.

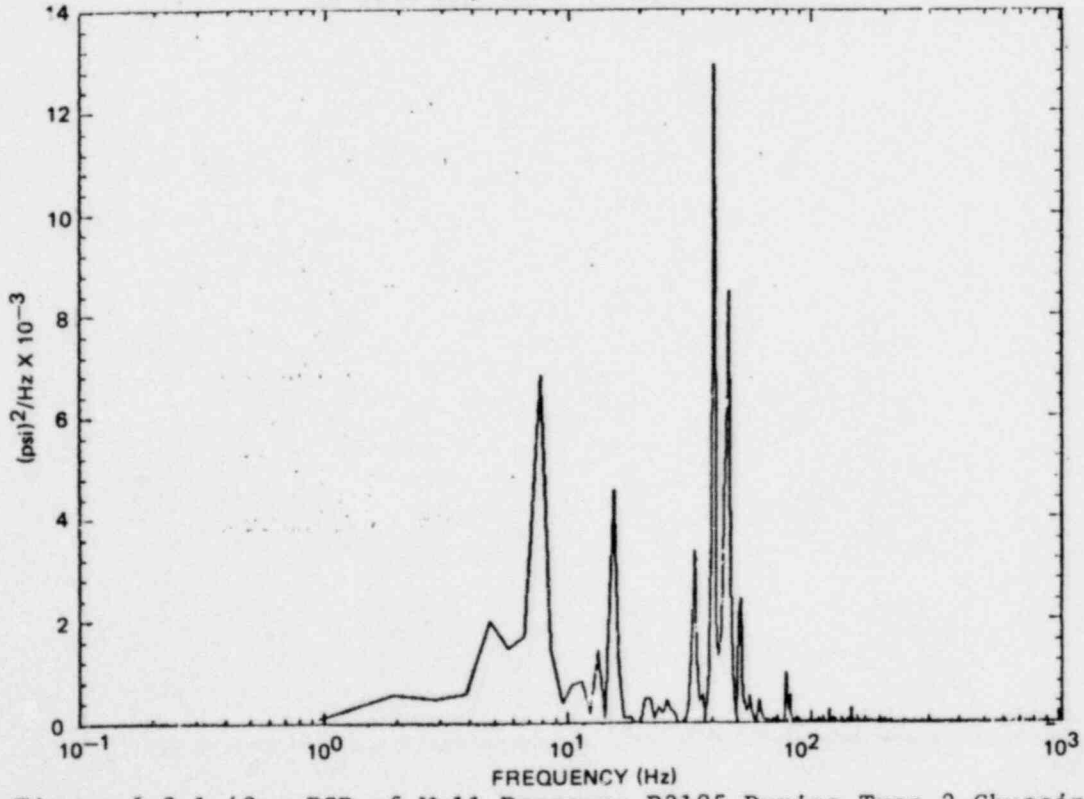

Figure 6.2.1-43. PSD of Wall Pressure P3185 During Type 2 Chugging in Test M4, 37.4 to 38.5 Secs.

1157 293

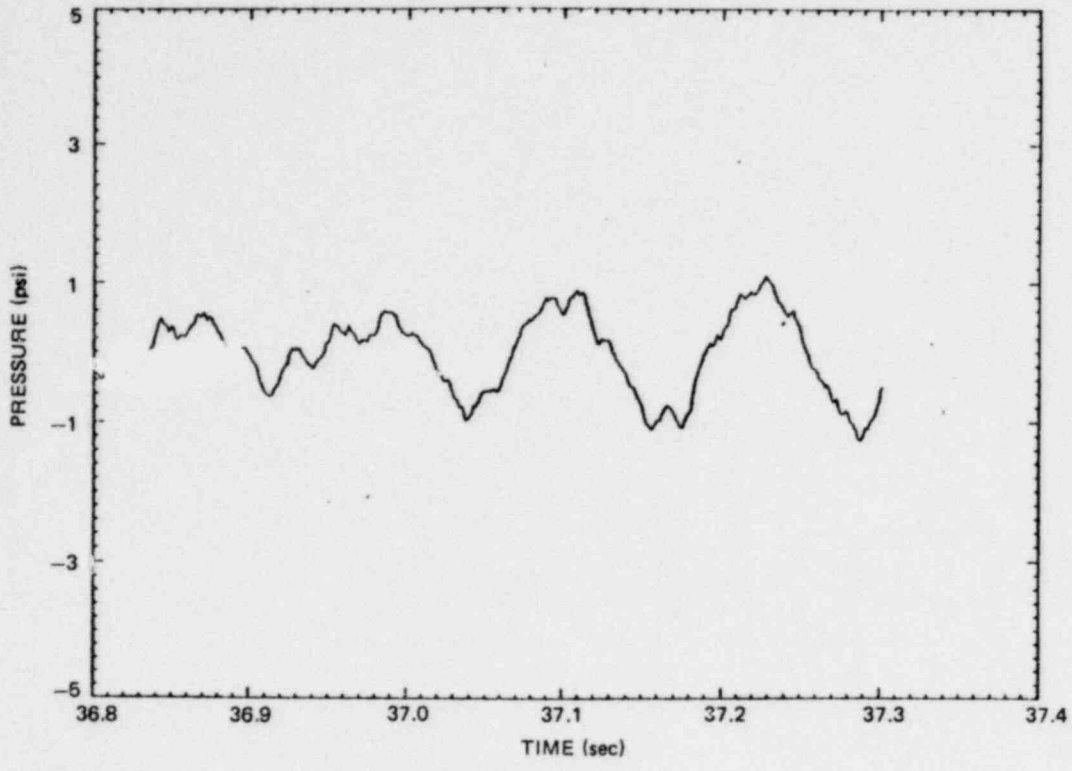

Figure 6.2.1-44. Average Wall Pressure During Type 2 Chugging in Test M4, 36.8 to 37.3 Secs.

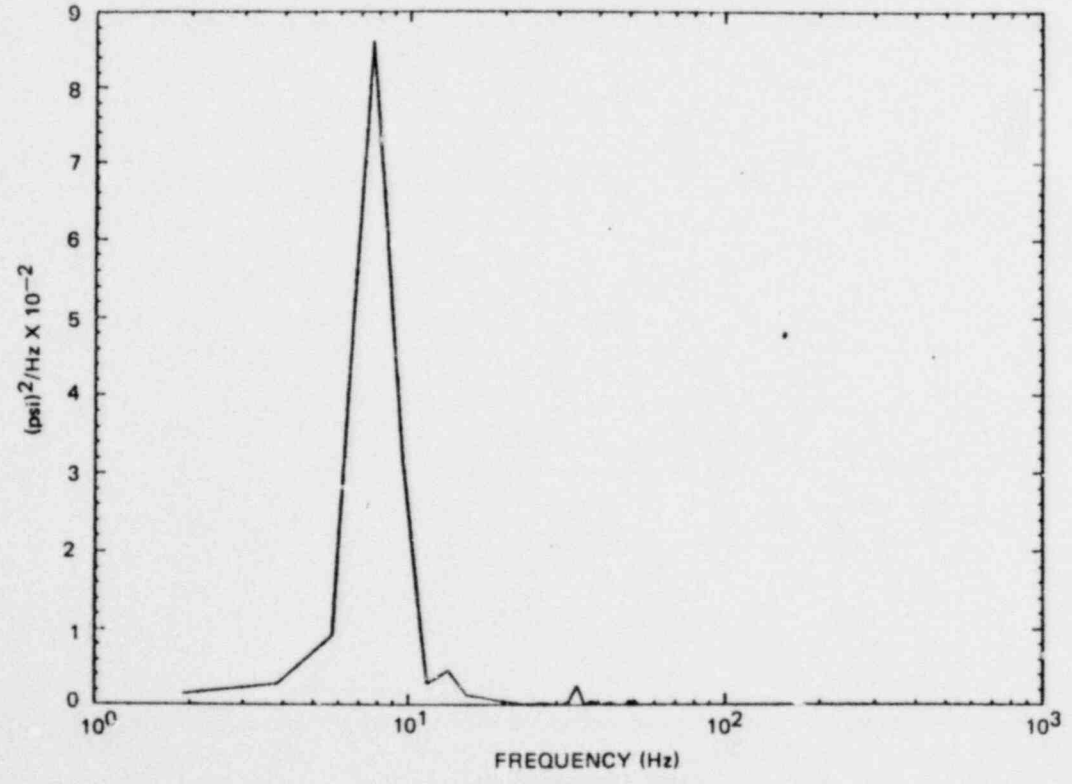

Figure 6.2.1-45. PSD of Average Wall Pressure During Type 2 Chugging in Test M4, 36.8 to 37.3 Secs.

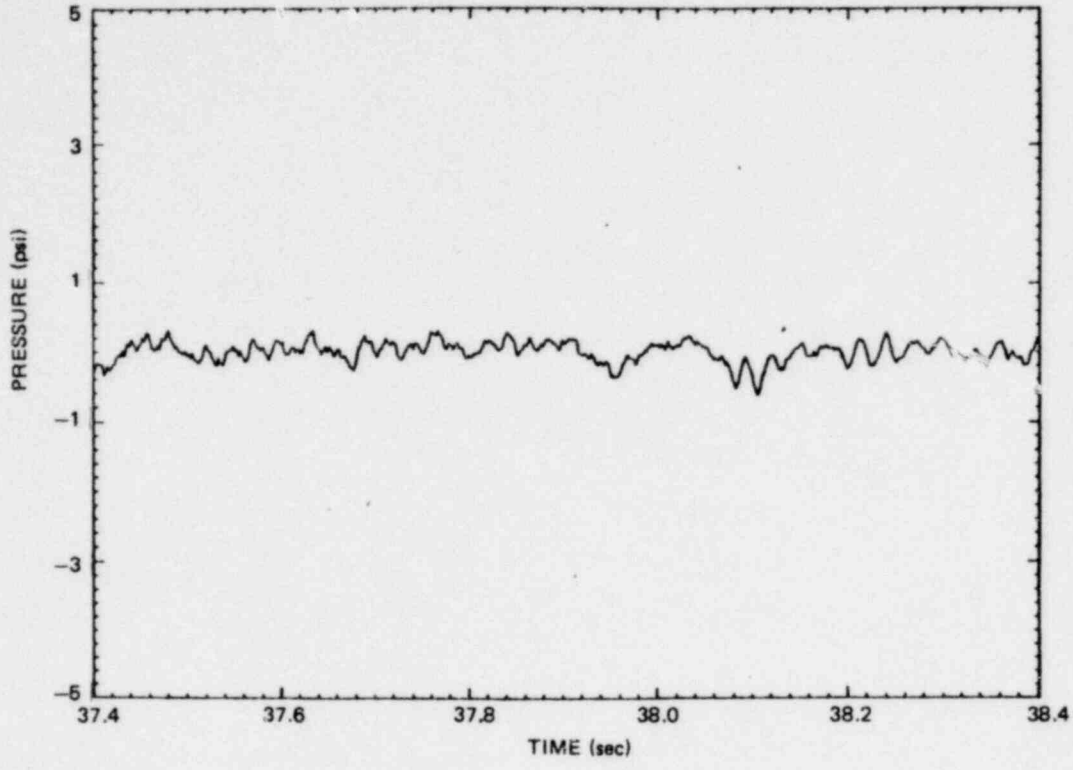

Figure 6.2.1-46. Average Wall Pressure During Type 2 Chugging in Test M4, 37.4 to 38.4 Secs.

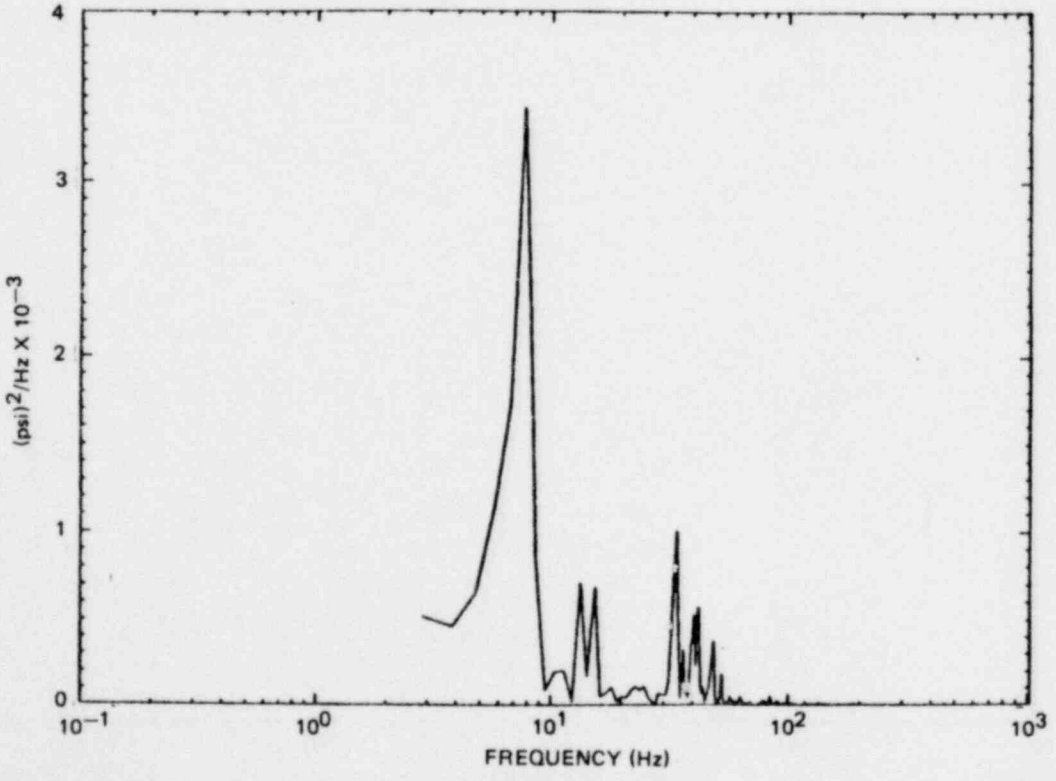

Figure 6.2.1-47. PSD of Average Wall Pressure During Type 2 Chugging in Test M4, 37.4 to 38.4 Secs.

1157 295

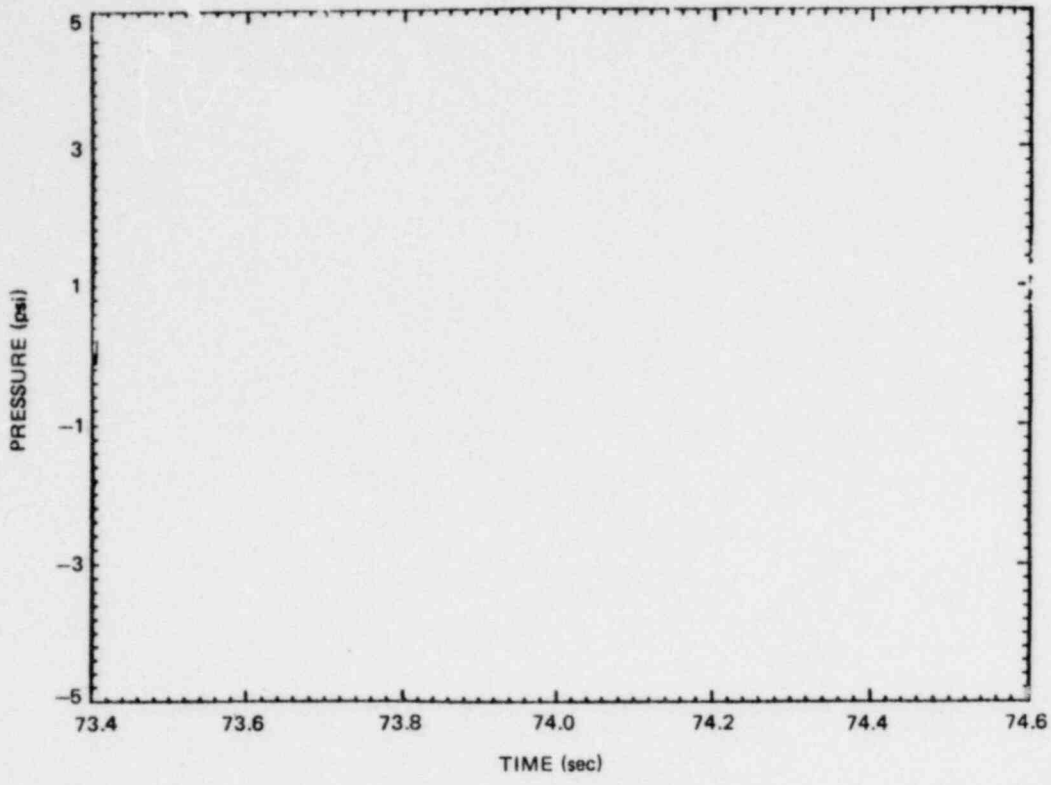

Figure 6.2.1-48. Wall Pressure P3185 During Type 2 Chugging in Test M9, 73.4 to 74.5 Secs.

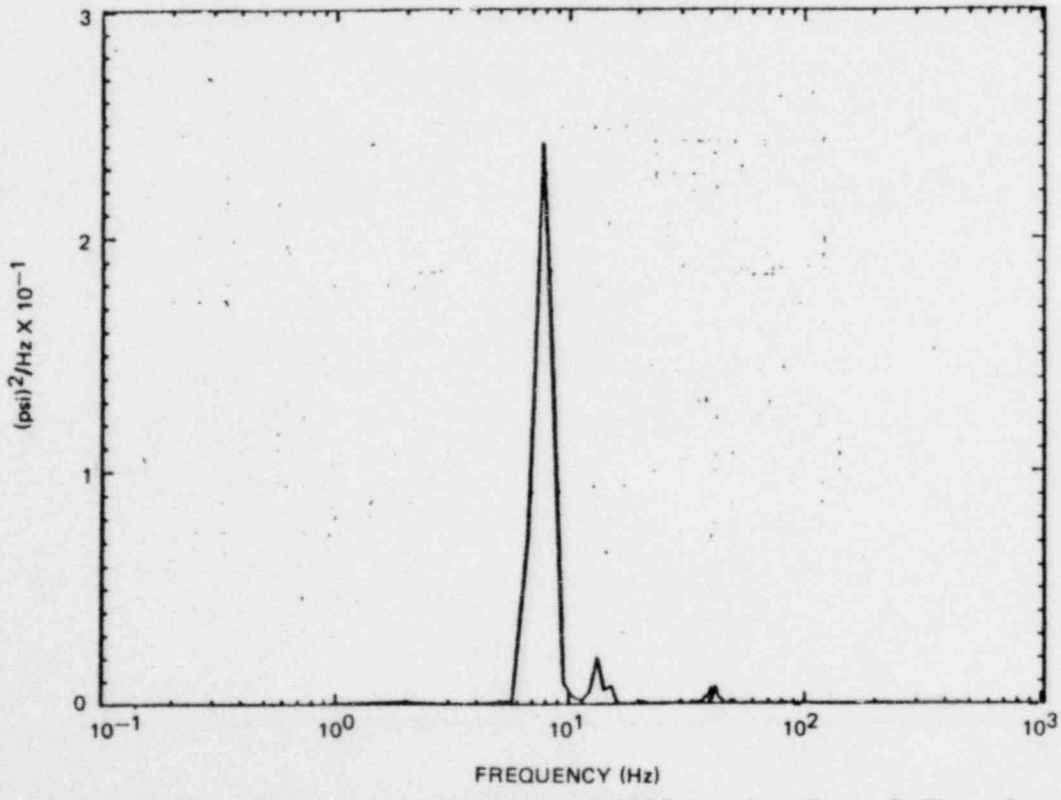

Figure 6.2.1-49. PSD of Wall Pressure P3185 During Type 2 Chugging in Test M9, 73.4 to 74.5 Secs.

1157 2

*Proprietary information deleted

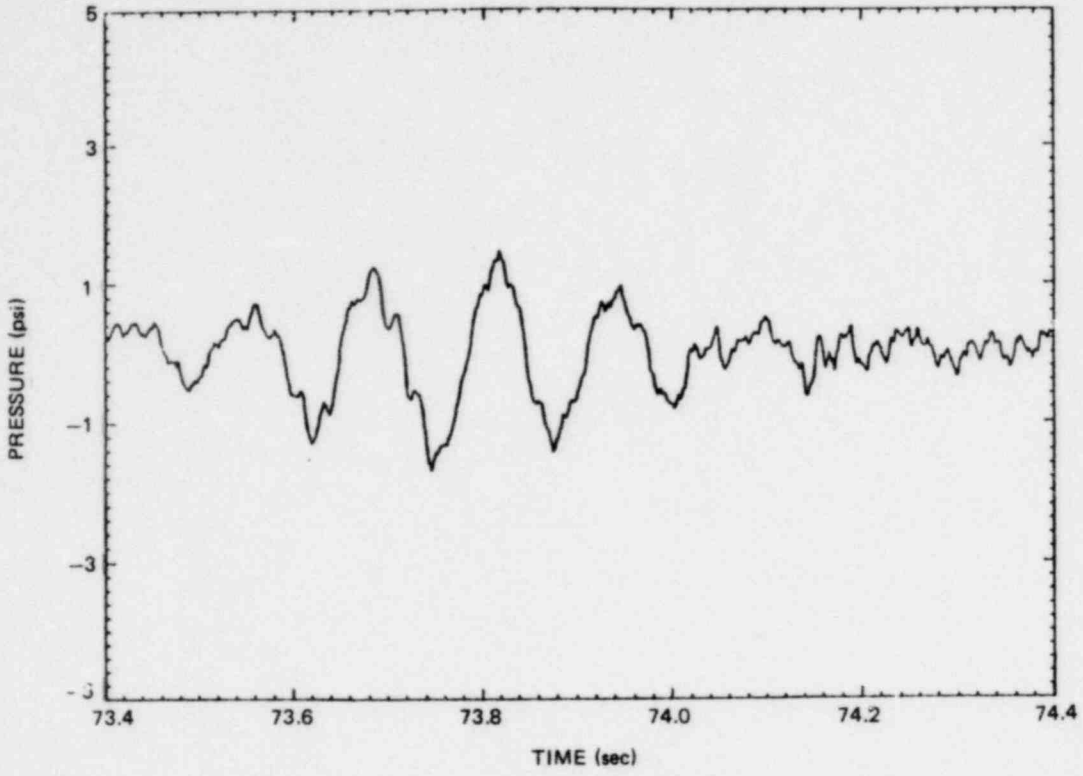

Figure 6.2.1-50. Average Wall Pressure During Type 2 Chugging in Test M9, 73.4 to 74.4 Secs.

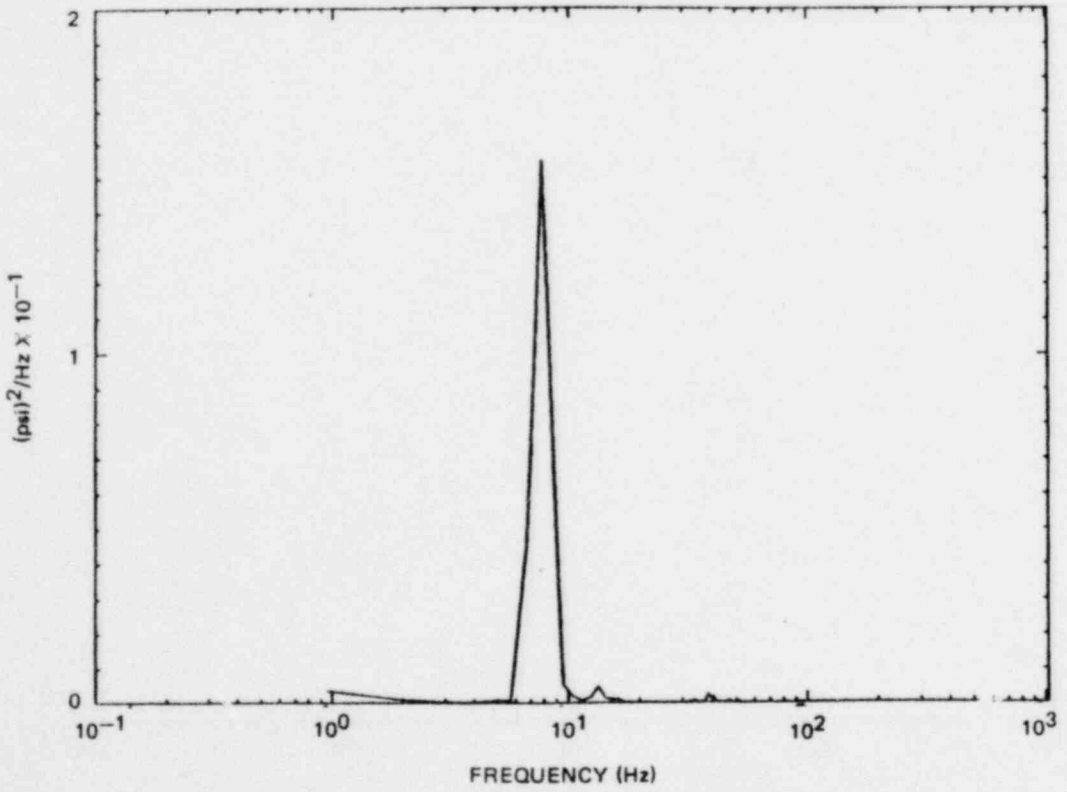

Figure 6.2.1-51. PSD of Average Wall Pressure During Type 2 Chugging in Test M9, 73.4 to 74.4 Secs.

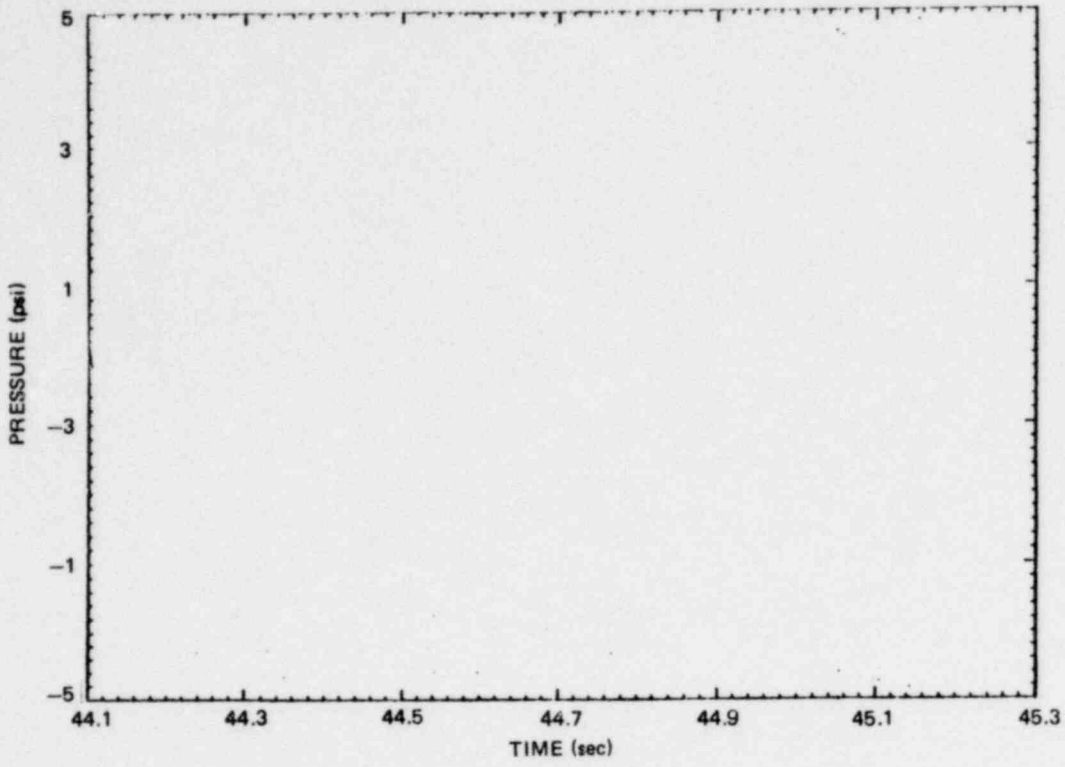

Figure 6.2.1-52. Wall Pressure P3185 During Type 2 Chugging in Test M10, 44.1 to 45.2 Secs.

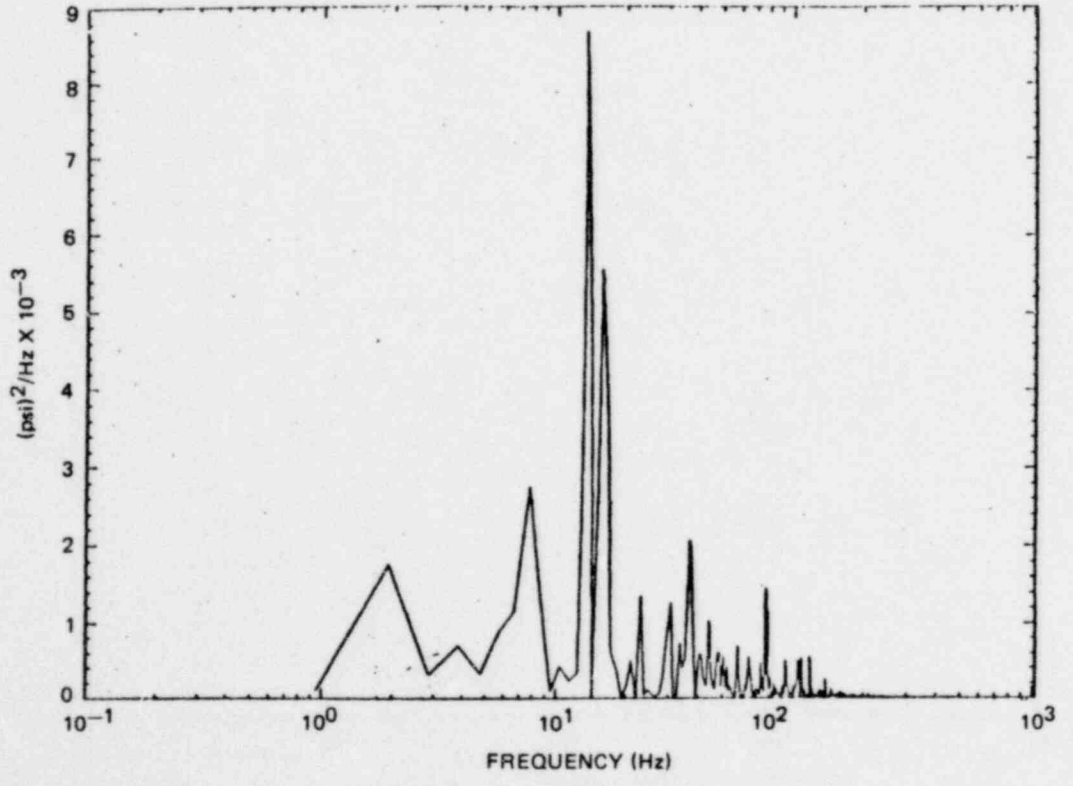

Figure 6.2.1-53. PSD of Wall Pressure P3185 During Type 2 Chugging in Test M10, 44.1 to 45.2 Secs.

1157 298

*Proprietary information deleted

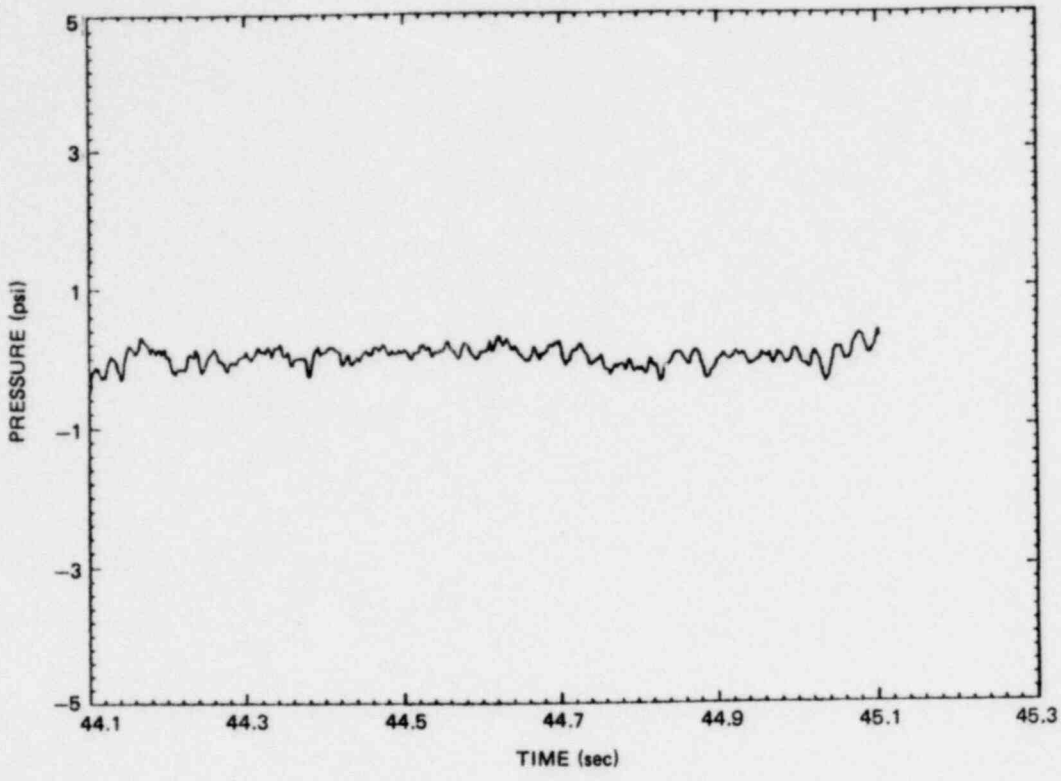

Figure 6.2.1-54. Average Wall Pressure During Type 2 Chugging in Test M10, 44.1 to 45.1 Secs.

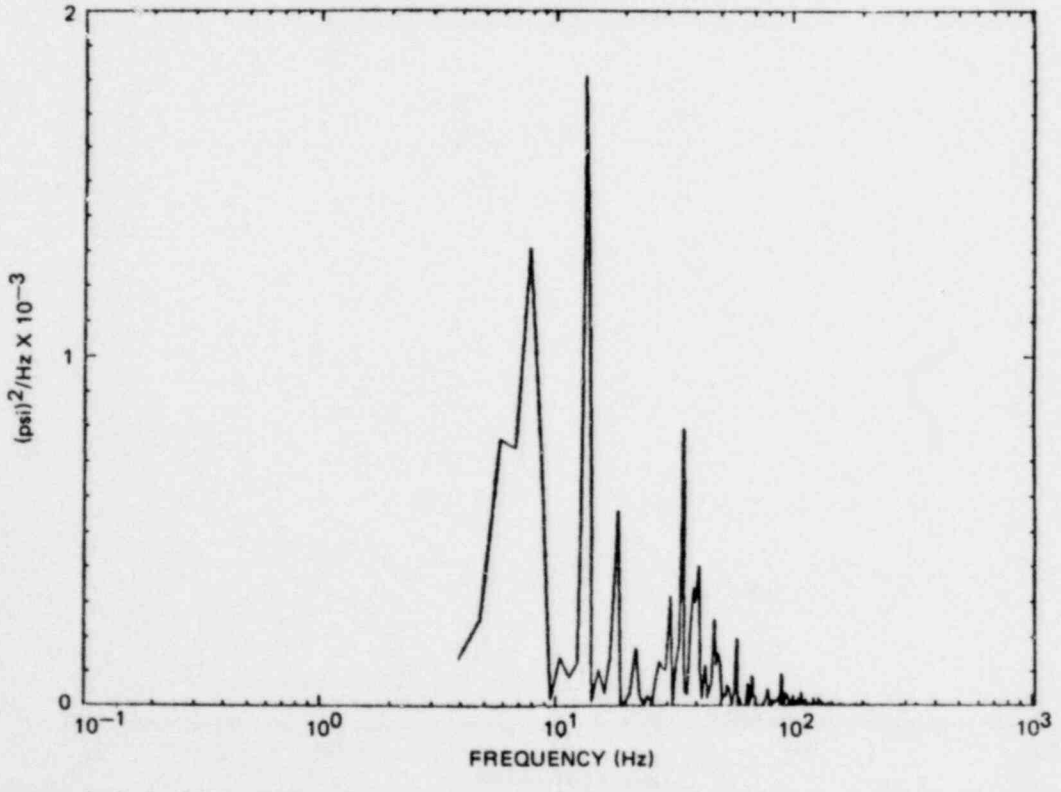

Figure 6.2.1-55. PSD of Average Wall Pressure During Type 2 Chugging in Test M10, 44.1 to 45.1 Secs.

Figure 6.2.1-56. Circumferential Wall Pressure Profiles Before a Type 2 Chug in Test M1, 41.453 and 41.391 Seconds

Figure 6.2.1-57. Axial Wall Pressure Profiles Before a Type 2 Chug in Test M1, 41.453 and 41.391 Seconds

*Proprietary information deleted

1157 200

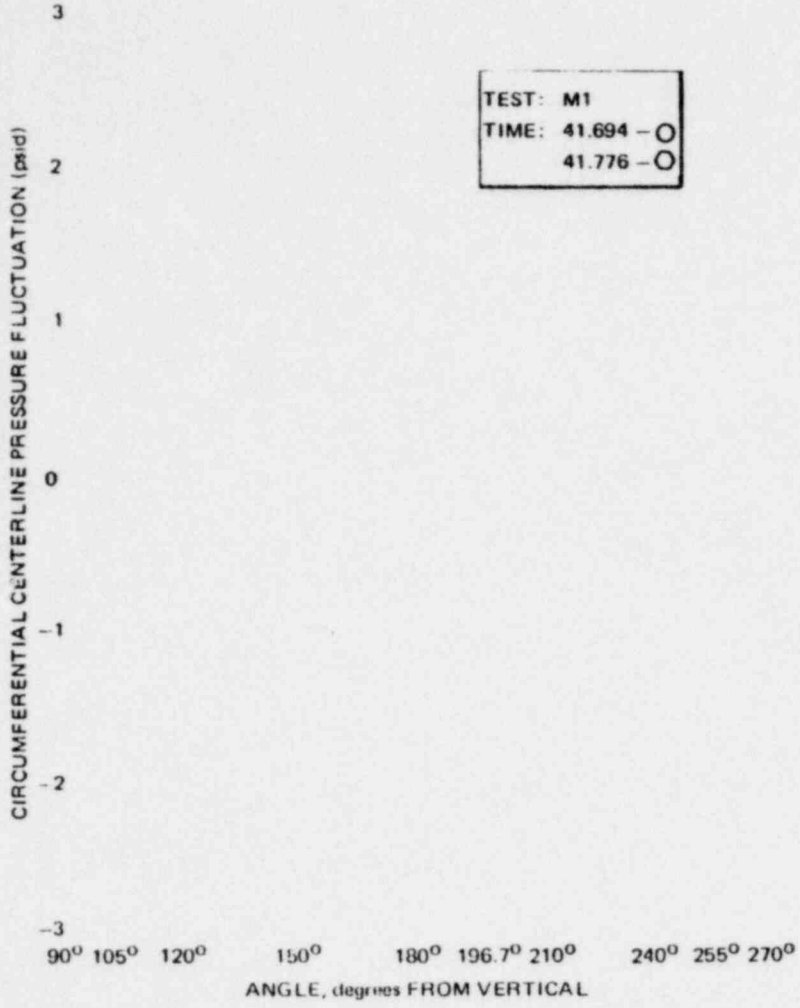

Figure 6.2.1-58. Circumferential Wall Pressure Profiles Following a Type 2 Chug in Test M1, 41.694 and 41.776 Seconds

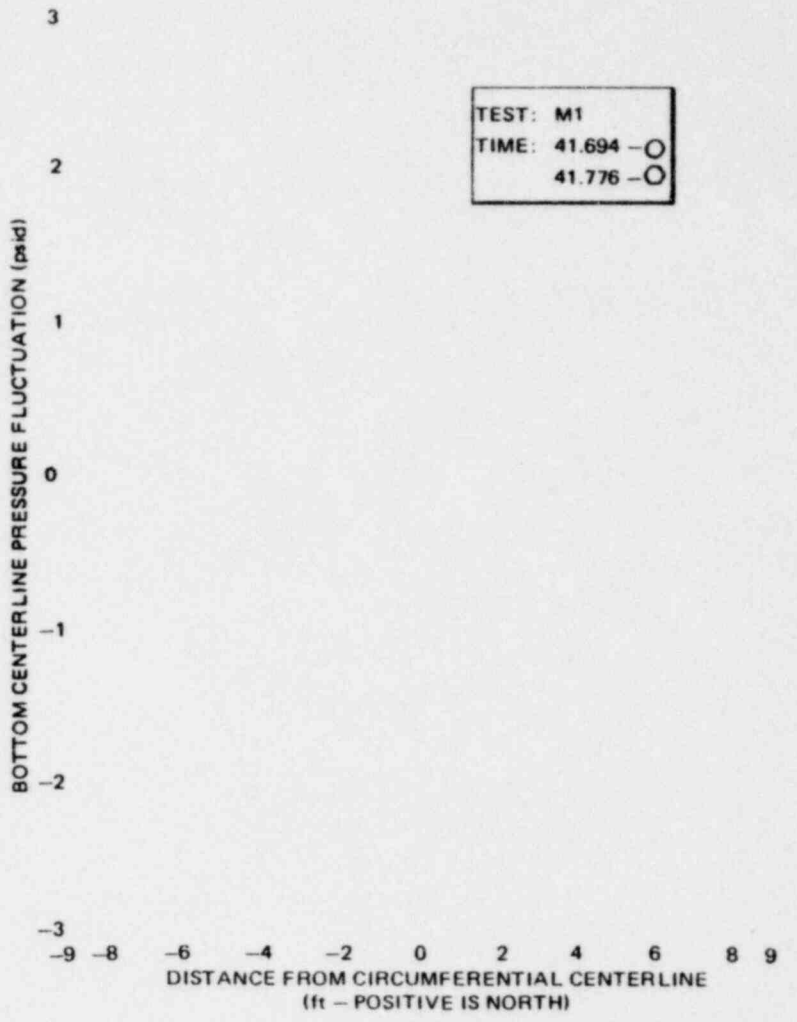

Figure 6.2.1-59. Axial Wall Pressure Profiles Following a Type 2 Chug in Test M1, 41.694 and 41.776 Seconds

*Proprietary information deleted

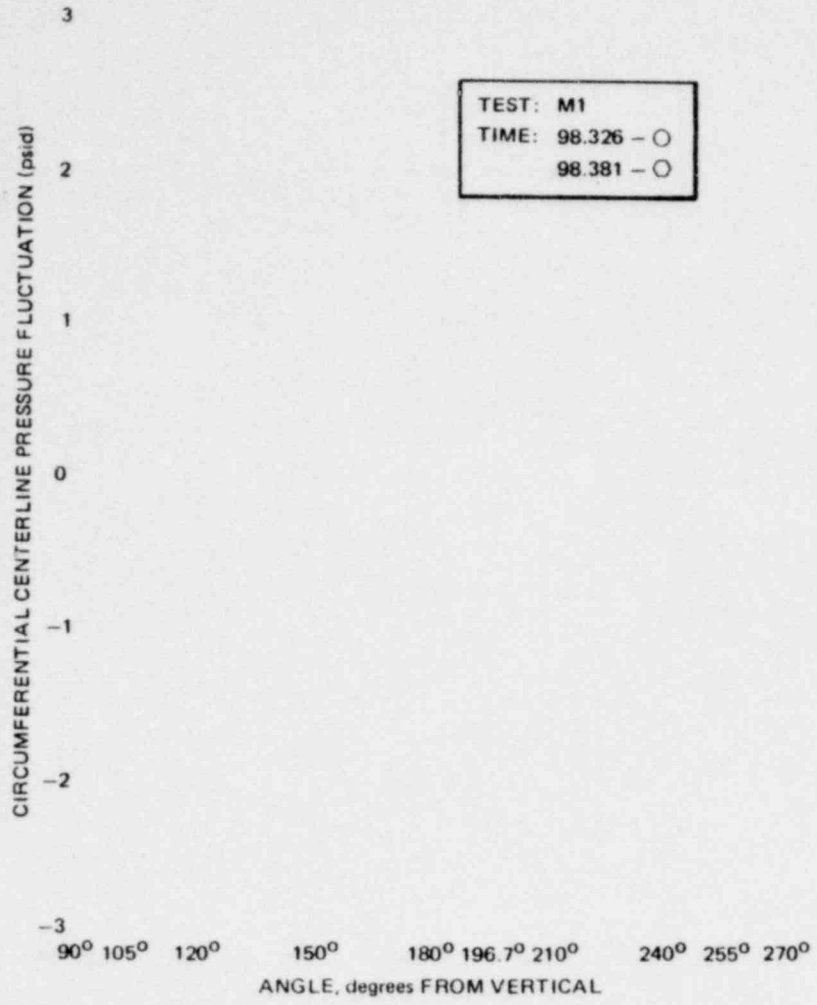

Figure 6.2.1-60. Circumferential Wall Pressure Profiles Before a Type 1 Chug in Test M1, 98.326 and 98.381 Seconds

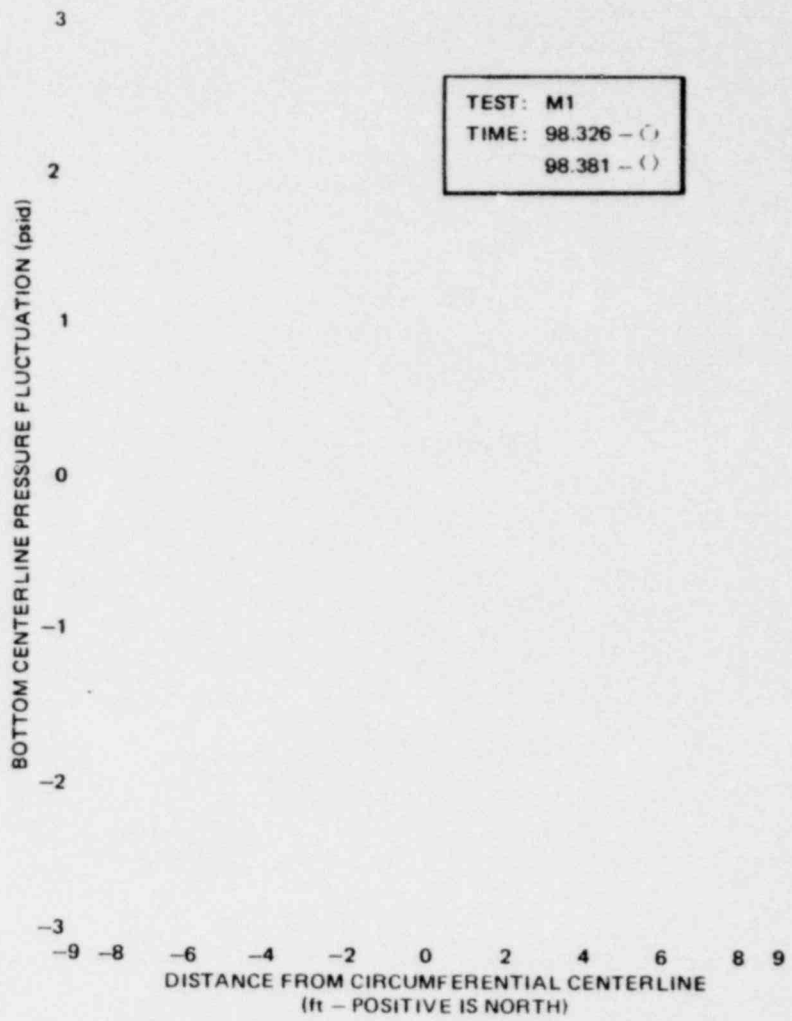

Figure 6.2.1-61. Axial Wall Pressure Profiles Before a Type 1 Chug in Test M1, 98.326 and 98.381 Seconds

*Proprietary information deleted

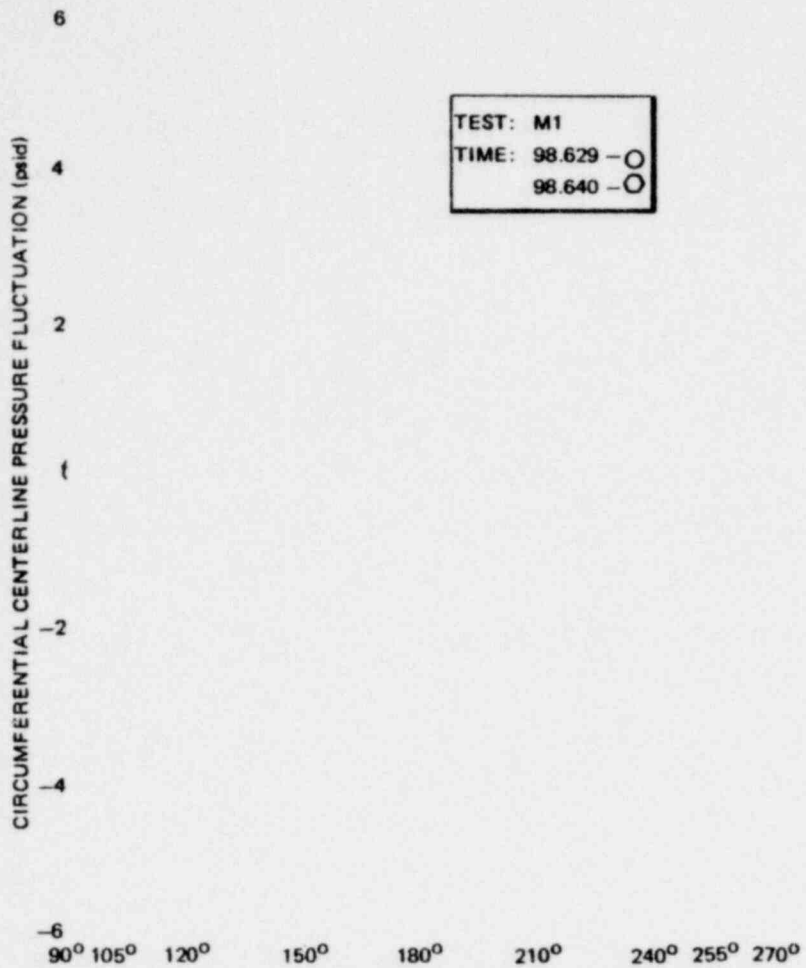

Figure 6.2.1-62. Circumferential Wall Pressure Profiles Following a Type 1 Chug in Test M1, 98.629 and 98.640 Seconds

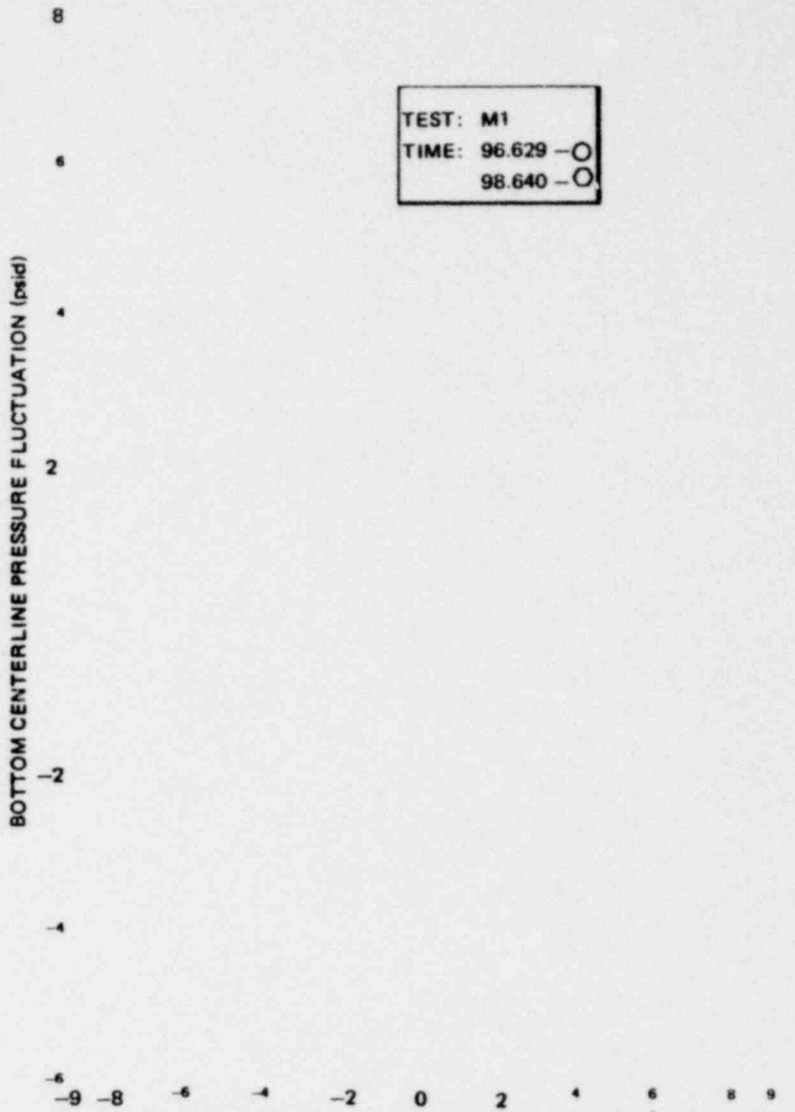

Figure 6.2.1-63. Axial Wall Pressure Profiles Following a Type 1 Chug in Test M1, 98.629 and 98.640 Seconds

*Proprietary information deleted

1157 203

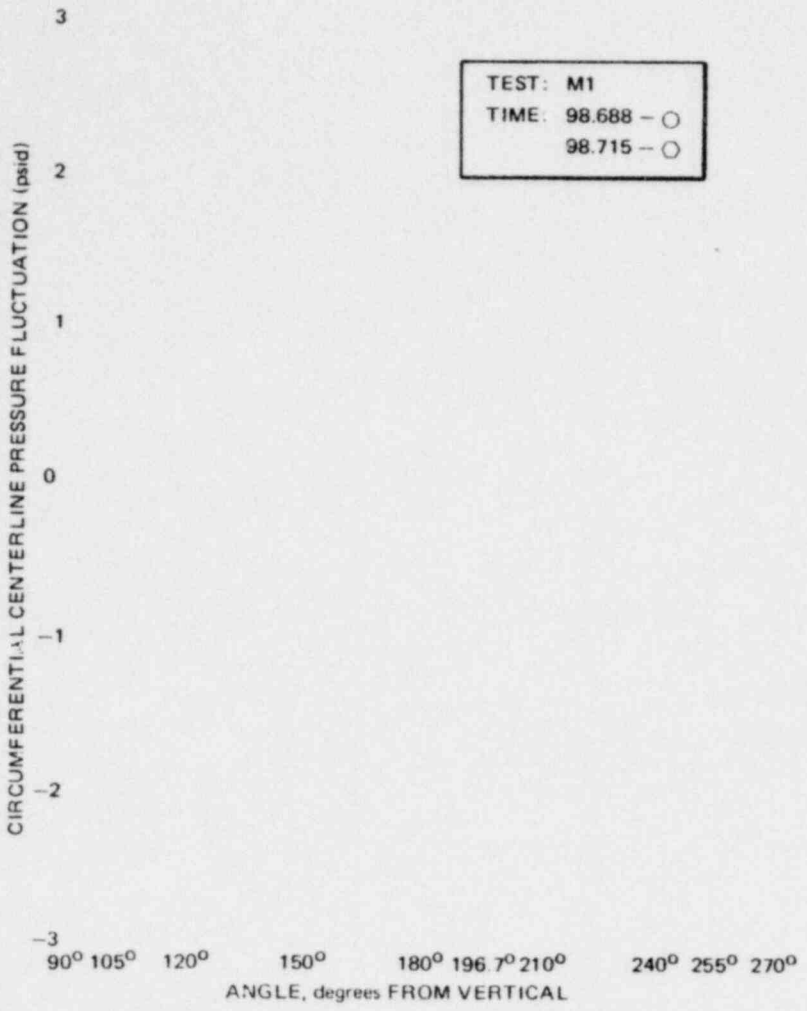

Figure 6.2.1-64. Circumferential Wall Pressure Profiles Following a Type 1 Chug in Test M1, 98.688 and 98.715 Seconds.

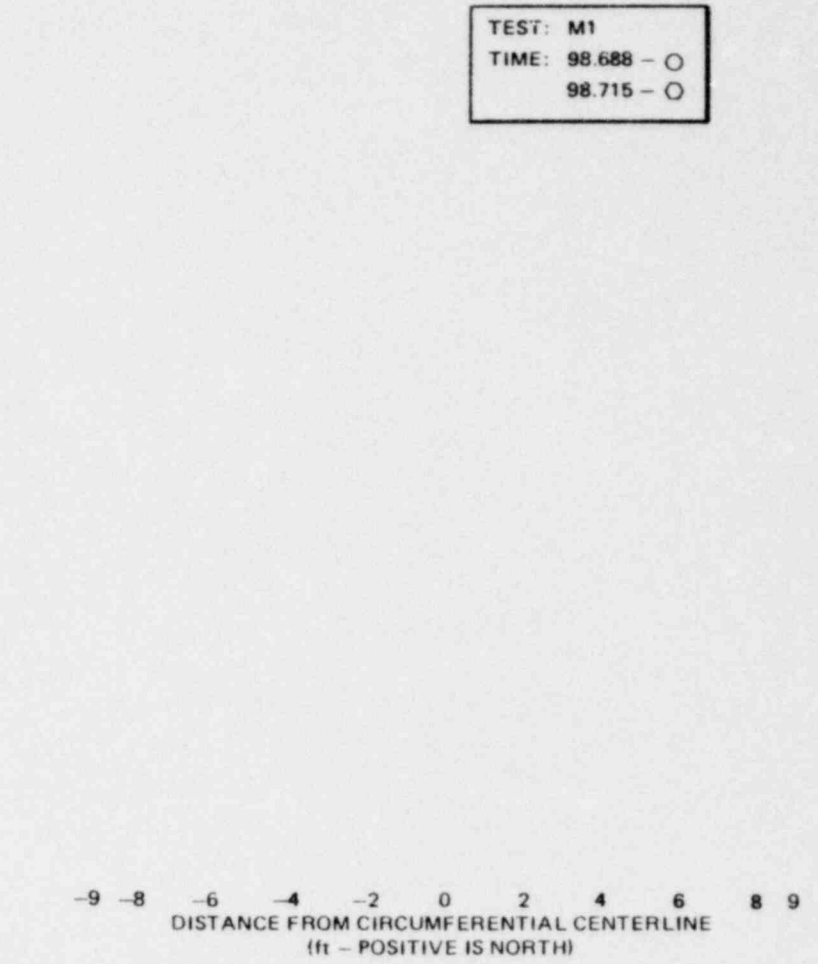

Figure 6.2.1-65. Axial Wall Pressure Profiles Following a Type 1 Chug in Test M1, 98.688 and 98.715 Seconds

*Proprietary information deleted

Figure 6.2.1-66. Circumferential Wall Pressure Profiles Before a Type 2 Chug in Test M9, 49.417 and 49.487 Seconds

Figure 6.2.1-67. Axial Wall Pressure Profiles Before a Type 2 Chug in Test M9, 49.417 and 49.487 Seconds

*Proprietary information deleted

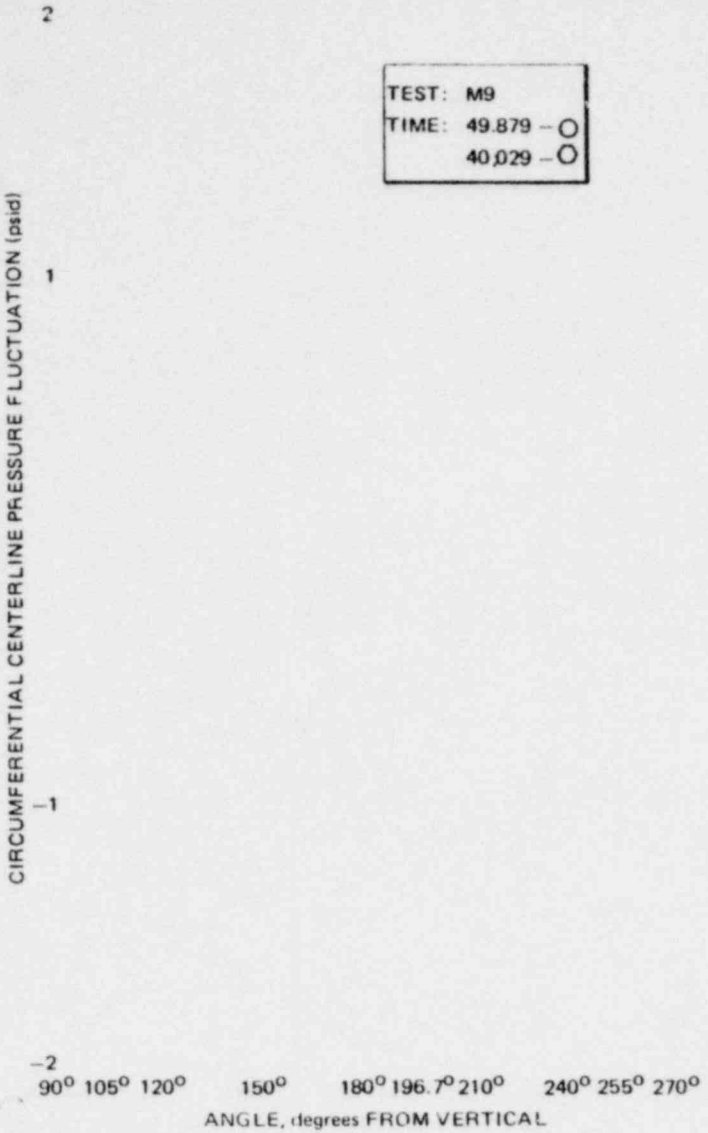

Figure 6.2.1-68. Circumferential Wall Pressure Profile Following a Type 2 Chug in Test M9, 49.879 and 49.928 Seconds

Figure 6.2.1-69. Axial Wall Pressure Profiles Following a Type 2 Chug in Test M9, 49.879 and 49.928 Seconds

*Proprietary information deleted

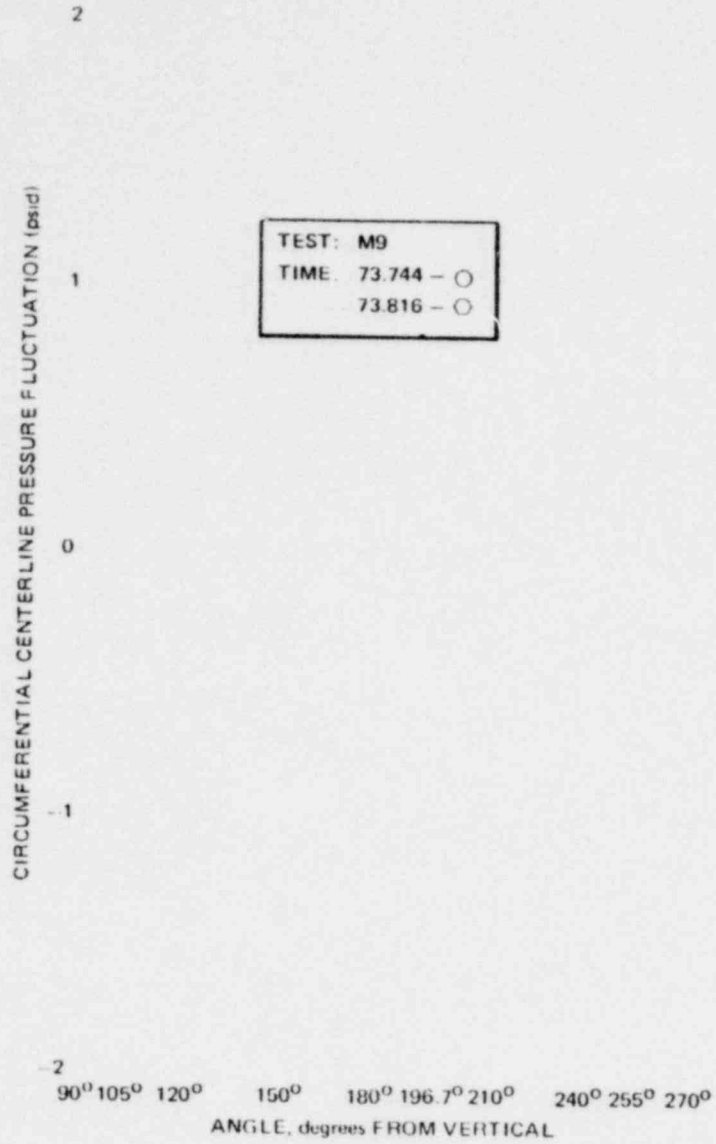

Figure 6.2.1-70. Circumferential Wall Pressure Profiles Before a Type 2 Chug in Test M9, 73.744 and 73.816 Seconds

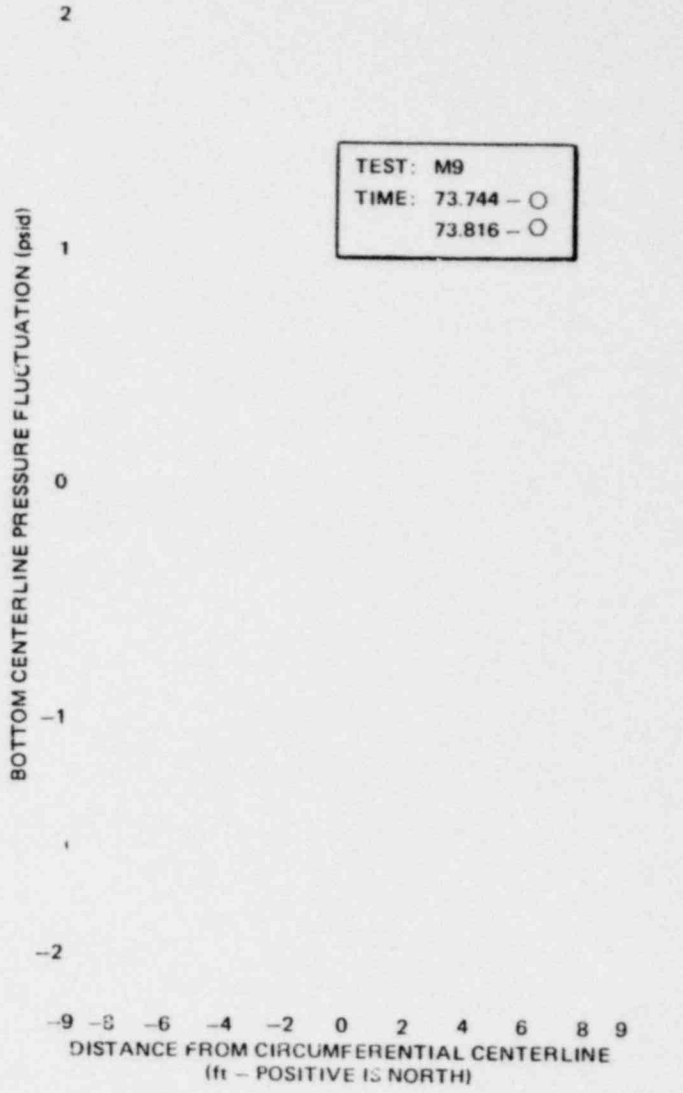

Figure 6.2.1-71. Axial Wall Pressure Profiles Before a Type 2 Chug in Test M9, 73.744 and 73.816 Seconds

*Proprietary information deleted

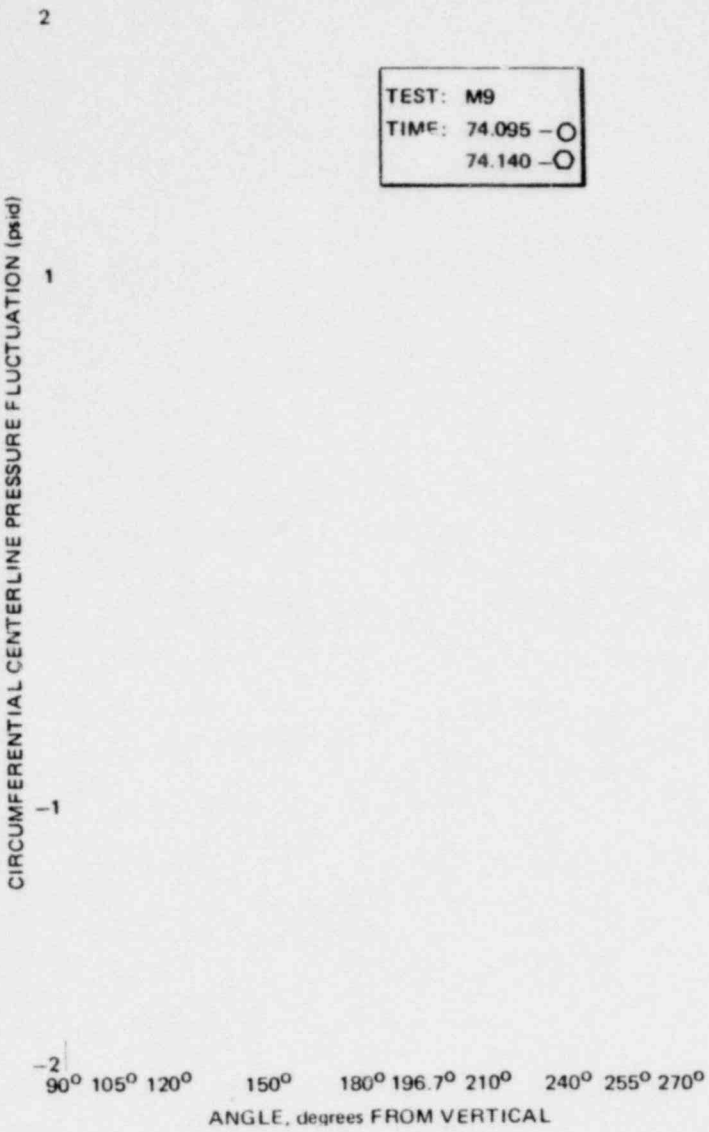

Figure 6.2.1-72. Circumferential Wall Pressure Profiles Following A Type 2 Chug in Test M9, 74.095 and 74.140 Seconds

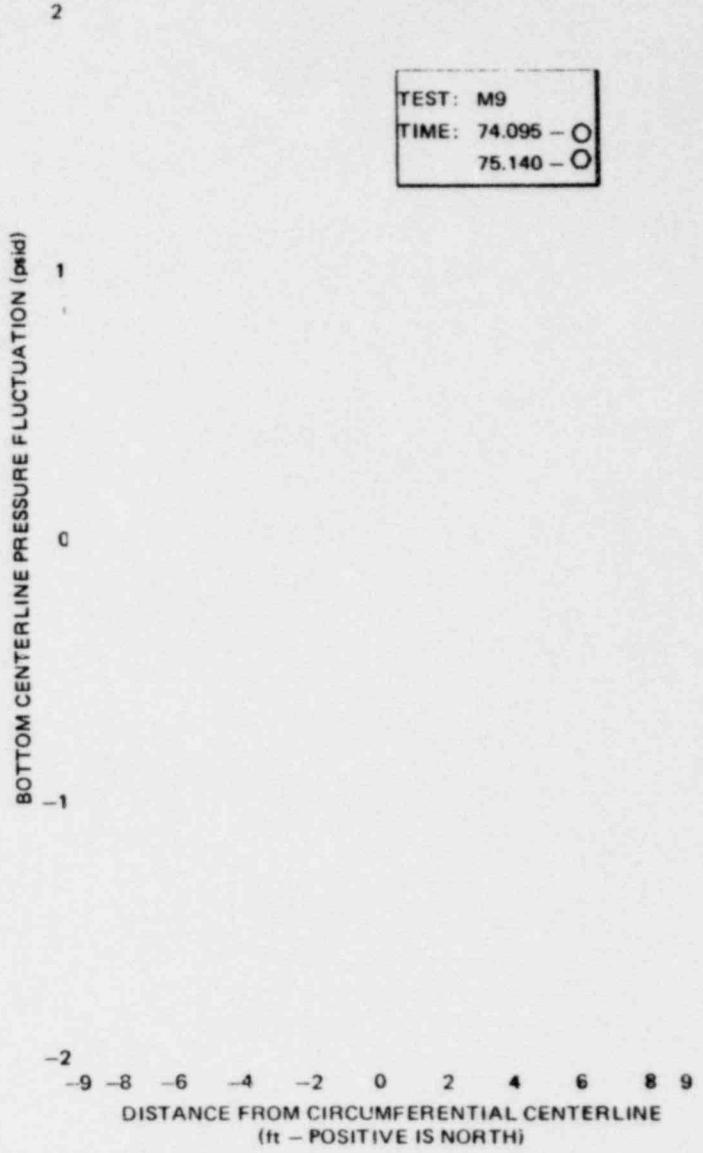

Figure 6.2.1-73. Axial Wall Pressure Profiles Following a Type 2 Chug in Test M9, 74.095 and 74.140 Seconds

*Proprietary information deleted

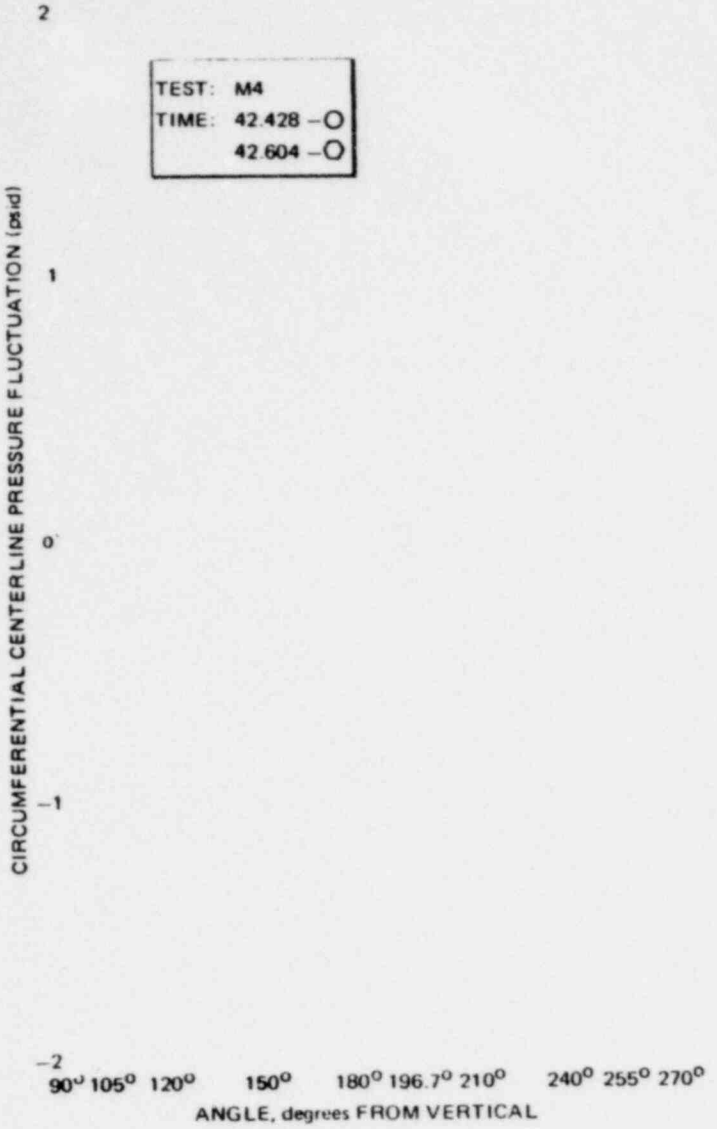

Figure 6.2.1-74. Circumferential Wall Pressure Profiles Before a Type 2 Chug in Test M4, 42.428 and 42.604 Seconds

Figure 6.2.1-75. Axial Wall Pressure Profiles Before a Type 2 Chug in Test M4, 42.428 and 42.604 Seconds

*Proprietary information deleted

Figure 6.2.1-76. Circumferential Wall Pressure Profiles Following a Type 2 Chug in Test M4, 42.793 and 42.845 Seconds

Figure 6.2.1-77. Axial Wall Pressure Profiles Following a Type 2 Chug in Test M4, 42.793 and 42.845 Seconds

*Proprietary information deleted

Figure 6.2.1-78. Circumferential Wall Pressure Profiles Before a Type 2 Chug in Test M4, 67.294 and 67.347 Seconds

Figure 6.2.1-79. Axial Wall Pressure Profiles Before a Type 2 Chug in Test M4, 67.294 and 67.347 Seconds

*Proprietary information deleted

Figure 6.2.1-80. Circumferential Wall Pressure Profiles Following a Type 2 Chug in Test M4, 67.540 and 67.586 Seconds

Figure 6.2.1-81. Axial Wall Pressure Profiles Following a Type 2 Chug in Test M4, 67.540 and 67.586 Seconds

*Proprietary information deleted

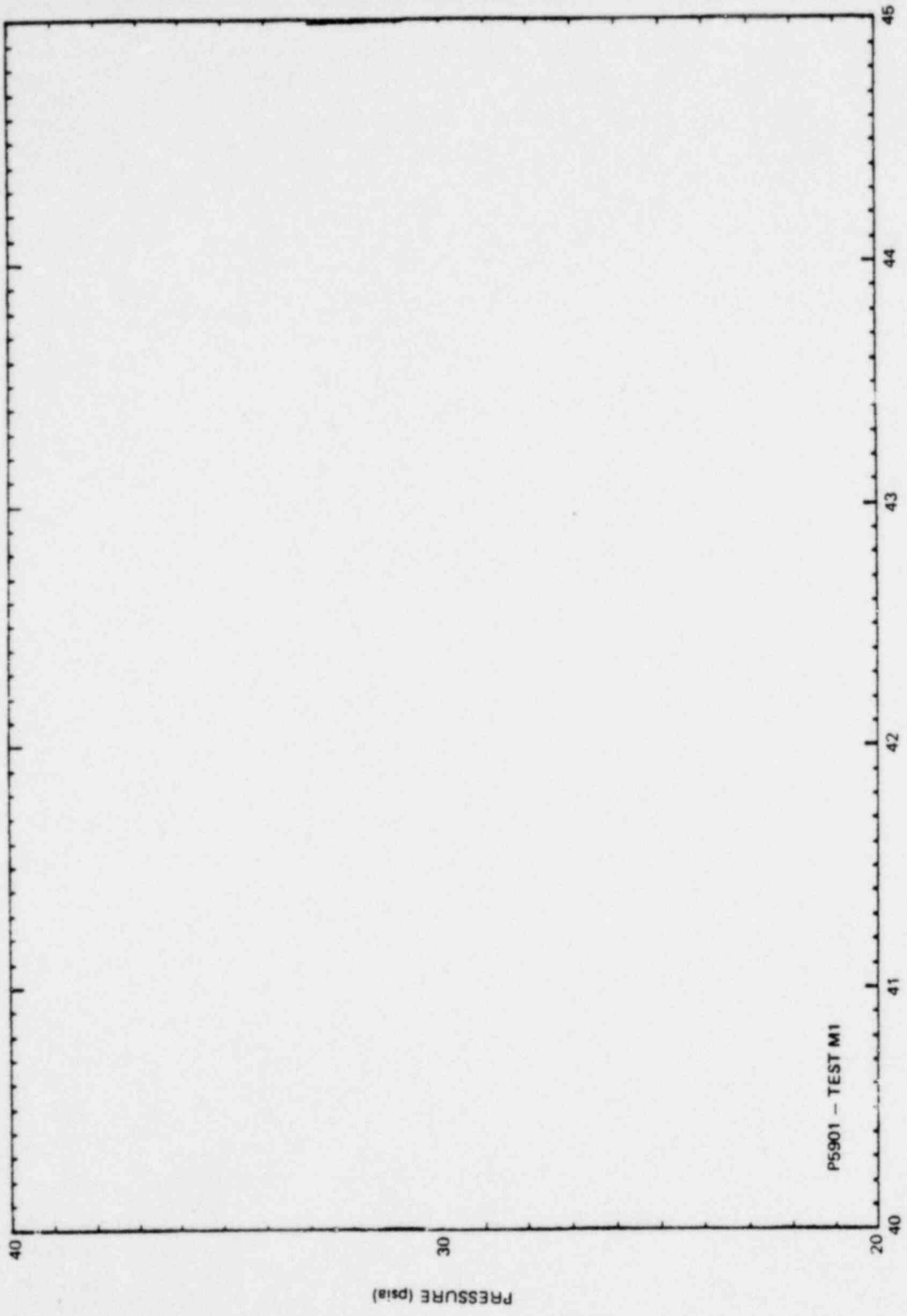

Figure 6.2.1-82. Typical Vent Header Pressure Signal During Type 2 Chugging

*Proprietary information deleted

1157 313

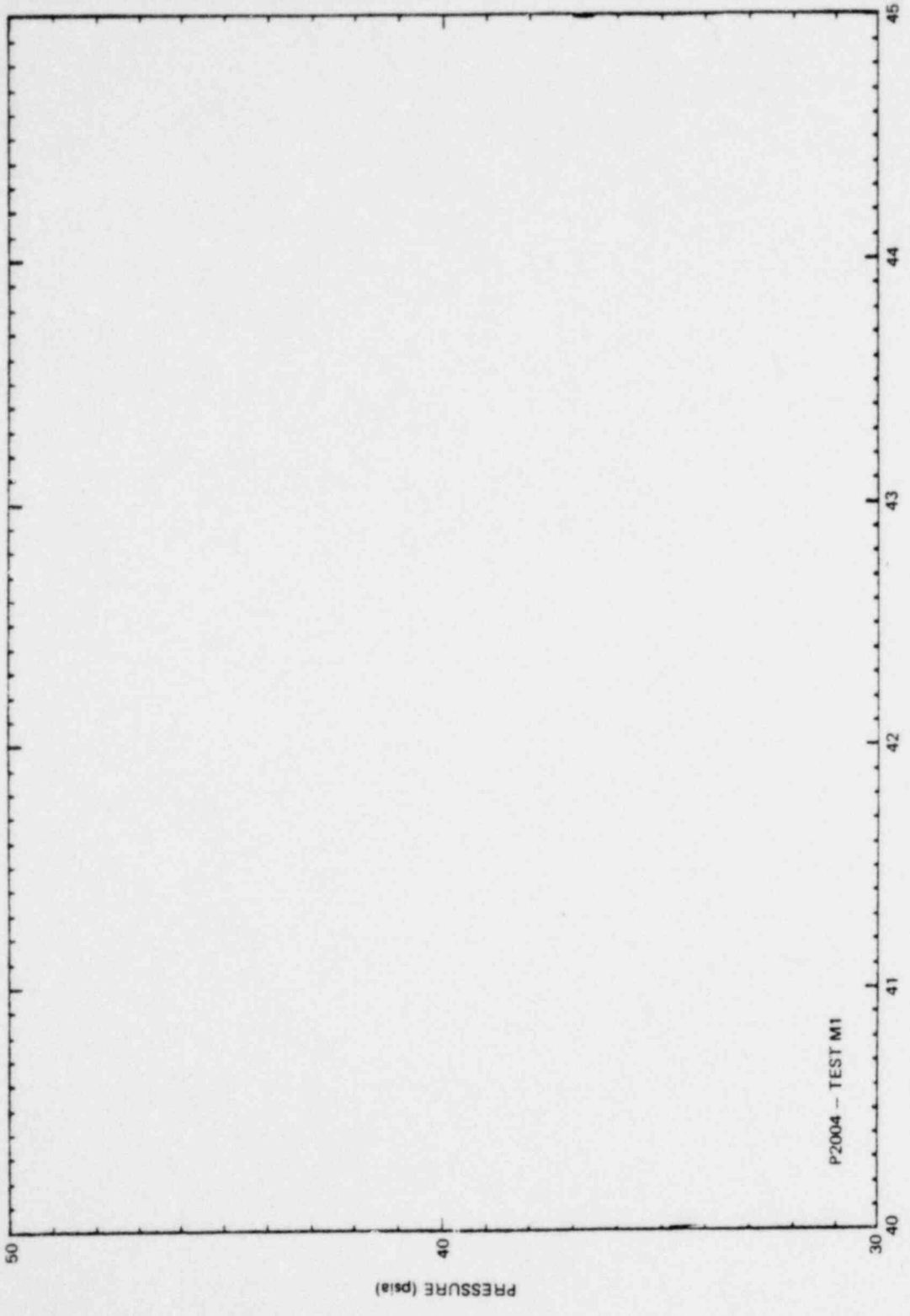

Figure 6.2.1-83. Typical Vent Line Pressure Signal During Type 2 Chugging

*Proprietary information deleted

1157 314

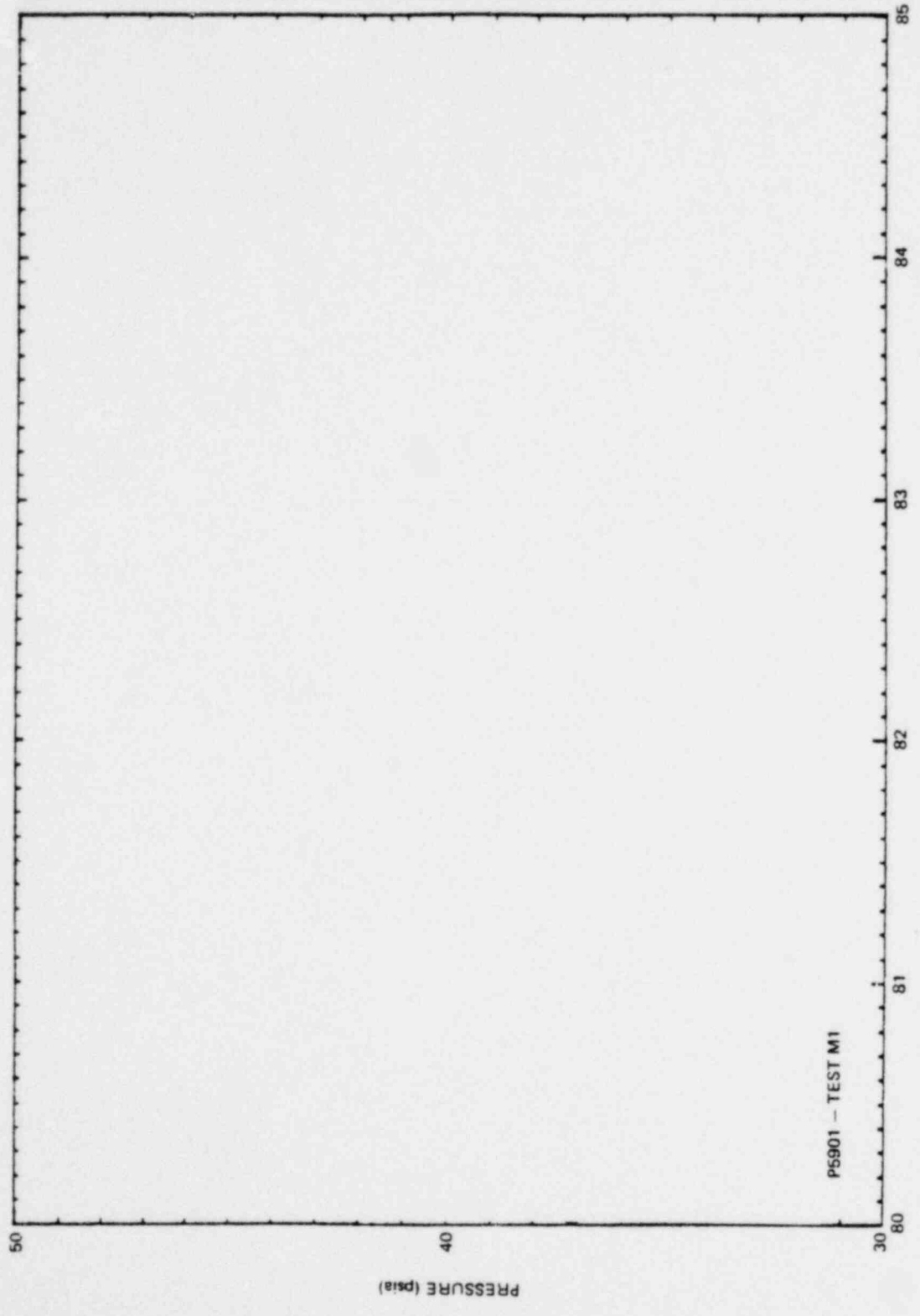

Figure 6.2.1-84. Typical Vent Header Pressure Signal During Type 1 Chugging

*Proprietary information deleted

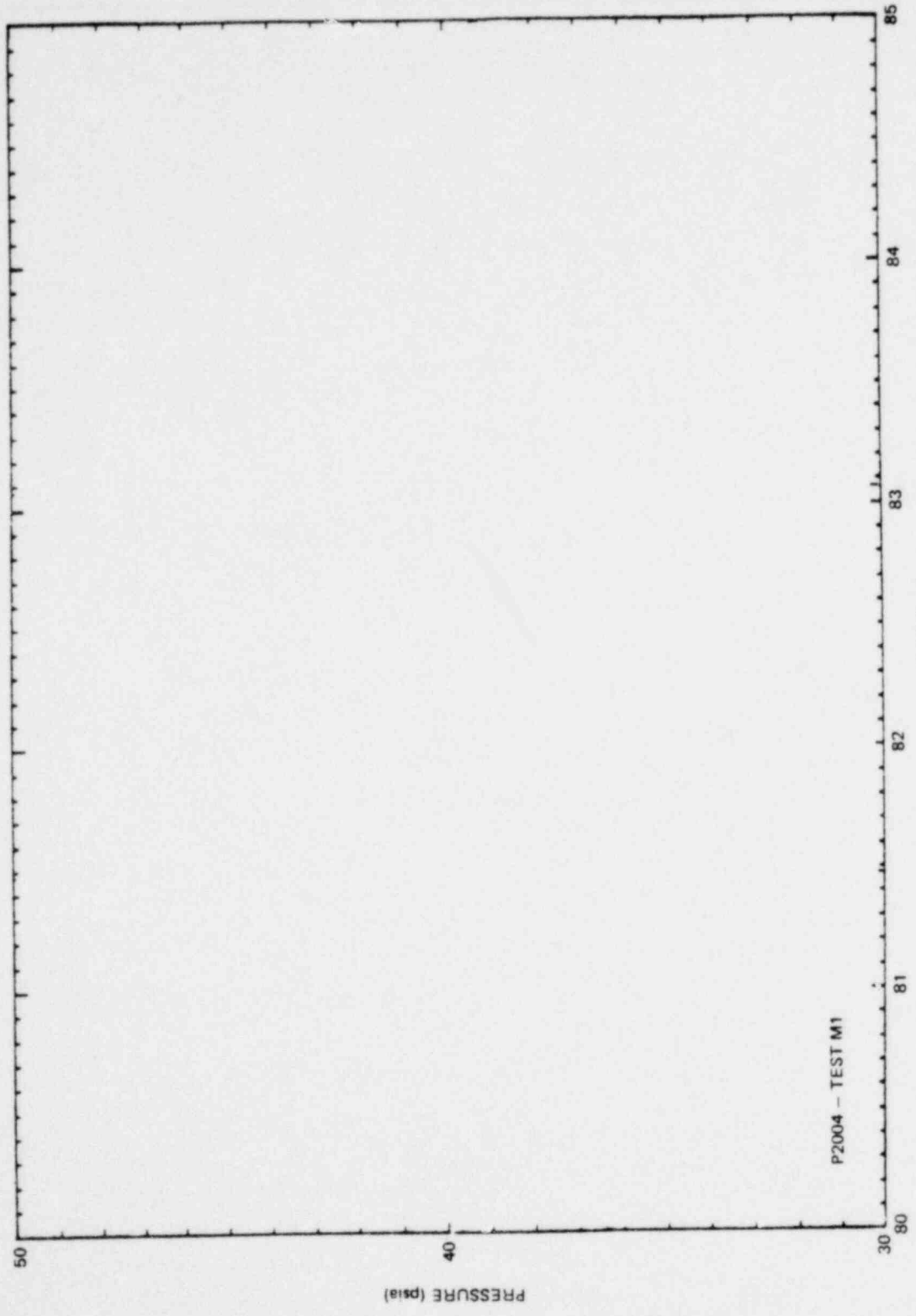

Figure 6.2.1-85. Typical Vent Line Pressure Signal During Type 1 Chugging

*Proprietary information deleted

6.2.2 Condensation Oscillations

After the pool swell event following blowdown in the FSTF tests, a short period (5-10 seconds) of irregular, relatively low-amplitude pressure oscillations occurs throughout the wetwell. These oscillations, which are also present in the drywell and vent system, build up gradually to become continuous and regular. This is the start of the condensation oscillation (CO) period.

During this period, a small portion of the steam exiting the downcomers goes into forming a "bubble" at the exit while the major portion of the steam condenses at the bubble interface. It is this condensation process (governed in part by the convection heat transfer at the interface) that causes the oscillating behavior of CO.

To define more precisely the time period of condensation oscillations, the traces of the pressure transducer located in the vent header (P5901) are used, mainly because these traces exhibit similar behavior as the wetwell wall pressure transducers but are generally much cleaner. The start time of CO in every run is then defined as the time when P5901 exhibits a sinusoidal waveform. The CO period is defined to terminate at the time of the first chugging event. If no chugging is present in a run as defined by the chugging criteria given in Section 6.2.1, the CO period is defined as extending to the end of the run.

Table 6.2.2-1 gives the CO time interval for every run. All time references in Section 6.2.2 refer to start time of the data acquisition system. Also tabulated are the ranges of measured independent key parameters associated with each run over the CO interval. The parameters are

- Air content in steam flow (% mass)
- Blowdown flowrate measured at nozzle (lbs/s)
- Wetwell airspace pressure (psia)
- Local pool temperatures in the vicinity of downcomers 5 and 6 (°F)

6.2.2.1 General Pattern of Wetwell Pressure Dynamics. Run M7 had the largest pressure amplitudes of the steam-break runs and Run M8, the large liquid break test, produced the largest amplitudes of the entire test matrix. For these reasons, most of the data used for the analysis presented here are from these

two runs. Figures 6.2.2-1 to 6.2.2-13 give the time history of a transducer located at the bottom of the wetwell equidistant from downcomers 1, 2, 3 and 4 (P3183) over the CO period for these two runs. The signals are subjected to linear trend removal prior to plotting.

The signal becomes sinusoidal at approximately 19 seconds for M7 and is followed 3 seconds later by a time period where the amplitudes are the highest of the run. This period lasts about 10 seconds after which the signal appears to be amplitude-modulated with a beat frequency of about 0.6 Hz. The amplitude decreases as a function of time until about 100 seconds where it becomes relatively insignificant (<1.0 psi peak-to-peak). The dynamic behavior of P3183 during M7 shown in Figures 6.2.2-1 to 6.2.2-9 is typical of most pool boundary transducer signals observed throughout the steam break runs.

The typical dynamic behavior of a pool boundary transducer signal throughout M8 is shown in Figures 6.2.2-10 to 6.2.2-13. After vent clearing and pool swell (∿9s) the waveform is irregular at low amplitudes until 20 seconds. The time period from 20 to 35 seconds is the crucial period where the amplitudes are high and the frequency of the signal is predominantly ∿5 Hz. The waveform is also characterized by the presence of sharp spikes during the ascending mode of the wave. This pattern changes to an irregular, low amplitude signal from 35 to 38 seconds. This change is probably due to the change of flow rate at this time from two-phase flow to single-phase steam flow. The sinusoidal behavior picks up again after 38.2 seconds with low amplitude and a dominant frequency and decays away at 44 seconds.

Detailed reduction of the amplitudes and frequencies of pool boundary transducer signals is given in Section 6.2 2.4.

6.2.2.2 Comparison of Drywell, Vent, Downcomer and Pool Boundary Pressure Dynamics. Figures 6.2.2-14 - 6.2.2-18 give the sample pressure traces of transducers located in the drywell (P2001), the elbow part of the vent (P2007), the vent header (P5901), a downcomer exit (P5443), and the pool boundary (P3185) for the time period of 31-32.1 seconds. In comparing amplitudes, it can be seen that the pool boundary transducer detects the highest values while

1157 318

the drywell transducer shows the lowest. The dominant CO frequency is present throughout the drywell, vent system and the wetwell for the entire test matrix.

To compare waveforms of the signals from transducers located throughout the facility, cross-power spectral density analyses (CPSD) were performed for M8 between pairs of data channels. Two signals were compared by denoting one as input and another as output in a dynamic linear system. The cross-power spectral density between the input and the output is equal to the transfer function times the power spectral density of the input. The following transducers were compared:

P2000 - transducer on top of drywell, cavity-type
P2001 - near middle of drywell, flush-mount
P2002 - vent line, near drywell, flush-mount
P2003 - near middle of vent line, cavity-type
P2004 - vent line, near wetwell, flush-mount
P5901 - vent header, above downcomers 5 & 6, flush-mount
P5443 - near exit of downcomer #4, flush-mount
P5523 - near exit of downcomer #2, flush-mount
P5643 - near exit of downcomer #6, flush-mount
P3185 - at centerline wetwell 180°, equidistant from downcomers #'s 3, 4, 5, 6, flush-mount
P3155 - at centerline wetwell 150°, flush-mount

CSPDs for eight time-blocks were averaged to yield the values for the time period from 24 to 32.4 seconds. These values are tabulated in Table 6.2.2-2. For every pair of transducers in the table, the first transducer is the input and the second is the output in the analysis. The dominant frequency appeared to be somewhere between 4.77 and 5.72 Hz; the uncertainty being due to the bandwidth of the CPSD algorithm (0.954 Hz). The frequency relationships (PSDs, phase angles, transfer functions, etc.) corresponding to these two frequencies are given in the table. Aside from the individual PSD values and the cross-spectral functions (CPSD's), the phase angles, transfer functions, and coherence functions are tabulated. The transfer function is defined by the ratio of the Fourier transform of one signal and the Fourier

transform of the other and in effect is a comparison of the amplitudes of the two signals at a given frequency. The coherence function is a measure of the coherence at a given frequency of two signals (a perfect coherence is achieved at the value of unity).

It can be seen from Table 6.2.2-2 that the coherence of the dominant frequency is very good for the transducers compared. There is a phase shift between the drywell transducer (P2001) and any vent system transducer, with a maximum shift of close to -180° between P2001 and the vent header transducer (P5901). As expected, coherence is very good and the phase shift is small for a pair of downcomer transducers (P5523 and P5643), between a downcomer transducer and wetwell transducer (P5643 and P3185), and for a pair of wetwell transducers (P3185 and P3155).

In general, the magnitude of the pressure oscillations increases as the downcomer exit is approached. The peak-to-peak amplitude measured by a downcomer transducer is of the same order of magnitude as measured by a wetwell transducer. An indication of this is shown in Figure 6.2.2-19 where the values of the ratios between the averaged (over a 1.1-second time interval) peak-to-peak amplitude of the downcomer #4 transducer (P5443) and a wetwell transducer (P3185) are graphed as a function of steam mass flow rate for all runs. As shown in the figure, the wetwell amplitudes are higher than downcomer amplitudes at high steam flow rates and the trend is reversed for lower steam flow rates. This amplitude ratio appears to be a function of other independent parameters as well, such as the wetwell airspace pressure (c.f. value from test M4 in Fig. 6.2.2-19).

Figure 6.2.2-19 also indicates that possible fluid structure interaction effects might be significant in the wetwell transducer signals for M8 and M7 (cf. Section 6.4). Since the pressure oscillations are transmitted from the vent exit to the wetwell pool bottom, a certain amount of attenuation can be expected thereby decreasing the amplitude (i.e., M > 1.0 for Figure 6.2.2-19). When the wetwell pressure amplitude is higher than the vent pressure amplitude, one would suspect other phenomena affecting the magnitude of the wetwell pressures.

1157 320

PSD's performed on wetwell transducers (e.g., P3185) downcomer transducers (e.g., P3443), and the vent header transducer (P5901) show the dominant waveform frequency is identical (within a ∿1 Hz resolution) in all locations. Generally wetwell transducer signals have more pressure spikes than the downcomer transducer signals; this is especially evident in the large liquid (M8) and large steam (M7) break runs. The vent header transducer (P5901) signals remain relatively 'clean' throughout each run and high pressure spikes are not evident. The corresponding PSD plots are given in Figures 6.2.2-20, -22 for M8 at the 31-32 second time interval. The dominant frequency common to all locations is 4.8 Hz at that time interval.

6.2.2.3 Downcomer Pressures and Frequencies. At a given time, the magnitudes of the pressure oscillations for the eight downcomers are different from one another. This is shown in Figures 6.2.2-23 - 6.2.2-26 where the peak-to-peak downcomer amplitudes are plotted for M7 and M8.

The downcomer signals are also amplitude modulated, similar to wetwell pressure signals, with the modulation especially evident in the middle of the CO time interval. The time variation of the pressure amplitudes is complicated due to the modulation, but the amplitude appears to build up at the beginning of CO and slowly declines thereafter. This trend is also observed for wetwell transducers (cf. Figure 6.2.2-2 to Figure 6.2.2-6).

Figures 6.2.2-23 and 6.2.2-24 show that for M7 the downcomers at the narrow side of the wetwell generally have slightly higher pressure magnitudes than the wide side ones. This is not so for M8, where the magnitudes are about the same (see Figures 6.2.2-25 and 6.2.2-26). In the above figures, the time interval "width" over which the peak-to-peak pressure magnitudes were determined ranged from ∿0.06 seconds for M7 to ∿0.14 seconds for M8. The magnitudes are also observed to be generally uniform traversing from the south end to the north end. In both M7 and M8, (particularly the latter) the downcomer amplitudes are characterized by regular oscillations with irregularly occurring pressure spikes. These spikes contribute significantly to the non-uniformity of the spatial and time variation of amplitude.

Figures 6.2.2-27 and 6.2.2-28 show the time variation of the important frequencies for a transducer located in the downcomer (P5443) for M7 and M8. The frequency values are obtained from power spectral density (PSDs) analyses performed on the signals with linear trend removal and over a one second period. The solid circles on the figures identify the dominant frequency as characterized by the highest PSD values. If two solid circles appear for the same time, then the PSD values are comparable at those frequencies. The criteria for selecting the frequencies to be plotted is

$$PSD(f) > 0.1 \{PSD(f)\}_{\text{dominant frequency}}$$

The frequency increment (Δf) is 0.954 Hz and the bandwidths are shown by vertical lines. In Figure 6.2.2-28 the time when the flow is suspected to change to steam only (break uncovered) in M8 is marked.

Figure 6.2.2-27 shows that the dominant frequency stays at about 7 Hz throughout most of the M7 CO time interval. There is a significant frequency of ~45 Hz at later times and this frequency dominates towards the end of the period. The 45-Hz frequency is present in downcomer and wetwell transducer signals but is absent in the vent header signal; it has been shown to be one of the natural higher mode downcomer acoustic frequencies.

The downcomer signal for M8 is comprised of more frequencies, as shown in Figure 6.2.2-28. The dominant frequency during the CO period stays constant between 4.8 and 5.7 Hz and changes to 6.7 Hz after the time of downcomer flow change (break uncovered).

6.2.2.4 Wetwell Pressures and Frequencies. The wetwell pressure transducer data are especially important for containment loading function definition. In the following sections, data results are used to describe the spatial distribution of pool boundary loads. The amplitude values of the pressure oscillations are described, and different reduction methods are performed to investigate parametric effects and frequency relationships. A table consisting of representative amplitude and frequency data results and their corresponding independent system parameter values are given. A comparison

of the parametric trends of the data is made with other available full-scale data. This is followed by a description of the wetwell oscillation frequency results.

6.2.2.4.1 Spatial Distribution of Pool Boundary Pressures - The net vertical pressure force exerted on the submerged portion of the wetwell wall is determined by multiplying each pressure transducer with its assigned area and summing the calculated vertical force components. The spatial distribution of the pressure is investigated over the time period corresponding to the largest vertical forces existing on the shell. Figure 6.2.2-29 gives the calculated total vertical force for the time period of 24 to 33 seconds in M8. The high peaks at the time period of 26.3-27.3 seconds and 31-32 seconds are investigated further and their expanded time scale plots are given in Figures 6.2.2-30 and 6.2.2-31.

The times corresponding to the maximum/minimum vertical forces do not necessarily correspond to the times of the peaks of the individual pressure signals. This is caused mainly by the presence of irregularly occurring pressure spikes on the fundamental waveform. However, because the vertical force values calculated this way indicate best the resultant wetwell response as a system to CO pressure oscillations, the spatial distribution of pressure amplitudes is best described at the times corresponding to the maximum/minimum vertical forces.

Figures 6.2.2-32 - 6.2.2-33 show the wall pressure azimuthal profile through the centerline of the wetwell as measured by the transducers at two different instants of time. The highest pressure values are located at the bottom and the magnitude tends to decrease near the pool surface. The positive pressure loads are higher than the negative ones. Figure 6.2.2-33 shows an unusually high pressure at 150 deg from the top of the wetwell, which is attributed to the presence of a short-duration high spike at the time.

Figures 6.2.2-34 - 6.2.2-37 show the wall pressure profile beneath downcomers 5 and 6 and near the south end of the shell (beneath downcomers 7 and 8) at the same times. The profile patterns are similar to those through the centerline described earlier.

1157 323

The wall pressure axial profiles from the south end (-) to the north end (+) of the wetwell at 180° and 196.7° from the top are shown in Figures 6.2.2-38 - 6.2.2-41. The figures show that there is no consistent trend of pressure distribution at the bottom of the wetwell.

By comparison, the variation of the magnitude of pressure oscillations in the downcomers has been shown to be more uniform along each row of downcomers for a given time (see Figures 6.2.2-25 and 6.2.2-26).

A similar investigation was performed for M7; Figures 6.2.2-42 and 6.2.2-43 give the total vertical force for two time periods and Figures 6.2.2-44 - 6.2.2-47 show some spatial distribution of loads at these times. In general, the amplitudes of M7 are smaller than that of M8 and the spatial distributions from the south end to the north end of the shell are more uniform.

6.2.2.4.2 Magnitudes of Wetwell Pressure Oscillations - There are several ways to interpret the magnitudes of wetwell pressure oscillations. The first step common to all methods presented in this report is to time-average the magnitude of the oscillations over some time interval. The reason for doing this is because pressure spikes appear sporadically on the dominant waveform and the averaging process provides a mean value of the amplitude of the oscillations for a particular time. The data are thus averaged over a 1.1-sec time interval. Because amplitude modulation is observed (beat frequencies range from 0.6 Hz for M1 to 1 Hz for M8), these time intervals are chosen for the average so that the maximum and minimum peak-to-peak amplitudes in a beat period are included.

Wetwell wall pressure signal amplitudes may be broken up into components of frequencies by using values yielded by PSD analyses. Assuming that the waveform consists of a combination of sinusoidal waves, the PSD is composed of delta functions of height $A^2/2$ at the particular frequency of the sinusoids where A is the amplitude component. The zero-to-peak amplitudes associated with each of these frequencies may then be calculated by first calculating the area under the PSD spikes. This type of analysis has been performed for M8 at the 31 - 32 second time period and the results are presented below.

For M8, PSD plots show one dominant spike centering around 5 Hz and two smaller spikes centering around 11 and 16 Hz. The area under the spikes are calculated by using trapezoidal integration with the following boundaries:

Frequency (Hz)	Boundary of spikes (Hz)
5	2.86 - 7.63
11	8.58 - 13.4
16	14.3 - 19.1

The amplitude associated with the 5-Hz frequency contributes the most case to the overall value. The summation of the amplitude components of the three frequencies may be compared to the actual amplitudes of the waveform; this is shown in Figure 6.2.2-48 for the bottom center transducer (P3185). Furthermore, similar calculations can be done for other transducers located in the wetwell and the resulting values plotted to show the spatial distribution of calculated loads on the pool shell. This is shown in Figure 6.2.2-49 (circumferential direction at the centerline) and in Figure 6.2.2-50 (axial distribution at 180°). These plots may be compared to the actual data values plotted in a similar fashion (see Figures 6.2.2-33 and 6.2.2-39). This type of amplitude analysis is helpful in relating amplitudes to their corresponding frequencies.

To investigate the variation of wetwell shell loads with system parameters, the overall load experienced by the submerged portion of the wetwell should be noted. This is accomplished by first multiplying each of the 24 applicable submerged transducers by their areas of influence and summed together to get the vertical component of the force. Next the time averaged (over ~1.1-sec interval) value of the maximum/minimum forces is divided by the projected area (76012 $in.^2$) to yield a time and spatial averaged peak-to-peak pressure. The peak-to-average amplitudes obtained this way are tabulated in the seventh column of Table 6.2-3. The maximum peak-to-peak amplitudes of a particular time interval are also tabulated in the sixth column.

As a comparison, the time-averaged peak-to-peak amplitudes of the bottom center transducer (P3185) at the same time periods are tabulated, next to their maximum amplitude counterparts. The ratios of the time-average local

amplitudes to the time average overall amplitudes are graphed as a function of steam flow rate in Figure 6.2.2-51. These ratios lie between 1.75 to 3 and appear to be insensitive to flow rate magnitudes.

The first entry in the 8th column of Table 6.2.2-3 is the dominant waveform frequency as given by PSD analysis of P3185. Subsequent frequencies for each time period are values detected by PSDs to be significant via the criterion given in Section 6.2.2.3. For some time intervals, PSDs are not available and the dominant frequency tabulated is obtained by counting the peaks of a short-time history data plot. Frequencies obtained this way are identified with an asterisk in the table.

The important independent system parameters are extracted from data plots and listings at the midpoint ($\bar{t}$) of the time interval, Δt. The total flow rate is the nozzle blowdown flow rate. The wetwell airspace pressures in psia are obtained from the time history plots of P3009. The air content values in percentage mass are taken as the average values of the simultaneous grab sample measurements from the two vents performed for each run. For Runs M4 and M5 no measurements were taken, so the values listed for these runs are taken from the mean of all small steam-break grab samples (cg. Figure C-32). The last five columns in the table show the pool temperatures from the thermocouple string between downcomers 5 and 6. The column labelled 3186-4 give the temperatures of the pool nearest to the vent exit.

From the tabulated values of Table 6.2.2-3, an attempt is made here to show system parametric effects on the vertical component of the overall wetwell shell amplitudes. From Figure 6.2.2-52 where the amplitudes are graphed versus blowdown steam flow rate, amplitudes for the large liquid blowdown test M8 are observed to be at least a factor of two higher than the amplitudes of steam blowdown test data at similar steam flow rates.* Amplitudes decrease as the steam flow rates decrease.

*The steam flow rates in the vents of liquid break tests are calculated using a flow quality of 30%. This quality approximate that obtained assuming isenthalpic expansion of the blowdown flow throughout the transient.

1157 26

Figure 6.2.2-53 shows amplitude vs pool temperature for windows from Figure 6.2.2-52 where liquid-break and steam-break amplitudes appear at the same steam flow rate. The air content values appear in parentheses. This graph confirms the increase by a factor of two between the different breaks as observed in Figures 6.2.2-52. At later times in M8 when the break is uncovered and most likely steam only is flowing through (i.e., quality = 100%) the amplitude is very near that of a steam-break at similar steam flow rate.

The wetwell airspace pressure effect on amplitude is shown in Figure 6.2.2-54 where the steam-break average amplitudes at a steam flow rate of 150 lbm/s are plotted versus wetwell airspace pressure. It appears that within the pressure range of 30-40 psia, the wetwell airspace pressure does not appear to affect pressure magnitudes.

No definitive trends are observed for amplitudes as a function of local pool temperature. To study the initial submergence effect on amplitudes, steam-break values are plotted at three different vent submergences. Amplitudes appear to increase as submergence increase, as shown in Figure 6.2.2-55.

Consistent trends are difficult to observe for the amplitude values versus air content values in the fluid flow.

Steam-break amplitude data appear to correlate well with liquid-break amplitude data when the energy ('heat') rates are taken into account, as shown in Figure 6.2.2-56, where the amplitudes increase linearly as a function of energy rate. The energy rate ($\dot{H}$) is defined as

$$\dot{H} = \dot{M}_{total}(x\, h_g + (1 - x)\, h_f)$$

where x is the flow quality.

The flashing fractions calculated assuming an adiabatic expansion at transient system conditions varied by ±16% of 0.30. For simplicity in plotting this graph, a constant flow quality of 30% is assumed for all liquid-break data before the break is uncovered. For M8 data enthalpy values h_g and h_f are taken at a pressure of 45 psia of saturated steam. For all other runs enthalpy values are taken at a pressure of 35 psia. These are the pressures in the vent system during CO.

The energy rate ($\dot{H}$) is a good correlating parameter from a phenomenological standpoint. The wetwell wall pressure oscillations (and therefore their magnitudes) are produced by the bubble interface motion. This interface motion is caused by the time-variations of the condensation rate, which, although affected by local pool temperature and steam air content, should be directly proportional to the incoming energy or heat rate into the bubble (especially if steam air content and pool temperature remain approximately constant during CO).

The M7 and M8 data bank had been fairly exhausted in plotting Figure 6.2.2-56, so beyond the energy rate of 4×10^5 Btu/second, the difference in amplitude values between liquid-break and steam-break data having the same energy rate values is not due to data scatter. In other words, the highest average amplitude value from the M7 test is approximately 2.64 psi peak-to-peak, and the lowest average amplitude value for the M8 test during two-phase flow is 2.83 psi peak-to-peak.

The amplitude values plotted in Figure 6.2.2-56 are calculated directly from test results. However, there is evidence that fluid/structure interaction effects exist in the large-break tests. Therefore, the data trends as plotted may change appreciably when FSI effects are separated from the data.

All the wetwell transducer signals show an increase of amplitude as a function of time during the start period of C.O. This is evident in Figure 6.2.2-56 where data points at the start period are asterisked in the plot. They are seen to be lower in value than their neighboring points. This increase is not observed in the transducer signals of the downcomers and therefore is

probably related to the wetwell pool and/or structure response as the system underwent the transition from the pool swell period to a stable C.O. period.

Table 6.2.2-4 provides several average (over a ~1.0 second period) pressure amplitudes from downcomers #6 (P5643) and from the calculated wetwell vertical forces ($\bar{A}$ (24)) at time intervals during the start of C.O. Note that the downcomer pressure amplitudes do not change much compared to the large increase of the wetwell amplitudes. For this reason, it is expected that if averaged downcomer pressure amplitudes are plotted versus their enthalpy rates, the drop in amplitude of the asterisked points of Figure 6.2.2-56 will not occur. Indeed, the downcomer pressure readings are devoid of fluid/structure interaction effects which are shown to affect wetwell pressure readings in Section 6.4.

The vertical forces on the wetwell calculated from the output of the submerged pressure transducers may be compared to the vertical forces on the wetwell calculated from the output of the strain gage bridges on the support columns. Figures 6.2.2-57 and 6.2.2-58 show the results of the latter for test M8 at the 26.3-27.3 seconds and 31.0-32.0 seconds time period, where the Young's Modulus is taken as 27.9 psi/(μin./in.). These figures, compared to Figures 6.2.2-30 and 6.2.2-31, show that the vertical forces from strain gage calculations are similar in waveform and magnitude to the forces calculated from transducers.

6.2.2.4.3 Wetwell CO Frequencies - The time variation of the dominant frequencies yielded by PSDs of wall pressures are plotted in Figures 6.2.2-59 for M7 and Figures 6.2.2-60 and 6.2.2-61 for M8. In general, they behave similarly to the time variation of downcomer dominant frequencies as discussed in Section 6.2.2.2. The criterion for selecting the frequencies to be plotted is the same as stated in that section. As is shown, the dominant frequency varies between 5.7 - 7.6 Hz during the major portion of the CO interval in M7. Higher frequencies are insignificant. At approximately 90 seconds, the dominant frequency shifts up to ~45 Hz, although the 7.6 Hz signal is still significant. The shifting trend is observed for all runs during very low flow

rates (∿30 lbm/s) and can also be seen in the downcomers. Since this high frequency is observed in the downcomer and wetwell pressure transducers only, it is believed that it is associated with the resonance frequency of the downcomer portion of the vent system.

For the large liquid break test (M8), the pressure signals are less 'clean' than for the steam break tests, as shown in Figures 6.2.2-60 and 6.2.2-61.

The dominant frequency varies between 4.8-5.7 Hz during the two phase flow period and increases to 6.7 Hz after the break has uncovered. At the time period of 37.5 seconds, the dominant frequency is ∿32 Hz and is not shown in the plots. The reason of such a change of dominant frequency is not clear, but since this time corresponds to the time of the uncovering of the break, this high frequency may possibly be associated with the transition of the system from two-phase flow to steam only flow.

Frequencies around 11 and 16 Hz are also shown to be significant, and their contribution to the overall pressure amplitude may be seen from Figures 6.2.2-49 and 6.2.2-50. Recent shake tests on the test facility yield system resonance frequencies of similar values (cf. Section 6.4.1.4 and Appendix D).

The dominant frequencies of the CO waveform of all the runs are plotted versus their corresponding total flow rates in Figure 6.2.2-62. Most of the frequencies are obtained from PSD analyses. The figure shows that the dominant frequency is not very sensitive to flow rate although it tends to increase as the flow rate decreases. Another data trend that was observed is that higher amplitudes are associated with lower dominant frequencies.

1157 330

Table 6.2.2-1

FSTF TESTS: CONDENSATION OSCILLATION TIME INTERVAL AND PARAMETER RANGES

Test	Special Features	CO Time + Interval(s)	Air Content (% Mass)	Blowdown Flowrate(lbm/s)	Wetwell Airspace Pressure (psia)	Local Pool Temperature °F*				
						T3186-6	T3186-4	T3186-3	T3186-2	T3186-1
M1	Small steam break									
M2	Medium steam break									
M3	Small liquid break									
M4	Small steam break Increased airspace pressure									
M5	Small steam break Increased pool temperature									
M6	Small steam break Decreased submergence Increased pool temperature									
M9	Small steam break Increased submergence									
M10	Small steam break									
M7	Large steam break									
M8	Large liquid break									

+From start of data recording; and for runs with no chugging, the time interval is defined as extending to the end of the run.

*c.f. Figure 3.4-2 for precise location of thermocouples.

◊No data available, so values taken from average of all small steam-break data.

•Proprietary information deleted

6.2-95

NEDO-24539

1157 331

Table 6.2.2-2

RESULTS OF CPSDs PERFORMED FOR DRYWELL, VENT, WETWELL TRANSDUCER TEST M8

t = 24-32.4 s Dominant frequencies: 4.77 & 5.72 Hz

I.D.*	PSD (psi^2/Hz)		Angle (°)		CPSD		Transfer		Coherence	
P2000	0.47×10^{-2}	0.56×10^{-2}	25.8	27.7	0.37×10^{-2}	0.41×10^{-2}	0.80	0.73	0.97	0.98
P2001	0.31×10^{-2}	0.30×10^{-2}								
P2001	0.31×10^{-2}	0.30×10^{-2}	-277	-277	0.18×10^{-1}	0.18×10^{-1}	5.99	6.15	0.97	0.96
P2002	0.114	0.120								
P2001	0.31×10^{-2}	0.30×10^{-2}	-239	-237	0.36×10^{-1}	0.38×10^{-1}	11.6	12.6	0.95	0.95
P2003	0.44	0.51								
P2001	0.31×10^{-2}	0.30×10^{-2}	-212	-207	0.37×10^{-1}	0.40×10^{-1}	11.9	13.3	0.94	0.94
P2004	0.46	0.57								
P2001	0.31×10^{-2}	0.30×10^{-2}	-196	-192	0.45×10^{-1}	0.47×10^{-1}	14.6	15.5	0.95	0.93
P5901	0.69	0.79								
P5901	0.69	0.79	-319	-320	0.96	1.12	1.38	1.42	0.95	0.95
P5443	1.39	1.66								
P5523	1.06	1.05	-0.98	-4.28	0.99	1.00	0.94	0.96	0.96	0.98
P5643	0.96	0.98								
P5643	0.96	0.98	3.01	3.06	1.35	1.38	1.40	1.41	0.98	0.99
P3185	1.91	1.96								
P3185	1.91	1.96	0.79	0.75	1.7[illegible]	1.76	0.90	0.90	1.0	1.0
P3155	1.56	1.59								

*Transducers locations identified in Figures 3.4-1 through 4.

Table 6.2.2-3 (1 of 3)

CONDENSATION OSCILLATION DATA SUMMARY

Test I.D.	Δt (s)	$\bar{t}$ (s)	P3185(psi)		24 Transducers (psi)		ν(hz)	Total Flowrate (lbm/s)	Wetwell Airspace (psia)	Air Content (% mass)	Wetwell Temperature (°F)				
			A_{max}	$\bar{A}$	A_{max}	$\bar{A}$					3186-1	3186-2	3186-3	3186-4[0]	3186-6
M1															
M1															
M2															
M2															
M2															
M2															
M2															
M2															
M2															
M3															
M3															
M3															
M3															
M3															
M3															
M3															
M3															
M4															
M4															

*Proprietary information deleted

6.2-97

1157 773

NEDO-24539

Table 6.2.2-3 (2 of 3)

CONDENSATION OSCILLATION DATA SUMMARY

Test I.D.	Δt (s)	$\bar{t}$ (s)	P3185(psi)		24 Transducers (psi)		ν(hz)	Total Flowrate (lbm/s)	Wetwell Airspace (psia)	Air Content (% mass)	Wetwell Temperature (°F)				
			A_{max}	$\bar{A}$	A_{max}	$\bar{A}$					3186-1	3186-2	3186-3	3186-4◊	3186-6
M5															
M5															
M5															
M5															
M6															
M6															
M6															
M6															
M6															
M7															
M7															
M7															
M7															
M7															
M7															
M7															
M7															
M7															
M7															
M7															

•Proprietary information deleted

6.2-98

NEDO-24539

1157 334

Table 6.2.2-3 (3 of 3)

CONDENSATION OSCILLATION DATA SUMMARY

Test I.D.	Δ (s)	$\bar{t}$ (s)	P3185(psi)		24 Transducers (psi)		ν(hz)	Total Flowrate (lbm/s)	Wetwell Airspace (psia)	Air Content (% mass)	Wetwell Temperature (°F)				
			A_{max}	$\bar{A}$	A_{max}	$\bar{A}$					3186-1	3186-2	3186-3	3186-4[0]	3186-6
M7															
M7															
M7															
M8															
M8															
M8															
M8															
M8															
M6															
M9															
M10															

•Proprietary information deleted

6.2-99

1157 335

NEDO-24539

Table 6.2.2-4

COMPARISON OF DOWNCOMER PRESSURE AMPLITUDES VS WETWELL PRESSURE AMPLITUDES NEAR THE START TIME OF C.O.

Test	Time Interval (s)	Downcomer No. 6 (PS643) (psi)	$\bar{A}$(24) Wetwell (psi)
M7	19 - 19.9	3.98	1.92
M7	20 - 20.9	3.90	1.53
M7	23.5 - 24.5	4.17	2.64
M8	22.6 - 23.6	7.84	3.60
M8	24.2 - 25.2	8.40	5.92
M8	25.3 - 26.3	7.92	5.71

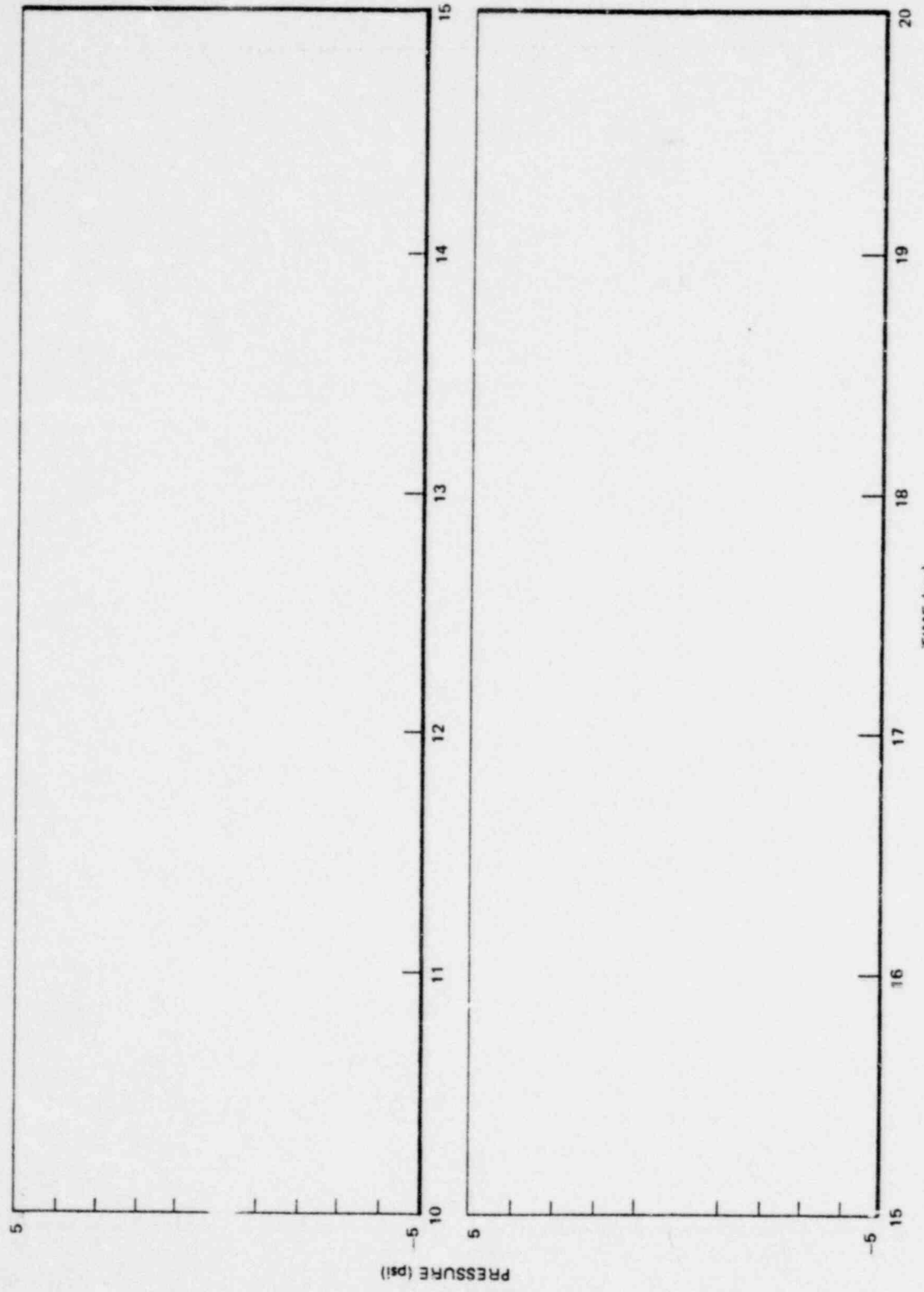

Figure 6.2.2-1. Dynamic Portion of Wetwell Pressure Transducer (P3183) Output, 10-20 Seconds, M7

*Proprietary information deleted

1157 337

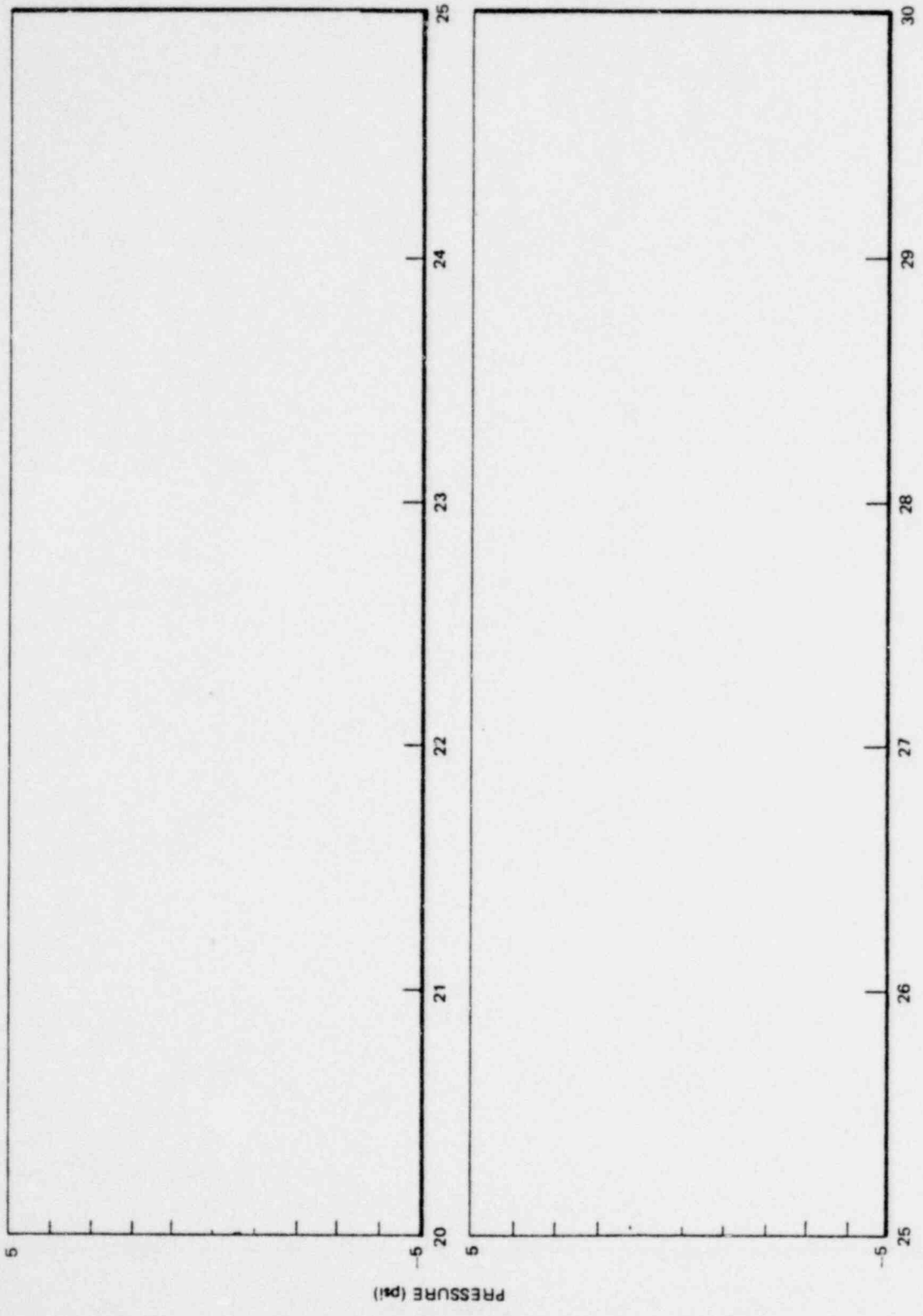

Figure 6.2.2-2. Dynamic Portion of Wetwell Pressure Transducer (P3183) Output, 20-30 Seconds, M7

*Proprietary information deleted

1157 338

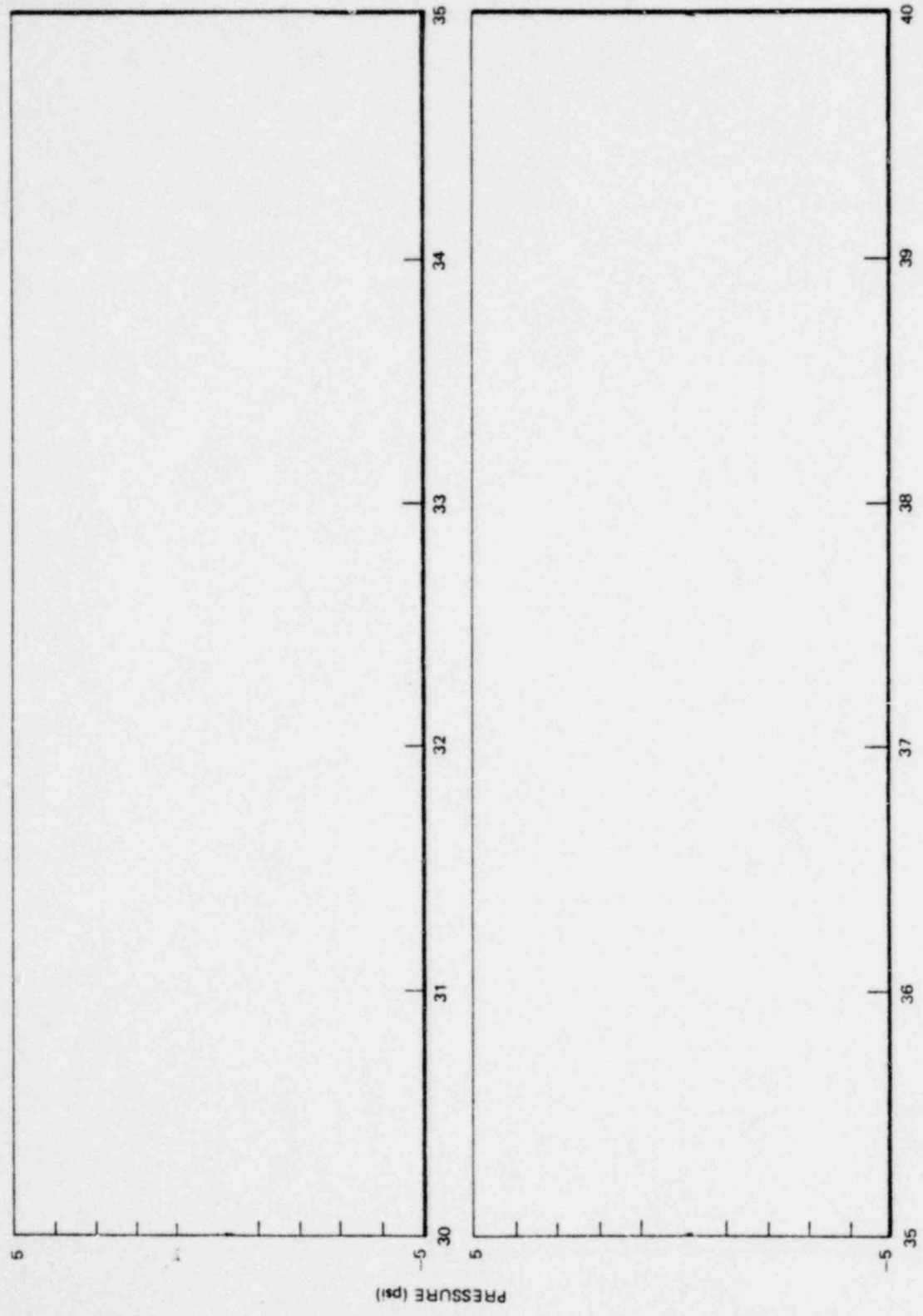

Figure 6.2.2-3. Dynamic Portion of Wetwell Pressure Transducer (P3183) Output, 30-40 Seconds, M7

*Proprietary information deleted

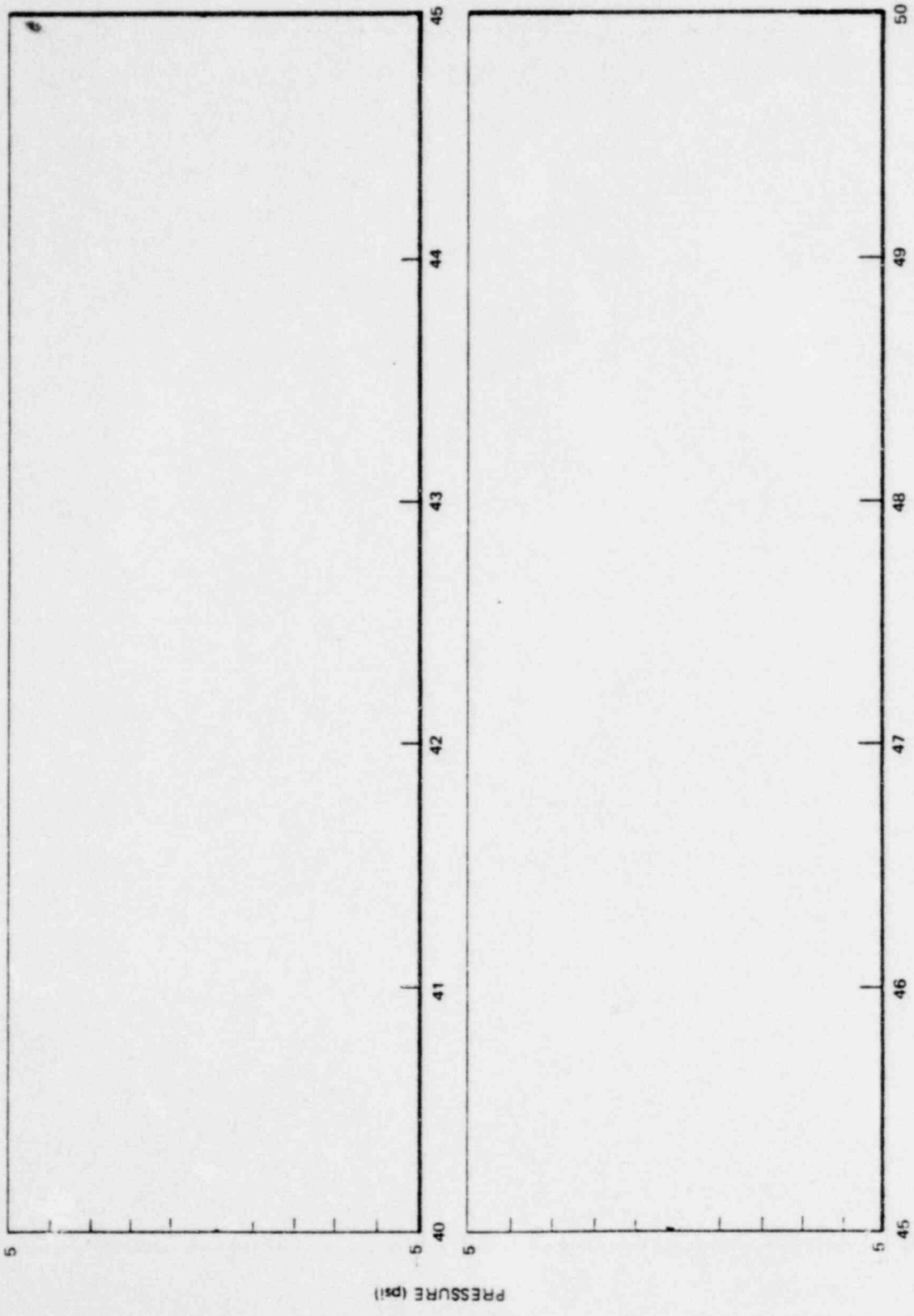

Figure 6.2.2-4. Dynamic Portion of Wetwell Pressure Transducer (P3183) Output, 40-50 Seconds, M7

*Proprietary information deleted

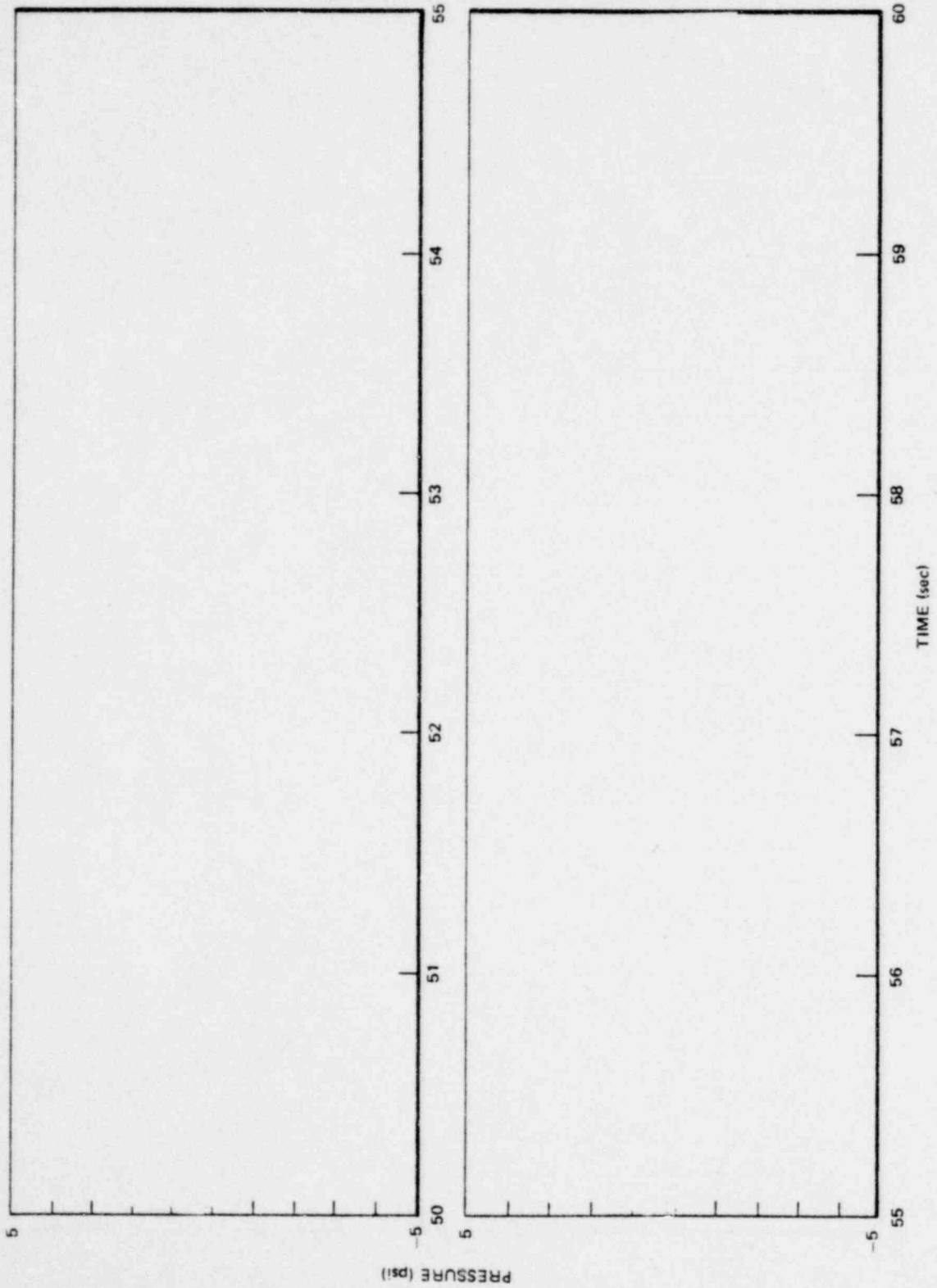

Figure 6.2.2-5. Dynamic Portion of Wetwell Pressure Transducer (P3183) Output, 50-60 Seconds, M7

*Proprietary information deleted

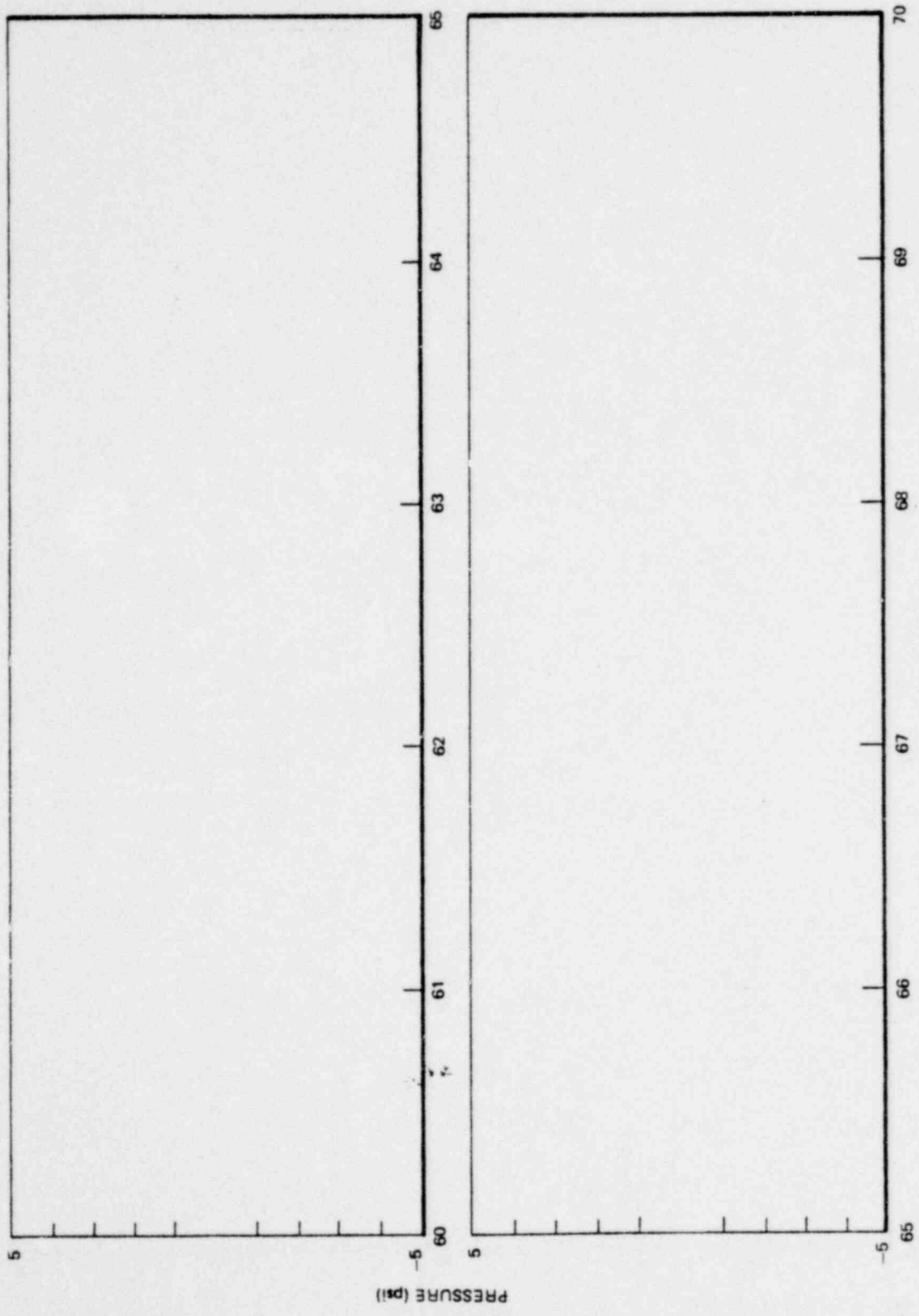

Figure 6.2.2-6. Dynamic Portion of Wetwell Pressure Transducer (P3183) Output, 60-70 Seconds, M7

*Proprietary information deleted

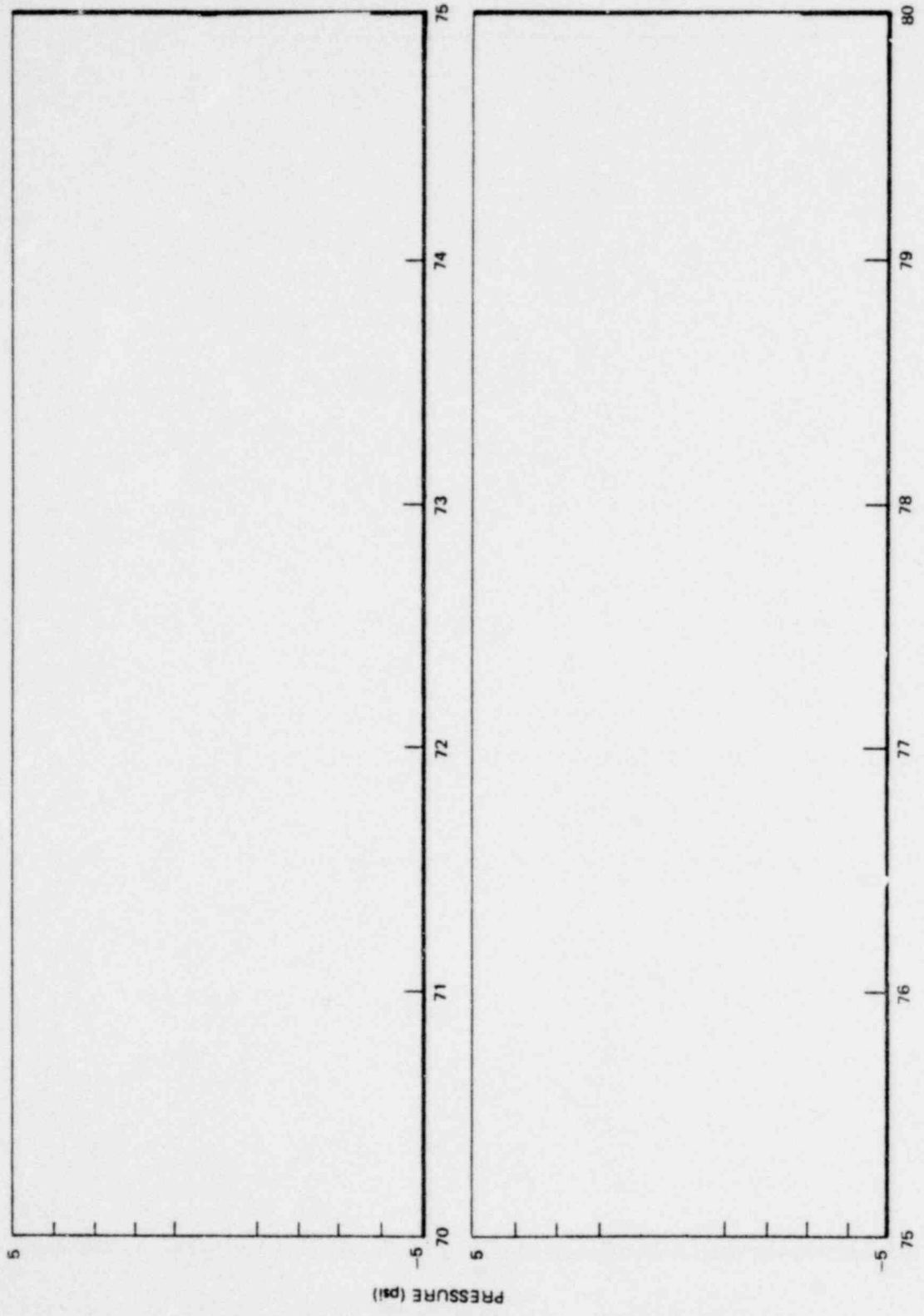

Figure 6.2.2-7. Dynamic Portion of Wetwell Pressure Transducer (P3183) Output, 70-80 Seconds, M7

*Proprietary information deleted

1157 343

Figure 6.2.2-8. Dynamic Portion of Wetwell Pressure Transducer (P3183) Output, 80-90 Seconds, M7

*Proprietary information deleted

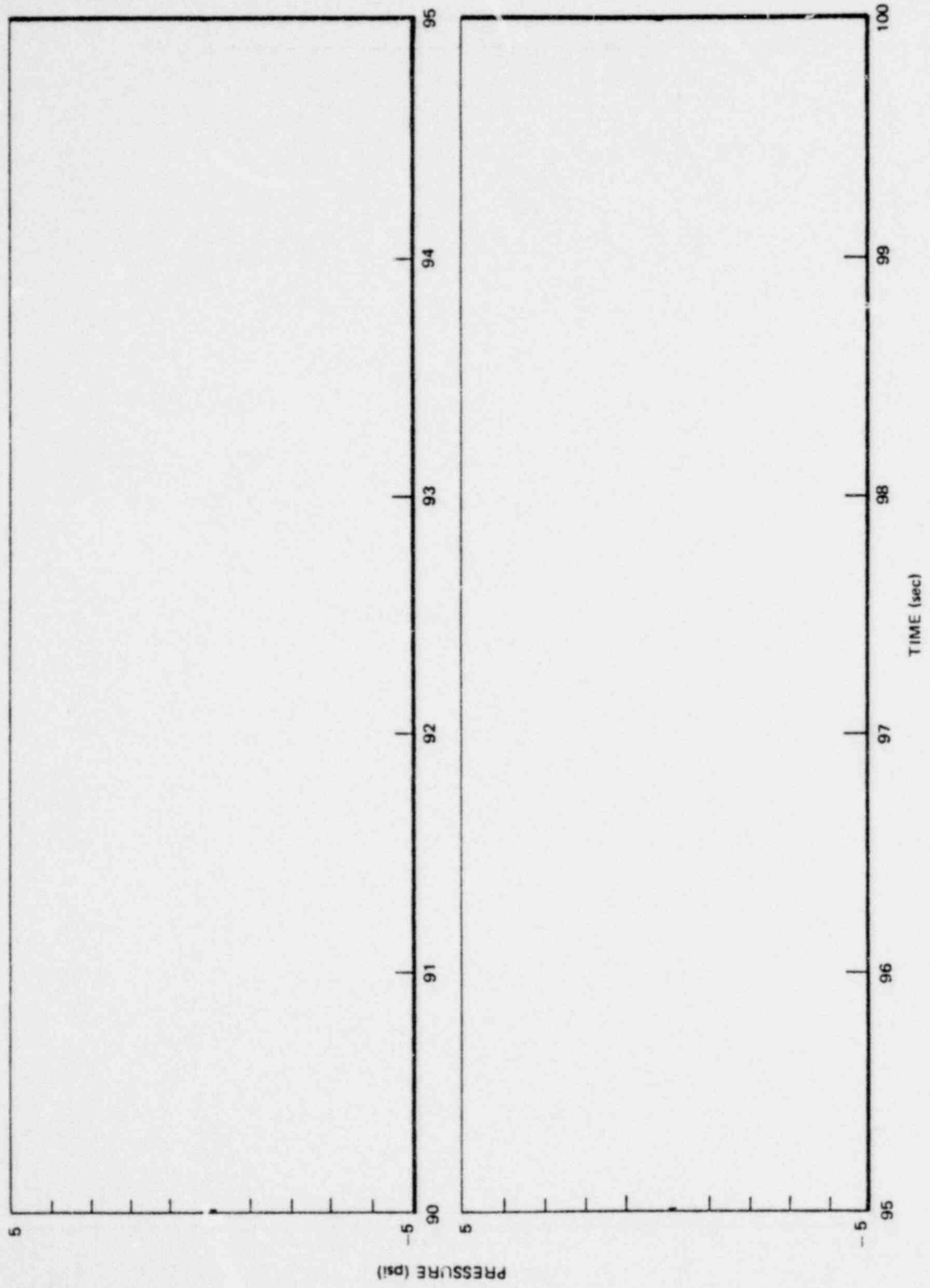

Figure 6.2.2-9. Dynamic Portion of Wetwell Pressure Transducer (P3183) Output, 90-100 Seconds, M7

*Proprietary information deleted

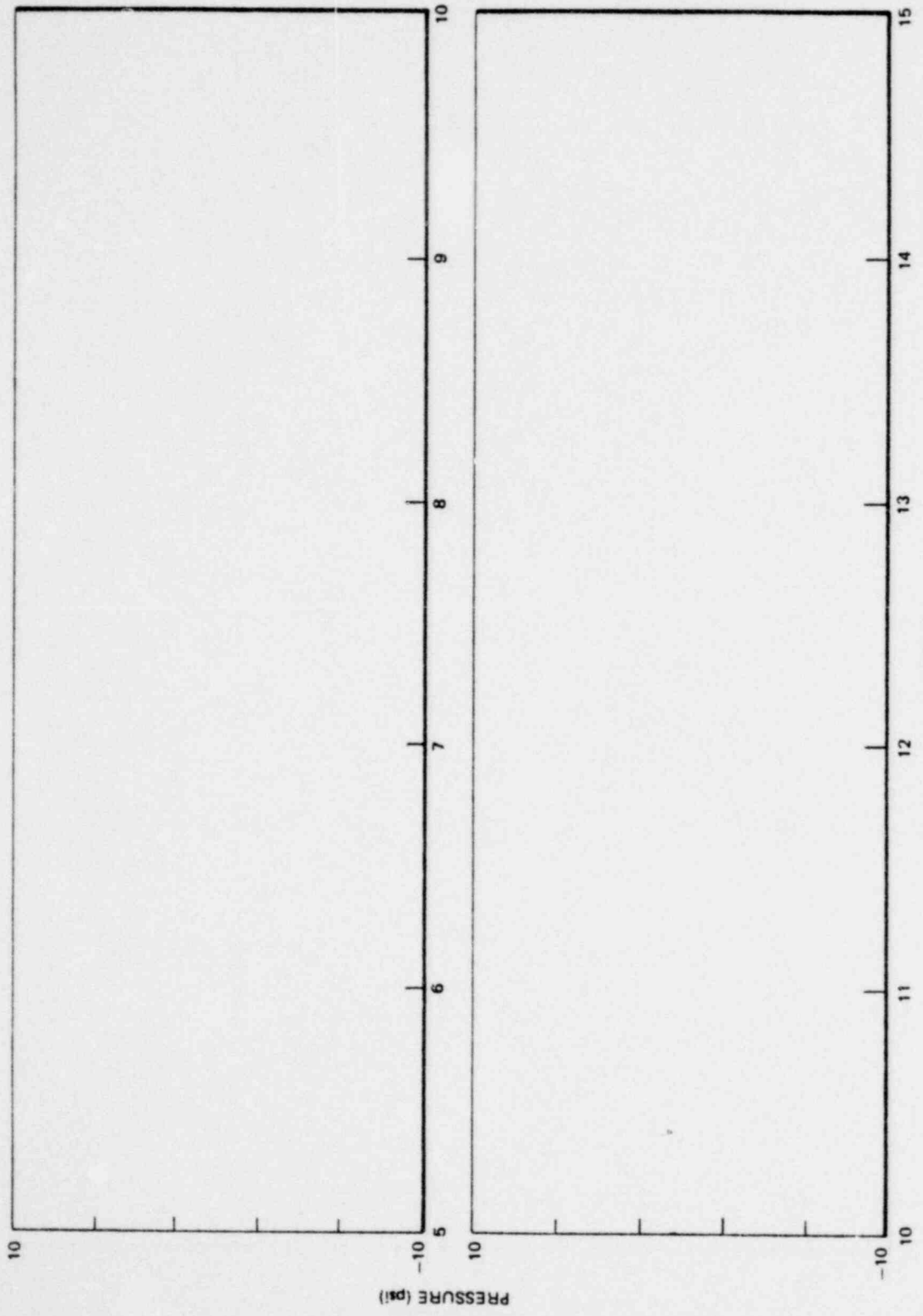

Figure 6.2.2-10. Dynamic Portion of Wetwell Pressure Transducer (P3183) Output, 5-15 Seconds, M8

*Proprietary information deleted

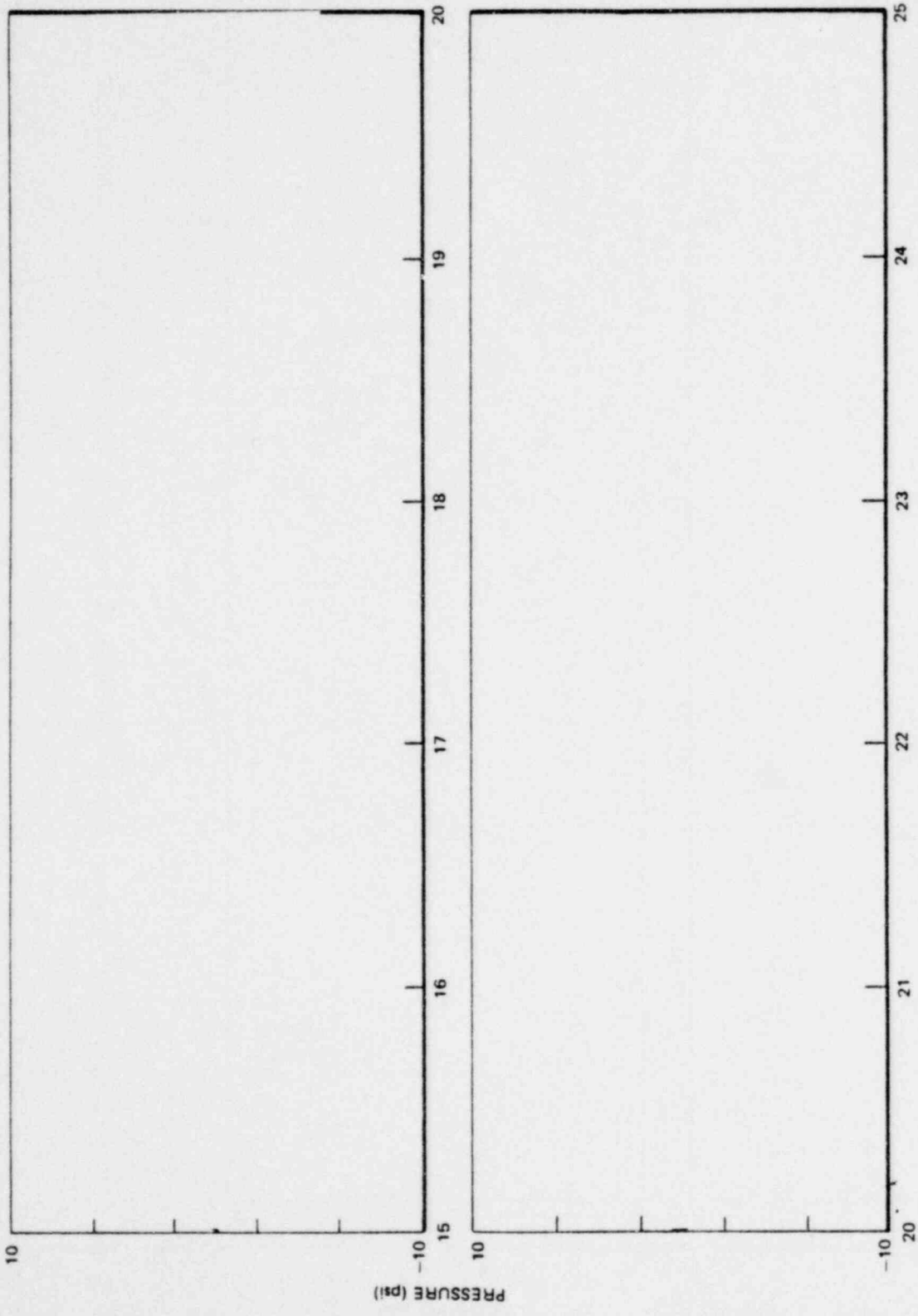

Figure 6.2.2-11. Dynamic Portion of Wetwell Pressure Transducer (P3183) Output, 15-25 Seconds, M8

*Proprietary information deleted

1157 347

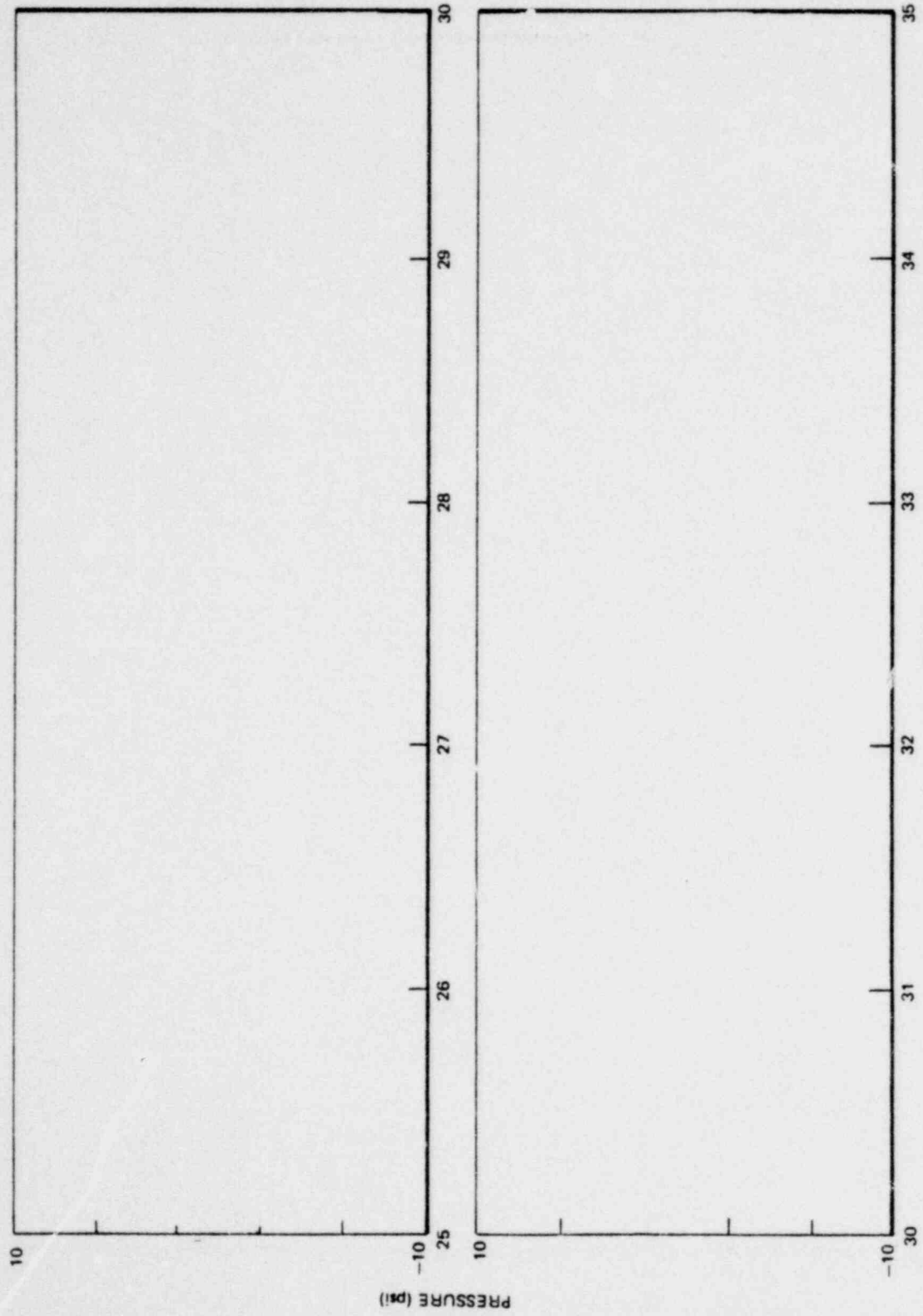

Figure 6.2.2-12. Dynamic Portion of Wetwell Pressure Transducer (P3183) Output, 25-35 Seconds, M8

*Proprietary information deleted

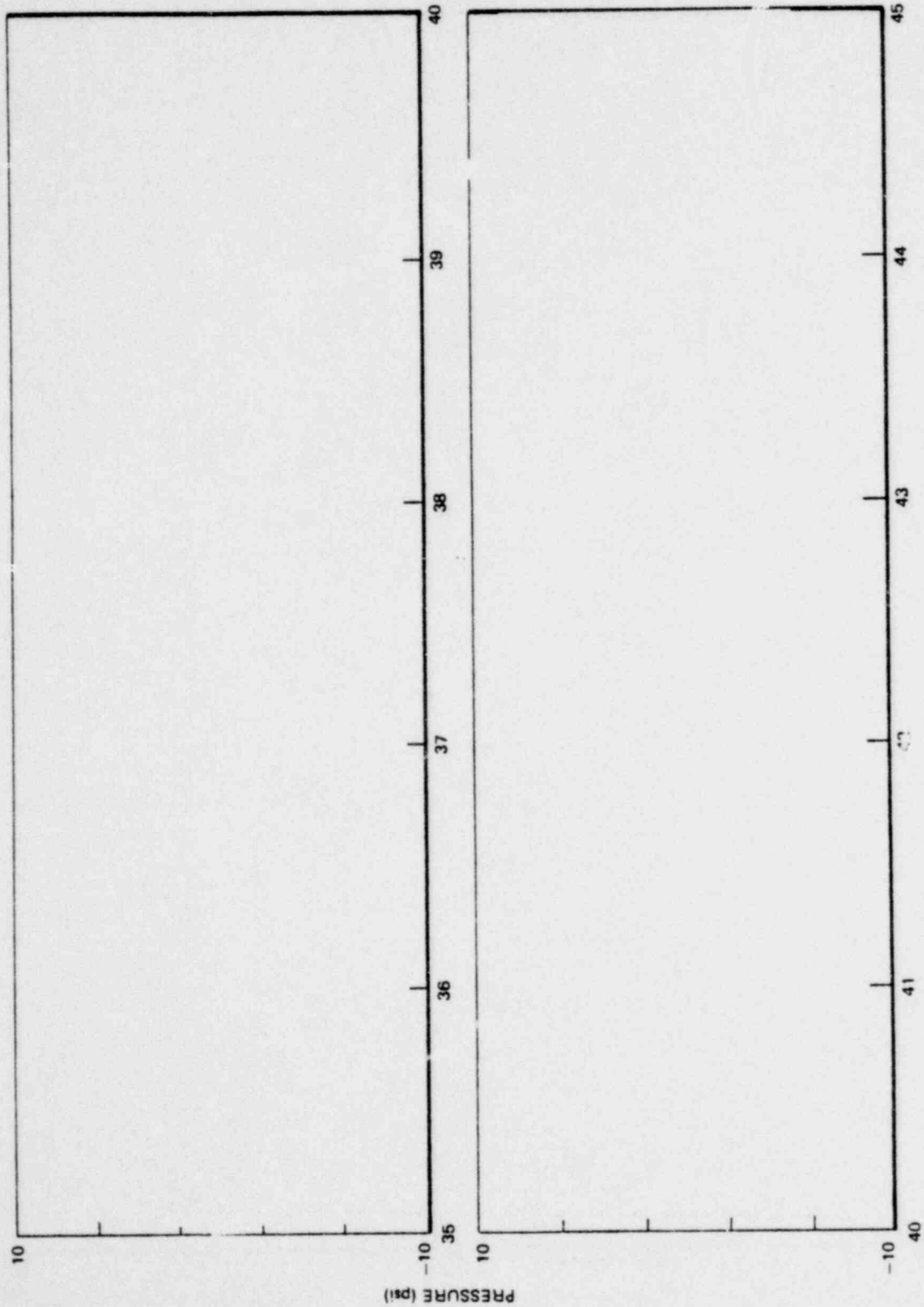

Figure 6.2.2-13. Dynamic Portion of Wetwell Pressure Transducer (P3183) Output, 35-45 Seconds, M8

*Proprietary information deleted

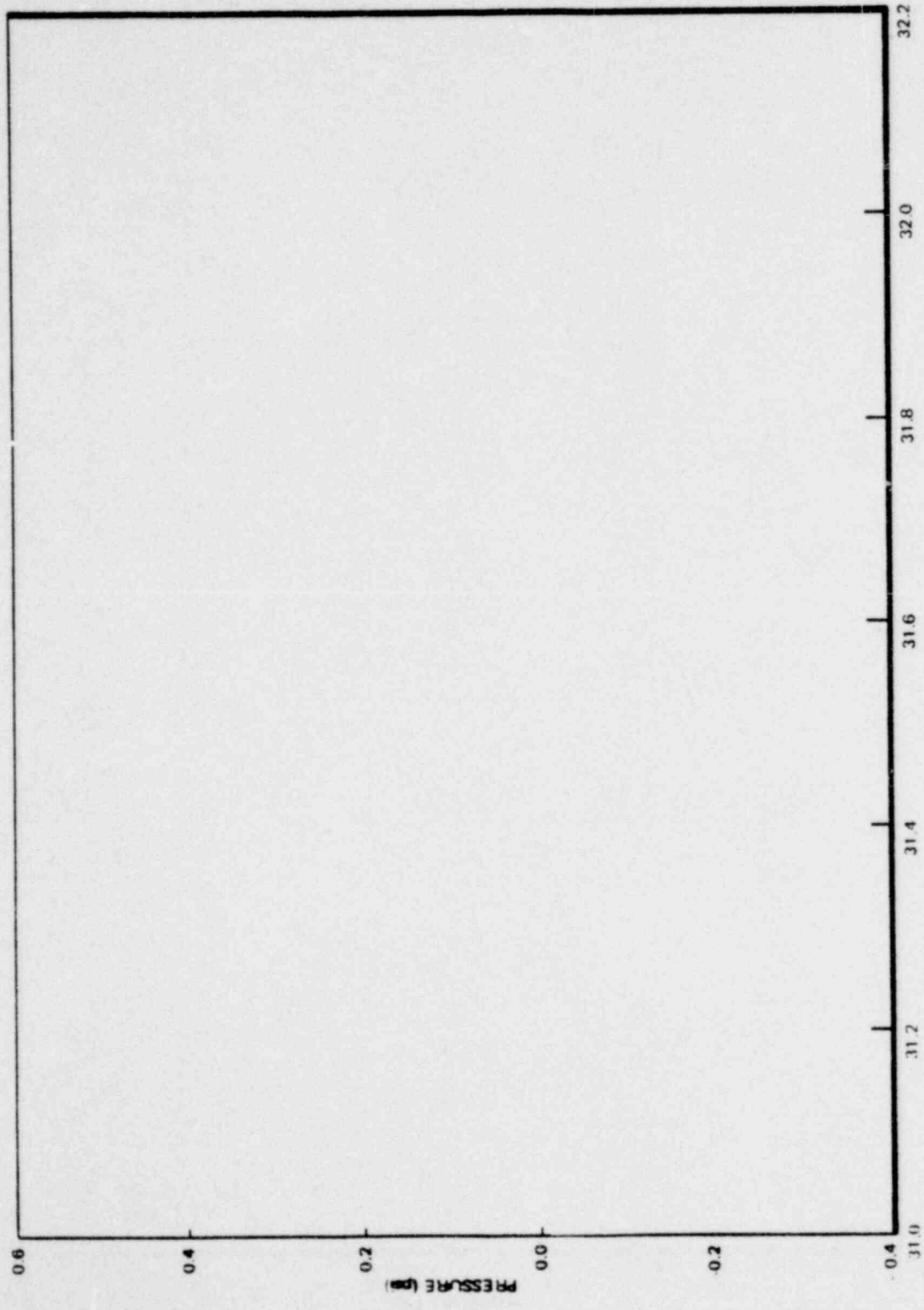

Figure 6.2.2-14. Dynamic Portion of Drywell Pressure Transducer (r2001) Output, 31-32.1 Seconds, M8

*Proprietary information deleted

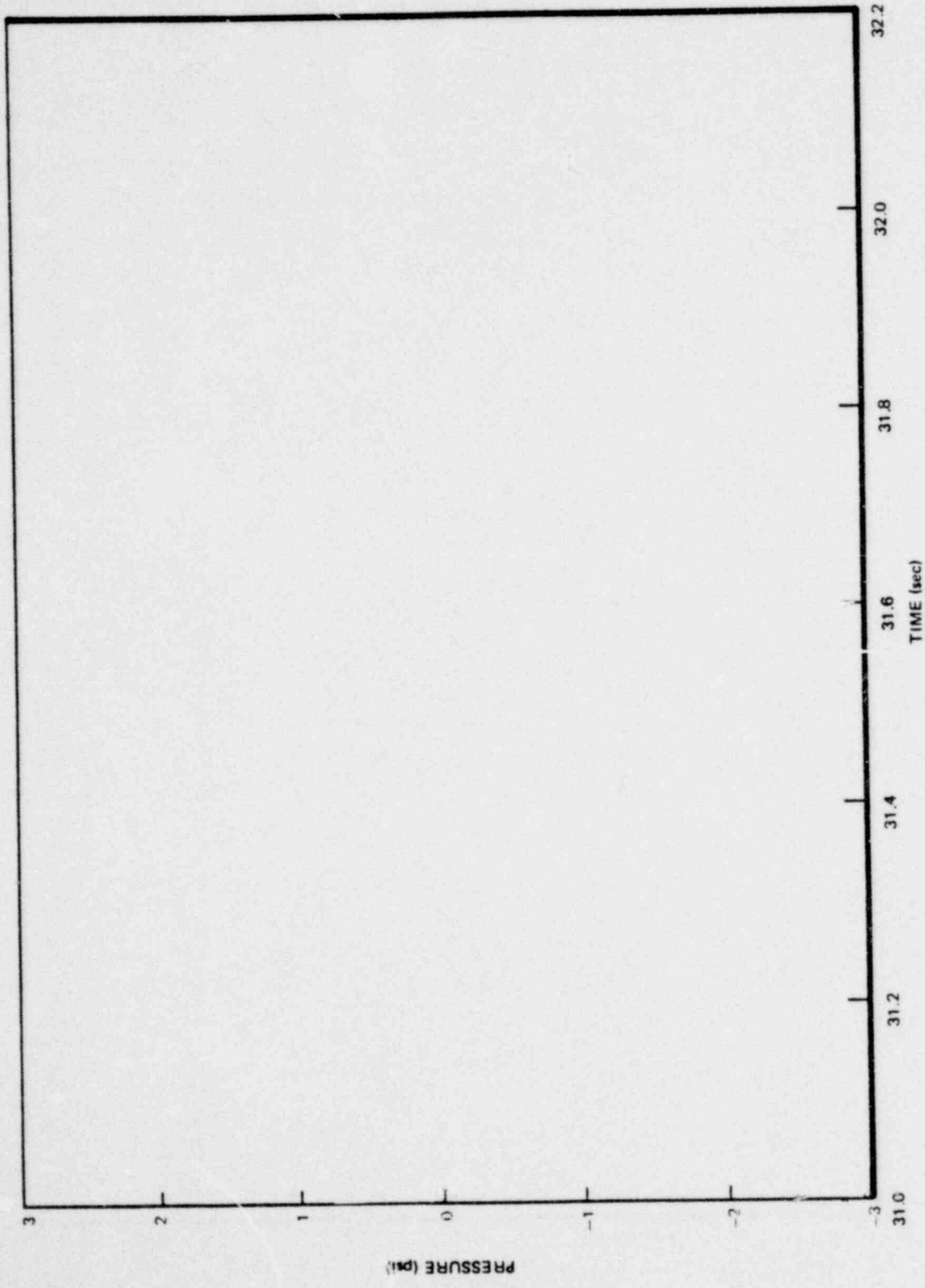

Figure 6.2.2-15. Dynamic Portion of Vent Pressure Transducer (P2004) Output, 31-32.1 Seconds, M8

*Proprietary information deleted

1157 351

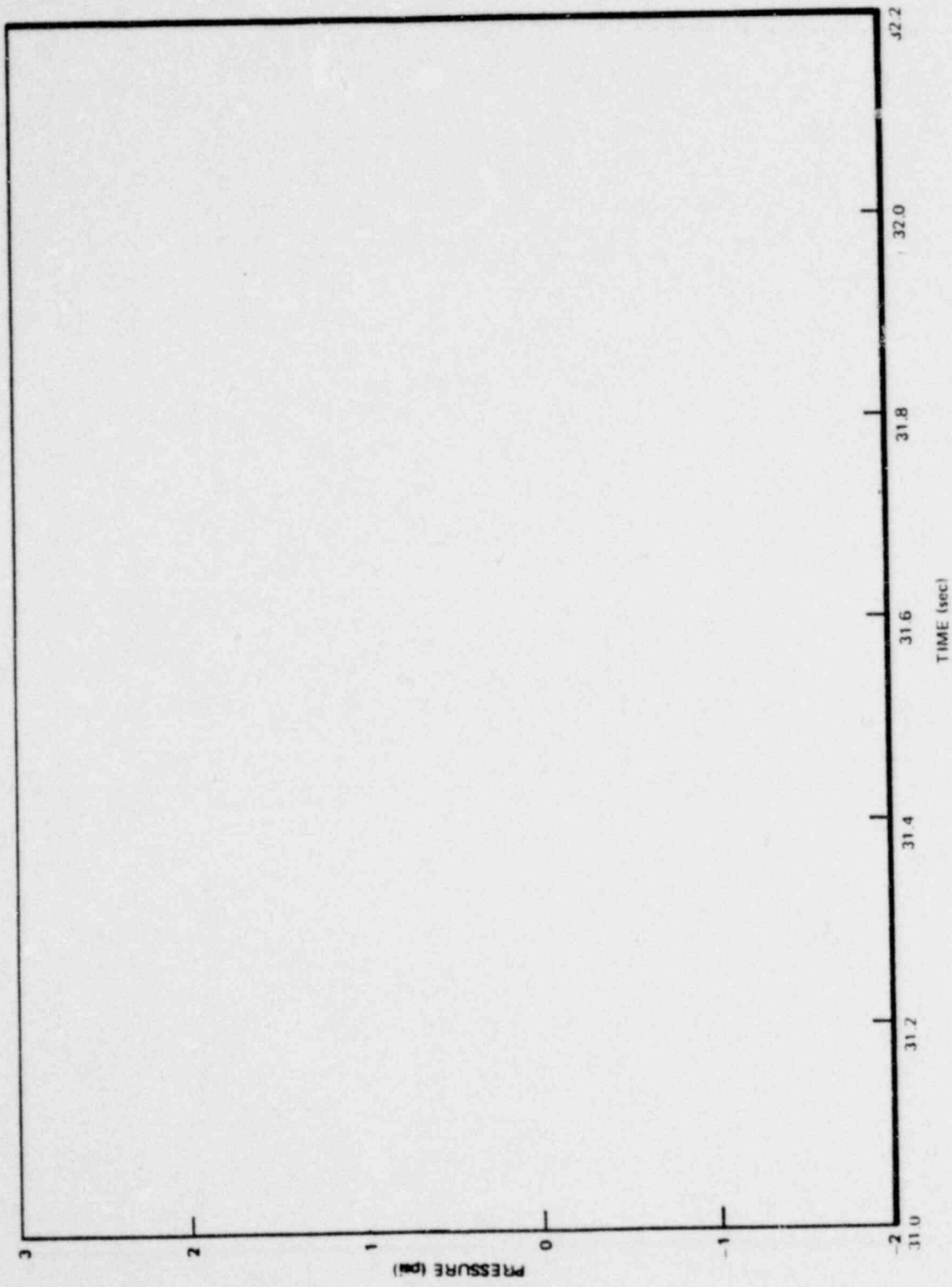

Figure 6.2.2-16. Dynamic Portion of Vent Header Pressure Transducer (P5901) Output, 31-32.1 Seconds, M8

*Proprietary information deleted

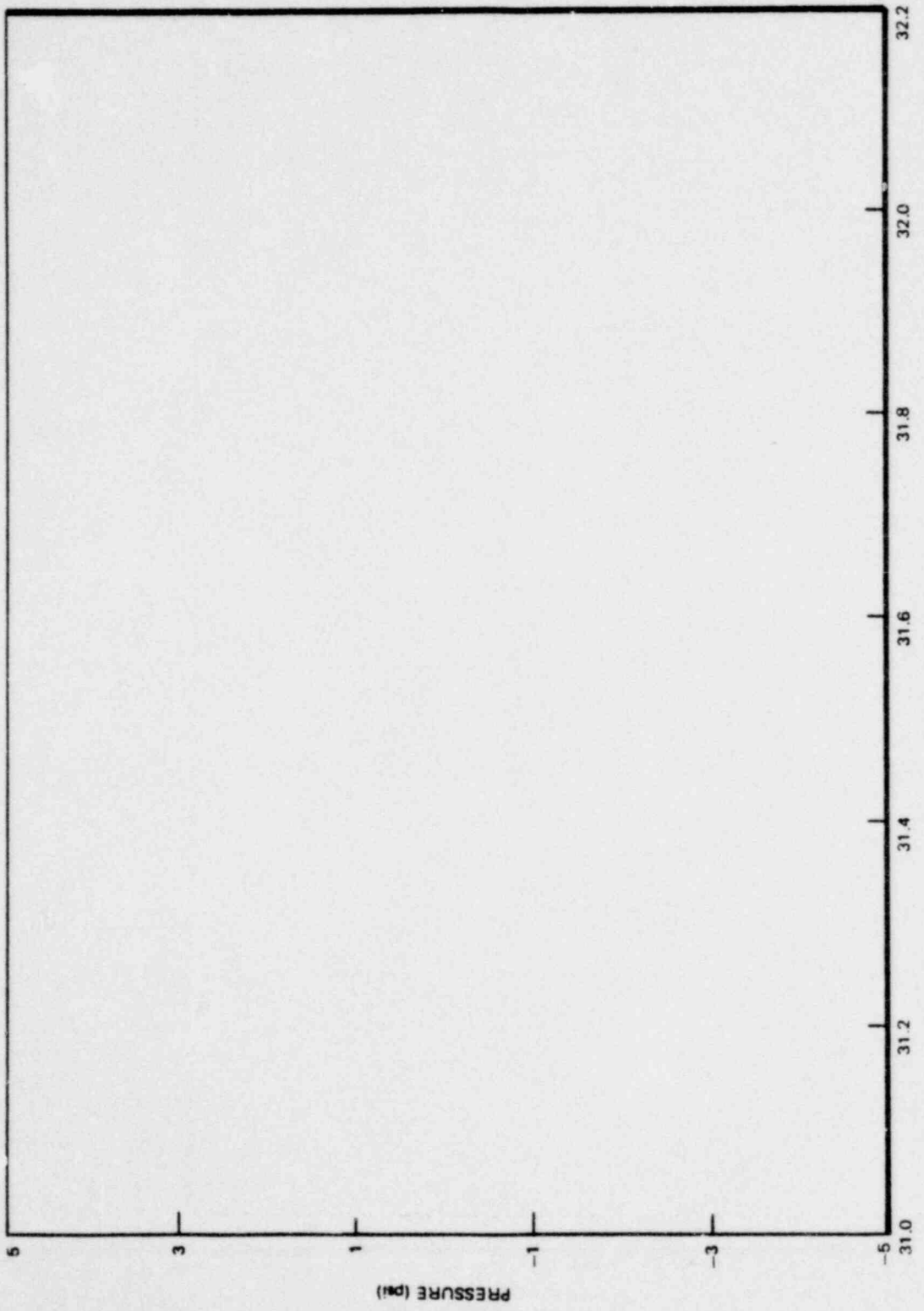

Figure 6.2.2-17. Dynamic Portion of Downcomer No. 4 Pressure Transducer (P5443) Output, 31-32.1 Seconds, M8

*Proprietary information deleted

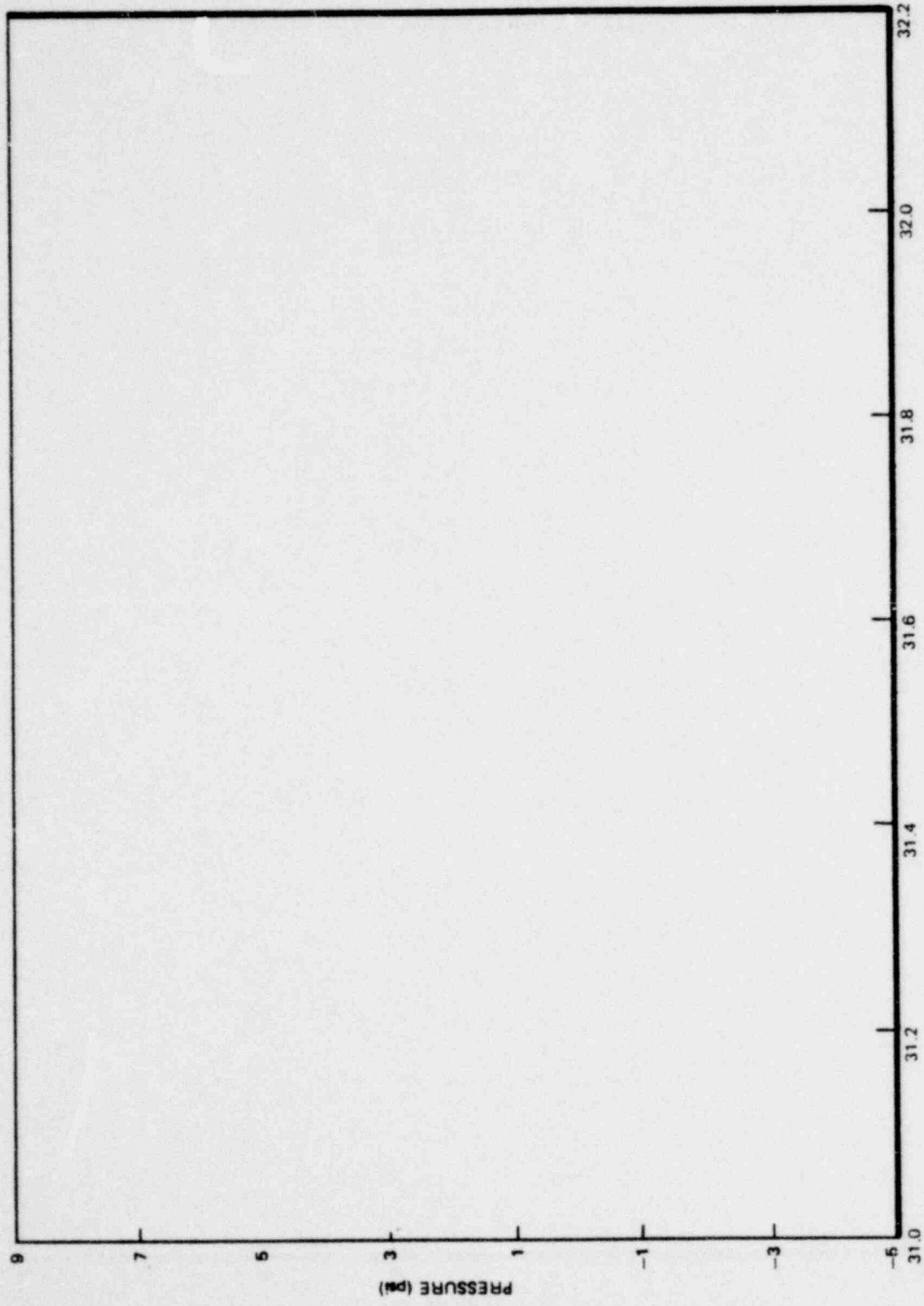

Figure 6.2.2-18. Dynamic Portion of Wetwell Pressure Transducer (P3185) Output, 31-32.1 Seconds, M8

*Proprietary information deleted

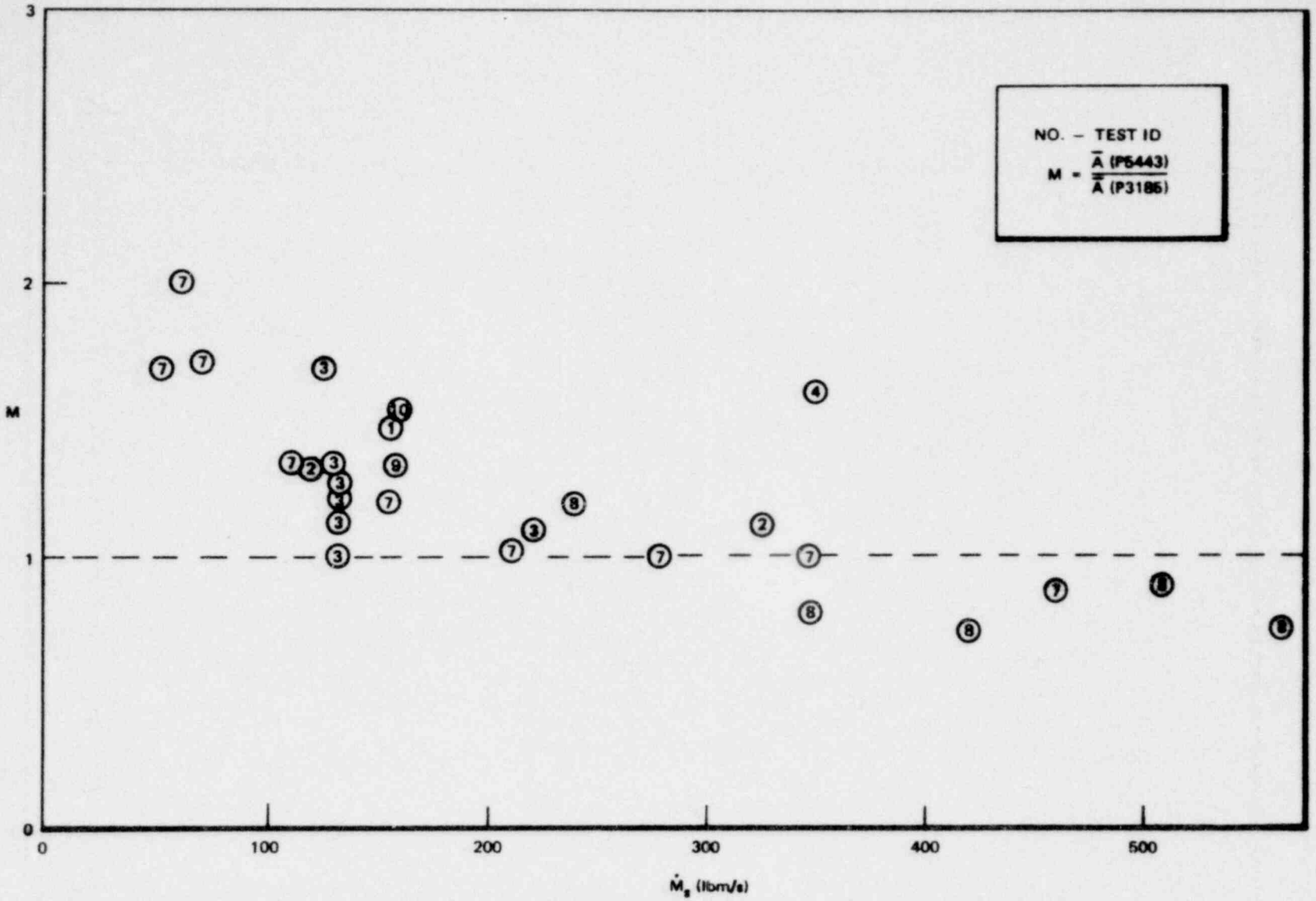

Figure 6.2.2-19. Ratios of Averaged Peak-to-Peak Amplitudes of Downcomer No. 4 (P5443) and Wetwell Bottom Center (P3185) vs Steam Flow Rate

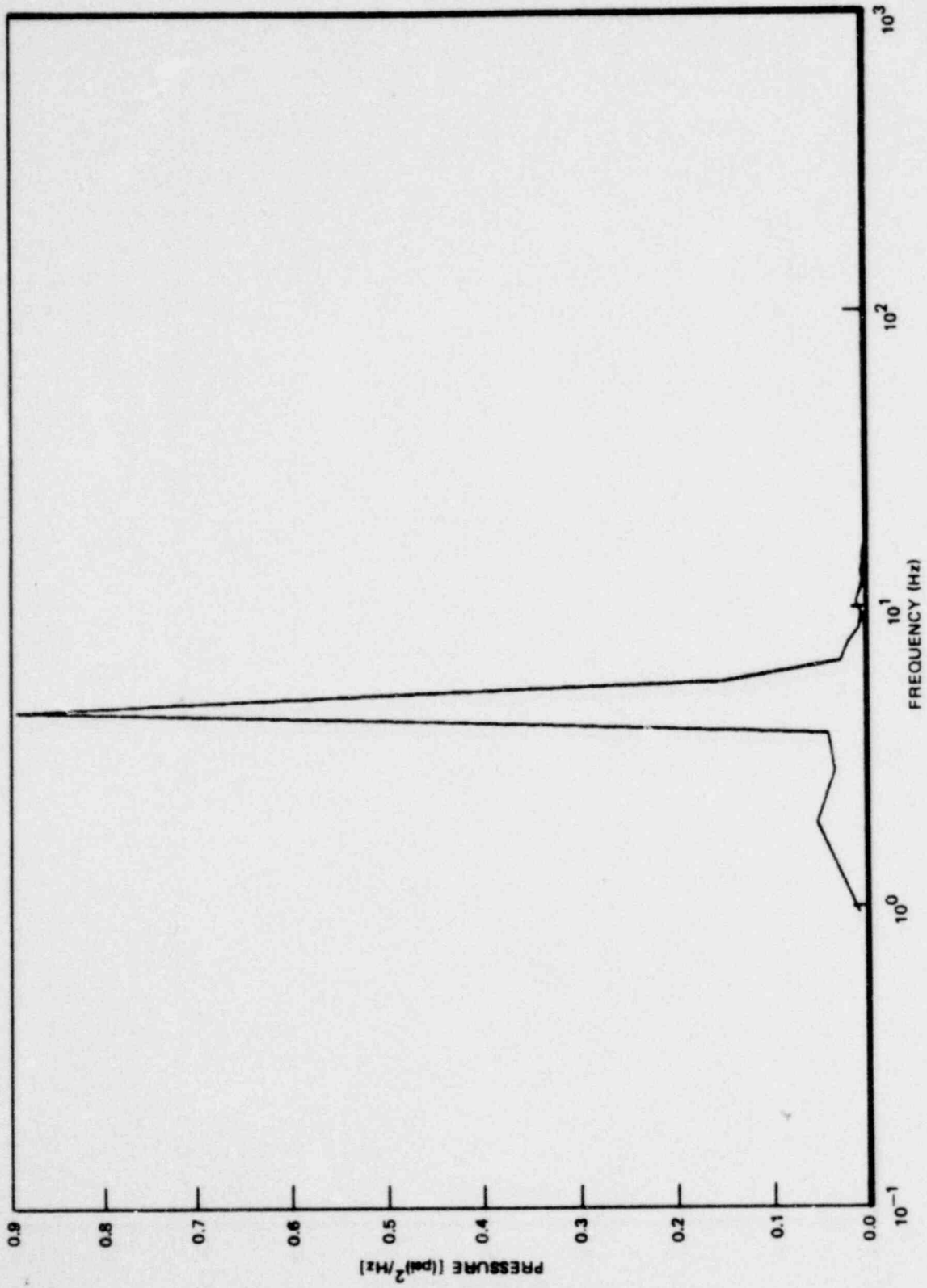

Figure 6.2.2-20. Calculated PSDs for Vent Header Pressure Transducer (P5901) Signal, 31-32.05 Seconds, M8

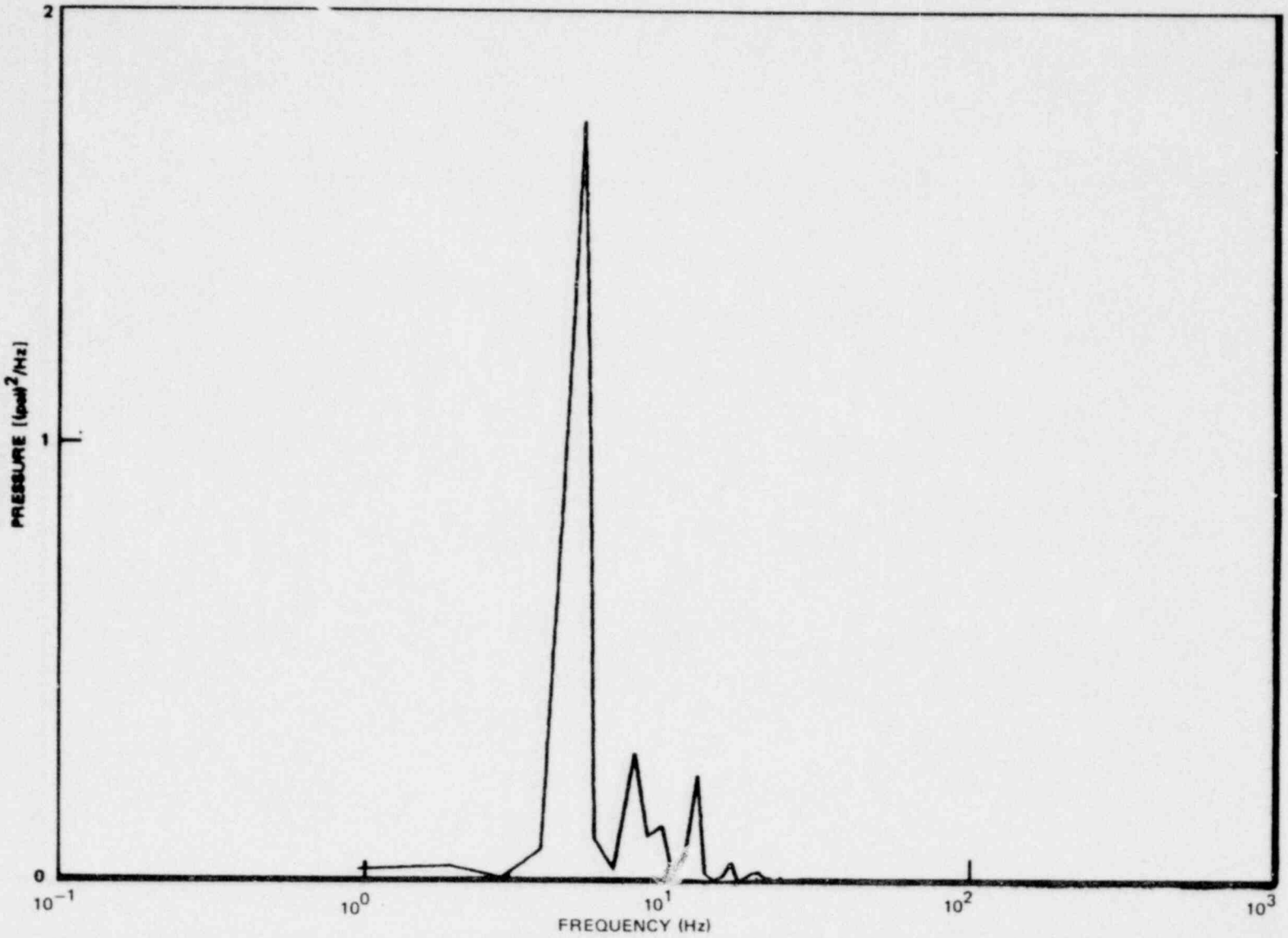

Figure 6.2.2-21. Calculated PSDs for Downcomer No. 4 Pressure Transducer Signal (P5443), 31-32.05 Seconds, M8

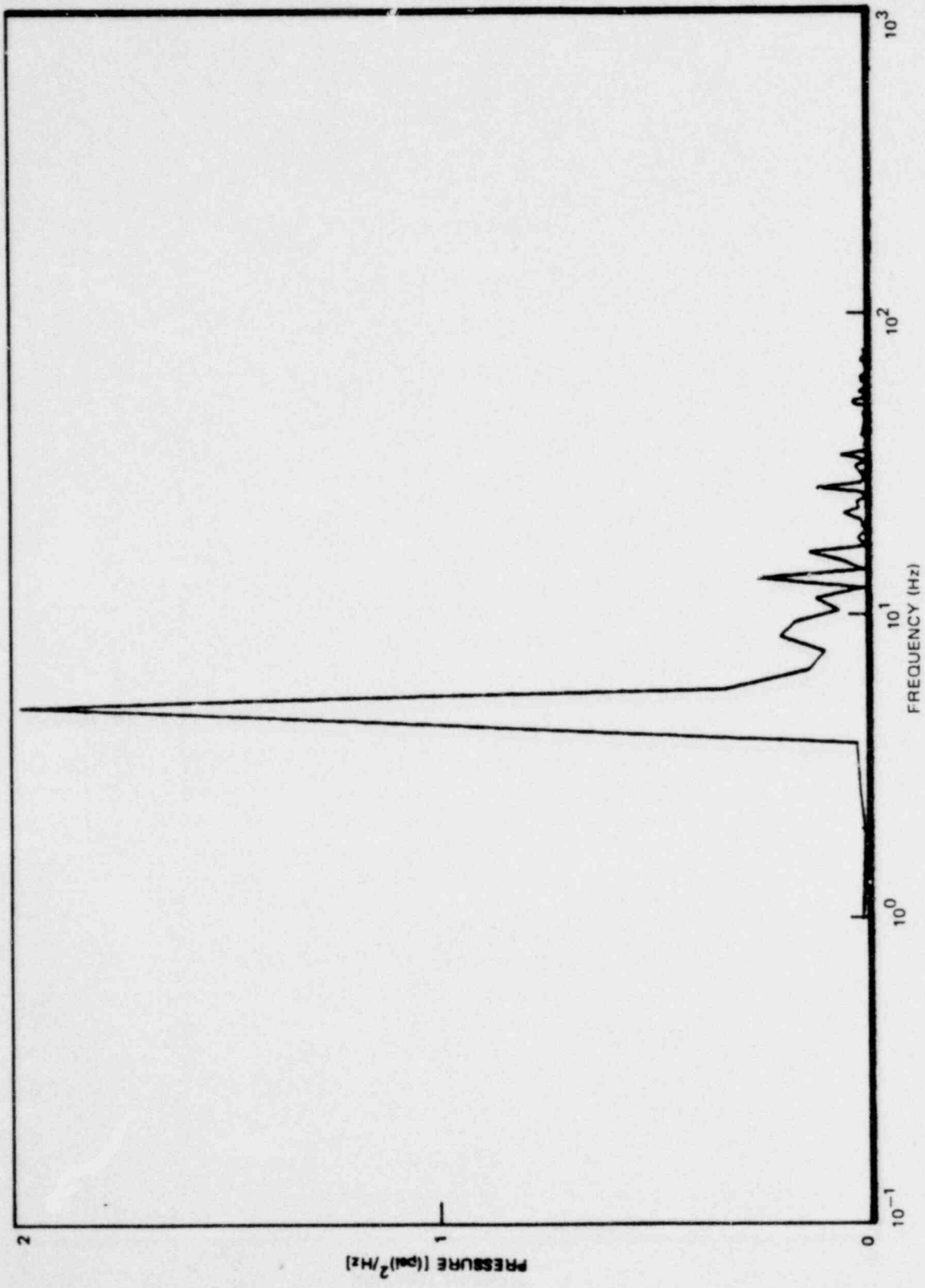

Figure 6.2.2-22. Calculated PSDs for Wetwell Pressure Transducer (P3185) Signal, 31-32 Seconds, M8

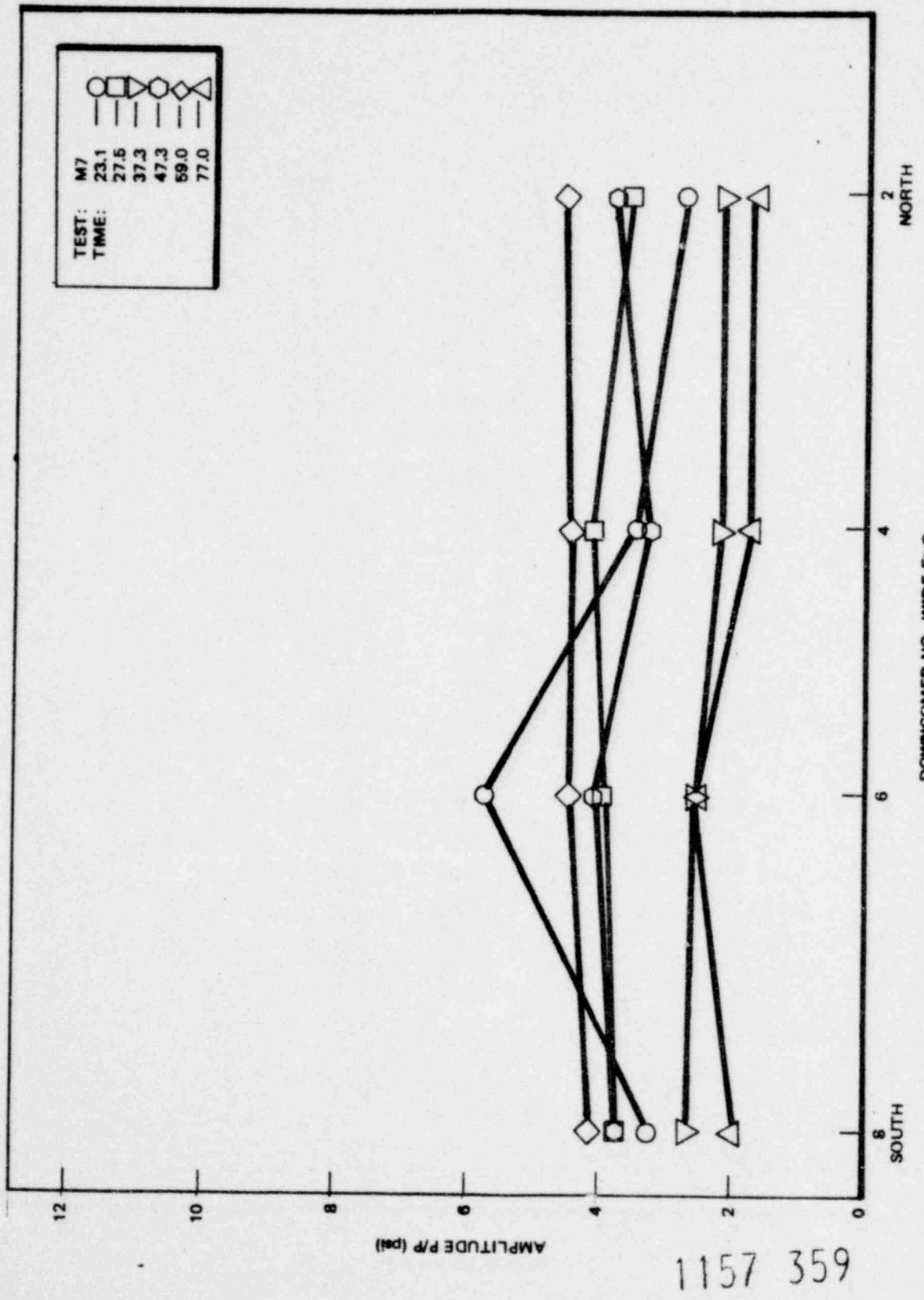

Figure 6.2.2-23. Peak-to-Peak Amplitudes for Wide-End Downcomers for Different Times During the C.O. Period

1157 359

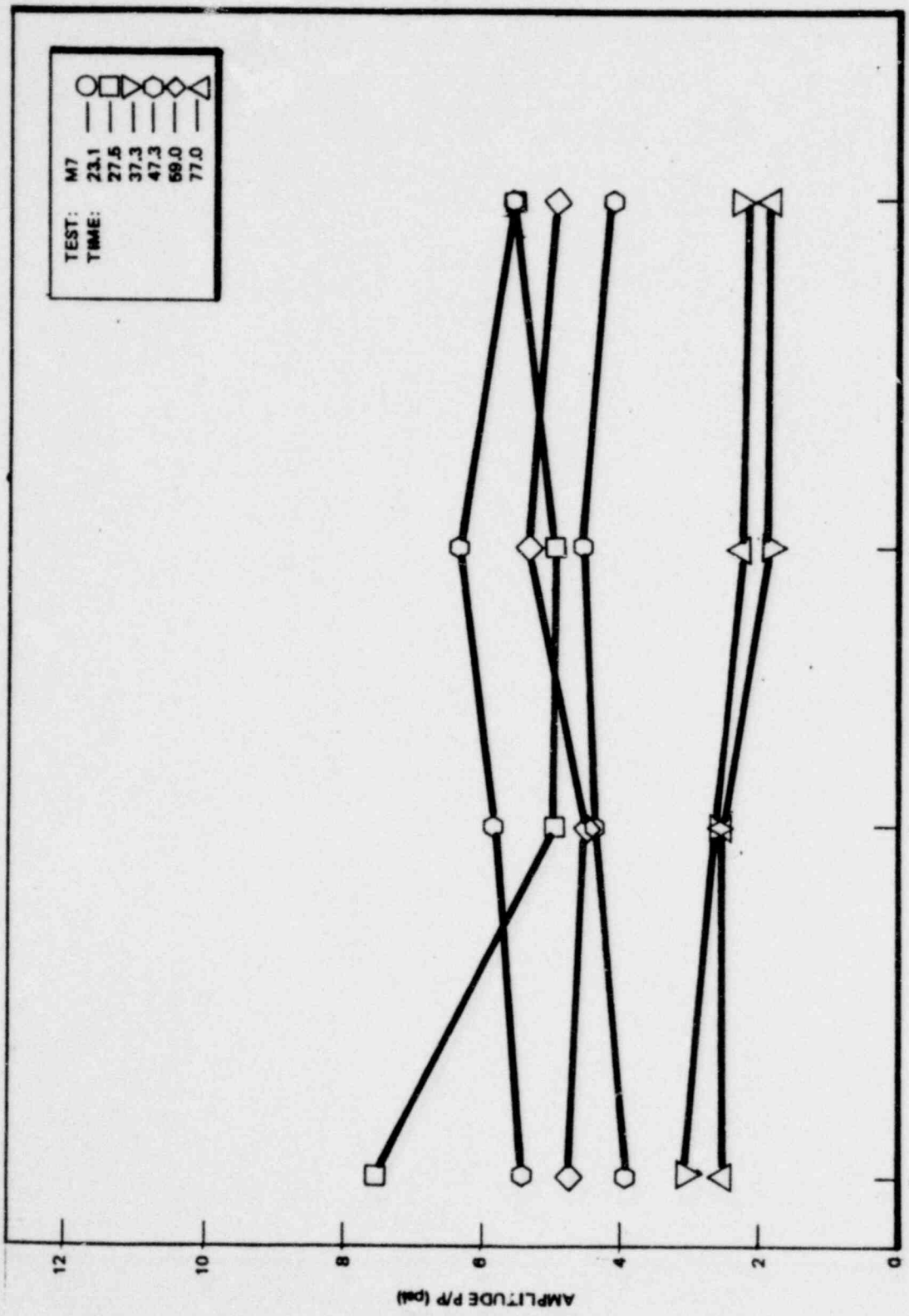

Figure 6.2.2-24. Peak-to-Peak Amplitudes for Narrow-End Downcomers for Different Times During the C.O. Period

1157 360

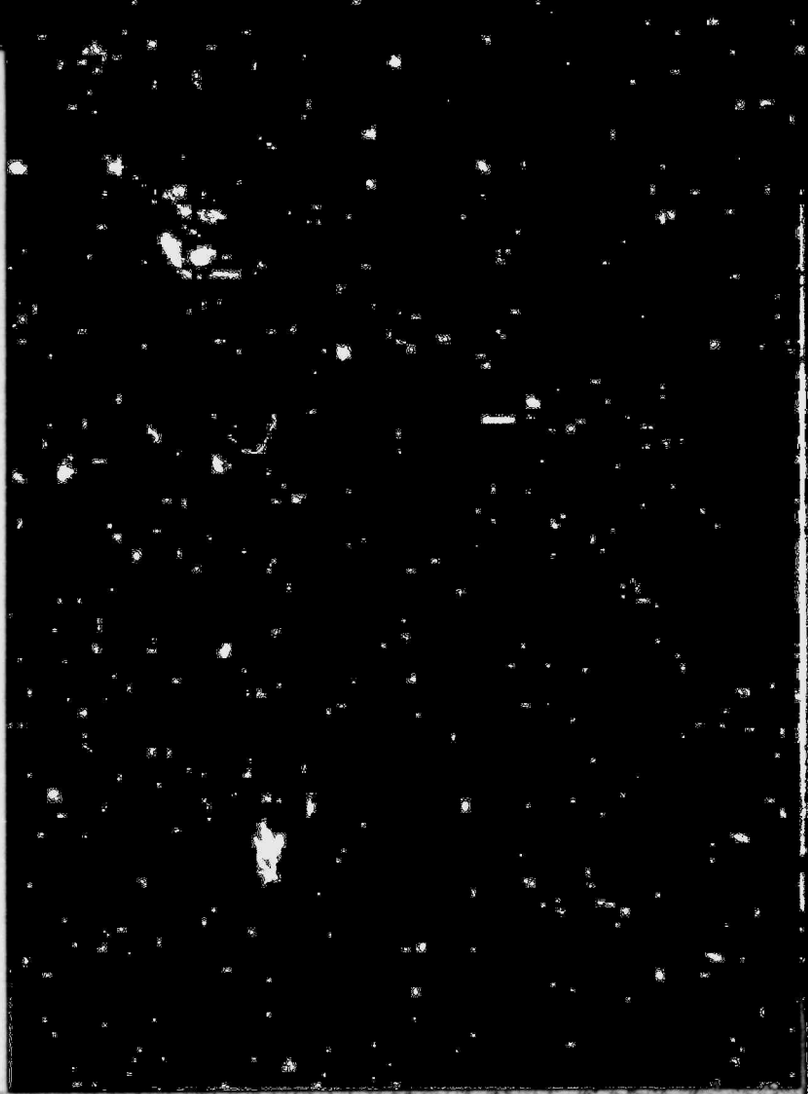

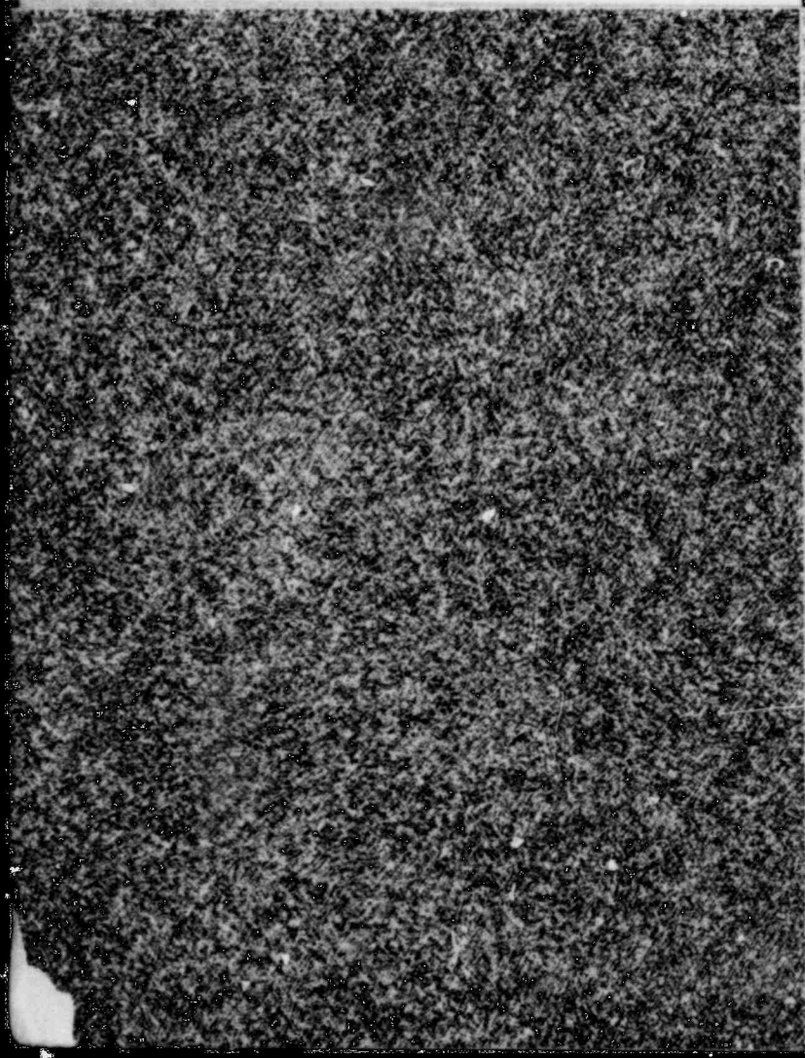

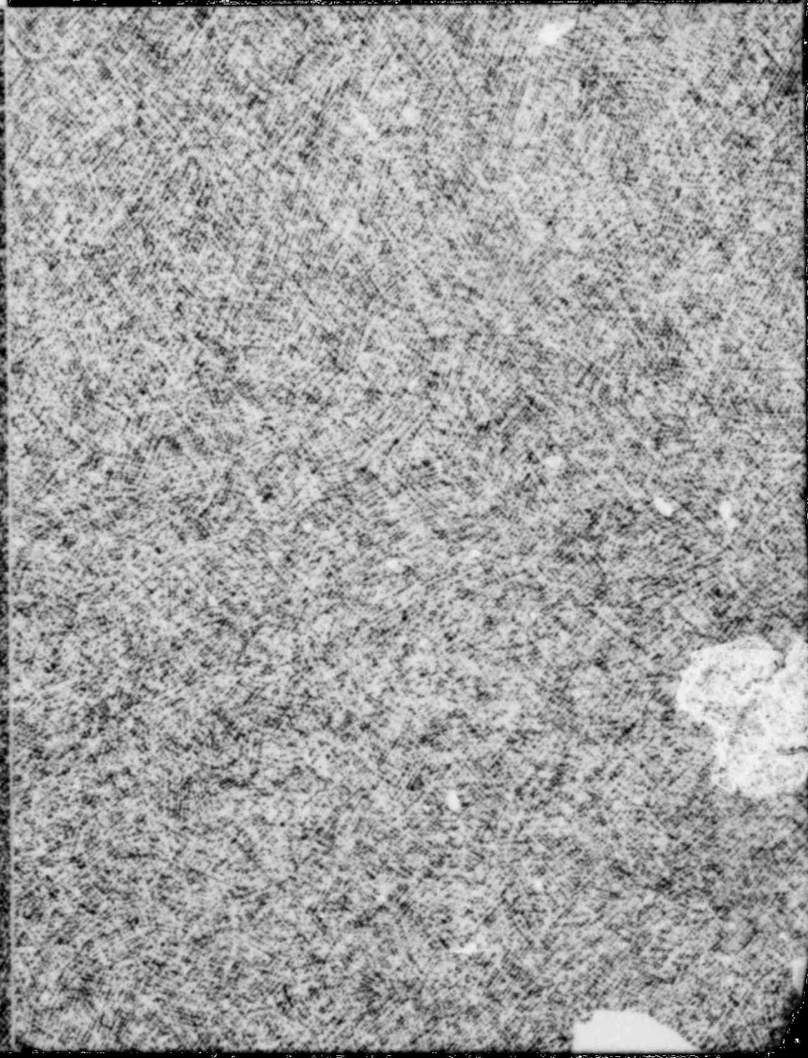

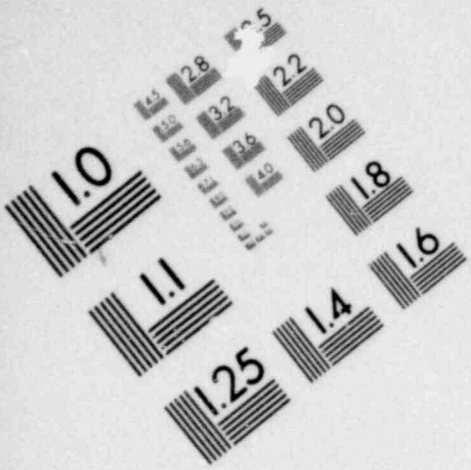

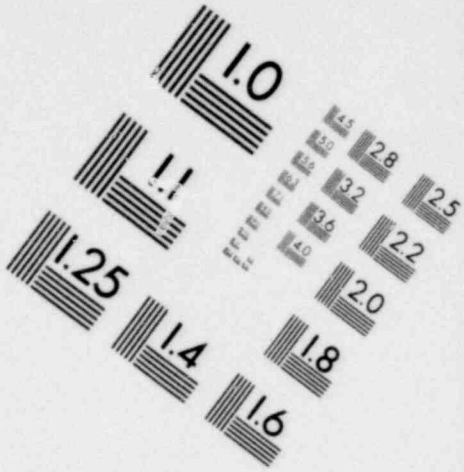

IMAGE EVALUATION TEST TARGET (MT-3)

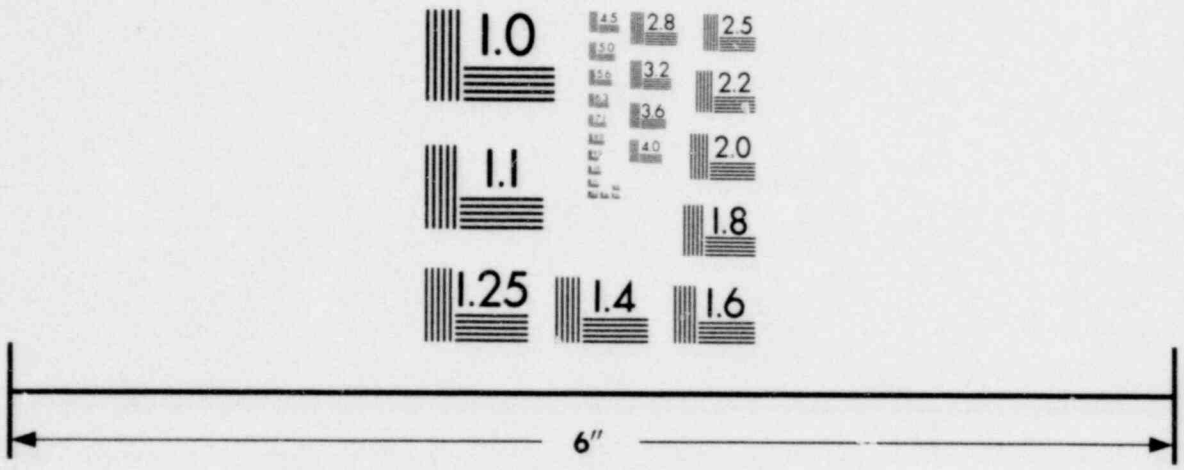

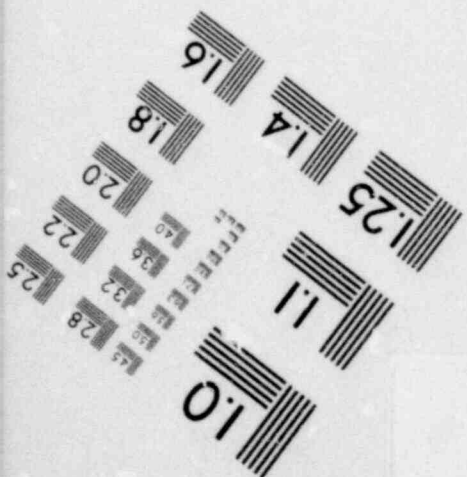

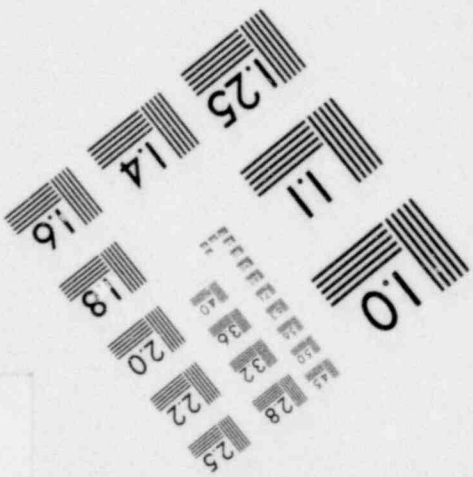

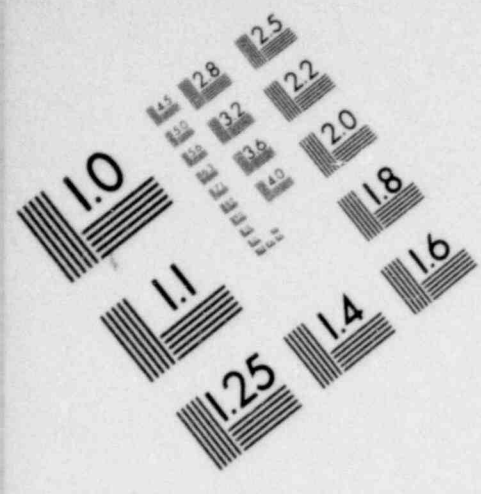

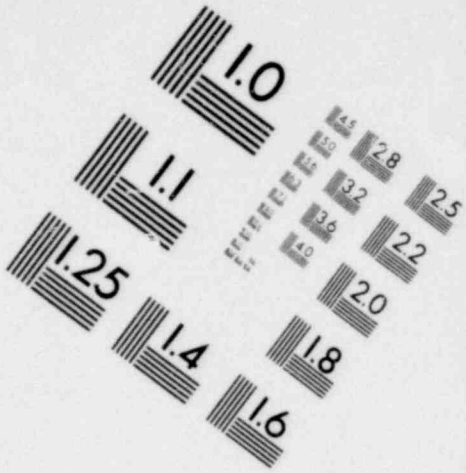

IMAGE EVALUATION
TEST TARGET (MT-3)

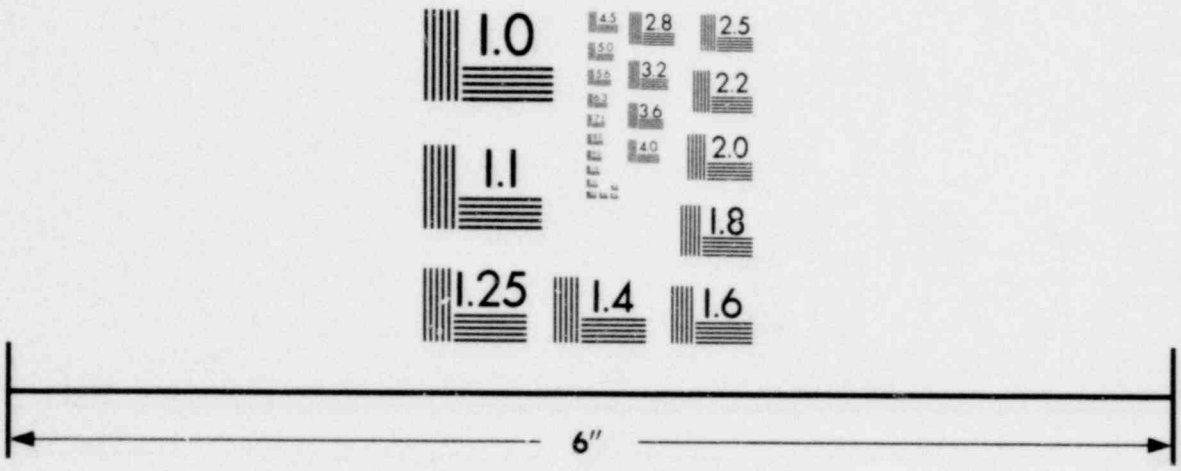

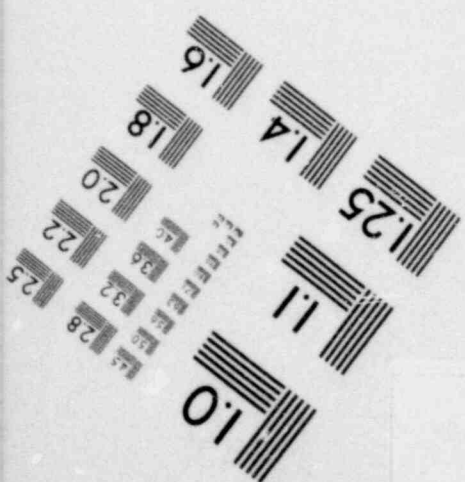

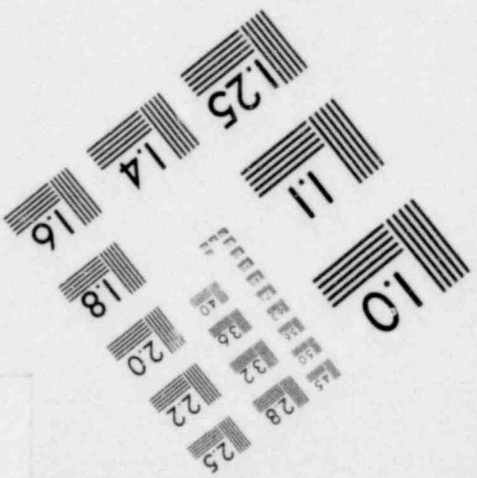

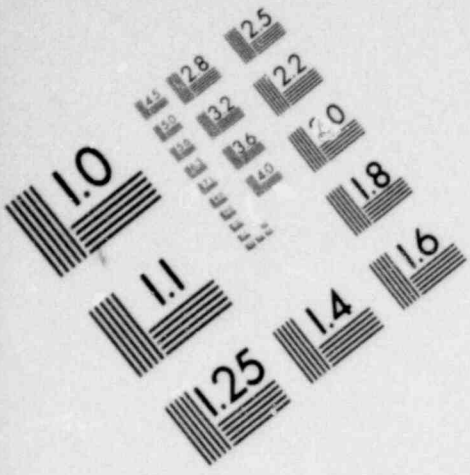

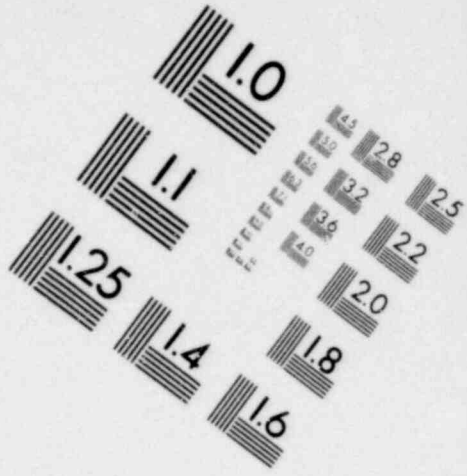

IMAGE EVALUATION TEST TARGET (MT-3)

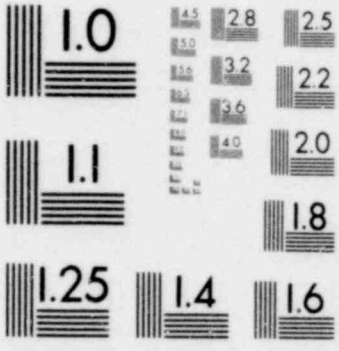

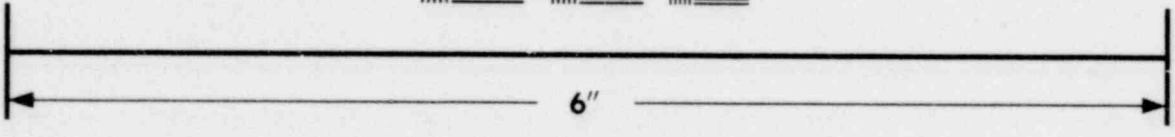

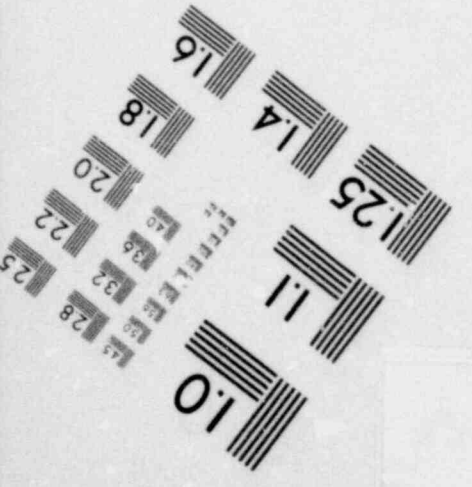

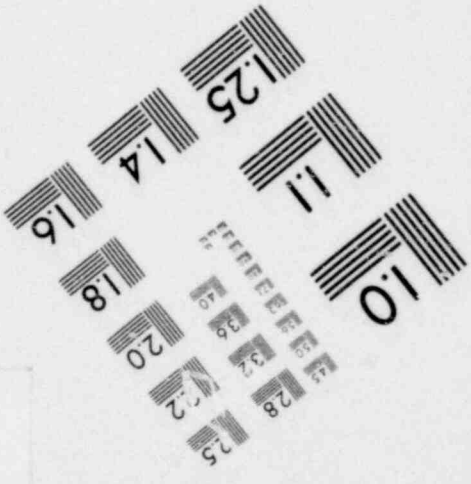

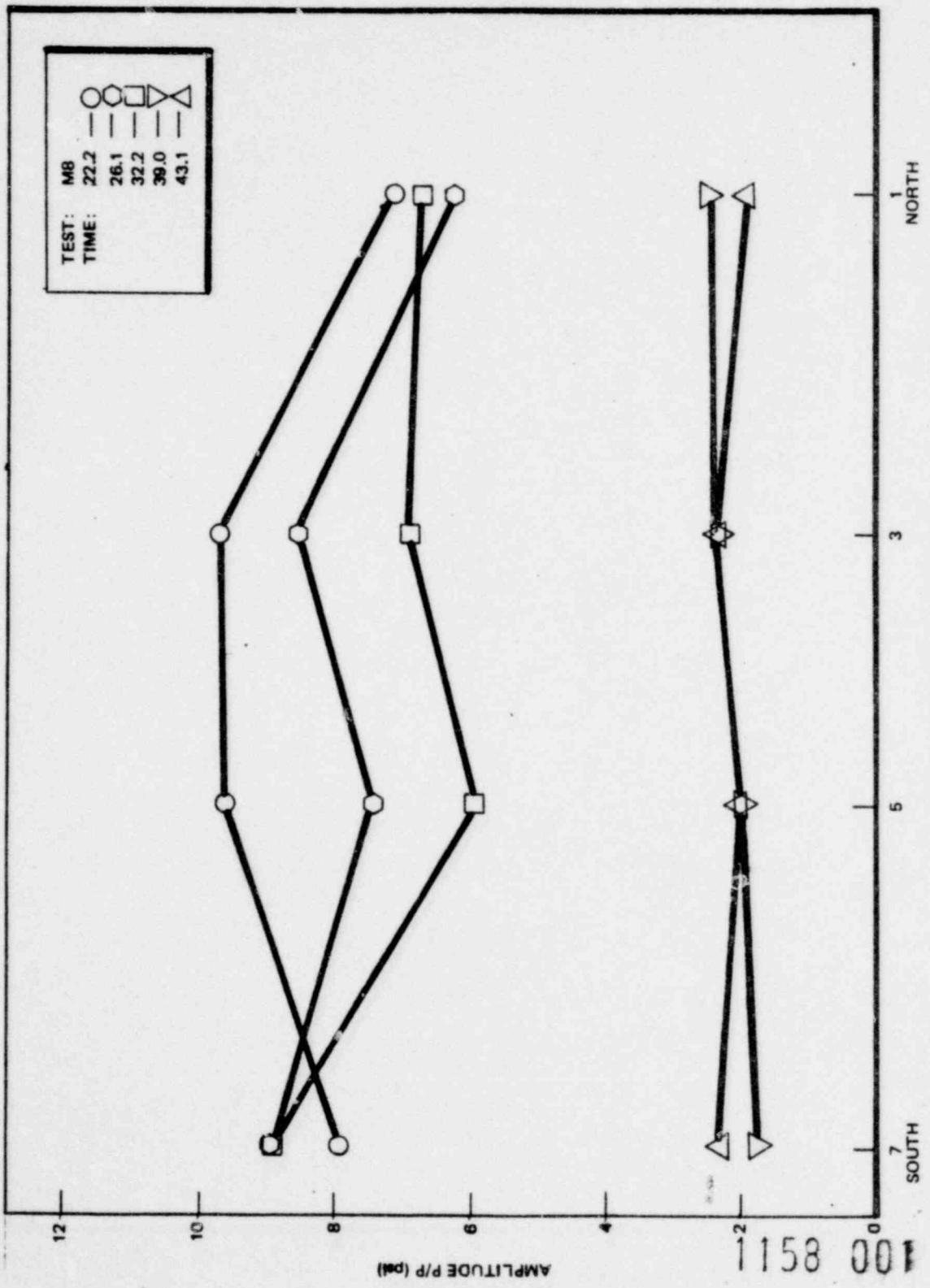

Figure 6.2.2-25. Peak-to-Peak Amplitudes for Narrow-End Downcomers for Different Times During C.O. Period

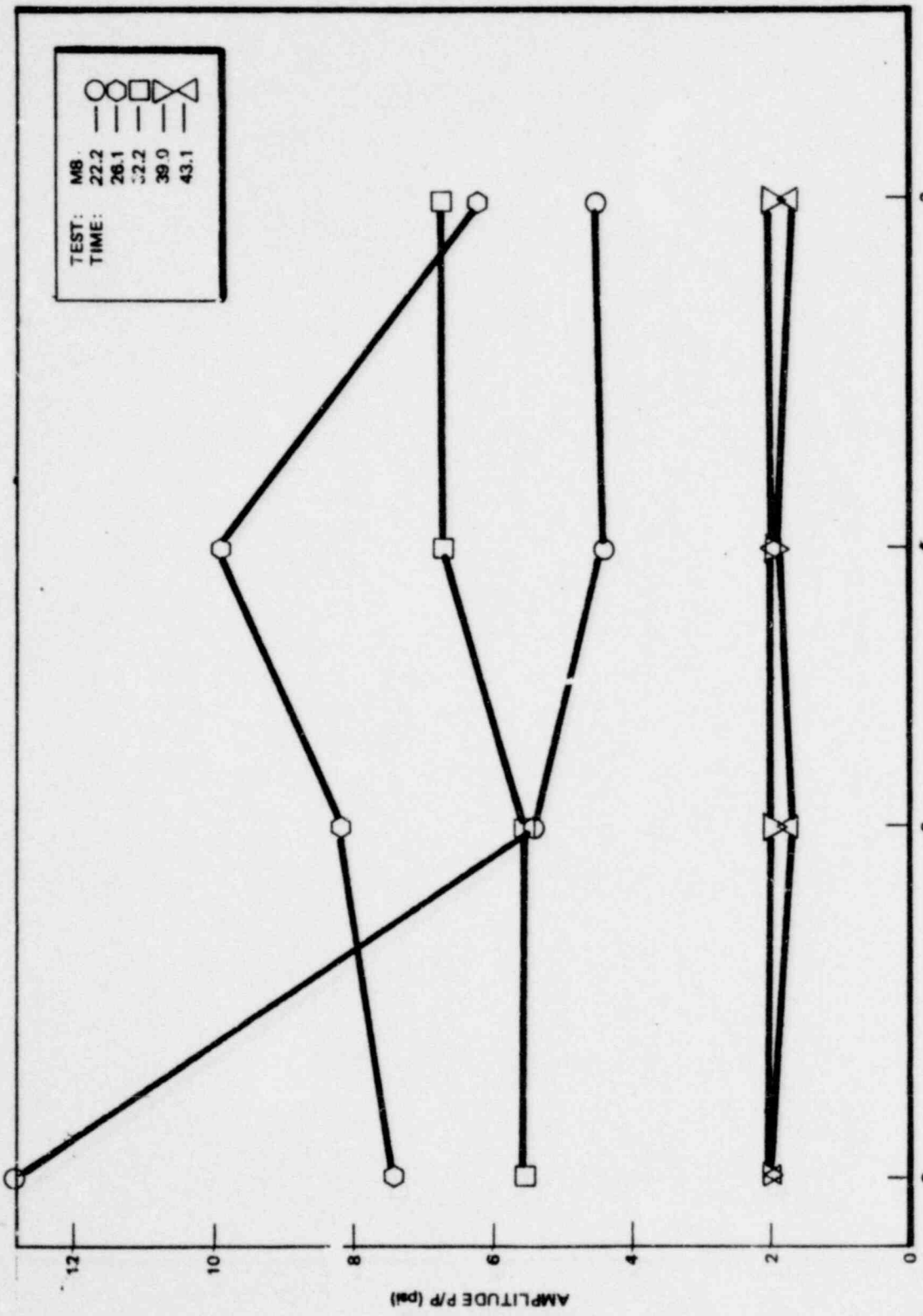

Figure 6.2.2-26. Peak-to-Peak Amplitudes for Wide-End Downcomers for Different Times During C.O. Period

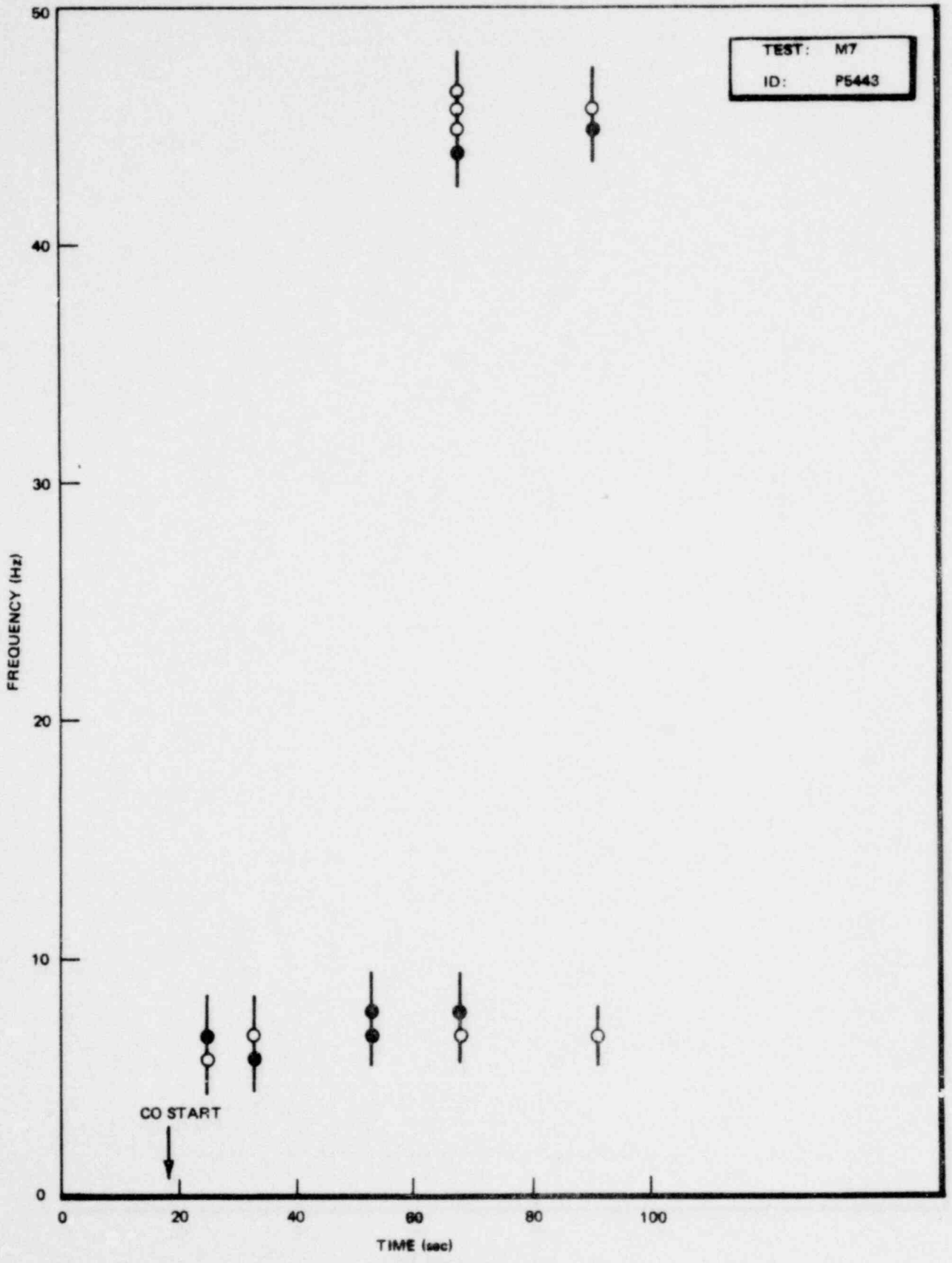

Figure 6.2.2-27. Significant Frequencies in the Pressure Waveform in Downcomer No. 4, M7

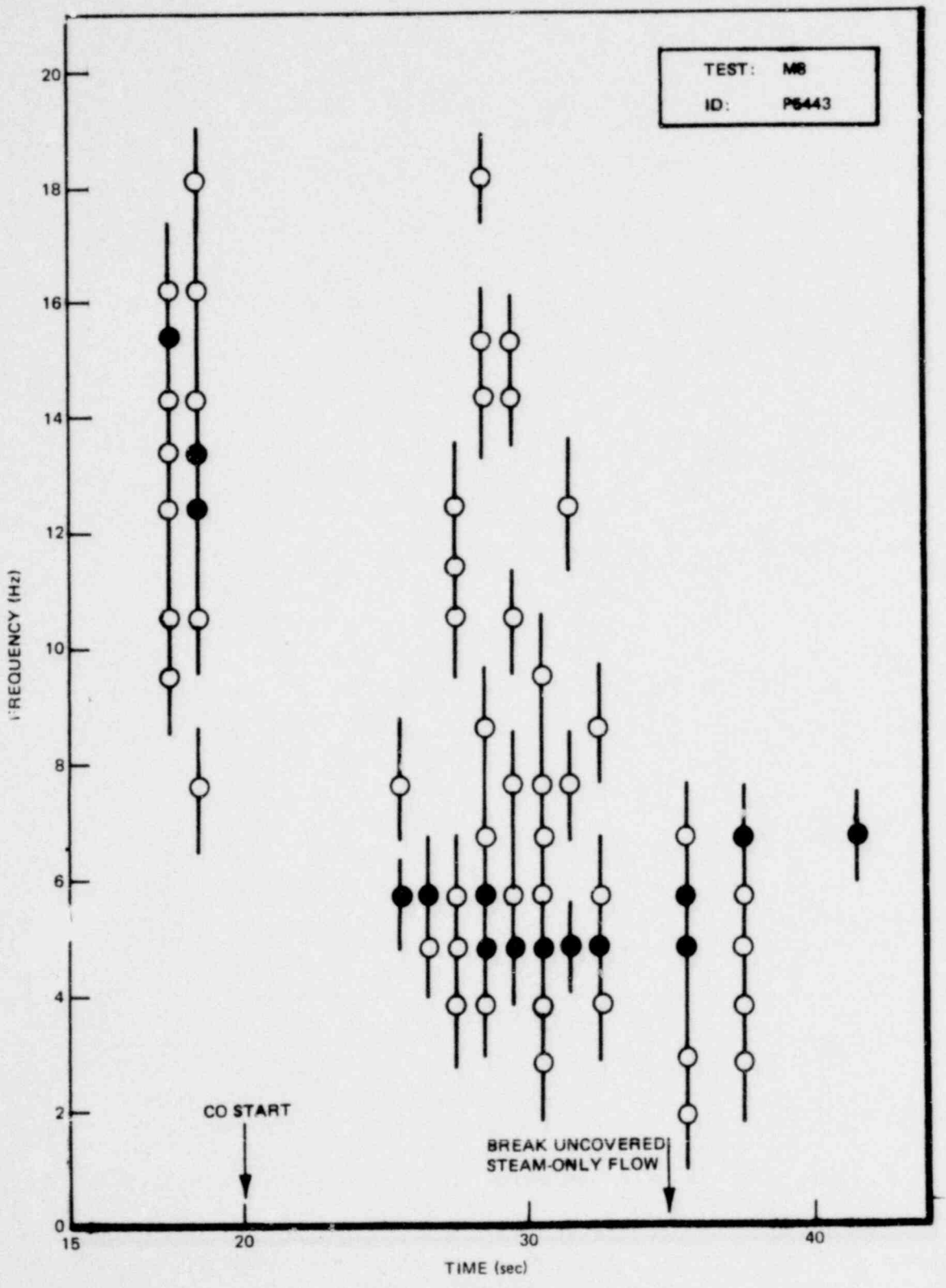

Figure 6.2.2-28. Significant Frequencies in the Pressure Waveform in Downcomer No. 4, M8

1158 004

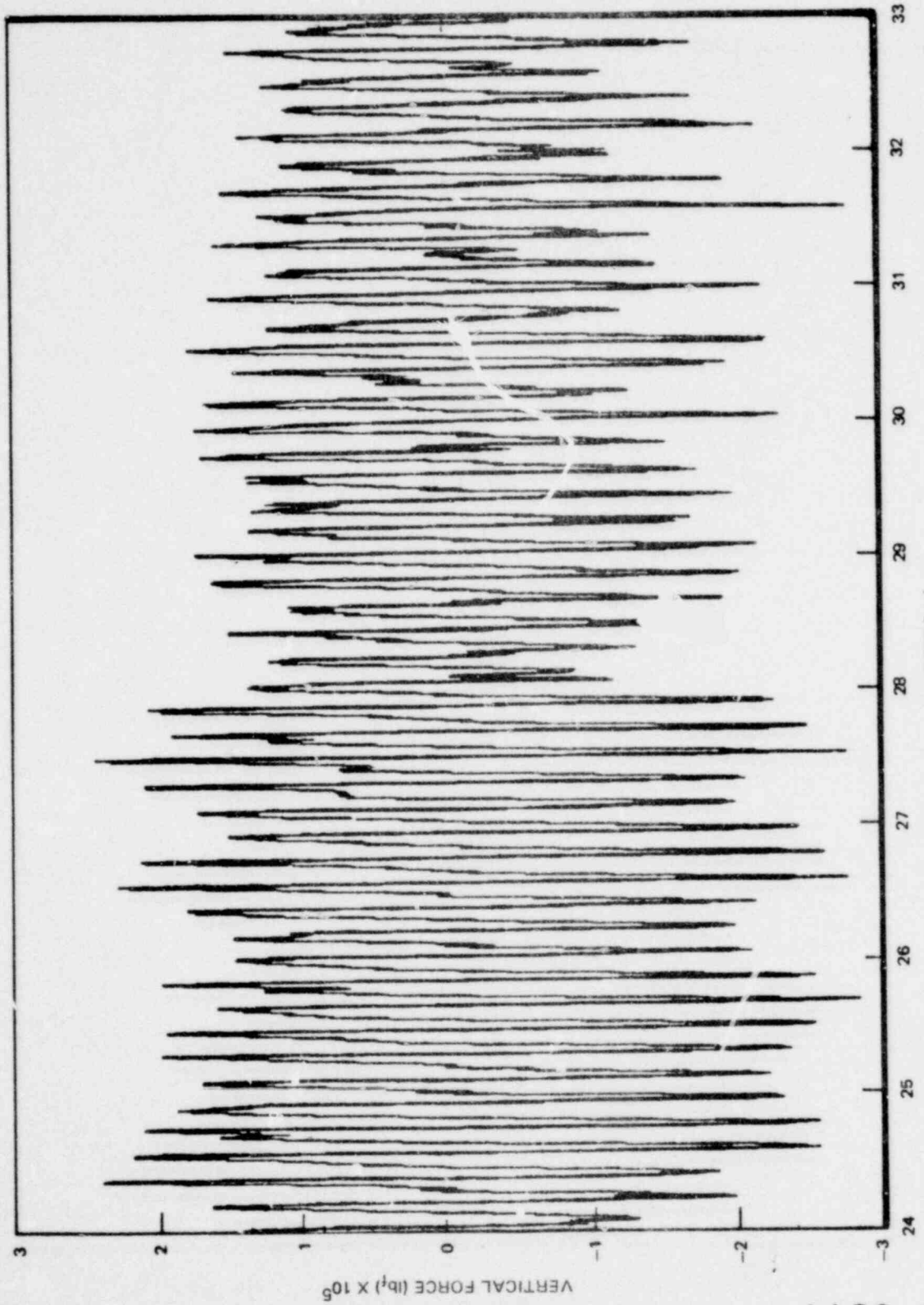

Figure 6.2.2-29. Vertical Force Exerted on Wetwell Shell as Calculated From 24 Wetwell Pressure Transducer Outputs, 24-33 Seconds, M8

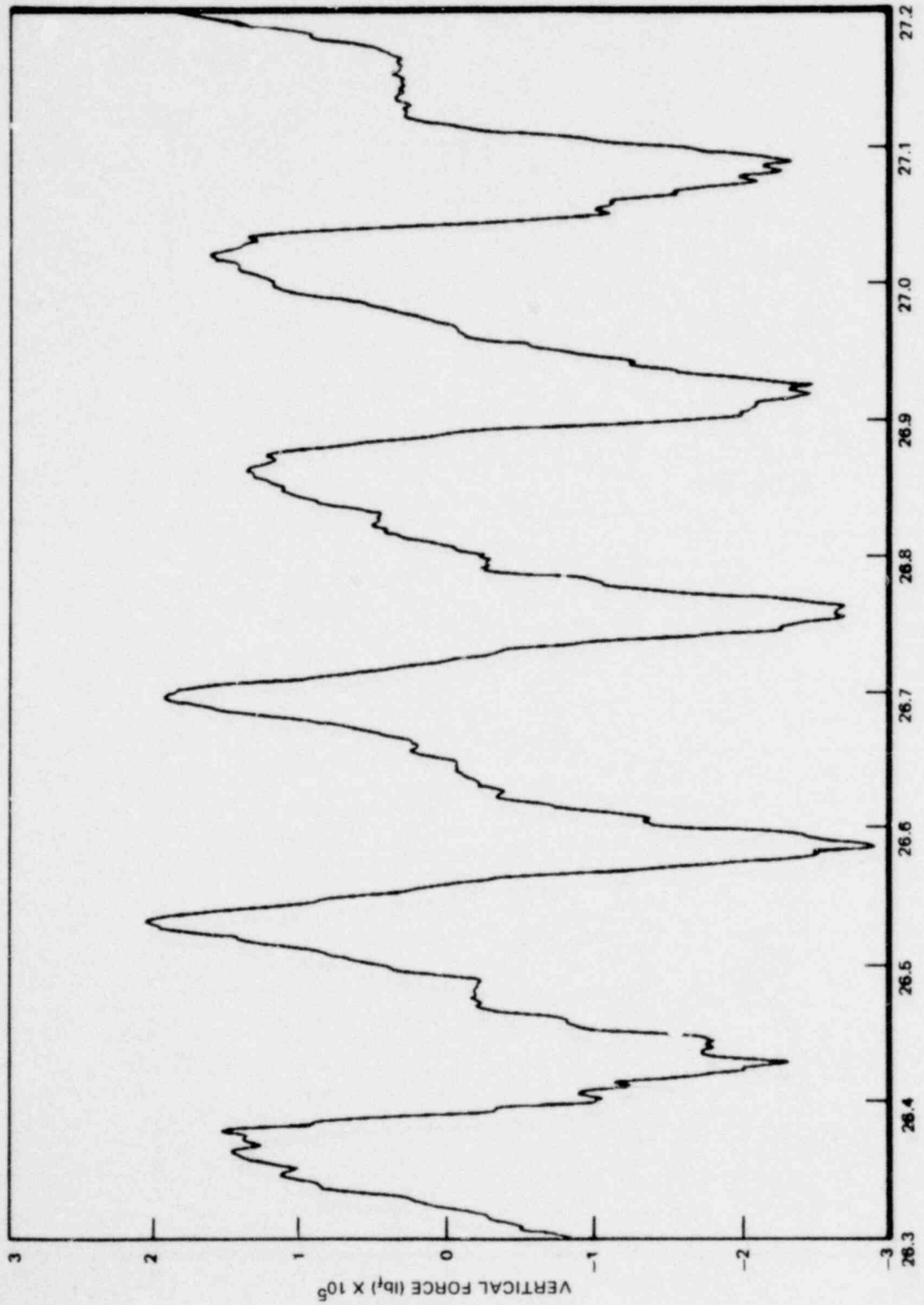

Figure 6.2.2-30. Vertical Force Calculations Graphed On An Expanded Time Scale, 26.3-27.2 Seconds, M8

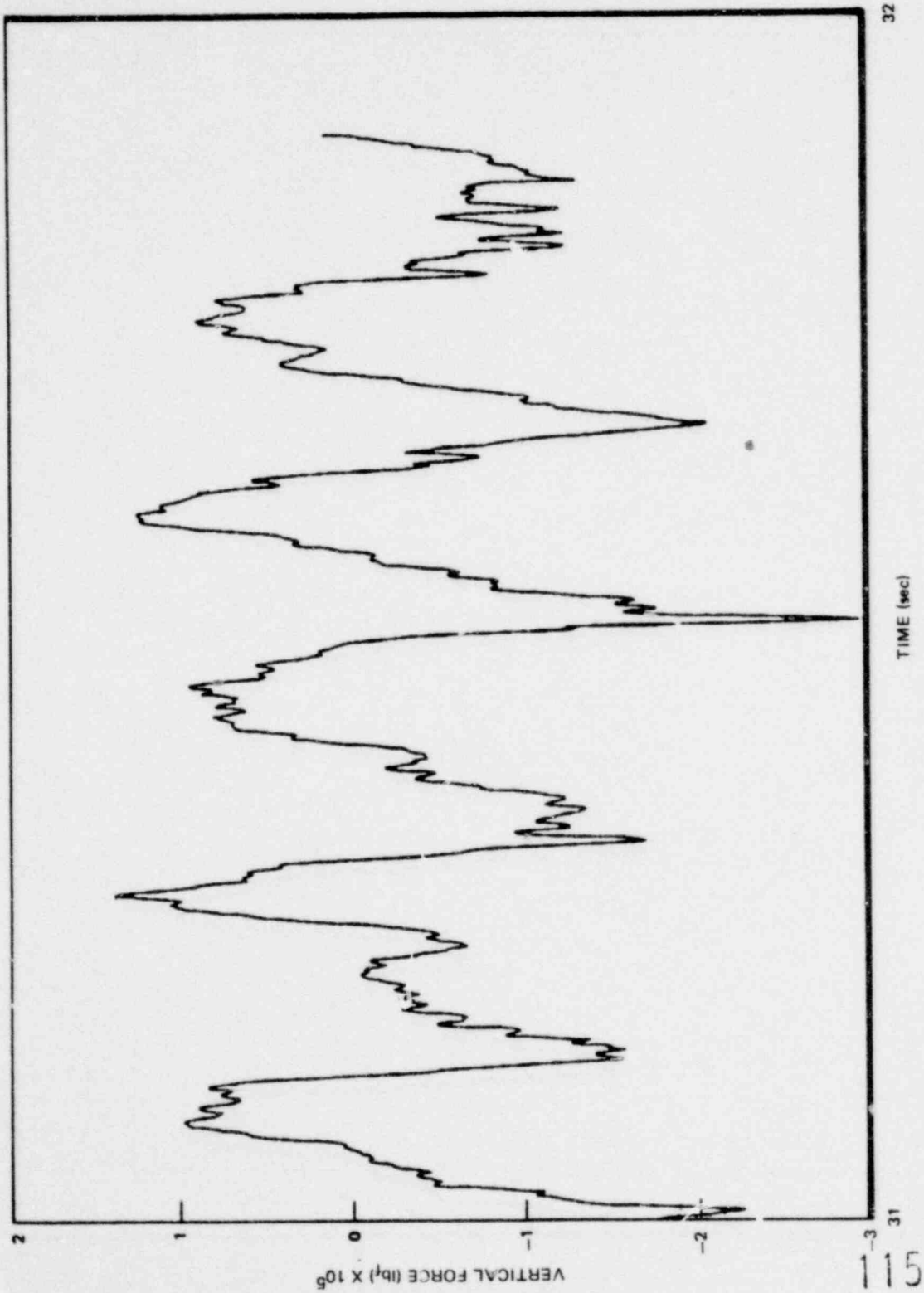

Figure 6.2.2-31. Vertical Force Calculations Graphed On An Expanded Time Scale, 31-32 Seconds, M8

1158 007

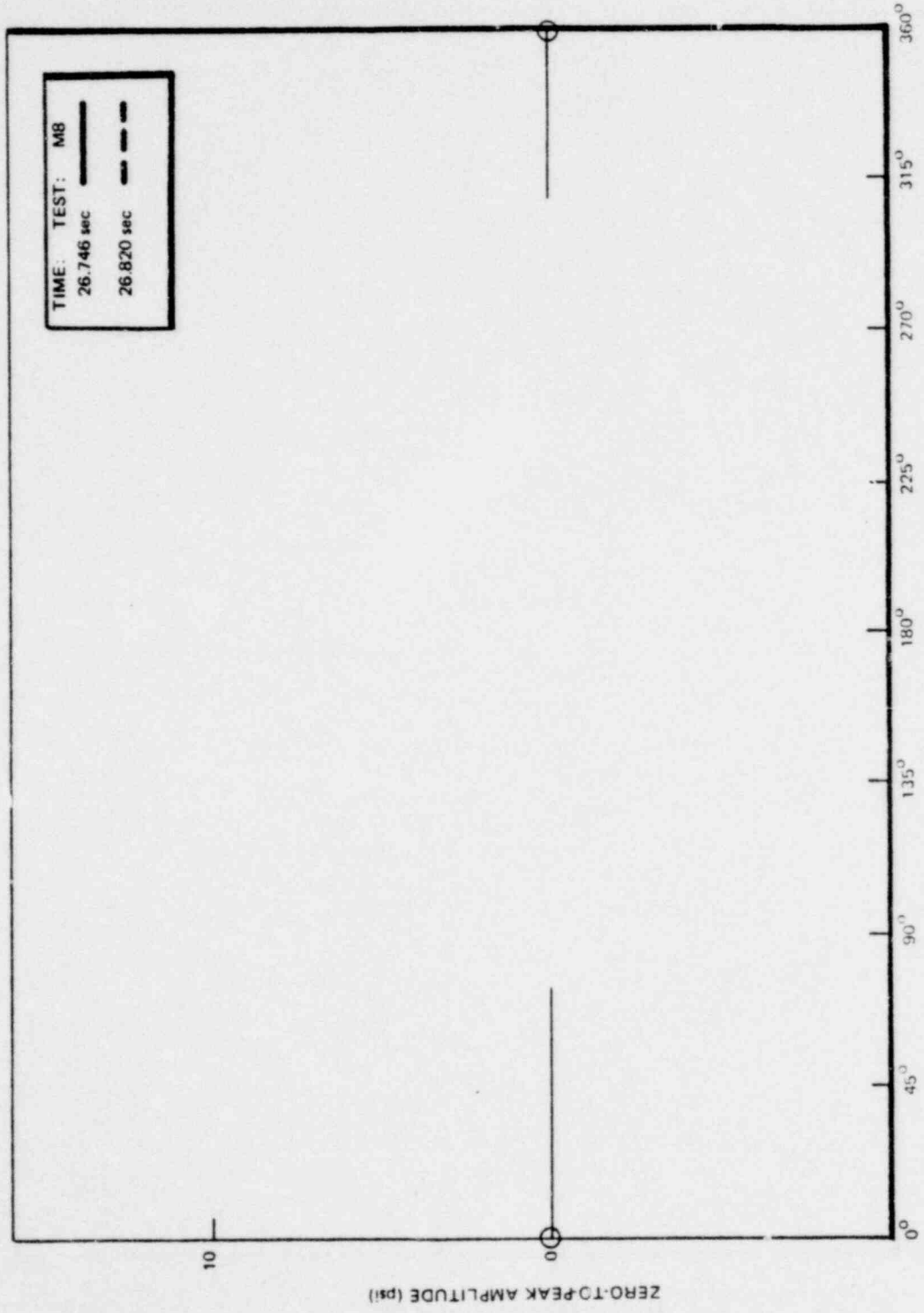

Figure 6.2.2-32. Wall Pressure Profile at Centerline of Wetwell

*Proprietary information deleted

1158 008

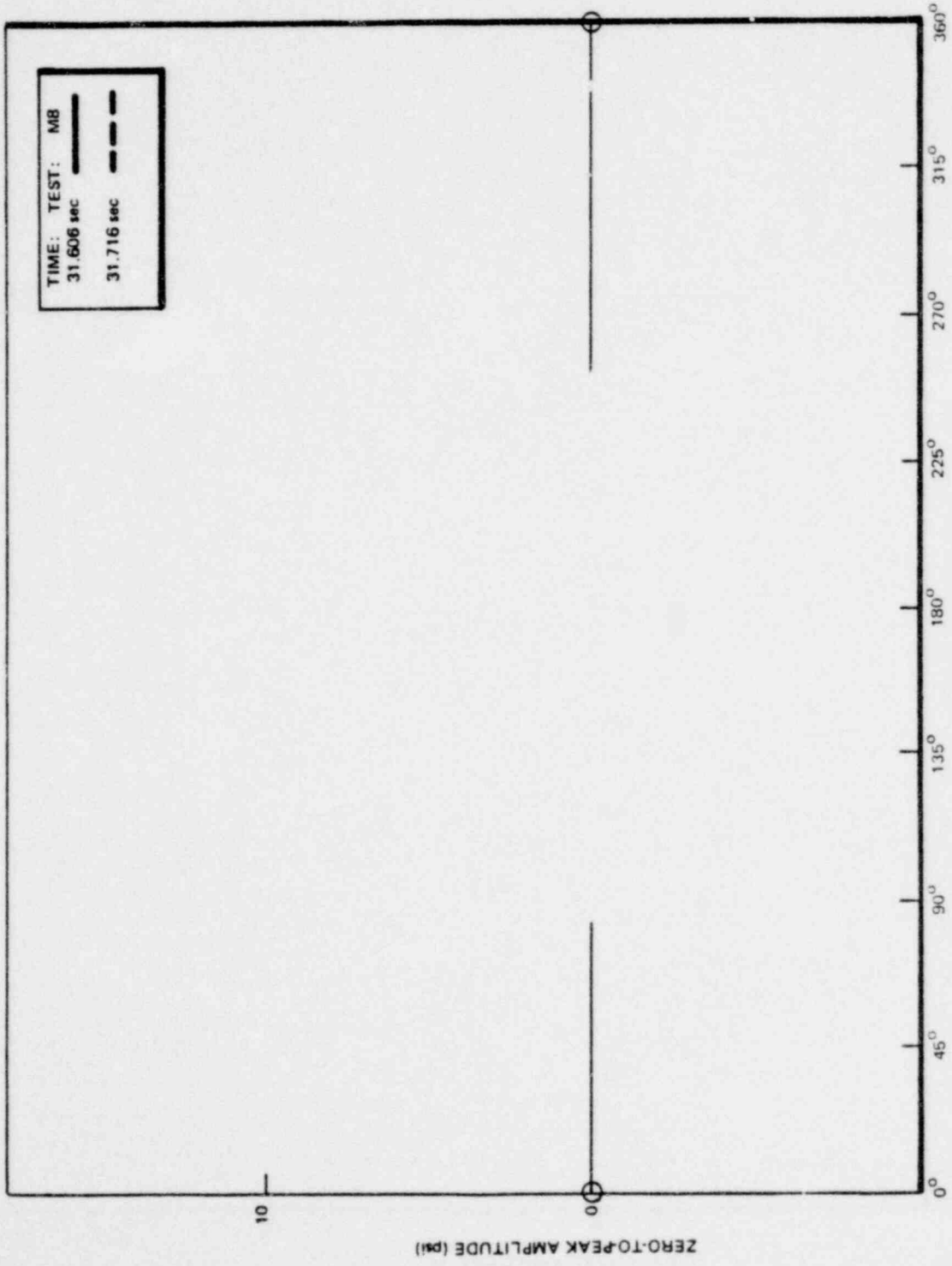

Figure 6.2.2-33. Wall Pressure Profile at Centerline of Wetwell *

*Proprietary information deleted

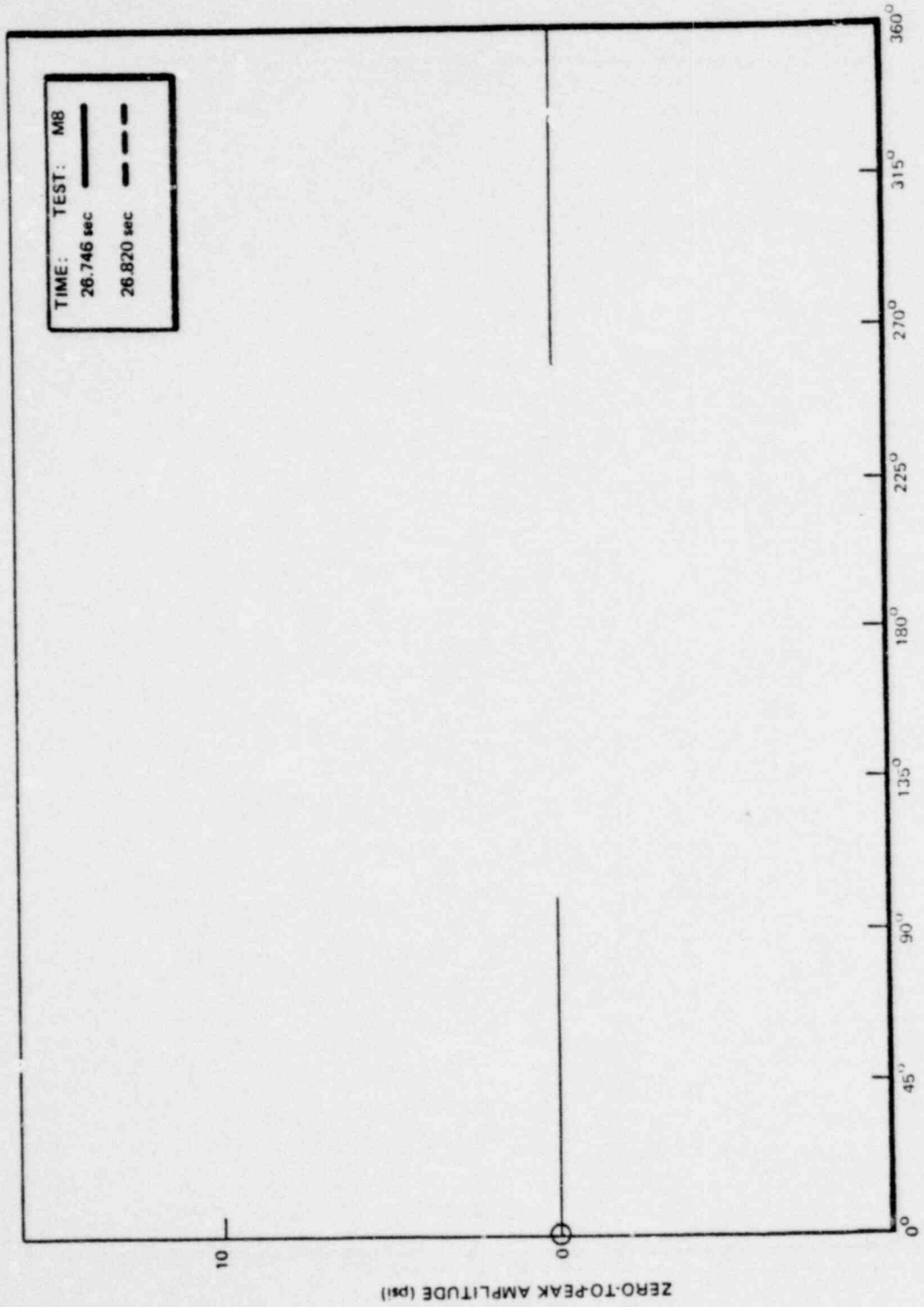

Figure 6.2.2-34. Wall Pressure Profile of Wetwell Beneath Downcomers 5 and 6

*Proprietary information deleted

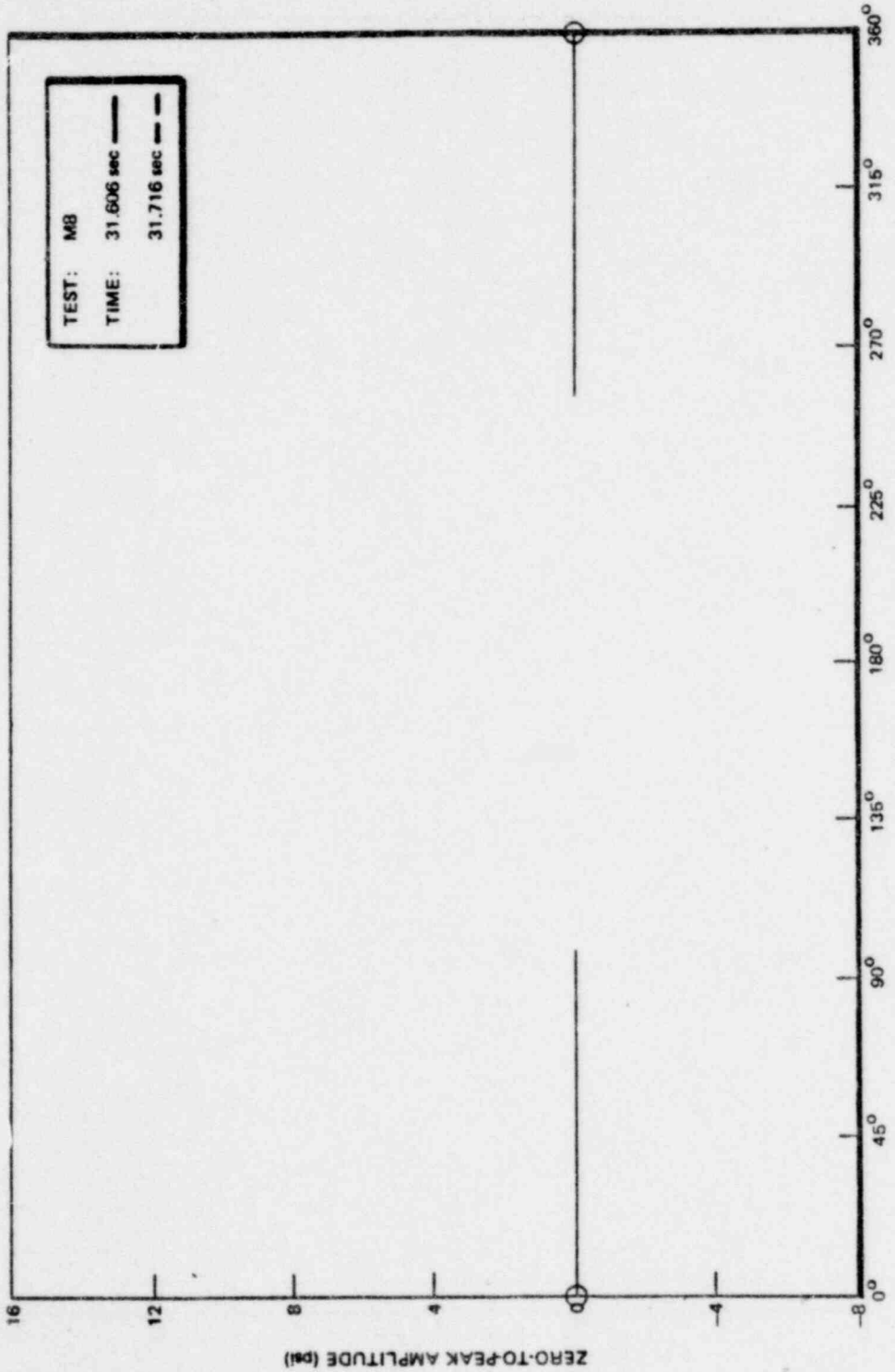

Figure 6.2.2-35. Wall Pressure Profile of Wetwell Beneath Downcomers 5 and 6

*Proprietary information deleted

1158 011

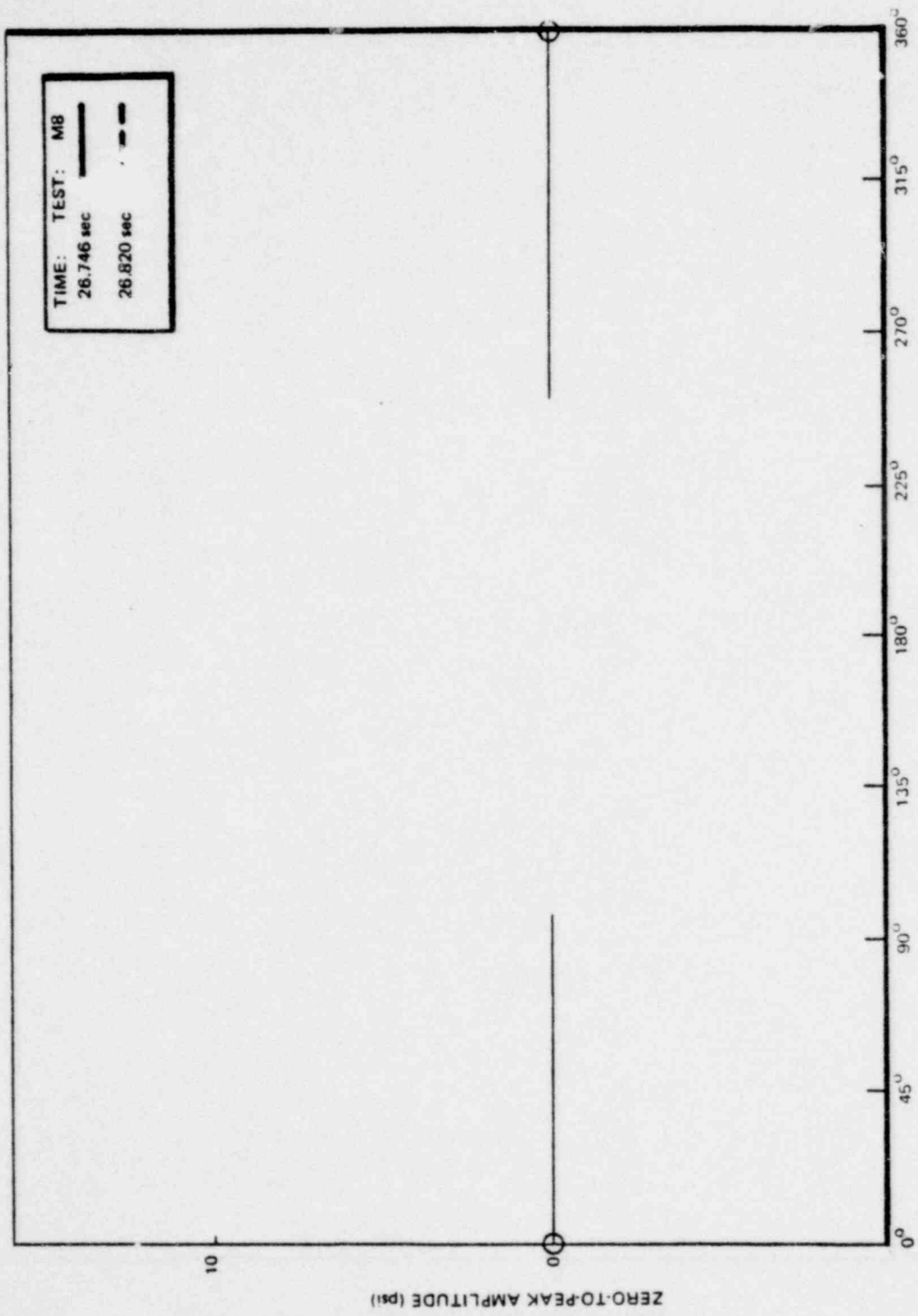

Figure 6.2.2-36. Wall Pressure Profile of Wetwell Beneath Downcomers 7 and 8

*Proprietary information deleted

1158 012

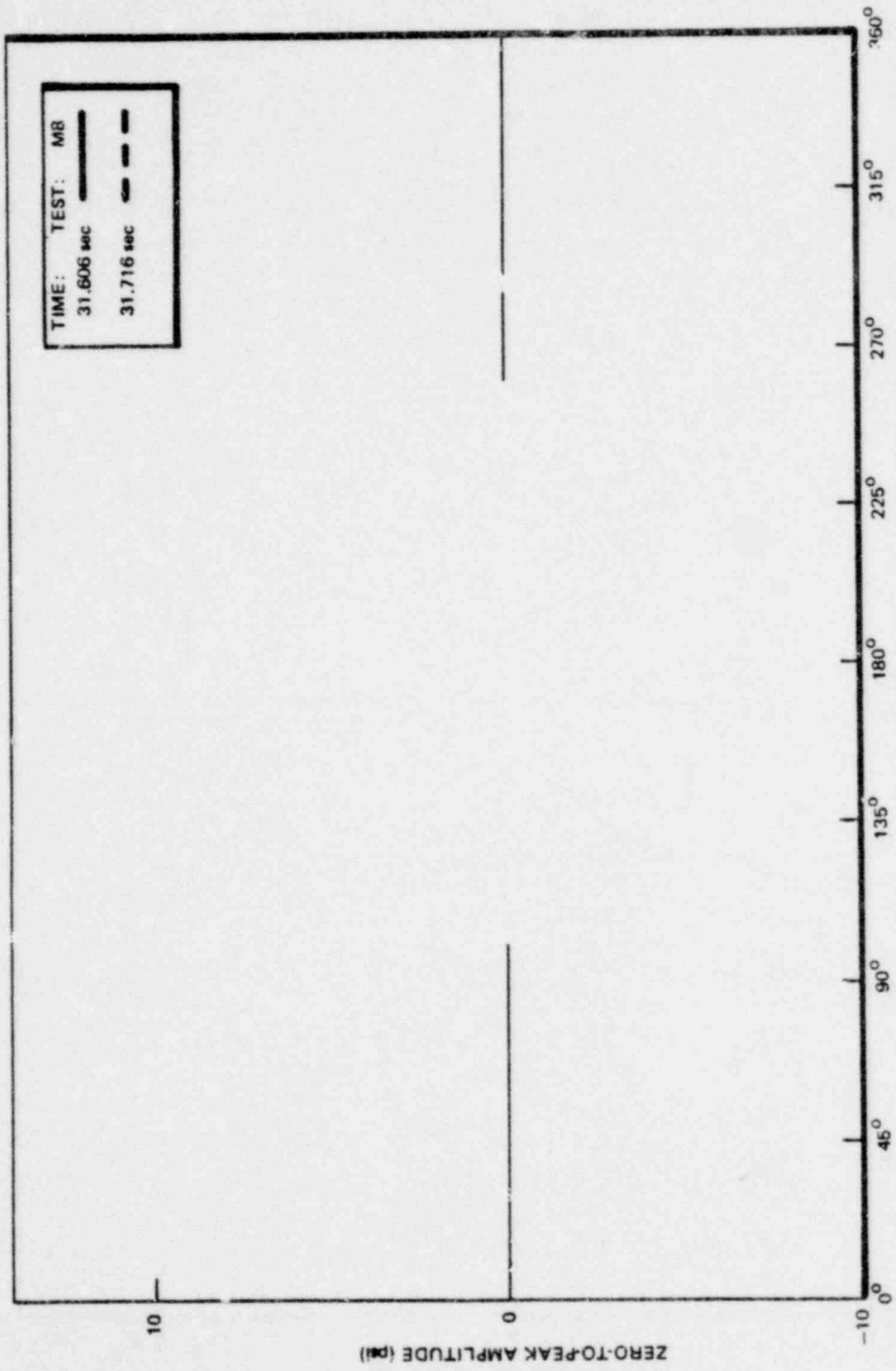

Figure 6.2.2-37. Wall Pressure Profile of Wetwell Beneath Downcomers 7 and 8

*Proprietary information deleted

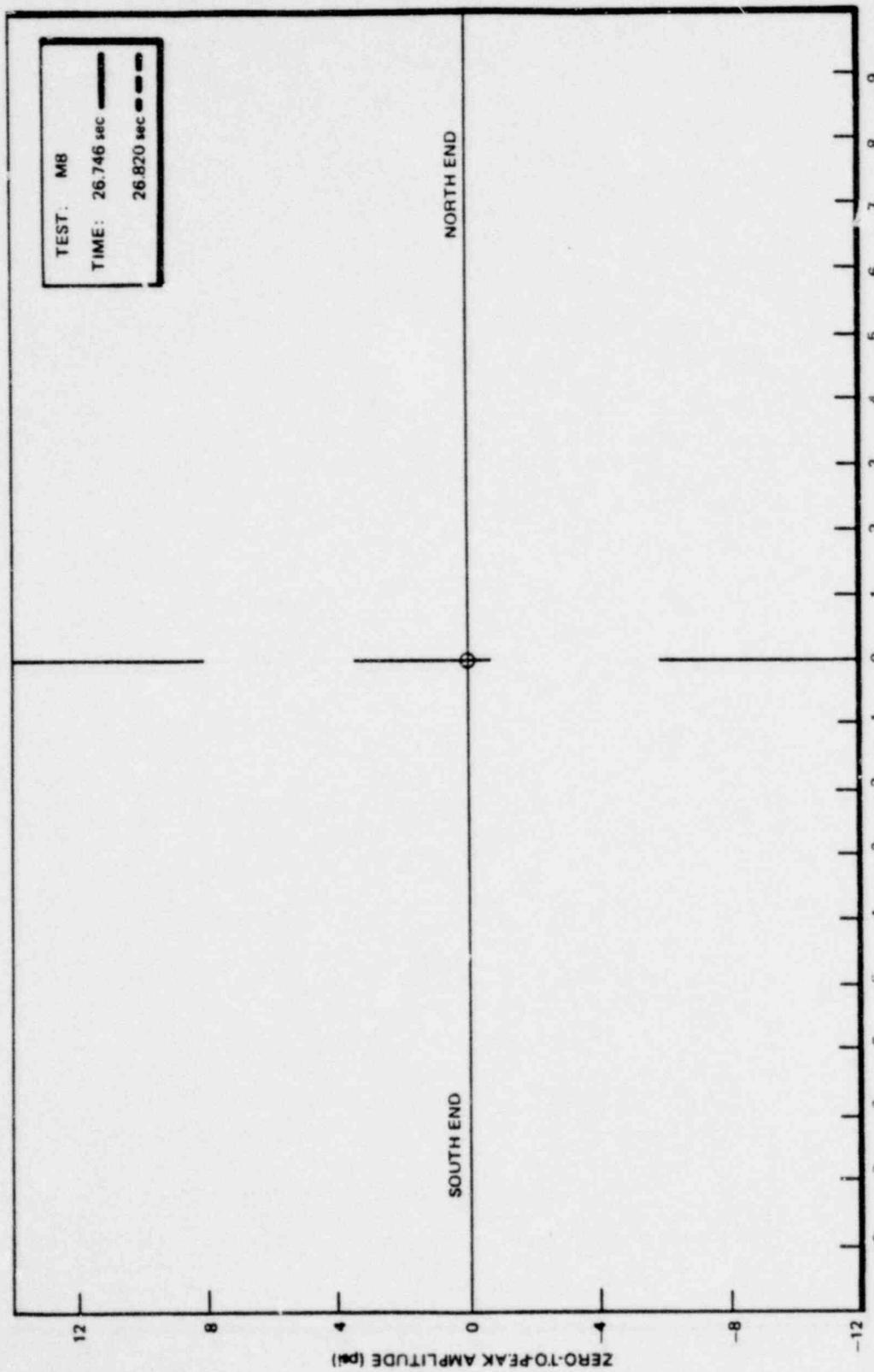

Figure 6.2.2-38. Wall Pressure Profile at Wetwell Bottom Center (180°)

*Proprietary information deleted

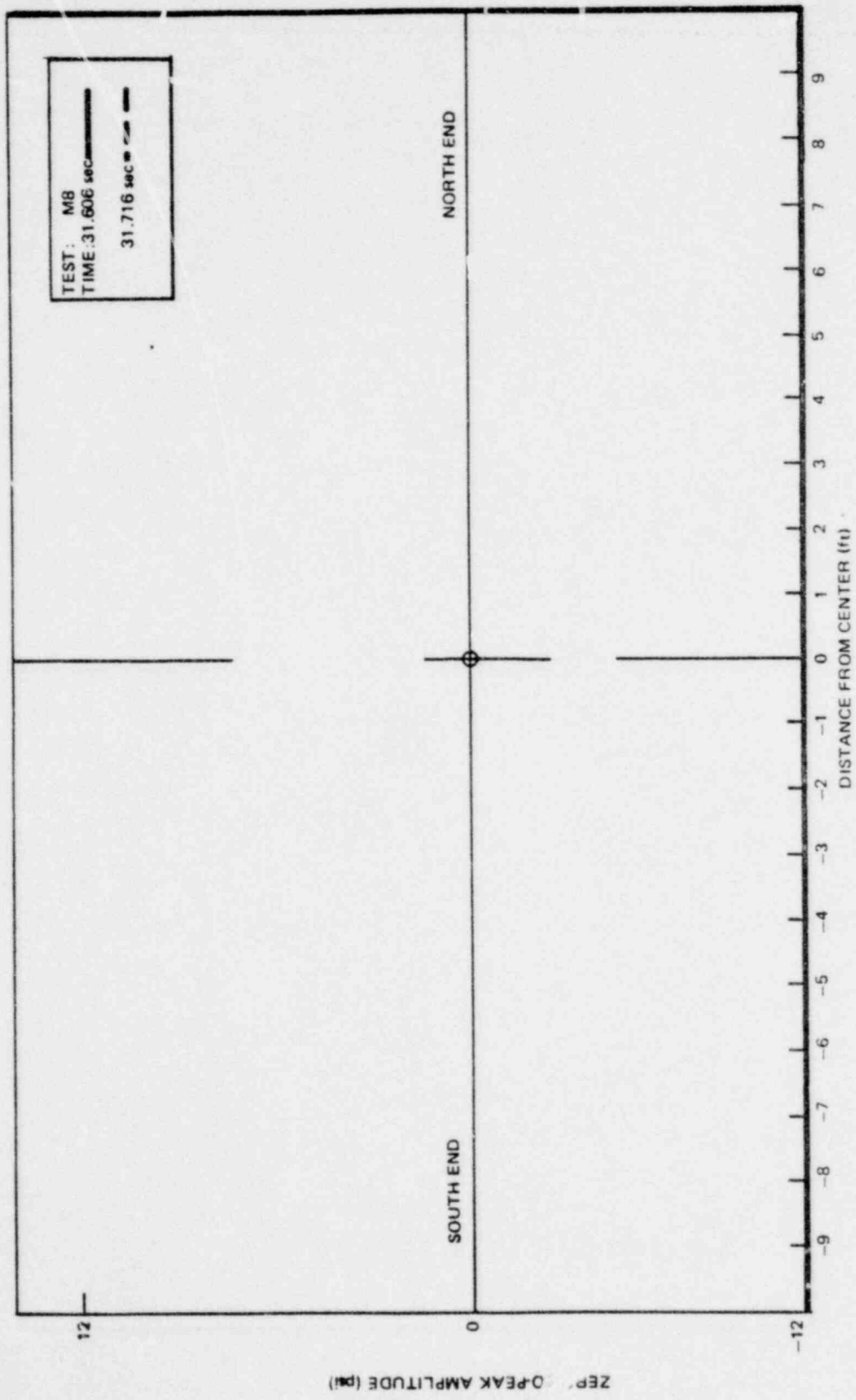

Figure 6.2.2-39. Wall Pressure Profile of Wetwell Bottom Center (180°)

*Proprietary information deleted

1158 015

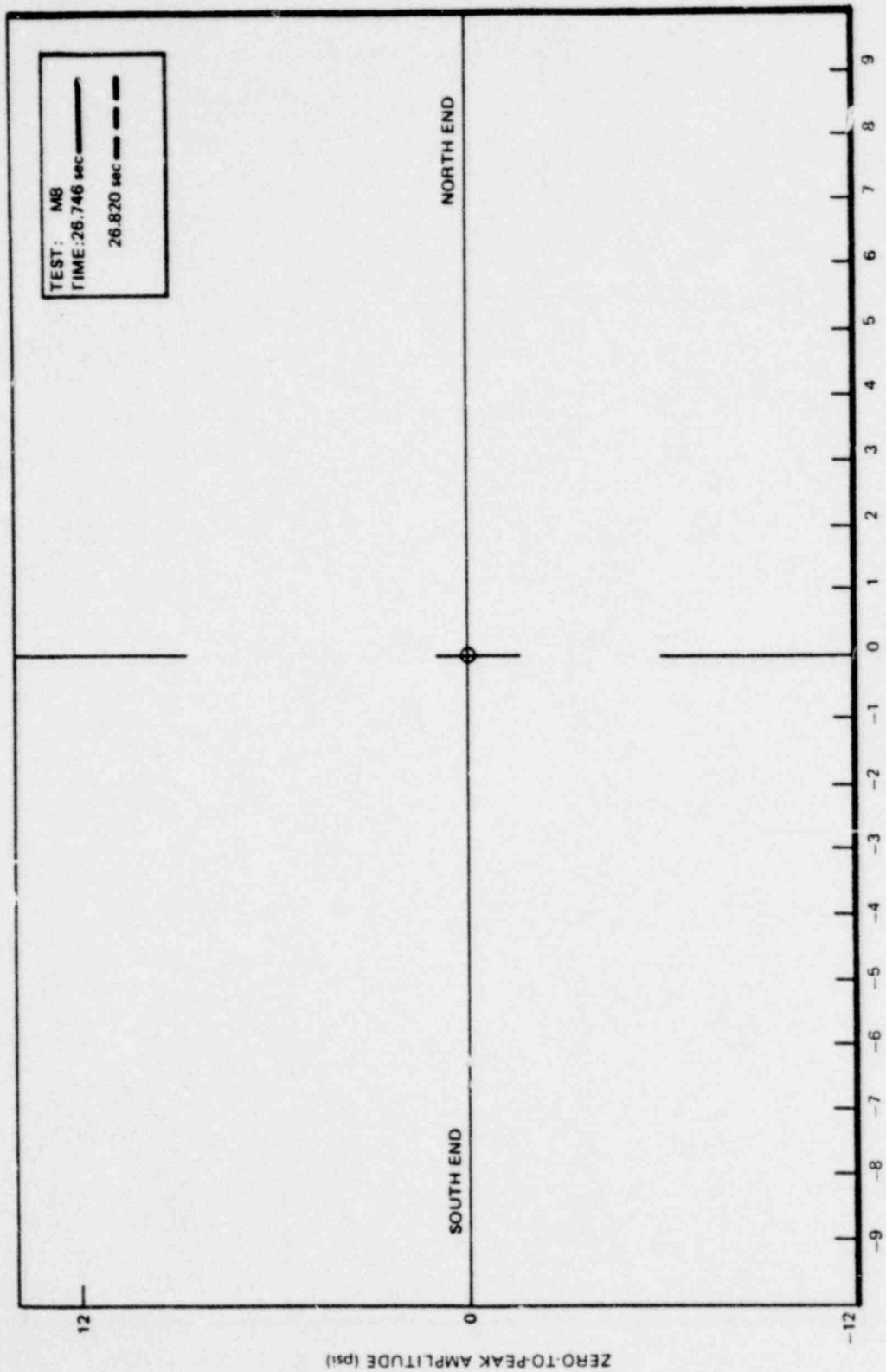

Figure 6.2.2-40. Wall Pressure Profile of Wetwell Bottom at 196.7° from Top (Below Even # DC)

*Proprietary information deleted

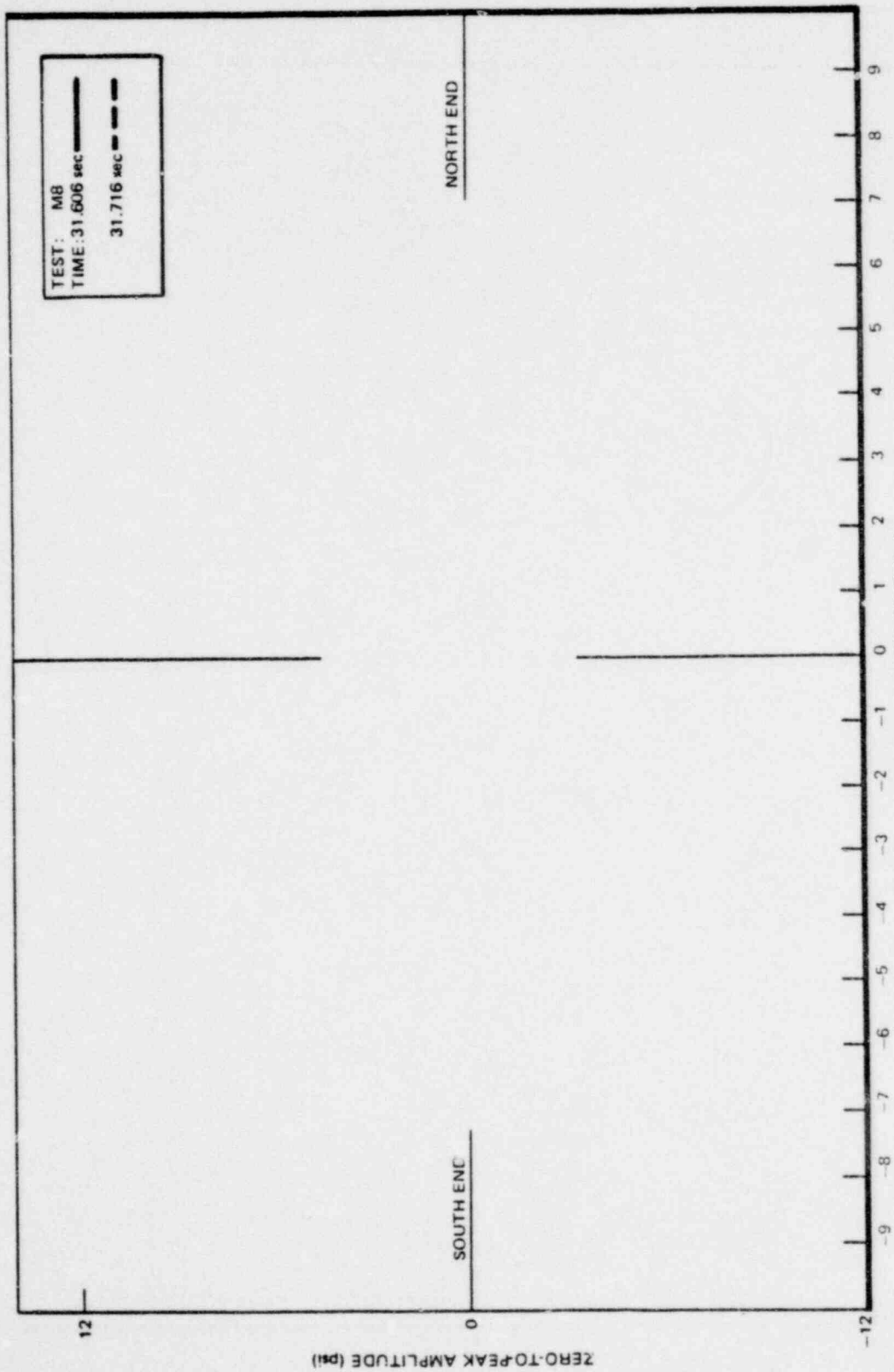

Figure 6.2.2-41. Wall Pressure Profile of Wetwell Bottom at 196.7° from Top (Below Even # D.C.)

*Proprietary information deleted

1158 017

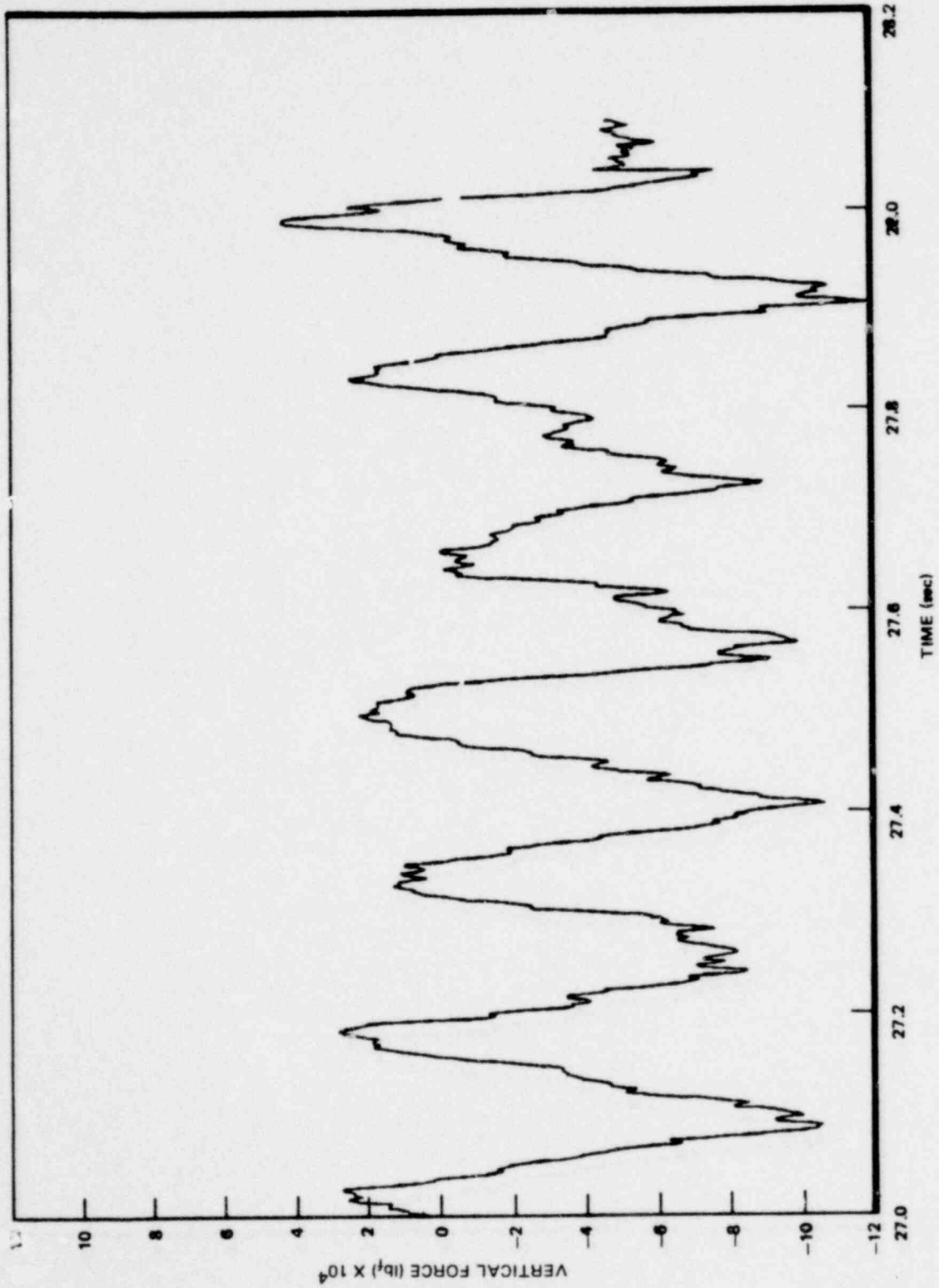

Figure 6.2.2-42. Vertical Force Calculations Graphed On An Expanded Time Scale; 27-28 Seconds, M7

1158 018

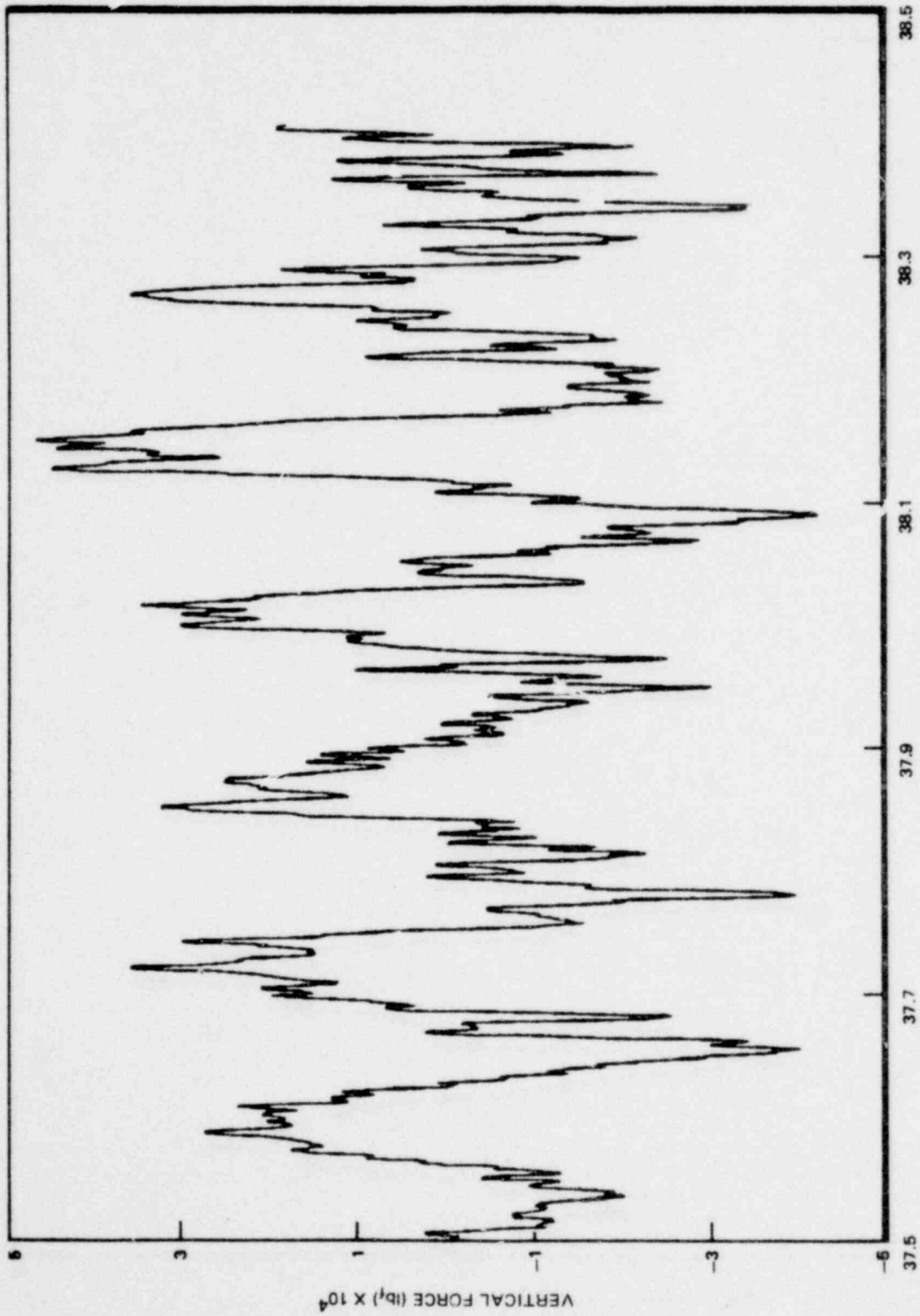

Figure 6.2.2-43. Vertical Force Calculations Graphed On An Expanded Time Scale, 37.5-38.5 Seconds, M7

1158 019

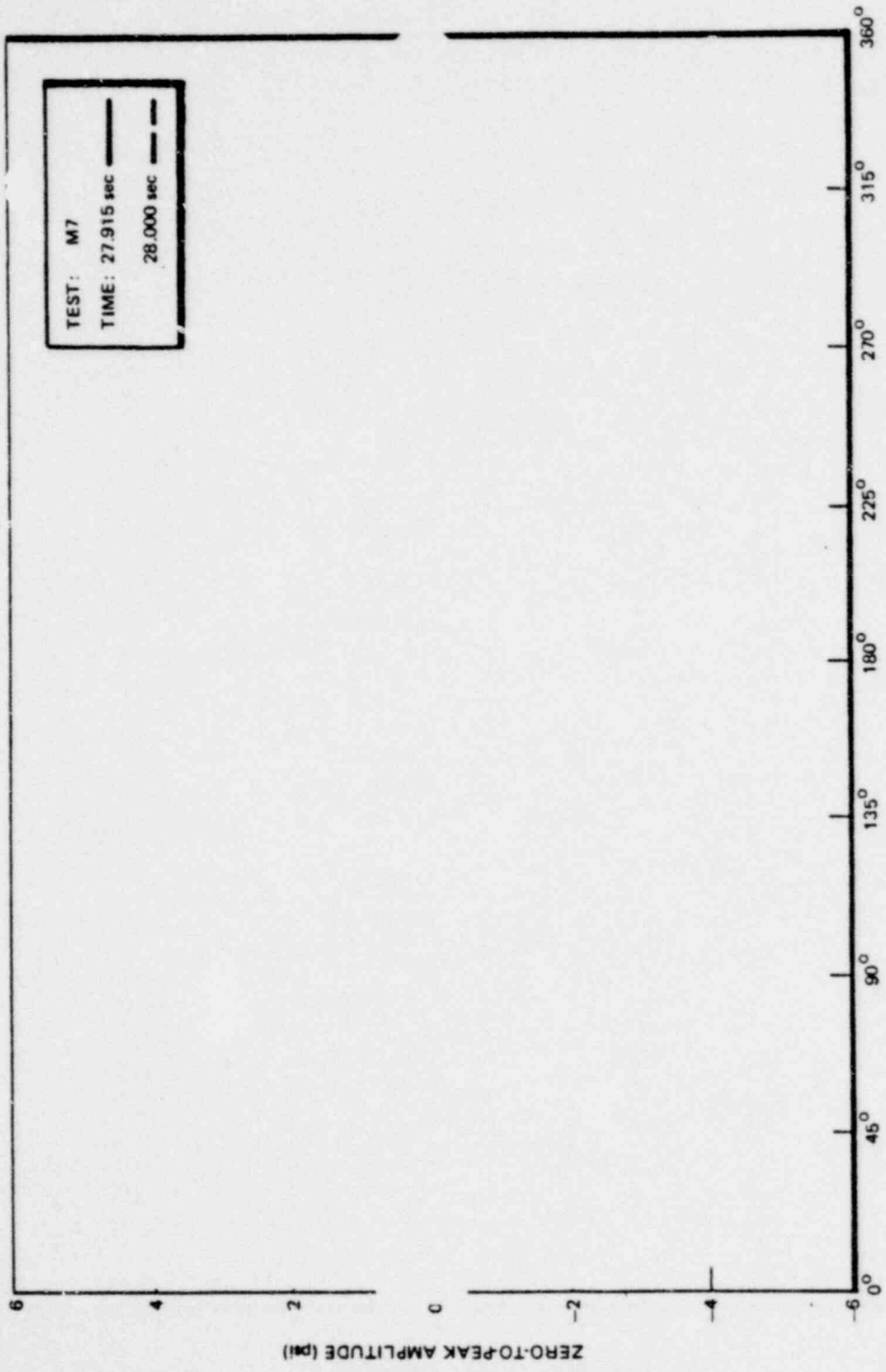

Figure 6.2.2-44. Wall Pressure Profile at Centerline of Wetwell

*Proprietary information deleted

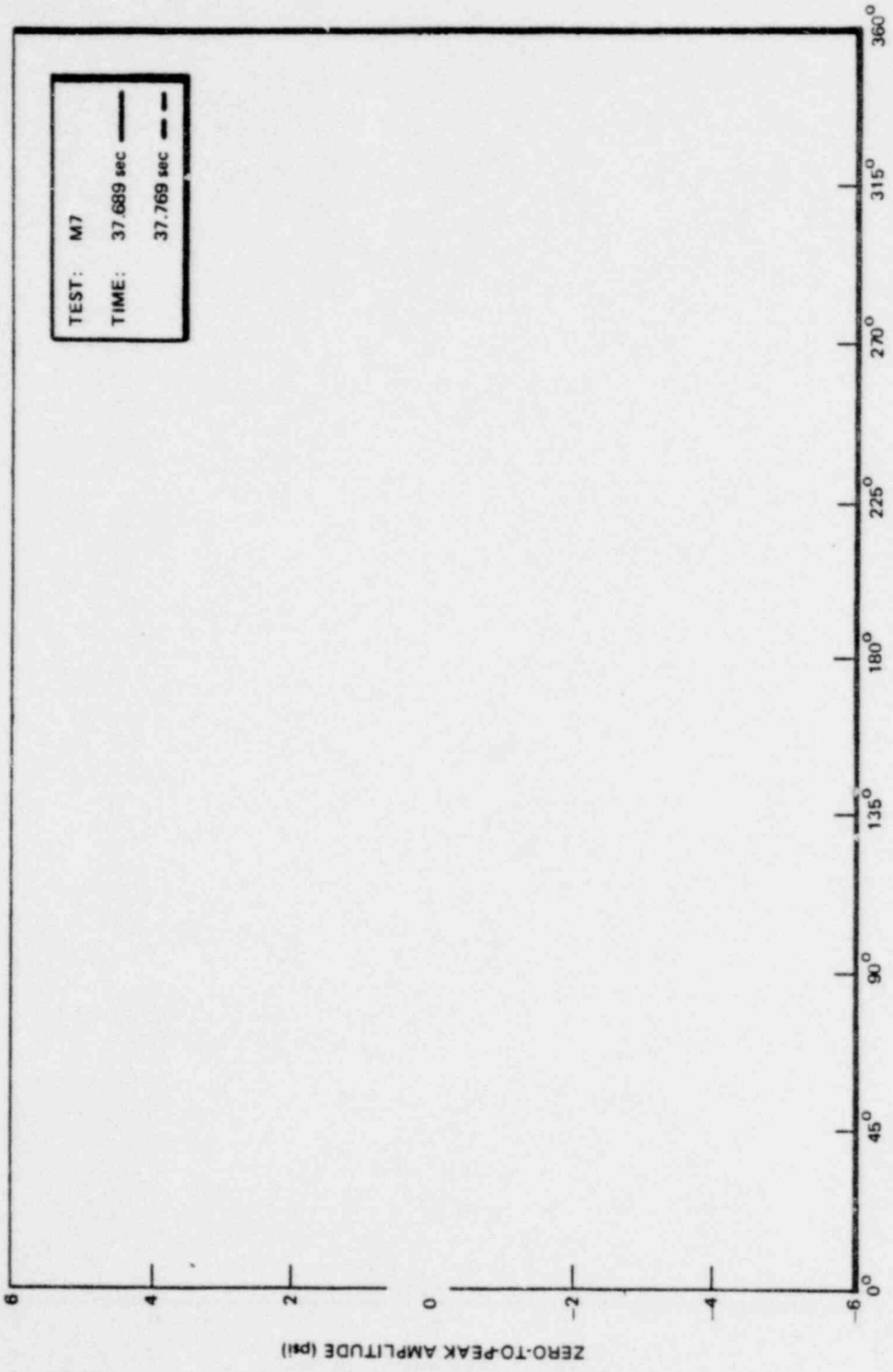

Figure 6.2.2-45. Wall Pressure Profile at 180° Centerline of Wetwell

*Proprietary information deleted

1158 021

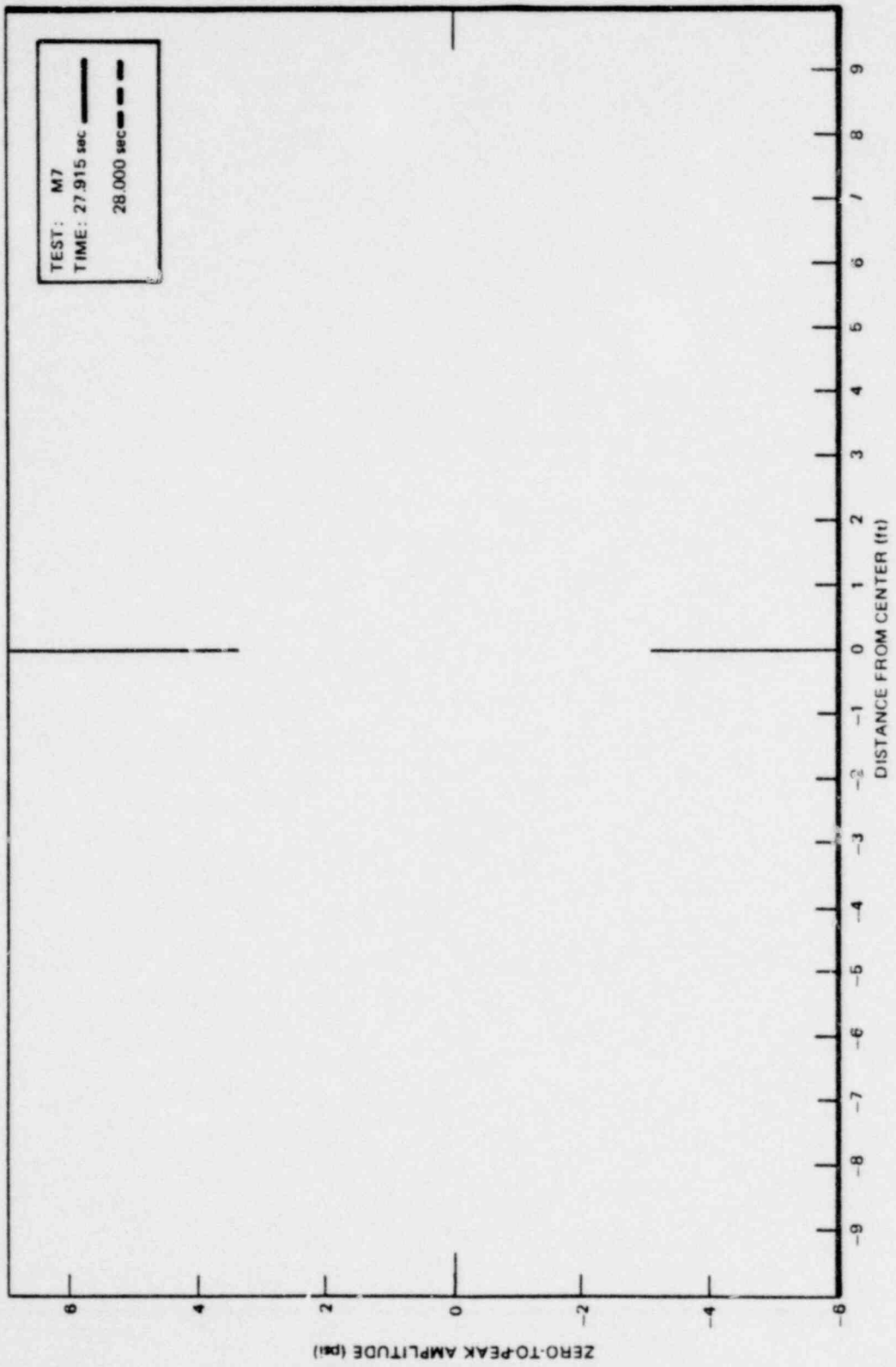

Figure 6.2.2-46. Wall Pressure .rofile at Wetwell Bottom Center (180°)

*Proprietary information deleted

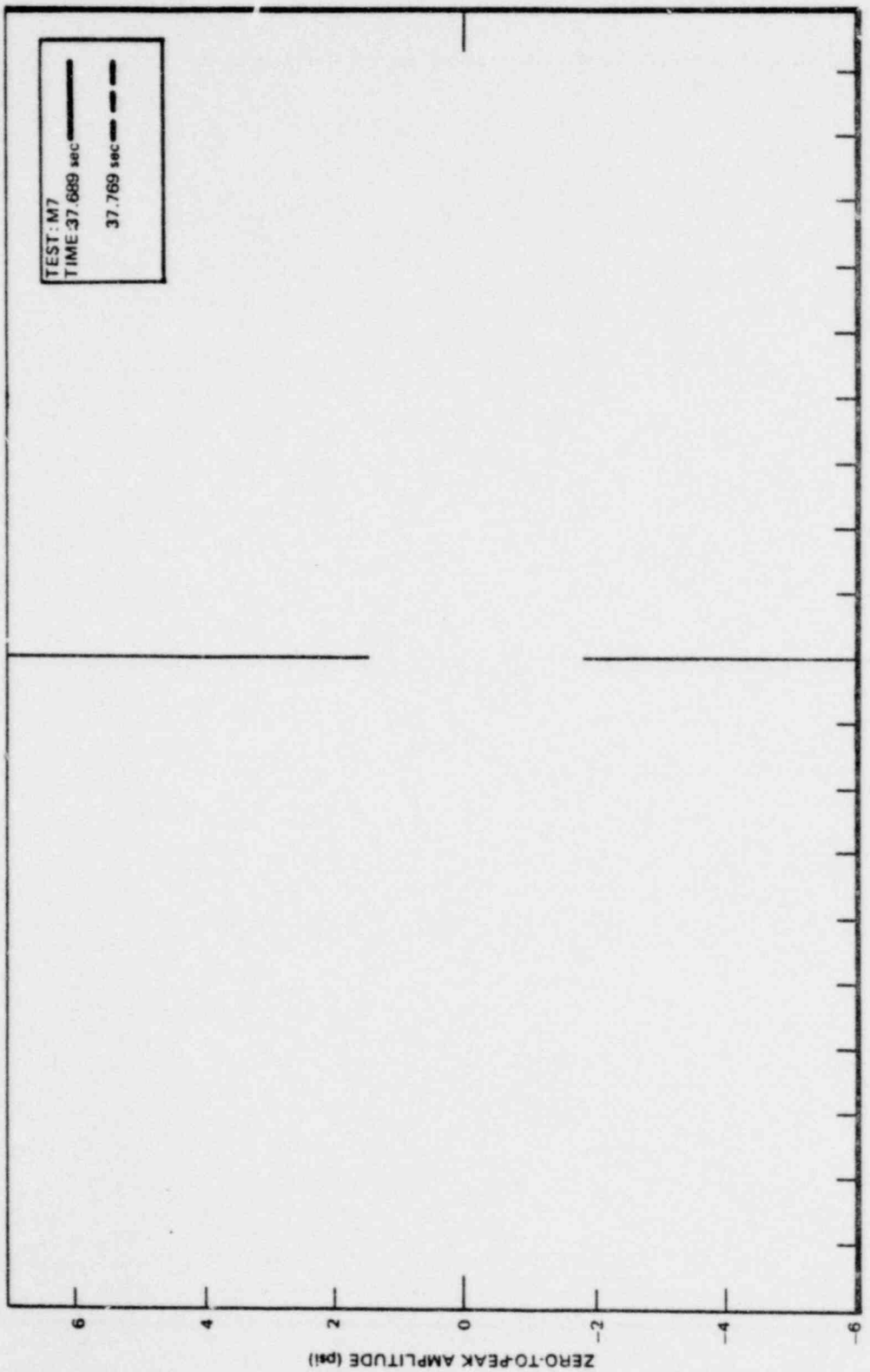

Figure 6.2.2-47. Wall Pressure Profile at Wetwell Bottom Center (180°)

*Proprietary information deleted

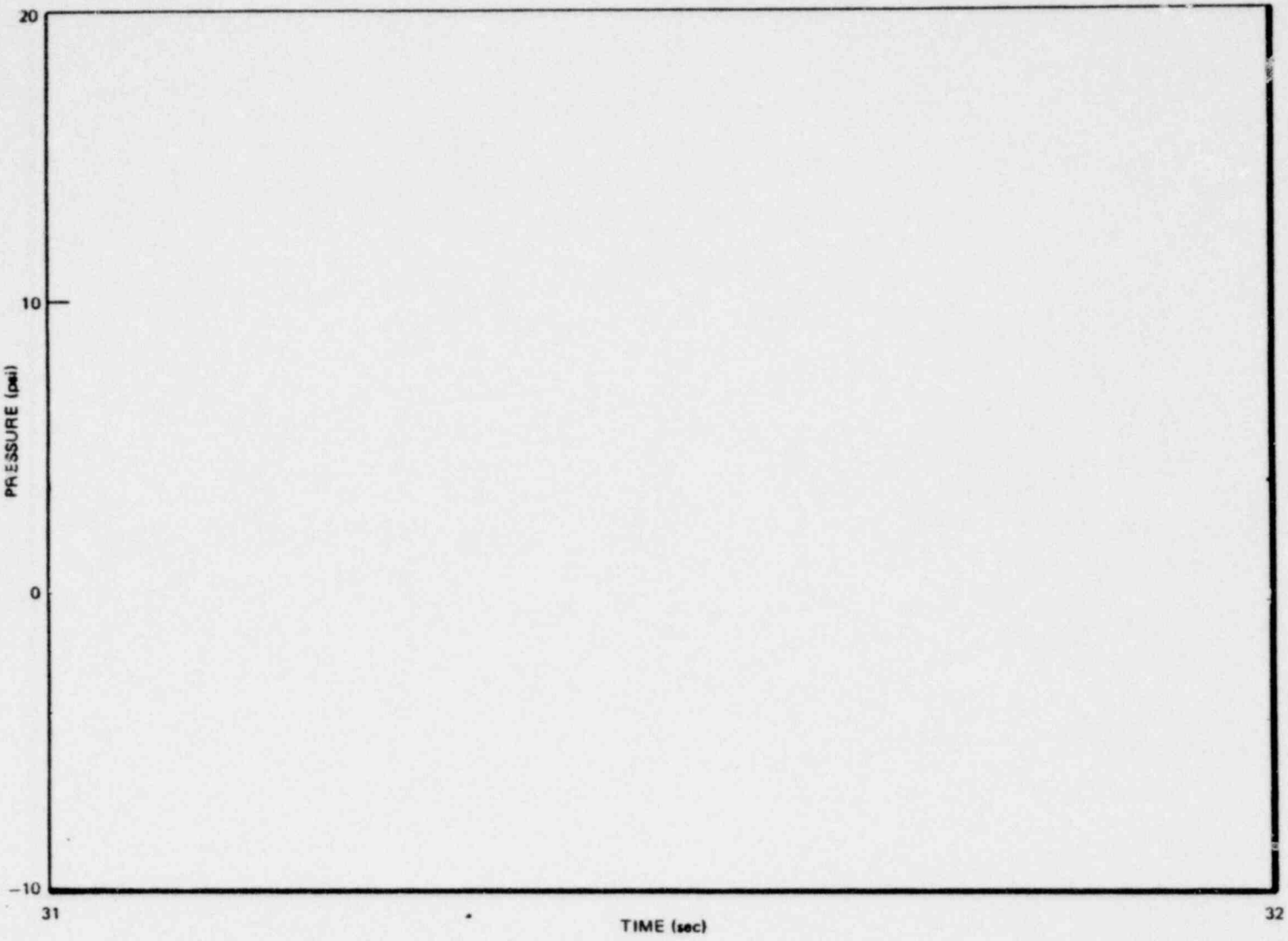

Figure 6.2.2-48. Comparison of the Summation of Amplitude Components to Actual Wetwell Pressure Tra..sduc:r (P3185) Signal, 31-32 Seconds, M8

*Proprietary information deleted

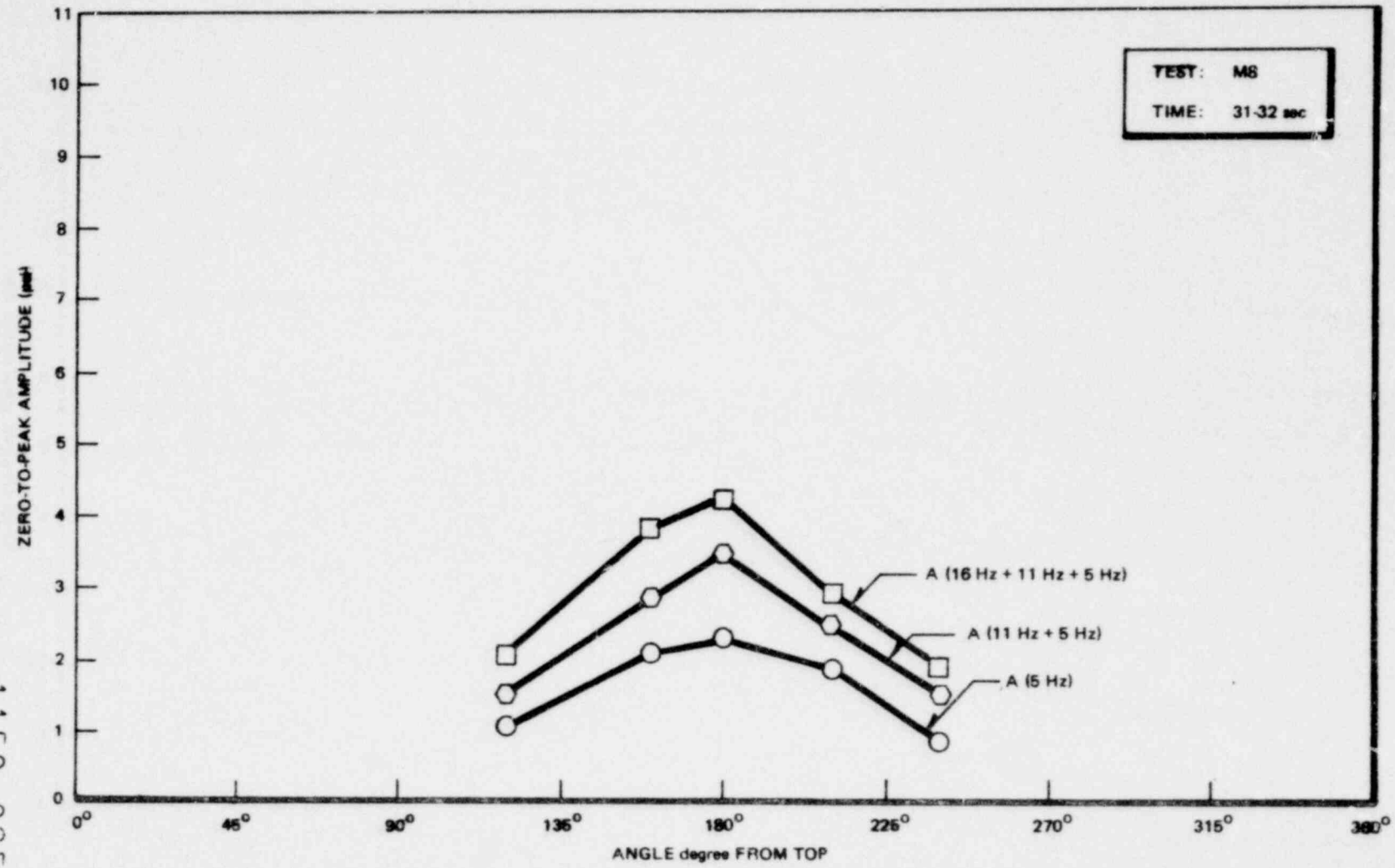

Figure 6.2.2-49. Circumferential Pressure Distribution at Wetwell Centerline Calculated from PSDs

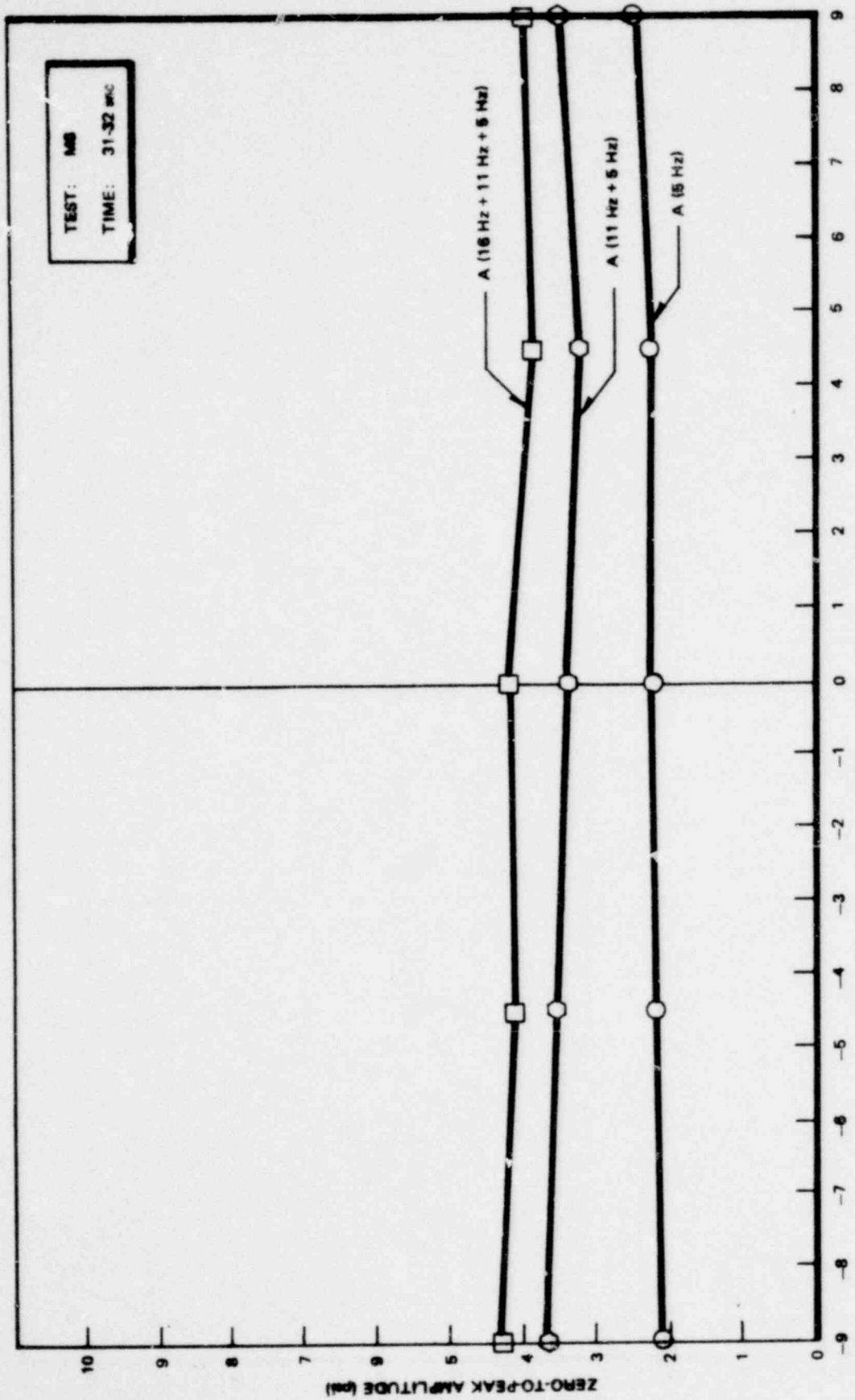

Figure 6.2.2-50. Axial Pressure Distribution at Wetwell Bottom Center (180°) Calculated From PSDs

1158 026

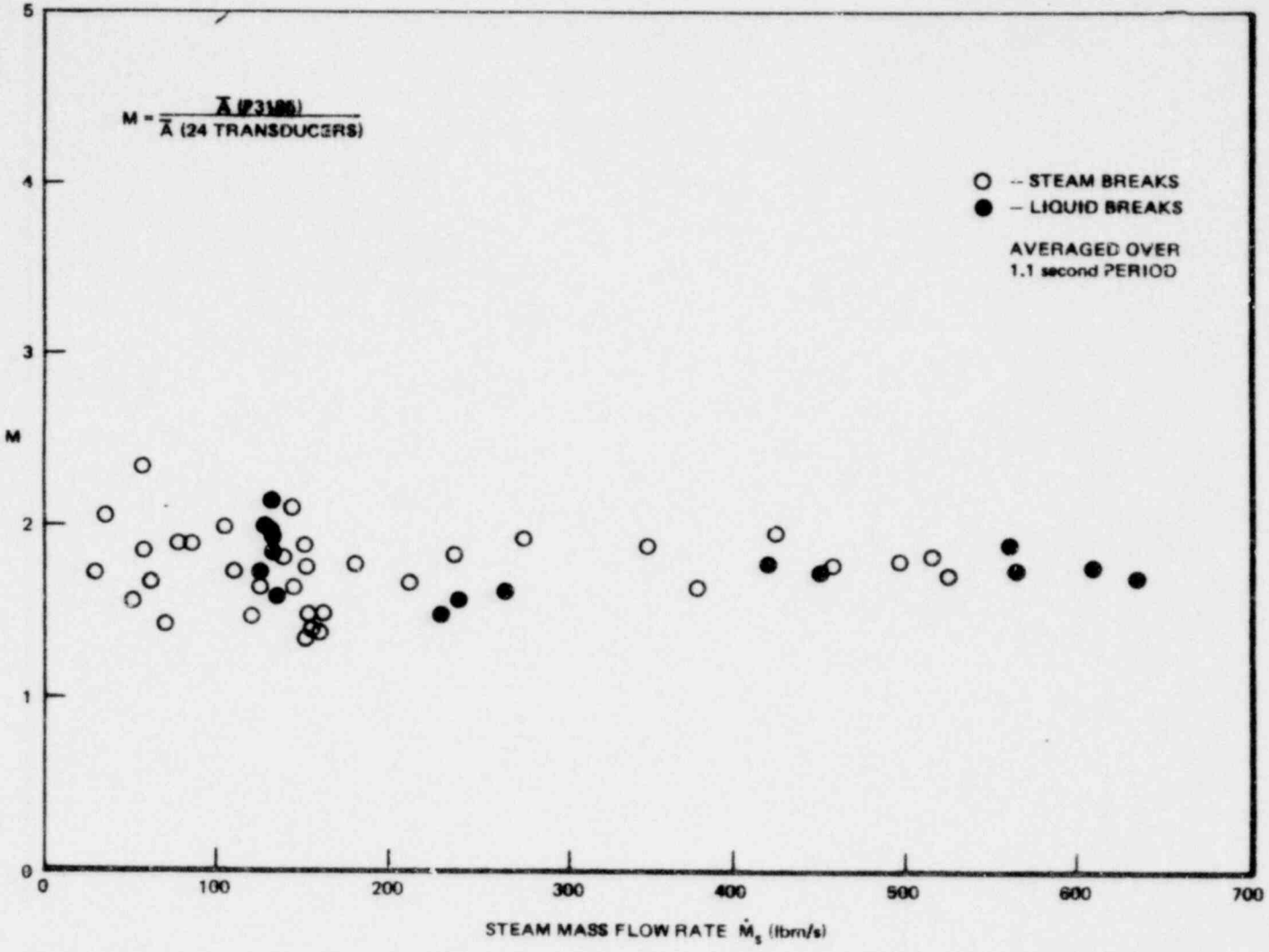

Figure 6.2.2-51. Ratios of Averaged Loop Amplitude to Averaged Amplitude of 24 Wetwell Transducers Due to Vertical Force vs Steam Flow Rate

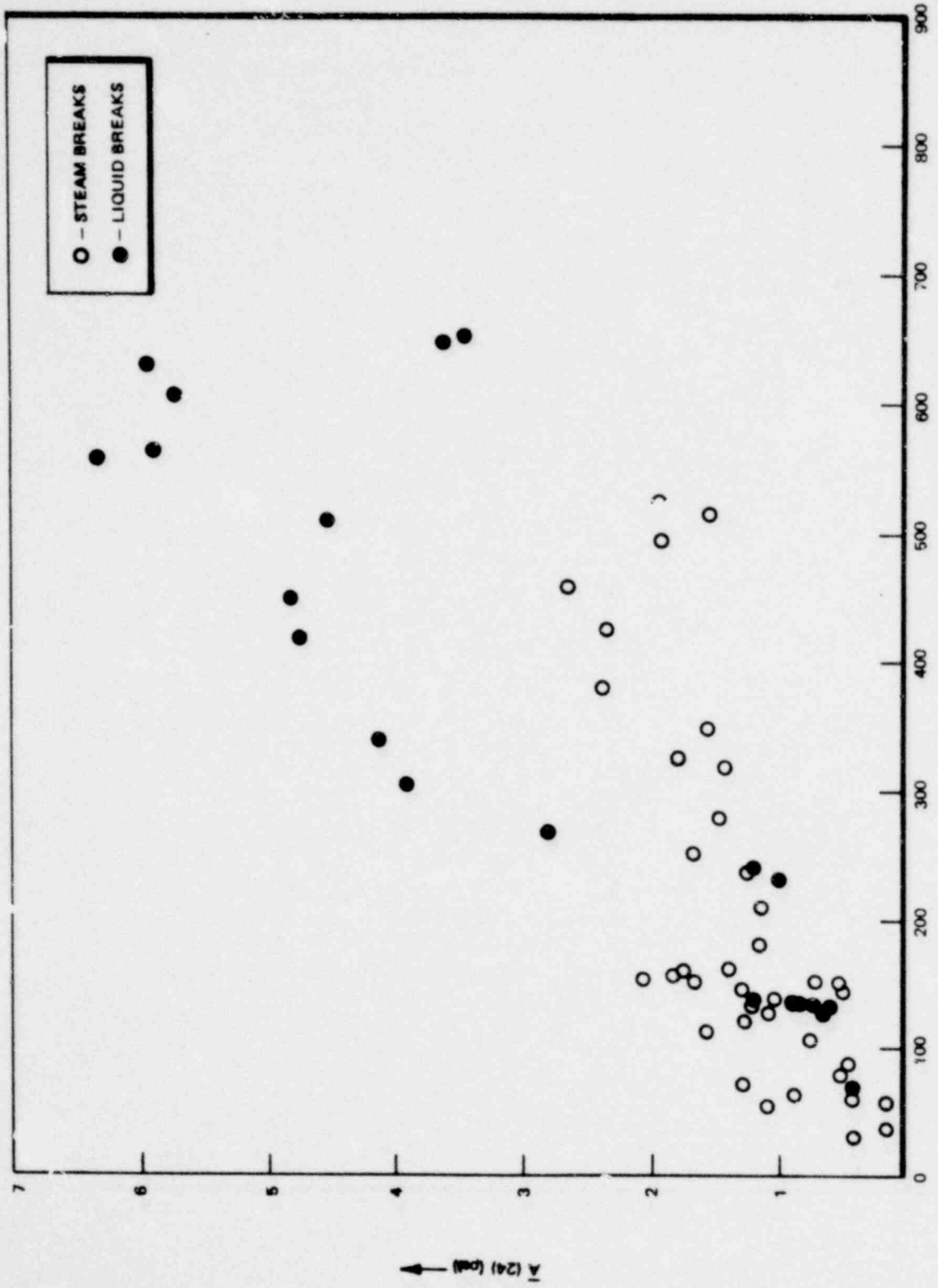

Figure 6.2.2-52. $\bar{A}$ (24 transducers) vs Steam Flow Rate $\dot{M}_s$

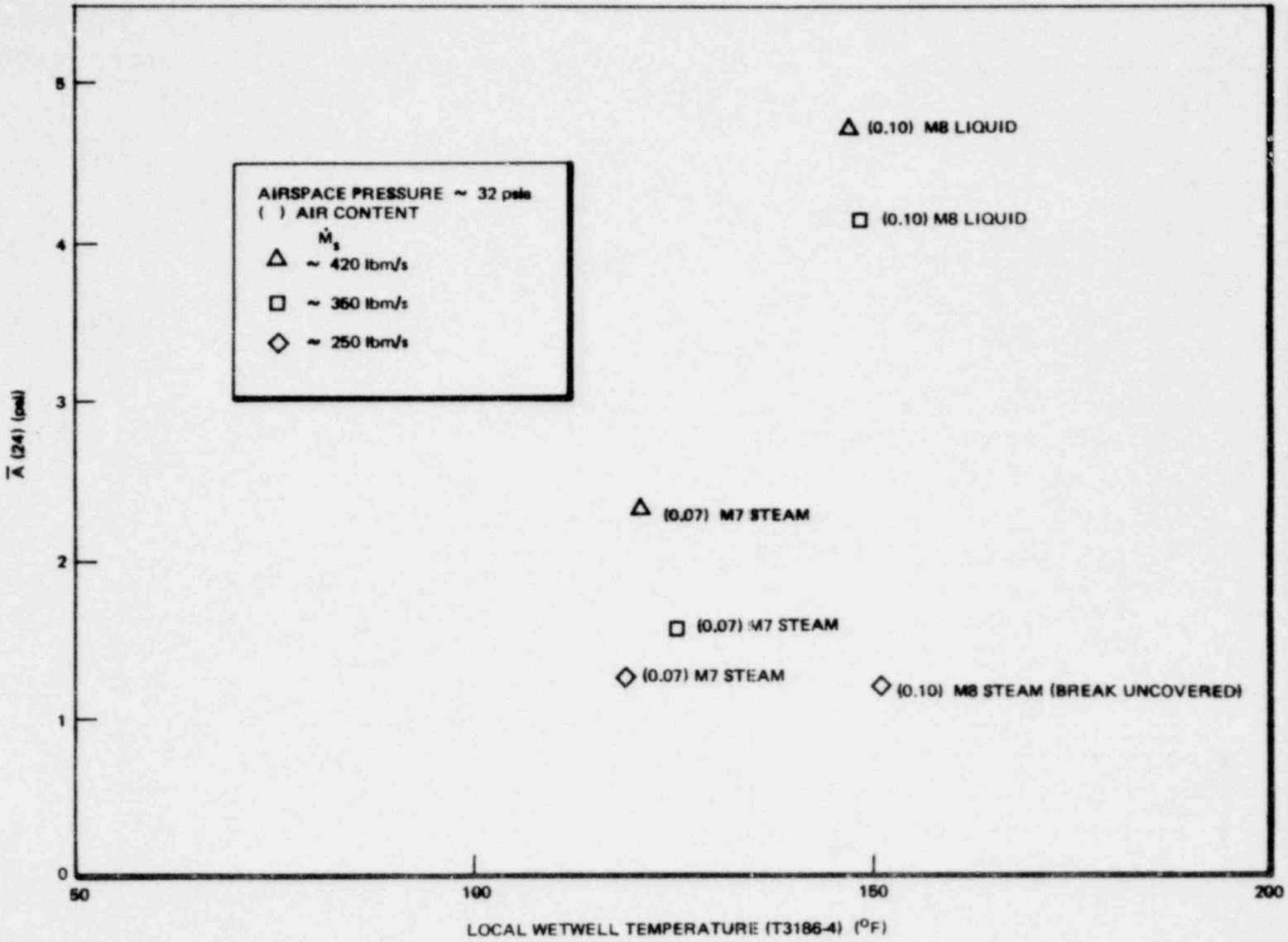

Figure 6.2.2-53. Comparison of Liquid Break and Steam Break Average Amplitudes

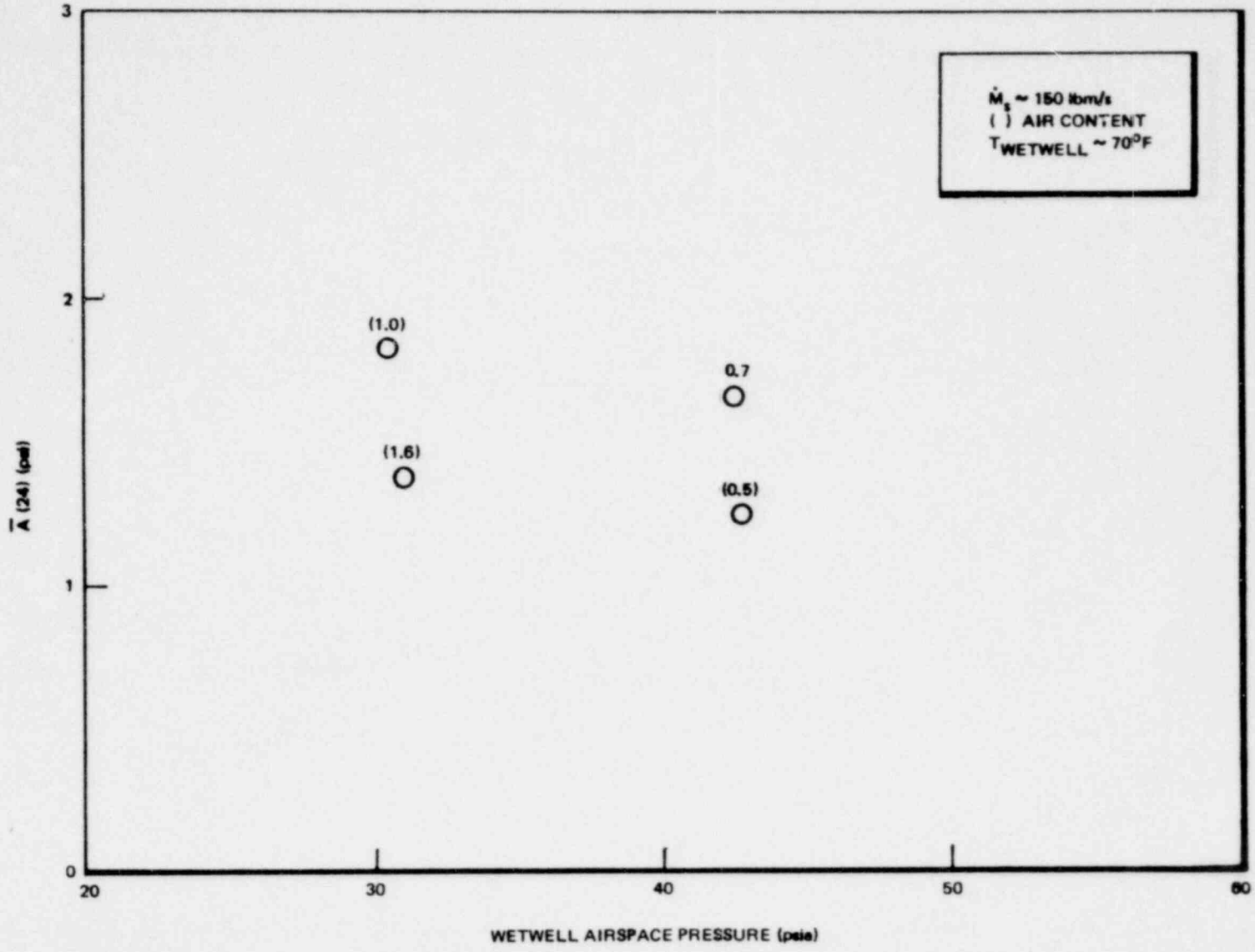

Figure 6.2.2-54. Steam Break Average Amplitude vs Wetwell Airspace Pressure

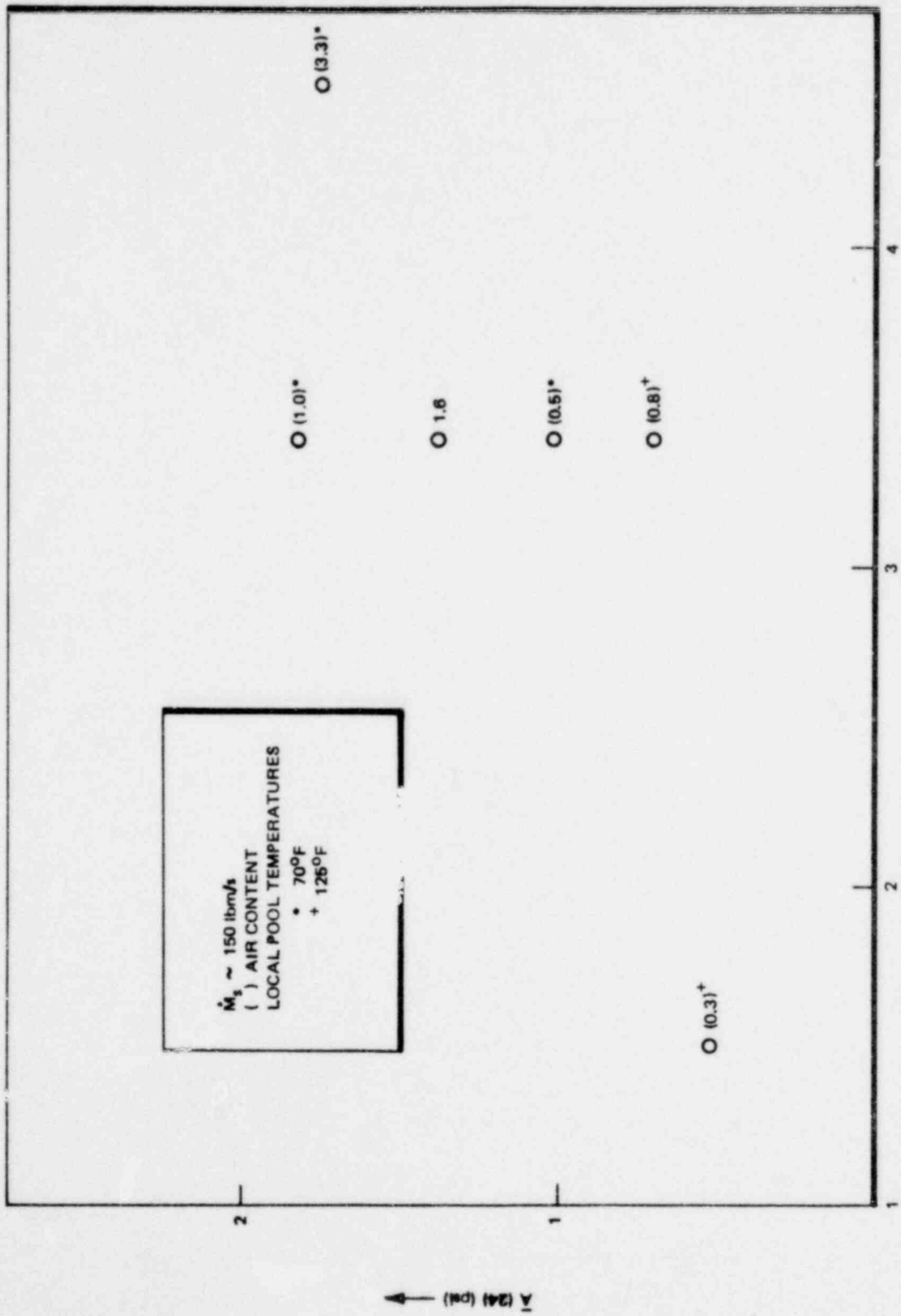

Figure 6.2.2-55. Steam Break Average Amplitude vs Initial Downcomer Submergence

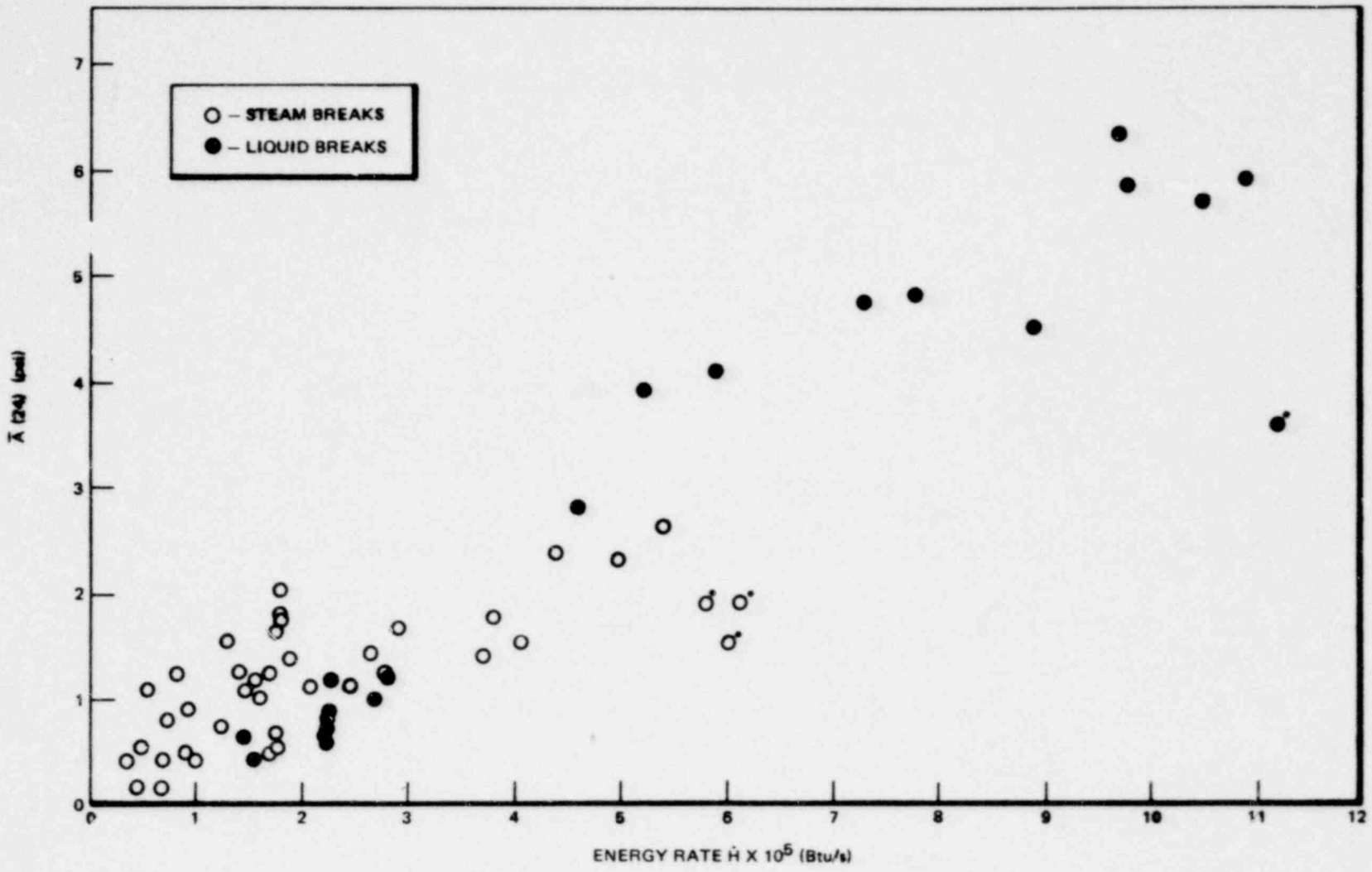

Figure 6.2.2-56. Average Amplitude of 24 Wetwell Transducers vs Energy Rate

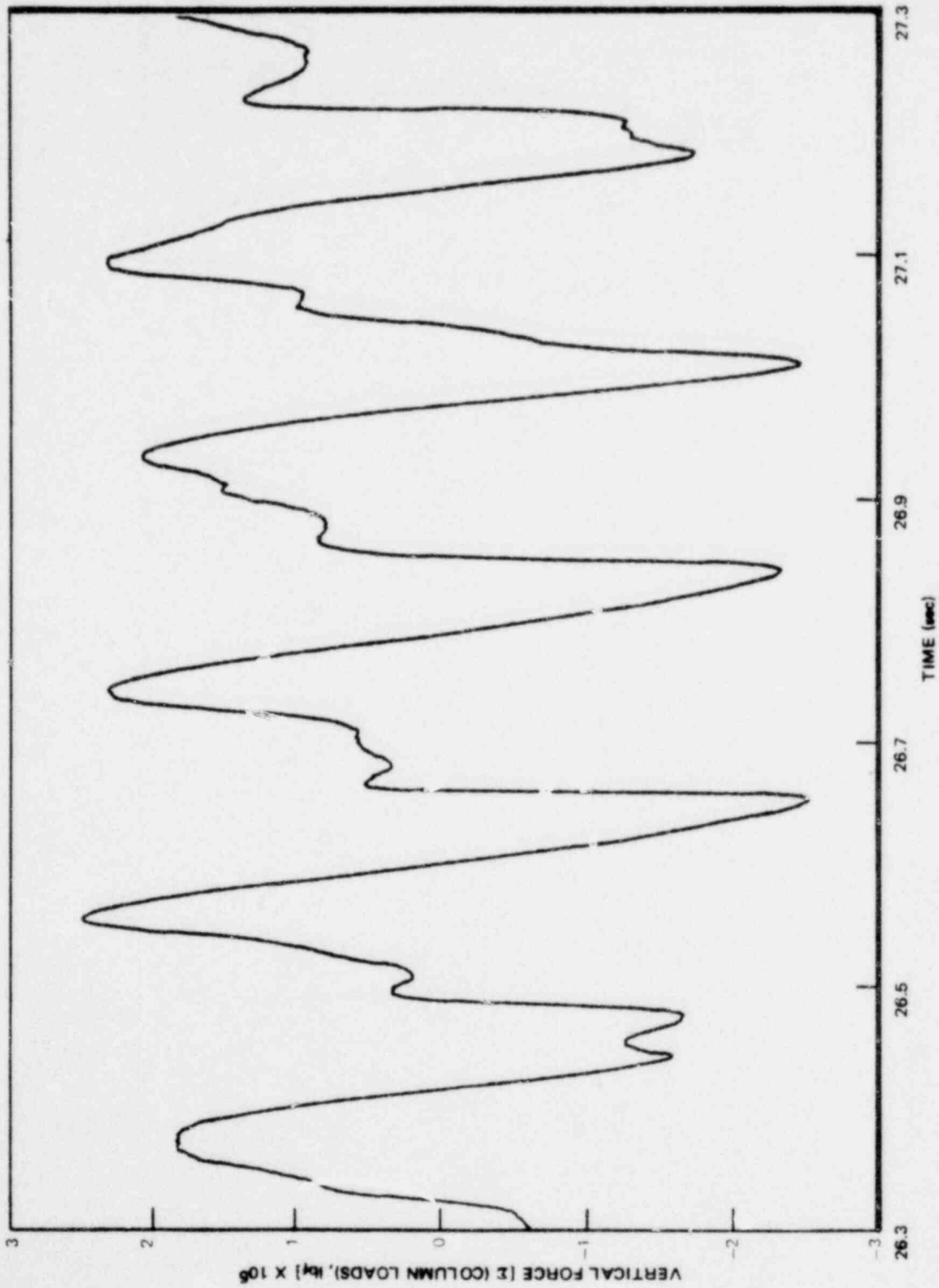

Figure 6.2.2-57. Vertical Component of Forces Exerted on the Wetwell Calculated From Output of Strain Gage Bridges on the Support Columns, M8

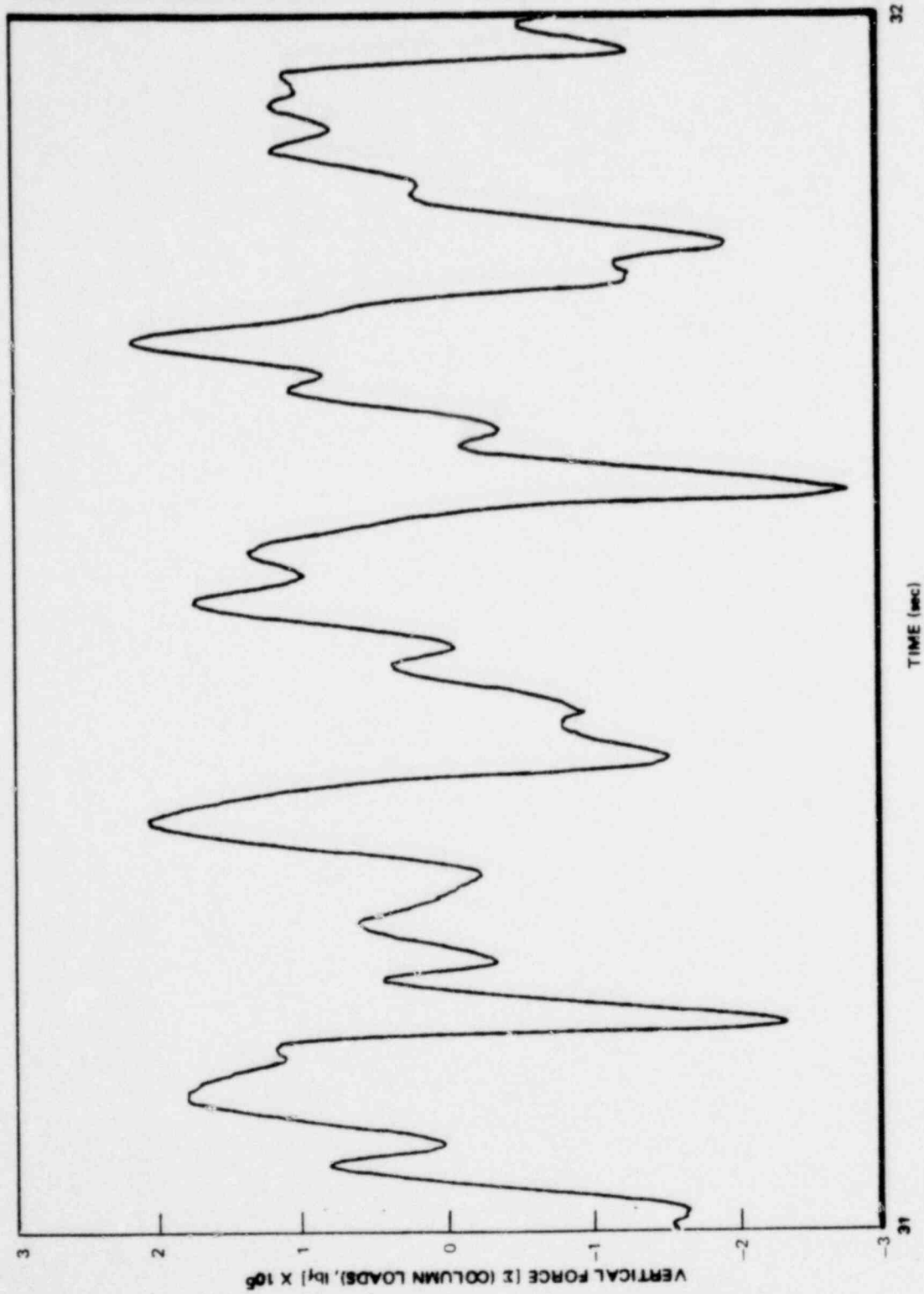

Figure 6.2.2-58. Vertical Component of Forces Exerted on the Wetwell Calculated from Output of Strain Gage Bridges on the Support Columns, M8

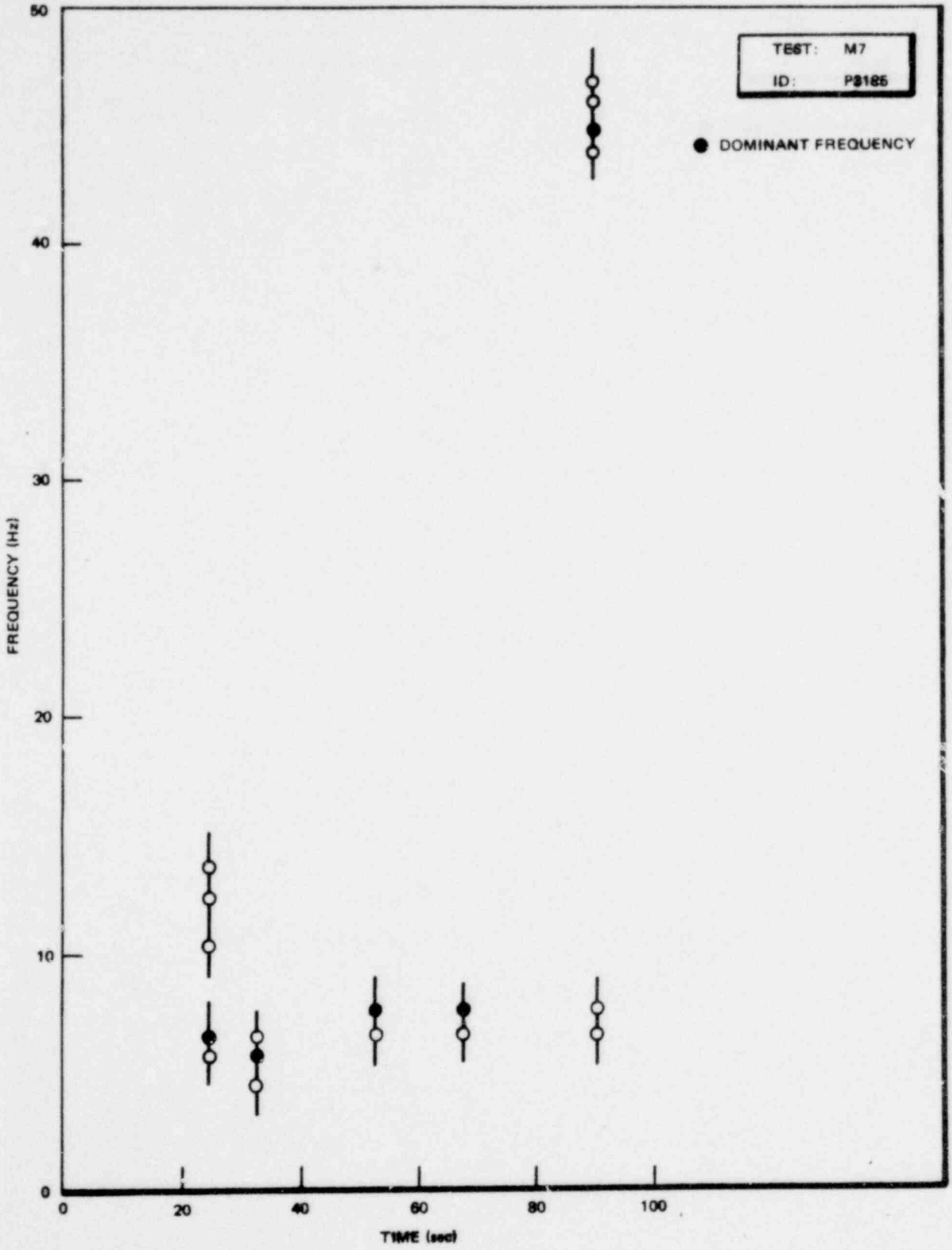

Figure 6.2.2-59. Significant Frequencies in the Wetwell Bottom Center Pressure Waveform

1158 035

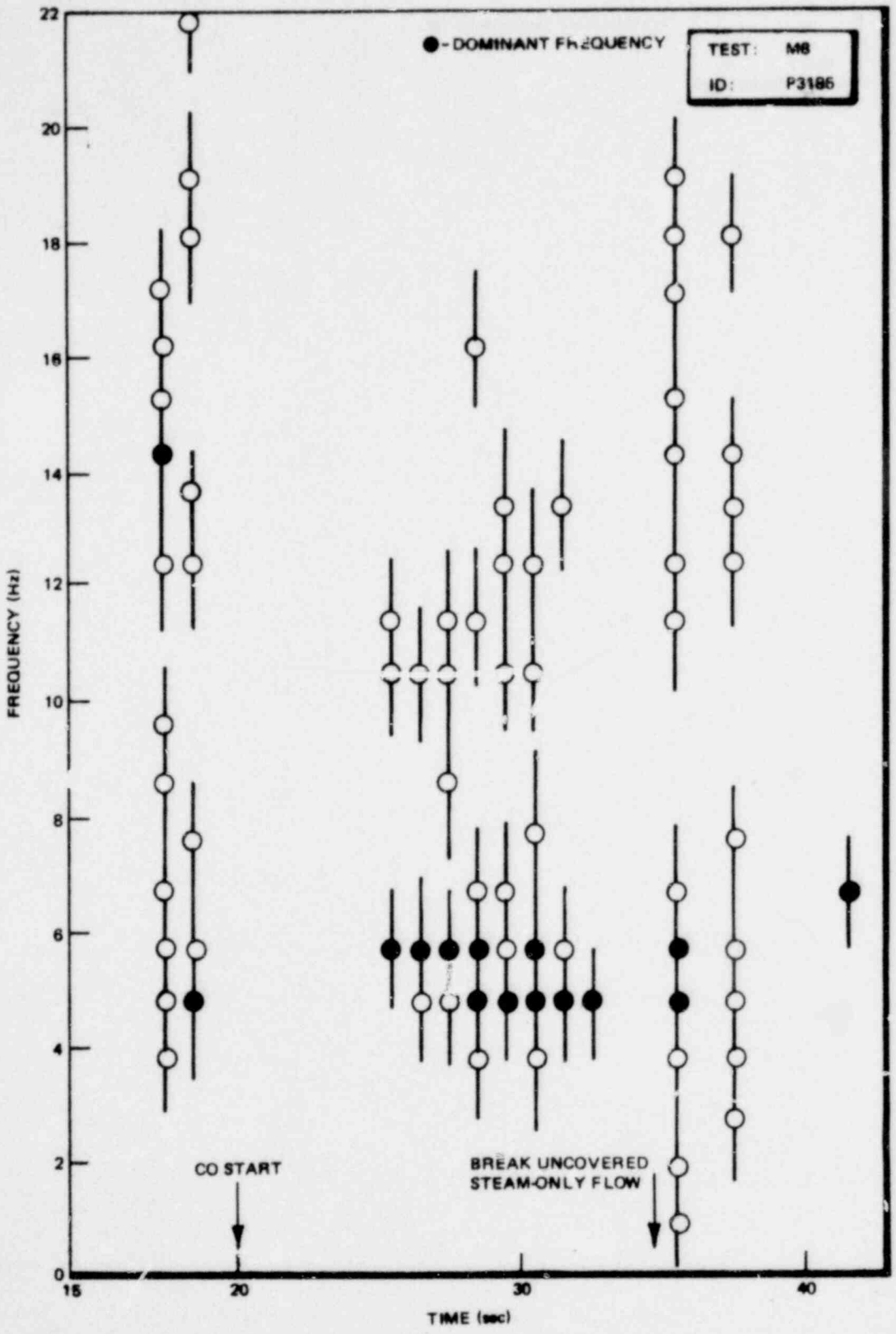

Figure 6.2.2-60. Significant Frequencies in the Wetwell Botton Center Pressure Waveform

1158 036

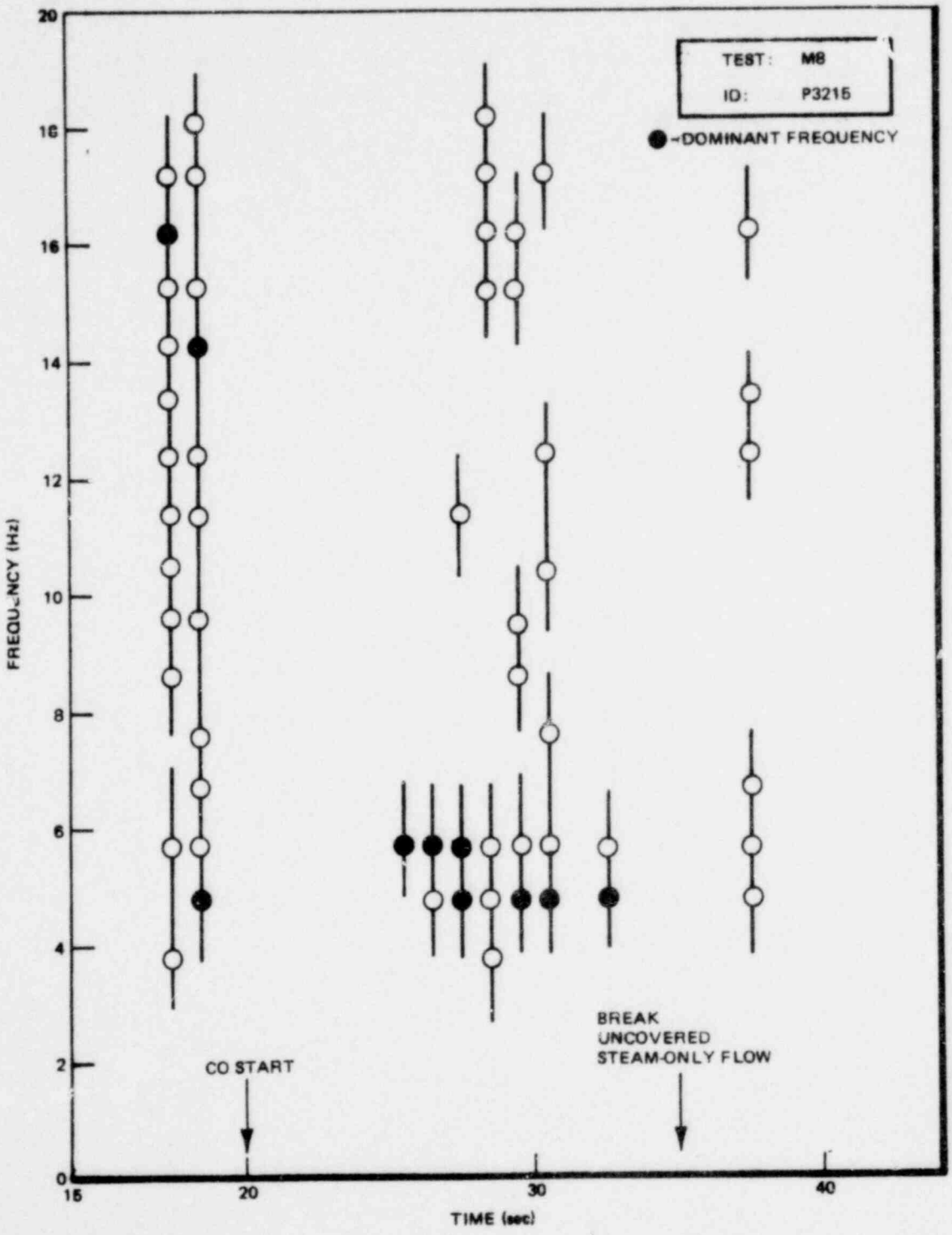

Figure 6.2.2-61. Significant Frequencies of the Pressure Waveform at the Wetwell Centerline and 210° From the Top

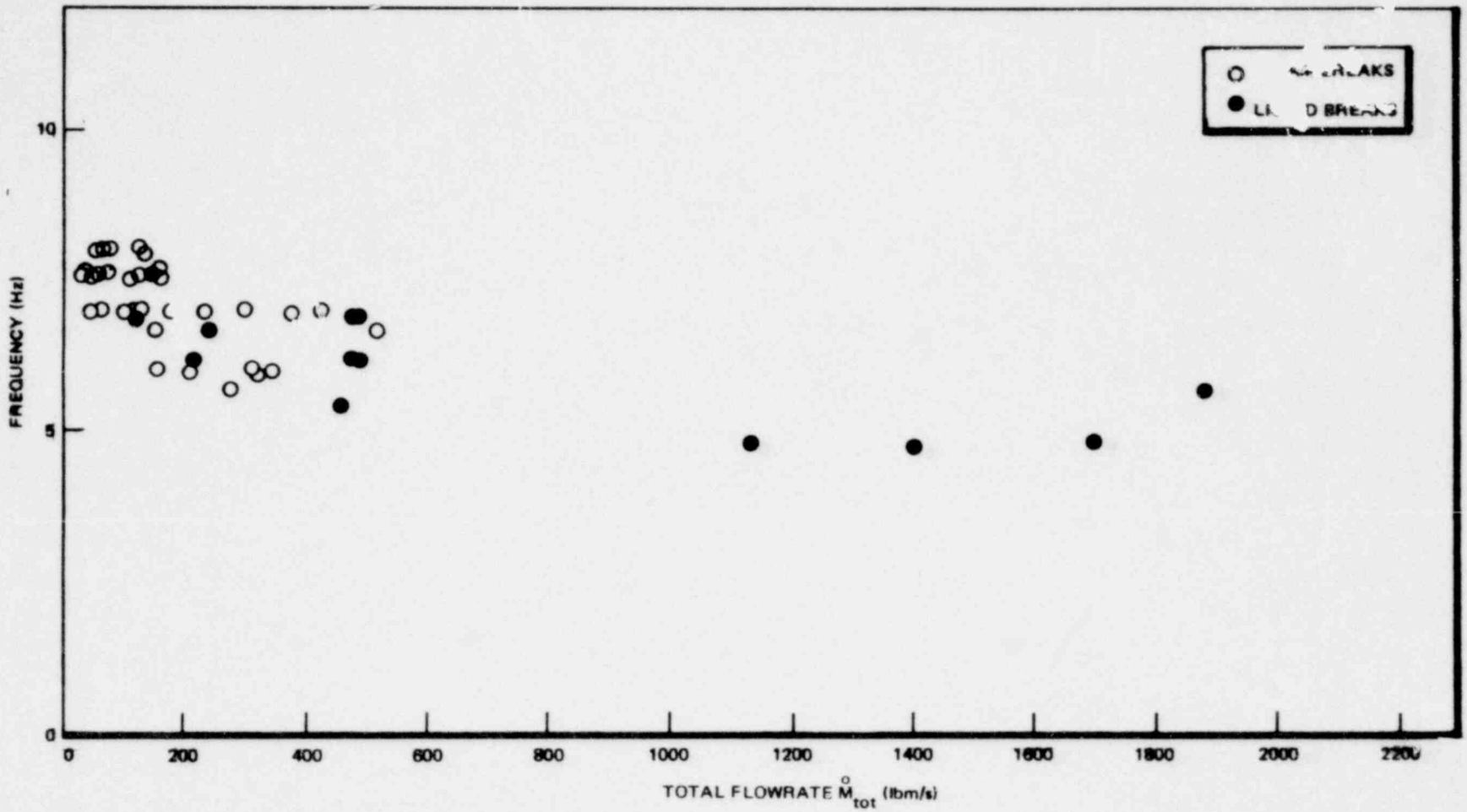

Figure 6.2.2-62. Dominant Condensation Oscillation Frequency vs Total Flowrate

6.3 STRUCTURAL RESPONSE

6.3.1 Dynamic Response During Condensation Oscillation and Chugging

Each of the major structural components of the FSTF wetwell and internal structures - the wetwell shell wetwell support columns, vent header shell and downcomers - were instrumented with numerous strain gauges. Specific information on the location and arrangement of these gauges (e.g., biaxial, rosette, bending strain bridges, etc.) is given in Subsection 3.4.

Maximum values of stress measured during either CO or chugging are presented in Table 6.3.1-J. These values represent total stresses; that is, they result from the combined effects of wetwell pressurization, wetwell heatup and pool pressure fluctuations during CO and chugging. The test and test period (CO or chugging regime) in which maximum stresses were observed are also identified in Table 6.3.1-1.

Table 6.3.1-2 tabulates dynamic stresses during condensation oscillation (CO) and chugging for major structural components. For CO, dynamic stresses were based on the period around 25 seconds of the large liquid break test (M8). Dynamic stresses for chugging were based on periods around either 98 or 2[illegible] seconds of the small steam break test (M1).

In addition to measuring stresses levels, visual inspections of the facility were made after each test to ensure that no structural damage had occurred. No structural damage was identified from these inspections; however, an inspection of the wetwell after the large liquid break test (M8) revealed that one of the pins that secures the clevis of the vent header support column to the collar around the vent header had backed completely out. The column involved was the inside column at the south end of the facility. In the FSTF the pins were simply driven into the clevis with no keeper since there was very little clearance between the vent header collar and the end closure. Since the pins were held only by a frictional, close tolerance fit in the FSTF, it is likely that the vibration experienced by the header support column assembly

during the course of testing caused the pin to progressively back out. Sometime during the large liquid break test (the final test) the pin backed out completely. Examination of the column axial strain data does not clearly indicate precisely when this occurred.

6.3.1.1 Wetwell Shell

With the exception of the shell membrane stress intensity, each of the maximum wetwell shell stress intensities was measured during the CO period of the large liquid break test (M8). Each of the peak stress components observed during the large liquid break test resulted from the combined effects of wetwell pressurization, wetwell heatup and pool pressure fluctuations. In contrast, the peak shell membrane stress intensity occurred at the termination of the small liquid break test (M3). The location at which this peak stress occurred was midbay - 270°.

General transient characteristics of wetwell shell strains, as well as the circumferential distribution of strain about midbay, are illustrated by Figures 6.3.1-1 through 6.3.1-4. These figures present, respectively, shell hoop strain on the outside surface at angular positions of 0°, 90°, 180° and 270° about midbay, for the large liquid break test transient. The hoop strain transients generally reflect the pressurization of the wetwell as can be seen by comparing the hoop strain transients (Figures 6.3.1-1 through 6.3.1-4) with the wetwell freespace pressure transient (refer to Appendix C - Figure C-56).

During condensation oscillation (approximately 20 to 35 seconds), significant strain fluctuations can be observed at each of the circumferential positions shown in Figures 6.3.1-1 through 6.3.1-4. As expected, the circumferential distribution of these strains fluctuations is non-uniform, with the highest strain fluctuations occurring in the lower shell. At 180° the peak to peak range of strain fluctuations is about 160 μ in/in, while at 0° the peak to peak range of strain fluctuations is only 40 μ in/in.

Figure 6.3.1-5 presents the axial strain transient corresponding to the hoop strain transient presented in Figure 6.3.1-4 (outside surface, midbay, at 270°). Comparison of Figures 6.3.1-5 and 6.3.1-4 indicates that the axial strain follows the same general trend as the hoop strain for the first 35 seconds, although the axial strain level is less than the hoop strain level. After this time the axial strain continues to increase, approaching a steady value of about 350 μ in/in at 150 seconds. In contrast, the hoop strain drops slightly and then approaches a steady value of about 200 μ in/in at 150 seconds.

Figures 6.3.1-6 through 6.3.1-9 illustrate the wetwell shell stress state directly beneath downcomer No. 6 during the large liquid break test transient (M8). These transients are for, respectively, the hoop and axial strain on the outside surface and the hoop and axial strain on the inside surface. The highest measured values of shell surface stress intensity and shell membrane bending stress intensity were measured at this location during the M8 CO period.

As Figures 6.3.1-6 and -7 illustrate, the characteristics of the hoop and axial strain on the outside surface, beneath downcomer No. 6, are similar to those of the strain data on the outside surface at midbay (see Figures 6.1.1-1 through -5). However, the hoop and axial strain transients on the inside surface beneath downcomer No. 6 have a markedly different behavior, during the period from about 10 to 35 seconds, than the equivalent strain measurements on the outside surface. On the inside surface both the hoop and axial strain decrease abruptly beginning at about 10 seconds. Hoop strain then begins to increase again, tracking the pressurization of the wetwell. Meanwhile, the axial strain continues to decrease, goes into compression, and then remains at nearly the same mean level until the end of CO (∿35 seconds). After this time the axial strain on the inside surface goes from compression into tension. Similar behavior is also observed at the bottom of midbay, though none of the strain measurements ever indicates that the inside surface goes into compression.

Apparently, the behavior just described is induced by thermal stresses related to through-wall temperature gradients. Examination of pool thermocouple measurements indicates that in the large liquid break the water deep in the pool, close to the wetwell shell, is heated early in the transient (the pool temperature jumps abruptly, by about 30°F, at 10 seconds). During CO the pool temperatures near the shell continue to increase with the highest temperature seen deep in the pool.

After cessation of CO the pool temperature levels stabilize and come to thermal equilibrium at about 60 seconds. Also by this time the stress state in the lower shell becomes uniform as the temperature gradient through the wall diminishes. This last point is apparent from comparisons of inside and outside hoop strains (Figures 6.3.1-6 and -8) and inside and outside axial strains (Figures 6.3.1-7 and -9) for the period at or after 60 seconds.

The highest wetwell shell bending stresses were measured during the period of the large liquid break test just discussed. Further, the shell location at which the membrane stresses were maximum was directly beneath downcomer No. 6. Referring to Table 6.3.1-1, it can be seen that the maximum shell bending stress was only 6,400 psi.

Figures 6.3.1-10 and -11 illustrate the maximum strain fluctuations observed during CO at the wetwell/ring girder intersection. Both of these strain transients are for the large liquid break test (condensation oscillation period: ∿20 to 35 seconds). The gauge presented in Figure 6.3.1-10 is located at 180° (wetwell bottom) while the gauge presented in Figure 6.3.1-11 is located at 270° (near the attachment of the wetwell support columns). Both gauges are the 45° elements of three element rectangular rosettes located on the inside surface of the wetwell shell. The strain fluctuations observed on the bottom inside surface of the shell/ring girder intersection, 750 μ in/in peak to peak (see Figure 6.3.1-10), are the highest measured on the wetwell. Correspondingly, the highest surface stress intensity measured on the wetwell, occurred at this location (refer to Table 6.3.1-1). Comparison of Figures 6.3.1-10 and -11 indicates that dynamic strain levels at the shell/ring

girder intersection are much lower at the support column/shell attachment than at the wetwell bottom (less by a factor of approximately ten).

The strain transients presented in Figures 6.3.1-12 through -15 illustrate the state of strain of the wetwell shell during the small steam break test (M1). All gauges are located beneath downcomer No. 6 and represent, respectively, outside surface - hoop strain, outside surface-axial strain, inside surface - hoop strain and inside surface-axial strain. Dynamic strain fluctuations in the wetwell shell during chugging (beginning at about 40 seconds) are very low, being no more than about 110 μ in/in peak to peak. During chugging, there are several periods in which the response of the shell strains suggests that effects due to through-wall temperature gradients are present (similar to the effects observed during the large liquid break test). The notable instance in which this effect is seen is at about 80 seconds. At this time the strain gauges on the outside surface show a sharp increase in tensile stress with the gauges on the inside surface indicating a sharp drop in tensile stress (with the axial gauge going in compression briefly).

Similar behavior is observed at midbay at 180° and 210°. Thermocouple measurements suggest thermal stress effects similar to those discussed regarding the large liquid break test. Just before the time at which marked changes in the shell stresses are observed (at about 70 seconds), the deep pool temperatures, near the shell, increase abruptly (by about 35°F). The nature of the change in strains (tensile strain increases on the outside surface and decreases on the inside surface) combined with the sudden change in deep pool temperatures suggest that the strain changes are caused by a through-wall temperature gradient.

Dynamic strain fluctuations at the wetwell shell/ring girder intersection, during chugging, are illustrated in Figure 6.3.1-16. This figure presents the axial strain transient on the outside bottom surface of the shell/ring girder intersection for the small steam break. The largest dynamic peak to peak strain fluctuation is only 160 μ in/in.*

*The strain levels on the inside surface would be expected to be greater, however, such data is not available for the small steam break test.

6.3.1.2 Wetwell Support Columns

Stresses in the wetwell columns result from the combined effects of thermal expansion of the wetwell shell and dynamic loads imposed on the shell during CO and chugging; water mass addition also results in a static axial load. Column bending stresses in both radial and longitudinal directions (relative to the torus center) primarily resulted as a consequence of the thermal expansion of the wetwell. Referring to Table 6.3.1-1, it can be seen that the maximum radial bending stresses in the inside and outside columns were measured at the end of test M6. Initial conditions for this test (hot pool (120°F) and low submergence) were the most severe from the standpoint of shell heatup. The maximum column radial bending stress was 10,800 psi in the outside columns. Maximum bending stresses in the longitudinal direction for the inside columns and outside columns were measured during the CO phases of the medium steam break test and the large steam break test, respectively. The maximum column longitudinal bending stress was less than 1,000 psi. The largest column axial (or tension/compression) stresses were measured during the CO phase of the large liquid break test. The maximum compressive stress was 2000 psi, while the maximum column tensile stress was 1,600 psi. It should be noted, and this will be discussed later, that these maximum column axial stresses do not result solely from pressure fluctuations during condensation oscillation; rather, a significant part of the maximum stresses measured results from the effect of the thermal growth of the wetwell.

Inside and outside column radial and longitudinal bending strain transients for the large liquid break test (M8) are presented in Figures 6.3.1-17 through -20. Similar plots for column axial strain are presented in Figures 6.3.1-21 and -22. Wetwell column bending and axial strain fluctuations resulting from condensation oscillation can be observed in Figures 6.3.1-17 through -22 over the period from about 20 to 35 seconds. The maximum peak to peak amplitudes observed in the column strain data during this period are about 100, 30 and 110 μ in/in for, respectively, the radial bending, longitudinal bending and axial strains. Comparisons of column axial strains for all four columns indicate that condensation oscillation loads are uniformly distributed among the four columns.

Due to the thermal expansion of the wetwell, bending strains in both inside and outside columns increase with time (see Figures 6.3.1-17 through -20). In the radial direction the wetwell grows outward (away from the torus center). The radial bending strain is about three times greater in the outside columns than in the inside columns. Thermal expansion of the wetwell in the longitudinal direction is also outward (wetwell ends move away from each other). However, the longitudinal bending strains are nearly the same in both the inside and outside columns. Longitudinal bending strains are considerably lower than radial bending strains. The ratio of the longitudinal to radial bending strain for the inside column is about one-third while this ratio for the outside columns is about one-tenth.

Ring girder displacement data indicate that column radial bending strains result from both "rigid body" displacement and ring girder deformation associated with wetwell expansion. This can be seen in Figure 6.3.1-23 which presents the radial displacements of the south ring girder at 0°, 90°, 180° and 270° at the end of the large liquid break test. It is particularly notable that the ring girder was moved radially outward by about 0.4 in. on the outside but only by 0.2 in. on the inside. This behavior is consistent with the column radial bending strain data. As was discussed above, the bending strains are in radially outward direction for both columns with greater bending strains in the outside columns than in the inside columns.

The ring girder displacement data indicate that outside columns would be in tension and the inside columns would be in compression. This result is consistent with column axial strain data. In Figure 6.3.1-21 it can be observed that the axial strain in the inside column shows a general trend of an increase in compressive strain with time. This trend parallels the general trend of the column radial bending strain for the inside column (Figure 6.3.1-17). A similar observation may be made regarding the axial strain in the outside column, although in this case, the general trend is an increase in tensile strain with time (see Figure 6.3.1-22).

As a further check of data consistency, the net vertical force on the wetwell, at test termination, was calculated by summing the vertical forces acting on

the four columns (force was calculated based on column stress and column load area). Calculations were performed for two tests - the large liquid break (M8) and small steam break (M1) tests. In both cases agreement within ten percent was obtained between the increase in compressive load measurement by the column axial strain bridges and the corresponding mass of water added over the test transient.

Dynamic fluctuations in wetwell column radial bending, longitudinal bending and axial strains during chugging are typified by Figures 6.3.1-24, -25, and -26, respectively. Each of the strain transients presented in Figures 6.3.1-24 through -26 is for the small steam break test (M1). In all cases peak to peak strain fluctuations during chugging (beginning at about 40 seconds) are very low. Peak to peak strains are less than 20 μ in/in for radial and longitudinal bending strains and less than 35 μ in/in for axial strains.

6.3.1.3 Vent Header Shell and Downcomers

Stresses in the downcomer/vent header attachment region of the vent header shell and the downcomers were measured. More specifically, the downcomer/vent header region at downcomers No. 6 and No. 8 were instrumented with uniaxial strain gauges arranged radially about the downcomers (every 45°), and both downcomers were instrumented with strain gauge bridges to measure bending strain in the radial (perpendicular to the vent header axis) and longitudinal (parallel to the vent header axis) directions. The measurement of downcomer bending strains provides the data base for defining downcomer lateral loads.

Figure 6.3.1-27 shows the uniaxial strain at the top dead center (TDC) or 0° location at downcomer No. 8 for the large liquid break test transient. Prototypical tie-straps were installed between downcomers No. 8 and No. 7. The largest dynamic strains are observed in the TDC location during the CO period of the test (∿ 20 to 35 seconds).

Uniaxial strains in the radial and longitudinal planes at the downcomer/vent header attachment region of downcomer No. 8 are illustrated by Figures 6.3.1-28 and -29, respectively. The peak surface stress measured in the downcomer/vent header attachment region was 14,000 psi. This stress was measured at both the TDC (0°) and BDC (180°) locations. At these locations most vent shell stress cycles ranged over 12,000 psi peak to peak (tension/compression) during CO.

Stress levels in the downc r/vent header attachment region at downcomer No. 6 were considerably higher than at downcomer No. 8. Downcomers No. 5 and No. 6 were not interconnected with tie-straps or bracing (tension-compression bars). Figures 6.3.1-30 and -31 illustrate strains observed in the downcomer/vent header attachment region at downcomer No. 6 during the CO period of the large liquid break test. During this period, the peak surface stress measured in the downcomer/vent header attachment region of downcomer No. 6 was 46,000 psi. This stress was measured at the TDC location (Figure 6.3.1-30). At this location most stress cycles ranged over 50,000 psi peak to peak (tension/compression) during CO.

The small steam break test with low submergence (1 ft 6 in.) and heated pool (120°F) - matrix test No. 6 - was the most severe test from the standpoint of the duration of cyclic stresses in the downcomer/vent header attachment region of the vent header shell. During the CO period of this test, from about 20 seconds to test termination (∿ 300 sec.), most stress cycles in the TDC location at downcomer No. 6 (no tie-straps or bracing) ranged over 40,000 psi peak to peak (tension/compression). The CO related stress cycles were much lower for downcomer No. 8, which was connected to downcomer No. 7 by tie-straps. At the TDC location of downcomer No. 8, the stress cycles ranged just over 10,000 psi peak to peak during CO.

Figures 6.3.1-32 and -33 present, respectively, the radial and longitudinal bending strains measured at downcomer No. 8 during the CO period of the large liquid break test (M8). The same measurements for downcomer No. 6 are presented in Figures 6.3.1-34 and 6.3.1-35.

Dynamic strain levels in the downcomer/vent header attachment region of the vent shell during chugging are illustrated by Figure 6.3.1-36. In this figure the vent shell strain measured at the TDC location at downcomer No. 6 is shown for the small steam break test (M1) transient. It should be noted that all downcomers were free for this test (i.e., downcomer pairs were not intra-connected with tie-straps or bracing). The peak surface stresses occurred at approximately 80 seconds. The peak tensile stress was about 23,000 psi while the peak compressive stress was about 25,000 psi. Uniaxial strains in the radial and longitudinal planes are shown in Figures 6.3.1-37 and -38, respectively, for a period from 75 to 85 seconds. Stresses resulting from a number of chugs can be observed during this period. Figures 6.3.1-39 and -40 present, respectively, the downcomer bending strains in the radial and longitudinal directions for the same period.

Uniaxial strains in the radial and longitudinal planes at the downcomer/vent header attachment region of downcomer No. 8 are illustrated by Figures 6.3.1-28 and -29, respectively. The peak surface stress measured in the downcomer/vent header attachment region was 14,000 psi. This stress was measured at both the TDC (0°) and BDC (180°) locations. At these locations most vent shell stress cycles ranged over 12,000 psi peak to peak (tension/compression) during CO.

Stress levels in the downcomer/vent header attachment region at downcomer No. 6 were considerably higher than at downcomer No. 8. Downcomers No. 5 and No. 6 were not interconnected with tie-straps or bracing (tension-compression bars). Figures 6.3.1-30 and -31 illustrate strains observed in the downcomer/vent header attachment region at downcomer No. 6 during the CO period of the large liquid break test. During this period, the peak surface stress measured in the downcomer/vent header attachment region of downcomer No. 6 was 46,000 psi. This stress was measured at the TDC location (Figure 6.3.1-30). At this location most stress cycles ranged over 50,000 psi peak to peak (tension/compression) during CO.

The small steam break test with low submergence (1 ft 6 in.) and heated pool (120°F) - matrix test No. 6 - was the most severe test from the standpoint of the duration of cyclic stresses in the downcomer/vent header attachment region of the vent header shell. During the CO period of this test, from about 20 seconds to test termination ($\sim$ 300 sec.), most stress cycles in the TDC location at downcomer No. 6 (no tie-straps or bracing) ranged over 40,000 psi peak to peak (tension/compression). The CO related stress cycles were much lower for downcomer No. 8, which was connected to downcomer No. 7 by tie-straps. At the TDC location of downcomer No. 8, the stress cycles ranged just over 10,000 psi peak to peak during CO.

Figures 6.3.1-32 and -33 present, respectively, the radial and longitudinal bending strains measured at downcomer No. 8 during the CO period of the large liquid break test (M8). The same measurements for downcomer No. 6 are presented in Figures 6.3.1-34 and 6.3.1-35.

Dynamic strain levels in the downcomer/vent header attachment region of the vent shell during chugging are illustrated by Figure 6.3.1-36. In this figure the vent shell strain measured at the TDC location at downcomer No. 6 is shown for the small steam break test (M1) transient. It should be noted that all downcomers were free for this test (i.e., downcomer pairs were not intra-connected with tie-straps or bracing). The peak surface stresses occurred at approximately 80 seconds. The peak tensile stress was about 23,000 psi while the peak compressive stress was about 25,000 psi. Uniaxial strains in the radial and longitudinal planes are shown in Figures 6.3.1-37 and -38, respectively, for a period from 75 to 85 seconds. Stresses resulting from a number of chugs can be observed during this period. Figures 6.3.1-39 and -40 present, respectively, the downcomer bending strains in the radial and longitudinal directions for the same period.

Table 6.3.1-1

MAXIMUM MEASURED STRESSES DURING
CONDENSATION OSCILLATION AND CHUGGING

Measurement Location	Test	Test Period	Measured Valve (psi)
Wetwell Shell - General*			
a. Membrane Stress Intensity	M3	CO (Test End)	11,500
b. Bending Stress Intensity	M8	CO	6,400
c. Surface Stress Intensity	M8	CO	13,900
Wetwell Shell/Ring Girder Intersection - Local Stress	M8	CO	17,000
Wetwell Column Bending Stress			
a. Longitudinal			
1. Inside Column	M3	CO	920
2. Outside Column	M7	CO	750
b. Radial			
1. Inside Column	M6	CO (Test End)	2,800
2. Outside Column	M6	CO (Test End)	10,800
Wetwell Column Axial Stress			
a. Inside Column			
1. Compression	M8	CO	3,000
2. Tension	M8	CO	700
b. Outside Column			
1. Compression	M8	CO	4,700
2. Tension	M8	CO	1,600
Downcomer/Vent Header Attachment - Local Stress			
a. "Tied" Downcomers**	M8	CO	14,000
b. "Free" Downcomers	M8	CO	46,000

* Refers to regions away from discontinuties
** Prototypical tie-straps

1158 051

Table 6.3.1-2

DYNAMIC STRESSES DURING CONDENSATION OSCILLATION AND CHUGGING

	Condensation Oscillation (M8) (psi)	Chugging (M1) (psi)
Wetwell Shell*		
Wetwell Shell	3,800	2,500
Wetwell Shell/Ring Girder Intersection	14,800	2,900
Wetwell Support Columns		
Radial Bending	1,500	300
Longitudinal Bending	500	300
Tensile/Compressive	1,600	500
Vent Header Shell		
Downcomer/Vent Header Intersection		
• "Tied" Downcomers**	14,000	-
• "Free" Downcomers	46,000	25,000

* Maximum surface stress intensity.
** Monticello prototypical tie-straps.

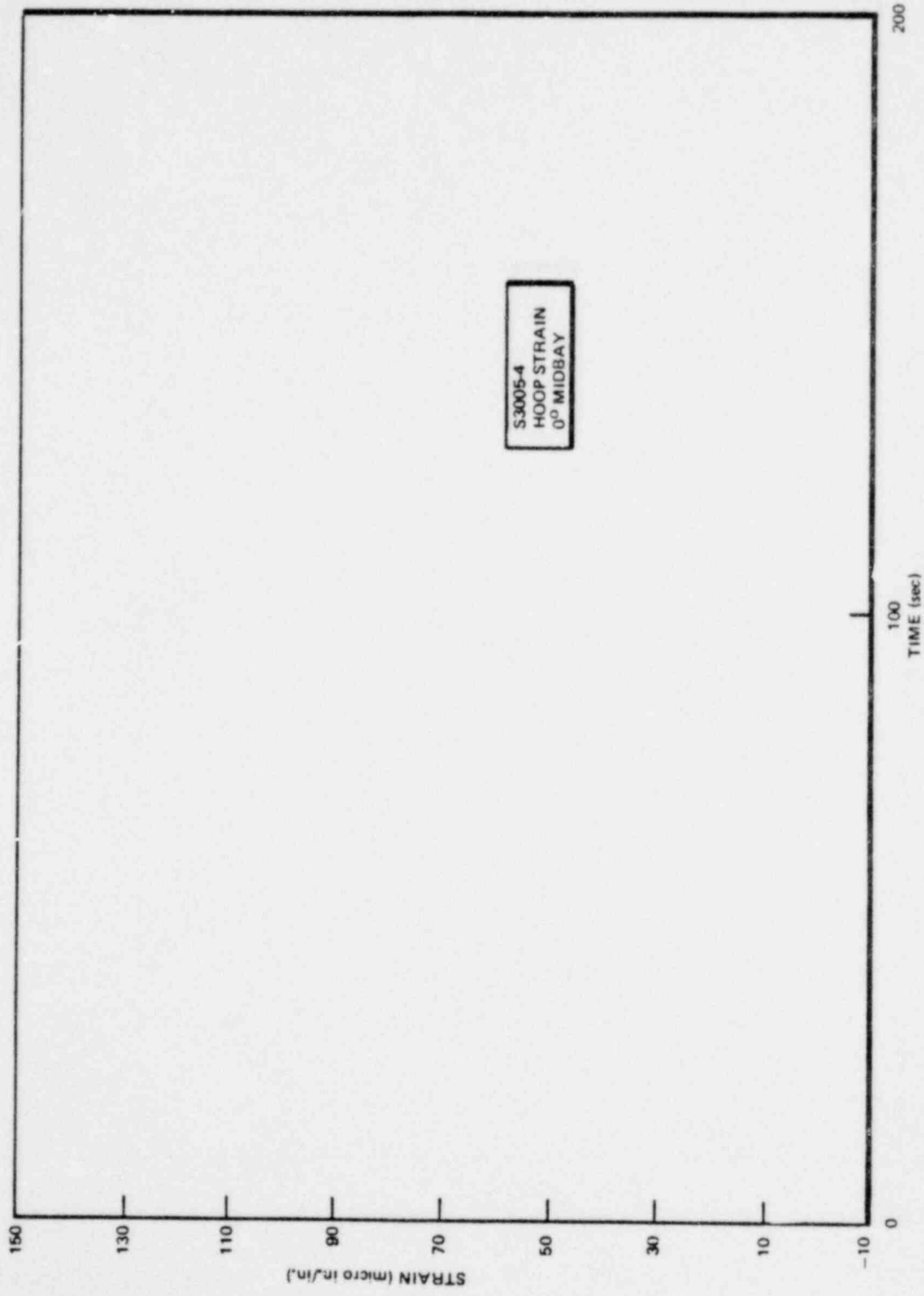

Figure 6.3.1-1. Wetwell Shell Hoop Strain at 0° Midbay (Large Liquid Break Test - M8)

*Proprietary information deleted

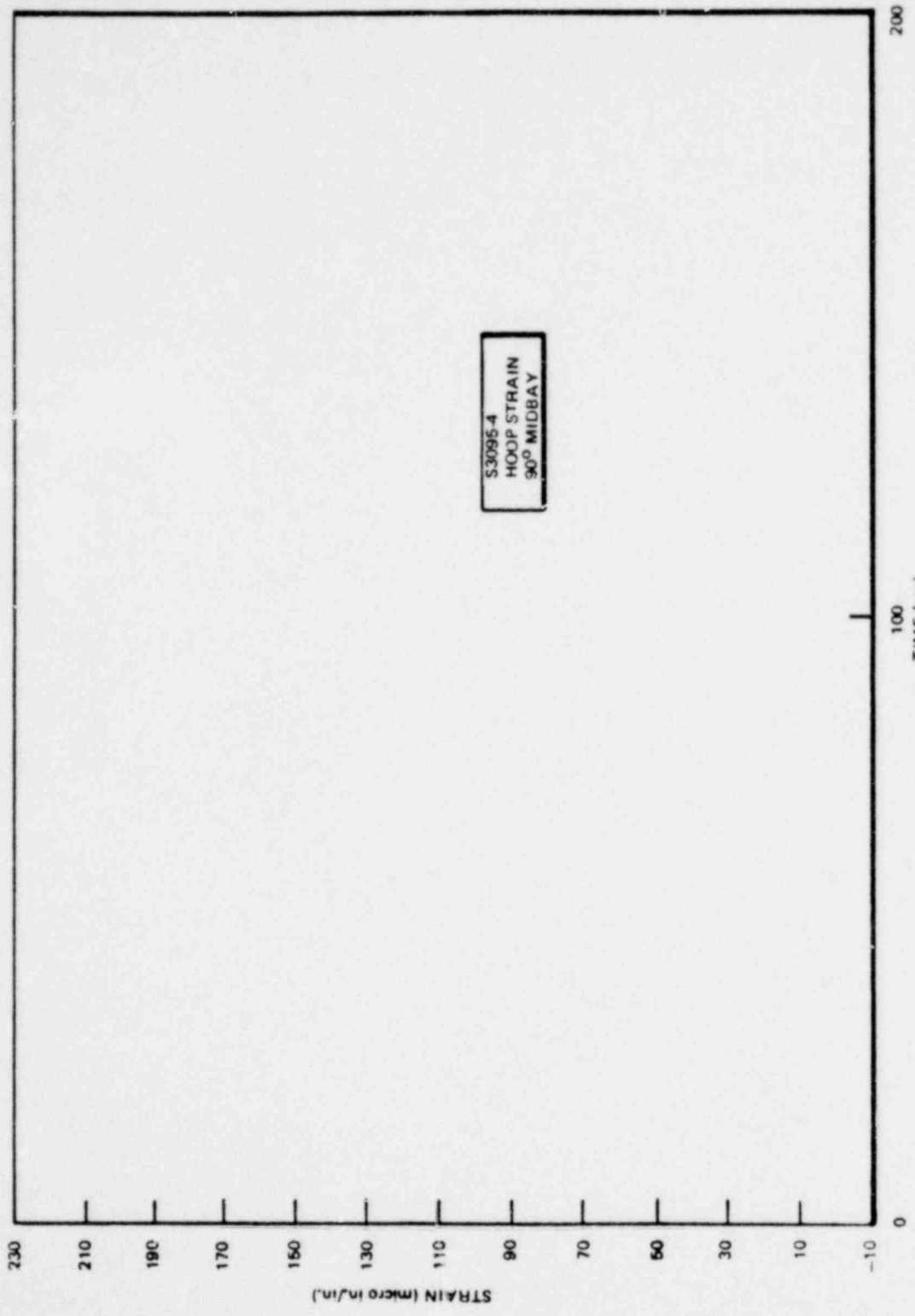

Figure 6.3.1-2. Wetwell Shell Hoop Strain at 90° Midbay (Large Liquid Break Test - M8)

*Proprietary information deleted

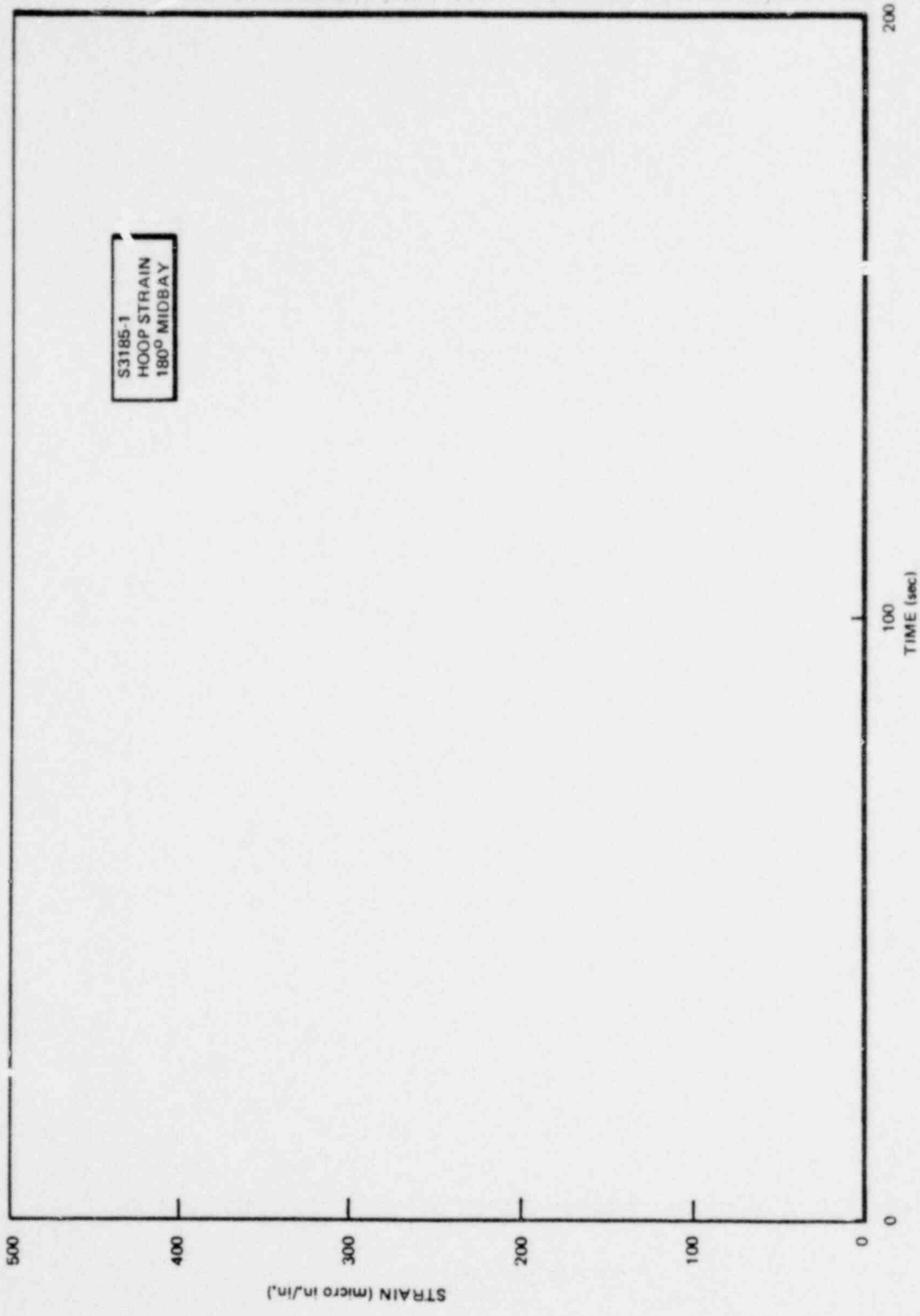

Figure 6.3.1-3. Wetwell Shell Hoop Strain at 180° Midbay (Large Liquid Break Test - M8)

*Proprietary information deleted

1158 055

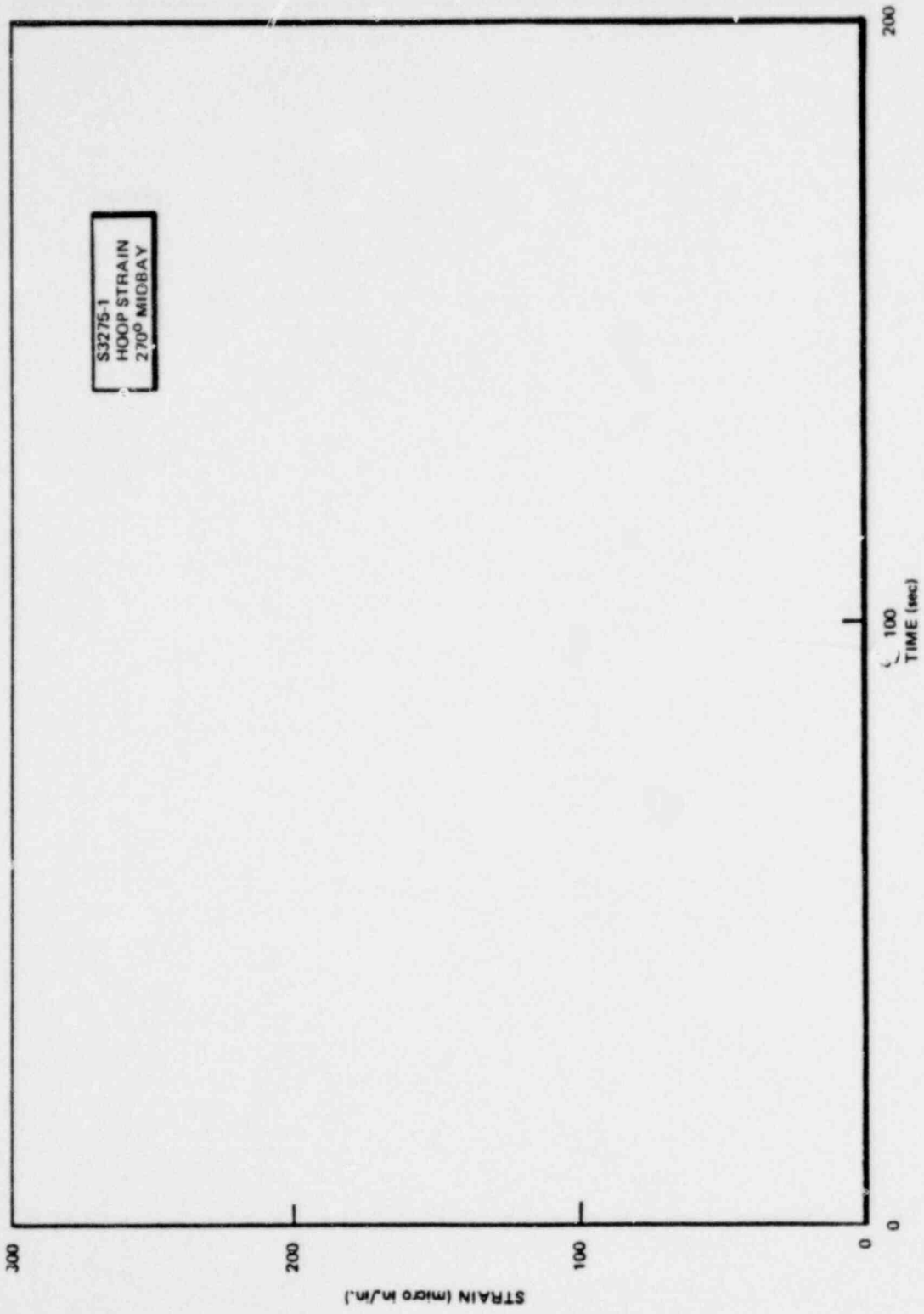

Figure 6.3.1-4. Wetwell Shell Hoop Strain at 270° Midbay (Large Liquid Break Test - M8)

*Proprietary information deleted

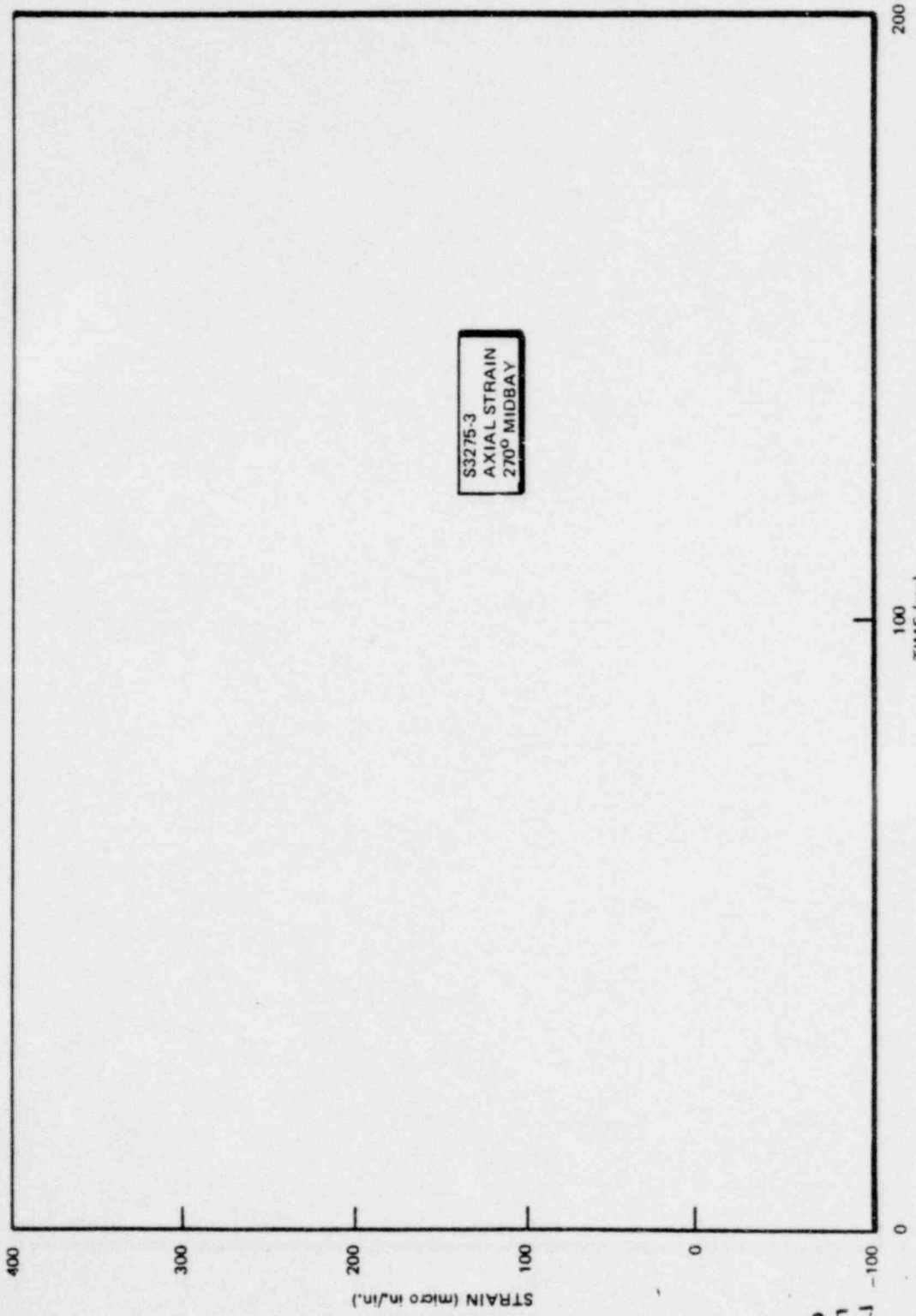

Figure 6.3.1-5. Wetwell Shell Axial Strain at 270° Midbay (Large Liquid Break Test - M8)

*

1 53 057

*Proprietary information deleted

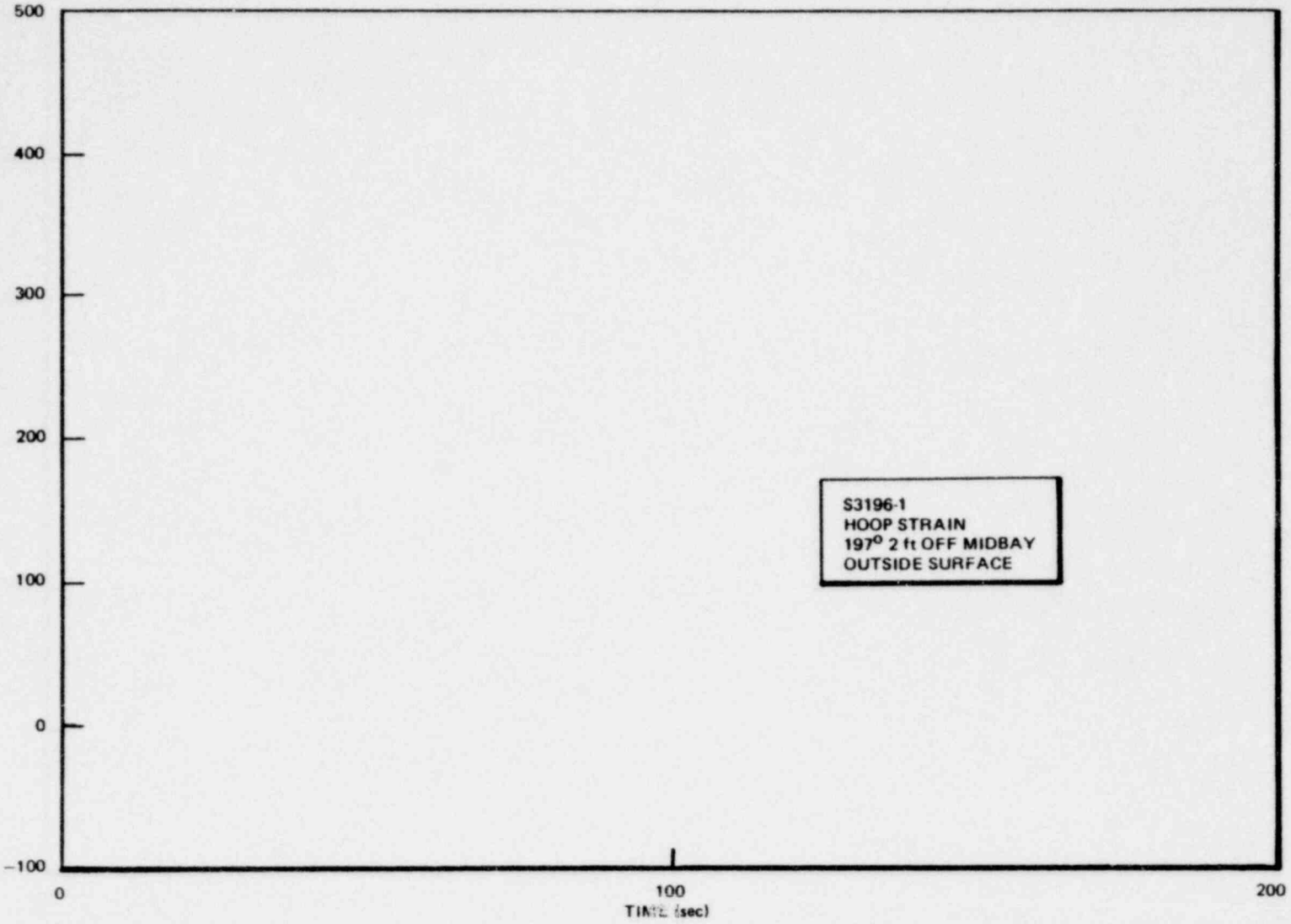

Figure 6.3.1-6. Wetwell Shell Hoop Strain Beneath Downcomer No. 6 - Outside Surface (Large Liquid Break Test - M8)

*Proprietary information deleted

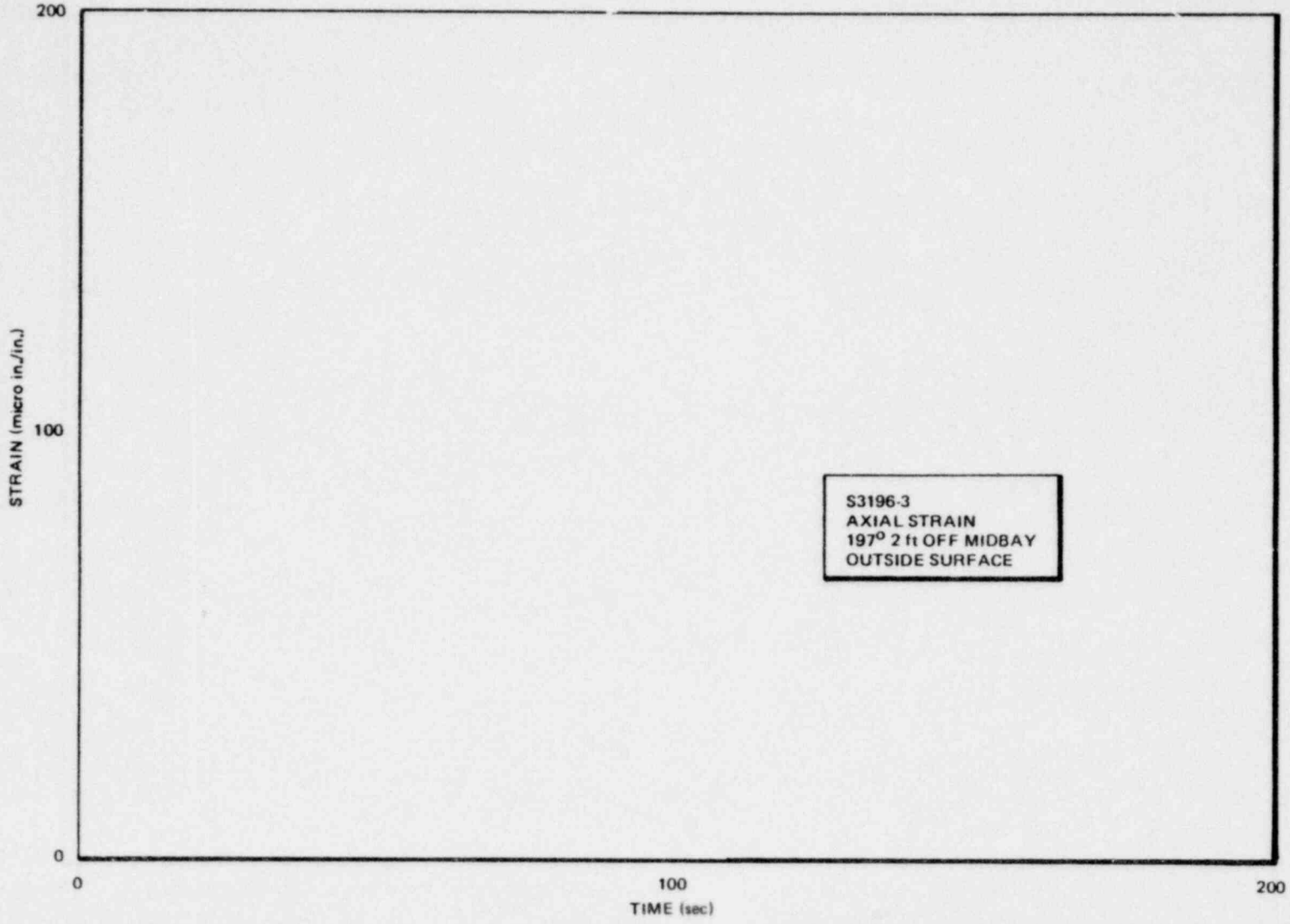

Figure 6.3.1-7. Wetwell Shell Axial Strain Beneath Downcomer No. 6 - Outside Surface (Large Liquid Break Test - M8)

*Proprietary information deleted

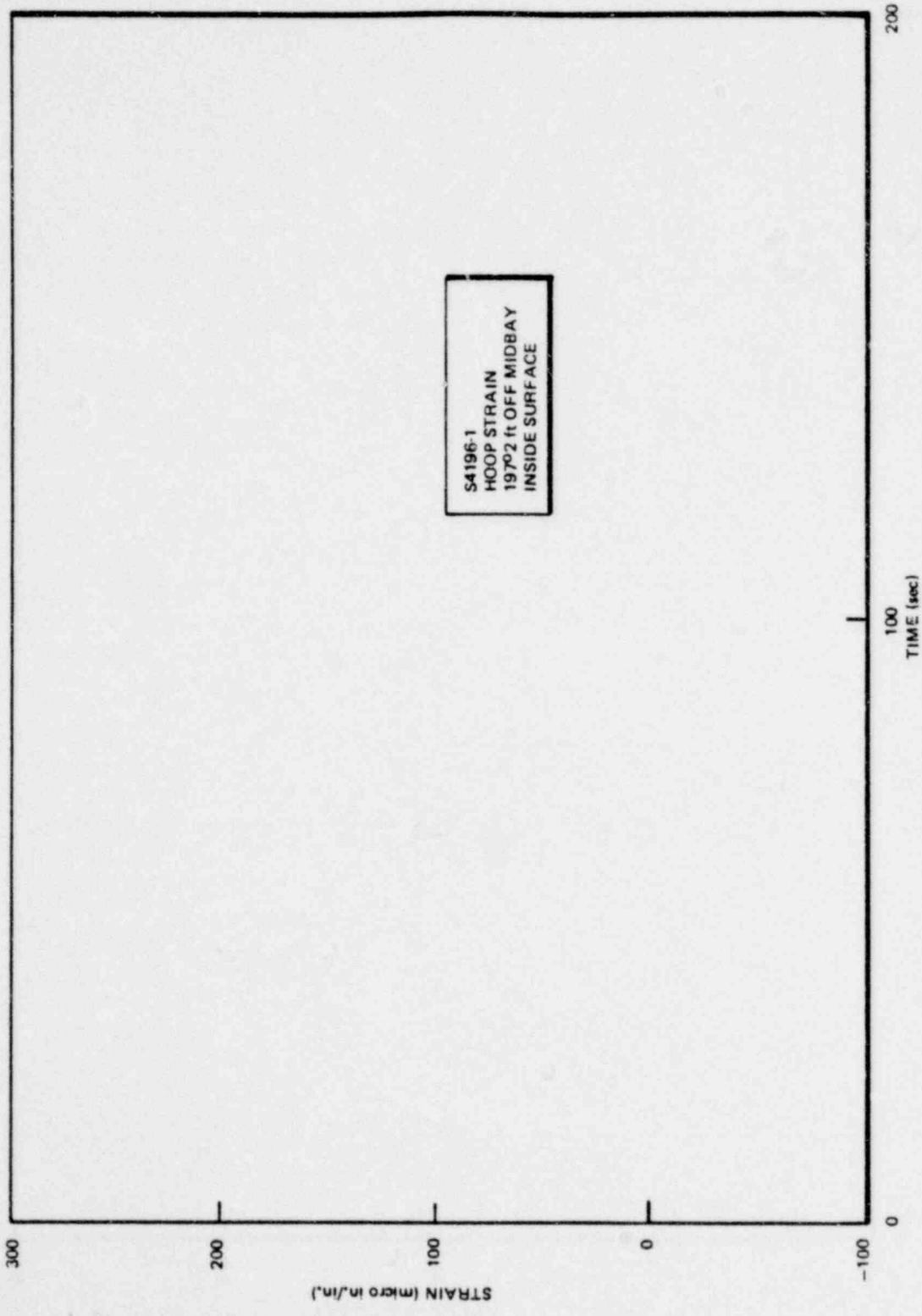

Figure 6.3.1-8. Wetwell Shell Hoop Strain Beneath Downcomer No. 6 - Inside Surface (Large Liquid Break Test - M8)

*Proprietary information deleted

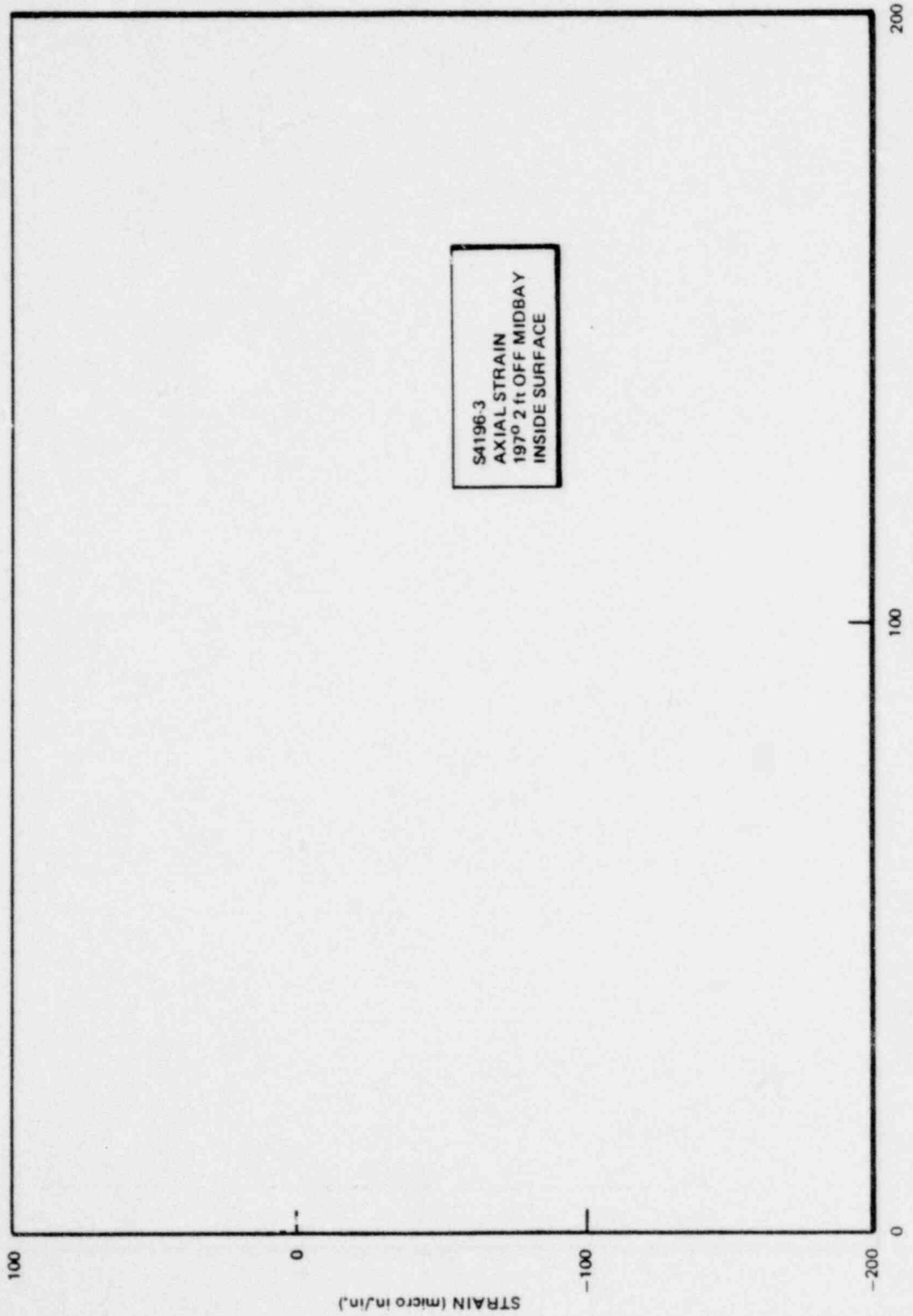

Figure 6.3.1-9. Wetwell Shell Axial Strain Beneath Downcomer No. 6 - Inside Surface (Large Liquid Break Test - M8)

*Proprietary information deleted

1158 061

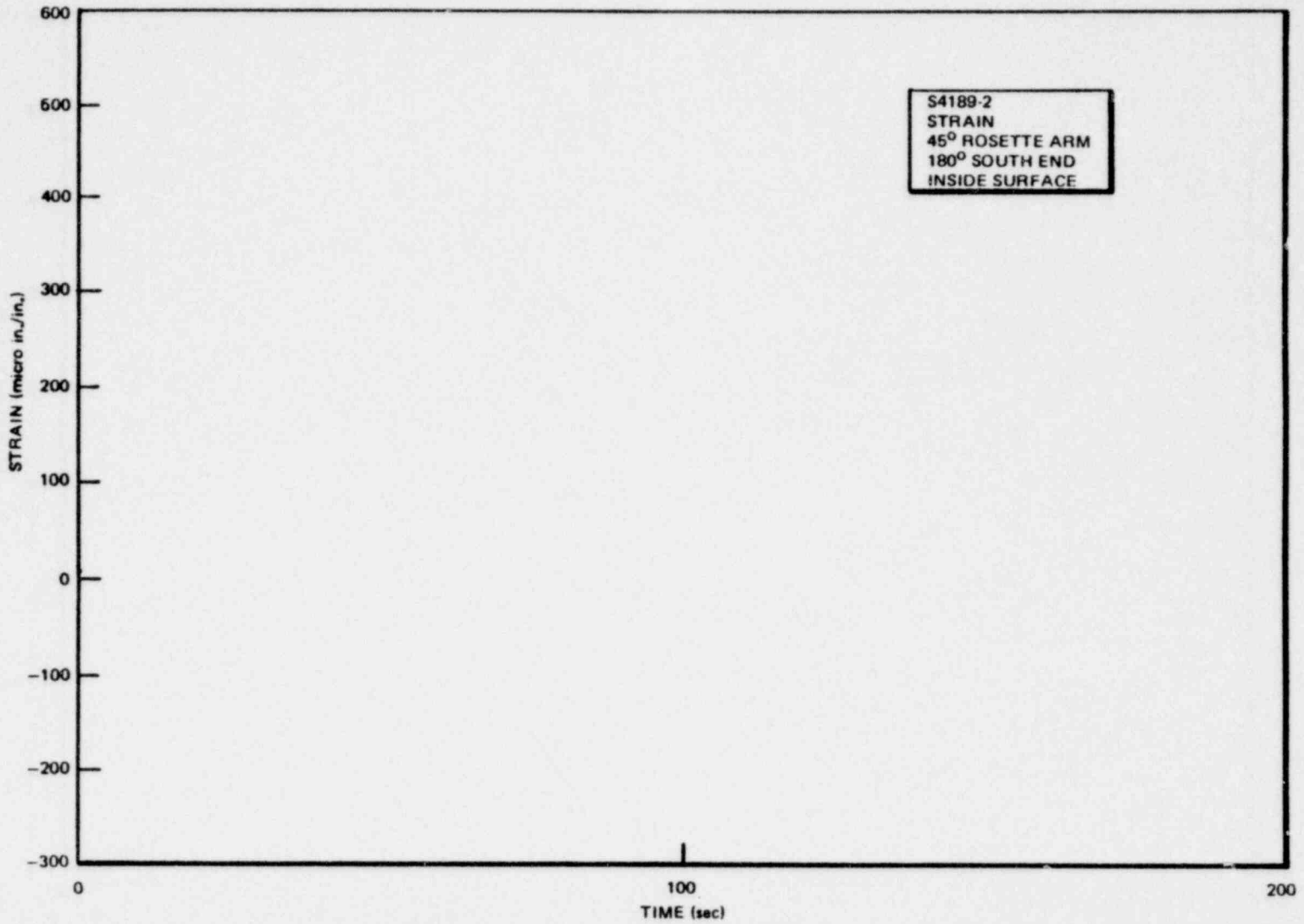

Figure 6.3.1-10. Wetwell Shell/Ring Girder Attachment Strain 180° South End (Large Liquid Break Test - M8)

*Proprietary information deleted

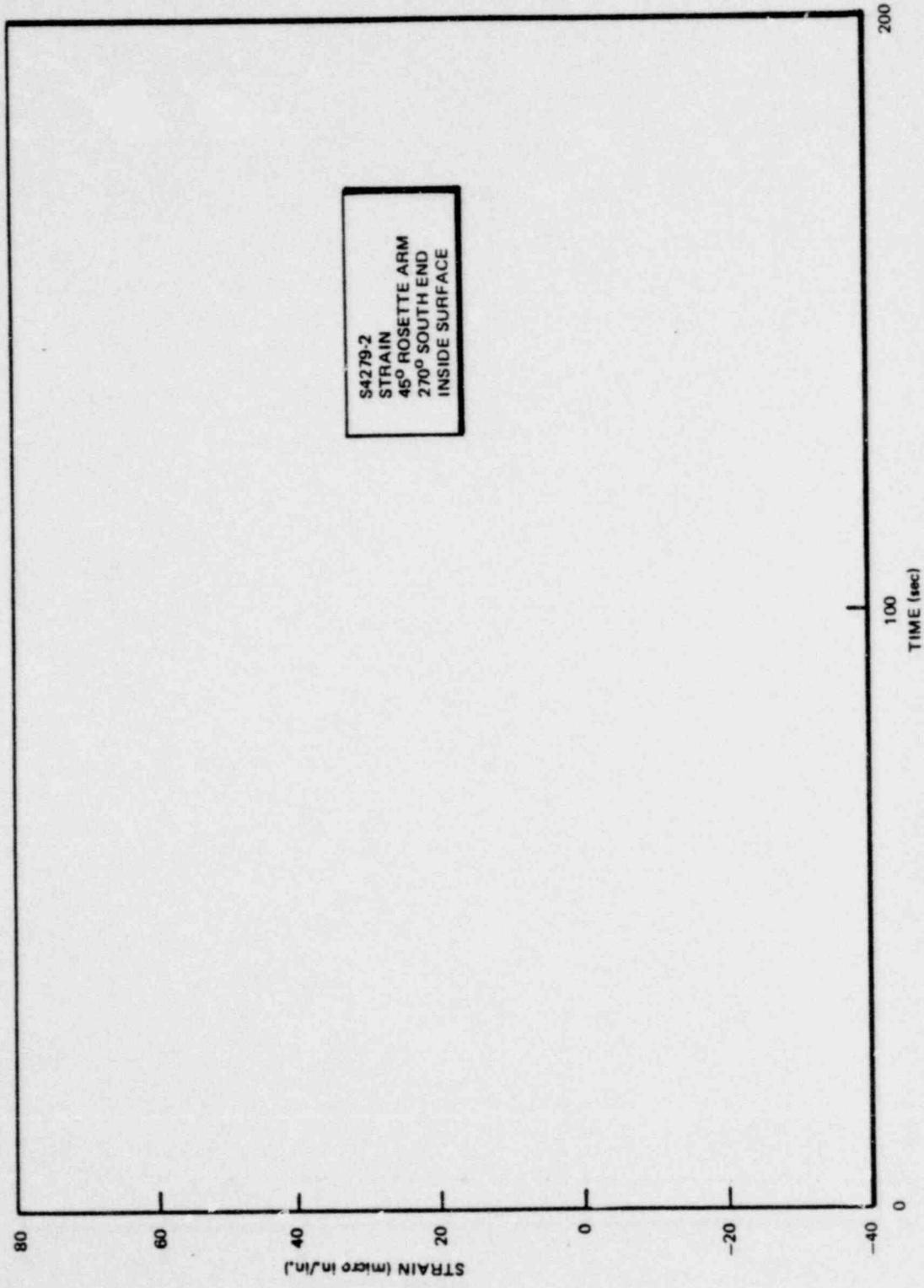

Figure 6.3.1-11. Wetwell Shell/Ring Girder Attachment Strain 270° South End (Large Liquid Break Test - M8)

*Proprietary information deleted

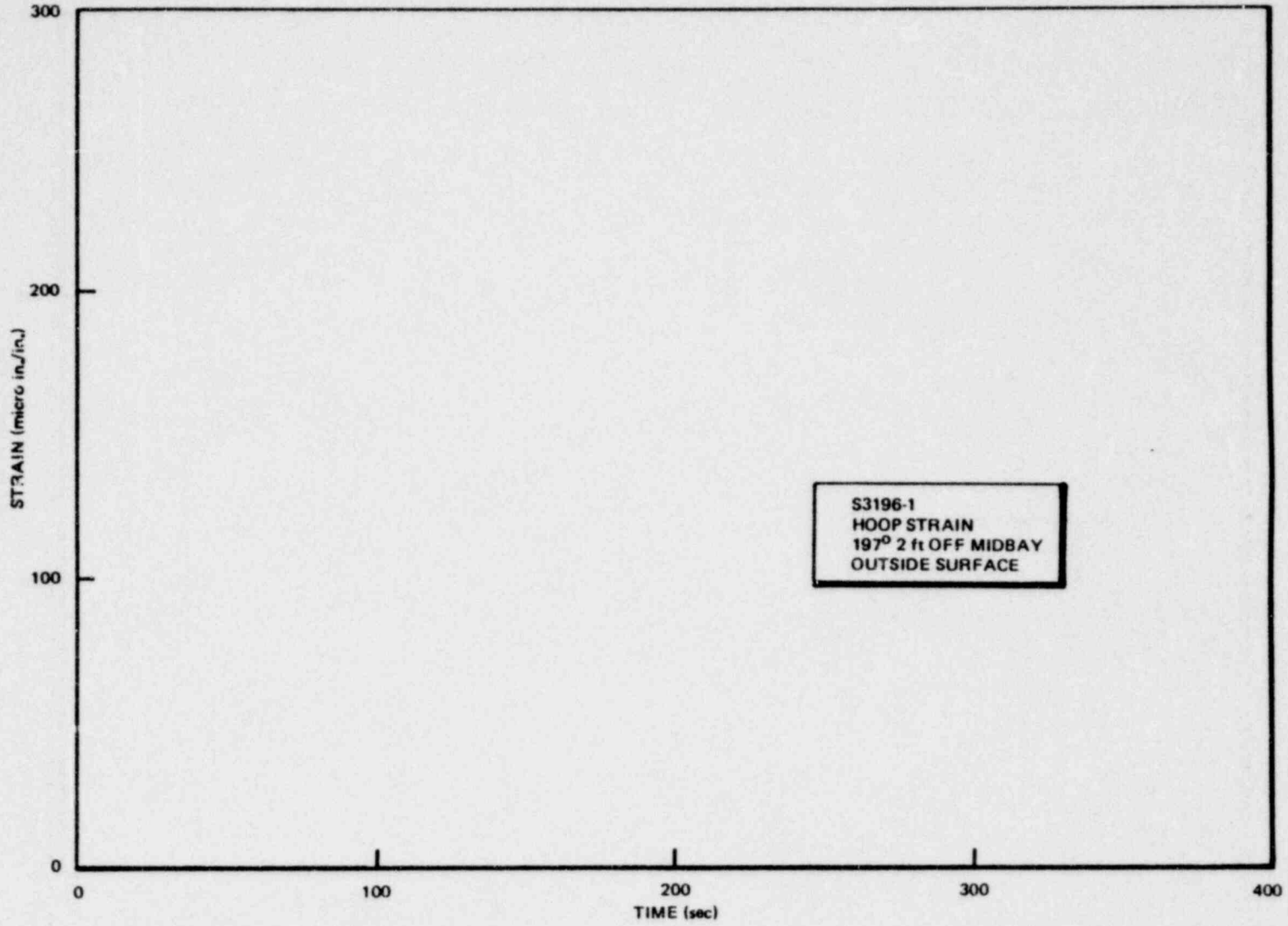

Figure 6.3.1-12. Wetwell Shell Hoop Strain Beneath Downcomer No. 6 - Outside Surface (Small Steam Break Test - M1)

*Proprietary information deleted

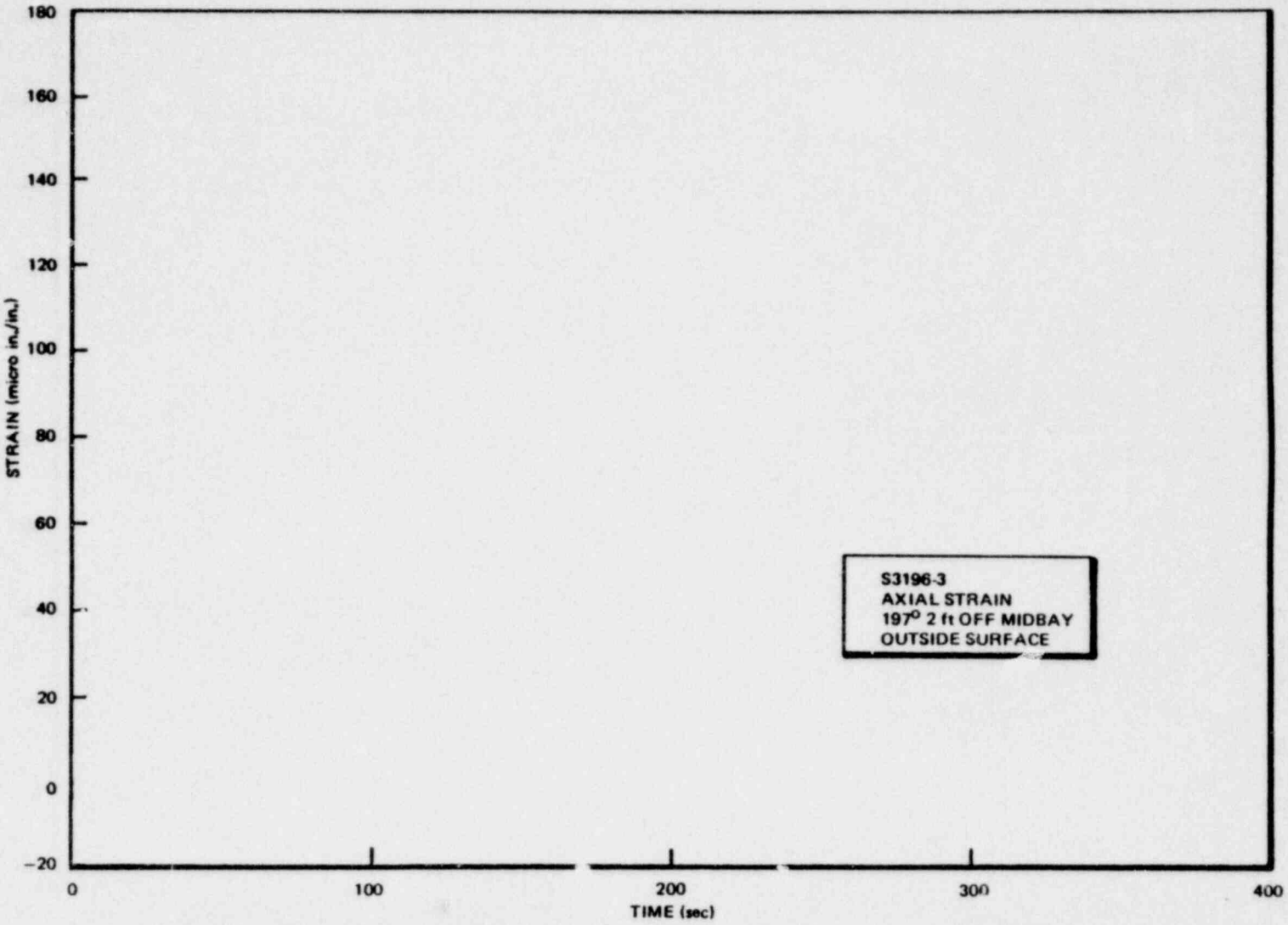

Figure 6.3.1-13. Wetwell Shell Axial Strain Beneath Downcomer No. 6 - Outside Surface (Small Steam Break Test - M1)

*Proprietary information deleted

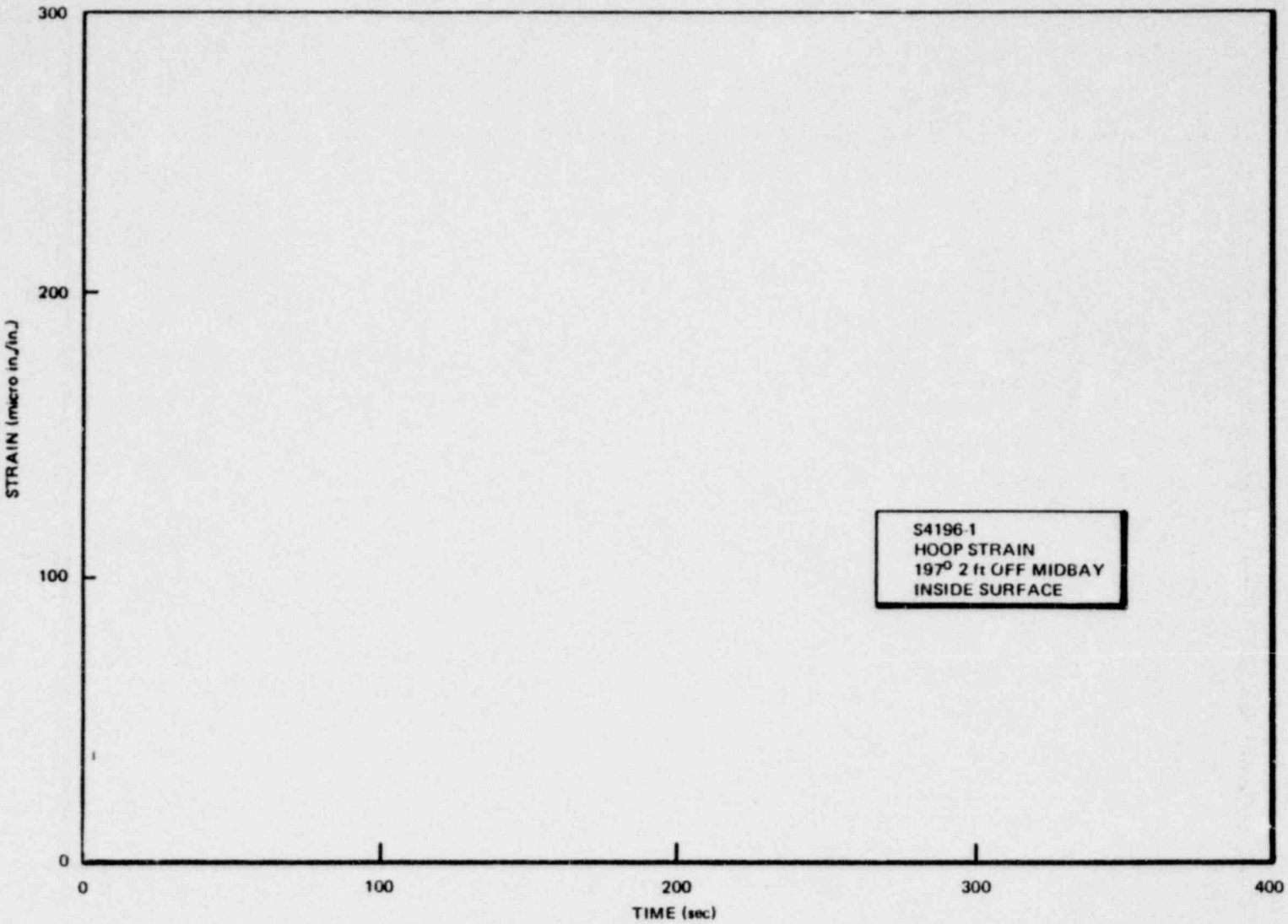

Figure 6.3.1-14. Wetwell Shell Hoop Strain Beneath Downcomer No. 6 - Inside Surface (Small Steam Break Test - M1)

*Proprietary information deleted

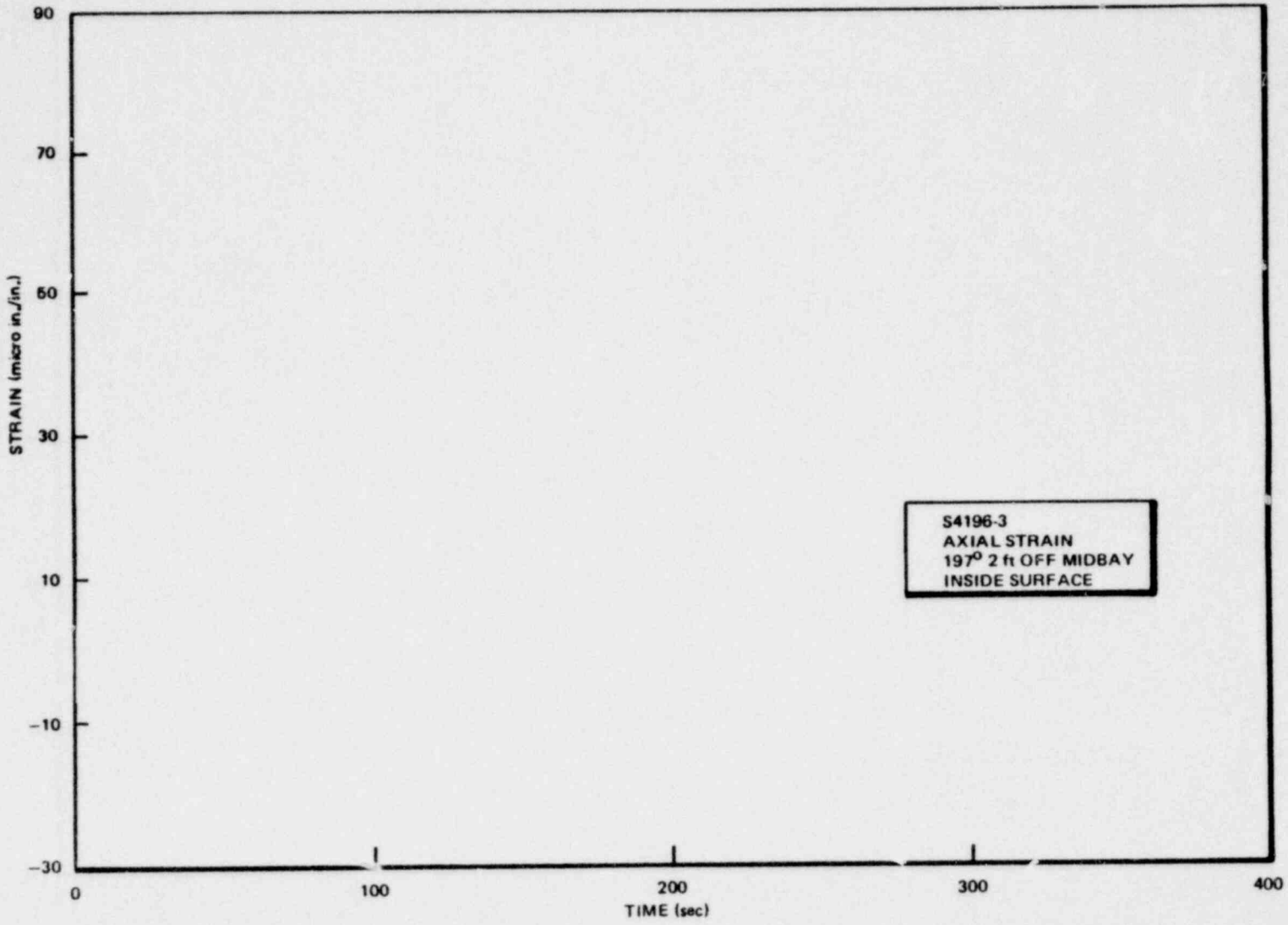

Figure 6.3.1-15. Wetwell Shell Axial Strain Beneath Downcomer No. 6 - Inside Surface (Small Steam Break Test - M1)

*Proprietary information deleted

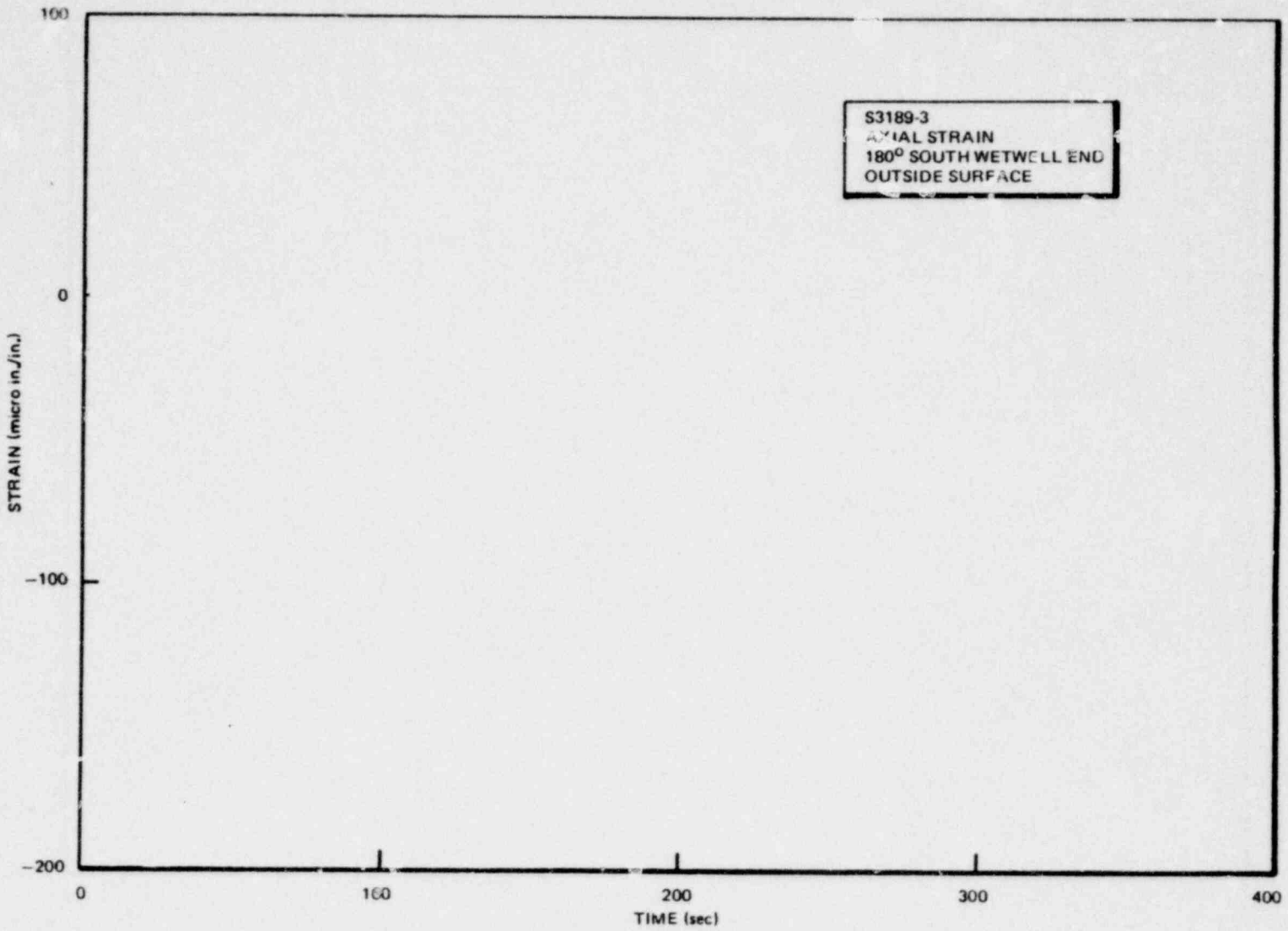

Figure 6.3.1-16. Wetwell Shell/Ring Girder Attachment Strain 180° South End (Small Steam Break Test - M1)

*Proprietary information deleted

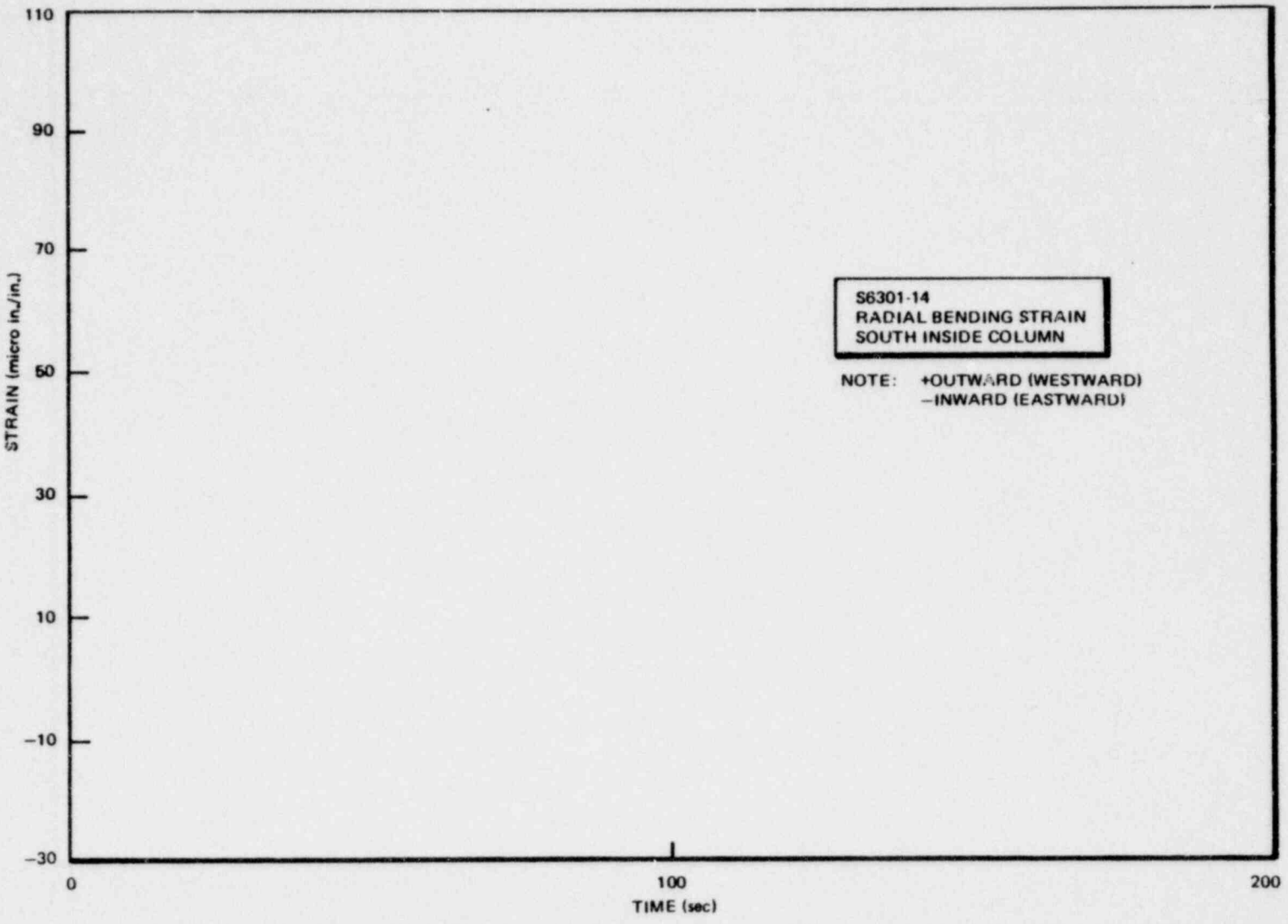

Figure 6.3.1-17. Wetwell Support Column Radial Bending Strain - South Inside Column (Large Liquid Break Test - M8)

*Proprietary information deleted

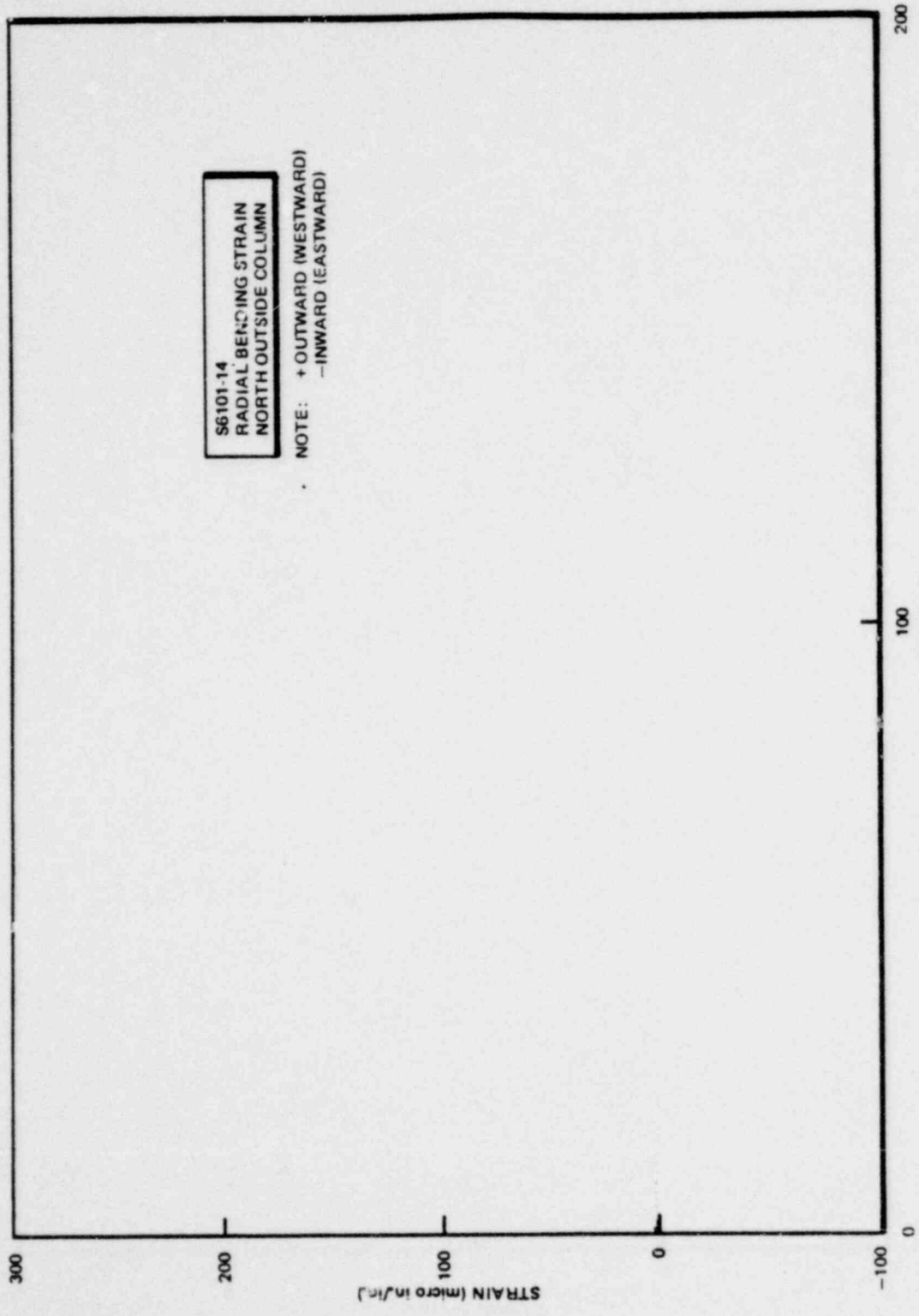

Figure 6.3.1-18. Wetwell Support Column Radial Bending Strain - North Outside Column (Large Liquid Break Test - M8)

*Proprietary information deleted

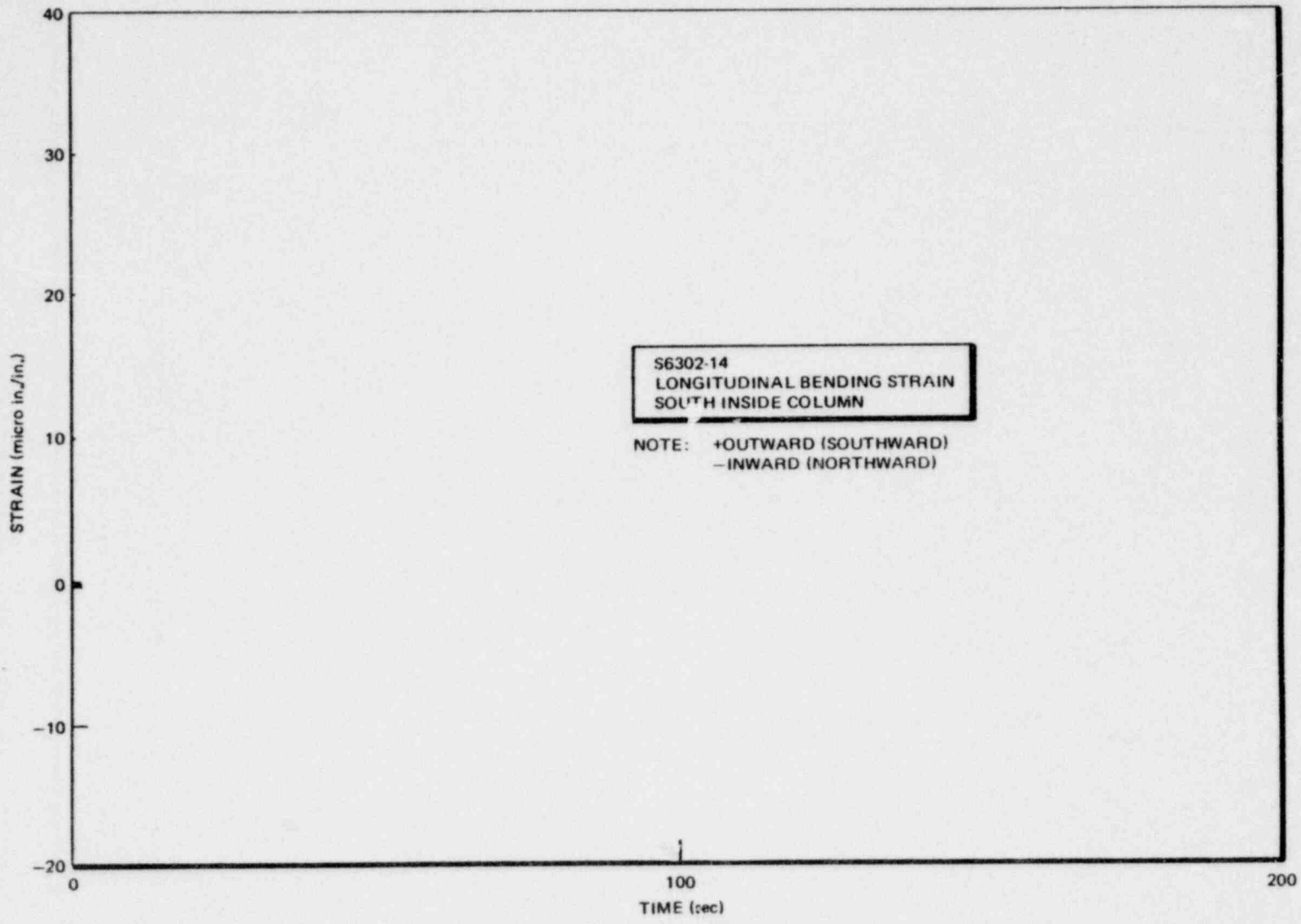

Figure 6.3.1-19. Wetwell Support Column Longitudinal Bending Strain - South Inside Column (Large Liquid Break Test - M8)

*Proprietary information deleted

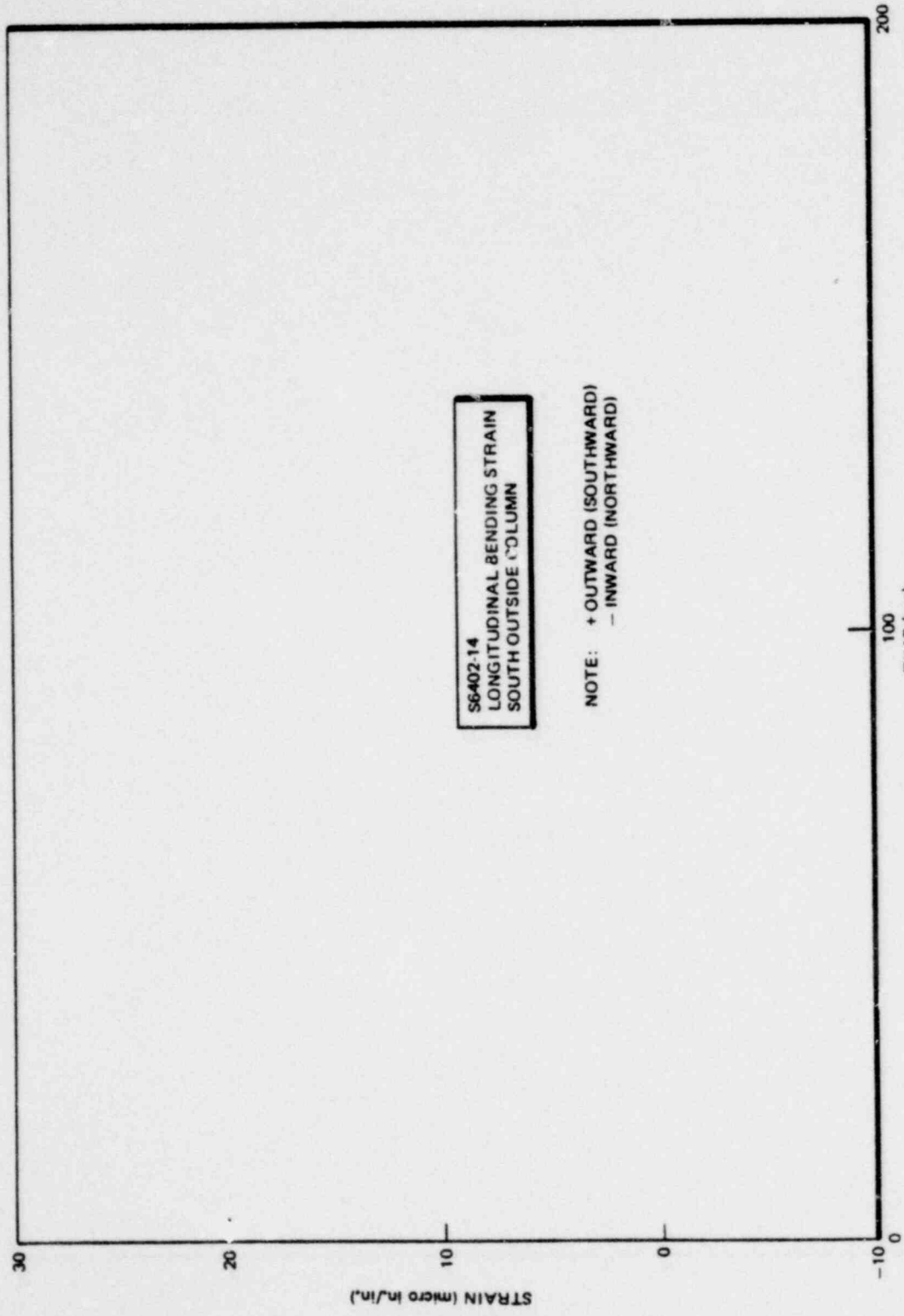

Figure 6.3.1-20. Wetwell Support Column Longitudinal Bending Strain - South Outside Column (Large Liquid Break Test - M8)

*Proprietary information deleted

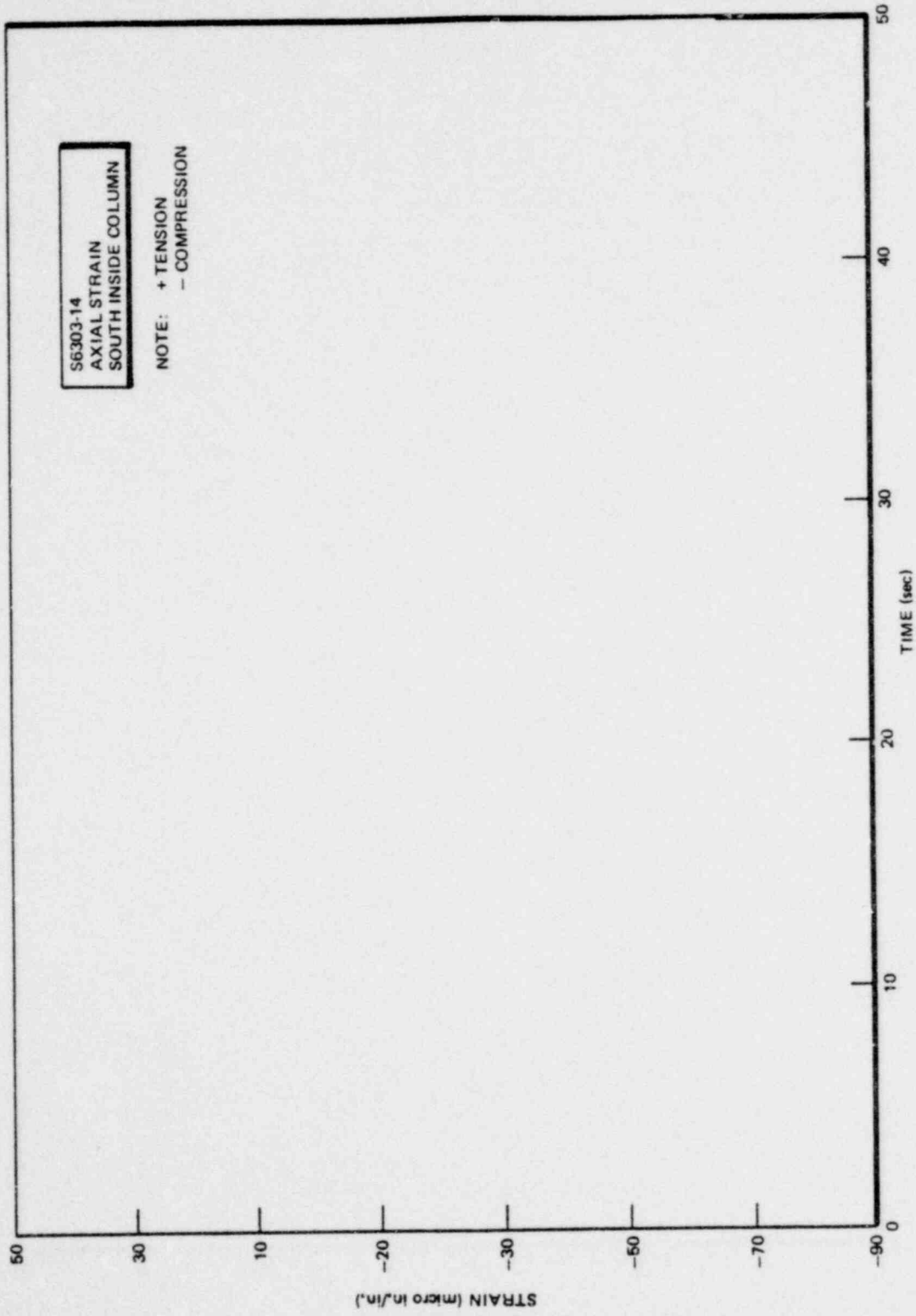

Figure 6.3.1-21. Wetwell Support Column Axial Strain - South Inside Column (Large Liquid Break Test - M8)

*Proprietary information deleted

1158 073

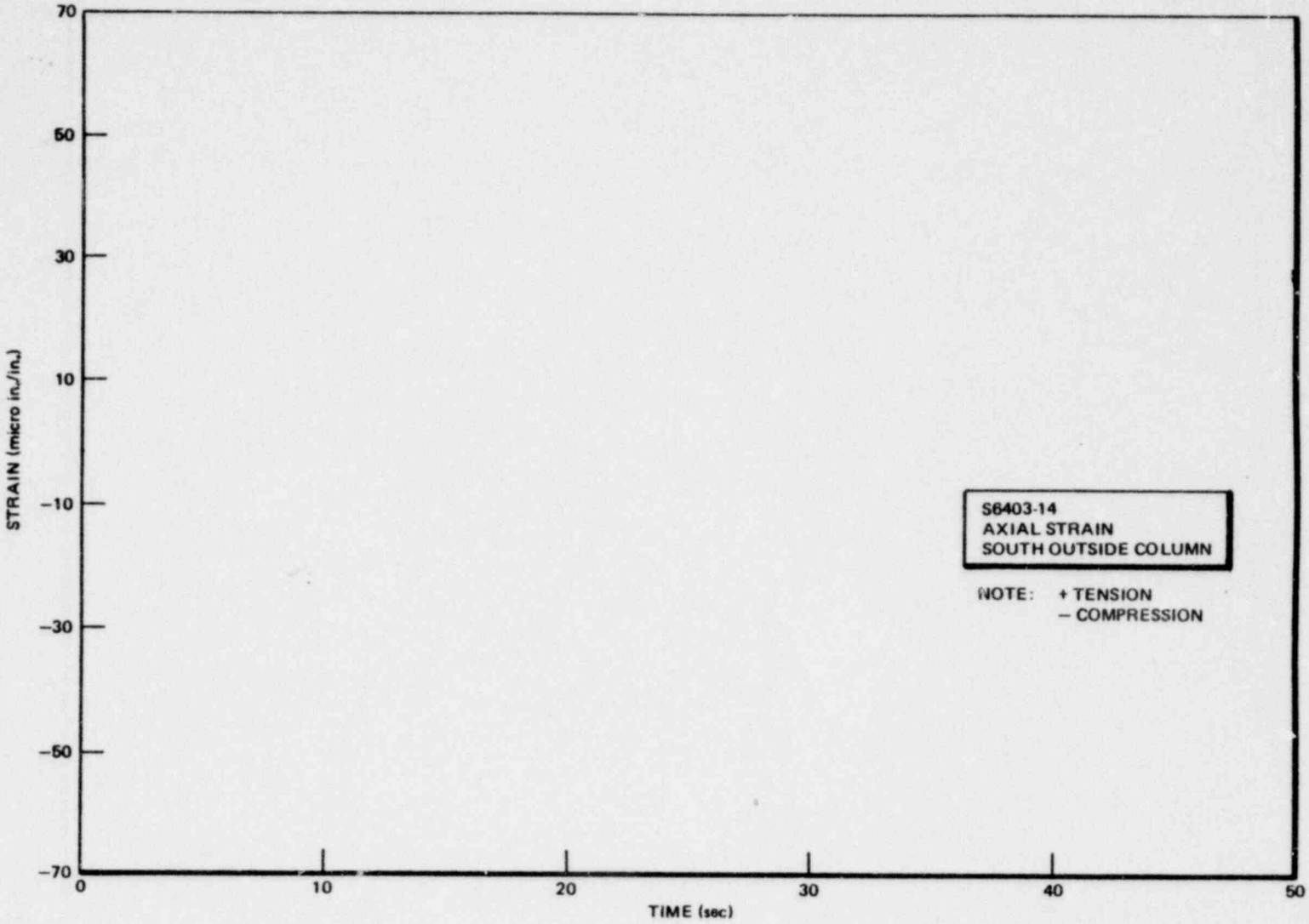

Figure 6.3.1-22. Wetwell Support Column Axial Strain - South Outside Column (Large Liquid Break Test - M8)

*Proprietary information deleted

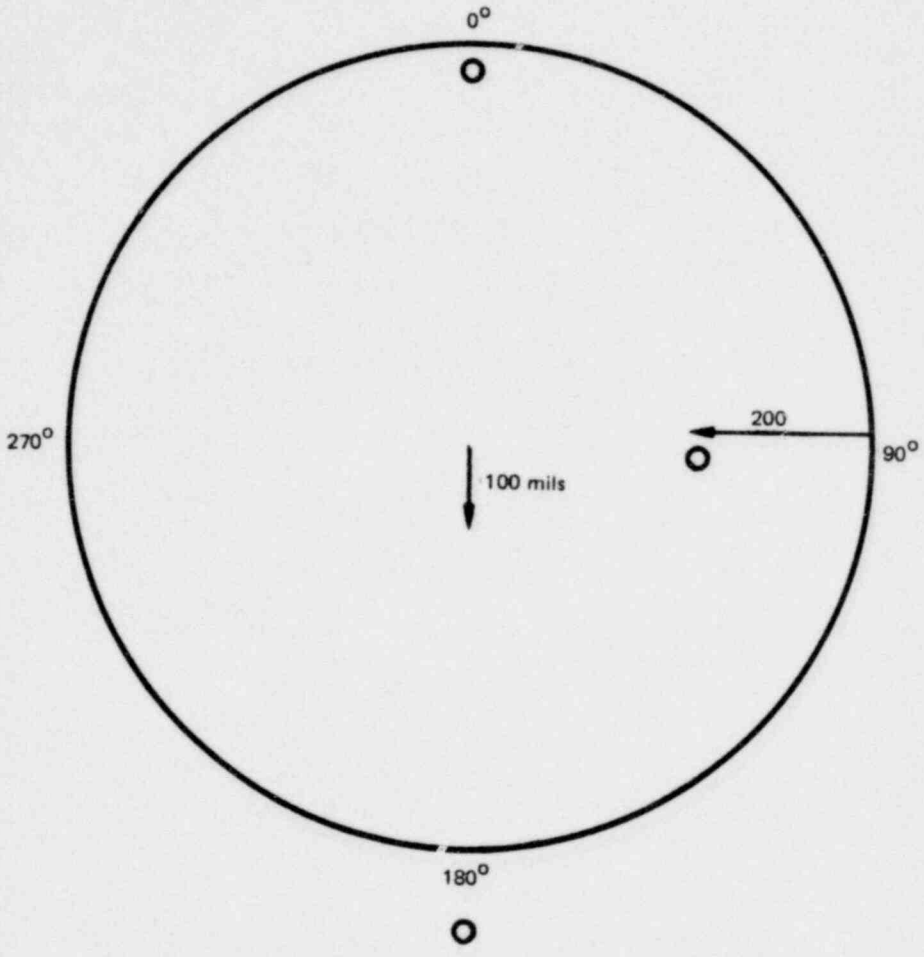

Figure 6.3.1-23. Ring Girder Deformation at the Termination of the Large Liquid Break Test - M8

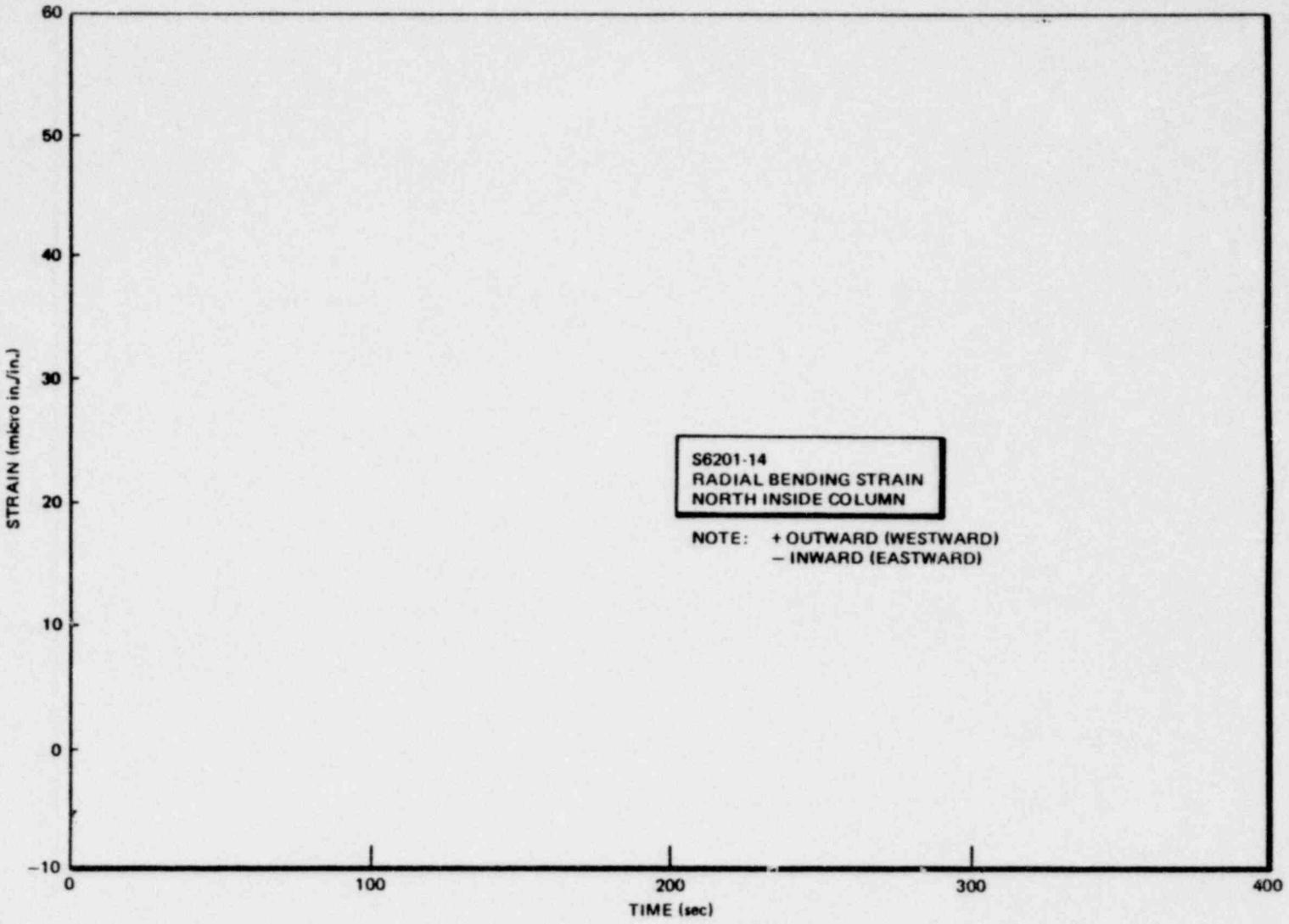

Figure 6.3.1-24. Wetwell Support Column Radial Bending Strain - North Inside Column (Small Steam Break Test - M1)

*Proprietary information deleted

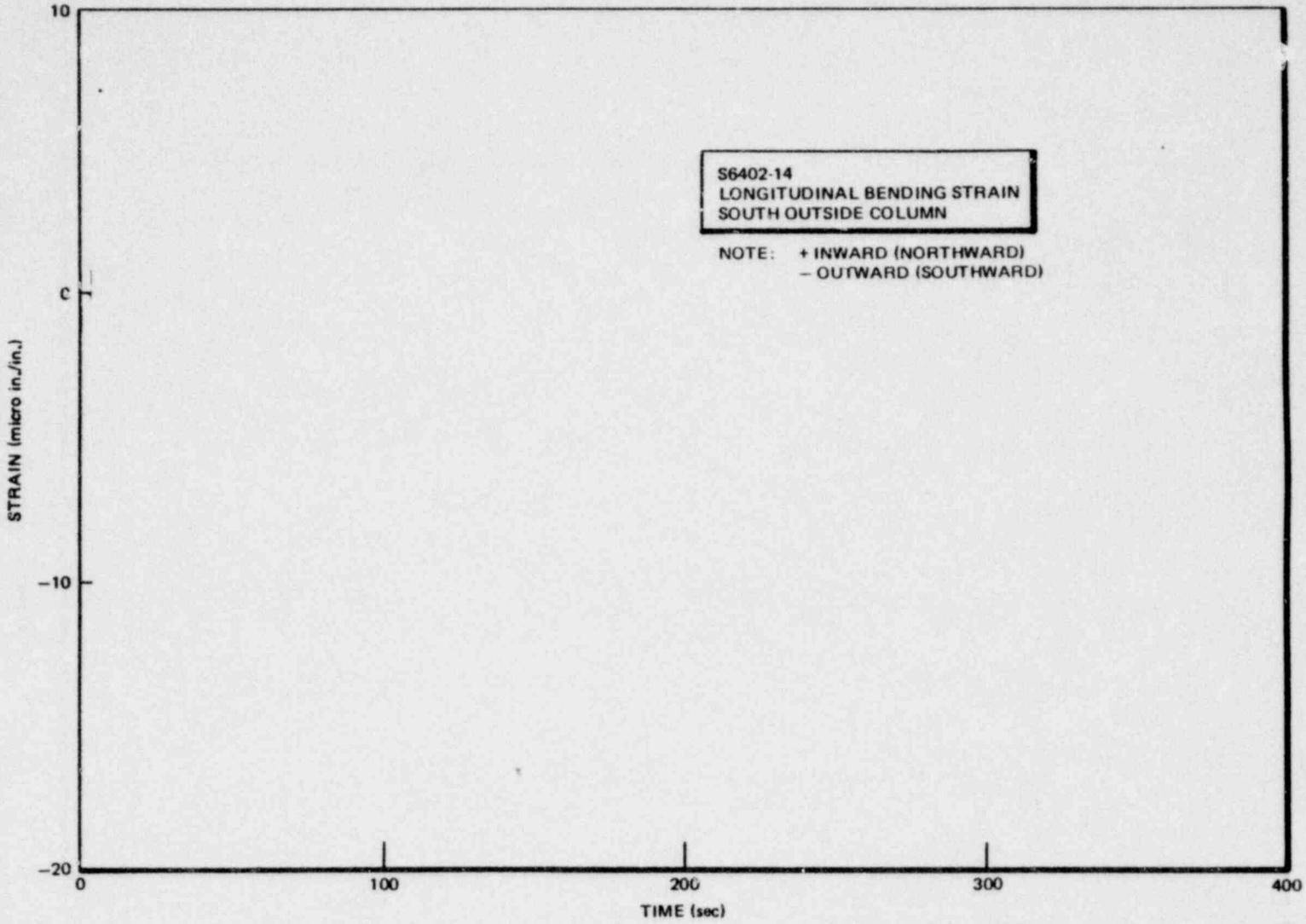

Figure 6.3.1-25. Wetwell Support Column Longitudinal Bending Strain - South Outside Column (Small Steam Break Tests - M1)

*Proprietary information deleted

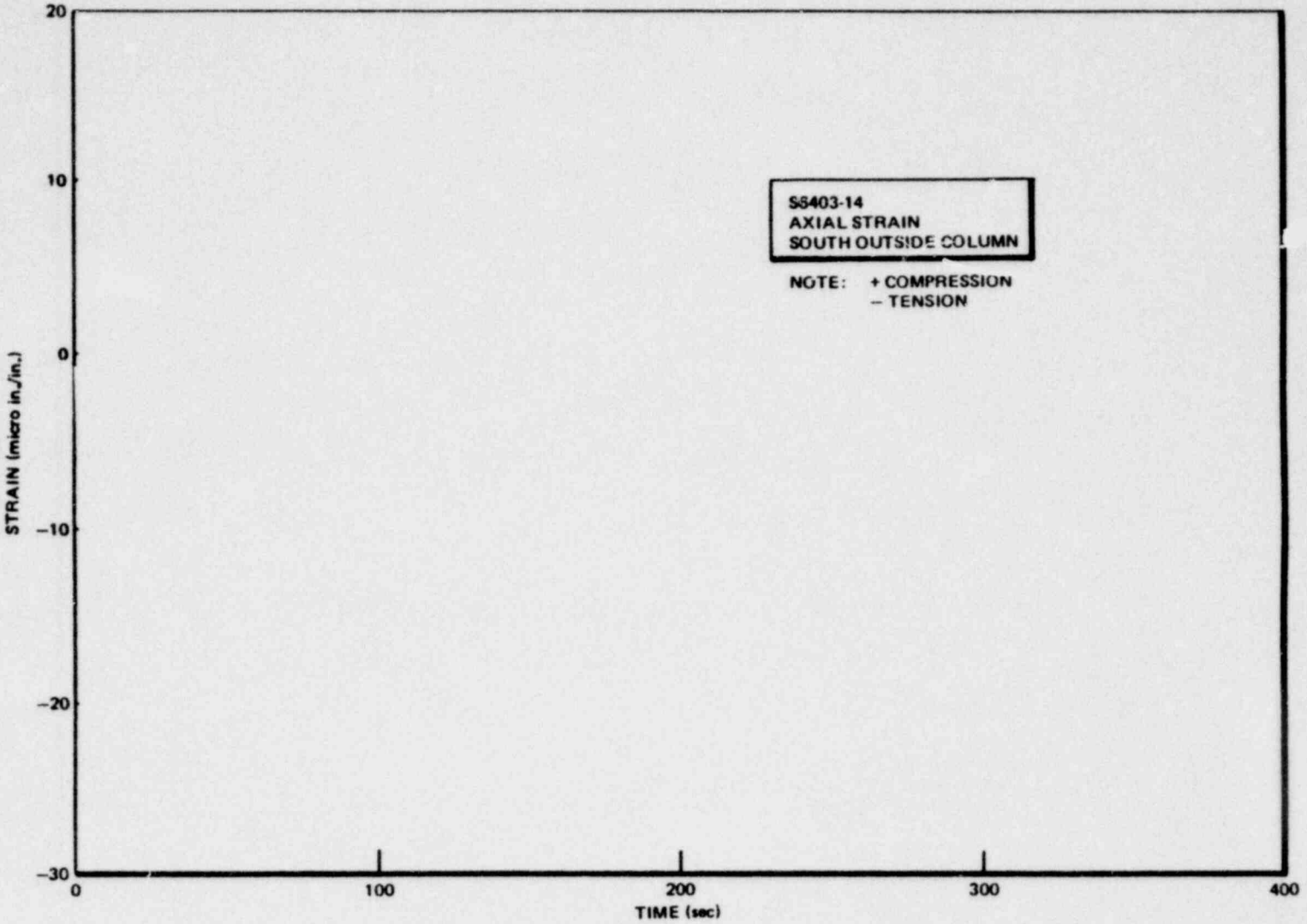

Figure 6.3.1-26. Wetwell Support Column Axial Strain - South Outside Column (Small Steam Break Test - M1)

*Proprietary information deleted

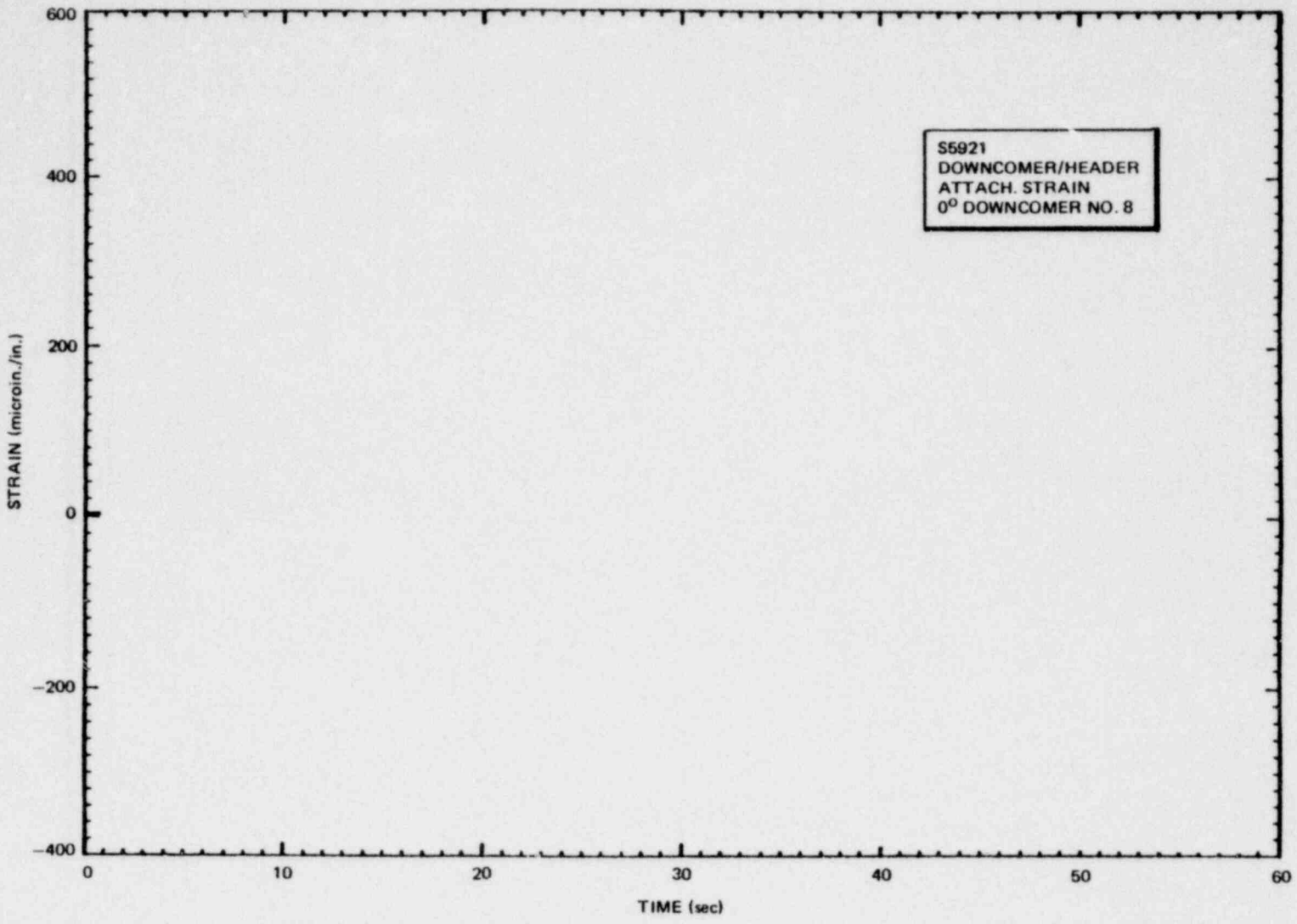

Figure 6.3.1-27. Downcomer/Header Attachment Strain During Large Liquid Break Test - 0° Downcomer No. 8

*Proprietary information deleted

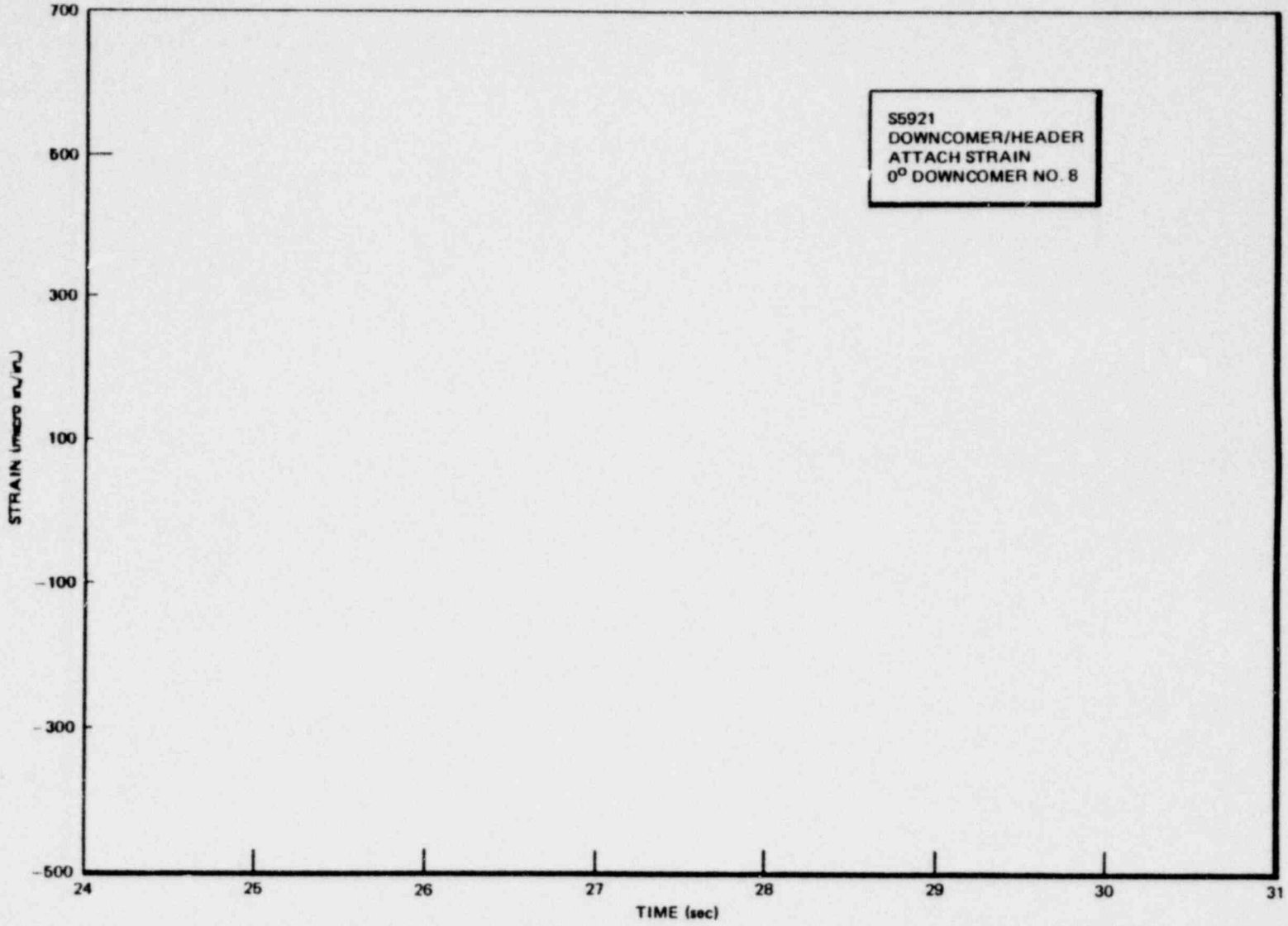

Figure 6.3.1-28. Downcomer/Header Attachment Strain During Condensation Oscillation - 0° Downcomer No. 8 (Large Liquid Break Test - M²)

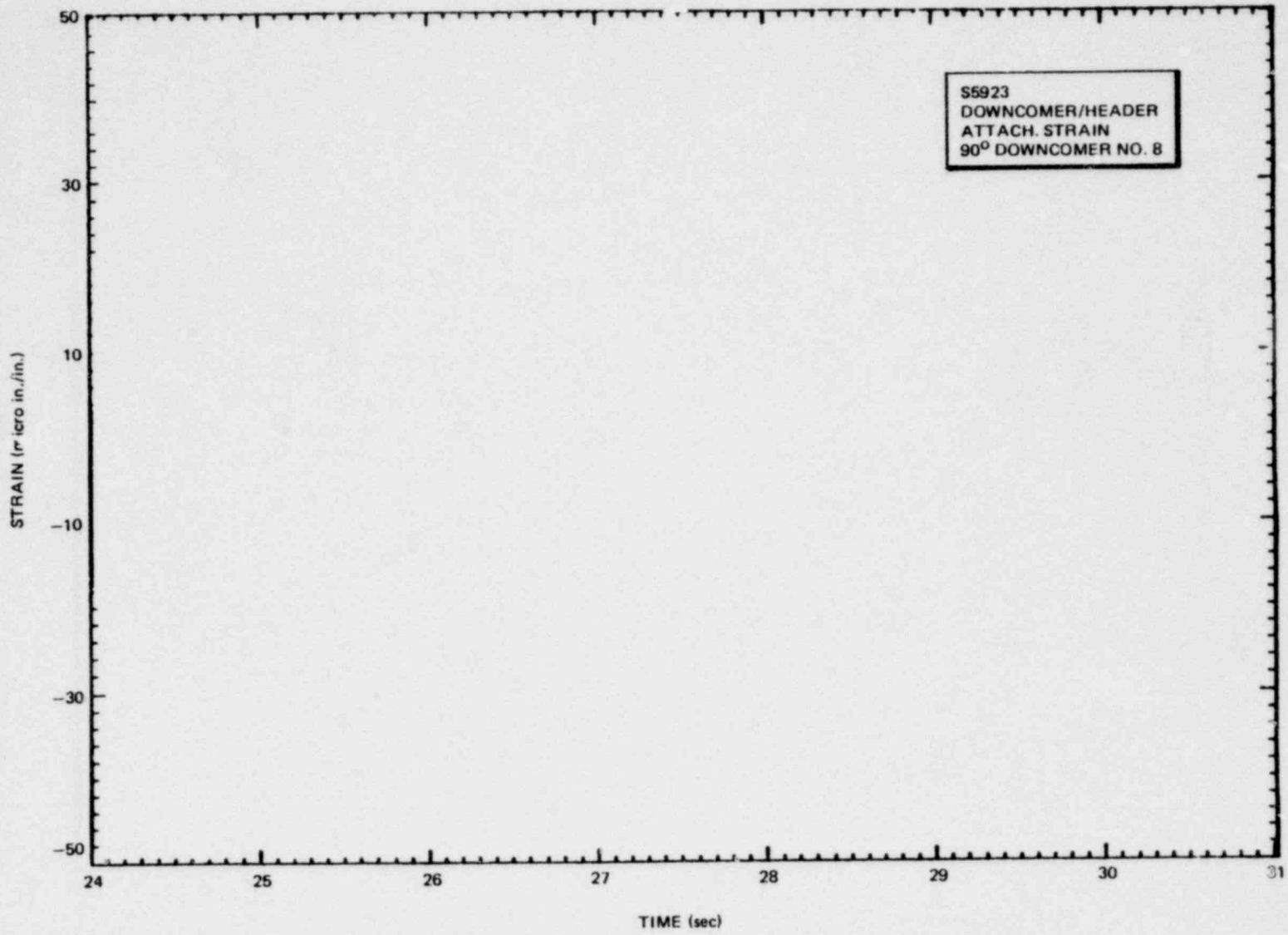

Figure 6.3.1-29. Downcomer/Header Attachment Strain During Condensation Oscillation - 90° Downcomer No. 8 (Large Liquid Break Test - M8)

*Proprietary information deleted

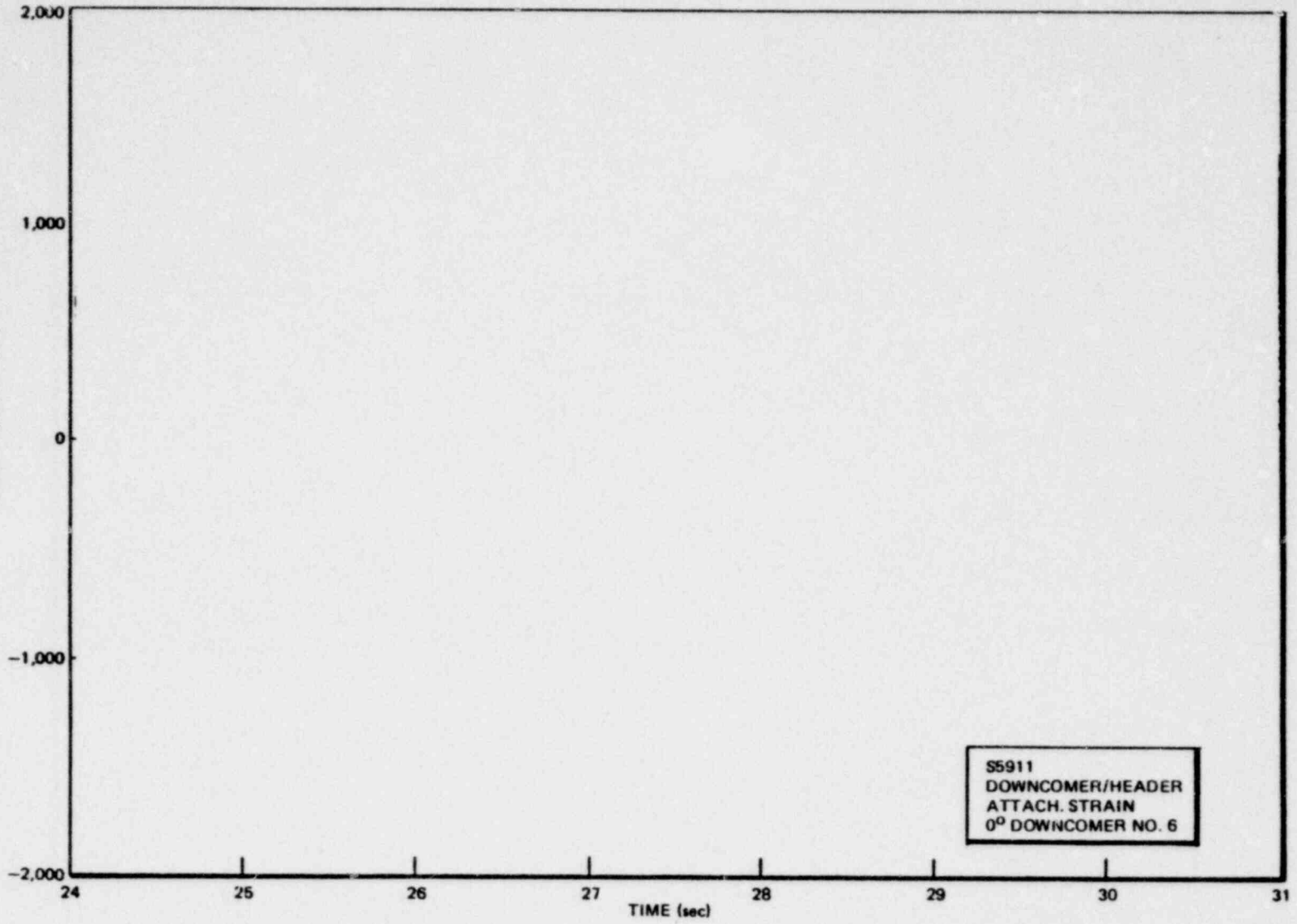

Figure 6.3-30. Downcomer/Header Attachment Strain During Condensation Oscillation - 0° Downcomer No. 6 (Large Liquid Break Test - M8)

*Proprietary information deleted

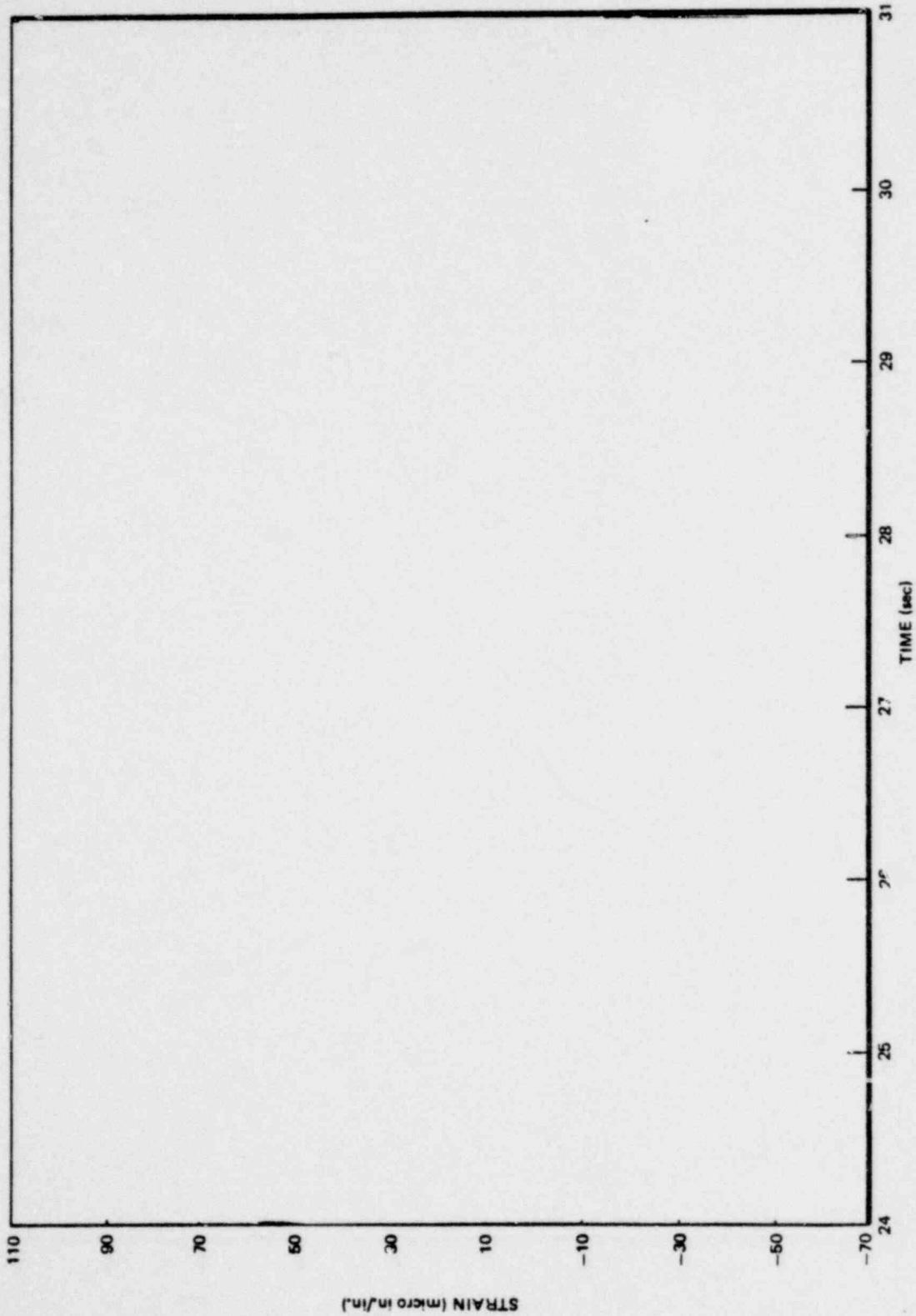

Figure 6.3.1-31. Downcomer/Header Attachment Strain During Condensation Oscillation - 90° Downcomer No. 6 (Large Liquid Break Test - M8)

*Proprietary information deleted

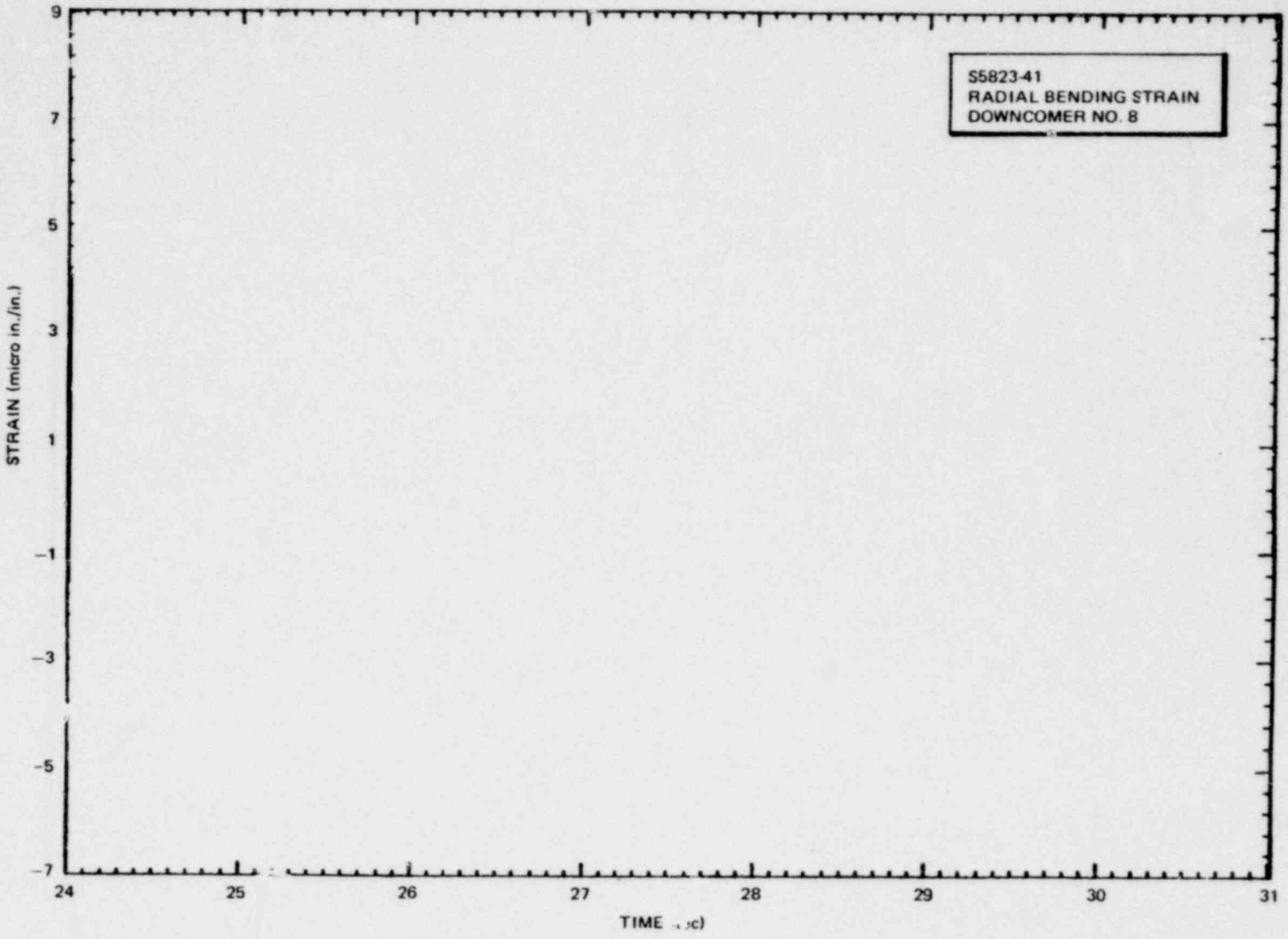

Figure 6.3.1-32. Downcomer Radial Bending Strain During Condensation Oscillation - Downcomer No. 8 (Large Liquid Break Test - M8)

*Proprietary information deleted

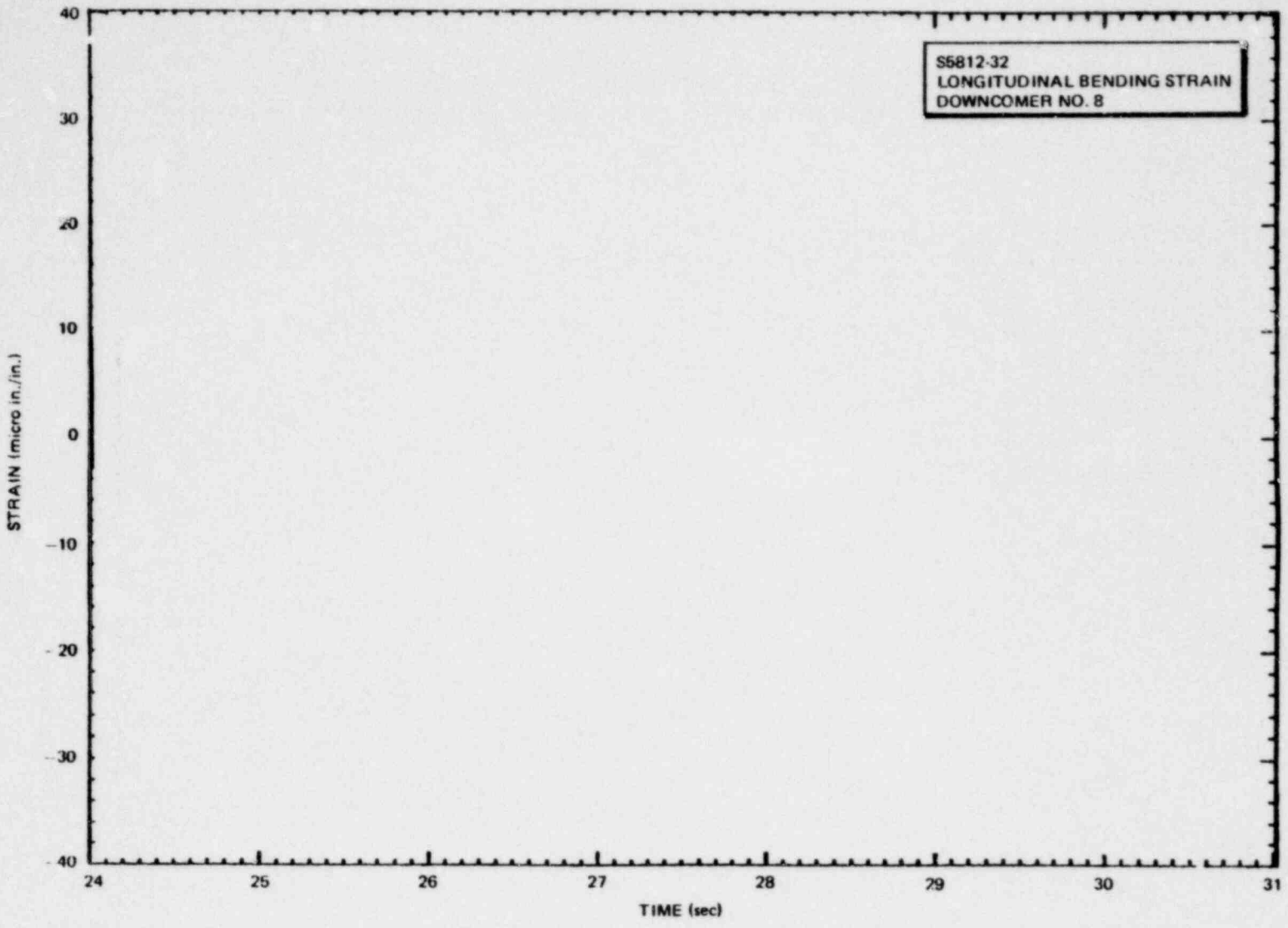

Figure 6.3.1-33. Downcomer Longitudinal Bending Strain During Condensation Oscillation - Downcomer No. 8 (Large Liquid Break Test - M8)

*Proprietary information deleted

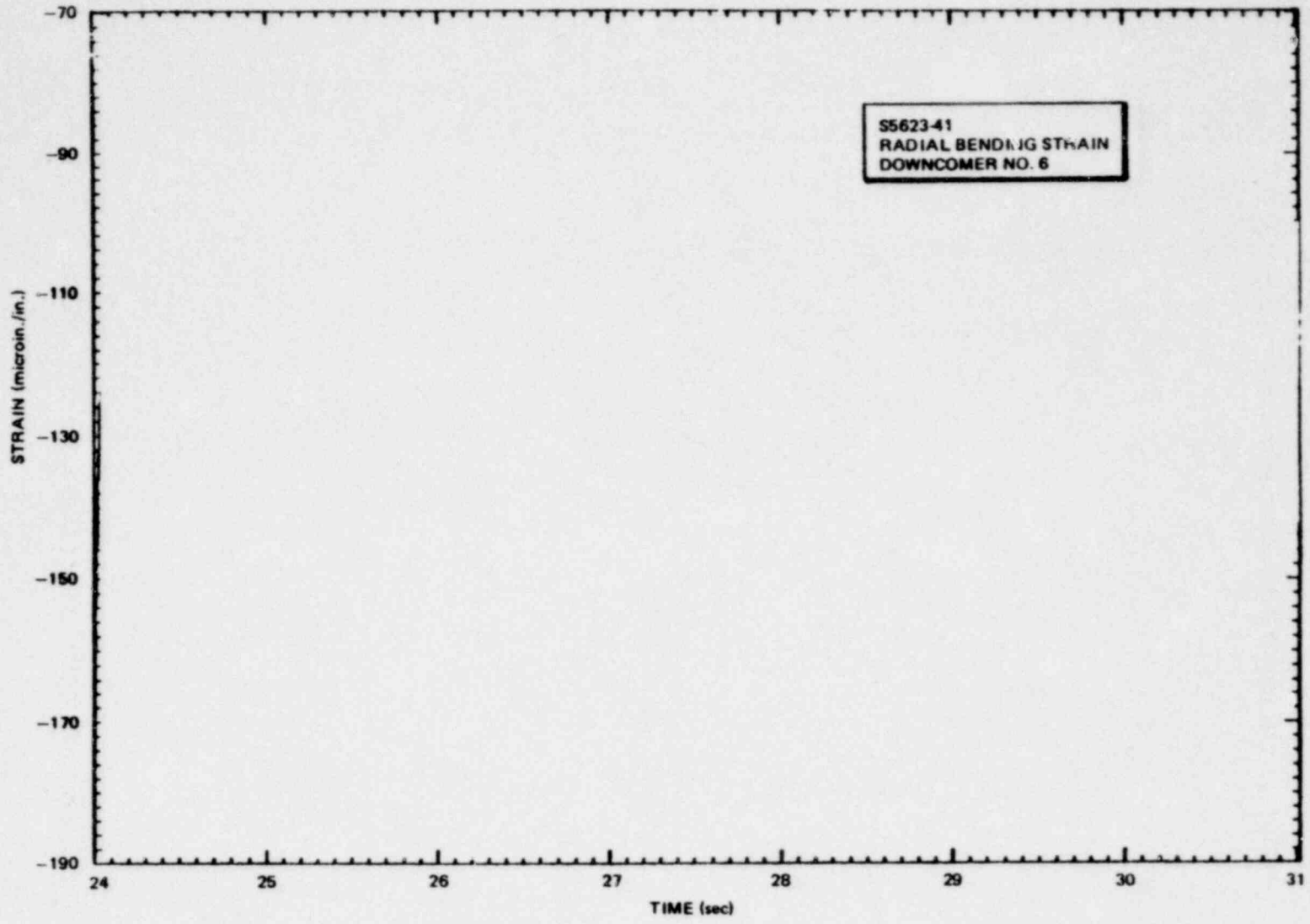

Figure 6.3.1-34. Downcomer Radial Bending Strain During Condensation Oscillation - Downcomer No. 6 (Large Liquid Break Test - M8)

*Proprietary information deleted

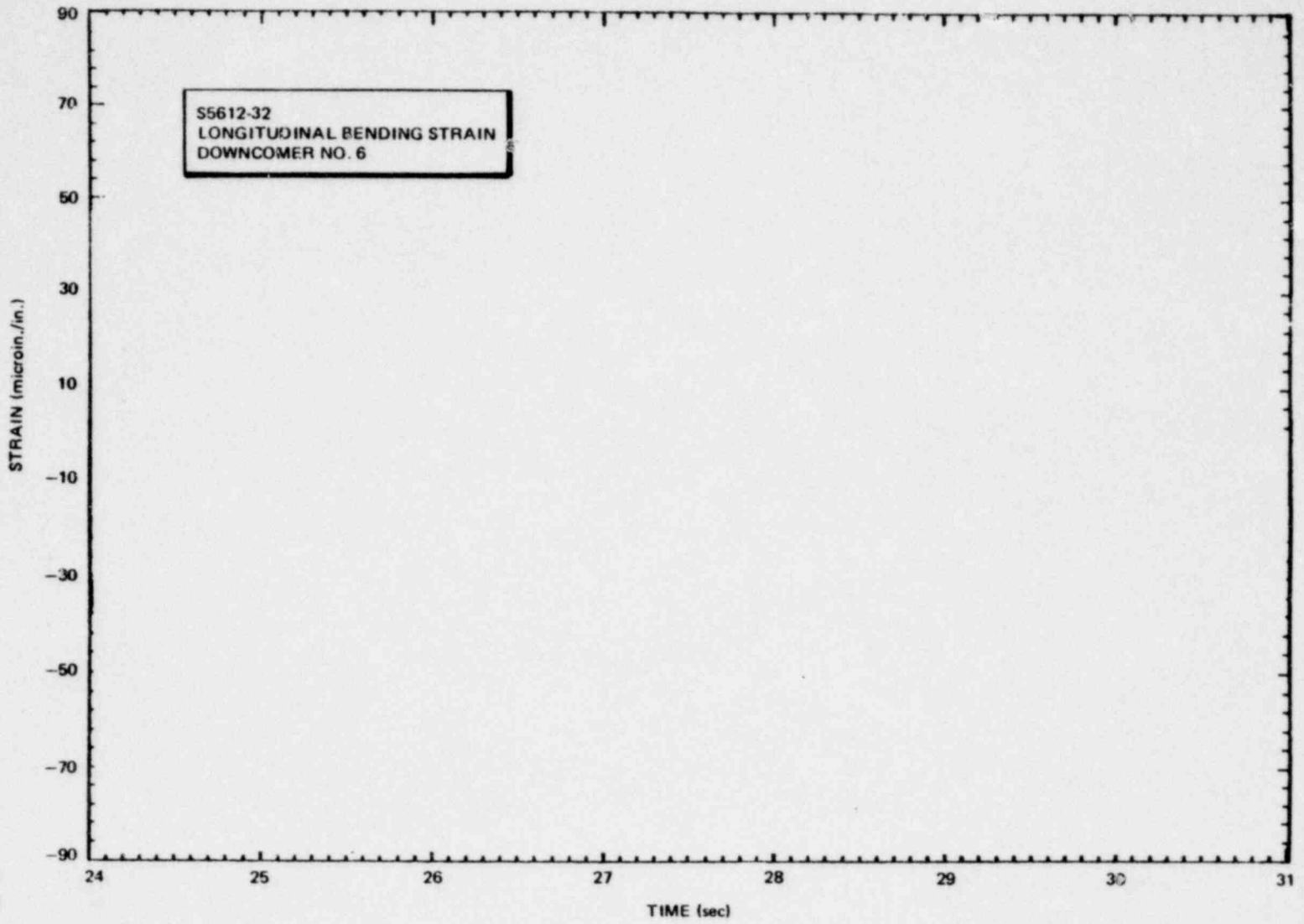

Figure 6.3.1-35. Downcomer Longitudinal Bending Strain During Condensation Oscillation - Downcomer No. 6 (Large Liquid Break Test - M8)

*Proprietary information deleted

11158 087

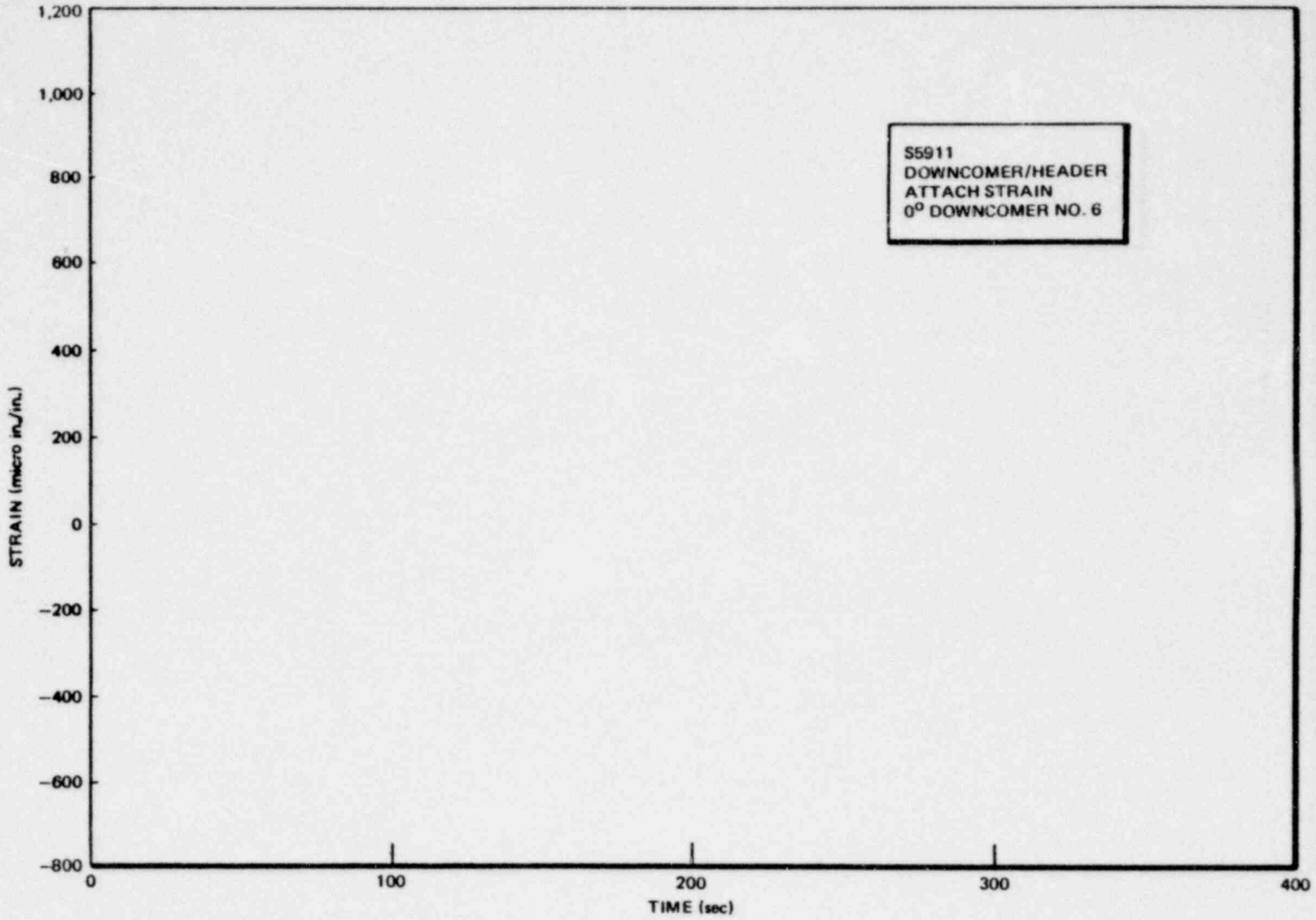

Figure 6.3.1-36. Downcomer/Header Attachment Strain During Small Steam Break Test - 0° Downcomer No. 6

*Proprietary information deleted

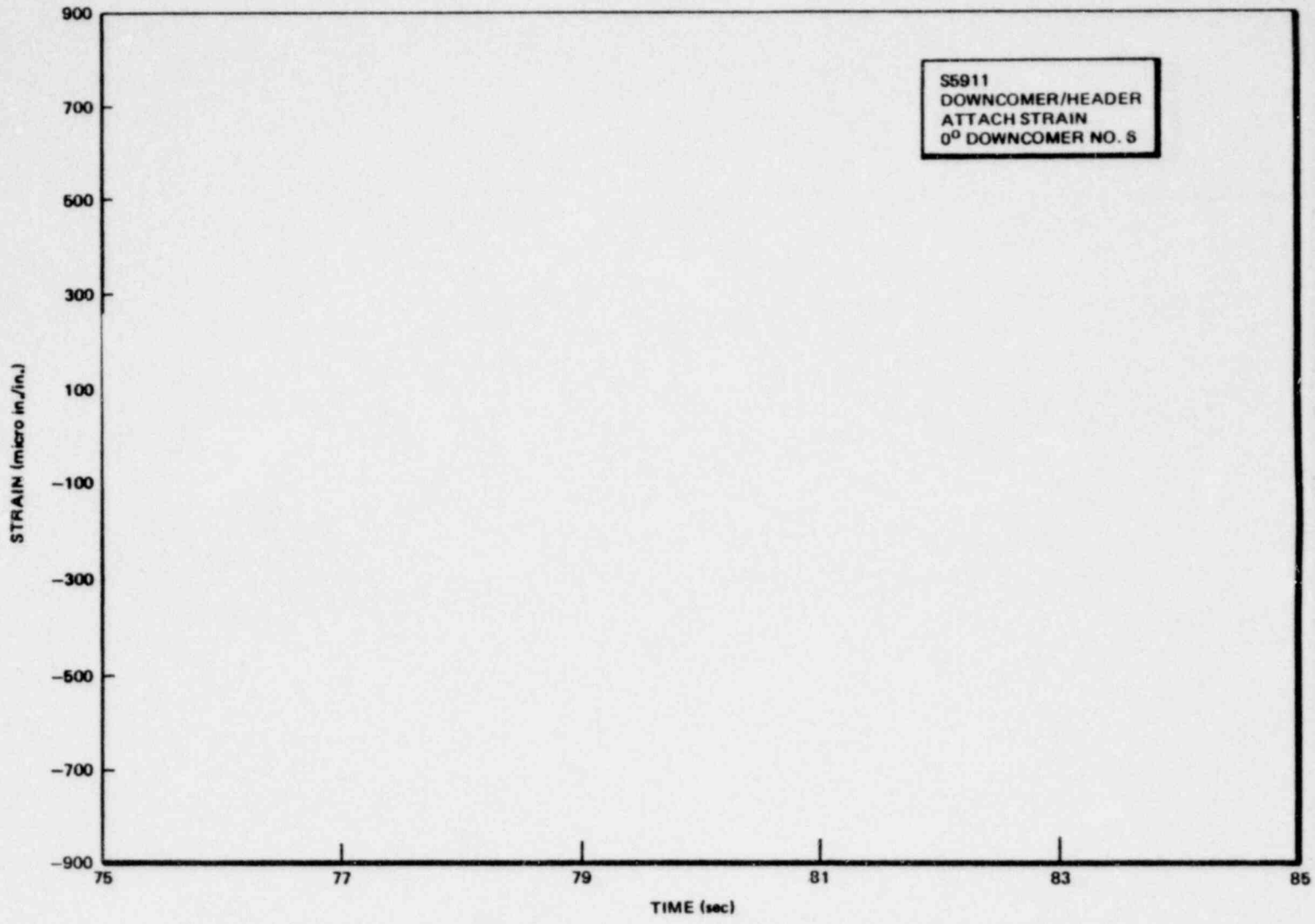

Figure 6.3.1-37. Downcomer/Header Attachment Strain During Chugging - 0° Downcomer No. 6 (Small Steam Break Test - M1)

*Proprietary information deleted

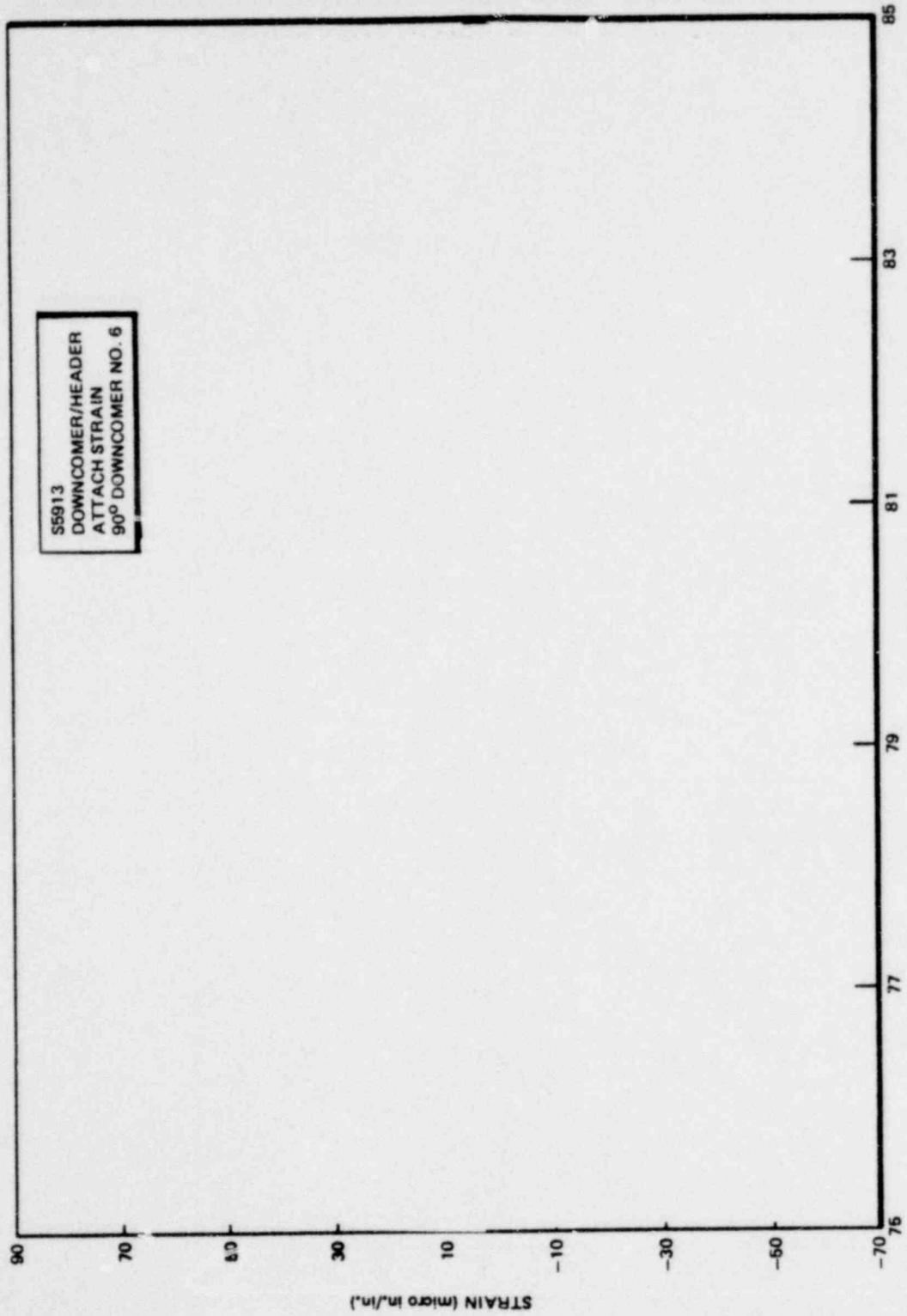

Figure 6.3.1-38. Downcomer/Header Attachment Strain During Chugging - 90° Downcomer No. 6 (Small Steam Break Test - M1)

*Proprietary information deleted

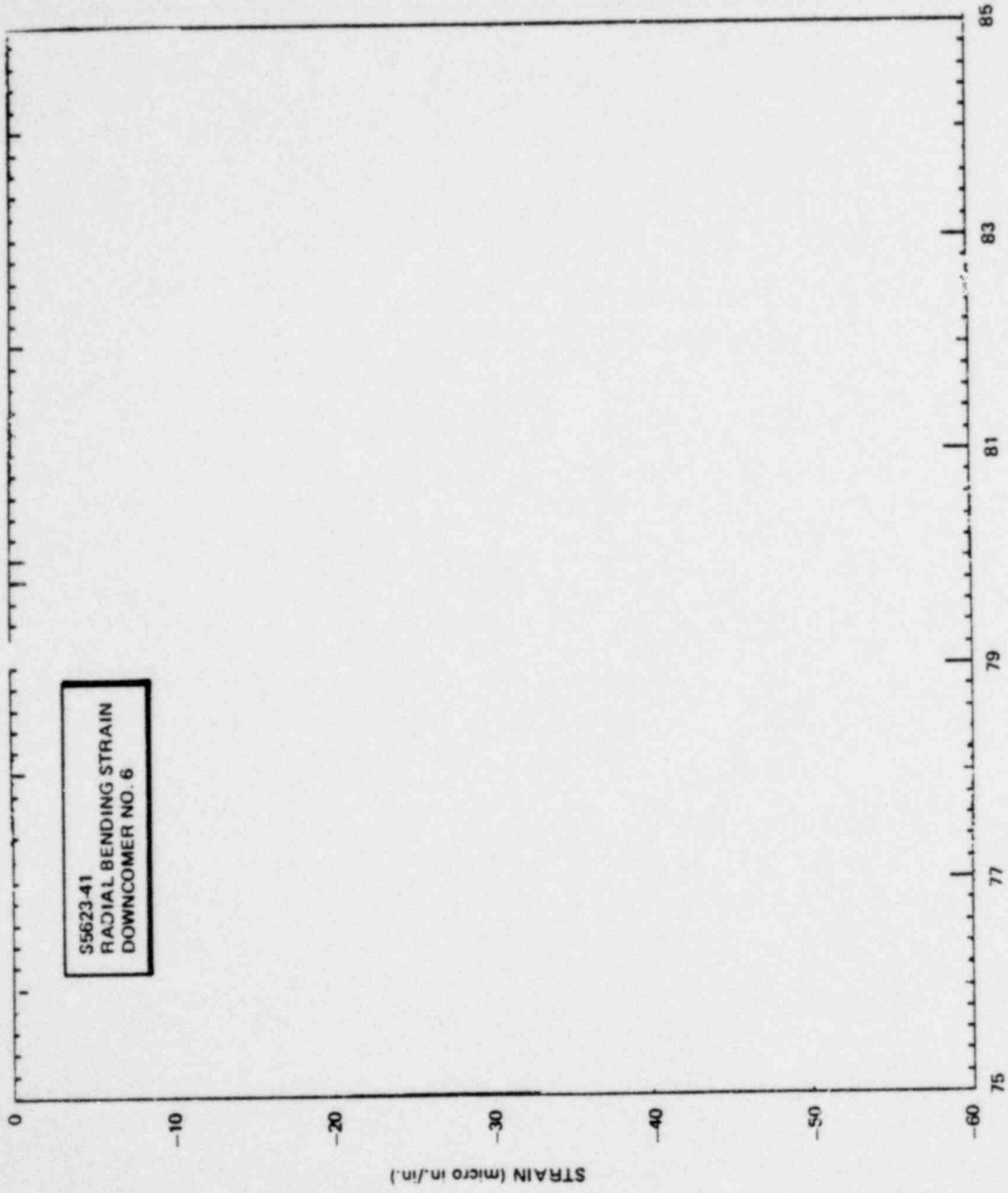

Figure 6.3.1-39. Downcomer Radial Bending Strain During Chugging - Downcomer No. 6 (Small Steam Break)

*Proprietary information deleted

1158 091

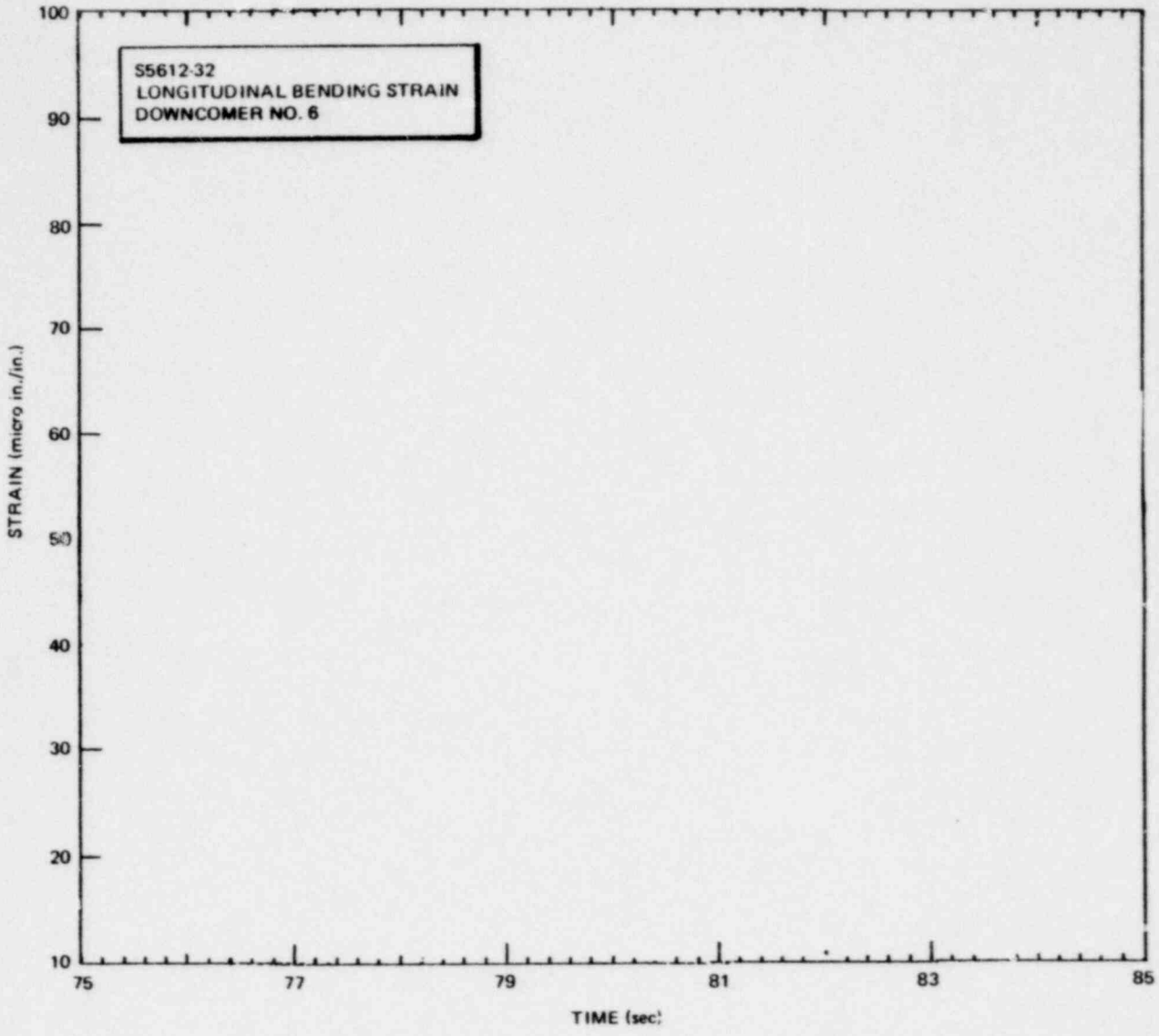

Figure 6.3.1-40. Downcomer Longitudinal Bending Strain During Chugging - Downcomer No. 6 (Small Steam Break)

*Proprietary information deleted

6.3.2 Facility Resonant Frequencies

A primary design criteria for FSTF was that its structural response accurately simulate the structural response of Monticello's torus. To ensure that FSTF met this design criteria, extensive structural calculations, including finite element modeling, were performed. Resonant frequencies determined from these calculations are summarized in Table 6.3.1-3. This table also summarizes resonant frequencies determined from experimental data.

Of the resonances identified in Table 6.3.2-1 those corresponding to the shell ovalization, vertical "bounce", "breathing" and "accordion" modes represent prototypical modes. Vibratory motions associated with these modes are, respectively: free shell radial wall motion; vertical motion of the wetwell on its support columns; lateral motion of the wetwell in a radial direction (relative to the torus center); and motion of the ring girders towards and away from each other (alternately compressing and stretching the wetwell shell). The "axial" and "piston" modes are unique to FSTF. The "axial" mode, which consists of lateral motion of the wetwell along its axis, results from the structural boundary conditions associated with the end restraint system. The "piston" mode corresponds to the motion of the end closure structures relative to the ring girders. Vibrations associated with the end closures, which simulate planes of hydrodynamic symmetry between adjacent bays of the torus, obviously do not represent a prototypical effect.

Experimental determination of wetwell shell resonant frequencies was based on dynamic vibration tests performed on the FSTF. In these tests controlled dynamic excitation was applied to the wetwell (via a hydraulic ram, or "shaker") and the response of the wetwell was measured by monitoring shell displacements and accelerations. The frequency range covered during these tests was 3 to 30 Hz. A full test description, including additional test results, is given in Appendix D.

Determination of other resonances for the FSTF, on experimental bases, relied on test data from the chugging period of the small steam break test (M1).

Fast Fourier transform methods were utilized to perform frequency decomposition of selected acceleration, displacement and strain data (i.e., PSDs were analyzed). The specific time period analyzed (from 98.5 to 99.7 seconds) included an eight-downcomer chug (or "pool" chug). Table 6.3.2-1 identifies which measurements were examined to determine each of the resonances for FSTF. The range of frequencies observed in these measurements, near the calculated resonant frequency, are also tabulated in Table 6.3.2-1. Examples of time histories and related PSDs used in this analysis are presented in the following discussion.

The radial bending strain of the wetwell support column was examined to determine the frequency of the radial or "breathing" mode. The time history of this strain, for the outside-south column, is shown in Figure 6.3.2-1. The frequency composition of this signal is discernible from the PSD presented in Figure 6.3.2-2. A strong frequency component can be observed at 14.4 Hz. The calculated resonant frequency for the radial mode of the wetwell is 14.2 Hz. Other prominent frequency components appear at 11.0, 21.2 and 28.0 Hz. The first two of these frequencies corresponds to shell ovalization modes (at 11.0 and 19.5 Hz) while the highest frequency corresponds to the vertical bounce mode of the wetwell on its support columns (calculated first and second modes being 27.3 and 28.7, respectively).

Confirmation of the calculated resonant frequency for the wetwell bounce mode is provided by the frequency composition of the wetwell column axial strain measurements. Figures 6.3.2-3 and -4 present, respectively, the time history and related PSD for the axial strain in the outside-south column. The predominant frequency components are 28.0 Hz, which is close to the calculated resonants for the first two bounce modes (27.3 and 28.7 Hz), and 11.9 Hz. Again, the 11.9 Hz component corresponds to an ovalization mode of the wetwell.

Figures 6.3.2-5 and -6 present, respectively, the time history and PSD for axial strain on the outside surface of the wetwell shell. Frequencies near the predicted resonant frequencies for the "axial" and "accordion" modes (34.5 and 52.5 Hz, respectively) are present in the shell strain PSD (at

36.5 Hz and 54.4 Hz). Numerous other frequencies also appear in this PSD. The frequencies of 11.9-12.7, 14.4-15.3 and 21.2 Hz appear to correspond to shell resonances while the 28.0 Hz frequency corresponds to the wetwell vertical "bounce" mode. The frequency of 42.5 Hz appears to be associated with vent system acoustics during chugging (similar frequencies are observed in downcomer pressure measurements). Finally, the 63.7 Hz frequency is near the predicted frequency for the end closure "piston" mode (66.5 Hz). As will be discussed later in subsection 6.4.2.4, frequencies in the range from 60 to 70 Hz appear in the shell displacement and acceleration data; so the 63.7 Hz frequency that appears in the shell axial strain data may correspond to a higher shell mode.

Lateral accelerations of the end closures were examined to determine the response frequency of the end closures. Time histories and PSD plots of the north end closure accele ion are presented in Figures 6.3.2-7 and -8, respectively. Signifi signal power is indicated in the PSD over a range from 62.9 to 68.0 Hz. The calculated resonant frequency for the "piston" mode of the end closures, 66.5 Hz, falls within this frequency range. Significant signal power is also indicated at 54.4 Hz and 40.8 Hz. Evidently, 54.4 Hz corresponds to the "accordion" mode for the wetwell. The 40.8 Hz component again appears to be associated with vent system acoustics during chugging.

Table 6.3.2-1

SUMMARY OF CALCULATED AND OBSERVED FACILITY FREQUENCIES

Mode	Calculated Resonant Frequency (Hz)	Observed Frequency	Indicative Instrumentation
Wetwell Shell Ovalization		7.4 9.7 11.0 15.0 17.4 19.5	Wetwell Shake Tests
Wetwell Vertical "Bounce"	1st 27.3 2nd 28.7	27 - 29 Hz	Wetwell Column Axial Strain Ring Girder Displ. and Accel.
Radial or "Breathing"	14.2	12 - 15 Hz	Wetwell Column Radial Bending Strain Ring Girder Displ. and Accel.
Rigid Body or "Axial"	34.5	31 - 37 Hz	Wetwell Shell Axial Strains Wetwell Column Longitudinal Bending Strain End Closure Accel.
"Accordion"	52.5	52 - 56 Hz	
End Closure "Piston"	66.5	62 - 68 Hz	

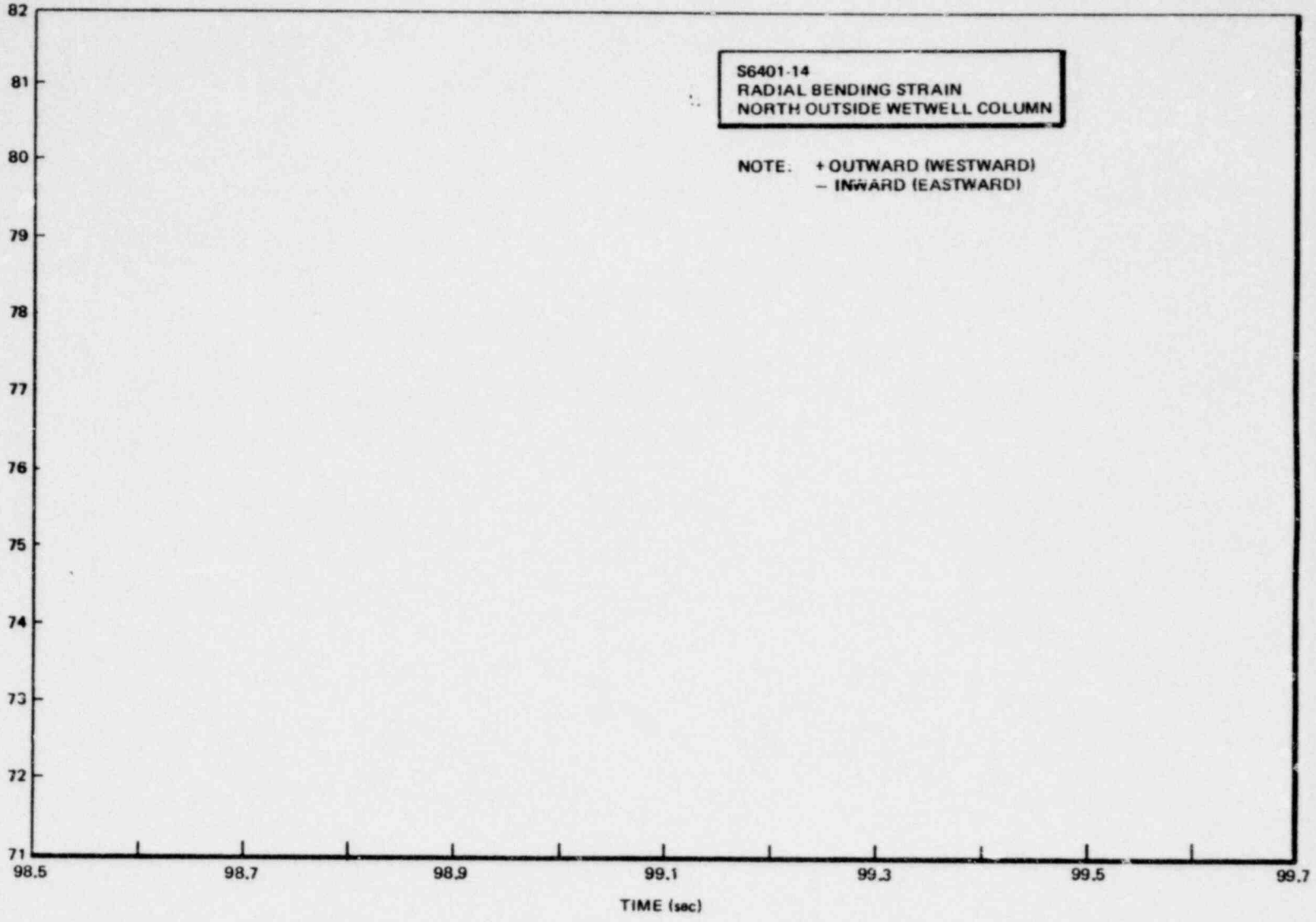

Figure 6.3.2-1. Wetwell Support Column Radial Bending Strain During Chugging - North Outside Column (Small Steam Break Test - M1)

*Proprietary information deleted

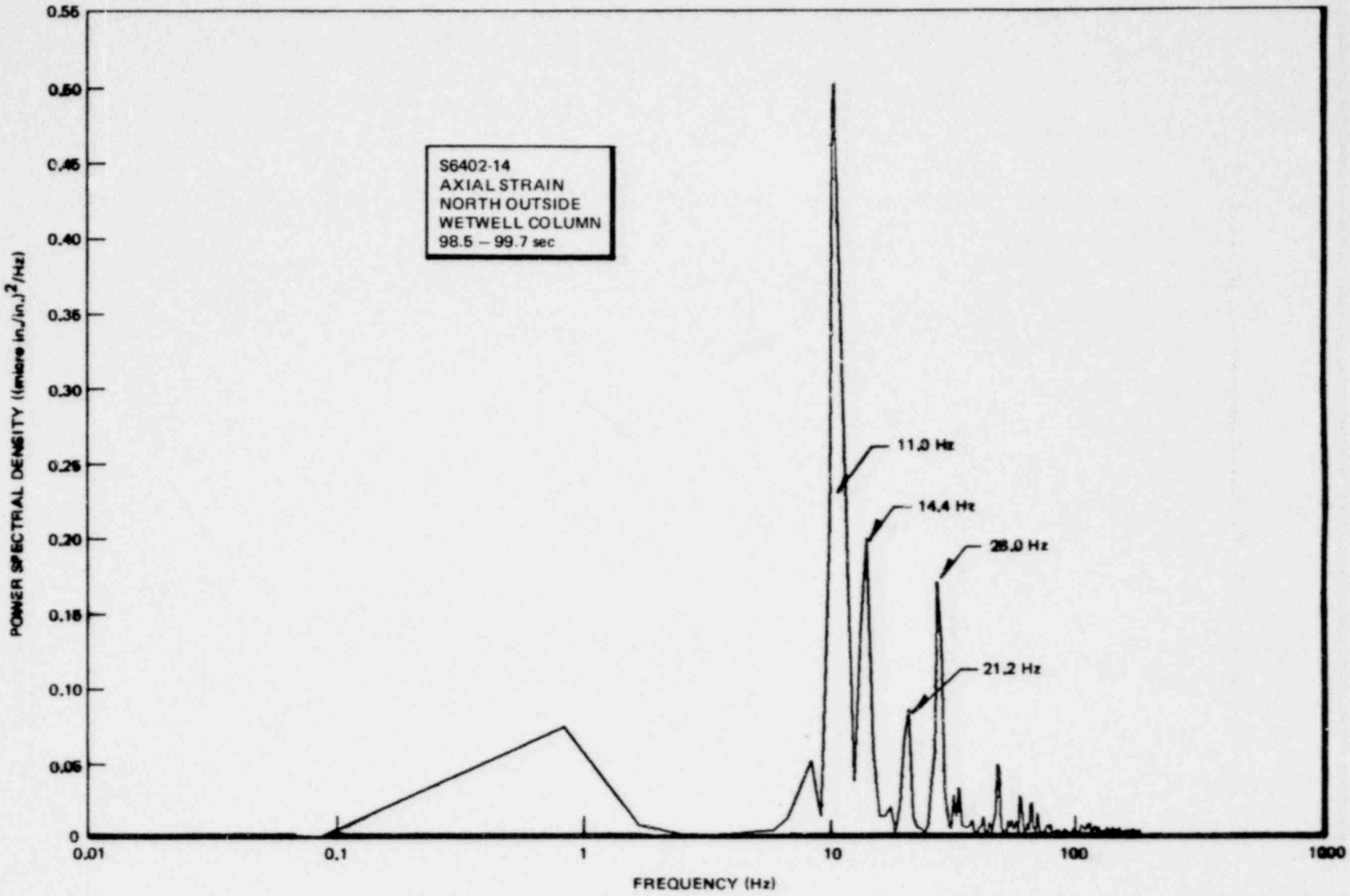

Figure 6.3.2-2.. Power Spectral Density of Wetwell Support Column Radial Bending Strain

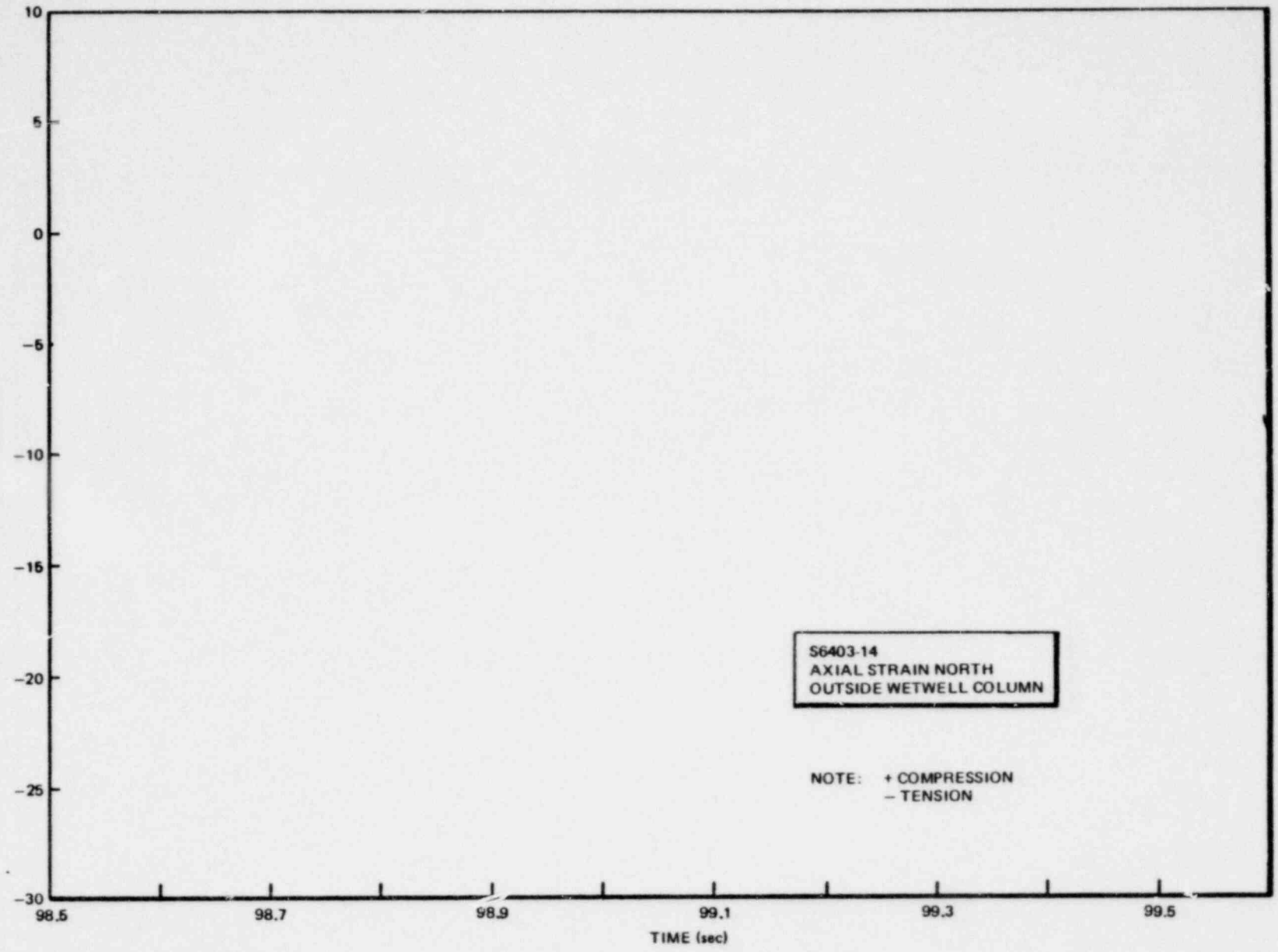

Figure 6.3.2-3. Wetwell Support Column Axial Strain During Chugging - North Outside Column (Small Steam Break Test - M1)

*Proprietary information deleted

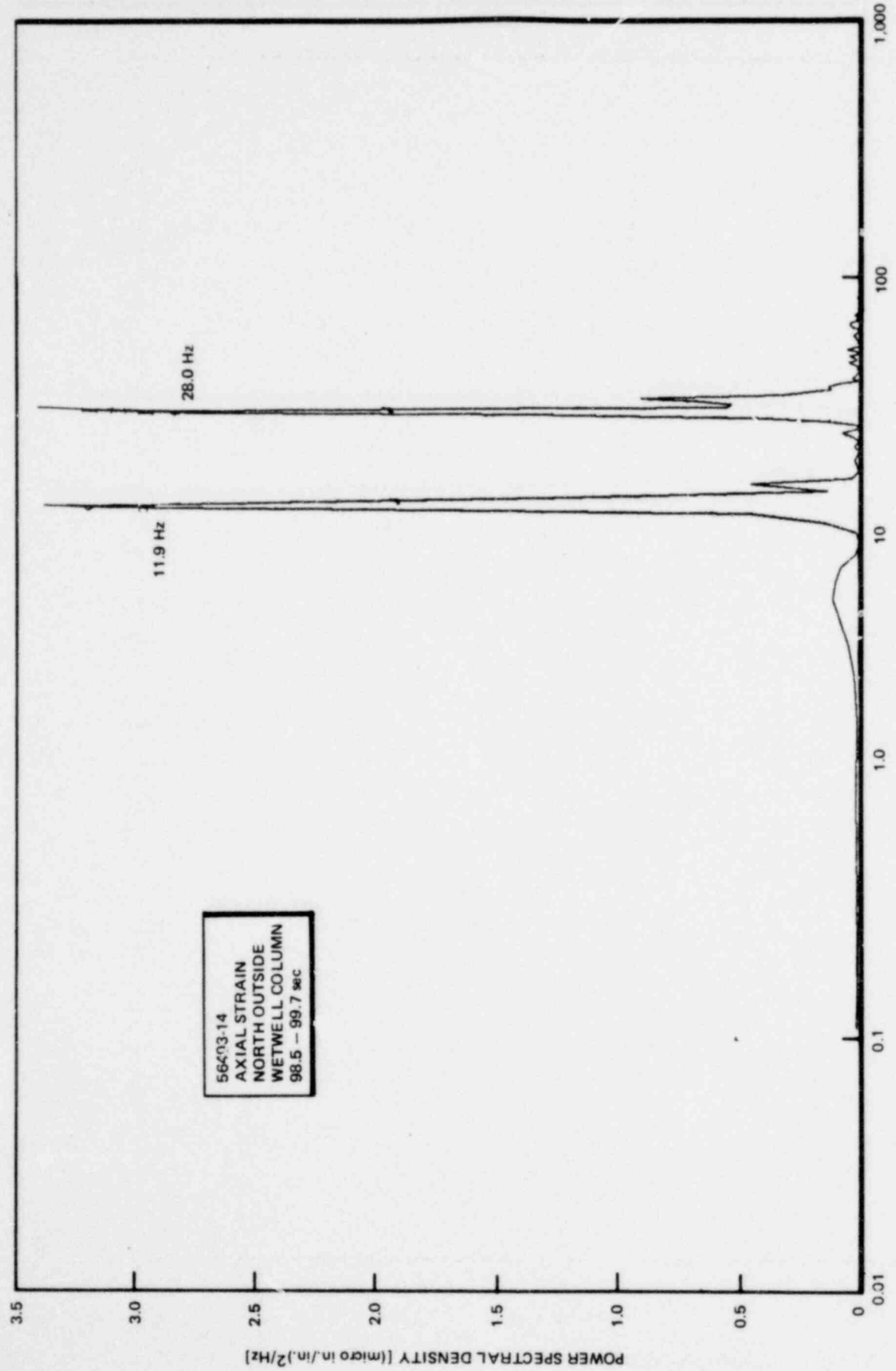

Figure 6.3.2-4. Power Spectral Density of Wetwell Support Column Axial Strain

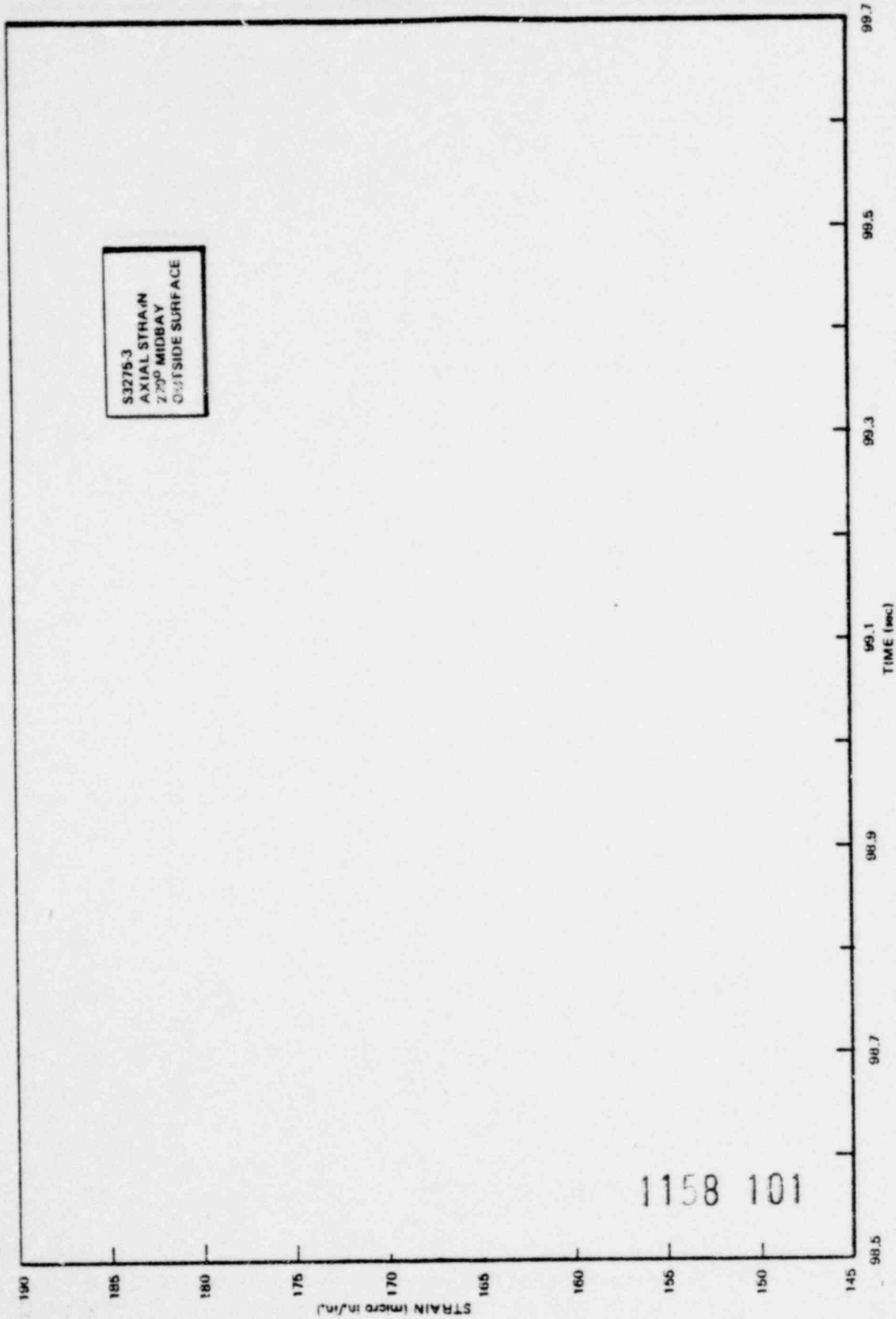

Figure 6.3.2-5. Wetwell Shell Axial Strain During Chugging - 290° Midbay (Small Steam Break Test - M1)

*Proprietary information deleted

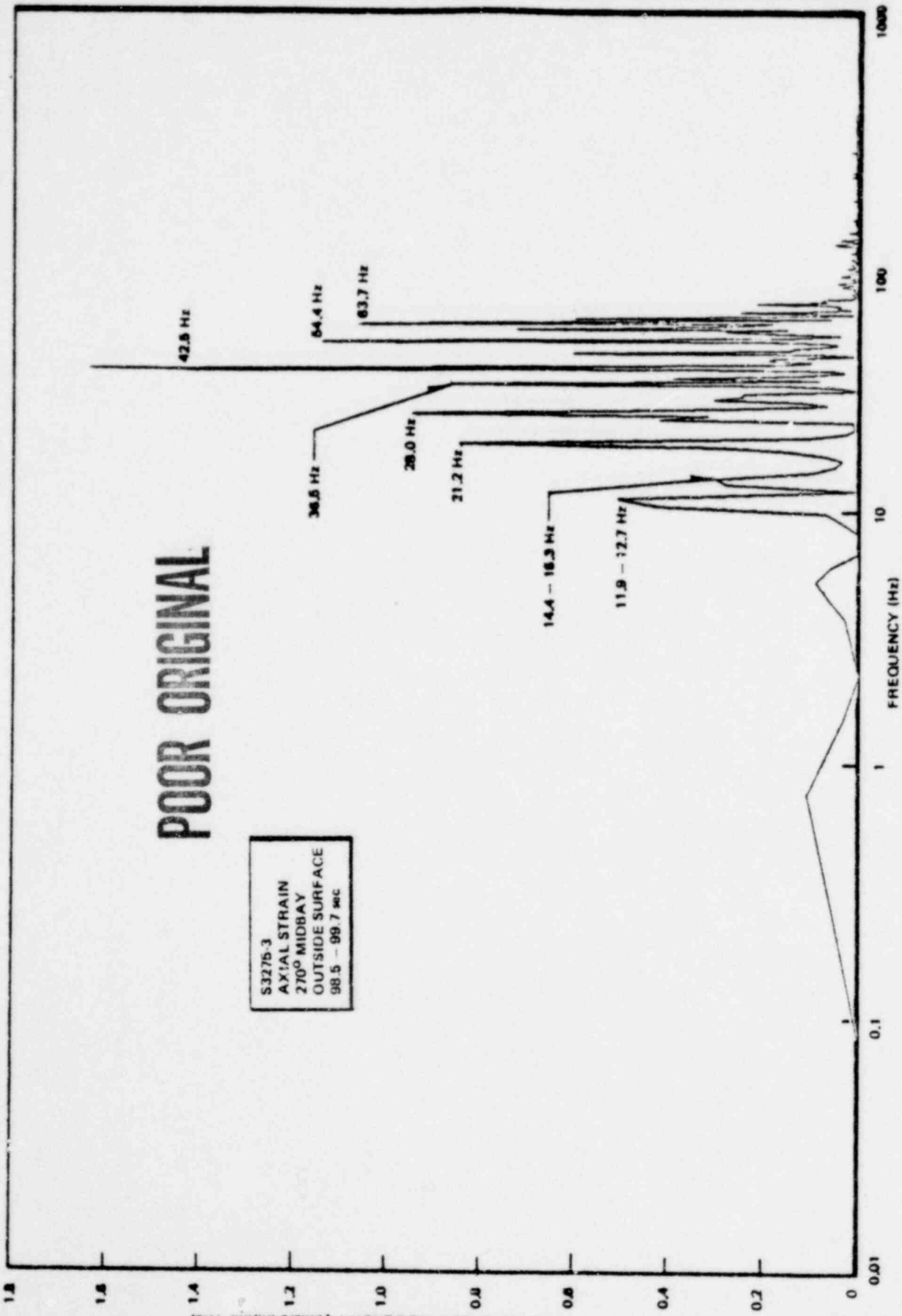

Figure 6.3.2-6. Power Spectral Density of Wetwell Shell Axial Strain

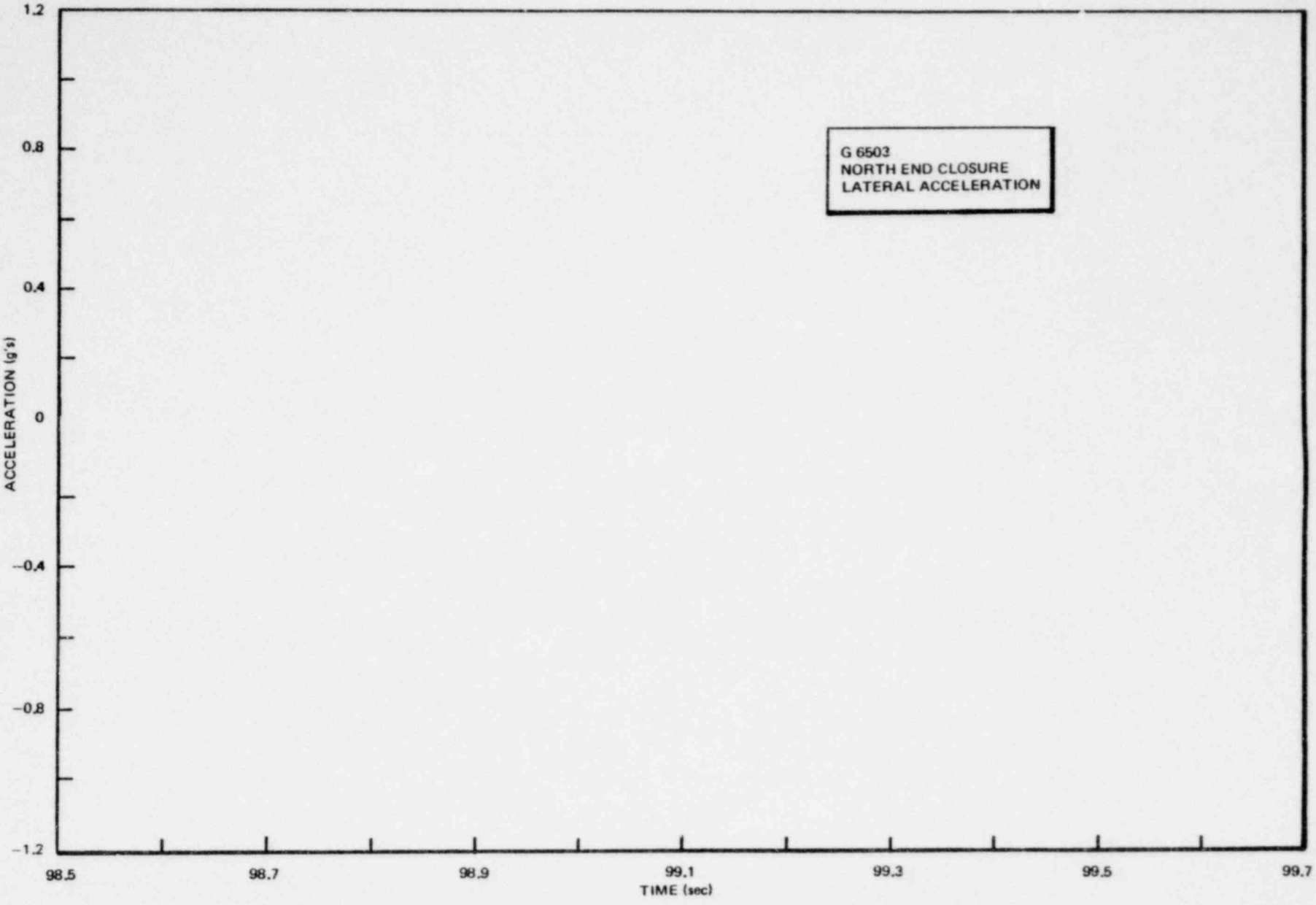

Figure 6.3.2-7. Lateral Acceleration of North End Closure During Chugging (Small Steam Break Test - M1)

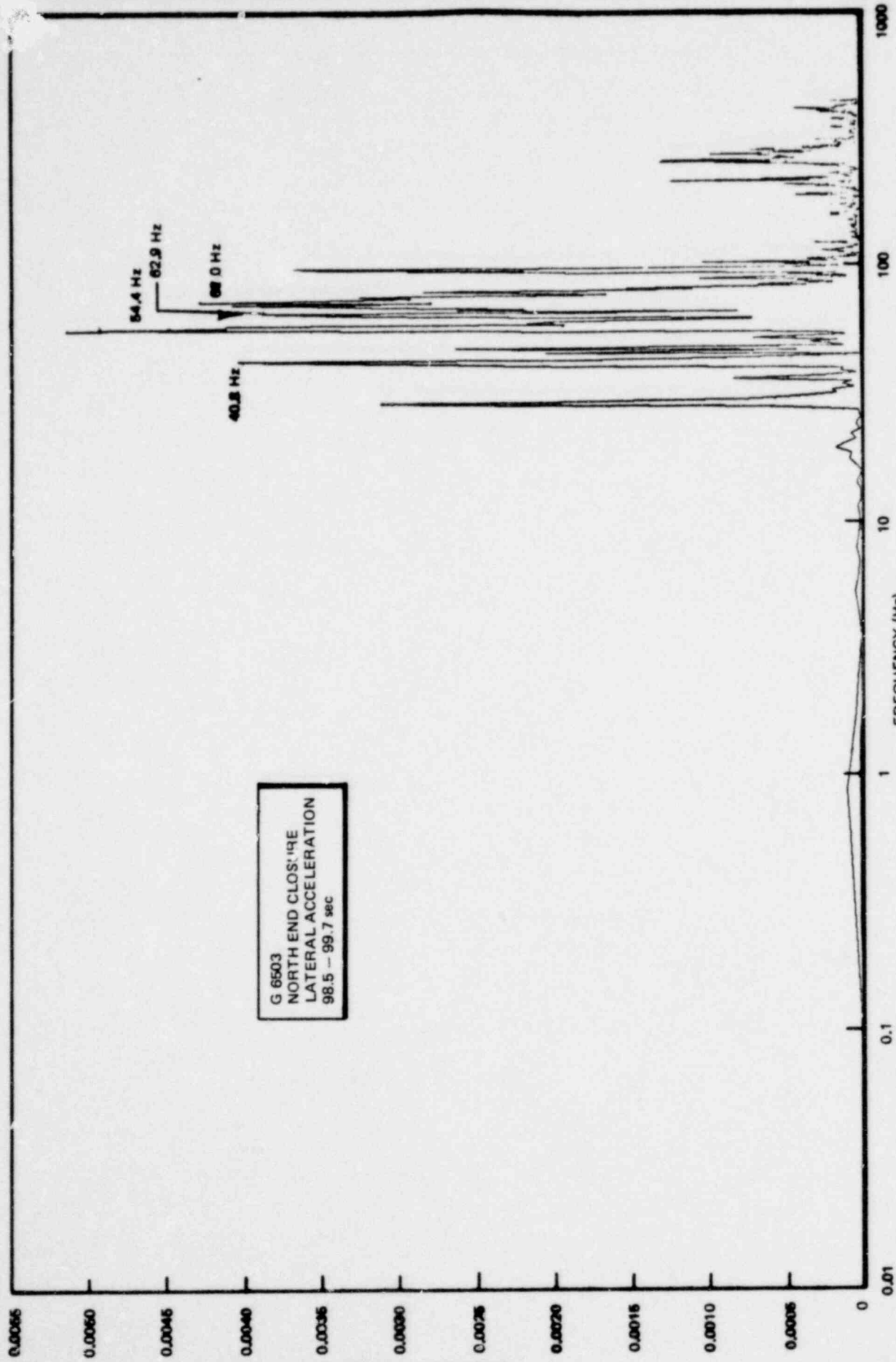

Figure 6.3.2-8. Power Spectral Density of North End Closure Lateral Acceleration

6.4 FLUID-STRUCTURE INTERACTION

Pool boundary pressures measured in FSTF tests reflect hydrodynamic phenomena and also, potentially, the coupled pool-structure response. This last effect is referred to as fluid-structure interaction (FSI) and arises from the mutual effects of transient fluid pressure and structural response on each other. FSI effects result in a modification of the pressure measured at the pool boundary relative to the pressure that would be measured if there were no structural response (i.e., if the structure were rigid and the pressures were defined entirely by hydrodynamic phenomena and pool acoustic effects). Modification of transient fluid pressures related to hydrodynamic phenomena may involve amplification or attenuation of pressure magnitudes and an alteration of the dominance of various frequency components.

A number of structural response modes of FSTF may introduce FSI effects into the measured pool boundary pressures. The rigid body vibration of the wetwell on its support columns (considering the wetwell itself to be rigid) may affect pool pressures due to pool inertia. Vibration of the facility's wetwell end closures could affect pool pressures, at least locally, due to the dynamic motion of the end closure wall into the adjacent fluid. (Note that this effect is unique to FSTF and is not prototypical for actual plants). A similar effect may arise from the response of the wetwell shell. Fluid-structure interaction effects associated with the shell response can be prominent if resonant frequencies of the coupled pool-structure system are excited.

FSTF was instrumented to measure pressure, acceleration and displacement at numerous locations on the wetwell shell and ring girders. These measurements serve as the primary data base for the investigation of fluid-structure interaction effects. Strain measurements were also made at numerous locations and these measurements provide valuable supporting data. Exact instrument locations and specifications are detailed in Subsection 3.4.

In the following, selected data for condensation oscillation (CO) and chugging will be investigated with respect to FSI. The purpose of this investigation is to provide summaries of the data to aid separate investigations in establishing the significance of FSI effects. No attempt is made to quantify the extent of fluid-structure interaction effects for the FSTF.

6.4.1 FSI Effects During Condensation Oscillation

The large liquid break test (M8) serves as the basis for investigation of FSI effects during CO. The largest amplitude pressure oscillations observed during the course of testing occurred during the CO phase of the large liquid break test. More specifically, data analysis will be limited to the period from 31 to 32 seconds of the large liquid break test. Prominent structural responses were observed during this period.

In the analysis which follows, it will be shown that:

a. FSI effects due to the rigid body vibration of the wetwell on its support columns and end closure vibration do not appear to be important during CO.

b. FSI effects related to wetwell shell vibration are evident during CO. Several facets of the data provide such evidence. Frequencies are observed mutually in pool pressure and shell response data near the 9.5, 11.0, [illegible] and 19.5 Hz shell resonant frequencies determined from shake [illegible]s of the FSTF. Further, when pool pressure and shell acceleration oscillations are of the same frequency, it can be observed that pool pressure increases as the shell accelerates into the pool. This data trend suggests that the pool pressure is at least partly induced by wall motion.

6.4.1.1 Vent and Pool Boundary Pressures.

1158 106

Comparison of downcomer and pool boundary pressures provides a first level assessment of whether or not there is reason to believe that the hydrodynamic

source pressure has been modified at the wall by wall motion. Examples of downcomer and pool boundary pressures during CO are presented in Figures 6.4.1-1 and -2, respectively.* Power spectral density distributions (PSDs) corresponding to these downcomer and pool pressures are presented in Figures 6.4.1-3 and -4. General similarities between the downcomer and pool pressures are apparent from comparisons of the time history and PSD plots. More specifically, most of the signal power for both the downcomer pressure and pool pressure is concentrated at 4.8 Hz (compare Figures 6.4.1-3 and -4). Further, the fundamental frequency components of the downcomer and pool pressure, 4.8 Hz, appear to be very nearly in phase (compare Figure 6.4.1-1 and -2).

The positive pressure spikes superimposed on the low frequency component of the pool pressures constitute one facet of the data which suggests that FSI effects are present. In Figure 6.4.1-2, two of these spikes can be observed at about 31.38 and 31.62 seconds. At both instants, the pool pressure is considerably greater than the downcomer pressure. For example, at 31.62 seconds the downcomer pressure is approximately +3 psi while the pool pressure is approximately +8 psi. The pulse width of the pool spikes (20 to 30 milliseconds) suggests the presence of frequency components from about 16 to 25 Hz in the pool pressure data. The PSD of the pool pressure (Figure 6.4.1-4) indicates frequency components in the range of 7 to 27 Hz, though, the signal power associated with frequencies in this range is not great and therefore they are not sharply defined. Higher frequency components are also in evidence in the PSD of the downcomer pressure (Figure 6.4.1-3). In this case, they appear in the range from 7 to 20 Hz.

6.4.1.2 Rigid Body Response.

Figure 6.4.1-5 illustrates the responses of the wetwell support columns and ring girders during CO. In this figure the outside support column axial strain and ring girder bottom center acceleration and displacement are shown concurrently.

*These pressure transients were processed with a linear trend removal routine (based on linear regression data fitting). Hence, only the dynamic component of the signal is represented. All data presented in Subsection 6.4 has been processed in a similar manner unless otherwise noted.

Peak values of axial strain, acceleration and displacement occur at approximately 31.62 seconds, which is the time (for the 31-to 32-second period) when the peak download is observed. These peak values are rather low; being 65 in/in (compression) for axial strain, 3 g's (upward) for ring girder acceleration and 40 mils (downward) for ring girder displacement. Both the column axial strain and ring girder displacement data suggest that the rigid body response of the wetwell is at the lowest frequency associated with the pool pressures (4.8 Hz). A PSD of the column axial strain, shown in Figure 6.4.1-6, delineates this point. Most of the signal power of the axial strain is at 4.8 Hz - corresponding to the fundamental frequency component of the downcomer pressure signal (see Figure 6.4.1-3). Appreciable ring girder acceleration levels are seen only at higher frequencies (50 Hz or greater based on the time data at 31.6 seconds). These higher frequency accelerations probably result from high frequency ringing of the wetwell shell and ring girder so do not reflect the rigid body response of the wetwell.

On the basis of column strain, it is possible to infer the rigid body displacement of the wetwell and then, in turn, to infer the rigid body acceleration of the wetwell at a frequency of 4.8 Hz. (The ring girder displacement and acceleration measurements are not good indicators of the rigid body motion of the wetwell because they are influenced by wetwell vibration modes - ovalization of the shell and ring girders, etc.). The values inferred for rigid body displacement and acceleration are, respectively, 7 mils and 0.02 g's. If the wetwell shell is considered rigid and assuming that both the wetwell and entire pool accelerate at 0.02 g, then the pressure at the bottom of the pool, due to the effect of pool inertia, would be calculated to be about 0.1 psi [acceleration (0.02 g) times maximum depth (12.4 ft) times density of water (62.4 lb/ft^3) x 1/144 in^2/ft^2]. Hence, the influence of the rigid body response of the wetwell on pool pressures is considered to be insignificant.

6.4.1.3 End Closure Response.

Lateral acceleration of the end closure* and ring girder, at the north end of the wetwell, are shown together in Figure 6.4.1-7. Pool pressure, just adjacent

*The accelerometers are located on the outside plates; 32 inches off the wetwell vertical centerline; and about midway between the wetwell horizontal centerline and wetwell bottom. At this location there is an intersection of vertical and horizontal ribs of the end closure "egg crate" structure (refer to Subsections 3.3 and 3.4).

to the end closure and at the bottom of the wetwell, is also shown for reference. Figure 6.4.1-8 shows the same type of data for the south end of the facility. In these Figures it can be seen that (1) the peak end closure and ring girder lateral acceleration levels are low (less than 3 g's maximum) and (2) no strong relationship between the pool pressure adjacent to the end closure and the end closure vibration is generally indicated.

The data for the south wetwell end (Figure 6.4.1-8) are particularly graphic in illustrating the two observations made above. At about 31.6 seconds, the peak end closure and ring girder lateral acceleration at the south end are observed (about +2.5, -2.0 g's for the end closure and about +2.8, -1.6 g's for the ring girder). The peak pool pressure, at the bottom of the wetwell and adjacent to the end closure is not observed until after the end closure vibration has ceased (this pressure peak lags the peak end closure acceleration by about 10 milliseconds). Further, several other pressure spikes occur, over the period from 31 to 32 seconds, with little indication of a significant concurrent end closure acceleration. Therefore, there is little reason to believe that the dynamic response of the end closures contributes significantly to pool pressure fluctuations during condensation oscillation.

6.4.1.4 Wetwell Shell Response.

During condensation oscillation, prominent local wetwell shell responses were observed coincident with local pool pressure fluctuations. In each of Figures 6.4.1-9 through -13, local shell pressure, acceleration and displacement are presented concurrently for the midbay circumferential positions of 120°, 150°, 180°, 210° and 240°. Local shell accelerations and displacements are measured in the radial direction (relative to the wetwell center). For reference, the pool pressure at the bottom south end of the wetwell (near the ring girder) and the south ring girder bottom center acceleration and displacement are presented in Figure 6.4.1-14. The multifrequency composition of the pool pressures, throughout the pool, is evident from these figures. However, the fundamental CO frequency, 4.8 Hz, is generally apparent throughout the pool. Local shell response data (acceleration and displacement) is also composed of many frequency components.

Peak dynamic pool pressures and shell radial accelerations and displacements observed about midbay, over the period from 31 to 32 seconds, are tabulated in Table 6.4.1-1. The highest local pool pressure is observed at 150° with the next highest pool pressure being observed at 180°. Peak values of pool pressure tend to be lower at shell location nearer to the pool free surface with the exception of the positive peak value at 150°. Another trend that can be noted with regards to peak pool pressures is that the positive peaks are greater on the narrow-side of the torus (120° and 150°) than on the wide-side of the torus (210° and 240°). Negative pool pressure peaks are nearly the same on the narrow-side and wide-side locations of the torus. Both peak inward and outward radial shell accelerations are greater for the narrow-side of the torus than for the wide-side of the torus.

There is significant evidence to suggest that pool pressures are affected by wetwell shell responses. Referring back to Figures 6.4.1-9 through -13, it can be observed that pool pressure spikes are coincident with prominent shell accelerations. This observation is particularly apparent at 120° and 150° around the time of 31.6 seconds. What is significant from the standpoint of FSI is how pool pressures vary with shell accelerations. At both 120° and 150°, it can be observed that: (1) as the shell begins to accelerate inwards (into the pool), the pool pressure starts to rise; (2) the peak pool pressure occurs at about the time the peak inward shell acceleration is reached; and (3) as the inward shell acceleration begins to decrease, the pool pressure also starts to decrease. Such behavior is consistent with what would be expected if pressures were induced by wall motion. Further, at instants of time wherein the shell acceleration is peak outward the dynamic component of the pool pressure is either near zero or slightly negative. At these instants of time, it might be expected the pool pressure would decrease even further if it were not for the influence of the general rise in pool pressures associated with the fundamental CO pressure signal - the oscillation at 4.8 Hz apparent in the pool pressures. Consideration of these trends suggests that the pressure "spikes" superimposed on the fundamental CO pressure signal are due in some part to wetwell shell responses.

The phase relationships between pool pressures and shell responses at adjacent locations also suggests that FSI effects are present. Comparing the time histories present in Figures 6.4.1-9 through -13 it can be noted that pool pressures and shell responses at adjacent locations are not in phase (with the exception of the 4.8 Hz component of the pool pressure which is in phase throughout the pool). This observation, together with the previous observation that the local pool pressure follows the local shell acceleration, implies that the pool pressure (with the exception of the 4.8 Hz component) follows the local shell response and hence FSI effects are present.

A graphic illustration of (1) the dynamic effect of shell acceleration on pool pressure and (2) the rather localized nature of this effect, is provided by Figures 6.4.1-15 through -20. In these figures, the midbay distribution of pool pressure and shell radial acceleration are shown for five instants of time covering an interval of 21 milliseconds. Illustration of the two points made above is best provided by the 150° and 180° locations. At these locations, the pool pressure and shell accelerations are much more prominent than at other locations around the shell during the time period under examination. From 31.603 to 31.612 seconds (Figures 6.4.1-16, -17 and -18), the pool pressure at 150° rises significantly as the shell accelerates into the pool and then falls (almost to zero) as the shell accelerates away from the pool. During this time period, the pool pressure and shell acceleration at 180° indicate little change. The pool pressure at 180° rises by about 3 psi between 31.612 and 31.615 seconds although there is little change in the local shell acceleration (see Figures 6.4.1-18 and -19). However, the pressure rise at this time is due to the rise in the 4.8 Hz cycle of the CO source pressure (refer to Figures 6.4.1-1 and -2). Between 31.615 and 31.620 seconds, the shell accelerates inward at 180° with the pool pressure reaching a maximum value at 31.620 seconds. Although the rise in pressure at 180° at this time is partly attributable to the CO source pressure nearing its maximum value, the significant difference in the peak pool and peak downcomer pressures at this time (pool pressure - 8 psi; downcomer pressure - 3 psi) indicates that effect of the shell motion is pronounced.

PSDs were utilized to identify the frequency content of pool pressure and structural response data. Example PSDs for shell radial displacement and acceleration are presented in Figures 6.4.1-21, -22 and -23. An example pool pressure PSD was previously shown in Figure 6.4.1-4. The frequencies associated with pool pressures, shell displacements and shell accelerations (all at midbay) are tabulated in Table 6.4.1-2. Only frequencies of 20 Hz or less could be identified from PSDs of pool pressure and shell displacement data. The frequencies identified from PSDs of shell acceleration data represent a broader frequency bandwidth. The shell acceleration data includes several high range frequencies (32-34 Hz, 50-60 Hz and 68 Hz) as well as lower range frequencies (12 to 20 Hz). It should be noted that for the high range shell acceleration frequencies (above 20 Hz) only the three most prominent frequencies Hz are tabulated in Table 6.4.1-2.

Higher frequencies which appear in PSDs of shell acceleration data, are in some instances, clearly present in time histories of pool pressure and shell displacement data even though they are not present in their related PSDs. For example, around 31.6 seconds a frequency of 65 Hz is clearly present in both pool pressure and shell acceleration time histories at midbay 150° (see Figure 6.4.1-10). This frequency also appears, though less conspicuously in the midbay 150° displacement time history. As this frequency is highly damped (only two cycles), the signal power associated with it is small. In the case of PSDs of the pool pressure and shell displacement data, the 65 Hz frequency is totally obscured by the signal power associated with the low frequencies (particularly the 4.8 Hz component).

The frequency content of the shell displacement and acceleration data suggests that several wetwell shell resonances are excited by CO. Comparison of the frequencies tabulated in Table 6.4.1-2 with shell resonant frequencies identified by shake tests of FSTF in (Appendix D) indicate that shell resonances at frequencies of 9.7, 11.0, 15.0 and 19.5 Hz are excited. The participation of the 11.0 Hz resonance appears to be more limited than the other resonances; this frequency does not appear in pool pressure and shell response data to the same extent as frequencies corresponding to other shell resonances. The fact that shell resonances are excited implies that FSI effects are present. However, the extent of FSI effects associated with each shell resonance is not readily apparent.

From linear system considerations it is expected that the excitation of shell resonances would require the frequency content of the pressure source to include components corresponding to the shell resonances excited. As was previously discussed in Subsection 6.4.1.1, the frequency content of the pressures measured in downcomer No. 6 was dominated by the 4.8 Hz frequency, but other frequencies in the range from 7 to 20 Hz were indicated. In examing PSDs of all eight downcomers (31 to 32 second period) only the frequencies of 9.5 and 12.4 Hz appear often in the 7 to 20 Hz range. Pressure signals at these frequencies are probably responsible for exciting the 9.7 and 11.0 Hz shell resonant frequencies.

The frequency content of the downcomer pressure measurements give no clear indication of why shell resonances at 15.0 and 19.5 Hz are excited or why higher frequencies are observed in the shell acceleration data. The downcomer pressure measurement reflects the fundamental frequency associated with CO phenomena and related vent system acoustics but cannot reflect the frequency content associated with phenomena such as bubble collapse.

In addition to the frequencies corresponding to shell resonances, two other prominent frequencies are observed in the pool pressure and shell response data - 4.8 and 13.4 Hz. As was discussed before, 4.8 Hz corresponds to the fundamental frequency of the CO source pressure (inferred from downcomer pressure). Although this frequency is the dominant component for the pool pressures, it is generally a less signifcant frequency component for shell displacements. At 180°, the 4.8 Hz component of the shell displacement has nearly as much signal power associated with it as some of the higher frequency components present (see Figure 6.4.1-21). However, for shell displacements at 150° and 210°, the signal power associated with the 4.8 Hz frequency component is much less than that associated with higher frequency components. No significant signal power is even indicated at 4.8 Hz for shell displacements at 120° and 240°; hence, the wetwell shell response to the 4.8 Hz frequency pressure signal appears to be very restricted.

In contrast, the signal power associated with 13.4 Hz is quite significant for shell displacements at a number of locations (180°, 210° and 240°). This frequency is also observed at 180°, 210° and 240° locations for the shell acceleration data but only at the 180° and 240° locations for the pool pressure data.

To illustrate wetwell deformations associated with shell resonances excited during CO, radial displacements of the wetwell shell about midbay (at 120°, 150°, 180°, 210° and 240°), about the south ring girder (at 0°, 90°, 180° and 270°) and along the bottom of the wetwell (north and south ring girders; north and south quarterbay; and midbay) were plotted for five instants of time. Figures 6.4.1-24 through -29 show the wetwell shape at each of the five instants of time. The period of time covered by these plots begins, roughly when the dynamic pressure is approximately zero (relative to the 4.8 Hz pressure cycle) and extends through a quarter of the 4.8 Hz cycle (when the peak midbay bottom pressure occurs).

At 31.582 seconds the dynamic component of the pool pressures is near zero and the configuration of the wetwell corresponds, nearly, to its static shape (see Figure 6.4.1-24).

Eight milliseconds later, at 31.590 seconds (Figure 6.4.1-25), the wetwell shell appears to ovalize at midbay with the major axis inclined at about 30° to the vertical (through the 150° position). Along the bottom the wetwell is drawn in at north quarterbay and midbay but nearly undisturbed at south quarterbay, suggesting that the outward deformation of the shell around 150° is more pronounced for the north section of the wetwell. There is some ovalization of the ring girder at this time (about the horizontal plane), but the principal ring girder motion appears to be rigid body (towards the inside or in the eastward direction).

Indications of the participation of a "breathing" type of mode of the wetwell shell are seen at 31.599 seconds (Figure 6.4.1-26). The shell motion at 180°, 210° and 240° are out of phase with the shell moving inward at 210° but outward at 180° and 240°. An asymmetric mode shape is seen along the bottom of the wetwell with north quarterbay moving outward; south quarterbay moving inward; and midbay being a null point. Little change is noted at the ring girder compared to the previous instant examined.

Little change to the shape of the wetwell at midbay is apparent at 31.607 seconds (Figure 6.4.1-27). However, it should be noted that the shell deflection reaches

a maximum at 150°. An inverted "beam bending" shape is seen along the bottom of the wetwell as the ring girder ovalizes along the vertical axis but little downward deflection is seen at midbay bottom. Since little deflection is noted at the top of the ring girder, the ring girders must also be experiencing rigid body motion downward at the same time.

For the next instant, 31.615 seconds (Figure 6.4.1-28), the shape of the wetwell still suggests a "breathing" mode, but at this instant the maximum outward shell deflection is seen at 180° rather than at 150° (where the shell is now deflected slightly inward). The ring girder shape remains about the same as for the previous instant examined. A non-symmetric shape is seen along the bottom of the wetwell with greatest outward deflections at south quarterbay and midbay.

At the last instant examined, 31.620 seconds (Figure 6.4.1-29), the wetwell shape suggests shell ovalization along the vertical axis but with "breathing" modes still present as evidence by the outward deflection at 120°. Correspondingly, the ovalization of the south ring girder, also along the vertical, is at a maximum. The non-symmetric shape along the bottom of the wetwell is maintained; however, the maximum outward deflection is now at midbay rather than south quarterbay.

The analysis above illustrates the possible participation of various breathing and ovalizing shell modes during CO. Shell deformations at any instant are, of course, a result of various combinations of participating shell resonances. As was discussed previously, the frequency content of the shell response data suggested that the resonant frequencies of 9.7, 11.0, 15.0 and 19.5 Hz are excited. Modal shapes corresponding to each of these resonant frequencies are shown in Appendix D.

Table 6.4.1-1

PEAK DYNAMIC PRESSURES, ACCELERATIONS AND DISPLACEMENTS AT MIDBAY DURING CONDENSATION OSCILLATION (LARGE LIQUID BREAK TEST-M8; 31-32 SEC.)

Position	Pressure (psi)	Acceleration (g's)	Displacement (mils)
120°			
150°			
180°			
210°			
240°			

*

*Proprietary information deleted

1158 116

Table 6.4.1-2

FREQUENCIES OBSERVED IN POOL PRESSURE AND SHELL RESPONSE DATA DURING CONDENSATION OSCILLATION (LARGE LIQUID BREAK TEST -M8; 31-32 SEC.)

Midbay Position	Pool Pressure						
120°	4.8	8.6			15.3	19.1	
150°	4.8	8.6			16.2	19.1	
180°	4.8	8.6	11.4	13.4	16.2		
210°	4.8	7.6			15.3	18.1	
240°	4.8	7.6		13.4	15.3	18.1	

Midbay Position	Shell Displacement						
120°		9.5	11.4		15.3	20.0	
150°	4.8	9.5		13.4	15.3	18.1	
180°	4.8	9.5	11.4	13.4	16.2		
210°	4.8	7.6	10.5	13.4	15.3	18.1	
240°		9.5		13.4	15.3	18.1	

Midbay Position	Shell Acceleration					
	(Low Range: 0-20 Hz)					
120°					20.0	
150°				16.2	19.1	
180°			12.4	16.2		
210°			13.4	15.1	20.0	
240°			13.4	16.2	18.1	
	(High Range: 20-70 Hz)					
120°				55.3,	57.2	67.7
150°			48.6	51.5		67.7
180°		34.3		51.5	57.2	
210°		32.4, 34.3			56.3	
240°		34.3		50.5,	59.1	

NOTE: (1) All values in Hz
(2) PSD incremental frequency is 0.954 Hz

1158 117

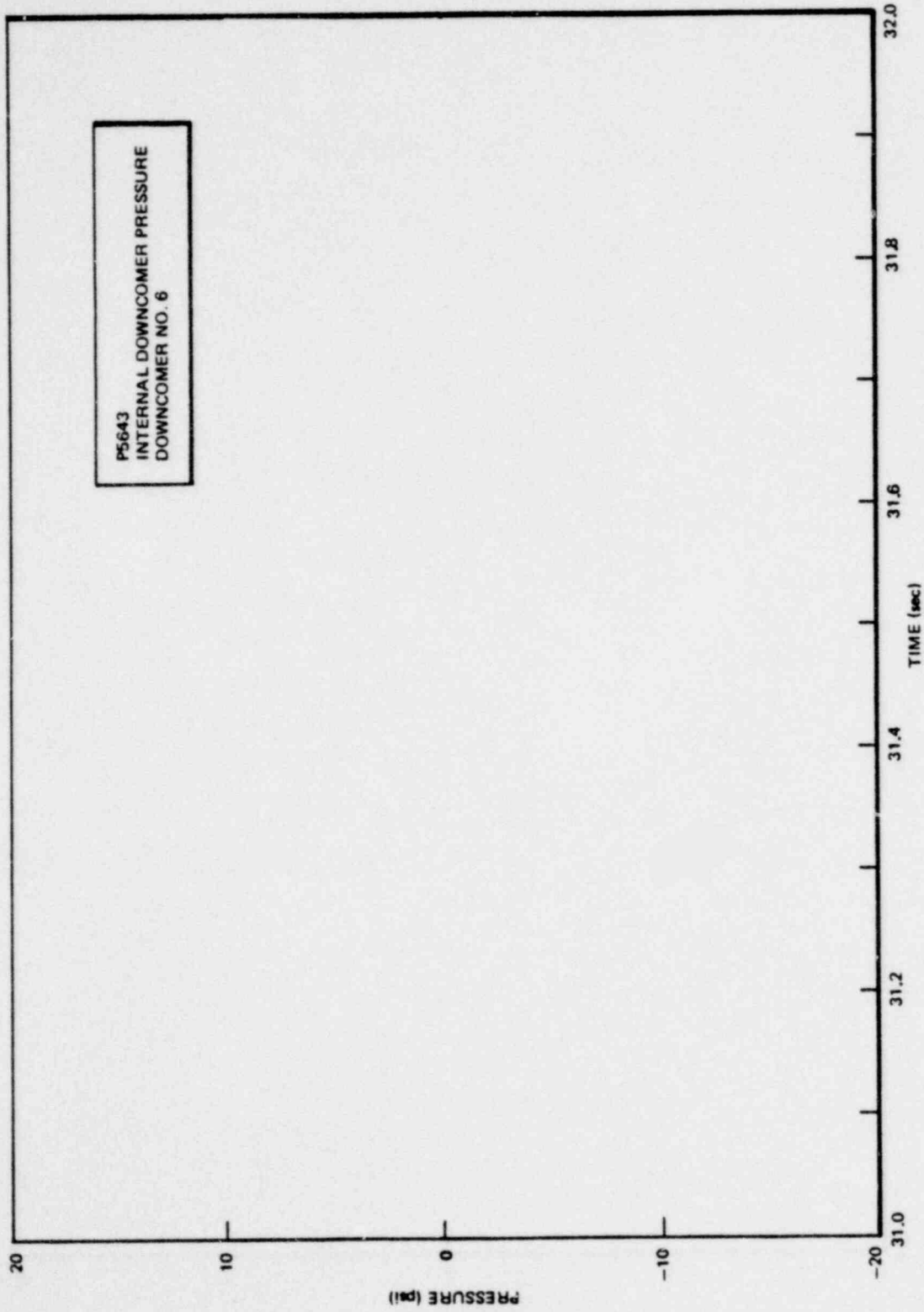

Figure 6.4.1-1. Dynamic Downcomer Pressure During Condensation Oscillation - Downcomer No. 6 (Large Liquid Break Test - M8)

*Proprietary information deleted

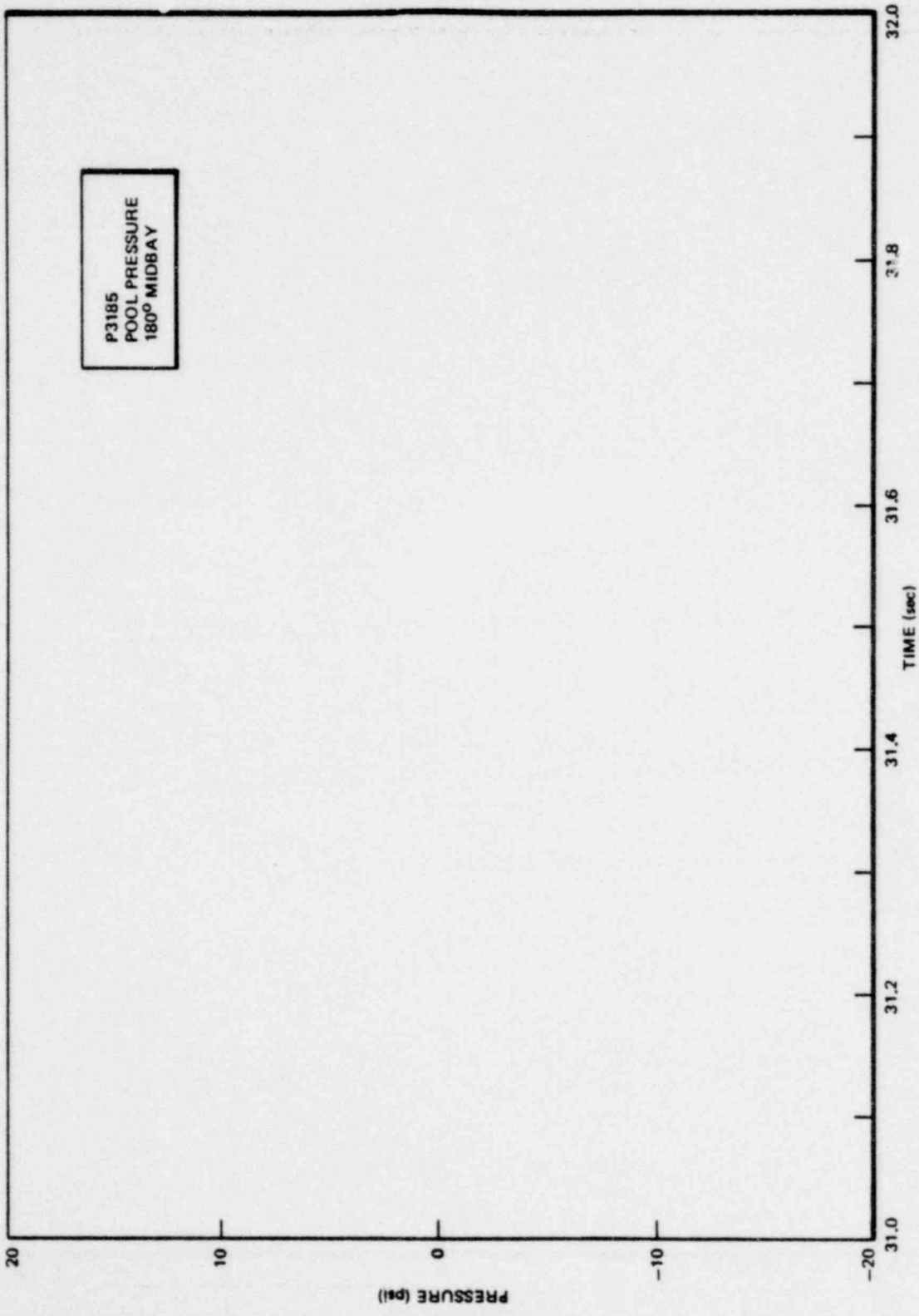

Figure 6.4.1-2 Dynamic Pool Boundary Pressure During Condensation Oscillation - 180° Midbay (Large Liquid Break Test - M8)

*Proprietary information deleted

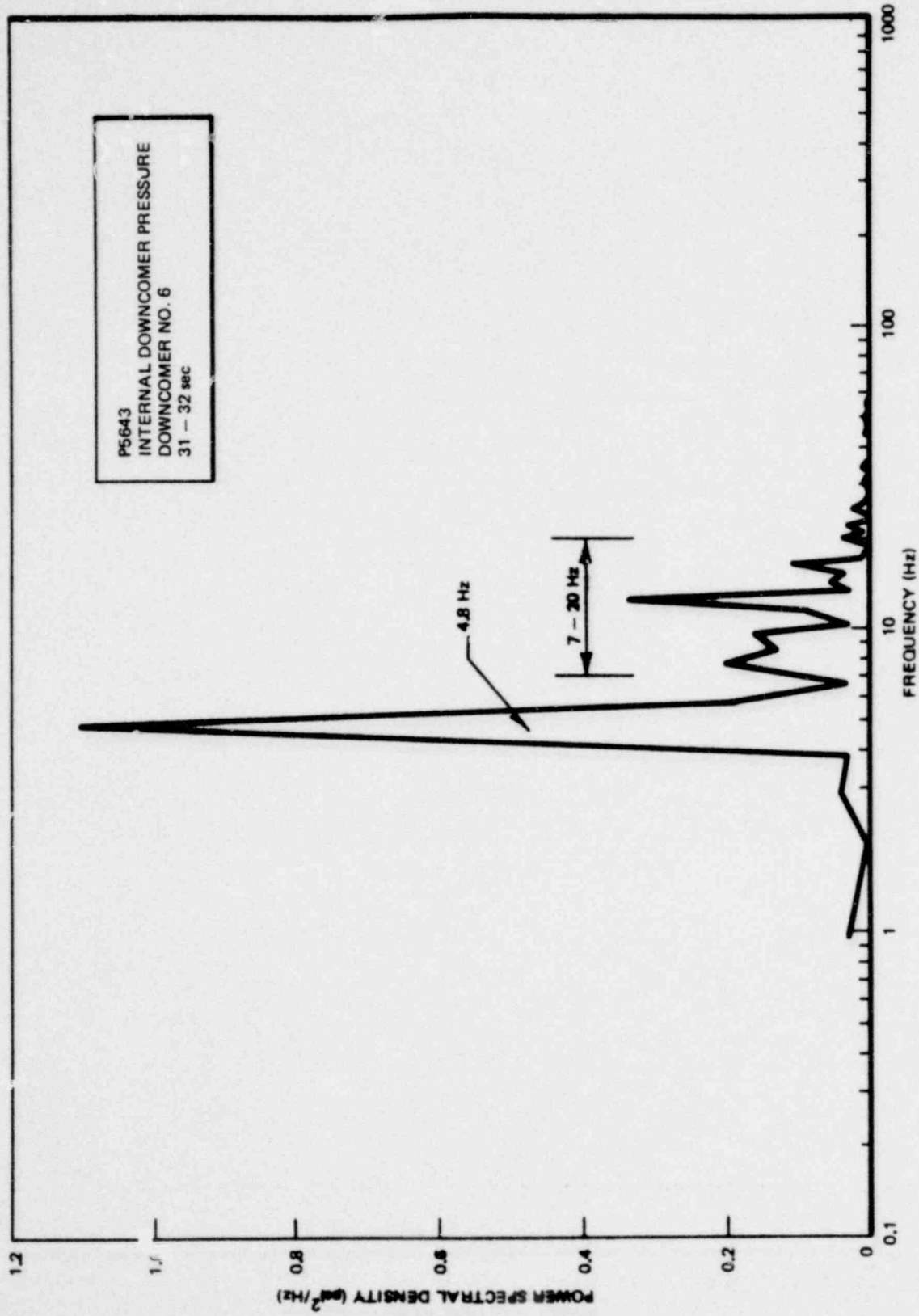

Figure 6.4.1-3. Power Spectral Density of Dynamic Downcomer Pressure (Downcomer No. 6)

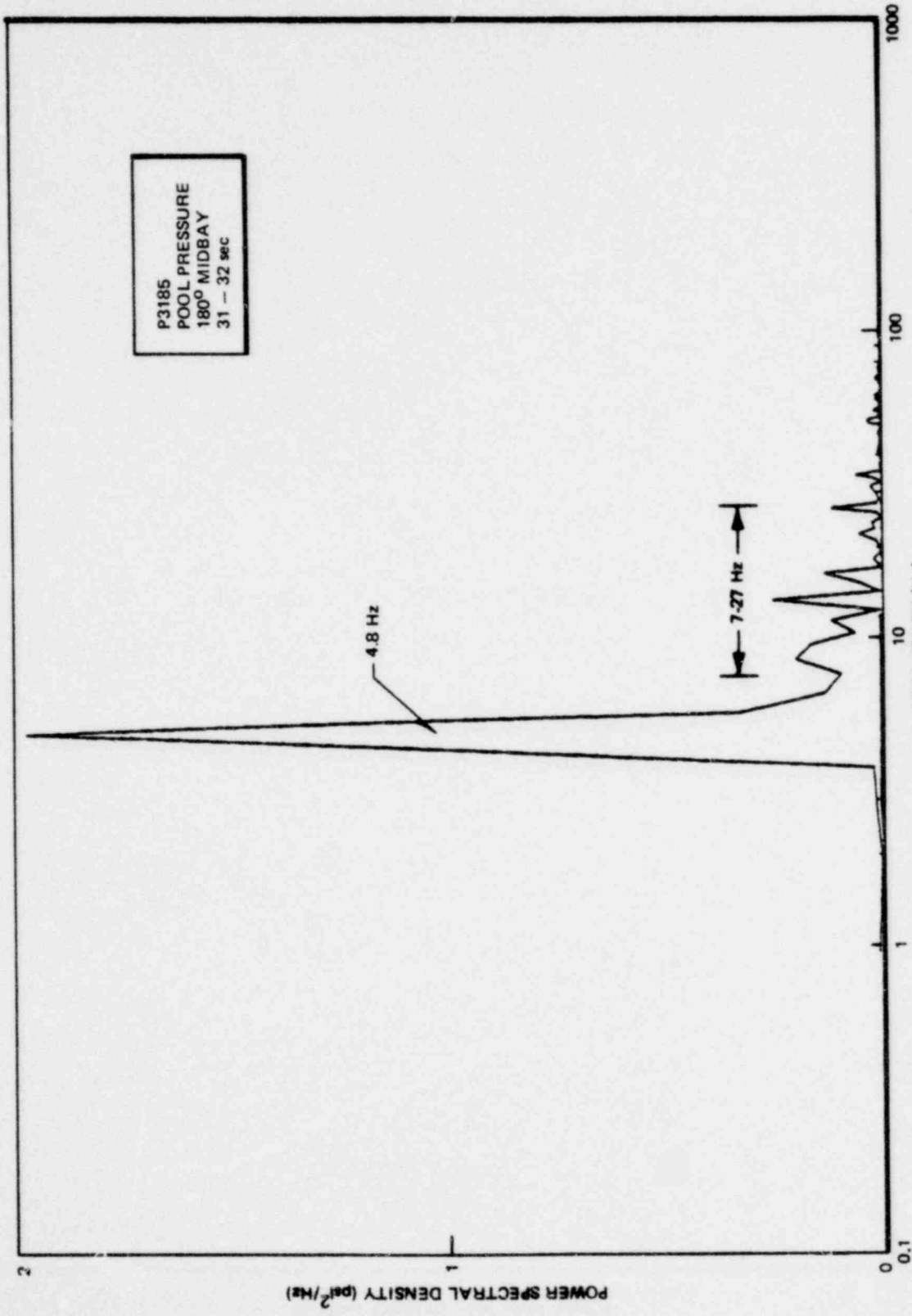

Figure 6.4.1-4. Power Spectral Density of Dynamic Pool Pressure at 180° Midbay

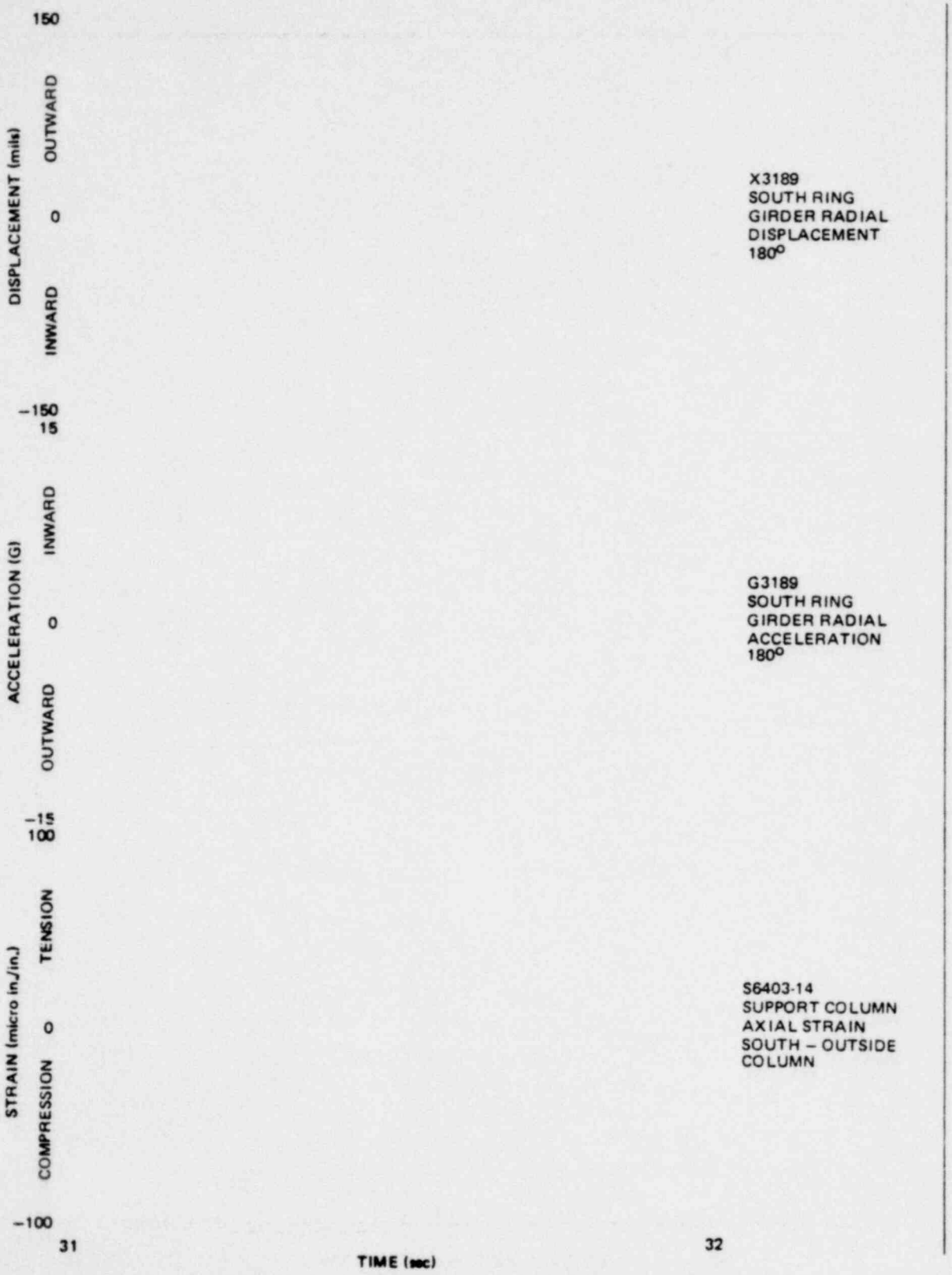

Figure 6.4.1-5. Ring Girder and Wetwell Support Column Responses During Condensation Oscillation (Large Liquid Break Test - M8)

*Proprietary information deleted

1158 122

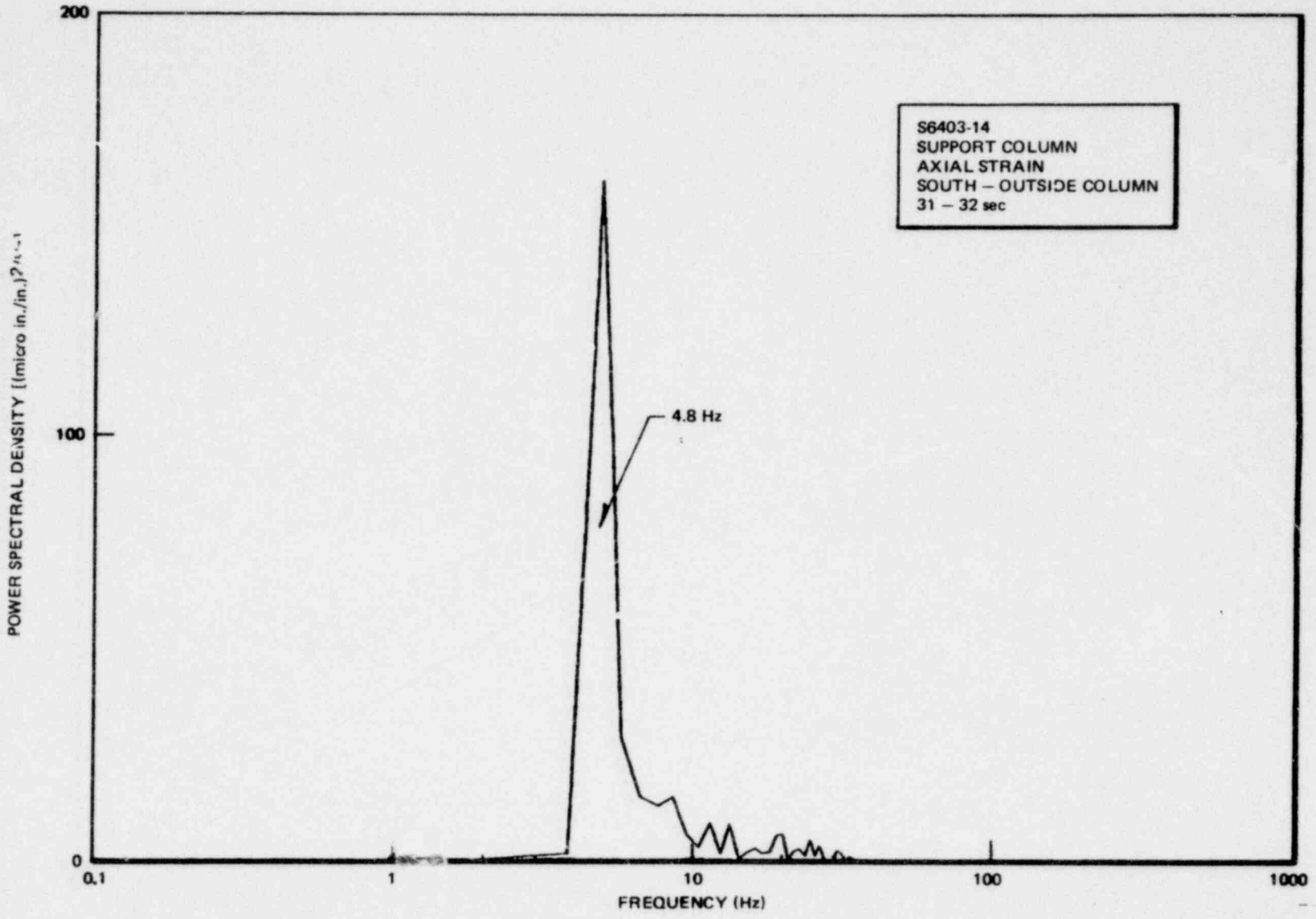

Figure 6.4.1-6. Wetwell Support Column Axial Strain Power Spectral Density

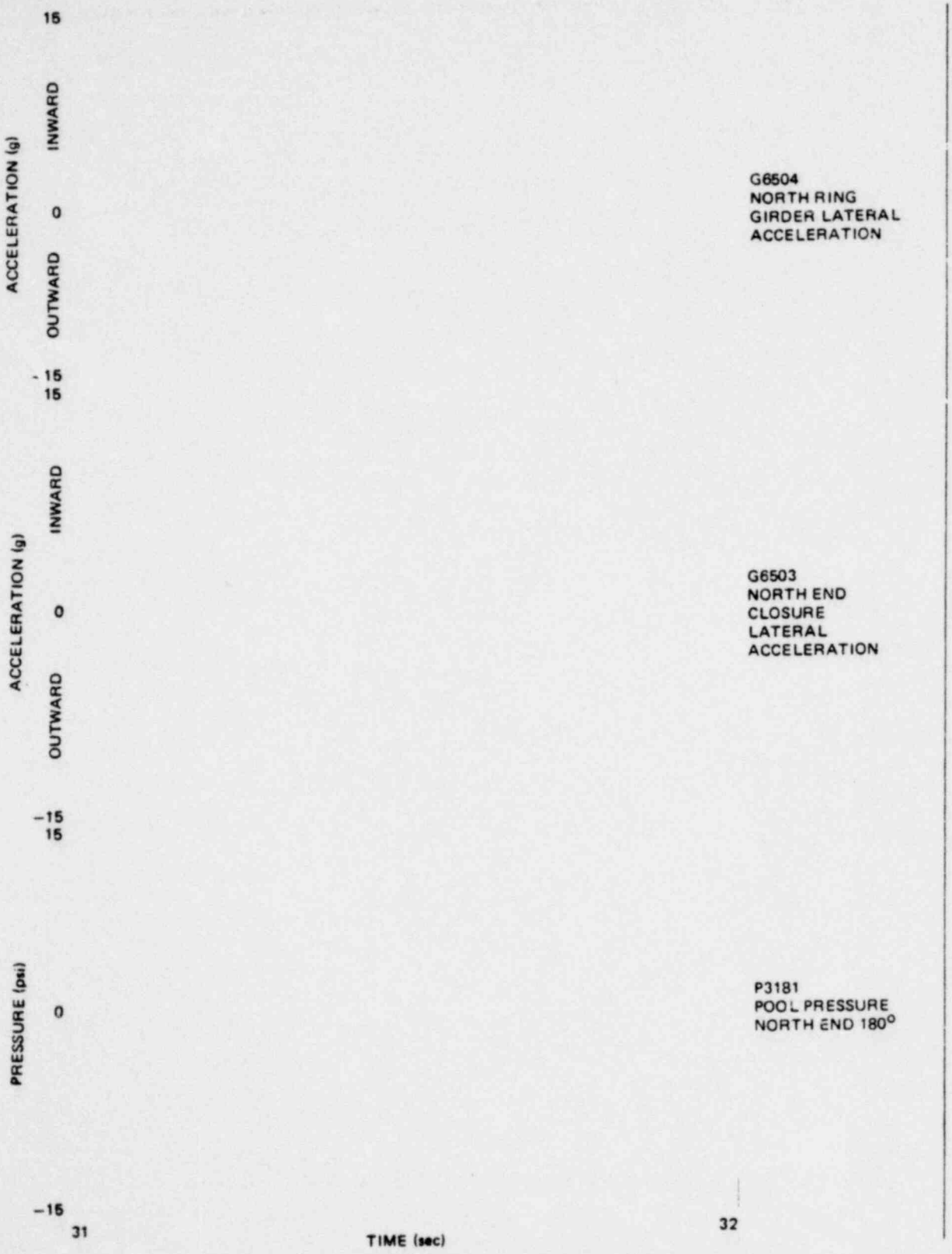

Figure 6.4.1-7. North End Closure Response During Condensation Oscillation (Large Liquid Break Test - M8

*Proprietary information deleted

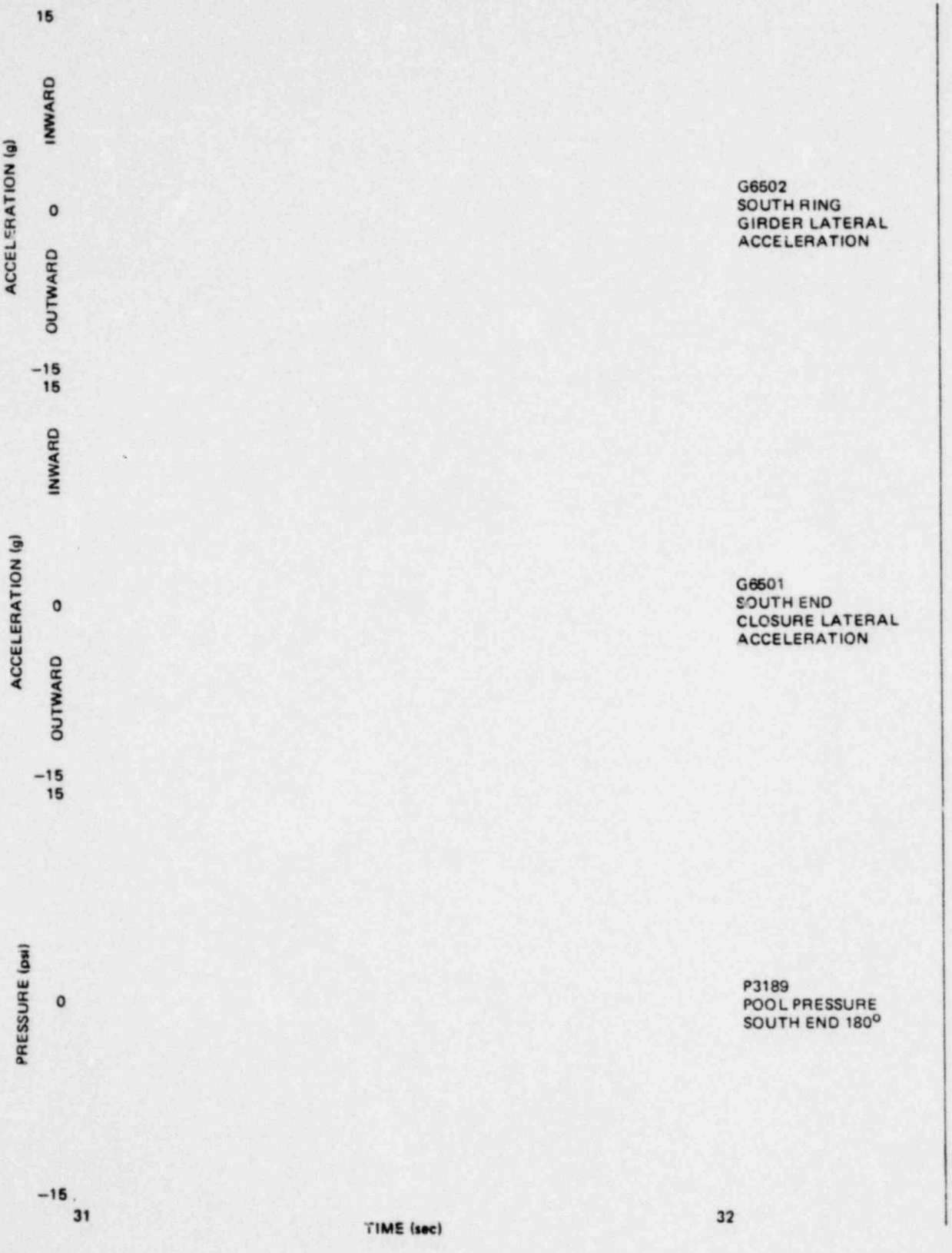

Figure 6.4.1-8. South End Closure Responses During Condensation Oscillation (Large Liquid Break Test - M8)

*Proprietary information deleted

1158 125

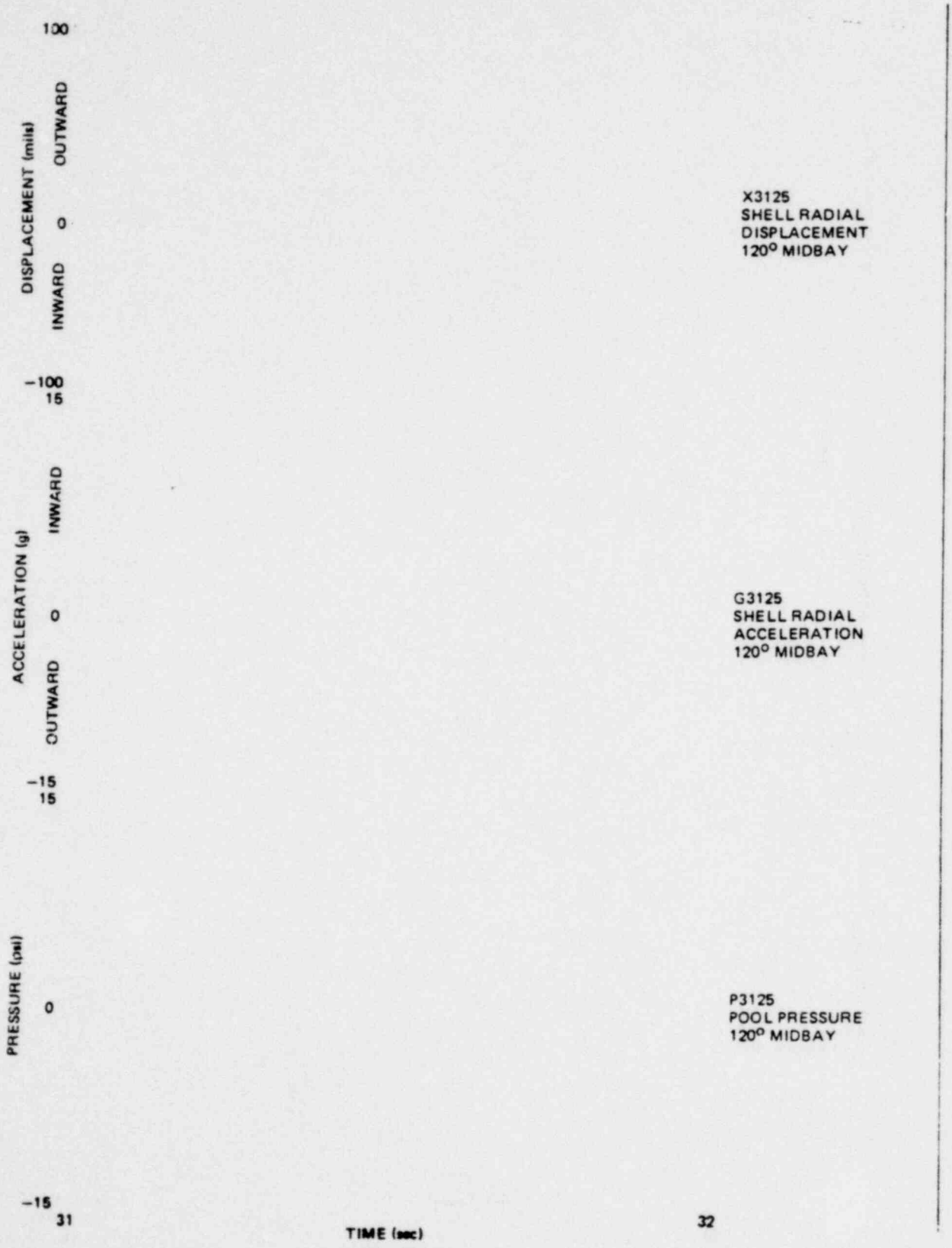

Figure 6.4.1-9. Wetwell Shell Response at 120° Midbay During Condensation Oscillation (Large Liquid Break Test - MS)

*Proprietary information deleted

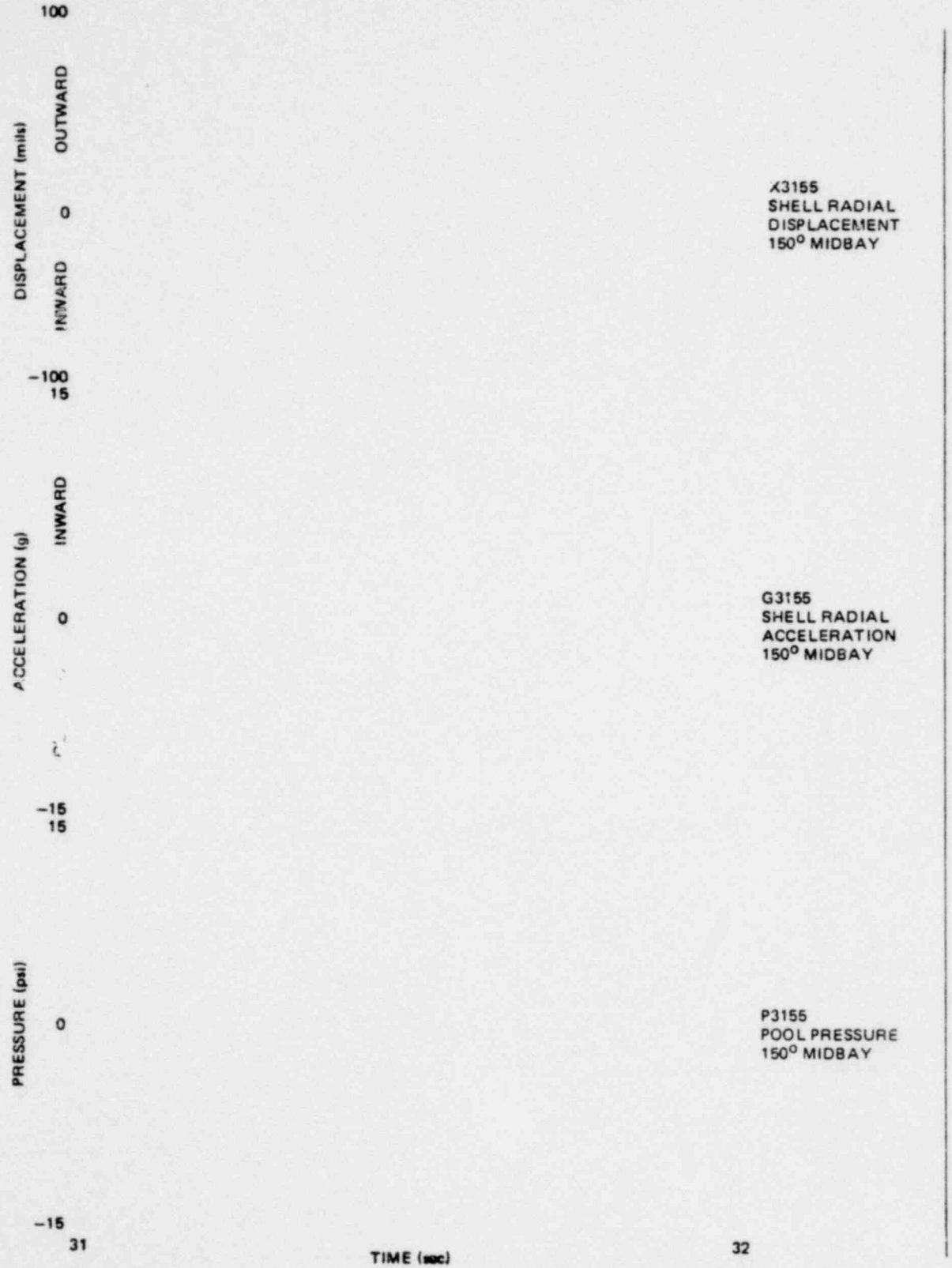

Figure 6.4.1-10. Wetwell Shell Response at 150° Midbay During Condensation Oscillation (Large Liquid Break Test - M8)

*Proprietary information deleted

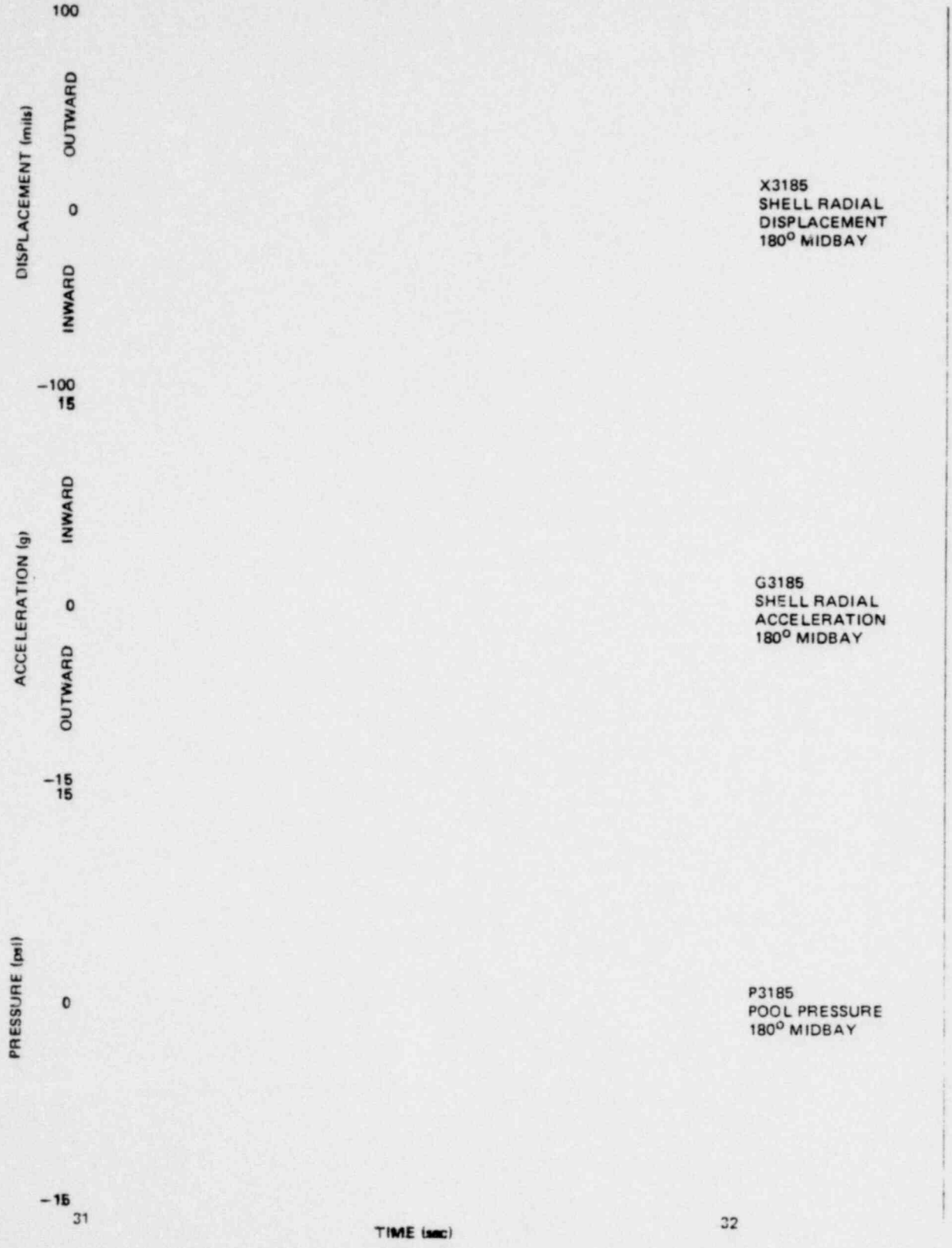

Figure 6.4.1-11. Wetwell Shell Response at 180° Midbay During Condensation Oscillation (Large Liquid Break Test - M8)

*Proprietary information deleted

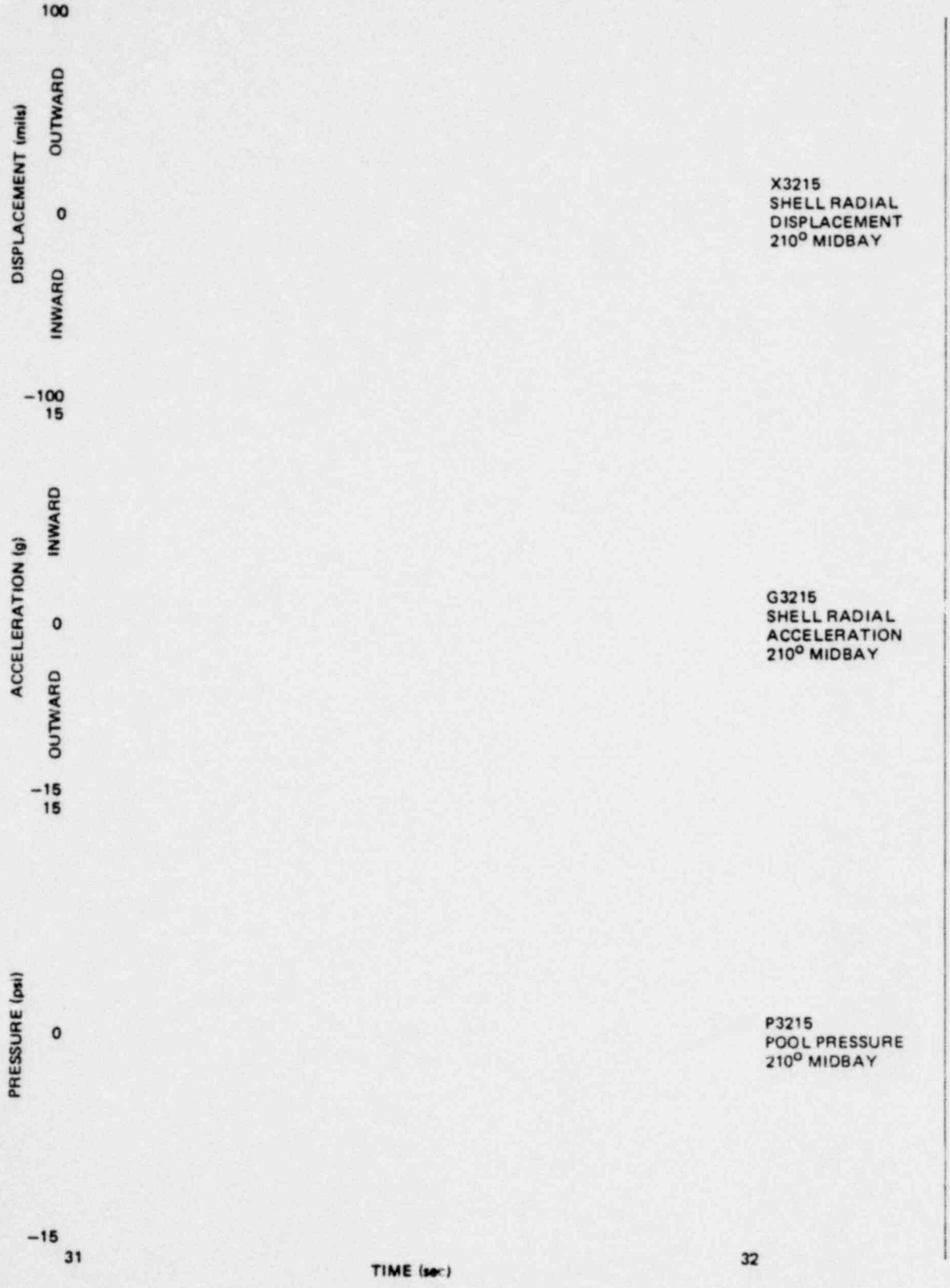

Figure 6.4.1-12. Wetwell Shell Response at 210° Midbay During Condensation Oscillation (Large Liquid Break Test - M8)

1158 129

*Proprietary information deleted

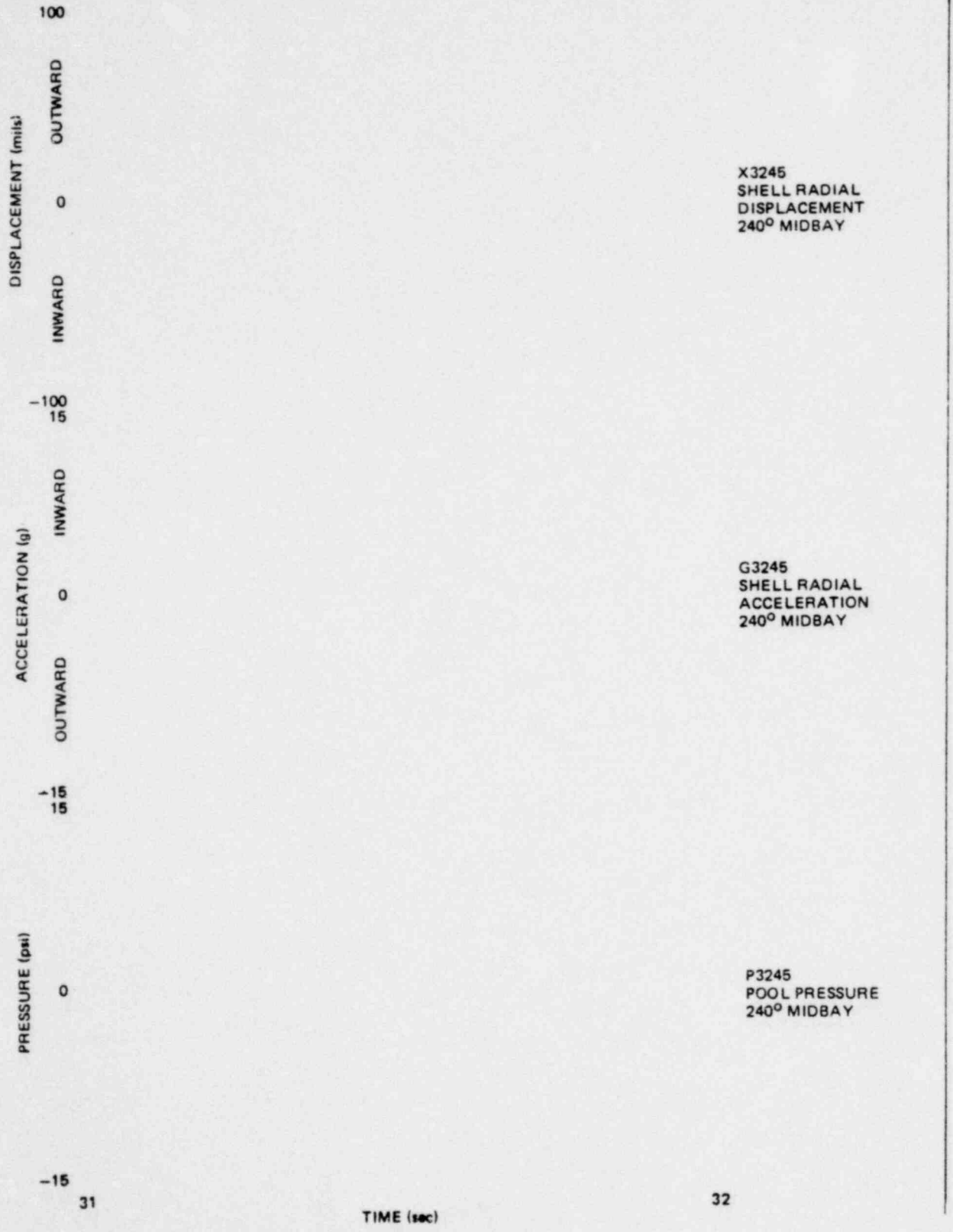

Figure 6.4.1-13. Wetwell Shell Response at 240° Midbay During Condensation Oscillation (Large Liquid Break Test - M8)

*Proprietary information deleted

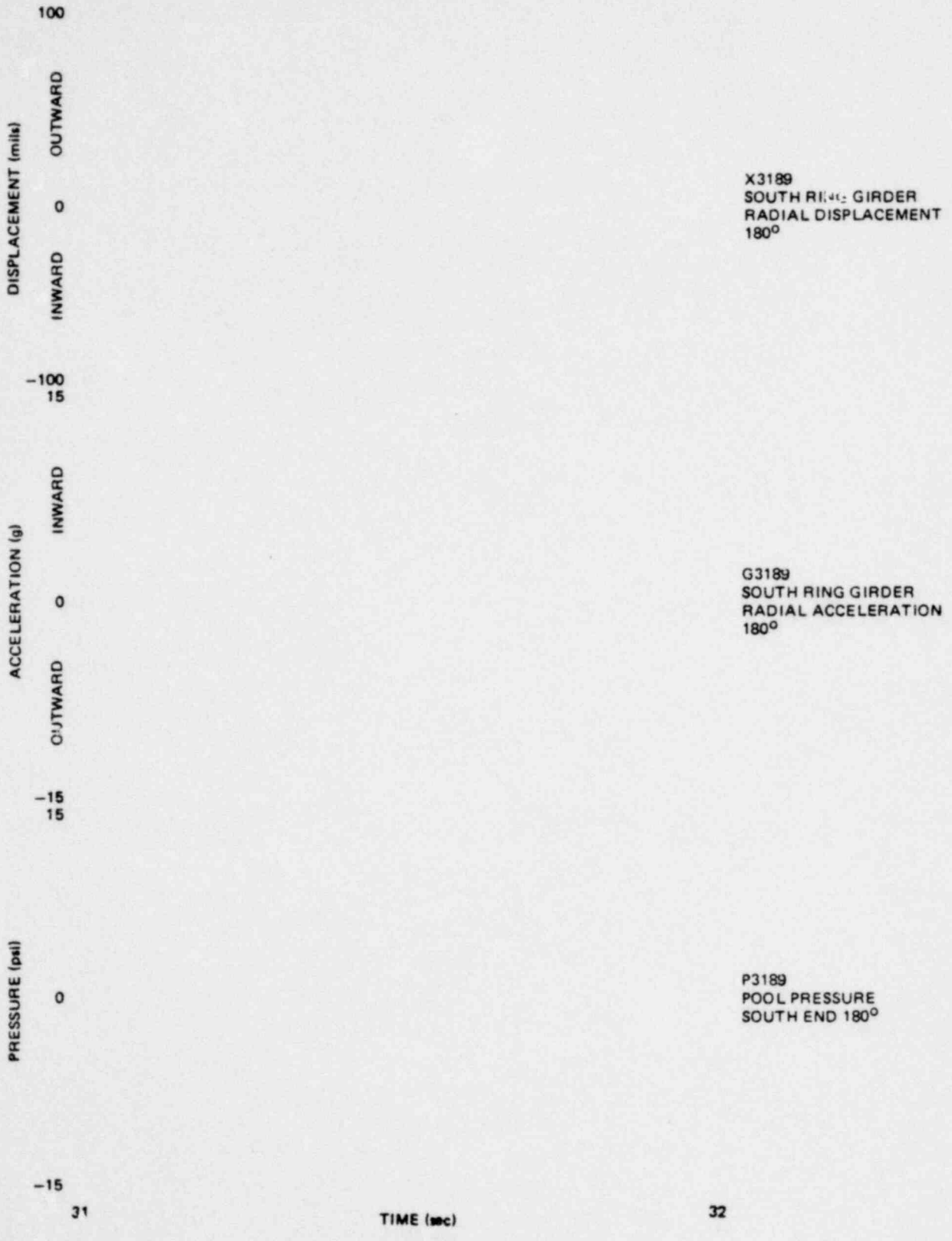

Figure 6.4.1-14. Wetwell Shell Response at 180° South End During Condensation Oscillation (Large Liquid Break Test - M8)

*Proprietary information deleted

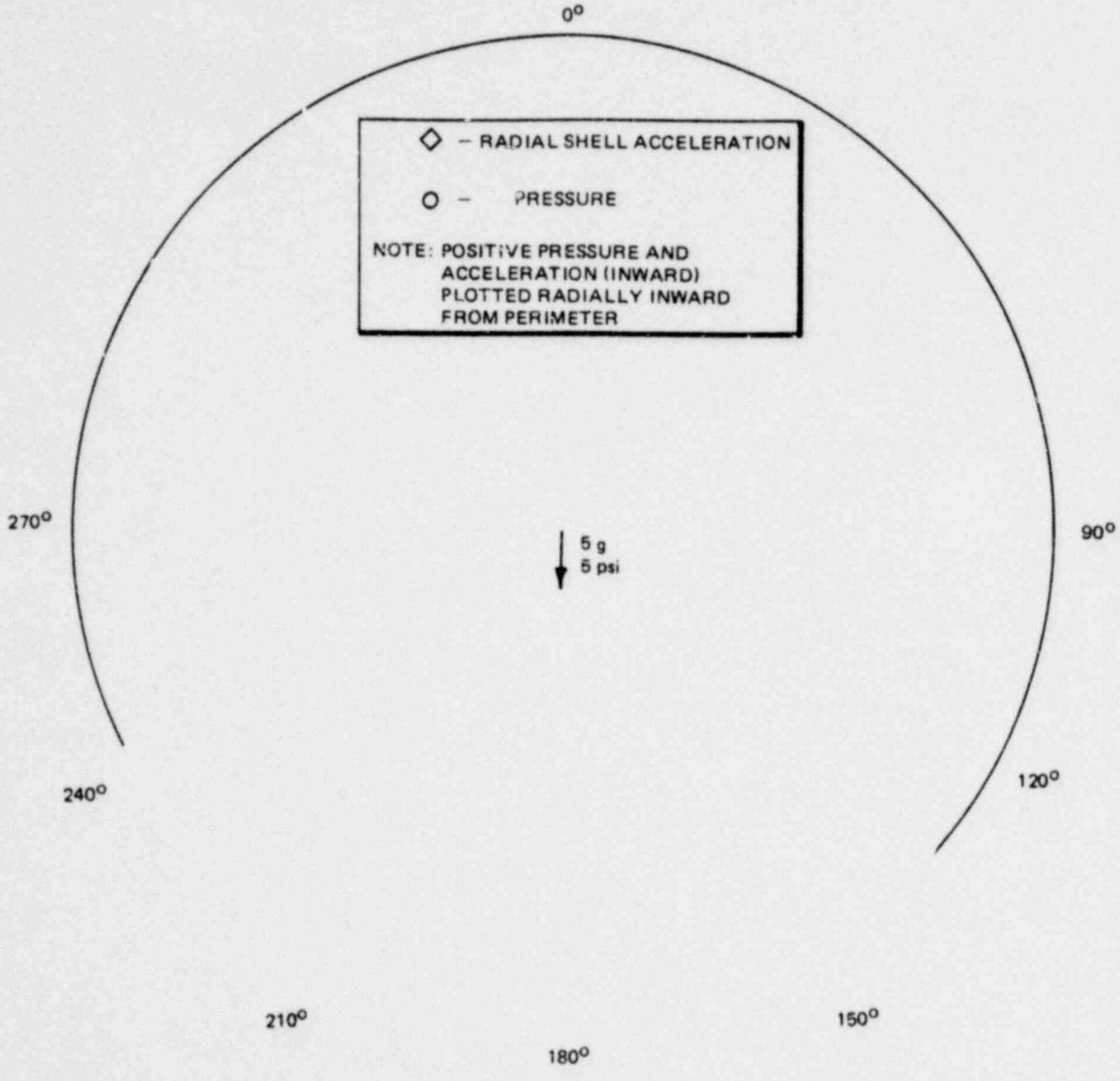

Figure 6.4.1-15. Pool Pressure and Shell Radial Accelerations About Midbay During Condensation Oscillation (31.599 sec)

1158 132

*Proprietary information deleted

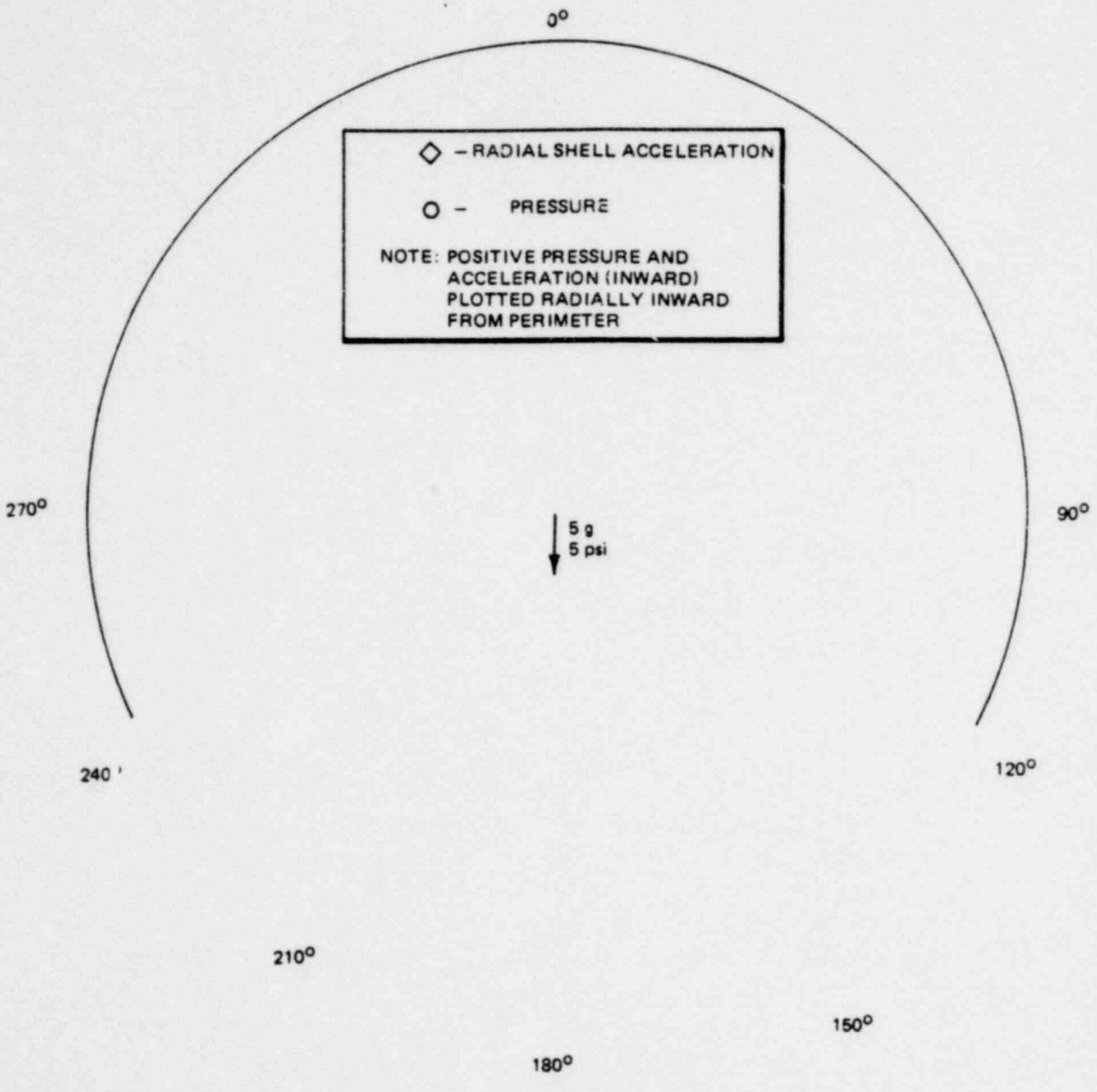

1158 133

Figure 6.4.1-16. Pool Pressure and Shell Radial Acceleration Distributions About Midbay During Condensation Oscillation (31.603 sec)

*Proprietary information deleted

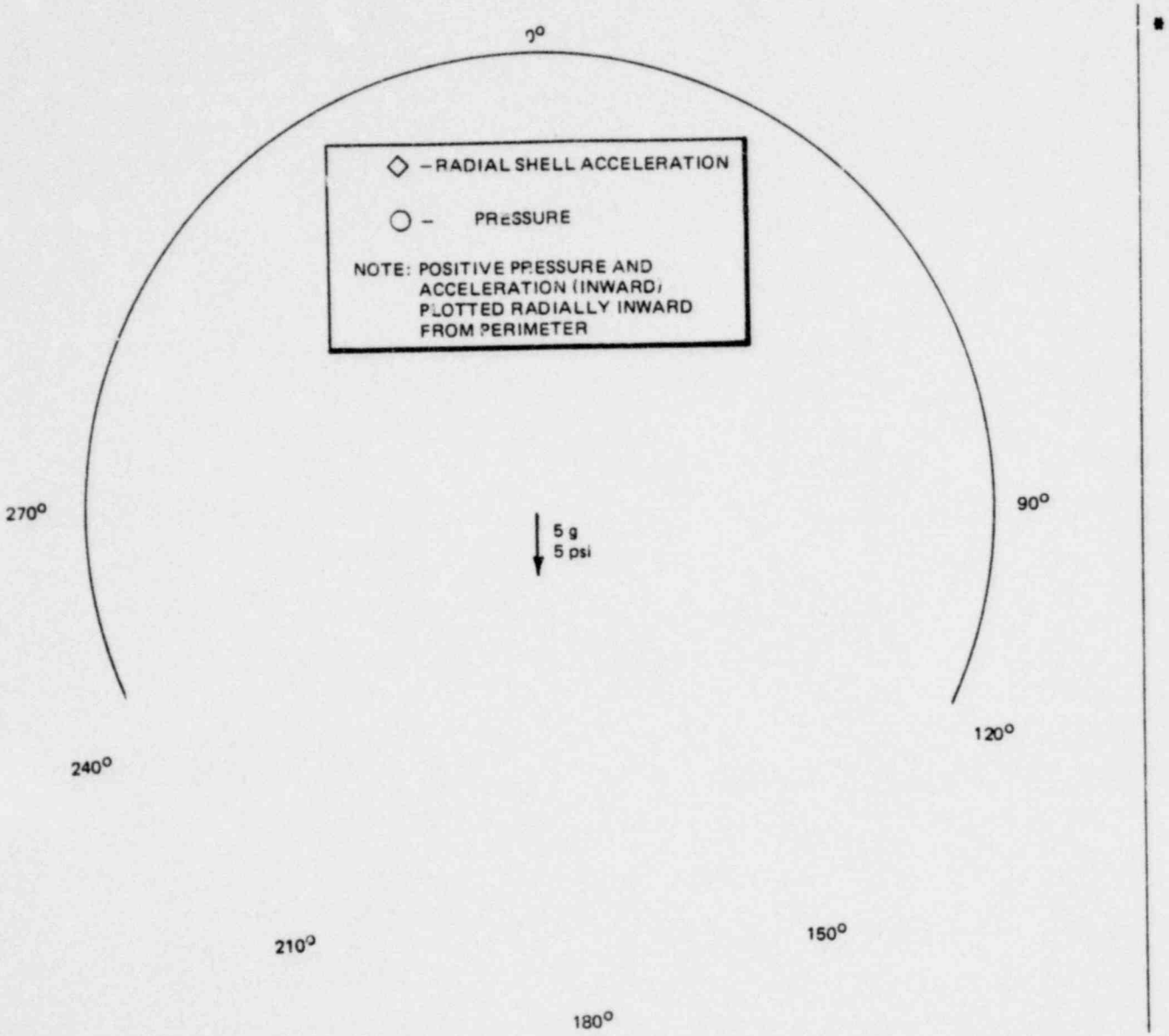

Figure 6.4.1-17. Pool Pressure and Shell Radial Acceleration Distributions About Midbay During Condensation Oscillation (31.607 sec.)

*Proprietary information deleted

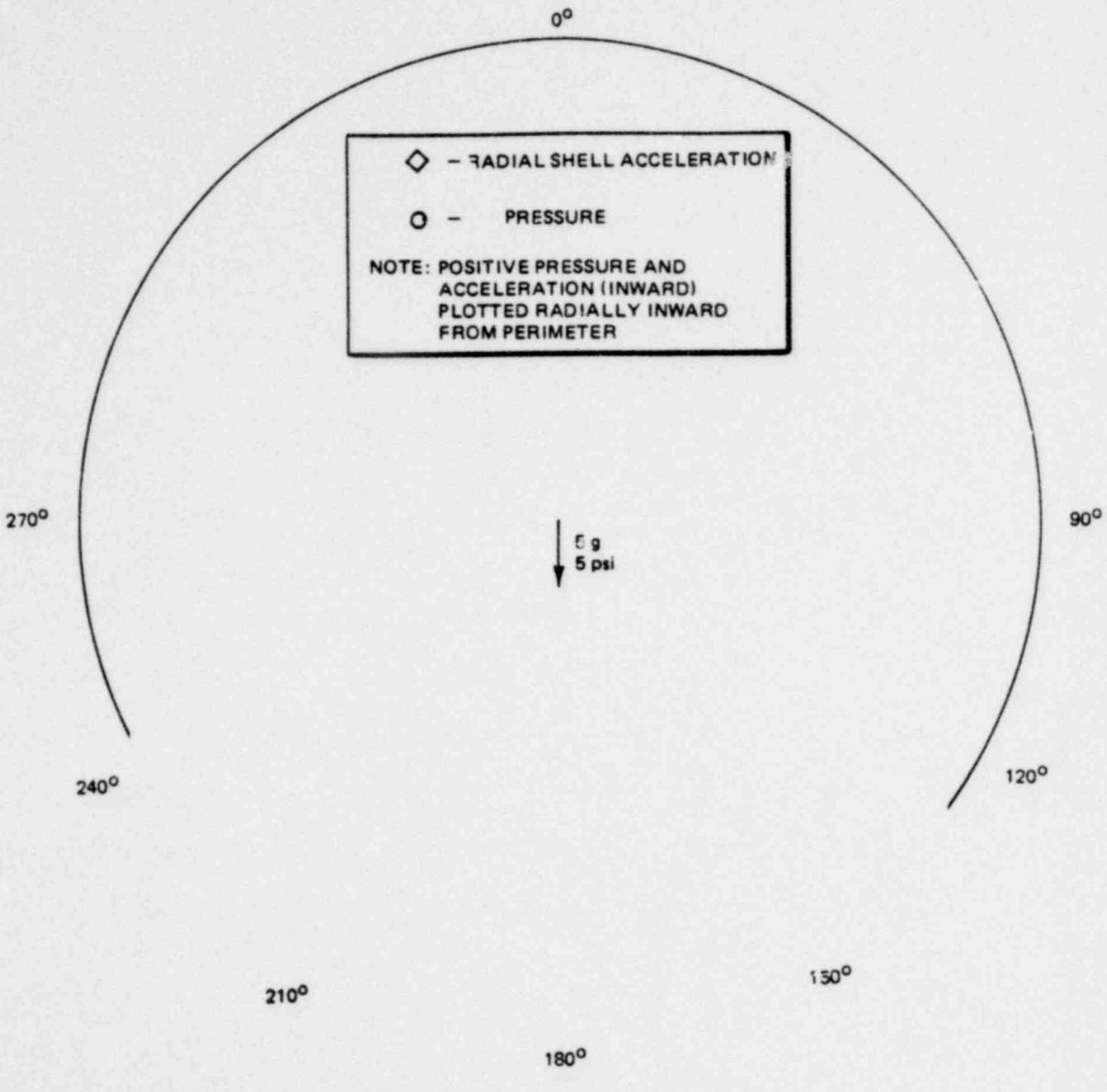

Figure 6.4.1-18. Pool Pressure and Shell Radial Acceleration Distributions About Midbay During Condensation Oscillation (31.612 sec)

*Proprietary information deleted

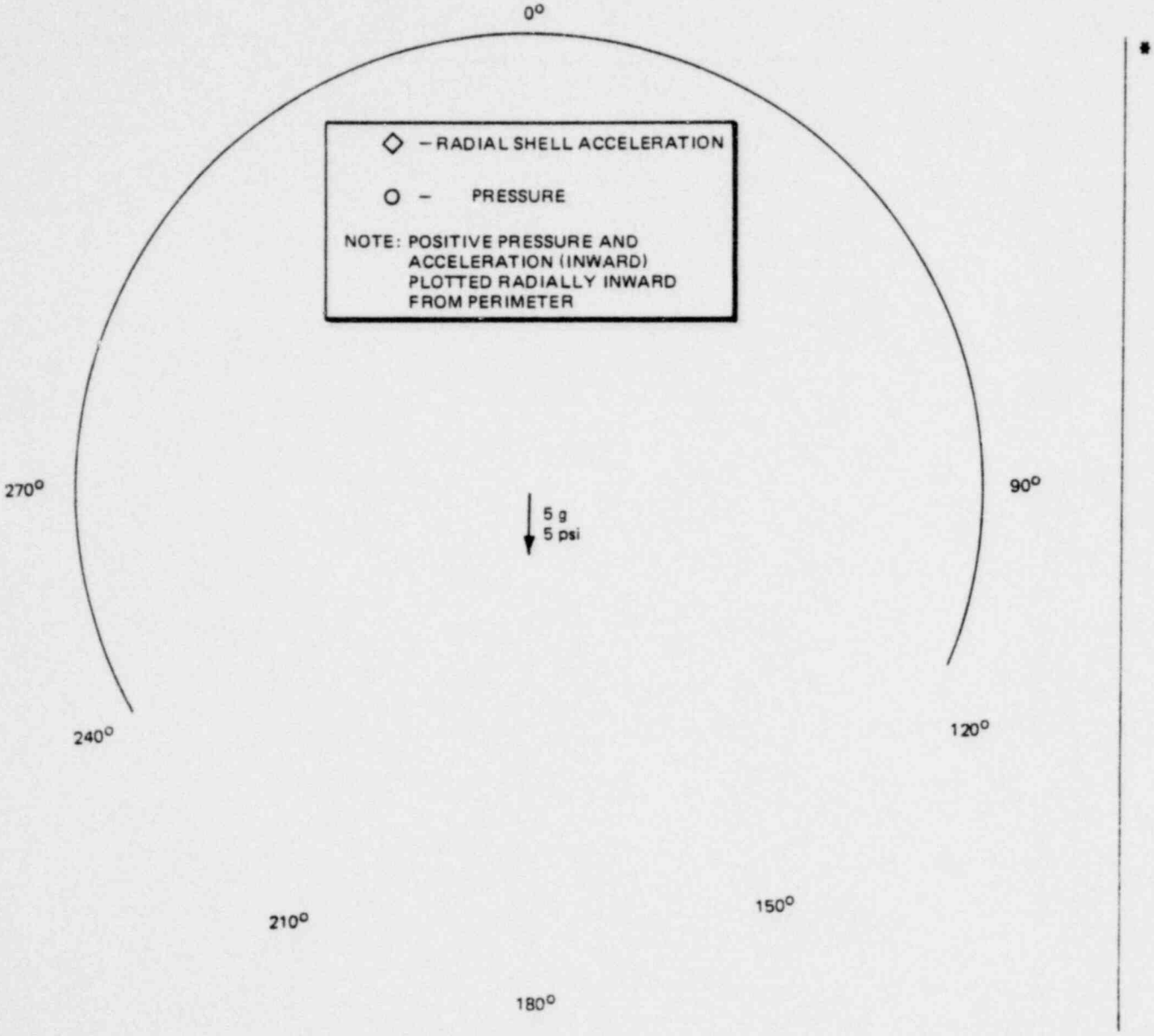

Figure 6.4.1-19. Pool Pressure and Shell Radial Acceleration Distributions About Midbay During Condensation Oscillation (31.615 sec)

*Proprietary information deleted

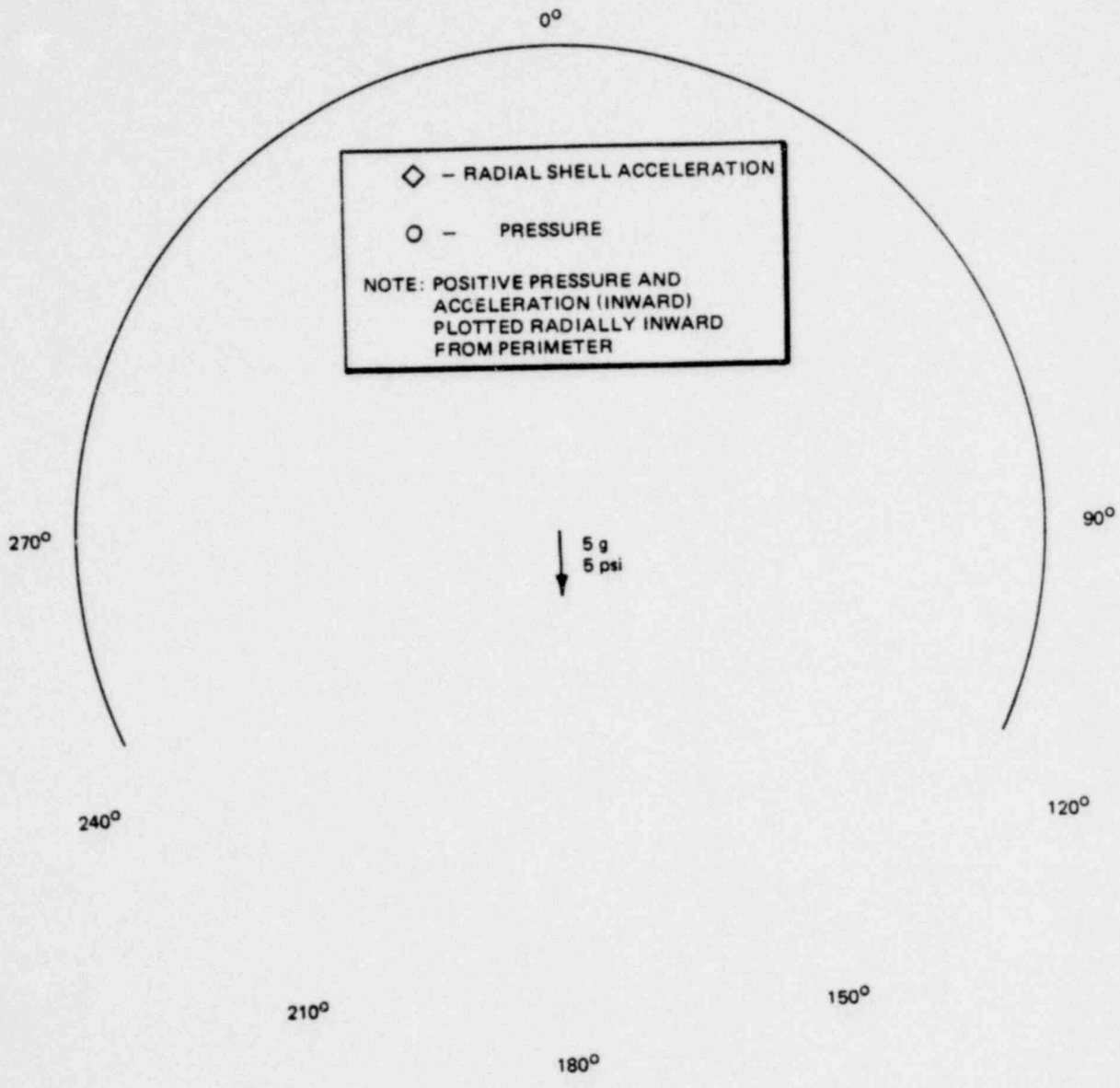

Figure 6.4.1-20. Pool Pressure and Shell Radial Acceleration Distributions About Midbay During Condensation Oscillation (31.620 sec)

*Proprietary information deleted

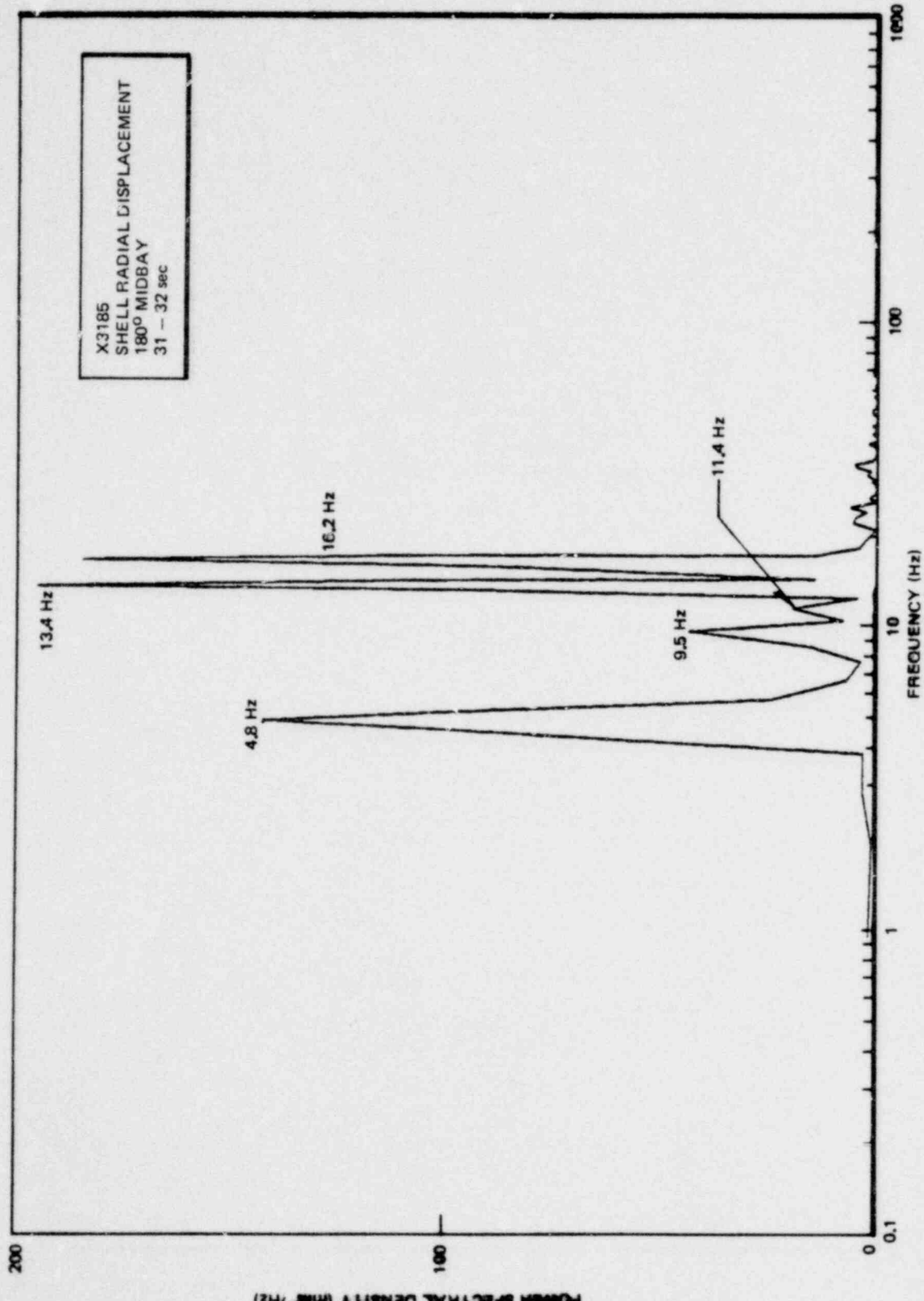

Figure 6.4.1-21. Power Spectral Density of Shell Radial Displacement at 180° Midbay

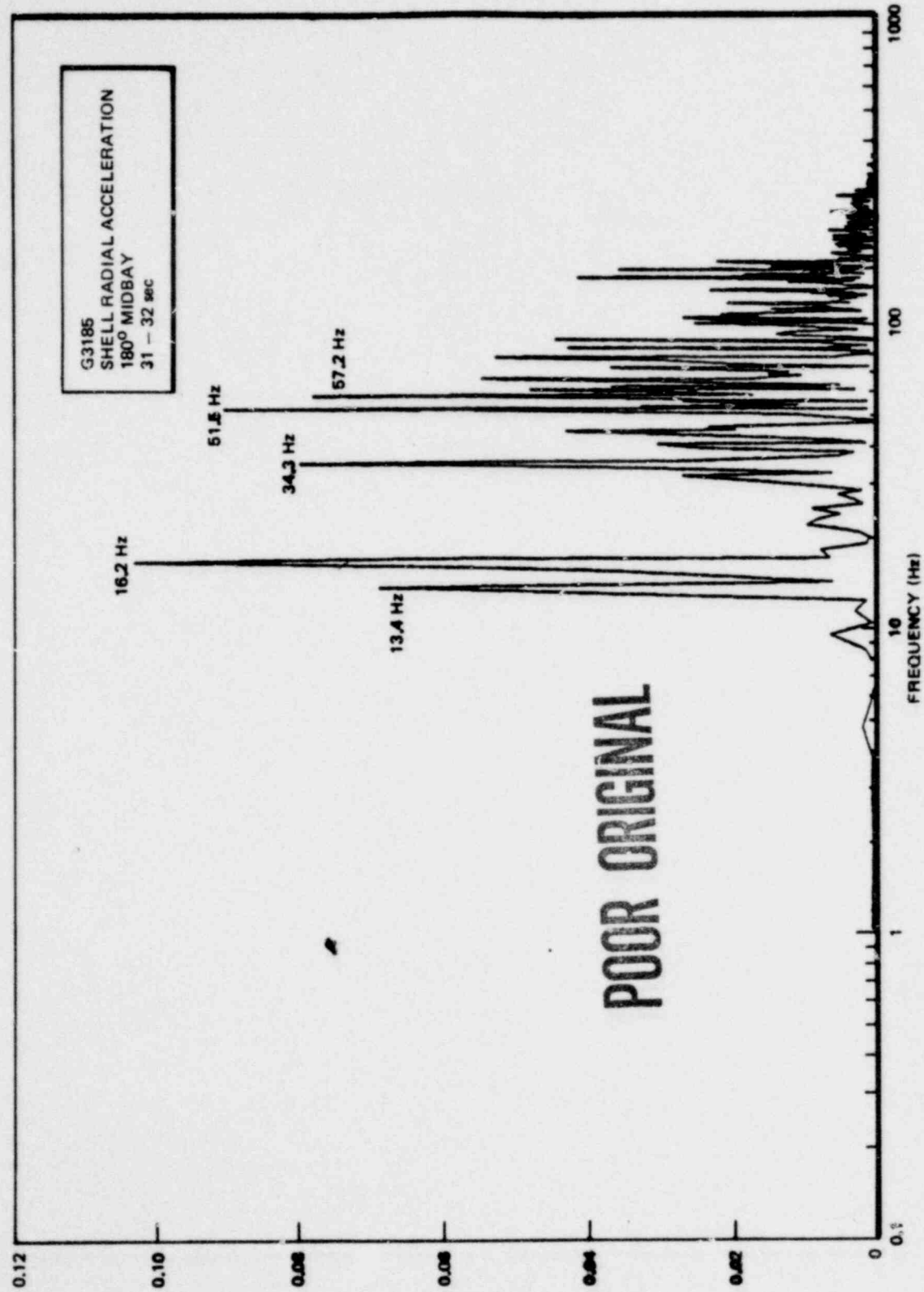

Figure 6.4.1-22. Power Spectral Density of Shell Radial Acceleration at 180° Midbay

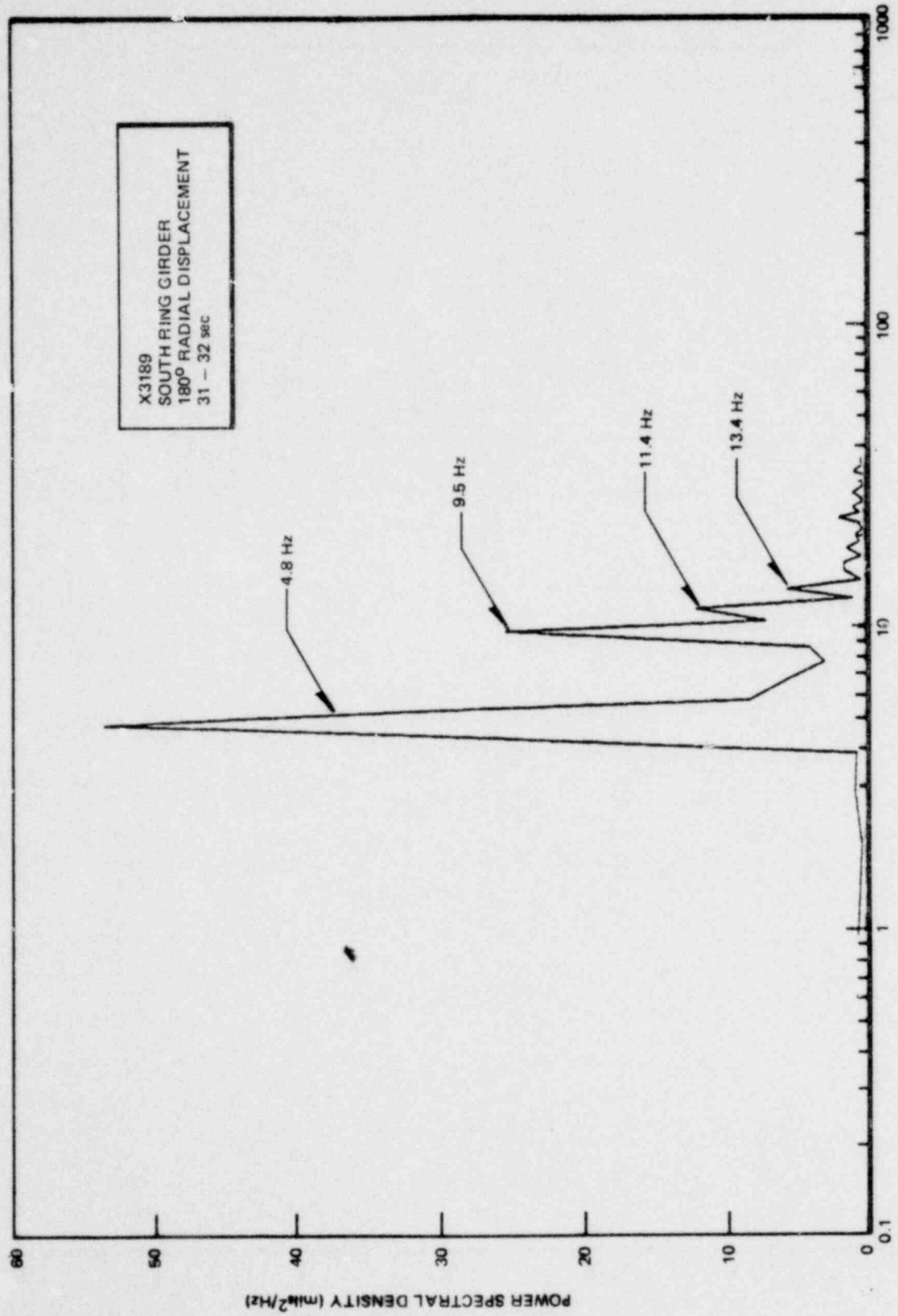

Figure 6.4.1-23. Power Spectral Density of Ring Girder Radial Displacement at 180° South End

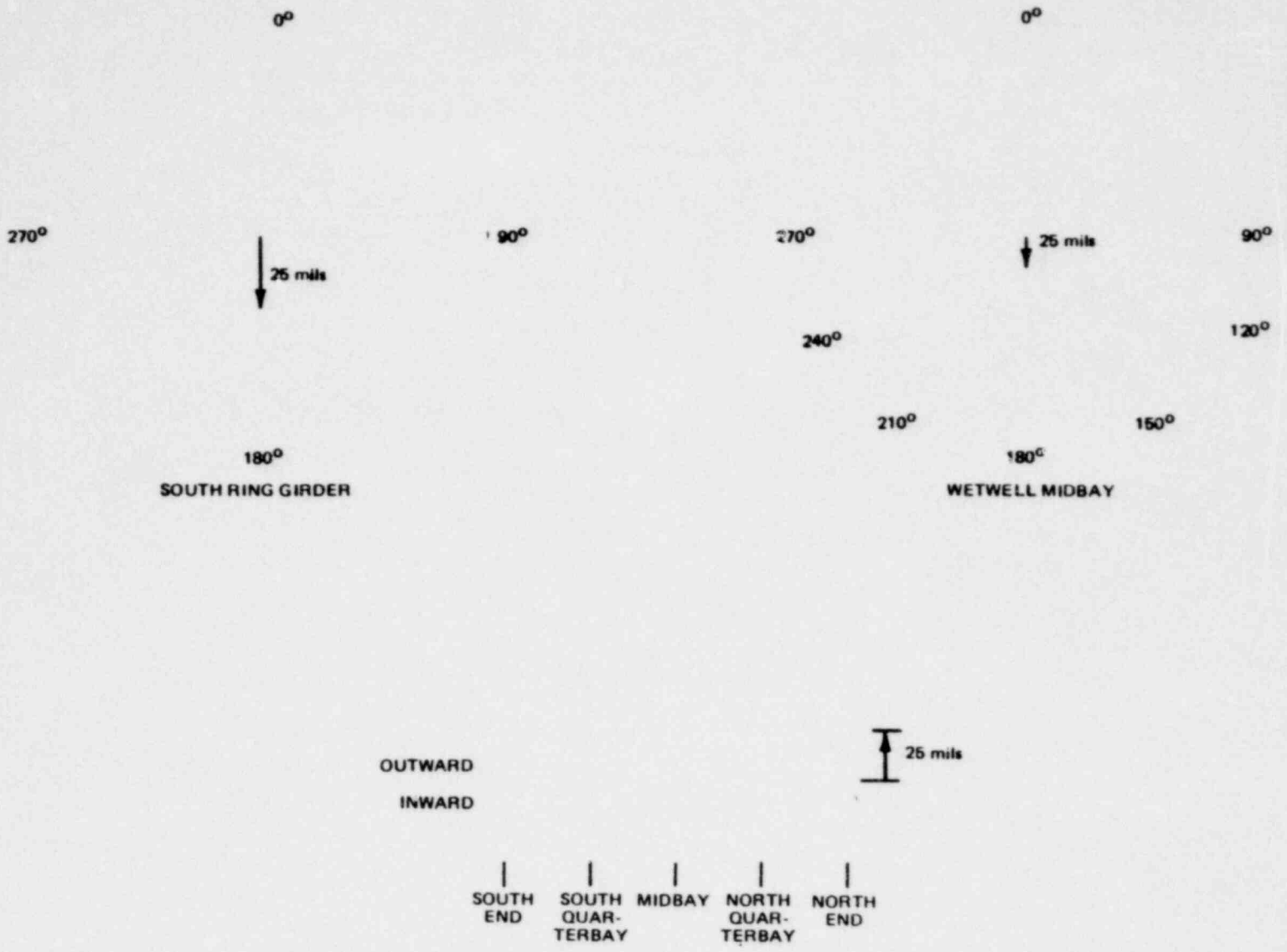

Figure 6.4.1-24. Wetwell and Ring Girder Deformation During Condensation Oscillation (31.583 sec)

*Proprietary information deleted

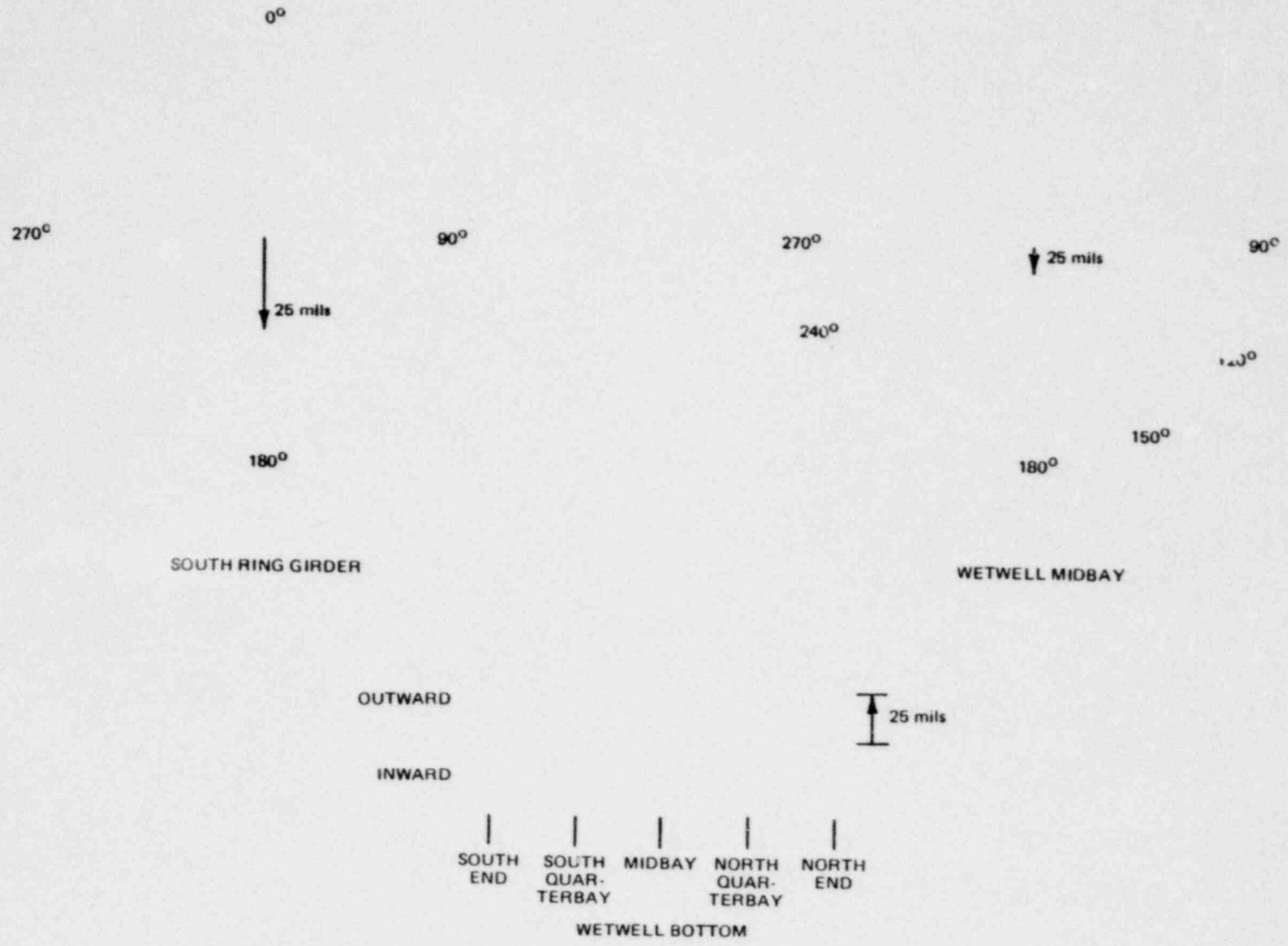

Figure 6.4.1-25. Wetwell and Ring Girded Deformation During Condensation Oscillation (31.590 sec)

*Proprietary information deleted

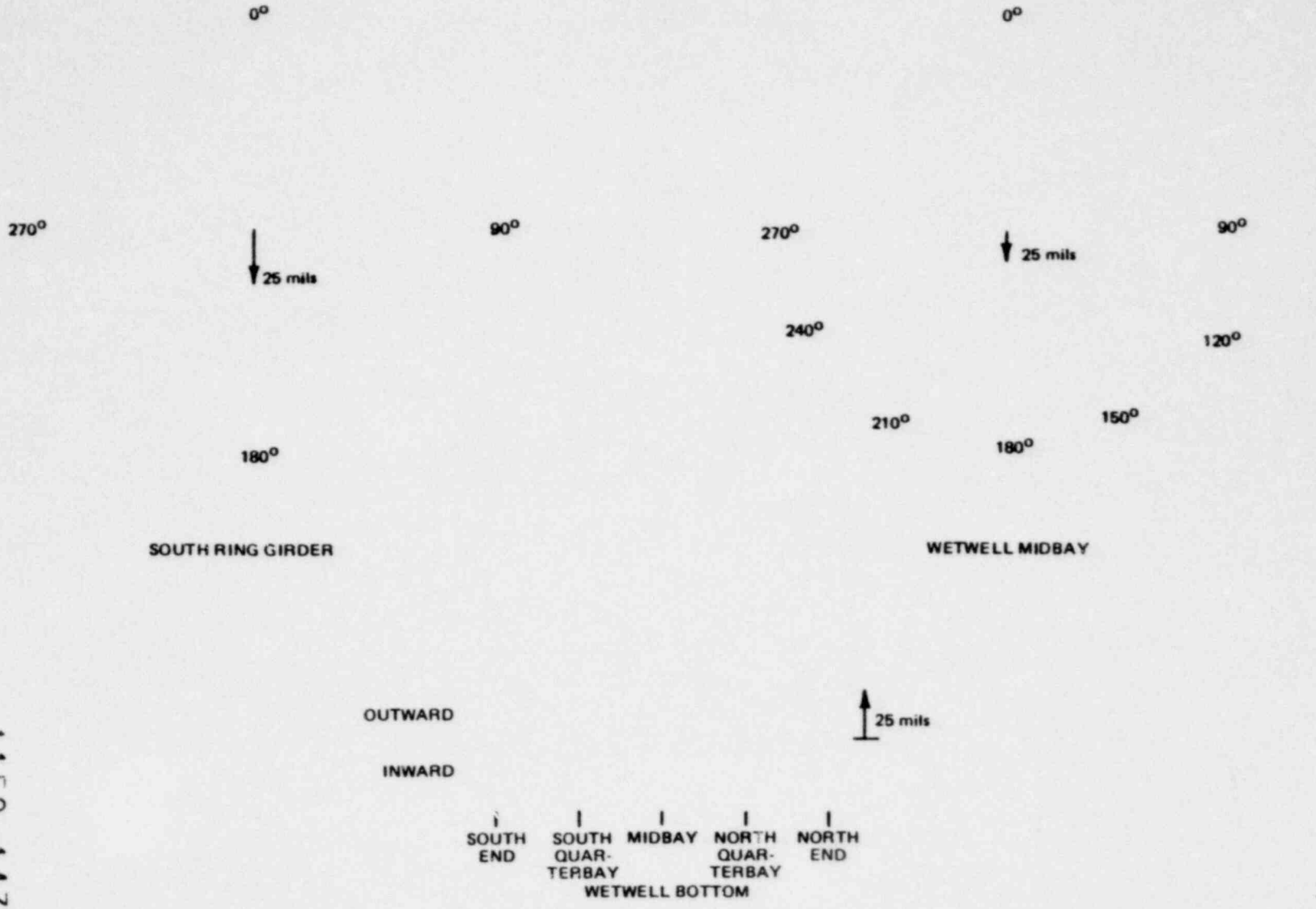

Figure 6.4.1-26. Wetwell and Ring Girder Deformation During Condensation Oscillation (31.599 sec)

*Proprietary information deleted

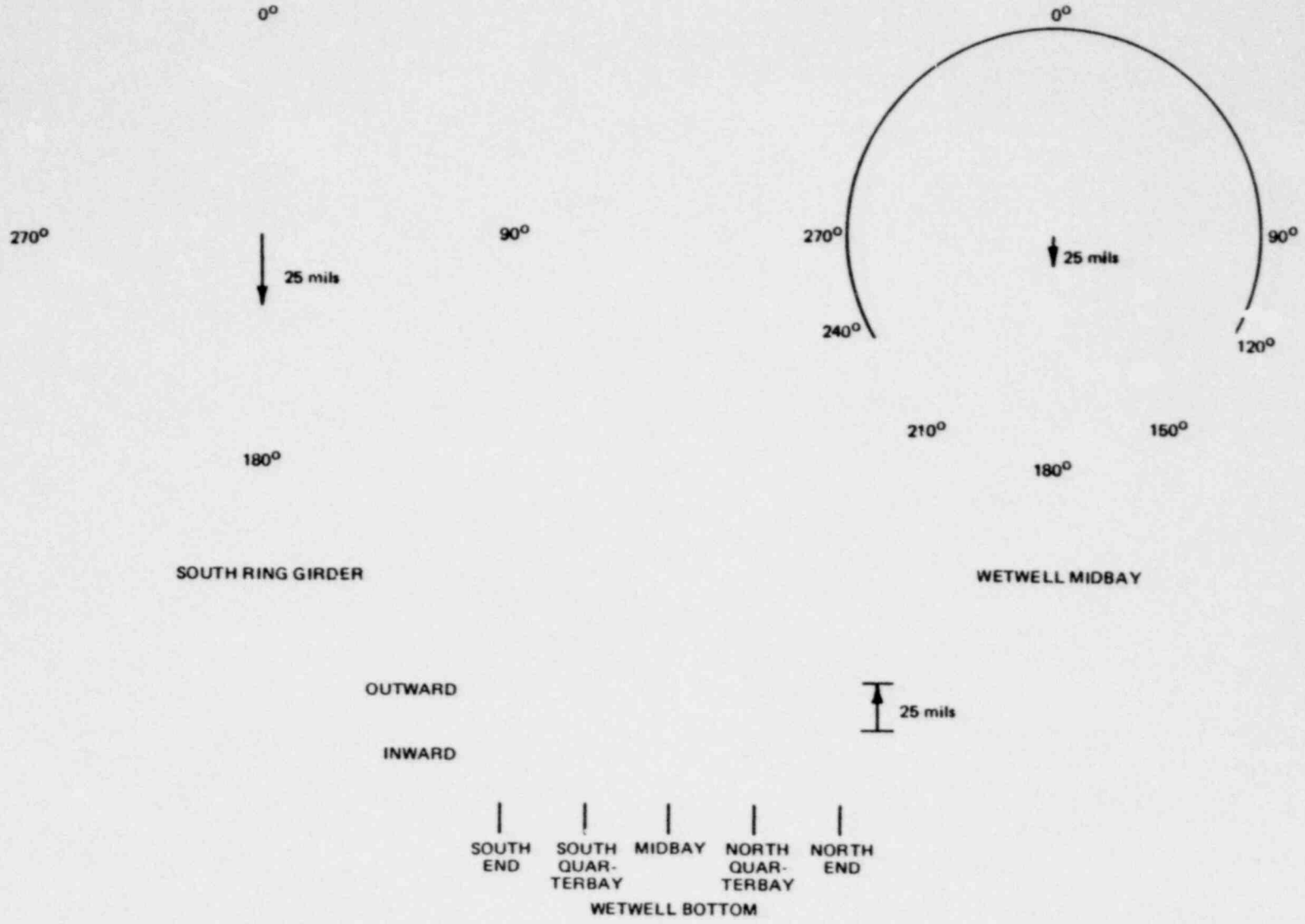

Figure 6.4.1-27. Wetwell and Ring Girder Deformation During Condensation Oscillation (31.607 sec)

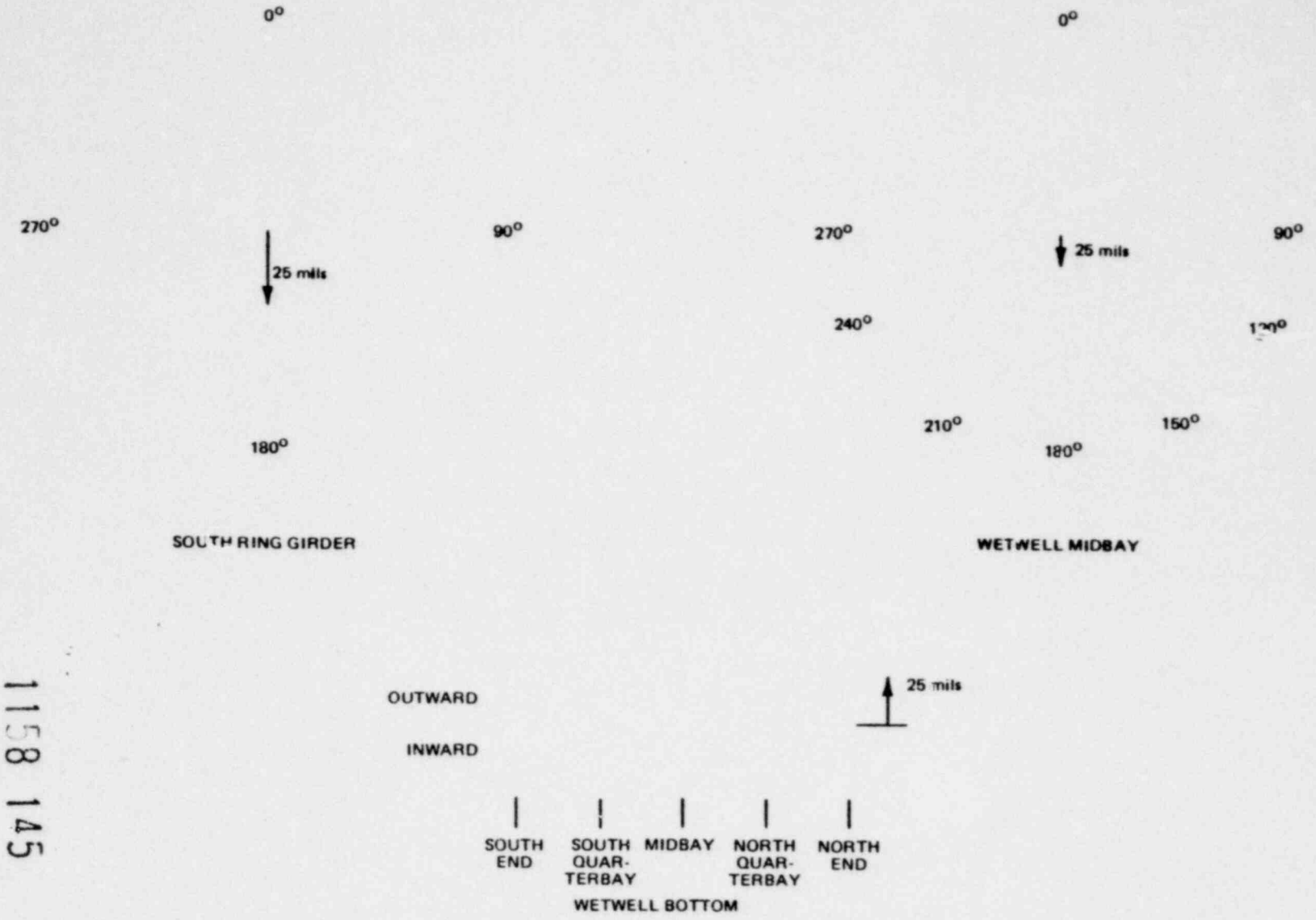

Figure 6.4.1-28. Wetwell and Ring Girder Deformation During Condensation Oscillation (31.615 sec)

*Proprietary information deleted

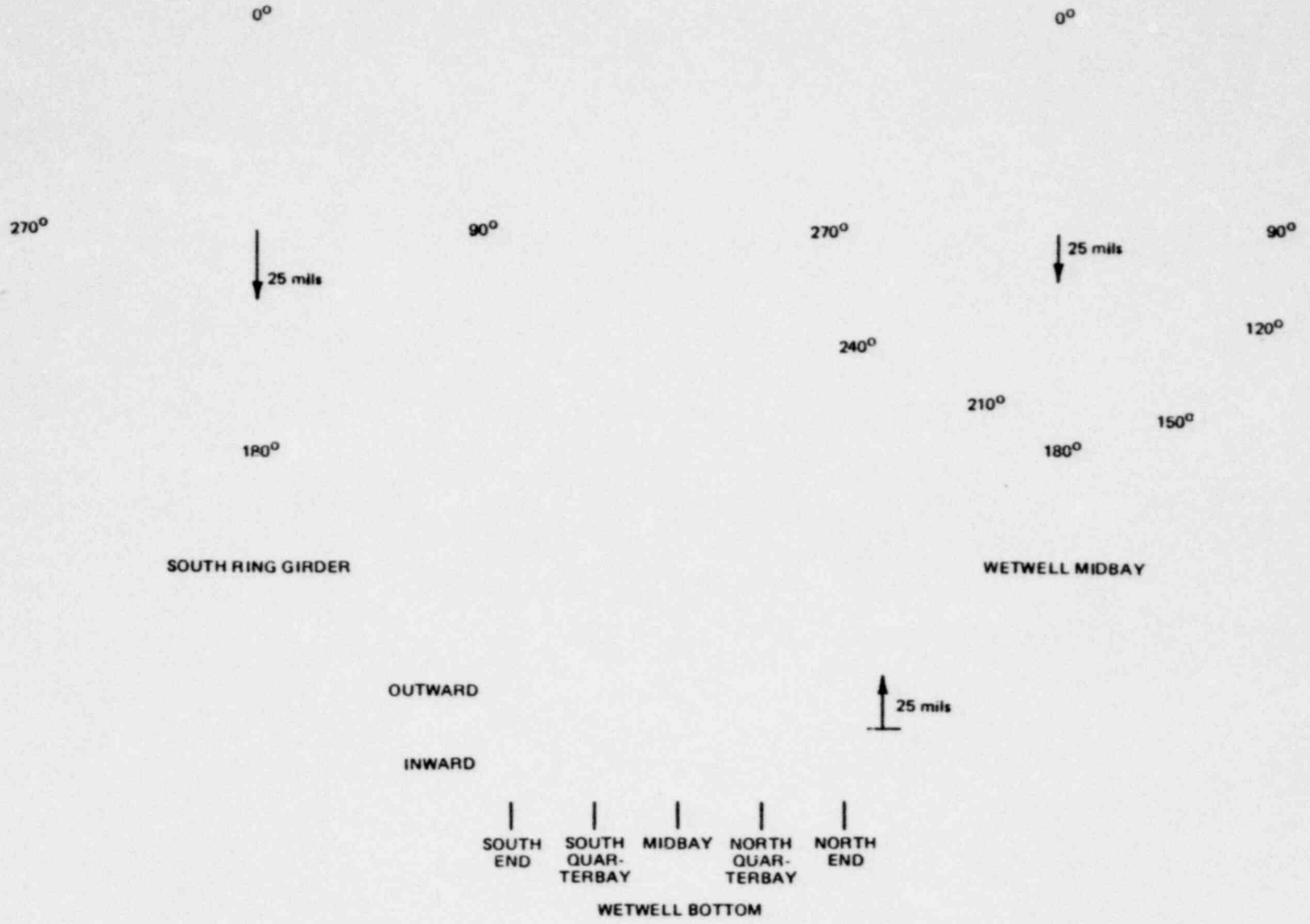

Figure 6.4.1-29. Wetwell and Ring Girder Deformation During Condensation Oscillation (31.620 sec)

6.4.2 FSI Effects During Chugging

To investigate FSI effects during chugging the small steam break test (M1) was selected as a data base. In particular, a detailed analysis of the time period following the initiation of a Type I Chug* will be made (98.5 to 99.5 seconds). During this time period some of the most prominent chugging related structural responses were observed.

The results of this analysis indicate that:

a. The rigid body vibration of the wetwell on its support columns does not result in significant FSI effects during chugging.

b. FSI effects due to the vibration of the end closures appear to be present during chugging. An increase in pressure in the pool region immediately adjacent to the end closures is observed as the end closures accelerate into the pool. The pressure signal associated with end closure vibration appears to attenuate toward midbay.

c. There is evidence that FSI results from wetwell shell vibrations during chugging. At shell locations where prominent structural responses are observed, the dynamic pool pressure appears to be mostly related to local shell acceleration. At these locations, the pool pressure increases as the shell accelerates into the pool and decreases as the shell accelerates away from the pool. These data trends are consistent with what would be expected if pressures are induced by wall motion. Additionally, the frequency compositic s of pool pressure and shell response data include some mutual components near the 11.0, 15.0 and 19.5 Hz shell resonances determined from shake tests of FSTF.

*Type I chugs are closely synchronized eight downcomer "Pool Chugs". A more detailed description of Type I chugging is available in Subsection 6.2.1.1.

6.4.2.1 Vent and Pool Boundary Pressures; Period of Analysis

An example downcomer pressure transient is presented in Figure 6.4.2-1* for the time interval which includes the pool chug of interest. The pool chug period, or the interval over which chugs are initiated at each of the 8 downcomers, is indicated on the figure.** The PSD associated with the downcomer pressure is shown in Figure 6.4.2-2. As can be seen in this figure, most of the signal power associated with the downcomer pressure is concentrated at 6.8 and 45.9 Hz. The presence of these two frequency components is most apparent prior to the pool chug.

In Figure 6.4.2-3 an example pool pressure transient (midbay bottom) is presented for the same time period as the downcomer pressure transient presented above. The related PSD is shown in Figure 6.4.2-4. In addition to frequency components near those seen in the downcomer pressure PSD at 7.6 and 41.6 Hz, the pool pressure PSD exhibits other prominent frequency components at 11.9 and 64.6 Hz.

In comparing the downcomer and pool pressure transients directly (compare Figure 6.4.2-1 with Figure 6.4.2-3), it can be noted that there is marked similarity between the two pressures only in the period prior to pool chug initiation. Prior to the pool chug, both the downcomer and pool pressure are dominated by the low frequency component (approximately 7 Hz). Also it can be noted at this time that the higher frequency component, $\sim$ 44 Hz, is more pronounced in the downcomer pressure than the pool pressure. Subsequent to pool chug initiation, the 7 Hz frequency is still apparent in the downcomer pressure but not in the pool pressure. The pool pressure is characterized, at this time, by relatively high frequencies. Examination of the PSD of the pool pressure for the period following pool chug initiation, Figure 6.4.2-5, indicates that the significant frequency components of the pool pressure, for this time period, are 11.9, 41.6 and 64.6 Hz.

---

* Linear trend removal was not used on this data

**Chug initiation times were obtained from computer programs described in Section 5

From the standpoint of FSI it is the period following pool chug initiation that is of primary interest. The basis of this conclusion rests with comparisons of the downcomer and pool pressures and, additionally, the differences in structural response for the periods preceding and following the pool chug. Again comparing Figures 6.4.2-1 and -3, it can be seen that prior to the pool chug the magnitude of downcomer pressure oscillations are greater than those of the midbay bottom pool pressure. The maximum peak to peak pressure range for the downcomer is 5.5 psi while the maximum peak to peak pressure range for the midbay bottom pressure is 3.5 psi. A similar difference in pressures would be expected due to spatial attenuation of a pressure source located at the downcomer exit.

Structural response data also suggest that FSI effects are more significant after the pool chug is initiated. Radial displacement and acceleration transients at the shell midbay bottom are shown in Figures 6.4.2-6 and -7, respectively. Although shell displacements amplitudes are comparable just prior to and during the pool chug, the frequency of the displacement fluctuations are obviously greater after the pool chug has been initiated. Here it is implied that shell acceleration amplitudes increase after the pool chug has been initiated. Actual shell acceleration data also indicates this pattern. Shell accelerations for the period after the pool chug is initiated are three times greater than for the period prior to the pool chug. Since the governing parameter for FSI is the shell acceleration it is reasonable to expect that FSI effects would be much more significant during the chugging period than during the period just preceding chugging.

6.4.2.2 Rigid Body Response

Structural responses of the ring girders and wetwell support columns were very low during chugging implying that the rigid body motion of the wetwell does not significantly affect pool pressures (due to water inertia effects). Figure 6.4.2-8 presents, concurrently, the outside support south column axial strain, ring girder acceleration and displacement at bottom center. Peak column axial strains are about ±18 μin/in.

1158 149

Peak ring girder accelerations and displacements are about ±1.8 g's and ±6 mils, respectively. As was the case for CO, the rigid body acceleration of the wetwell is probably not represented by the ring girder acceleration data which is characterized by rather high frequency components (42 and 62 Hz based on a PSD of the south ring girder bottom center acceleration). Reviewing the PSD of the column axial strain data, previously presented in Subsection 6.3.2, indicates that the "bounce" mode of the wetwell/support columns is excited. The rigid body acceleration inferred from the column axial strain data (a 2 mil deflection at 27 Hz - the bounce mode frequency), is 0.16 g's. At the bottom of the pool, this acceleration would result in a pressure of about 0.7 psi. A pressure of this magnitude is not insignificant compared to pool pressures during chugging. However, this estimate of the effect due to rigid body motion of the wetwell may be high as little signal power, at 27 Hz, is observed in pool pressure PSD's. It may well be that the effective water mass associated with the rigid body motion of the wetwell is considerably less than the total water mass.

6.4.2.3 End Closure Response

Lateral accelerations of the end closure and ring girder are shown together with the pool pressure, at the bottom of the wetwell, for the north end of the wetwell in Figure 6.4.2-9 and for the south end of the wetwell in Figure 6.4.2-10. Peak end closure accelerations are noted at about the time at which the peak pool pressures are observed at the bottom of the north and south ends of the wetwell. These times are not coincident for the two ends; the peak end closure acceleration at the south end is about 80 milliseconds in advance of peak end closure acceleration at the north end. At both ends pool pressure peaks are observed at times at which the end closures are accelerating towards the pool suggesting that closure vibration is amplifying the pressures in the adjacent region of the pool.

The extent to which end closure vibration influences pressures throughout the pool is not readily apparent. The region of influence for this effect appears to extend from the wetwell ends to at least the quarterbay position. Comparison

of pool pressures along the wetwell bottom - at the south end, south quarterbay and midbay - indicate that the pressure spike observed at the south end, corresponding to the end closure motion, is seen at south quarterbay but not at midbay. It should also be noted that the pressure spike at south quarterbay is attenuated relative to the pressure spike at the south end. Similar behavior can be noted in comparing pool pressures along the bottom of the wetwell at the north end, north quarterbay and midbay. Such behavior implies that the pressure signal associated with end closure vibration attenuates toward midbay; complete attenuation occurs somewhere between quarterbay and midbay.

6.4.2.4 Wetwell Shell Response

Pool pressure fluctuations measured circumferentially around midbay, during chugging, varied in terms of amplitude, frequency and phase. Corresponding variations in local shell responses are also observed. These points are illustrated by Figures 6.4.2-11 through -15. Each figure presents the pool pressure, radial shell acceleration and radial shell displacement, concurrently, at the indicated angular position about midbay. For reference, the pool pressure at bottom center of the south wetwell end, and south ring girder bottom center acceleration and displacement, are presented in Figure 6.4.2-16.

Peak values for pool pressure, shell radial acceleration and shell radial displacement are tabulated in Table 6.4.2-1 for the 120°, 150°, 180°, 210° and 240° midbay position over the 98.5-99.5 second interval. The highest peak pool pressures occur on the narrow-side of the torus (120° and 150°) and torus bottom (180°). At these positions the pressure peaks are nearly all of the same magnitude. On the wide-side of the torus the peak pressures decrease as the pool free surface is approached (i.e., the peak pressure at 210° is less than at 180° and, likewise, the peak pressure at 240° is less than at 210°). As was the case for CO_2 both the inward and outward radial shell accelerations are greater for the narrow-side of the torus than for the wide-side of the torus.

Comparisons of local shell acceleration and pool pressure time histories for the pool chug being examined suggests that pool pressures are affected by local

shell motions. At each of the midbay positions of 120°, 180°, 210° and 240°, it can generally be observed that as the shell accelerates into the pool the local pool pressure increases and as the shell accelerates away from the pool the local pool pressure decreases (see Figures 6.4.2-11, -13, -14 and -15). The 120° midbay position (Figure 6.4.2017) is a particularly graphic illustration of this relationship. This observation is consistent with what would be expected if pressures were induced by wall motion and suggests that FSI affects pool pressures.

The relationship between pool pressures and local shell accelerations, described above, consistently holds only for the locations at which the highest local shell responses are observed: at bottom of the wetwell and along the narrow-side of the torus (120° & 150°). Along the wide-side of the torus (210° & 240°) the pool pressures appear to be influenced more by the pressure state in the adjacent lower region of the pool than by local shell accelerations.

The above points are illustrated by Figures 6.4.2-17 through -22. These figures show the distribution of pool pressure and shell radial acceleration, about mid-bay, for five instants of a 12 millisecond interval.

The relationship between pool pressures and shell accelerations is sharply defined by Figures 6.4.2-17 through -22 at the 120° and 180° shell locations. At these locations the pool pressure increases as the shell accelerates inward. Further, at these locations, the pool pressures appear to track only the local shell acceleration and are independent of the pressure variations in the adjacent regions. For example, the pool pressure at 150° is nearly 180° out of phase with the pool pressures at 120° and 180° (refer to Figures 6.4.2-17 and -20).

In contrast, the pool pressure at 210° is apparently influenced more by the pressure state in the adjacent lower region of the pool than the local shell accelerations. Over the interval from 98.684 to 98.687 seconds the pool pressure at 210° remains nearly constant even though the shell has begun to accelerate away from the pool at this location (compare Figures 6.4.2-17 and -18). During the same interval the pool pressure at 180° has risen significantly - corresponding

to the inward acceleration of the shell at 180°. It can be noted that at 98.687 seconds, the magnitude of the shell acceleration at 180° is about four times greater than that observed at 210°. Similar behavior is observed in the time interval from 98.690 to 98.693 seconds. In this case the pool pressure at 210° falls, even though the shell is accelerating into the pool at this location. Simultaneously the shell sharply accelerates outward at 180° and the pool pressure at 180° goes negative. This indicates that the pool pressure at 210° is greatly influenced by variations in pool pressure at 180°. This behavior is reasonable considering that shell responses are more pronounced at 180° than at 210°. Also the effect of shell motions on pool pressures is expected to be greater for locations of greater submergence (i.e., locations which would have a greater associated hydrodynamic mass).

The behavior of the pool pressure at 240° during the interval from 98.684 to 98.696 seconds is very similar to that observed at 210°. That is, the changes in the pool pressure at 240° generally reflect changes in the pool pressure at 180° rather than the changes in shell acceleration at 240°. Apparently, during this time interval, the influence of the lower portion of the shell extends nearly to the free surface on the outside of the torus.

To quantify the frequencies associated with wetwell structural responses and to determine which of these frequencies also appeared in the pool pressures, PSDs of shell displacement, shell acceleration and pool pressures were analyzed. An example of a PSD of a pool pressure was previously given in Figure 6.4.2-5. Example shell displacement and accelerations are given in Figures 6.4.2-23 and -24. Significant frequency components of pool pressure, shell displacement and shell acceleration data are tabulated in Table 6.4.2-2. A number of frequencies appear mutually in the pool pressure and shell response data over a range from 11 to 65 Hz.

Some of the frequencies identified in Table 6.4.2-2 correspond to known structural resonances. Comparison of the test data and the resonant frequencies determined from shake tests of the FSTF (Appendix D) suggests that wetwell resonances of 11.0, 15.0 and 19.5 Hz are excited during chugging. These frequencies were also observed in the data during CO.

1158 153

Frequencies in the range from 42 to 50 Hz appear to be related to vent system acoustics. The basis for this conclusion is the frequency content of the downcomer pressure measurements. Take, for example, the PSD for the pressure measurement inside of downcomer No. 6 which is presented in Figure 6.4.2-12. A frequency in the 42 to 50 Hz range is clearly present (at 45.9 Hz).

Although a number of frequencies are apparent in the pool pressure data, several frequencies are clearly more dominant. In Table 6.4.2-3 the frequencies associated with pool pressures, about midbay, are classified in terms of whether they are primary or secondary components. For the purposes of this discussion, representative rather than actual values (obtained from PSD's) of frequency have been used. These representative values correspond either to shell resonant frequencies (11.0, 15.0 and 19.5 Hz) or are based on consideration of the frequencies appearing in both pool pressure and shell response data. The two primary frequencies of the pool pressure data are 11.0 and 62 Hz. The 62 Hz component is observed at each midbay position while the 11.0 Hz component is a primary frequency component only at two deep submergence locations - 180° and 210°. The dominance of the 62 Hz frequency is also directly evident in some of the pool pressure time histories. A good example is provided by the time history of the pool pressure at 120° (Figure 6.4.2-11). The shell acceleration time history at 120° also indicates a frequency of about 62 Hz. Both the pool pressure and shell acceleration "ring" at 62 Hz for about 0.6 seconds.

Table 6.4.2-1

PEAK DYNAMIC PRESSURES, ACCELERATIONS AND DISPLACEMENTS AT MIDBAY DURING CHUGGING* (SMALL STEAM BREAK TEST - M1; 98.5 - 99.5 SEC.)

Midbay Position	Pool Pressure (psi)	Shell Radial Acceleration (g's)	Shell Radial Displacement (mils)
120°			
150°			
180°			
210°			
240°			

* Based on period following pool chug initiation
** Accelerometer inoperative

•Proprietary information deleted

1158 155

Table 6.4.2-2

FREQUENCIES OBSERVED IN POOL PRESSURE AND SHELL RESPONSE DATA DURING CHUGGING*
(SMALL STEAM BREAK TEST - M1; 98.5 - 99.5 SEC.)

Midbay Position	Pool Pressure							
120°			21.2	27.2			56.9	61.2
150°	11.9	16.1	18.7			44.2		62.0
180°	11.9	16.1			36.5	41.6		64.6
210°	11.9		18.7		32.3	42.5	53.5	57.8
240°	12.7	15.3		28.0	32.3	49.3		61.2

Midbay Position	Shell Displacement							
120°			21.2	27.2				61.2
150°	12.7	16.1	18.7			45.9		62.0
180°	11.9	16.1			36.5	40.8		
210°	12.7		18.7		32.3			
240°	12.7	15.3		27.2	32.3			

Midbay Position	Shell Acceleration							
120°			21.2	27.2			56.1	59.5
150°**								
180°						42.5		62.0
210°	12.7				33.1	48.4	54.4	61.2
240°				27.2	32.3	42.5		64.6

NOTE: (1) All values in Hz
(2) PSD incremental frequency step is 0.850 Hz

* Based on period following pool chug initiation
**Accelerometer inoperative

1158 156

Table 6.4.2-3

PRIMARY AND SECONDARY FREQUENCY COMPONENTS
OF POOL PRESSURES DURING CHUGGING*
(SMALL STEAM BREAK TEST - M1; 98.5 - 99.5 SEC.)

Midbay Position	Primary Frequencies		Secondary Frequencies						
120°		62			19.5	27			54
150°		62	11.0	15.0	19.5			43	
180°	11.0	62		15.0			33	43	
210°	11.0	62			19.5		33	43	54
240°		62	11.0	15.0		27	33	43	

NOTE: All values in Hz

*Based on period following pool chug initiation

1158 157

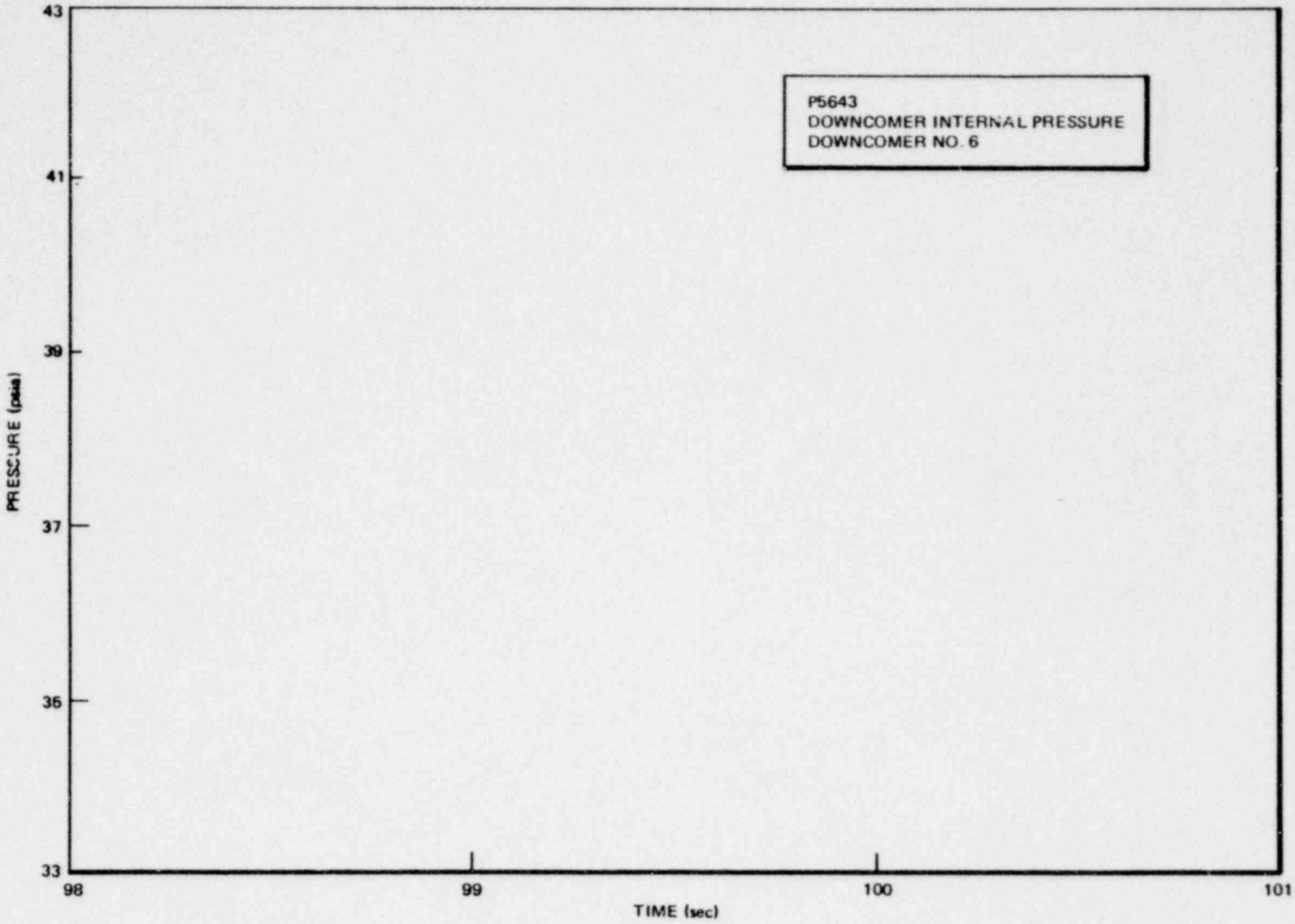

Figure 6.4.2-1. Downcomer Pressure During Chugging Downcomer No. 6 (Small Steam Break Test - M1)

*Proprietary information deleted

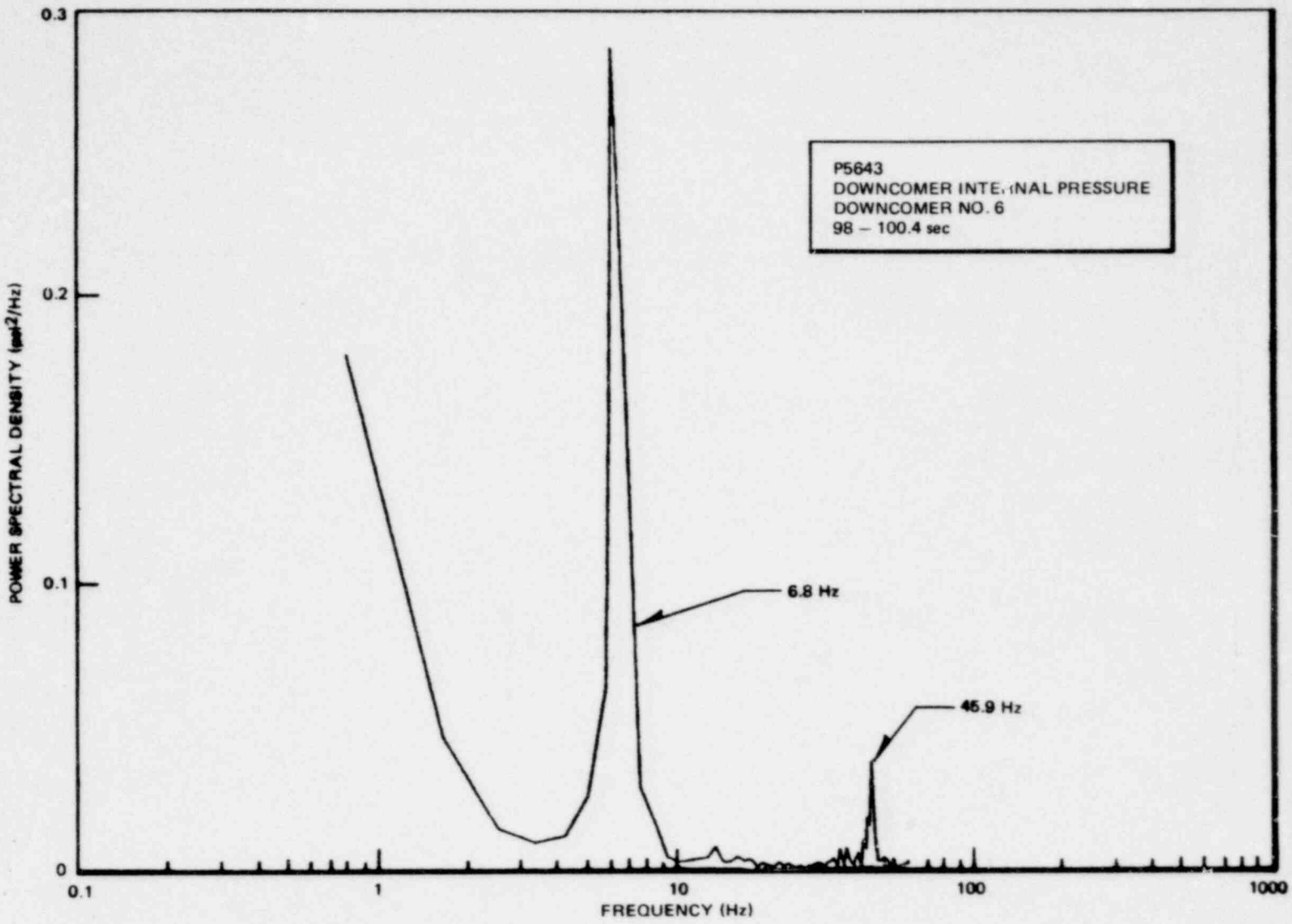

Figure 6.4.2-2. Power Spectral Density of Downcomer Pressure (Downcomer No. 6)

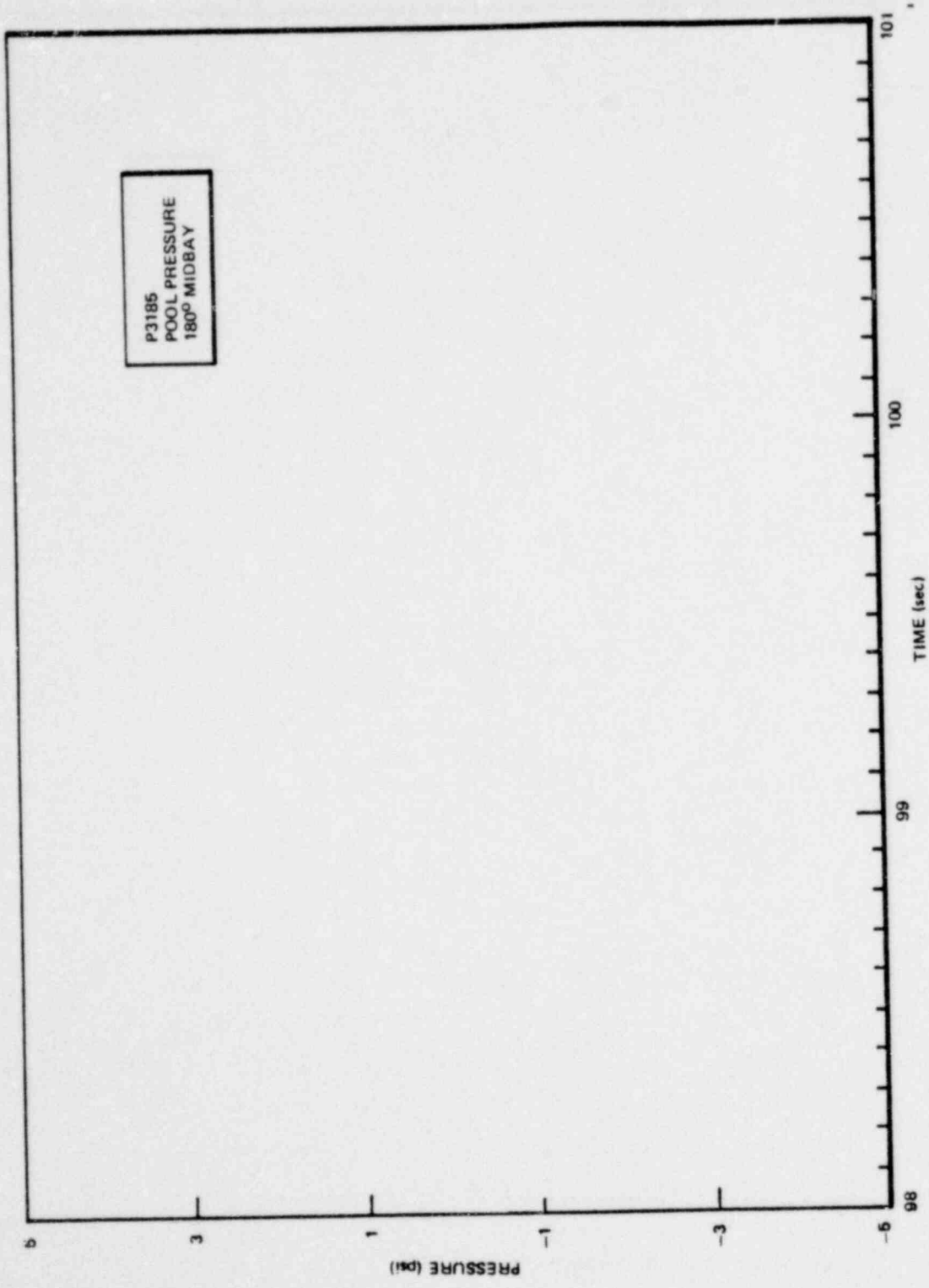

Figure 6.4.2-3. Pool Boundary Pressure During Chugging - 180° Midbay (Small Steam Break Test - M1)

*Proprietary information deleted

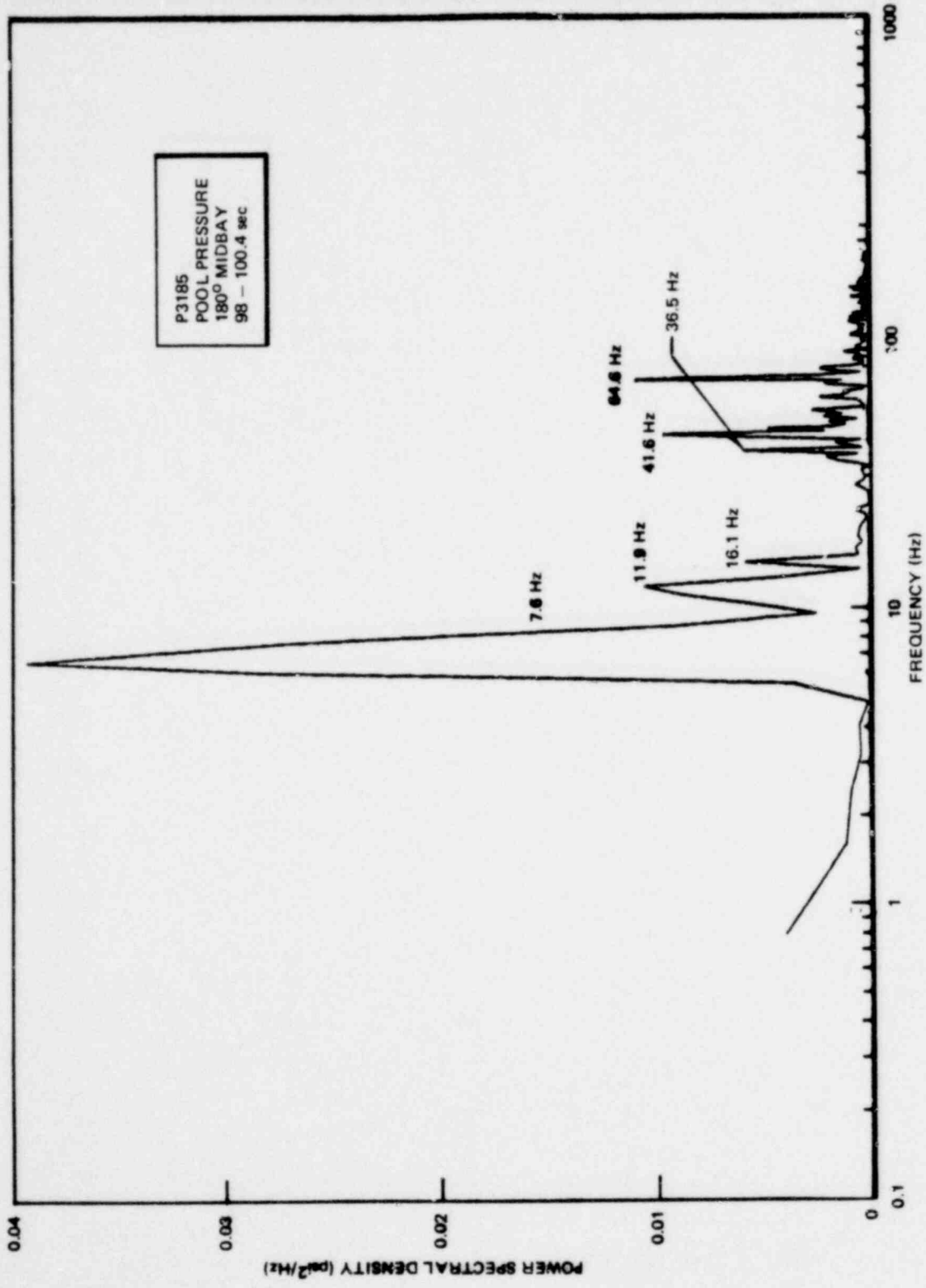

Figure 6.4.2-4. Power Spectral Density of Pool Pressure at 180° Midbay (Pre- and Post-Chug Period)

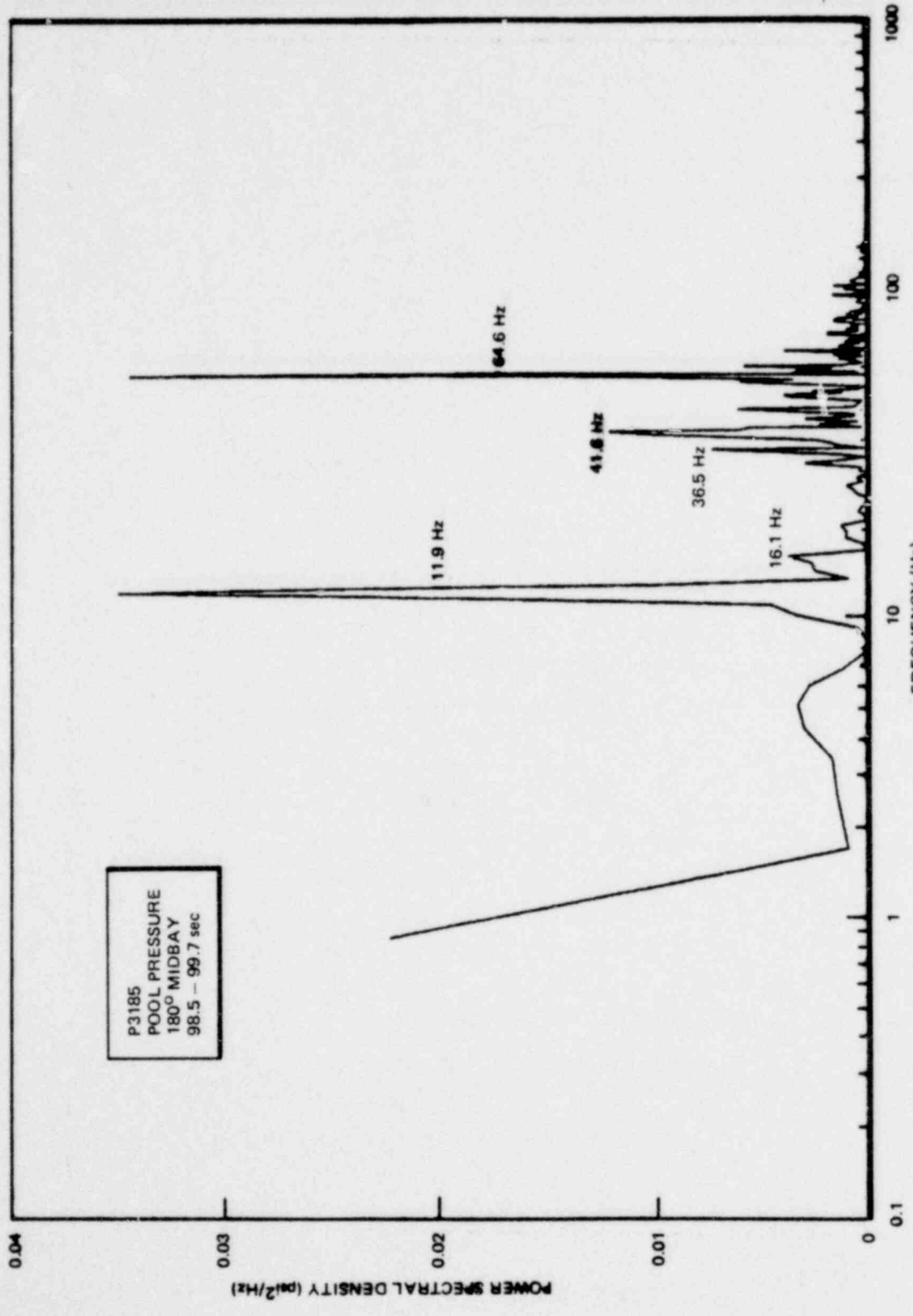

Figure 6.4.2-5. Power Spectral Density of Dynamic Pool Pressure at 180° Midbay (Chug and Post-Chug Period)

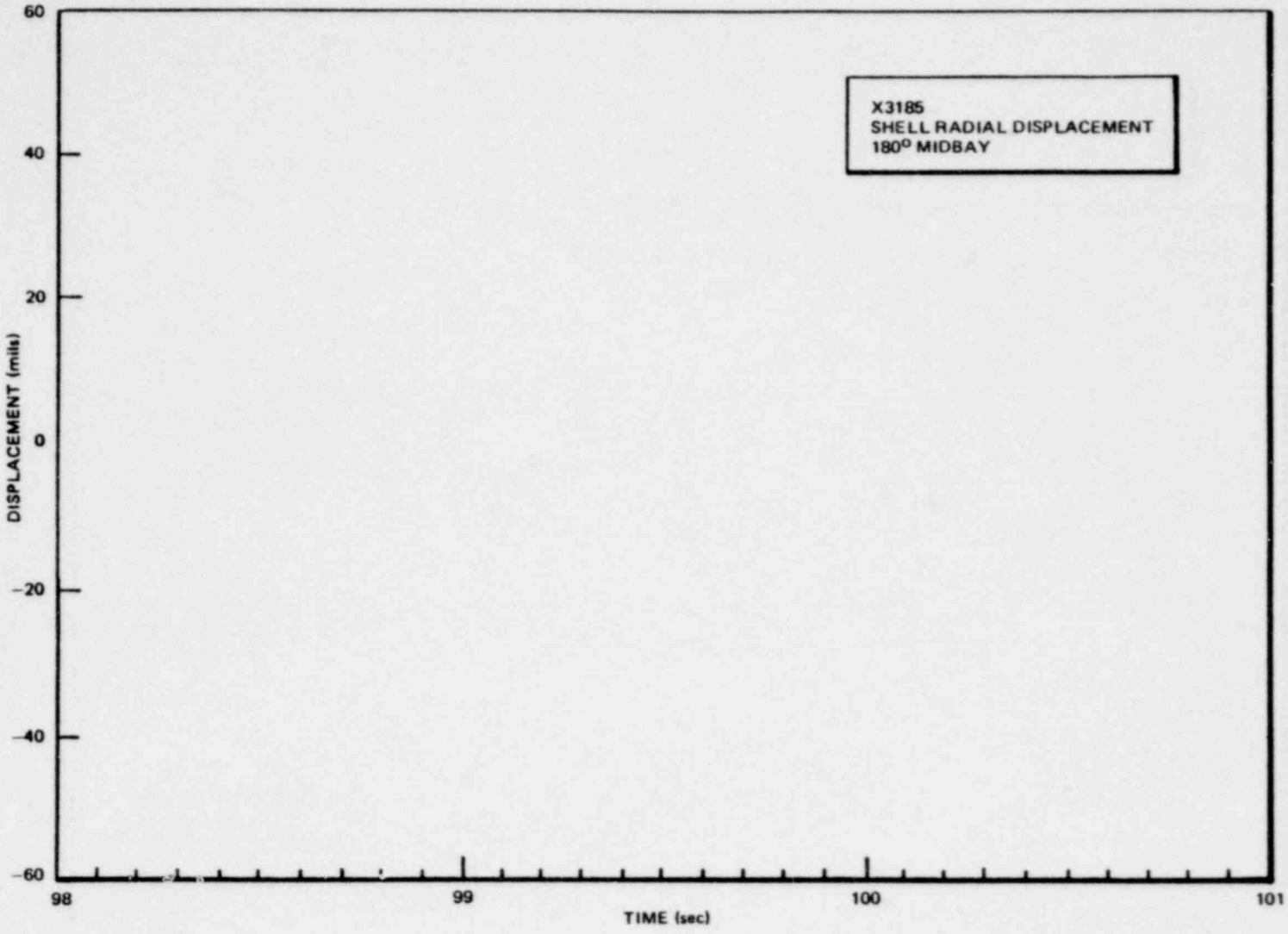

Figure 6.4.2-6. Shell Radial Displacement During Chugging - 180° Midbay (Small Steam Break Test - M1)

*Proprietary information deleted

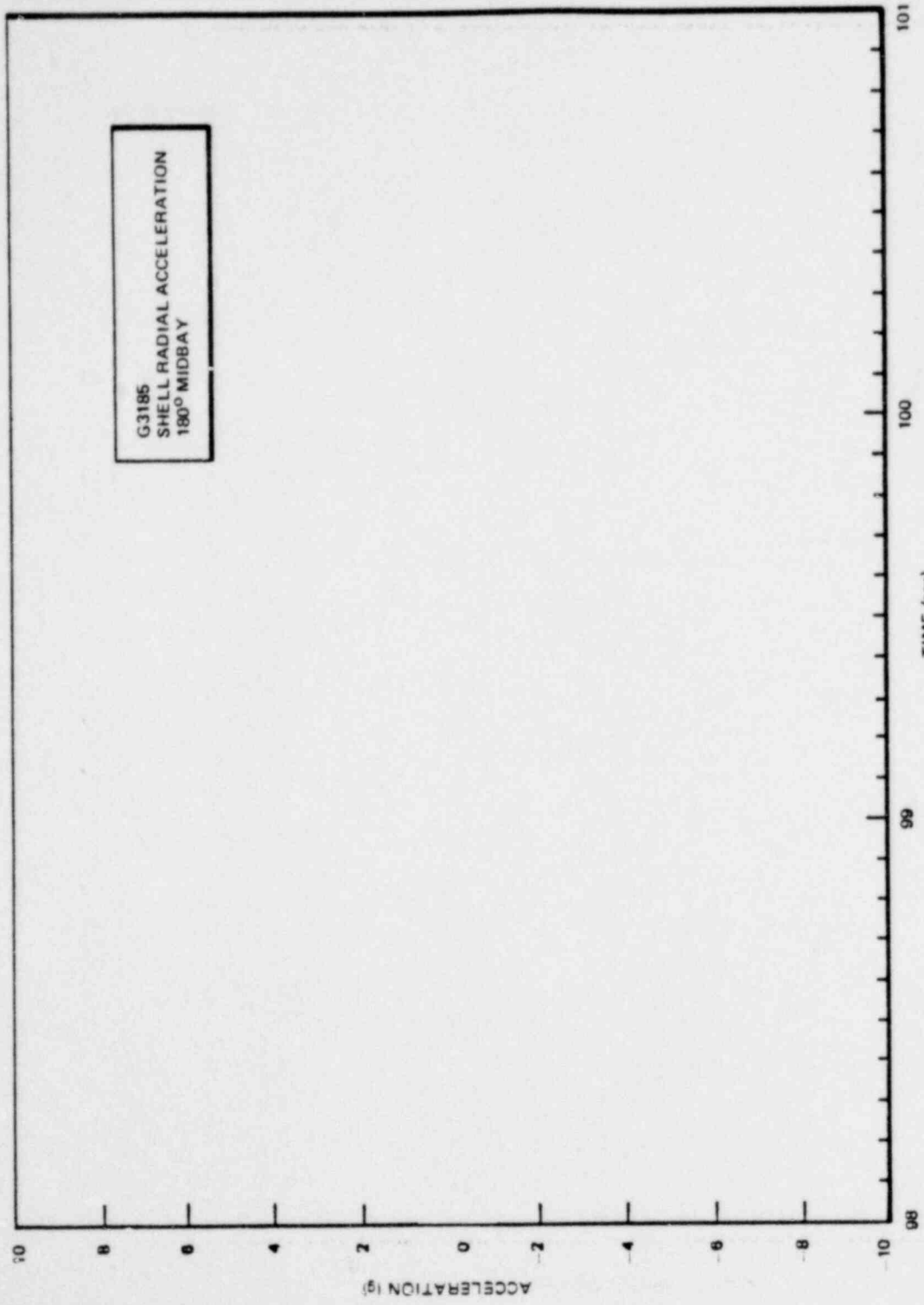

Figure 6.4.2-7. Shell Radial Acceleration During Chugging - 180° Midbay (Small Steam Break Test - M1)

*Proprietary information deleted

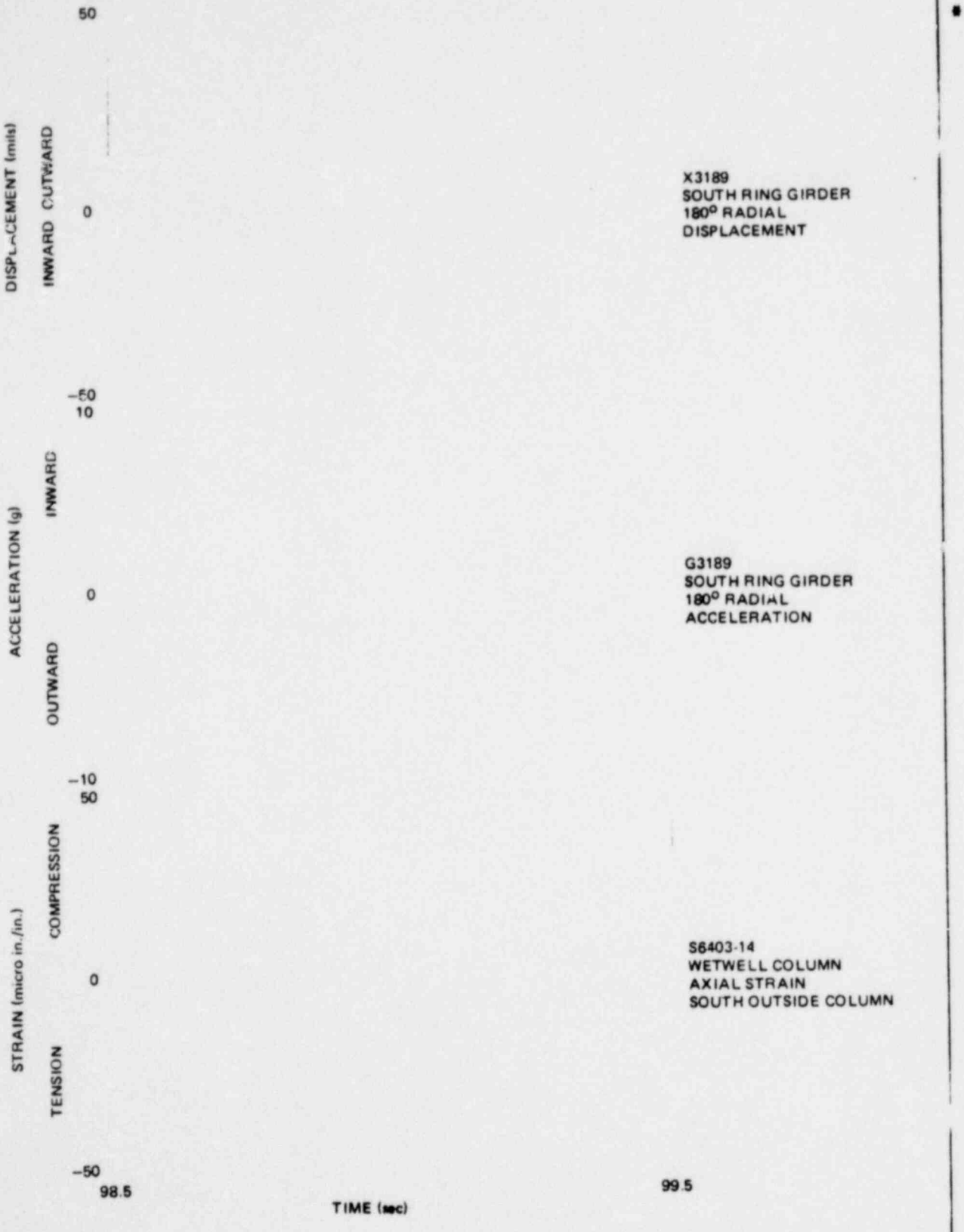

Figure 6.4.2-8. Ring Girder and Wetwell Support Column Responses During Chugging (Small Steam Break Test - M1)

*Proprietary information deleted

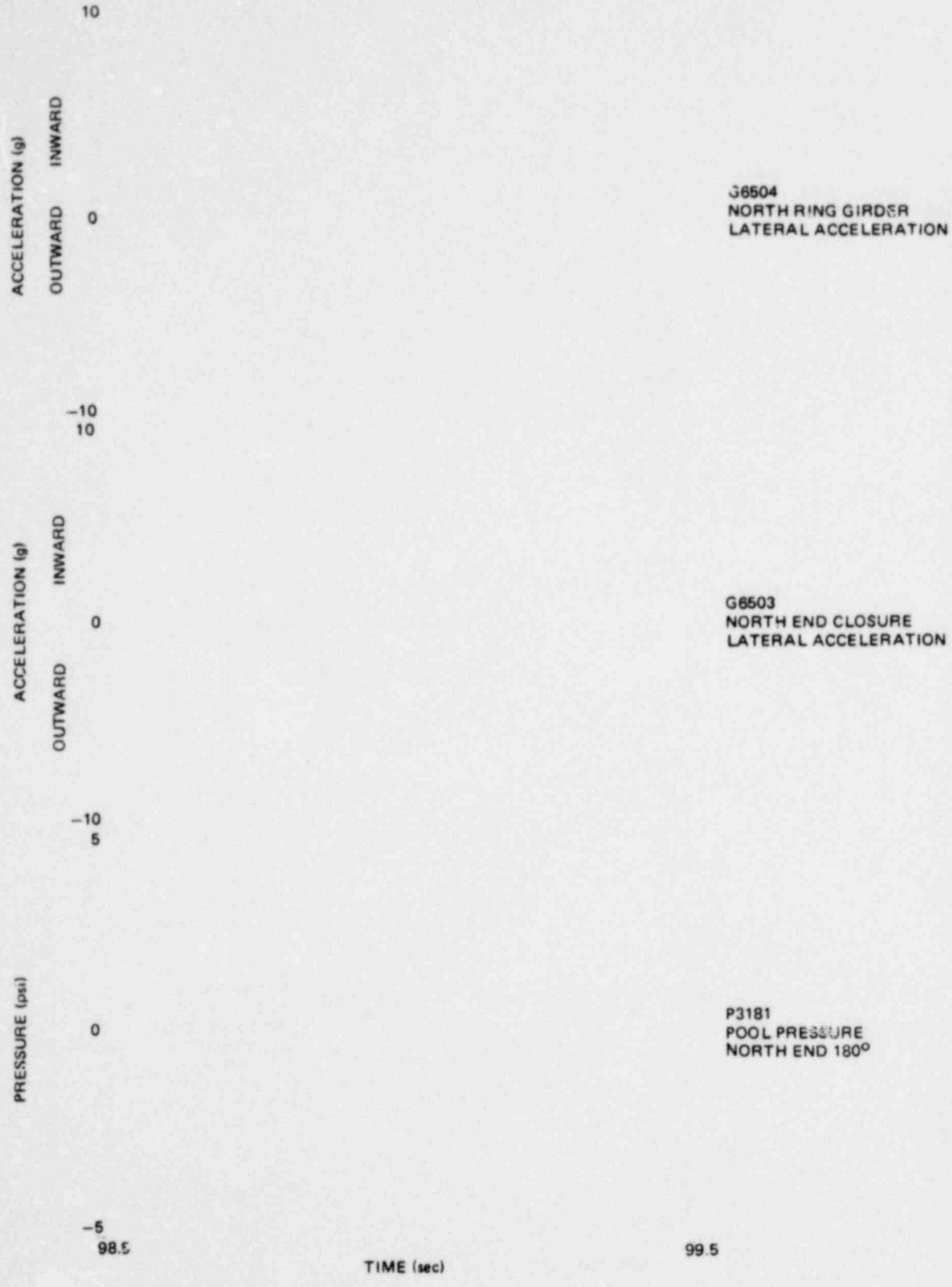

Figure 6.4.2-9. North End Closure Response During Chugging Small Steam Break Test - M1)

*Proprietary information deleted

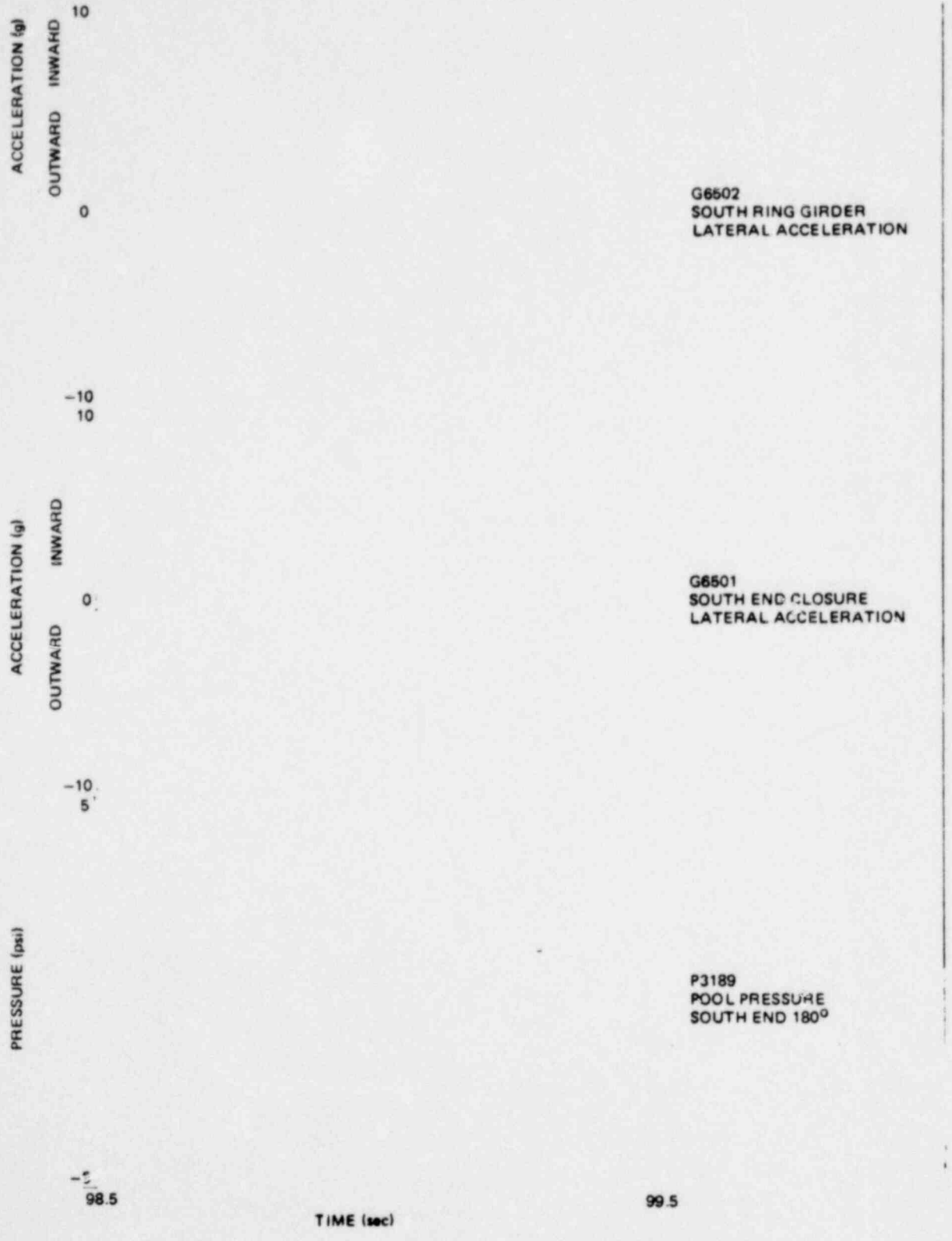

Figure 6.4.2-10. South End Closure Response During Chugging (Small Steam Break Test - M1)

*Proprietary information deleted

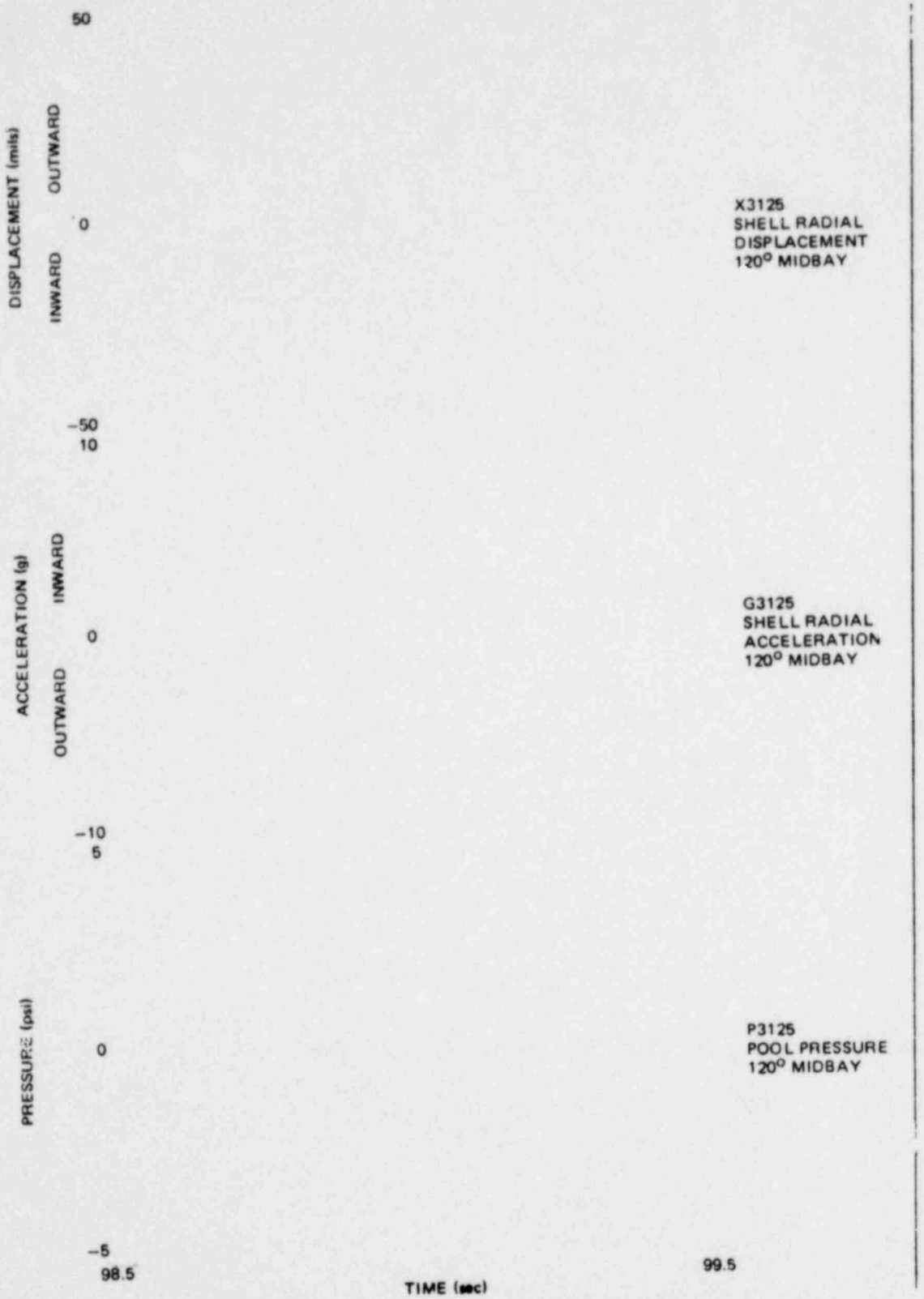

Figure 6.4.2-11. Wetwell Shell Response at 120° Midbay During Chugging (Small Steam Break Test - M1)

*Proprietary information deleted

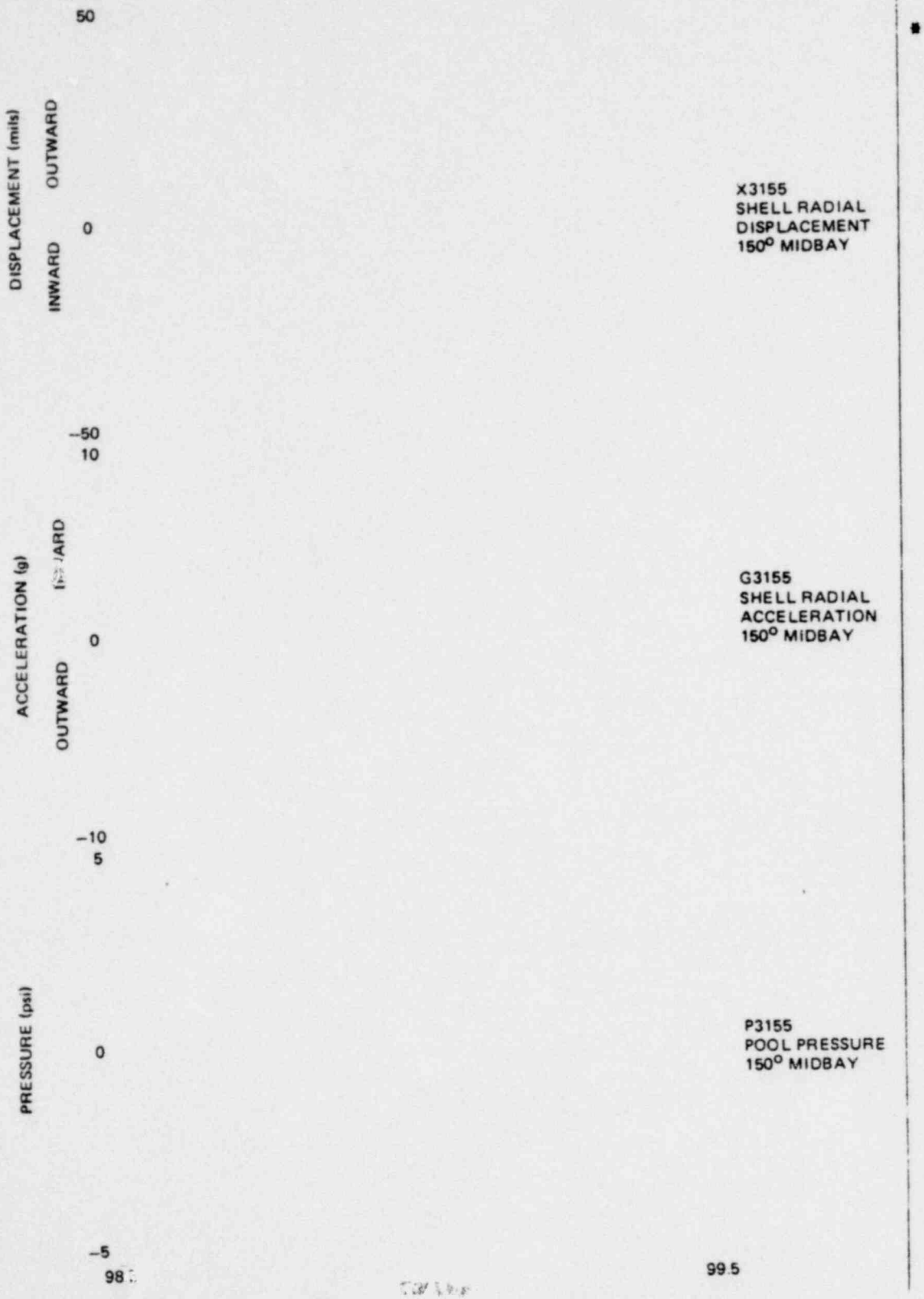

Figure 6.4.2-12. Wetwell Shell Response at 150° Midbay During Chugging (Small Steam Break Test - M1)

*Proprietary information deleted

1158 169

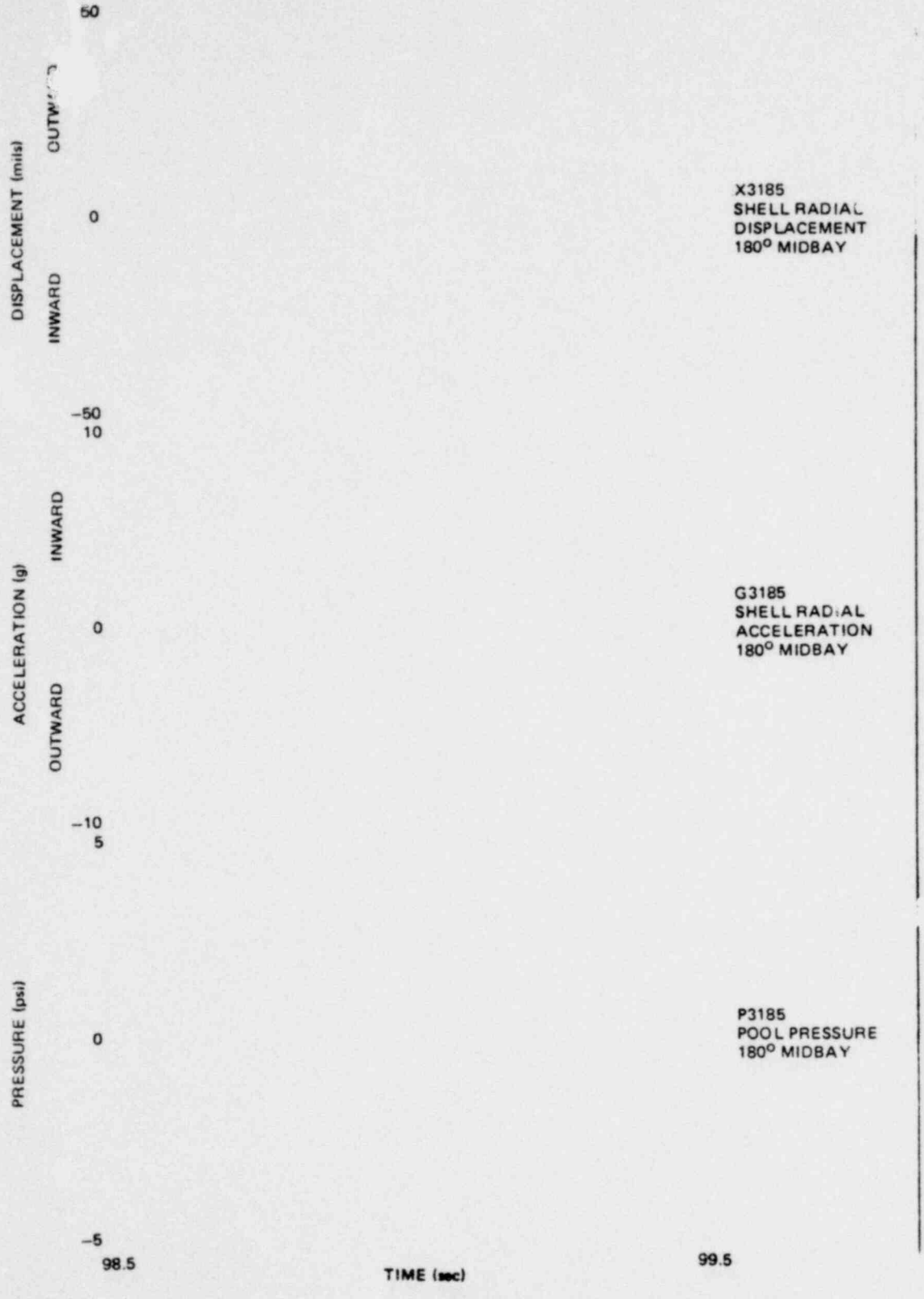

Figure 6.4.2-13. Wetwell Shell Response at 180° Midbay During Chugging (Small Steam Break Test - M1)

***Proprietary information deleted**

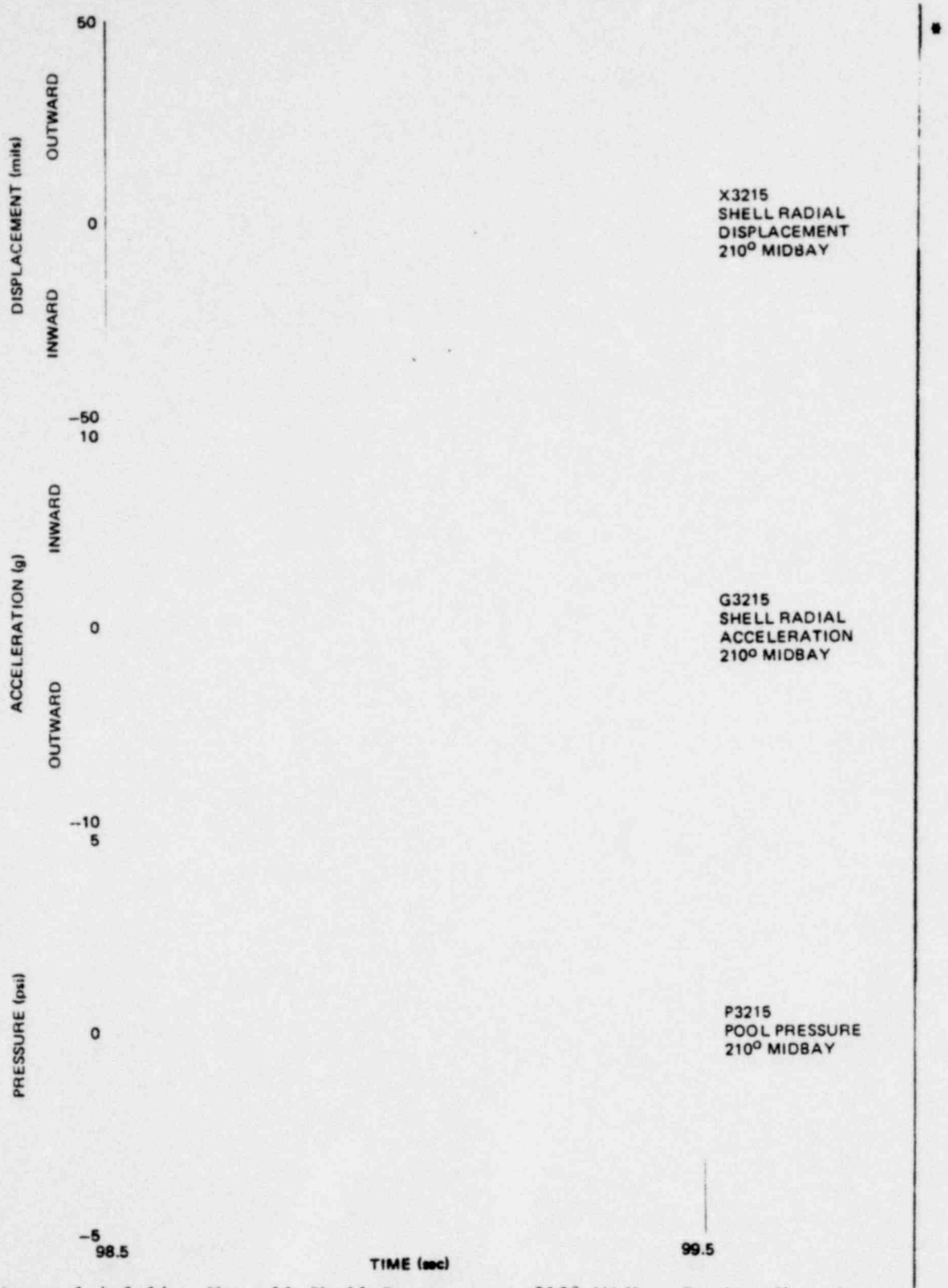

Figure 6.4.2-14. Wetwell Shell Response at 210° Midbay During Chugging (Small Steam Break Test - M1)

*Proprietary information deleted

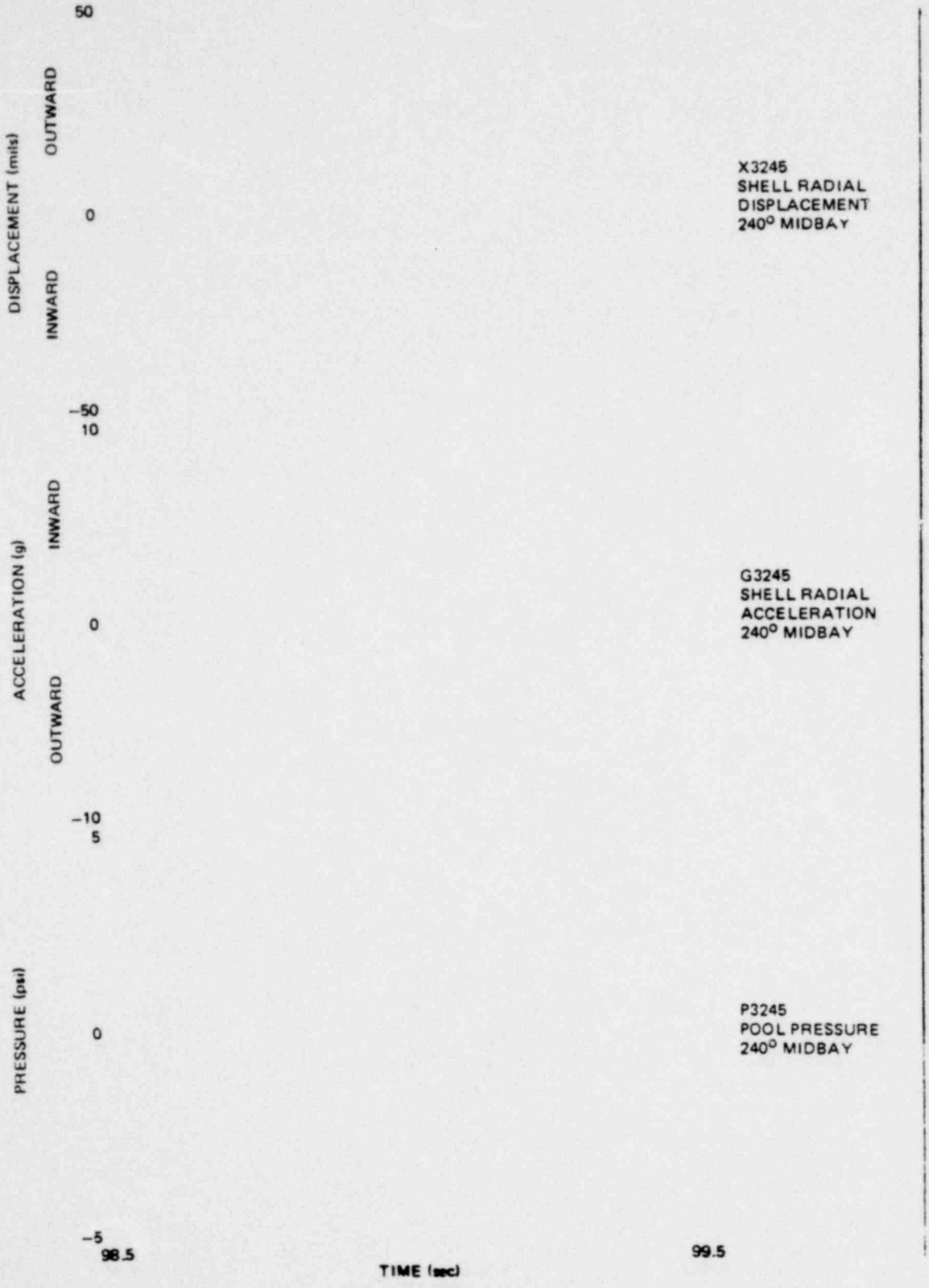

Figure 6.4.2-15. Wetwell Shell Response at 240° Midbay During Chugging (Small Steam Break Test - M1)

*Proprietary information deleted

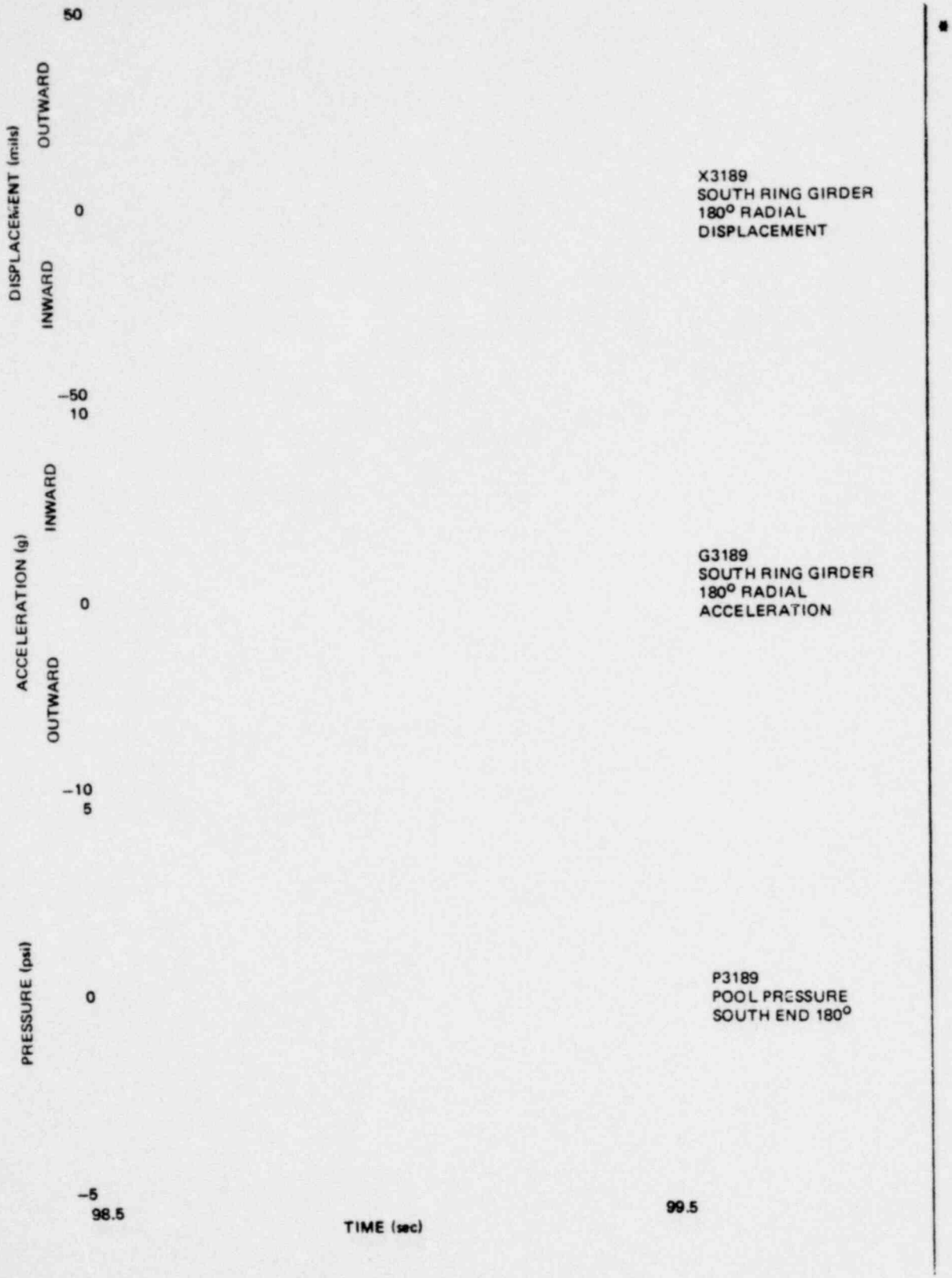

Figure 6.4.2-16. Wetwell Shell Response at 180° South End During Chugging (Small Steam Break Test - M1)

*Proprietary information deleted

1158 173

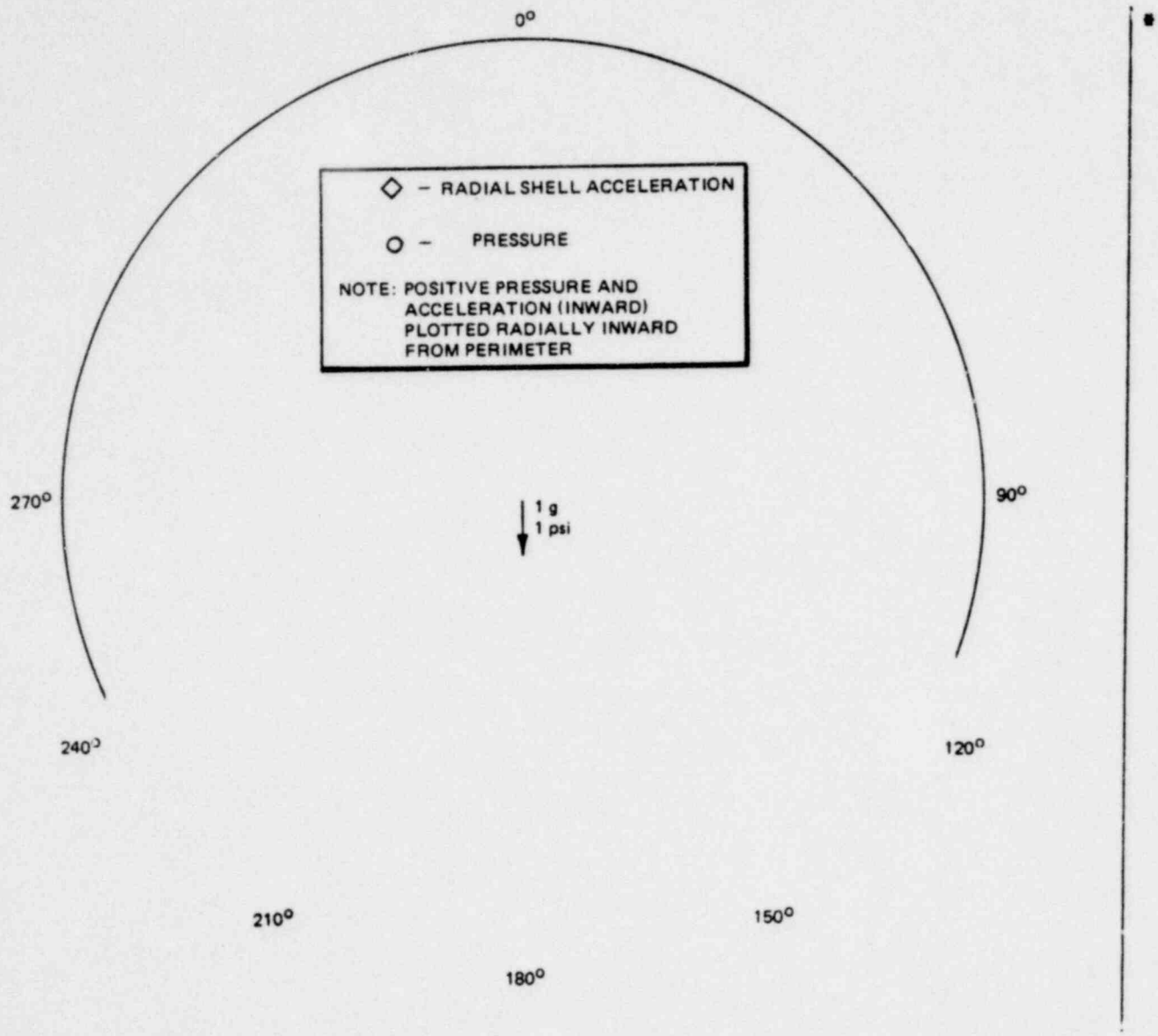

Figure 6.4.2-17. Pool Pressure and Shell Radial Acceleration Distributions about Midbay During Chugging (98.684 sec)

*Proprietary information deleted

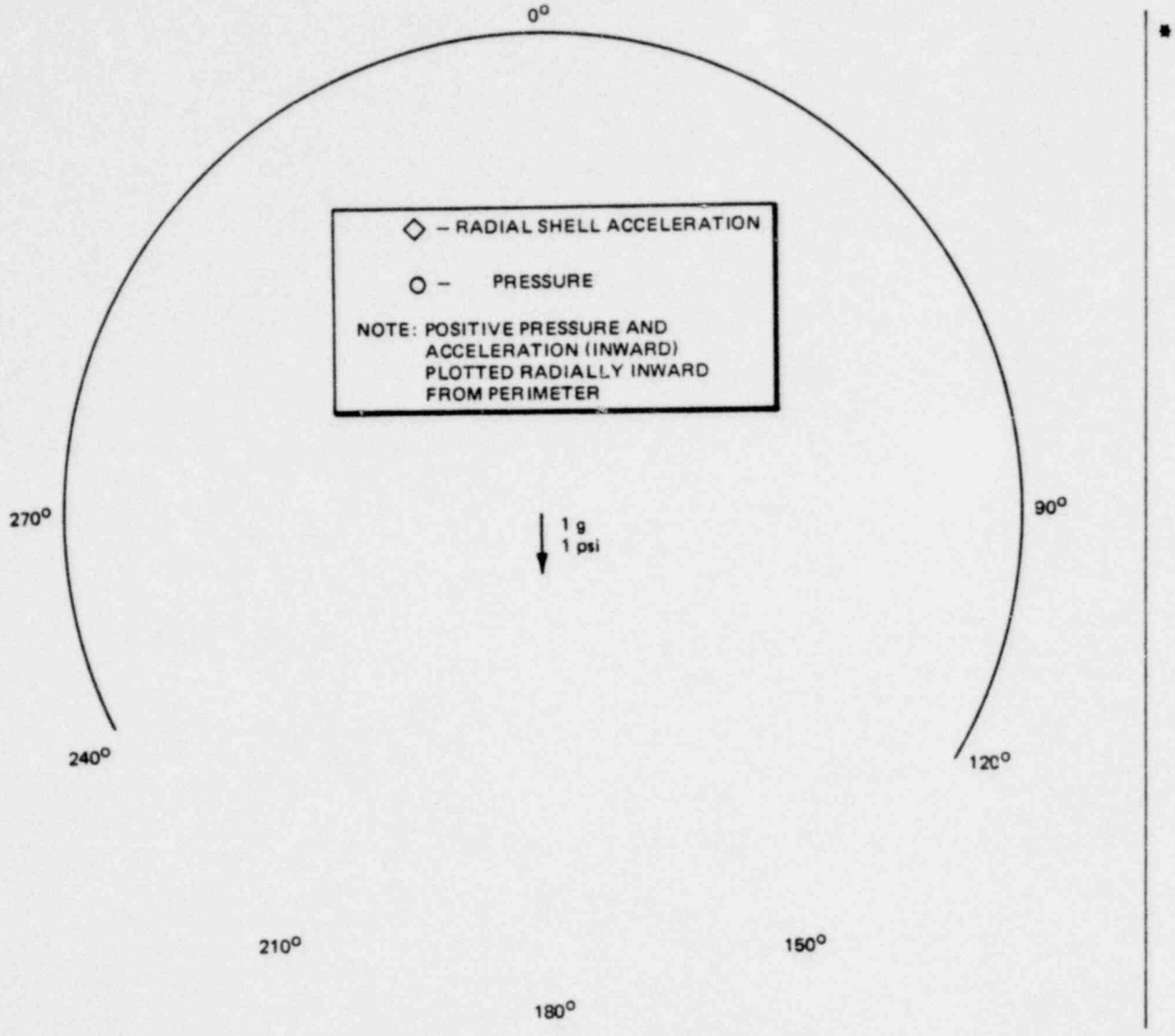

Figure 6.4.2-18. Pool Pressure and Shell Radial Acceleration Distributions about Midbay During Chugging (98.687 sec)

*Proprietary information deleted

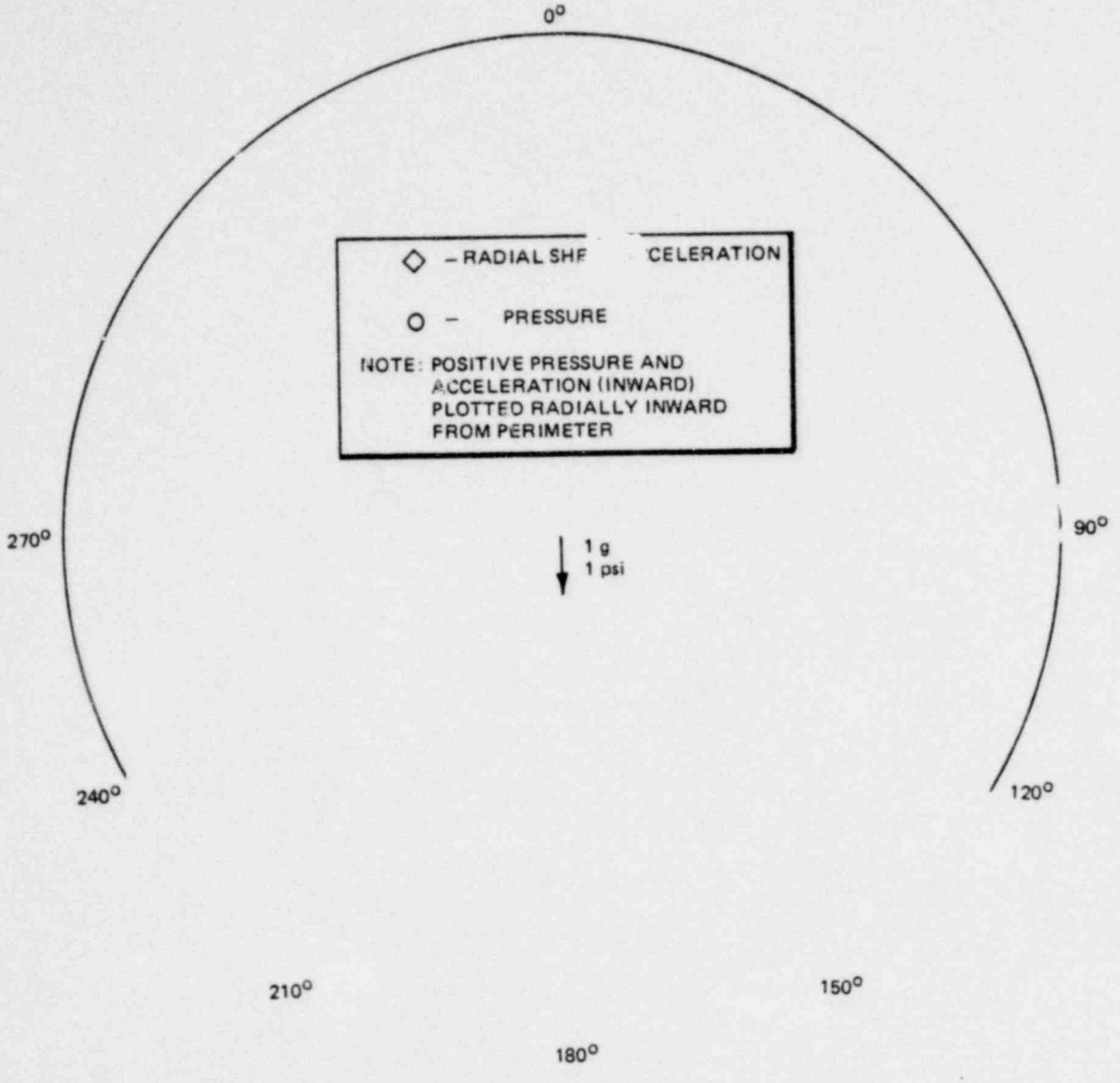

Figure 6.4.2-19. Pool Pressure and Shell Radial Acceleration Distributions about Midbay During Chugging (98.690 sec)

*Proprietary information deleted

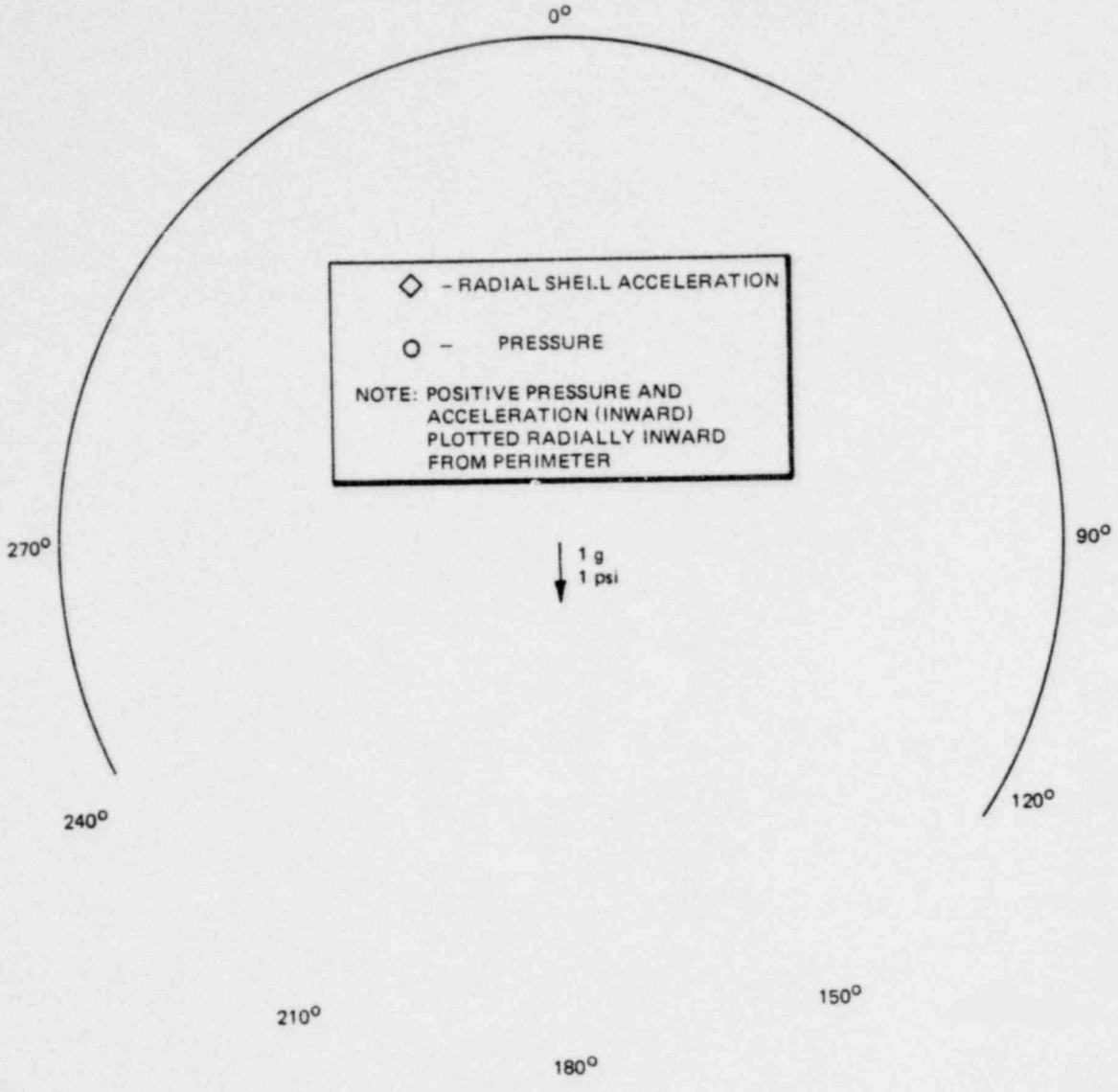

Figure 6.4.2-20. Pool Pressure and Shell Radial Acceleration Distributions about Midbay During Chugging (98.693 sec)

*Proprietary information deleted

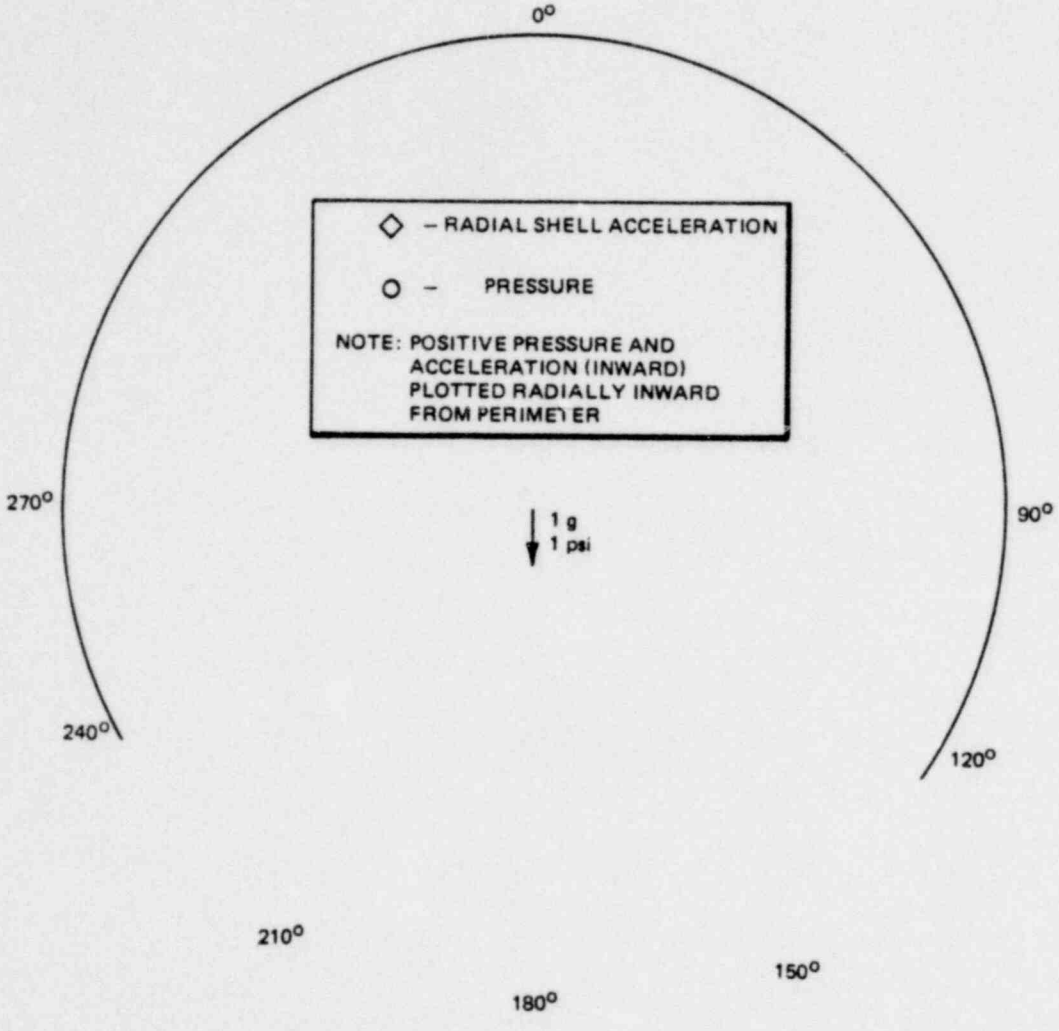

Figure 6.4.2-21. Pool Pressure and Shell Radial Acceleration Distributions about Midbay During Chugging (98.696 sec)

*Proprietary information deleted

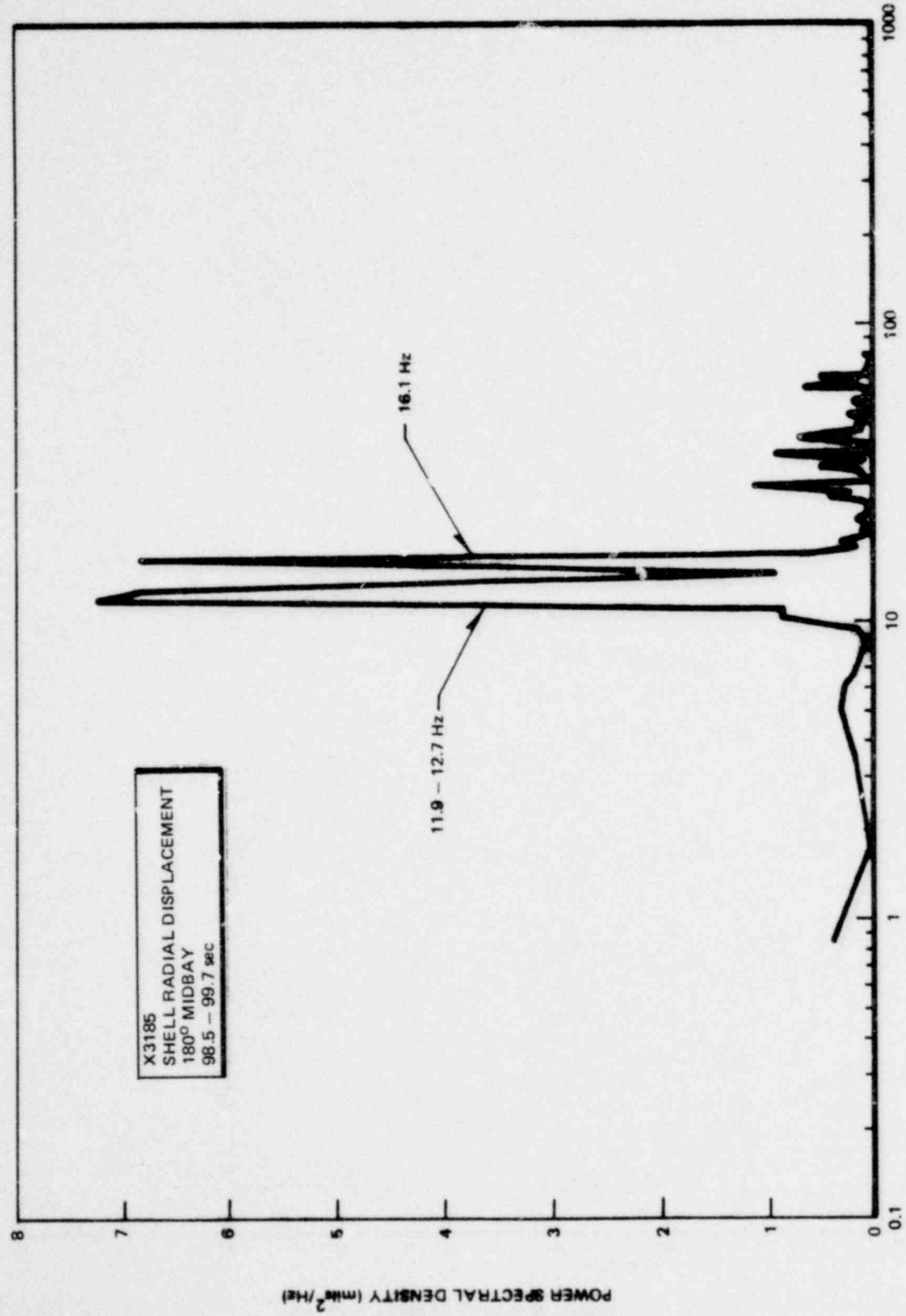

Figure 6.4.2-22. Power Spectral Density of Shell Radial Displacement at 180° Midbay

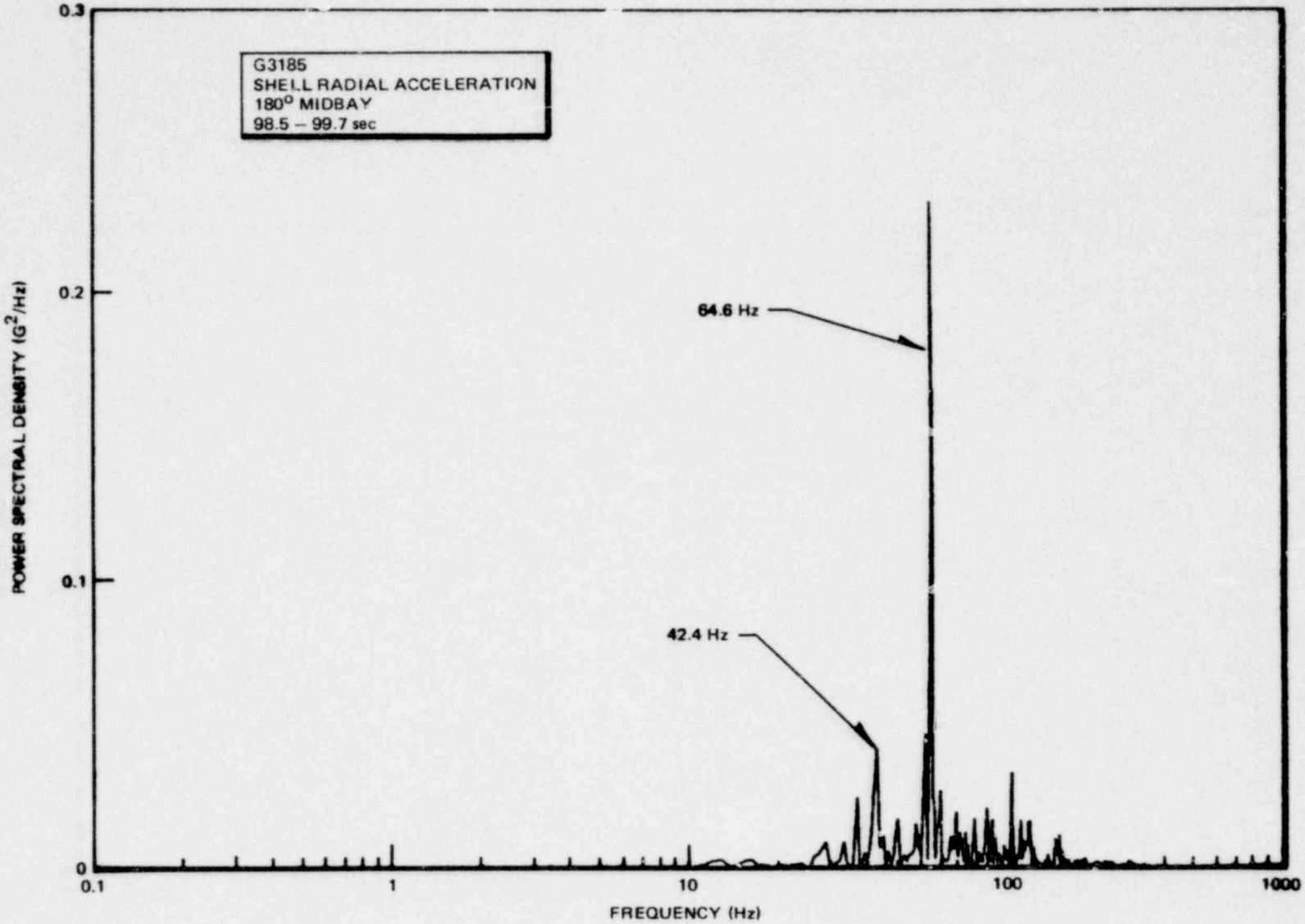

Figure 6.4.2-23. Power Spectral Density of Shell Radial Acceleration at 180° Midbay

6.5 MOVIE RESULTS

6.5.1 Above Water Movie Results

The above water films were taken in the FSTF with hardware described in Section 3.6 in an attempt to quantify the magnitude of post-LOCA surface waves and to evaluate condensation effectiveness of the suppression pool. The films also provided some qualitative observations regarding the visual effects of test parameter variations.

6.5.1.1 Surface Waves

For most of the test period, the waves observed consisted of rolling waves from 1 in. to 2 in. in amplitude (valley to peak) and 1-2 Hz. Only just after pool swell were any significant waves (1 ft - 2 ft valley to peak) recorded. These large waves appear to be a result of the energy imparted to the pool swell and the inertia of the pool. Wave frequency appears to be random for this period, which lasted from 12-30 sec after test initiation.

Mass flux (break size and type) and submergence were the two matrix parameters that significantly influenced post pool-swell pool waves. Higher mass flux (liquid in relation to steam and larger break size) imparts more energy to the pool and accordingly creates a more violent pool swell and larger post pool-swell waves. Increased submergence (increased water mass) extended the period of large post-LOCA waves as a result of higher pool inertia.

After the pool swell event during certain tests, standing waves appeared around the downcomers. These standing waves are believed to be a beat phenomenon in which the pressure pulses from adjacent downcomers reinforce and negate each other and result in the surface standing waves observed. Table 6.5.1-1 presents data on standing waves from the test matrix. Note that tests M5 and M6 have high frequency waves which are believed to be splashes from downcomer oscillations rather than the beat phenomenon described earlier.

6.5.1.2 Condensing Water Vapor in Wetwell Airspace

In all runs with above-water movies, small amounts of condensing water vapor are evident in the wetwell airspace. A relatively large amount of condensing vapor is observed only towards the end of one test, M6 (1 ft - 6 in. downcomer submergence, small steam break, and 120°F initial pool temperature). The source of this vapor cannot be distinguished in the movie.

6.5.1.3 Other Observations

Downcomer oscillations were among the few visual observations that could be related to instrument data. Cyclic motion of the downcomers was primarily in a vertical plane perpendicular to the ring header axis. Amplitudes were measured at the water surface. Table 6.5.1-2, Visual Observations of Downcomer Oscillations, presents frequency and amplitudes for the text matrix. Oscillation frequency varies from 5 to 10 Hz.

Parameter variations which resulted in increased downcomer oscillation amplitudes include increasing the initial pool temperature to 120°F and reducing the downcomer submergence to 1 ft 6 in. The medium steam break test indicates that increased mass flux results in increased downcomer oscillations. In M7, the large steam break, all the downcomers were tied in pairs and negligible oscillations were observed. In M8, the large liquid break, downcomers 5 and 6 were [illegible] and oscillations were observed in downcomer 5 which was in the field of view, but estimates of the amplitude were not possible because of the condensing vapor.

Table 6.5.1-1

POST POOL-SWELL STANDING WAVES

Test[4]	Frequency (Hz)	Amplitude[3] (in.)	Duration (sec. from test start)
M-1	None		
M-2	3.5	2-3	12-20
	7	2	20-60[2]
M-3	3	2-3	50-90[2] intermittent
M-4	3	2-4	40-80
M-5	3	2-4	20-60
	8	6-9	60-90 (See (1))
M-6	6	12-18	20-40 (See (1))
	5	6	>40
M-7	3.5	2	20-24, 30-40
M-8	6	2-3	13-30
M-9	None		
M-10	None		

(1) High frequency waves about downcomers in M-5 and M-6 appear to be splashing from severe downcomer vibration rather than standing waves.
(2) Observations were no longer possible after denoted time because of fogged viewport.
(3) Wave amplitudes were measured valley to peak for downcomers 3 and 5.
(4) Refer to Section 4.3 for status of downcomer strapping.

Table 6.5.1-2

VISUAL OBSERVATIONS OF DOWNCOMER OSCILLATIONS

Test[4]	Frequency (Hz)	Amplitude[3] (in.)	Duration (time from test start-sec)
M-1	None visible		
M-2	6-7	1-2	10-60(1)
M-3	None visible		
M-4	None visible		
M-5	10	1-2	10-40
	8 & 25	1-2	40-200 (2)
M-6	6	2	10-90
	5	2-3	90-120
M-7	None visible		
M-8	Some oscillations (8 sec.?) of downcomer #5 but indeterminable for fogged port.		
M-9	Some oscillations (10 sec-?) but indeterminable for fogged port.		
M-10	None visible		

(1) Observations no longer possible after denoted time because of fogged viewport.
(2) For the interval denoted in M-5 the basic oscillation frequency is 8 Hz but these oscillations are cyclicly damped at 2.5 Hz.
(3) Amplitudes are measured at water surface, valley-to-peak for downcomers 3 and 5.
(4) Refer to Section 4.3 for status of downcomer strapping.

APPENDIX A
MARK I
FULL SCALE TEST FACILITY
SCALING REPORT

TABLE OF CONTENTS

1.0 SUMMARY

A Full Scale Test Facility (FSTF) was designed, constructed and operated to establish experimental bounding hydrodynamic chugging loads and representative structural response of the Mark I suppression chamber. The facility was scaled from a reference Mark I plant, Monticello, which was selected so that resulting hydrodynamic data would be conservative and structural response data would be representative relative to the remaining Mark I plants. Facility components that were considered in the scaling criteria were:

- Wetwell (suppression chamber),
- Vent system (main vents, vent header, and downcomers),
- Drywell,
- Blowdown line and critical flow nozzle, and
- Reactor pressure vessel (steam vessel).

The FSTF scaling criteria were primarily based on the chugging phenomenon. Investigation of the condensation oscillation phenomenon was introduced late in the design phase of the project, but the chugging scaling criteria were adequate for scaling the condensation oscillation phenomenon.

A 22-1/2 degree segment (one bay) of the Monticello suppression chamber, vent header and downcomers was modeled to full scale dimensions. The selected Monticello bay modeled for FSTF was the one that contains the maximum number of downcomers and would result in maximum chugging loads. The main vents from the drywell to wetwell, the drywell simulation of the loss of coolant accident were appropriately scaled to represent the full scale plant. The primary scale parameters used to size the facility were the FSTF to Monticello suppression chamber volume ratio (1/16) and total number of downcomer ratio (8/96 = 1/12).

A summary of the specific scaling parameters used for each component is given in Table 1-1. Structural and hydrodynamic response of the suppression vessel duplicates the Monticello suppression chamber response because of the 1 to 1 scale factor. The vent system has been sized to duplicate Monticello fluid state, flow transient conditions and symmetry. Vent header and downcomer structural response is prototypical of the referenced Mark I plant. The pipe break area in Table 1-1 is for a large liquid break and is included to show that the Mark I plant DBA case has been bounded. Details on how these scaling parameters were determined are contained in the body of this Appendix.

Table A-1

MARK I FSTF S ALING PARAMETER SUMMARY

	Calculated Monticello	Scale Factor	Scaled Monticello	Calculated FSTF
SUPPRESSION CHAMBER				
All Dimensions for One Bay (22-1/2 segment)	1	1	1	1
Shell Frequency Response	3.46Hz	1	3.46Hz	3.35Hz
Vessel Radial Frequency Response	16Hz	1	16Hz	14.5Hz
Vessel Vertical Frequency Response	27Hz	1	27Hz	27Hz
End Closure Frequency Response	Not Applicable	Not Applicable	Based on Assumed Boundary Conditions $\geq$50Hz	66Hz
VENT SYSTEM				
Flow Resistance	5.2	1	5.2	4.8
Main Vent Pipe Area	35.6 ft^2	8/24	11.9 ft^2	11.9 ft^2
Volume	16,000 ft^3	1/12	1,134 ft^3	1,484 ft^3
Vent Header Vertical Structural Response for Unit Load	0.072 in	1	0.072 in	0.072 in
DRYWELL VESSEL				
Total Volume	134,000 ft^3	1/16	8,375 ft^3	8,375 ft^3
Liquid Hold Up Volume	905 ft^3	1/16	57 ft^3	57 ft^3

Table A-1 (Continued)

MARK I FSTF SCALING PARAMETER SUMMARY

	Calculated Monticello	Scale Factor	Scaled Monticello	Calculated FSTF
REACTOR PRESSURE VESSEL SIMULATOR				
Volume	13,950 ft^3	$\geq$1/12	$\geq$1,160 ft^3	1,444 ft^{3*}
Cross Sectional Area	229 ft^2	$\geq$1/12	$\geq$19 ft^3	33 ft^2
Pipe Break Area	4.02 ft^{2**}	$\geq$1/12	$\geq$0.335 ft^2	0.442 ft^2
Operating Pressure	1,050 psi	1	1,050 psi	1,050 psi
Operating Temperature	550°F	1	550°F	550°F
VACUUM BREAKER				
Flow Rate Through Breaker @ 0.5 psi	231 lb/sec	8/12	15 lb/sec	$\leq$15 lb/sec
Opening Pressure Set Point	0.1 psi	1	0.1 psi	0.1 psi

* Up to Flow Nozzle

** Design Basis Accident

2.0 SCALING CRITERIA

2.1 SCALING CONSIDERATIONS

To meet the project objectives defined in Section 1.0, structural and hydrodynamic simulation of the Mark I suppression chamber and LOCA is required. The facility components which were considered in establishing design criteria which will result in accurate structural and hydrodynamic scaling were:

- Wetwell (suppression chamber),
- Vent system,
- Drywell,
- Blowdown line and critical flow nozzle,
- Reactor pressure vessel (steam vessel).

Primary structural and hydrodynamic factors which affect the suppression chamber and LOCA simulation were identified and design criteria established to model the Mark I plants.

2.2 REFERENCE PLANT SELECTION

Review of the plant unique parameters resulted in the conclusion that no one plant could represent both the most severe hydrodynamic and structural configuration. It was therefore decided that the best approach was to select a reference plant which would result in a conservative hydrodynamic and representative structural configuration for the Mark I plants. The FSTF was to be directly scaled from the selected reference plant configuration.

The selected reference plant was Monticello, and the key parameters expected to influence the chugging loads which were used to make this selection are

given in Table 2-1. As indicated, Monticello parameters were all near the extreme condition which was expected to give the maximum chugging wall loads.

2.3 SUPPRESSION VESSEL

The wetwell vessel was the most critical component to simulate in establishing prototypical structural and hydrodynamic response due to chugging. The selection and sizing of the wetwell in turn govern the scaling criteria for the remaining facility components.

The FSTF wetwell was selected to be a 22-1/2 degree segment (1/16th) of the Monticello wetwell (see Figure 2-1). The single bay, with miter joints at each end, was chosen primarily because it would result in good structural simulation of the suppression chamber at mid-bay. This approach results in a three-dimensional test which simulates the most severe downcomer to pool surface area ratio (most severe hydrodynamic chugging condition) which exists in the Monticello plant.

Using the single bay approach, each end of the 22-1/2 degree segment was assumed to be a hydrodynamic and structural plane of symmetry. This in fact was not the case hydrodynamically but will result in conservative hydrodynamic chugging loads for the adjacent bays which actually have half the number of downcomers. Structurally, the most important simulation parameters were the radial (outward from torus center), vertical (bouncing), and shell response modes. With the one bay approach, these modes could and were modeled to duplicate Monticello. Attempting to simulate the non-symmetric structural response nodes of the torus would require building the full 360° torus, an approach which would be costly and result in no significant improvement in chugging data. The FSTF wetwell design was therefore scaled to duplicate:

(1) geometry of a single bay of the Monticello suppression chamber

(2) structural responses in the radial, vertical, and shell modes of the Monticello torus

In addition, since the ends of the FSTF wetwell were assumed to be planes of symmetry, very stiff closures (end plates) were used to preserve the symmetry and prevent fluid-end closure structure interaction with the hydrodynamic response of the vessel. With relatively stiff end closures, reflected hydrodynamic loads would not be amplified or attenuated and would be representative of chugging loads from adjacent bays. Effects of end closure stiffness on shell response were minimized with the use of shell extensions.

The scaling criteria established for the FSTF wetwell vessel and restraint system were as follows:

- The FSTF wetwell vessel would be a full scale 22-1/2° segment of the Monticello suppression chamber, including support columns. Using a full scale single bay results in reasonable structural simulation of the Monticello suppression chamber at mid-bay and allows the duplication of what is considered to be the most severe hydrodynamic chugging condition.

- Duplicate the Monticello suppression chamber shell, radial, and vertical structural response, i.e., match mode frequencies. Matching the mode frequencies insures fluid structure interactions would be duplicated and result in prototypical hydrodynamic and structural response data.

- Wetwell end closure natural frequencies would be as large as practical but not less than $50H_z$ (including the effects of the

water and shell). The mitre joints were assumed planes of symmetry and as such, maximum stiffness is desired to prevent fluid structure interaction effects which might result in hydrodynamic amplification of attenuation of the chugging loads due to closure motion. The enclosure was attached to a shell extended from the mitred joints to retain the structural response of the ring girder/support column combination.

2.4 VENT SYSTEM

The vent system connects the drywell vessel to the wetwell suppression pool and consists of the main vents, vent header, and downcomers. The primary scaling considerations were as follows:

Hydrodynamic

- Flow area and resistance
- Accustic path length
- Flow mixing and stratification characteristics
- Capacitance (volume)

Structural

- Downcomer response
- Vent header response.

The vent system transfers fluid (air, steam and/or water) from the drywell vessel to the wetwell vessel in the event of a LOCA. The fluid flow behavior in the vent system may govern some of the characteristics of chugging. Modeling the vent system was, therefore, an important objective. Parameters which were believed to affect the transient flow were carefully selected. Parameters believed to be critical in duplicating the transient flow condition between the drywell and wetwell were: system volume (capacitance effect); flow area and resistance which establish flow

velocity losses and fluid state; and acoustic path length which establishes the system acoustic frequency and may affect the transient flow behavior and frequency of chugs. Mixing and stratification were also important conditions along with the associated losses, to ensure the state of fluid entering the wetwell duplicates that which would occur in an actual Mark I plant. As stated in Section 2.3, the Monticello wetwell bay which contains the maximum number of downcomers was selected to be modeled to ensure upper bound loads were obtained. This bay contains eight downcomers. As shown in Figure 2-1, two main vent lines feed the vent header which in turn feeds a total of twenty-four downcomers. The FSTF vent system duplicates this flow configuration, and the main vent lines have been scaled to account for the reduced number of downcomers (eight) being fed. The vent header's actual diameter was retained within the test section, duplicating actual volume and flow losses in this region.

Structurally, it was desirable to de uple the main vents and vent header from the wetwell and duplicate the response of the Monticello plant. In this manner the structural response of the vent system would not interfere with the structural response of the wetwell and the wetwell would not interfere with the structural response of the vent system. Duplication of the Monticello vent header response and downcomer lateral response characteristics was also necessary in order to preserve the fluid structure interaction effects between the downcomers, discharging fluid and suppression pool in order to obtain prototypical chugging loads on the downcomer.

The scaling critieria established for the FSTF vent system were as follows:

1) Similar to Monticello, the vent system would feed the vent header at each end from two outlets located at the lower end of the drywell vessel. A prototypical Monticello jet deflector

would also be incorporated into the design to duplicate flow direction and fluid mixture in the vent system

2) The main vents would be sized to give the same average flow velocity as in the Monticello main vent lines with a cross-sectional area of 8/24 of the Monticallo main vent line cross-sectional area. The two main vent lines would be mirror images of each other.

3) The vent system would approximate the Monticello vent system geometry and have the same total flow resistance.

4) The vent header and downcomer system would be structurally decoupled from the wetwell except for the vent header support columns.

5) The vent header and vent header support system would approximate the Monticello vent header vertical response characteristics.

The vent header support system was designed to duplicate the structural deflection of the Monticello vent header support system under identical vertical loading conditions. Analyses conducted show that by reducing the FSTF vent header support column cross-sectional area by a factor of 1.84 resulted in deflection characteristics similar to Monticello. In Monticello, the main vent lines are directly coupled to the vent header and affect the vertical response of the vent header. In FSTF the main vent lines are not coupled; however, the effects of the main vent lines were considered in scaling the support column cross-sectional area. The vent header connection collar and clevis plates were reduced by a factor of two while the clevis pins remained the same size as Monticello since these components have little effect on the deflection characteristics of the vent header.

The downcomer structural response would be very close to Monticello since downcomers, vent headers and connection to the vent header were identical to Monticallo. Tie straps between downcomers prototypical of Monticello were used for some tests, and the specific test configuration is described in Section 4.3.

2.5 DRYWELL VESSEL

The purpose of the drywell vessel was to simulate as close as practical the reactor drywell enclosure. As such, the following scaling considerations were evaluated:

- Volume
- Air mass
- Liquid holdup/vent flow entrainment

Condensation rates are a principal factor in establishing chugging loads, since the fluid mixture (air, steam, and/or water) flowing through the vent system can affect the loads. Air mixing action, liquid entrainment, and heat losses in the drywell vessel and vent system will affect the condensation rate.

The Monticello Mark I wetwell suppression vessel consists of sixteen bays; the FSTF wetwell vessel was modeled after one of those bays. A scale factor of 1/16th was selected to size the drywell vessel in order to maintain the drywell to wetwell volume ratio the same as Monticello. Wetwell vessel pressurization transients would therefore come close to simulating that which would occur in Monticello in the event of a LOCA. The drywell liquid holdup volume was also scaled to the 1/16th factor in order to ensure duplication of liquid entrainment flow into the vent system.

A 1/12 (8/96) drywell volume scale factor was considered for accurate scaling of volume to exit flow area ratio; however, high wetwell free volume pressures would result and would not be representative of the Mark I plants. The wetwell freespace pressure was established to be an important chugging parameter, and an increased freespace pressure was expected to result in decreased chugging loads. The drywell volume to exit flow area ratio was concluded to be a secondary consideration relative to the final freespace pressure; therefore, a 1/16 scale factor was chosen.

A bounding approach was taken in modeling the drywell vessel due to the complexity of modeling the mixing and heat transfer characteristics of the Mark I drywell. The FSTF drywell was configured to minimize mixing, i.e., no internal structures, and the discharge from the blowdown line into the drywell was at the opposite end of the drywell from the vent lines, such that the air content of the vent flow during condensation phases would be at a minimum and thus result in upper bound loads. The FSTF drywell was insulated and heated to limit heat losses from the drywell and prevent condensation at test initiation.

Based on these considerations the following FSTF drywell vessel scaling criteria were established.

1) The drywell vessel and main vent lines would have a volume of 1/16 of the Monticello drywell vessel and vent system volume.

2) The drywell would be a symmetrical vessel with two vent system outlets located in the lower portion of the vessel and symmetrical to the inlet.

3) The liquid holdup volume in the vent system would be 1/16 of the Monticello liquid holdup volume.

4) The vessel would be insulated and be capable of being preheated in order to minimize heat losses.

2.6 REACTOR PRESSURE VESSEL SIMULATOR

A LOCA has to be accurately simulated to establish the correct mass and energy transients in the drywell vessel. In simulating a LOCA in the FSTF, a steam vessel (flash boiler) and blowdown line to the drywell were used. In scaling the steam vessel the following considerations were evaluated:

- Stored mass in vessel
- Stored energy in vessel
- Level swell in vessel

The mass in the vessel is limited only by the volume of the vessel and level swell requirements. The water mass in the vessel coupled with the discharge rate, (established from the fluid state and flow control nozzle size) determines the vessel blowdown time. The energy level is established solely by heating the water to the desired saturated water state. Since it is desired to simulate the operating reactor pressure vessel, this condition corresponds to a pressure of 1050 psia and a temperature of 550°F. To assure that energy and mass flow ratios could be bounded, the steam vessel volume must be equal to or greater than 1/12.

Steam vessel level swell was an important consideration in that it establishes the amount of liquid carryover during a steam break and vapor carryover during a liquid break, which would influence the rate of energy and the quality of flow to the drywell and ultimately to the wetwell. The Mark I blowdown flow conditions were bounded in the FSTF by conducting simulated steam breaks with liquid carryover less than expected for a Mark I steam line break and conducting simulated liquid breaks

with vapor carryover less than that expected for a Mark I recirculation line break. To assure the liquid carryover would be less during a steam line break, the ratio to FSTF steam vessel area to downcomer area was specified to be greater than the ratio of RPV area to downcomer area for a Mark I plant. This was specified so that the vapor velocities would be lower in the FSTF steam vessel. To assure the vapor carryover was less for the liquid line break, the liquid break outlet from the steam vessel was located as close to the bottom of the vessel as practical.

With fixed steam vessel conditions, the fluid discharge rate simulating a pipe break would be controlled by the blowdown line and flow control nozzle. Scaling considerations for the blowdown line were:

- Break size and location
- Flow mixing/stratification

The blowdown line transfers the fluid (liquid or steam) at a controlled rate from the steam vessel to the drywell vessel. The discharge rate would be controlled by a flow control nozzle where critical (choked) flow is established. The blowdown line length and frictional losses would be minimized, and the flow control nozzle would be positioned as close to the drywell inlet as practical. The blowdown piping would also be sized to prevent fluid stratification or slug flow.

The scaling criteria used to design the FSTF steam vessel and blowdown line were as follows:

Steam Vessel

(1) Volume equal to or greater than 8/96 of Monticello reactor pressure vessel volume

(2) Cross-sectional area equal to or greater than 8/96 of Monticello reactor pressure vessel area

(3) Nominal operation conditions of 1050 psia and 550°F

(4) Liquid volume equal to 25 to 95% of total volume.

Blowdown Line

(1) Simulation of discharge rates from scaled pipe break sizes up to 9 inches in diameter (a 9 inch diameter break area in the FSTF results in a ratio of the break flow to the total downcomer area which exceeds the same ratio for all Mark I plants)

(2) Frictional pressure losses less than 25 psi from the steam vessel to the flow control nozzle

(3) Piping length minimized with the flow control nozzle located as close to the drywell discharge location as practical

(4) Critical flow achieved at the flow control nozzle with no stratification or slug flow in the blowdown line

(5) Capability to simulate both liquid and steam pipe breaks.

2.7 VACUUM BREAKER

The Monticello plant uses ten 18-inch diameter vacuum breakers to equalize pressures between the wetwell and drywell after a LOCA. If the breakers operate during chugging, air would be transferred from the wetwell into the vent header and downcomers. Introduction of air to the downcomers may tend to mitigate the chugging loads. It was therefore imperative that the vacuum breakers used for FSTF be properly scaled to ensure conservative chugging loads resulted.

The scale factors which will affect the quantity of air into the vent header are:

- Vacuum breaker size and location
- Vacuum breaker opening set pressure
- Vacuum breaker response
- Total flow resistance from wetwell through vacuum breaker to vent header.

The ten Monticello vacuum breakers are located as shown in Figure 2-2. For the majority of the bays of the wetwell each vacuum breaker serves twelve downcomers. At two locations in the Monticello wetwell an additonal vacuum breaker is installed and thus, only six downcomers are served by the vacuum breaker.

Since the maximum chugging loads are expected when a minimum amount of air is allowed to enter the downcomers, it was concluded that for FSTF, one vacuum breaker per twelve downcomers should be used for scaling.

Breaker opening set pressure was also an important scaling parameter in that it affects the quantity of air which may be transferred from the wetwell free air space to the downcomers. If the set pressure was less than that used on the Mark I plants, additional air may enter the vent header and low chugging loads could result. Similarly, vacuum breaker response could also affect the amount of air entering the vent header.

The resulting FSTF vacuum breaker scaling criteria were as follows:

1) Using a prototypical vacuum breaker, the flow rate through the valve at a 0.5 psi pressure differential would be 8/12 of the flow rate developed in the Monticello plant at the same pressure differential.

2) The opening set pressure of the vacuum breaker would be 0.1 psi (prototypical of Mark I plants) or greater

3) Response characteristics of the vacuum breaker would be prototypical of the Mark I plants.

An 18-inch vacuum breaker was used in the FSTF and mounted on the vent header as shown in Figure 2-2. The opening set pressure of 0.1 psi and response characteristics of the breaker were prototypical of the Mark I plants. An orifice plate installed between the breaker and vent header reduced the flow rate through the breaker to 8/12 of the Monticello flow rate.

Table A-2

BASIS FOR SELECTING MONTICELLO

AS A REFERENCE FOR FSTF

PARAMETER	Mark I Range	Most Severe* Mark I Value	Monticello
Downcomer/Wall Spacing**	5.4' to 9.3'	5.4'	5.4'
Downcomer Submergence at Minimum Water Level**	3.0' to 4.75'	4.75'	4.5'
Pool Area Ratio	26.4 to 55.5	26.4	29.8
Drywell/Torus Air Volume Ratio	1.14 to 1.51	1.14	1.17

---

* Most severe from a chugging standpoint only

** These values were based on wetwell geometries as they existed prior to FSTF testing

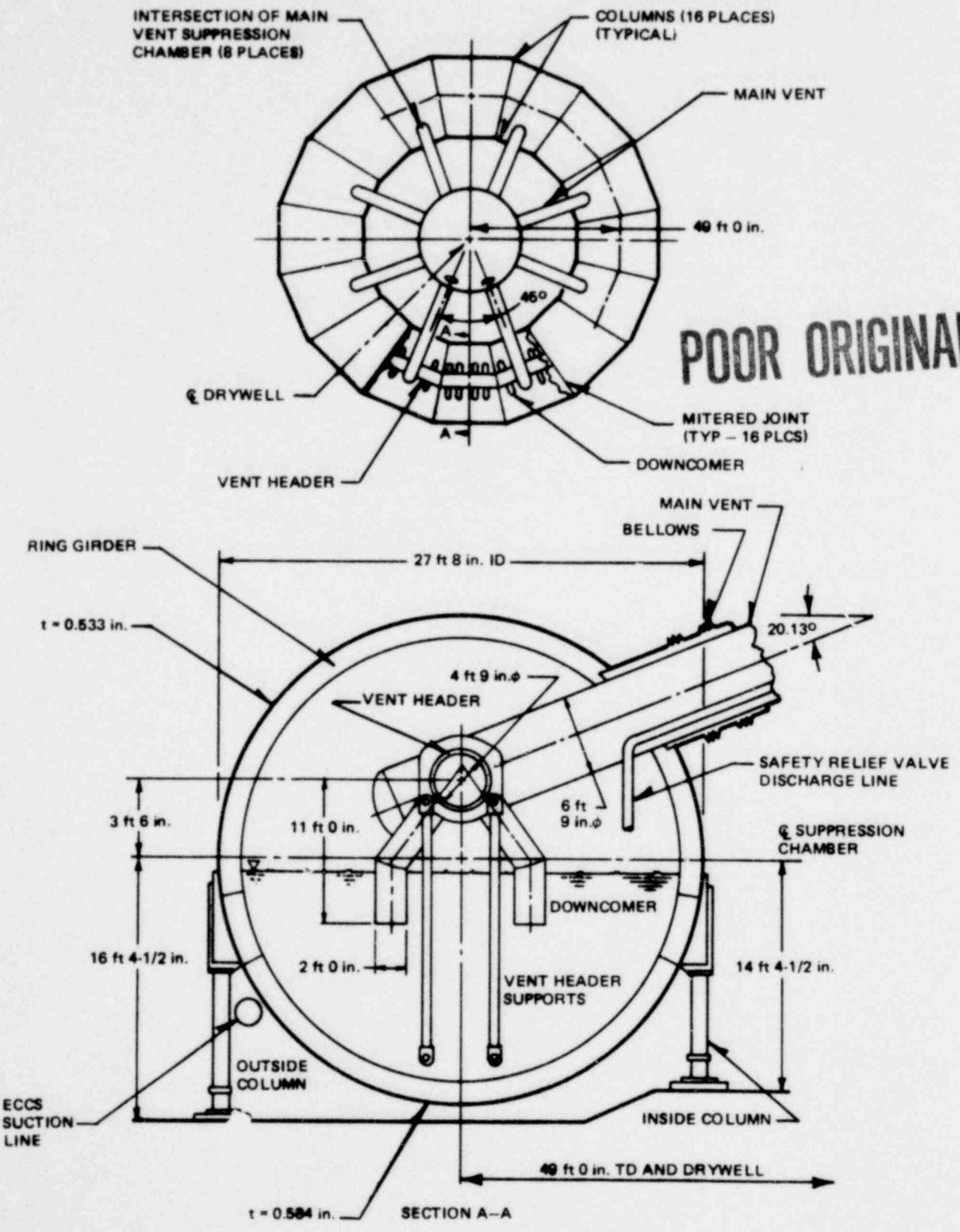

Figure A-1. Monticello Suppression Chamber

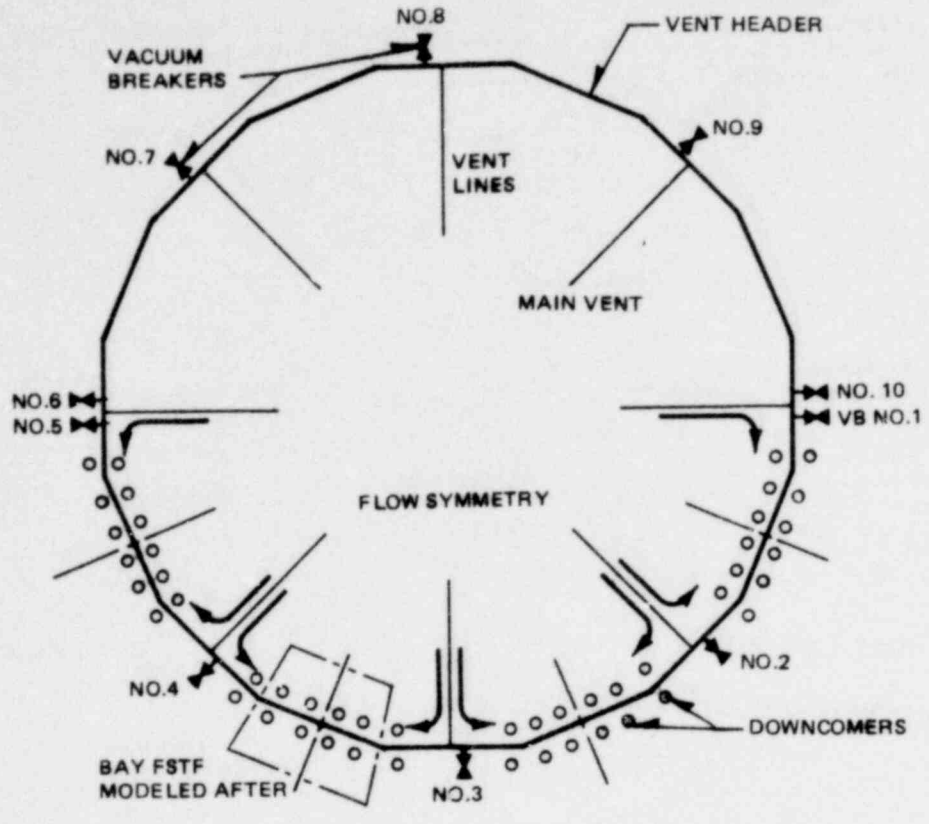

(A) LOCATION OF MONTICELLO VACUUM BREAKERS

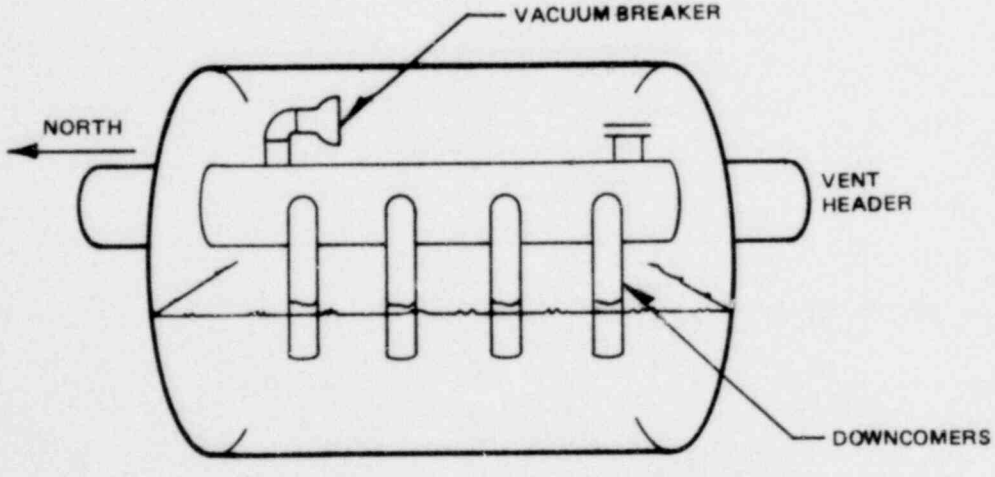

(B) LOCATION OF FSTF VACUUM BREAKER

Figure A-2. Vacuum Breaker Location

APPENDIX B

MARK I FULL SCALE TEST FACILITY UNCERTAINTY ANALYSIS OF INSTRUMENTS AND FLOWRATE CALCULATIONS

TABLE OF CONTENTS

Table of Contents
(Cont.)

LIST OF ILUSTRATIONS

Figures

NOMENCLATURE

A_p	Cross-sectional area of the blowdown line at the upstream pressure tap, ft^2
A_T	Cross-sectional area of the nozzle throat, ft^2
X_P	"Quality" of the fluid at the upstream pressure tap, fraction. (For a steam break, $X_p = 1.0$. For a liquid break, $X_p = 0$)
H_T	Elevation from the upstream pressure tap to the throat pressure tap, ft
g_c	Gravitational acceleration constant, 32.17 ft/sec^2
J	Mechanical equivalent of heat, 778.26 ft/lb/Btu
P_P	Static pressure measured in the pipe upstream of the flow nozzle, psia
P_T	Static pressure measured at the flow nozzle throat, psia
h_{ij}	Enthalpy of saturated liquid water or water vaper, i = f or g, j = P or T, Btu/lb
h_j	Enthalpy of the mixture at location j = P or T, Btu/lb
s_{ij}	Entropy of saturated liquid water (i=f) or water vapor (i=g), J = P or T, Btu/°F-lb
s_j	Entropy of the mixture at location j = P (pressure tap), or T (throat), Btu/°F lb
v_{ij}	Specific volume of saturated liquid water or water vapor, i = f or g, j = P or T, ft^3/lb
v_j	Specific volume of the mixture at location j = P or T, ft^3/lb
X_T	"Quality" of the mixture at the flow nozzle throat, fraction
U_j	Average velocity of the steam-water mixture at location j = P or T, ft/sec
w_N	Blowdown flowrate from flow nozzle pressure data, lb/sec
A_v	Average cross sectional area of steam vessel, ft^2
h	Height of the cold leg, ft
ρ_c	Density of water in the cold leg, lb/ft^3
ΔP_1	Differential pressure measured between the top and bottom of the steam vessel, psi

ΔP_2	Differential pressure measured between the top and the middle of the steam vessel, psi
ΔP_3	Differential pressure measured between the middle and bottom of the steam vessel, psi
$w_v(t)$	Blowdown flowrate at time, t, calculated by rate of change of vessel inventory, lb-mass/sec
C_j	Annubar flow coefficients, $ft.^{3/2}$ in/sec
A_{vj}	Vent line cross-sectional areas, ft^2
k_{11}, k_{12}	Isentropic exponent for air
D_0, D_1, D_2	Coefficients for calculating the isentropic exponent of steam as a function of pressure
K_1	Coefficient for calcualting air density as a function of pressure and temperature
B_0, B_1, B_2	Coefficients for calculating the density of saturated steam as a function of pressure
P_{vj}	Pressure measured upstream of the annubar in vent line j, psia
T_{vj}	Temperature measured upstream of the annubar in vent line j, ^oF
ΔP_{vj}	Annubar differential pressure in vent line j, psi
ρ_{ij}	Density of air or steam in vent line j, lb/ft^3
k_{2j}	Isentropic exponent for steam in vent line j
U_{ij}	Average velocity of air or steam in vent line j, upstream of the annubar, ft/sec
P_{Tij}	Total pressure of air or steam in vent line j, based on the average velocity V_{ij}, psia
V_{aij}	Adiabatic compression factor for air or steam in vent line j
W_{ij}	Flowrate of air or steam in vent line j, lb/sec
σ	Standard deviation
RTI	Reference to Input
RTO	Reference to Output

1.0 INTRODUCTION

This report analyzes the errors involved in the data acquisition system used in the GE MARK I Full Scale Test Facility test program. The data were acquired during a five-minute period during which the test facility was subjected to various loads which would result from a postulated loss of coolant accident (LOCA). These factors, in addition to external noise sources, inaccuracies in the measuring equipment and computational errors were all considered in this analysis.

The information used in this report was gathered from various sources including component vendors, specification sheets and discussions with cognizant Wyle personnel. Summaries of instrument errors and flowrate calculation errors are listed in Table 8 and Table 13 respectively.

2.0 ERROR TYPES

This report deals with two main aspects of errors: instrument error and error propagation. Within an experiment, the measurement process must deal with two general types of errors. The first is bias (or systematic) errors, such as those which result reproducibly from faulty equipment calibration or from observer bias. These are fixed errors that contribute to the difference between the true value and the average of many repeated experiments. (See Figure 1.)

The second error type is random (or precision) errors. These are the fluctuations in observations which yield results that differ from experiment to experiment and that require repeated testing to yield precise results. These errors are caused primarily by noise and tend to flatten out the distribution curve of Figure 1 about the most probable (or averaged measured value).

The sum of the bias and random errors constitutes the instrument error in the system. The instrument error is a measure of the uncertainty of the recorded data acquired during a test.

Error progation is concerned with the way in which uncertainties are propagated or carried over from the data points to the parameters and how the uncertainties of the determinations of some parameters of a test will be propagated to the final result. The equations used in the data analysis and reduction process will be investigated for propagation errors.

3.0 MATHEMATICAL CONSIDERATIONS

3.1 Instrument Error

The instrument error is composed of two (2) terms: bias and random errors. The bias error 'B' is defined as the square root of the sum

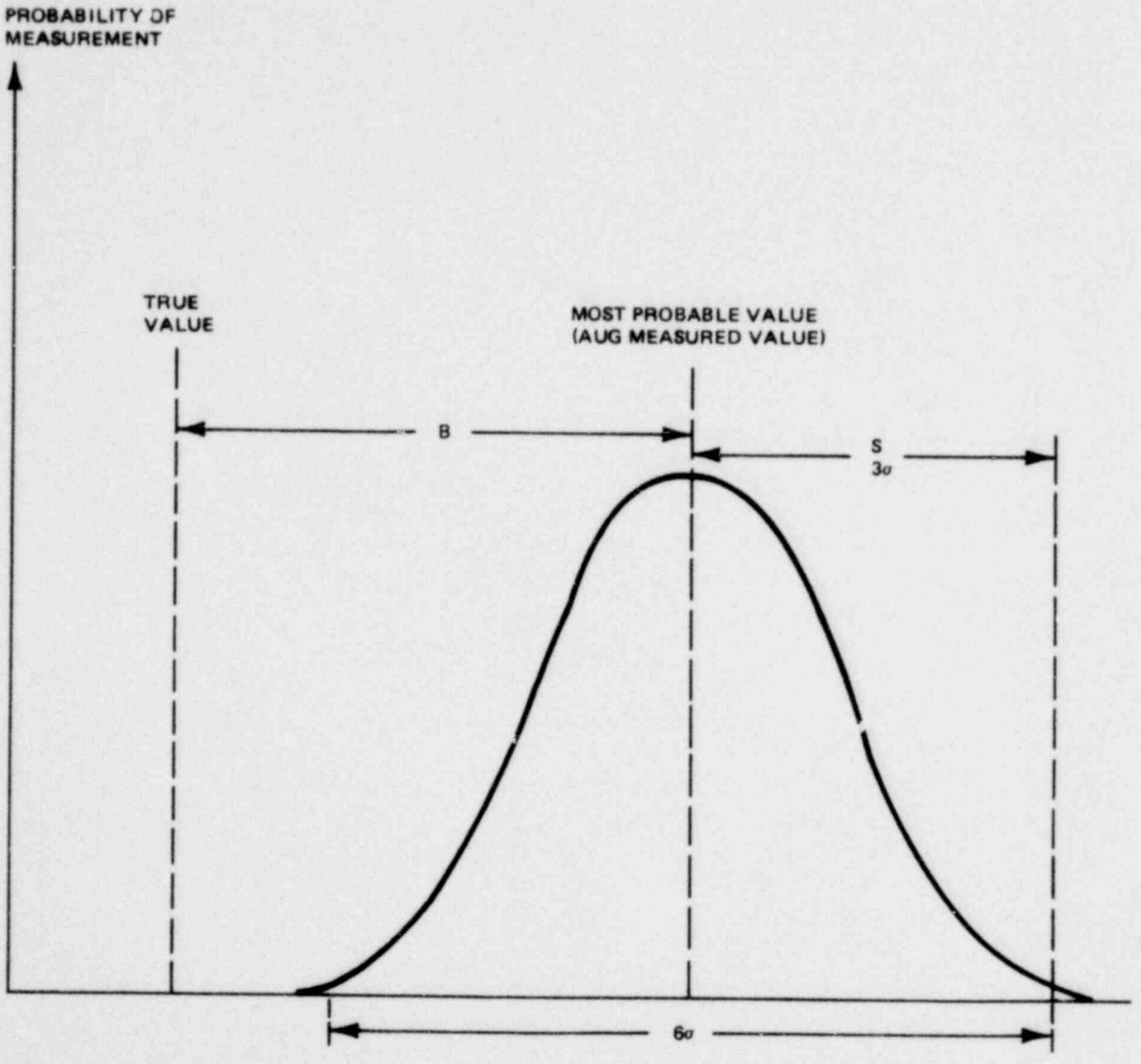

Figure B-1. Measurement Uncertainty

of the squares (RSS) of all known elemental errors. This can be written as:

$$B = (b_1^2+b_2^2+....b_n^2)^{1/2} \quad (1)$$

where the b_i are the individual bias errors of the system. This assumes that the bias errors are not self compensating and that the components have been calibrated. In general, the bias errors reflect the limits of calibration and hence the bias errors can be much greater when a unit is out of calibration. Only calibrated values will be used. The random error 'S' is similarly defined as the RSS of the elemental uncorrelated random errors of the system, or:

$$S = (s_1^2+s_2^2+....s_m^2)^{1/2} \quad (2)$$

where the s_i are the elemental random error terms. The instrument error is the combination of the B and S terms to obtain the total system error or measurement uncertainty U:

$$U = \pm(B + S) \quad (3)$$

3.2 Error Propagation

Error progation is a means of relating an error in a computed result to the input terms. The development will first proceed in general terms for error conditions from which an exact form applicable to this report will be developed.

Given an equation or set of equations relating a dependent variable y to a set of independent variables u, v, ... each with a known uncertainty, the goal is to seek the corresponding uncertainty in the dependent variable y. This is written as:

$$y = f(u, v, ...) \quad (4)$$

Let the value of y corresponding to a specific measurement of the variables u, v, ... be denoted as:

$$y_i = f(u_i,v_i, ...) \quad (5)$$

From equations (4) and (5), two (2) types of error propagation equations can be developed using Taylor's series. The first equation is termed the worst case error propagation equation and is developed below.

Expanding y in a Taylor's series for a specific measurement and retaining only the first order terms results in:

$$y_i-y=\frac{\partial y}{\partial u}(u_i-u)+\frac{\partial y}{\partial v}(v_i-v) \ldots \quad (6)$$

Use the notation $u_i-u = \Delta u$ and write (6) as:

$$\Delta y = \frac{\partial y}{\partial u}\Delta u+\frac{\partial y}{\partial v}\Delta v+.... \quad (7)$$

Equation (7) is referred to as a general formula for error propagation.

Two examples, one for addition and one for multiplication, will show how (7) is used. For addition, let

$$y = au+bv \tag{8}$$

where a and b are constants. Then the absolute error is:

$$\Delta y = a\Delta u + b\Delta v \tag{9}$$

Since the errors can be either positive or negative, the absolute values are used to get the worst case error which is:

$$\Delta y = |a\Delta u|+|b\Delta v| \tag{10}$$

The relative error $\Delta y/y$ is:

$$\Delta y/y = (|a\Delta u|+|b\Delta v|)/(au+bv) \tag{11}$$

For multiplication let:

$$y = auv \tag{12}$$

The absolute error is:

$$\Delta y = |av\Delta u|+|au\Delta v| \tag{13}$$

and the relative error is:

$$\Delta y/y = |\Delta u/u|+|\Delta v/v| \tag{14}$$

Thus given (7) the worse case relative error propagation can be determined as exemplified by (11) and (14).

The other approach is to use what is known as the most probable value error propagation or mean error propagation. For this, again start with Equation (4) and assume that it may be written using the most probable values for each variable as:

$$\bar{y}=f(\bar{u},\bar{v},....) \tag{15}$$

where $\bar{u}$ means the mean value of u. Now again using (5) expand (15) in a Taylor's series and retain only the first order terms. This results in:

$$y_i-\bar{y} = \frac{\partial y}{\partial u}(u_i-\bar{u})+\frac{\partial y}{\partial v}(v_i-\bar{v})+.... \tag{16}$$

Next the variances are obtained from (16) using standard statistical techniques. Squaring both sides of (16), summing over i from 1 to N measurements, dividing by N and taking the limit as $N\to\infty$ gives:

$$\sigma_y^2=\left(\frac{\partial y}{\partial u}\right)^2\sigma_u^2+\left(\frac{\partial y}{\partial v}\right)^2\sigma_v^2+2\left(\frac{\partial y}{\partial u}\right)\left(\frac{\partial y}{\partial v}\right)\sigma_{uv}^2+... \tag{17}$$

1158 216

This is the general mean error propagation equation where the variance is:

$$\sigma_u^2 = \lim_{N\to\infty} \frac{1}{N} \sum_{i=1}^{N} (u_i - \bar{u})^2 \qquad (18)$$

and similarly for σ_v^2 and σ_y^2. The covariance is:

$$\sigma_{uv}^2 = \lim_{N\to\infty} \sum_{i=1}^{N} (u_i - \bar{u})(v_i - \bar{v}) \qquad (19)$$

Again, two examples will be shown this time for (17). For addition, again use (8) and (17) becomes:

$$\sigma_y^2 = a^2\sigma_u^2 + b^2\sigma_v^2 + 2ab\sigma_{uv}^2 \qquad (20)$$

and

$$\sigma_y = (a^2\sigma_u^2 + b^2\sigma_v^2 + 2ab\sigma_{uv}^2)^{1/2} \qquad (21)$$

Then the relative error is:

$$\sigma_y/y = (a^2\sigma_u^2 + b^2\sigma_v^2 + 2ab\sigma_{uv}^2)^{1/2} / (au+bv) \qquad (22)$$

For multiplication, again use (12) and (17) to get:

$$\sigma_y^2 = (av)^2\sigma_u^2 + (au)^2\sigma_v^2 + 2a^2uv\sigma_{uv}^2 \qquad (23)$$

and the relative error is:

$$\sigma_y/y = ((\sigma_u/u)^2 + (\sigma_v/v)^2 + 2\sigma_{uv}^2/uv)^{1/2} \qquad (24)$$

If the unusual case occurs where u and v are perfectly correlated the covariance can be written (see (19)).

$$\sigma_{uv}^2 = \Delta u \Delta v \qquad (25)$$

Now defining $\Delta u = \sigma_u$ and $\Delta v = \sigma_v$ and using the corresponding notations, it can be shown that both cases of addition (see (11) and (22)) and both cases of multiplication (see (14) and (24)) are, in fact, equal. Further, it can be shown that if all variables are perfectly correlated (i.e. all interdependent) then the 2 error propagation methods given by (7) and (17) are equal.

In the general case, however, the variables will not be perfectly correlated and the error values given by (17) will be less than the worst case condition given by (7). Equation (17) represents a more general and more realistic estimate of errors arising from numerous sources and thus will be used in this report.

The error sources will be assumed independent here (or uncorrelated) since the individual functions operate in an open loop configuration (i.e. there is no control between functions) and each unit is specified independent of all other units. This being the case (17) simplifies to:

$$\sigma_y^2 = \left(\frac{\partial y}{\partial u}\right)^2 \sigma_u^2 + \left(\frac{\partial y}{\partial v}\right) \sigma_v^2 + \ldots\ldots \qquad (26)$$

The relative error for the two examples (22) and (24) becomes:

$$\sigma_y/y = (a^2\sigma_u^2+b^2\sigma_v^2)^{1/2}/(au+bv) \qquad (27)$$

and

$$\sigma_y/y = ((\sigma_u/u)^2+(\sigma_v/v)^2)^{1/2} \qquad (28)$$

3.3 Confidence Levels

It should be noted that the derivation for (17) and (26) was done in terms of the standard deviation σ. Thus, for normally distributed variables, u_i, v_i, ... with standard deviations σ_u, σ_v, ... there is a 68.3% probability that the corresponding y_i will be in the range $y \pm \sigma_y$. If, however, the deviations σ_u, σ_v, ... actually represent three standard deviations then the confidence level of the resulting σ_y is 99.7%.

For the case of Neff amplifier, Neff states that all of the specifications are 3σ limits. Furthermore, while tolerances can be related to any desired σ limit it is standard engineering practice to use 3σ limits, and this limit will be assumed in all cases.

In theory, these σ limits only hold for normal distributions. The central limit theorem, however, states that when many measurements or measurement types are combined, as is the case below, the conditions of normality can be assumed even when individual components do not have exactly normal distributions. Therefore, the confidence level for the error analysis to be discussed is 99.7%.

4.0 ANALYSIS COMPONENTS

This section discusses all of the components to be used in the error analysis. The error components included: transducers including strain gage thermal effects, lead wires, signal conditioning, amplifier, analog to digital conversion (ADC), computer hardware and flowrate equations. A block diagram of their relation to one another is shown in Figure 2.

4.1 Transducers

Nine types of transducers were used on the Mark I FSTF project. Pertinent information on the transducers is given in Table 1. With the exception of repeatability, the transducer errors are all bias errors.

4.2 Cable Leads

The cables used were all 22AWG with runs of 650 to 700 feet. The measured noise with a quiescent facility was ±12uv.

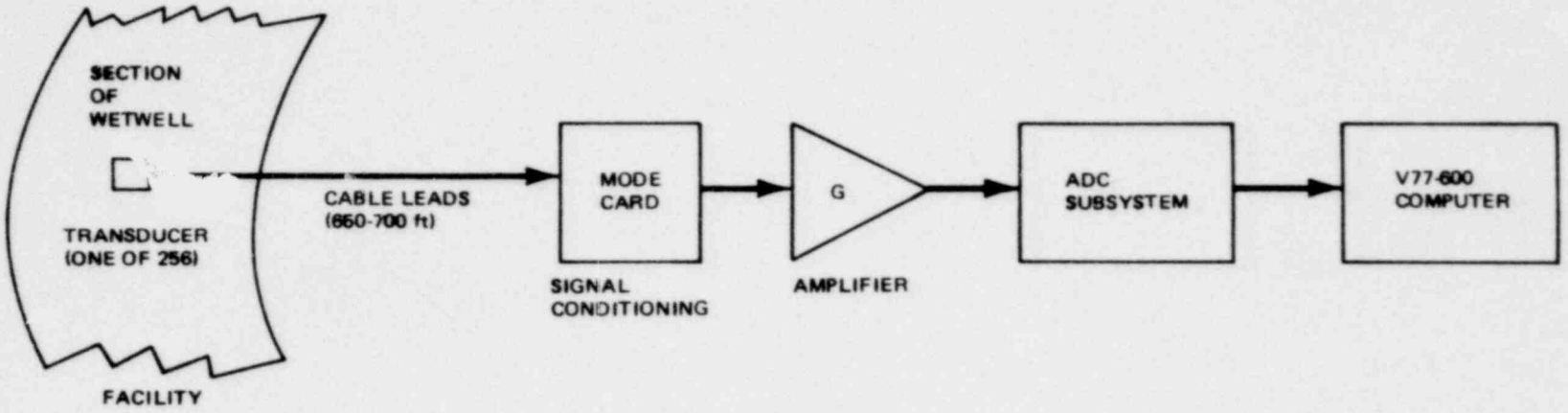

Figure B-2. Block Diagram of Overall Data Acquisition System

Table B-1

TRANSDUCER INFORMATION

Ailtech

Type: Strain
Model: SG-158-09H-XX-6S
Resistance: 350 ohms
Gage Accuracy: ±3%
Thermal Coefficient: =6.7 ppm /°F
Amplifier Gain: 1000
Typical Gage Factor: ≈2

Micro-Measurements

Type: Strain
Resistance: 350 ohms
Gage Accuracy: ± 1.5%
Thermal Coefficient: <6.7 ppm/°F
Amplifier Gain: 1000
Typical Gage Factor: ≈2

Endevco

Type: Accelerometer
Model: 7707-200
Gage Accuracy: ± 1.5%. Sensitivity increases 1% per 250 g up to 1000 g.
Stability: ±2%
Amplifier Gain: 1

Schaevitz

Type: LVDT
Model: 200Q HCD
Linearity: ± 0.25%
Stability: ± 0.125%
Ripple: <1%

Precise Sensor

Type: Pressure
Models: 70116-2, 70116-WP-4
Combined linearity and hysteresis: <± 0.25%
Repeatability: ± 0.08%
Amplifier Gain: 333

Table B-1 (Continued)

General Electric

Type: Liquid level probe
Model: 166B8943
Amplifier Gain: 1(Where possible) or 10

Conax

Type: Temperature - nonlinear, zero output at 150° F
Model: Various numbers all with prefix 'E'
Accuracy: ± 0.5%
Amplifier Gain: High level: 600, low level: 1000

Rosemount

Type: Differential Pressure
Accuracy: ±0.2%
Amplifier Gain: 1

Viatran

Type: Pressure
Repeatability: ± 0.1%
Hysteresis: <± 0.25%
Linearity: ≤ 0.4%
Amplifier Gain: 333

4.3 Signal Conditioning

The signal conditioning unit used was a Neff 300 conditioner plus mode cards and excitation supply. The pertinent signal conditioner specifications are shown in Table 2.

4.4 Amplifier

The instrumentation amplifier per channel used was a Neff 620050 low level amplifier. The pertinent specifications are shown in Table 3[4]

4.5 ADC System

The ADC system used was a Phoenix Data Model 6913 system. The pertinent specifications are shown in Table 4.

4.6 Computer System

The computer system used was a Varian V77. Since all computations were done using floating point arithmetic, the computer resolution is 1 part in 2^{22} or ± .000024%.

A potential source of error in the computer is due to the computer clock. The basic clock rate of the Varian V77 is 24.2424Mhz (41.25 nsec period) generated by a high quality crystal. Crystals typically have a frequency accuracy of $\pm$ 0.001% and a long term drift of 5 to 10 ppm/year. The data error is not a function of the frequency error since the date is acquired in real time from the facility but rather a function of drift. Over a period of about 5 minutes, the drift can be considered to be zero.

In displaying data, the delay of the signal from the facility to the computer can affect the results. The delay due to the 700 foot run for a signal traveling 1/2 foot per nsec (in twisted pair wire) is about $1400*10^{-9}$ seconds. An unrelated display problem arose during one analysis where the FORTRAN algorithm for computing time used insufficient precision. This was corrected using double precision arithmetic. This is not an inherent system problem and is thus not considered further here.

4.7 Flowrate Equations

For the ventline flowrate, a Taylor's expansion for direct computation was used. The equations are given in Table 5. Refer to the nomenclature for explanation of all terms.

Table B-2

NEFF SYSTEM 300 SIGNAL CONDITIONER IN CONSTANT VOLTAGE MODE SPECIFICATIONS

Output Voltage: Continuously adjustable from 2-10 volts by resistor adjustment on Mode Board.

Line Regulation: <0.01% or 200uv, whichever is greater, for a ± 10% input line voltage variation.

Ripple: <100uv p-p in a d.c. to 1 KH_z bandwidth.

Stability: ± 0.01% ± 0.005% per ^{o}C.

Mode card voltage resolution ± 10 mv.

1158 223

Table B-3

NEFF SYSTEM 620050 LOW LEVEL AMPLIFIER SPECIFICATIONS

Gain Stability: ± 0.01% ± 0.002%/^{o}C

Linearity: ± 0.01% f-s

Zero Stability: ± 4uv RTI + 15uv RTO

Zero Drift: ± 1uv RTI + 15uv RTO (60 days)

Noise (1 KH_z bandwidth): 6uv(p-p)RTI + 50uv(p-p)RTO

Maximum Operating Common Mode Voltage: ± 10v DC or peak AC ± 20 volts

Common Mode Rejection Ratio: (DC to 60Hz with up to 350 ohms source impedance independent of filter): 66db + gain (indb) up to 120db maximum

Table B-4

PHOENIX DATA ADC SUBSYSTEM SPECIFICATIONS

ADC Resolution: 1 part in 8192

Throughput Accuracy: <±0.03% of FS

System Gain Accuracy: ±0.01% FSR @ 25°C

System Linearity: ± 0.01% FSR @ 25°C

Cross Talk: 80db FSR @ 25°C

Common Mode Rejection: 80db @ DC @ 25°C

Multiplexer and SAH Settling Accuracy: ±0.008% in 5us @ 25°C

Table B-5

EQUATIONS USED FOR FLOWRATES

Nozzle Flowrate

$$S_p = (1 - X_p)S_{fp} + S_{gp}X_p \quad \text{(T1)}$$

$$X_T = (S_p - S_{fT})/(S_{gT} - S_{fT}) \quad \text{(T2)}$$

$$V_j = (1 - X_j)V_{fj} + X_jV_{gj} \quad \text{(T3)}$$

$$h_j = (1 - X_j)h_{fj} + X_jh_{gj} \quad \text{(T4)}$$

$$U_p = \left[\frac{2g_cJ(h_p - h_T - H_T/J)}{(V_TA_p/V_pA_T)^2 - 1}\right]^{1/2} \quad \text{(T5)}$$

$$W_N = U_pA_p/V_p \quad \text{(T6)}$$

Differential Pressure Flowrate

$$W_v(t_2) = 144A_v(\Delta P_2 - \Delta P_1)/(t_2 - t_1) \quad \text{(T7)}$$

$$\Delta P_2 + \Delta P_3 = \Delta P_1 \pm 1\% \quad \text{(T8)}$$

Ventline Flowrate

$$\rho_{1j} = (K_1P_{vj})/(T_{vj} + 460) \quad \text{(T9)}$$

$$\rho_{2j} = B_0 + B_1P_{vj} + B_2P^2_{vj} \quad \text{(T10)}$$

$$k_{2j} = D_0 + D_1P_{vj} + D_2P^2_{vj} \quad \text{(T11)}$$

Table B-5 (Continued)

For Range of Flows Used

$$\gamma_{ij} = (k_{ij} - 1)/k_{ij} \quad \text{(T12)}$$

$$C1_{ij} = C_j(\rho_{ij}\Delta P_{vj})^{1/2} \quad \text{(T13)}$$

$$C2_{ij} = 1/(288 g_c \rho_{ij} A^2_{vj} P_{vj}) \quad \text{(T14)}$$

$$W_{ij} = C1_{ij}/(1-1/2(1-\gamma_{ij})C2_{ij}C1^2_{ij})^{1/2} \quad \text{(T15)}$$

See Nomenclature for definition of terms.

5.0 ERROR COMPUTATION DETAILS

This section will take the components of Section 4.0 and develop detailed error values using the mathematical approaches discussed in Section 3.0.

5.1 Transducers

The transducer data is shown in Table 1. Applying equations (1) and (2), the instrument errors for all transducers are shown in Table 6. The GE level probes have no error terms and thus were not listed.

The strain gages (Ailtech and Micro-Measurements) have three errors, one due to standard bias error and the other two due to temperature drift. To obtain the temperature error terms, an assumed maximum stress level of 5000 psi was used along with two temperature ranges: 75^{o} - 120^{o}F ($\Delta T = 45$) for those gages immersed in wetwell water and 75^{o} - 250^{o}F ($\Delta T = 175$) for those gages in the vent header area[9]. Mild carbon steel has a thermal expansion factor of about 6.92 ppm in the 300^{o} F range.

For the assumed maximum stress level, the corresponding ΔR is found from:

$$S = \frac{E*\Delta R}{G*R} \qquad (29)$$

where

S = Stress in psi
E = Modules of elasticity = $30*10^{6}$psi
G = Gage factor = 2
R = Gage resistance = 350

Assuming S = 5000 then $\Delta R = 0.1167$ ohms

To find the ΔR for the thermal drift, the relation is:

$$\Delta R = R*\Delta T* (6.92 - 6.7) * 10^{-6} \qquad (30)$$

For $\Delta T = 45^{o}$F, ΔR = .00347 ohms and the error relative to the maximum reading is 2.97%. For $\Delta T = 175^{o}$F, ΔR = .0135 ohms and the error relative to the maximum reading is 11.57%

A typical computation for the other Table 2 entries is for the Schaevitz LVDT:

$$B = (.0025^{2} + .00125^{2} + .01^{2})^{1/2} = .0104 \text{ or } 1.04\%$$

5.2 Cable Leads

Given a noise signal level of 12uv and assuming a transducer data signal of 1mv, the signal to noise ratio is:

$$S/N = 1.0*10^{-3}/12 \times 10^{-6} = 83.3 \text{ or } 38.4 \text{ dB} \qquad (31)$$

Table B-6

TRANSDUCER INSTRUMENT ERRORS

			$\Delta T=45^{\circ}F$	$\Delta T=175^{\circ}F$
1.	Ailtech	± 3.00%	2.97%	11.57%
2.	Micro-Measurements	± 1.50%	2.97%	11.57%
3.	Endevco	± 2.50%		
4.	Schaevitz	± 1.04%		
5.	Precise Sensor	± 0.33%		
6.	Conax	± 0.50%		
7.	Rosemount	± 0.20%		
8.	Viatran	± 0.60%		

A S/N ratio of 38.4 dB will produce a data transmission error probability of less than 1 part in 10^5 which implies that the chance of the ADC producing improper codes due to lead noise is <0.001%.

5.3. Signal Conditioning

Using the data from Table 2 the instrumental errors are computed as follows:

b_1 = line regulation = ± 0.01%

b_2 = stability = ± 0.01% ± 0.005%/°C

Assuming 3°C range for the computer room:

b_2 = ± 0.01% ± 0.005%/°C★3°C = ± 0.025%

b_3 = ripple error = 100uv/10v = ± 0.001%

The bias error is, therefore:

$$B = (b_1^2 + b_2^2 + b_3^2)^{1/2} = (.01^2 + .025^2 + .001^2)^{1/2} = \pm 0.027\%$$

s_1 = Mode card voltage resolution = 10 mv/10v = ± 0.1%

The total signal conditioning uncertainty is:

$$U = \pm(B + S) = \pm 0.127\% \qquad (32)$$

5.4 Amplifier

Using the data from Table 3, the amplifier instrumental errors are computed as follows:

b_1= gain stability = ± 0.01% ± 0.002%/°C★3°C= ± 0.016%

b_2= gain linearity = ± 0.01% f-s.

b_3= zero stability = 4uv RTI + 15uvRTO

Assuming a signal condition of V_{in}= 4.0mv, V_{out} = 4.0 volt and gain = 1000 then:

$$b_3 = \frac{4\star10^{-6}}{4.0\star10^{-3}} + \frac{1.5\star10^{-6}}{4.0} = \pm 0.100\%$$

b_4 = zero drift=1uvRTI+15uvRTO/°C ★ 3°C

$$= \frac{1\star10^{-6}}{4\times10^{-3}} + \frac{15\star10^{-5}}{4.0}\star3 = \pm 0.025\%$$

b_5 = common mode rejection = $\frac{CMV}{CMR\ V_{in}}$

For an V_{in}= 4.0 mv assume a gain of 1000, then CMR = 120db = 1×10^6

$$b_5 = 1.0/(1*10^6 \times 4.0*10^{-3}) = \pm 0.025\%$$

The total bias error is:

$$B = (b_1^2 + b_2^2 + b_3^2 + b_4^2 + b_5^2)^{1/2} = \pm 0.107\%$$

$$s_1 = \frac{6uvRTI * 1000}{4.0v} \text{ (worst case gain)} = \pm 0.150\%$$

$$s_2 = 50uv/1.0 \text{ volt} = \pm 0.005\%$$

The random error is thus:

$$S = (s_1^2 + s_2)^{1/2} = \pm 0.150\%$$

The total uncertainty for the amplifier is:

$$U = \pm(B + S) = \pm 0.257\% \qquad (33)$$

5.5 ADC System

Using the data from Table 4, the ADC instrumental errors are:

b_1 = resolution = 2.44mv/10v = ± 0.024%

b_2 = throughput accuracy = ± 0.03%

b_3 = gain accuracy = ± 0.01%

b_4 = linearity = ± 0.01%

b_5 = common mode rejection = 80dB = ± 0.01%

The bias error is:

$$B = (b_1^2 + b_2^2 + b_3^2 + b_4^2 + b_5^2)^{1/2} = \pm 0.042\%$$

s_1 = Cross talk = 80db = ± 0.01%

s_2 = Settling accuracy = ± 0.008%

The random error is:

$$S = (s_1^2 + s_2^2)^{1/2} = \pm 0.013\%$$

The total uncertainty for the ADC system is, therefore:

$$U = \pm (B + S) = \pm 0.055\% \qquad (34)$$

1158 231

5.6 Computer

As shown in Section 4.6, the computational data error is ± 0.000024%.

The error due to drift as discussed in Section 4.6 is essentially zero. The display error due to delay is a function of the delay relative to the sampling rate. At 1000 Hz sampling rate the error due to delay is

$$\frac{1400*10^{-9}}{1*10^{-3}} = 1.4*10^{-3} \text{ or } 0.14\%$$

Note that this error affects the time at which the analyst perceives the data relative to a start pulse, but does not affect the value of the data. Therefore, it will not be considered as part of the data error terms.

5.7 Summary of Instrument Errors

The above instrument error terms for other than the transducers are shown in Table 7.

Combining Table 6 with Table 7 gives an overall instrument error for each transducer type. This overall instrument error is shown in Table 8. Again, three values are shown for the strain gages due to the thermal drift considerations discussed earlier.

5.8 Flowrate Equations

5.8.1 Equations

Given the equations in Table 5, Equation (26), the data from Table 8, constants and their relative errors given in Table 9 and typical data values in Table 10, the propagation errors may be determined. The uncertainty in steam-break flowrates were performed at an upstream pressure of 150 psia and a throat pressure of 79 psia. For liquid breaks, the flowrate uncertainty were done for an upstream pressure of 880 psia and a throat pressure of 640 psia. These pressures were observed to be the typical pressures at the midpoint of a flow transient.

The first propagation error function will be for the blowdown nozzle flowrate equations.

For $X_p = 0.0$ (T1) becomes:

$$S_p = S_{fp},\ V_p = V_{fp},\ h_p = h_{fp}$$

$$X_T = (S_{fp} - S_{fT})/(S_{gT} - S_{fT}) \qquad (35)$$

For $X_p = 1.0$ (T1) becomes:

$$S_p = S_{gp},\ V_p = V_{gp},\ h_p = h_{gp}$$

$$X_T = (S_{gp} - S_{fT})/(S_{gT} - S_{fT}) \qquad (36)$$

1158 232

Table B-7

SUMMARY OF INSTRUMENTAL ERRORS
OTHER THAN TRANSDUCERS

Cable Leads	± 0.001%
Signal Conditioning	± 0.127%
Amplifier	± 0.2[illegible]7%
ADC System	± 0.055%
Computer System	± 0.000024%
Total	± 0.44%

Table B-8

OVERALL SYSTEM INSTRUMENT ERROR
BY TRANSDUCER TYPE

		$\Delta T=45^{o}F$	$\Delta T=175^{o}F$
Ailtech - strain	3.4%,	3.4%,	12.0%
Micro-Measurements-strain	1.9%,	3.4%,	12.0%
Endevco-accelerometer	2.9%		
Schaevitz-LVDT	1.5%		
Precise Sensor - pressure	0.8%		
Conax-temperature	0.9%		
Rosemount-diff pressure	0.6%		
Viatran-pressure	1.0%		

Table B-9

CONSTANTS AND RELATIVE ERRORS

Name	Values		Errors (± %)	
	Small	Large	Small	Large
A_p	0.181 ft^2	1.402 ft^2	2.17	0.78
A_T	0.087 ft^2	0.442 ft^2	0.25	0.
H_T	0.0	2.0 ft	0.00	2.08

	Value	Error (± %)
X_p	1.0 (steam), 0.0 (liquid)	0.0
A_v	33.18	1.28
C_j	917.84	2.00
A_{vj}	11.95	1.07
K_{11}	1.395	0.0
D_0	1.3	0.0
D_1	0.0	0.0
D_2	0.0	0.0
B_0	$5.79 * 10^{-2}$	0.0
B_1	$1.9 * 10^{-3}$	0.0
B_2	$2.80 * 10^{-7}$	0.0
K_1	1.8	0.0
g_c	32.17	0.0
J	778.26	0.0

See Nomenclature for definition of names and units where applicable.

Table B-10

TYPICAL DATA VALUES*

Name	Value	
P_p	150	psia
P_T	79	psia
ΔP_1	10	psi
ΔP_2	5	psi
ΔP_3	5	psi
P_{vj}	35	psia
T_{vj}	250	^oF
ΔP_{vj}	0.2	psi

*Values presented here are median values for small steam breaks. See Nomenclature for definition of names.

Other terms are the same in all cases. Now define $x = S_{fp} - S_{fT}$, $y = S_{gT} - S_{fT}$, $z = S_{gp} - S_{fT}$ and using (26) obtain:

$$\sigma_x^2 = \sigma_{S_{fp}}^2 + \sigma_{S_{fT}}^2$$

$$\sigma_y^2 = \sigma_{S_{gT}}^2 + \sigma_{S_{fT}}^2$$

$$\sigma_z^2 = \sigma_{S_{gp}}^2 + \sigma_{S_{fT}}^2$$

For $X_p = 0.0$, $X_T = x/y$ so that

$$\sigma_{X_T}^2 = \frac{1}{y^2}\sigma_x^2 + \frac{x}{y^2}\sigma_y^2 \qquad (37)$$

For $X_p = 1.0$, $X_T = z/y$ and

$$\sigma_{X_T}^2 = \frac{1}{y^2}\sigma_z^2 + \frac{z}{y^2}\sigma_y^2 \qquad (38)$$

Expanding the above for $X_p = 0.0$ and using the approach of (28), then the error for (T2) is:

$$\sigma_{X_T}/X_T = \left[\frac{\sigma_{S_{fp}}^2 + \sigma_{S_{fT}}^2}{(S_{fp} - S_{fT})^2} + \frac{\sigma_{S_{gT}}^2 + \sigma_{S_{fT}}^2}{(S_{gT} - S_{fT})^2}\right]^{1/2} \qquad (39)$$

and for $X_p = 1.0$

$$\sigma_{X_T}/X_T = \left[\frac{\sigma_{S_{gp}}^2 + \sigma_{S_{fT}}^2}{(S_{gp} - S_{fT})^2} + \frac{\sigma_{S_{gT}}^2 + \sigma_{S_{fT}}^2}{(S_{gT} - S_{fT})^2}\right]^{1/2} \qquad (40)$$

Next given (T3) for $j = T$

$$V_T = (1 - X_T)V_{fT} + X_T V_{gT}$$

The propagation error terms are found as follows:

$$\sigma_{V_T}^2 = (1-X_T)^2 \sigma_{V_{fT}}^2 + (V_{gT} - V_{fT})^2 \sigma_{X_T}^2 + X_T^2 \sigma_{V_{gT}}^2$$

$$\sigma_{V_T}/V_T = \frac{\left[(1-X_T)^2\sigma_{V_{fT}}^2 + (V_{gT}-V_{fT})^2\sigma_{X_T}^2 + X_T^2\,\sigma_{V_{gT}}^2\right]^{1/2}}{(1-X_T)\,V_{fT} + X_T V_{gT}} \qquad (41)$$

Next given (T4) for $j = T$

$$h_T = (1-X_T)h_{fT} + X_T h_{gT}$$

It is obvious this takes the same form as the equation for V_T thus the final form can be written directly as:

$$\sigma_{h_T}/h_T = \frac{\left[(1-X_T)^2\sigma_{h_{fT}}^2 + (h_{gT}-h_{fT})^2\sigma_{X_T}^2 + X_T^2\sigma_{h_{gT}}^2\right]^{1/2}}{(1-X_T)h_{fT} + X_T h_{gT}} \quad (42)$$

Now define the intermediate terms for (T5).

$$x = 2g_c J(h_p - h_T - H_T/J) \quad (43)$$

$$y = (V_T A_p/V_p A_T)^2 - 1 \quad (44)$$

Then

$$\sigma_x^2 = (2g_c J)^2\left[\sigma_{h_p}^2 + \sigma_{h_T}^2 + (1/J^2)\sigma_{H_T}^2\right] \quad (45)$$

and for y

$$\sigma_y^2 = 4\left[\left(\frac{V_T A_p^2}{V_p^2 A_T^2}\right)^2\sigma_{V_T}^2 + \left(\frac{V_T^2 A_p}{V_p^2 A_T^2}\right)^2\sigma_{A_p}^2 + \left(\frac{V_T^2 A_p^2}{V_p^3 A_T^2}\right)^2\sigma_{V_p}^2 + \left(\frac{V_T^2 A_p^2}{V_p^2 A_T^3}\right)^2\sigma_{A_T}^2\right] \quad (46)$$

Then (T5) can be written as:

$$U_p = (x/y)^{1/2} \quad (47)$$

so that

$$\left(\sigma_{U_p}\right)^2 = 1/4\ (1/xy\ \sigma_x^2 + x/y^3\sigma_y^2)$$

and then

$$\sigma_{U_p}/U_p = 1/2(\ (\sigma_x/x)^2 + (\sigma_y/y)^2)^{1/2} \quad (48)$$

where the values for x, y, σ_x^2 and σ_y^2 are used in ((48).

Finally, using (28) directly, the error for (T6) is:

$$\sigma_{W_N}/W_N = (\ (\sigma_{U_p}/U_p)^2 + (\sigma_{A_p}/A_p)^2 + (\sigma_{V_p}/V_p)^2)^{1/2} \quad (49)$$

The second set of propagation error equations is for the differential pressure flowrate (see Table 5).

Given

$$W_v = 144\, A_v\, (\Delta P_2 - \Delta P_1)/(t_2 - t_1)$$

define $\Delta t = t_2 - t_2$ where Δt is a precise increment in time equal to the inverse of the sampling rate. Given a sampling rate, Δt is defined to the accuracy of the computer. As shown in Section 5.6 the only applicable error is that due to computer clock drift, which was shown to be zero for the test duration.

Therefore, $\sigma_{\Delta t} = 0$. The propagation error equation for (T7) is:

$$\sigma_{W_v}^2 = \left(\frac{144}{\Delta t}\right)^2 \left[(\Delta P_2 - \Delta P_1)^2 \sigma_{A_v}^2 + A_v^2 (\sigma_{\Delta P_2}^2 + \sigma_{\Delta P_1}^2)\right]$$

and

$$\sigma_{W_v/W_v} = \frac{\left[(\Delta P_2 - \Delta P_1)^2 \sigma_{A_v}^2 + A_v^2 (\sigma_{\Delta P_2}^2 + \sigma_{\Delta P_1}^2)\right]^{1/2}}{A_v(\Delta P_2 - \Delta P_1)} \quad (50)$$

The last set of propagation error equations is for the ventline flowrate (see Table 5). Referring to Table 9, all of the thermodynamic property constants have an error of 0.0%. This means their corresponding σ value is zero.

Given (T12)

$$\gamma_{ij} = (k_{ij} - 1)/k_{ij}$$

since $\sigma_{k_{11}} = 0.0$, then $\sigma_{\gamma_{ij}} = 0.0$.

Using (28) and (42) the error propagation for (T9) is:

$$\sigma_{\rho_{1j}}/\rho_{1j} = \left((\sigma_{P_{vj}}/P_{vj})^2 + (\sigma_{T_{vj}}/(T_{vj}+460))^2 \right)^{1/2} \quad (51)$$

The error equation for (T10) is:

$$\sigma_{\rho_{2j}}^2 = (B_1 + 2B_2)^2 \sigma_{\rho_{vj}}^2 \quad (52)$$

so that

$$\sigma_{\rho_{2j}}/\rho_{2j} = \frac{(B_1 + 2B_2)\sigma_{P_{vj}}}{B_0 + B_1 P_{vj} + B_2 P_{vj}^2} \quad (53)$$

Using the results for P_{2j} and (53), the error propagation term for (T11) can be written directly as:

$$\sigma_{k_{2j}}/k_{2j} = \frac{(D_1 + 2D_2)\sigma_{P_{vj}}}{D_0 + D_1 P_{vj} + D_2 P_{vj}^2} \quad (54)$$

Applying (26) and (28) the error propagation equation for (T13) is:

$$\sigma_{Cl_{ij}}/Cl_{ij} = \left((\sigma_{C_j}/C_j)^2 + (\sigma_{\rho_{ij}}/2\rho_{ij})^2 + (\sigma_{\Delta P_{vj}}/2\Delta P_{vj})^2 \right)^{1/2} \quad (55)$$

Using (26) and (28) for (T14) yields directly:

$$\sigma_{C2_{ij}}/C2_{ij} = \left((\sigma_{\rho_{ij}}/\rho_{ij})^2 + (2\sigma_{A_{vj}}/A_{vj})^2 + (\sigma_{P_{vj}}/P_{vj})^2 \right)^{1/2} \quad (56)$$

Expanding the denominator of (T15) and setting equal to intermediate variable y yields:

$$y = 1 - \frac{C2_{ij}}{2} Cl_{ij}^2 + \gamma_{ij} \frac{C2_{ij}}{2} Cl^2_{ij} \quad (57)$$

Applying (26) to y yields:

$$\sigma_y^2 = (\gamma_{ij}-1)^2 \left((Cl^2_{ij}/2)^2 \sigma_{c2_{ij}}^2 + (Cl_{ij}C2_{ij})^2 \sigma_{Cl_{ij}}^2 \right) \quad (58)$$

and

$$\sigma_y/y = \frac{Cl_{ij}(\gamma_{ij}-1)\left((Cl^2_{ij}/4)\sigma_{C2_{ij}}^2 + C2^2_{ij}\sigma_{Cl_{ij}}^2 \right)^{1/2}}{1-1/2(1-\gamma_{ij})C2_{ij}Cl^2_{ij}} \quad (59)$$

The last computation is:

$$\sigma_{W_{ij}}/W_{ij} = \left((\sigma_{Cl_{ij}}/Cl_{ij})^2 + (\sigma_y/y)^2 \right)^{1/2} \quad (60)$$

5.8.2 Numerical Results

Using the above derived propagation error equations, the error values can be determined.

5.8.2.1 Flow Nozzle Flowrate

The values for S, V, and h for the flowdown nozzle flow are obtained from steam tables. Computer curves were used to approximate the steam tables over the range of 13.5 to 1200 psia and were derived using least-squares fit techniques which were accurate to ± 0.036% relative to the table value. A sample listing of steam table values needed here is shown in Table 11.

Table B-11

STEAM TABLE VALUES USED IN COMPUTATIONS

Variable	Value At 79 psia (F_1)	Value at 150 psia (P_p)
v_f	0.01756	0.01809
v_g	5.540	3.015
s_f	0.4532	0.5138
s_g	1.6224	1.5694
h_f	281.30	330.51
h_g	1183.4	1194.1

See nomenclature for definition of variables and appropriate units.

The instrument errors used in the following computations from Table 8 are:

Pressure: $\pm$ 1.0%
Differential Pressure: $\pm$ 0.6%
Temperature: $\pm$ 0.9%

To obtain the corresponding σ^2 for S, V, and h, a percent error and typical data value are needed. The typical data values are given in Table 11. To obtain the percent error, it is first necessary to discuss the details of the computer curves used to approximate the steam tables. For the three variables over the range of pressures one of three general second order equations was used. The general equations are

$$F_1 = a_1 + a_2 P + a_3 P^2 \tag{61}$$

$$F_2 = a_1 + a_2/P^2 + a_3 P^{.22} \tag{62}$$

$$F_3 = a_1 + a_2 P + a_3 \ln P \tag{63}$$

The steam tables were divided into seven regions as follows:

Region	Pressure Range (psia)
1	13.5 - 34.0
2	34.0 - 75.0
3	75.0 - 123.0
4	123.0 - 220.0
5	220.0 - 490.0
6	490.0 - 800.0
7	800.0 - 1200.0

The coefficients a_1, a_2, a_3 are different for each function and each region. All the coefficients are maintained by the computer and accessed according to the specific function (F_1, F_2, F_3) and pressure region which applies.

For the three general forms given by (61) - (63) the error terms using the approach are

$$\sigma_{F_1} = (a_2^2 + 4 a_3^2 P^2)^{1/2} \sigma_p \tag{64}$$

$$\sigma_{F_2} = (4a_2^2 P^{-4} + .0484\, a_3^2 P^{-1.56})^{1/2} \sigma_p \tag{65}$$

$$\sigma_{F_3} = (a_2^2 + (a_3/P)^2)^{1/2} \sigma_p \tag{66}$$

For example, the two pressures of P_T = 79 psia and P_p = 150 psia the specific equations are as follows: (note the notation E for *10, e.g. 1.2E-2 means $1.2*10^{-2}$).

P_T Values

$$V_f = 1.672E\text{-}2 + 1.247E\text{-}5P - 2.292E\text{-}8P^2 \quad (67)$$

$$V_g = 1/(7.728E\text{-}3 + 2.222E\text{-}3P - 4.226E\text{-}7P^2 \quad (68)$$

$$h_f = -3.423E1 - 8.538E3/P^2 + 1.212E2P^{\cdot 22} \quad (69)$$

$$h_g = 1.161E3 + 3.290E\text{-}1P - 7.302E\text{-}4P^2 \quad (70)$$

$$S_f = 7.738E\text{-}2 + 1.152E\text{-}4P + 8.369E\text{-}2 \ln P \quad (71)$$

$$S_g = 1.72\_0 - 1.664E\text{-}3P + 4.196E\text{-}6P^2 \quad (72)$$

P_p Values

$$V_f = 1.695E\text{-}2 + 8.724E\text{-}6P - 7.880E\text{-}9P^2 \quad (73)$$

$$V_g = 1/(1.326E\text{-}2 + 2.134E\text{-}3P - 7.161E\text{-}8P^2) \quad (74)$$

$$h_f = -5.810E1 + 2.281E4/P^2 + 1.288E2P^{\cdot 22} \quad (75)$$

$$h_g = 1.169E3 + 2.328E\text{-}1P - 4.174E\text{-}4P^2 \quad (76)$$

$$S_f = 6.754E\text{-}2 - 2.724E1/P^2 + 1.487E\text{-}1P^{\cdot 22} \quad (77)$$

$$S_g = 1.910E0 + 7.848E1/P^2 - 1.142E\text{-}1P^{\cdot 22} \quad (78)$$

By applying the appropriate error equation above (61)-(63), to equations (67)-(78) Table 12 is obtained. A sample computation for $\sigma_{h_{gT}}$ is as follows:

$$\sigma_{h_{gT}} = \left((3.290E\text{-}1)^2 + 4(7.302E\text{-}4)^2(79)^2 \right)^{1/2} \sigma_p = .349\sigma_p \quad (79)$$

$$\text{For } \frac{\sigma}{P} p = 1.04\ \% \quad \sigma_p = .0104 \cdot 79 = .8216$$

$$\sigma_{h_{gT}} = .349(.8216) = .2864 \quad (80)$$

Table B-12

σ ERROR VALUES USED IN COMP''TATIONS

Variable	σ_T	σ_T^2	σ_P	σ_P^2
σ_{V_f}	1.70E-5	2.88E-10	1.394E-5	1.94E-10
σ_{V_g}	5.806E-2	3.371E-3	1.702E-2	2.90E-4
σ_{S_f}	1.641E-4	2.692E-8	7.25E-4	5.25E-6
σ_{S_g}	2.056E-3	4.227E-6	9.81E-4	9.63E-7
σ_{h_f}	0.827	0.684	0.586	0.344
σ_{h_g}	0.712	0.5075	0.647	0.419

where P_P = 150 psia, P_T = 79 psia

Next

$$\sigma_{h_{gT}}/h_{gT} = \pm\ (.0242 + .036)\% = \pm\ .0602 \tag{81}$$

Where the .036 is the table fit accuracy. Then

$$\sigma_{h_{gT}} = .000602 * h_{gT} = .000602(1183.4) = .712 \tag{82}$$

With this information, we may now perform the necessary detailed computations.

The first equations to be evaluated are (39) and (40). For (39) with $X_p = 0.0$

$$\sigma_{X_T}/X_T = \left[\frac{5.25E\text{-}6 + 2.69E\text{-}8}{(.5138 - .4532)^2} + \frac{4.23E\text{-}6 + 2.69E\text{-}8}{(1.6224 - .4532)^2}\right]^{1/2} \tag{83}$$

or

$$\sigma_{X_T}/X_T = .0379 \text{ or } 3.79\% \tag{84}$$

For (40) with $X_p = 1.0$

$$\sigma_{X_T}/X_t = \left[\frac{9.63E\text{-}7 + 2.692E\text{-}8}{(1.5694 - .4532)^2} + \frac{4.227E\text{-}6 + 2.692E\text{-}8}{(1.6224 - .4532)^2}\right]^{1/2} \tag{85}$$

or

$$\sigma_{X_T}/X_T = 1.97E\text{-}3 \text{ or } .197\% \tag{86}$$

The next equation is (41) which requires X_T and X_T^2 from (36), V_T from (T3), σ_{X_T} and $\sigma_{X_T}^2$. For $X_p = 0.0$

$$X_T = (.5138\text{-}.4532)/(1.6224\text{-}.4532) = 5.18E\text{-}2 \text{ and } X_T^2 = 2.69E\text{-}3 \tag{87}$$

$$V_T = (1\text{-}.0518)\ (0.1756) + 0.518\ (5.540) = .3036 \tag{88}$$

$$\sigma_{X_T} = .0379 \text{ or } \sigma_{X_T} = 1.963E\text{-}3\ \ \sigma_{X_T}^2 = 3.85E\text{-}6 \tag{89}$$

Now for (41)

$$\sigma_{V_T}/V_T = \frac{(1\text{-}.0518)^2(.288E\text{-}10)+(5.540\text{-}.01756)^2(3.85E\text{-}6)+(2.69E\text{-}3)(3.371E\text{-}3)}{.3036} \tag{90}$$

or

$$\sigma_{V_T}/V_T = 1.125E\text{-}2/.3036 = .0370 \text{ or } 3.7\% \tag{91}$$

The same computations for (41) with condition that X_p = 1.0 yields the following data:

$$X_T = .955,\ X_T^2 = .9115 \tag{92}$$

$$V_T = 5.29 \tag{93}$$

$$\sigma_{X_T} = 1.88E\text{-}3,\ \sigma_{X_T}^2 = 3.54E\text{-}6 \tag{94}$$

and finally for (41)

$$\sigma_{v_T}/V_T = 5.84E\text{-}4 \text{ or } .0584\% \tag{95}$$

$$\sigma_{V_T} = .00409$$

The evaluation of (42) is, for X_p = 0.0

$$\sigma_{h_T}/h_T = \frac{[(.9482)(.684) + (1183.4-281.3)^2\ 3.85E\text{-}6 + (2.69E\text{-}3)(.5075)]^{1/2}}{328.03} \tag{96}$$

$$\sigma_{h_T}/h_T = \frac{1.95}{328.03} = 5.93E\text{-}3 \text{ or } .593\% \qquad \sigma_{h_T} = 1.95 \tag{97}$$

Similarly for X_p = 1.0 (42) becomes

$$\sigma_{h_T}/h_T = \frac{3.342}{1142.5} = 2.93E\text{-}3 \text{ or } .293\% \tag{98}$$

The solution of (48) involves both X_p and steam line size as shown in Table 9. Each has two choices for a total of four combinations to check for. Define the four cases as:

Case 1 X_p = 0.0, small line

Case 2 X_p = 1.0, small line

Case 3 X_p = 0.0, large line

Case 4 X_p = 1.0, large line

In (48) the ratio σ_x/x is desired from (43) and (45) where

$$\sigma_x/x = \frac{\left(\sigma_{h_p}^2+\sigma_{h_T}^2+(1/J^2)\ \sigma_{H_T}^2\right)^{1/2}}{h_p-h_T-(H_T/J)} \tag{99}$$

Case 1 X_p=0.0, H_T=0.0, $h_p=h_{f_p}$, P_p = 880 psia, P_T = 640 psia.

A_p=.181 ft^2 $V_p=V_{fp}$, A_T=.087 ft^2, σ_{H_T}=0.0, V_T = 0.055

$$\sigma_x/x = \frac{(.344 + .380)^{1/2}}{(330.51-328.03)} = \frac{2.036}{2.48} = .821 \text{ or } 82.1\% \quad (100)$$

Taking the square root of (46) yields σ where $V_p = V_{fp} = .01809$ and

$$\sigma_y = 2\left[(4013.02)^2\ 1.265E\text{-}4 + (6735.45)^2\ (1.544E\text{-}5)\right.$$
$$\left.+(67391.7)^2\ 1.94E\text{-}10 + (14012.8)^2\ (4.73E\text{-}8)\right]^{1/2} \quad (101)$$

or

$$\sigma_y = 104.84 \quad (102)$$

and

$$y = 1218.1 \quad (103)$$

so

$$\sigma_y/y = 8.61E\text{-}2 = 8.61\% \quad (104)$$

Inserting these results in (48) gives

$$\sigma_{U_p}/U_p = (1/2)\left((.821)^2+(8.61E\text{-}2)^2\right)^{1/2} = .412 \text{ or } 41.3\% \quad (105)$$

Now (49) can be solved using Table 9, Table 12 and Equation (104).

$$\sigma_{W_N}/W_N = (.413^2+(.00393)^2+5.93E\text{-}7))^{1/2} \quad (106)$$

$$\sigma_{W_N}/W_N = .413 \text{ or } 41.3\% \quad (107)$$

This is the total progagation error for Case 1. Note that the final answer is determined mainly from Equation (100) which in turn comes from (99).

Case 2: $X_p = 1.0$, $h_p = h_{gp}$, $V_p = V_{gp}$, $V_T = 5.29$ Others same as Case 1.

$$\sigma_x/x = \frac{(.419+11.17)^{1/2}}{1194.1-1142.5} = \frac{3.40}{51.6} = .0660 \quad (108)$$

$$\sigma_y = 2((2.52)^2\ 5.84E\text{-}4 + (73.62)^2\ (1.54E\text{-}5)$$
$$+(4.42)^2\ 2.90E\text{-}4 + (153.2)^2\ (4.73E\text{-}8))^{1/2} \quad (109)$$

and

$$\sigma_y = .613 \quad (110)$$

plus

$$y = 12.32 \quad (111)$$

so

$$\sigma_y/y = .050 = 5.0\% \quad (112)$$

1158 247

Now inserting into (48) gives

$$\sigma_{U_p}/U_p = 1/2((.066)^2+(.050)^2)^{1/2} = 4.14E\text{-}2 \text{ or } 4.14\% \quad (113)$$

Solving for Equation (49) yields

$$\sigma_{W_n}/W_n = (.0414^2+.0217^2+(5.65E\text{-}3)^2)^{1/2}=4.71E\text{-}2 \text{ or } 4.71\% \quad (114)$$

This is the final propagation error result for Case 2.

Case 3: $H_T = 24.0$, $A_p = 201.89$, $A_T = 63.65$, $\sigma_{H_T} = .5$, others the same as Case 1.

$$\sigma_x/x = \frac{.344+3.80 + .25/778.26^2\ ^{1/2}}{330.51-328.03 - 24/778.26} = \frac{2.035}{2.449} \quad (115)$$

or

$$\sigma_x/x = .831 \text{ or } 83.1\% \quad (116)$$

$$\sigma_y = 2\left[(9334.2)^2\ 1.265E\text{-}3 + (2021.3)^2\ (1.196E\text{-}4) + (156653.)^2\ 1.94E\text{-}10 + (6411.4)^2\ (2.36E\text{-}7)\right]^{1/2} \quad (117)$$

or

$$\sigma_y = 107.35 \quad (118)$$

and

$$y = 2832.8 \quad (119)$$

so

$$\sigma_y/y = 3.79E\text{-}2 \quad (120)$$

The result for (48) is

$$\sigma_{U_p}/U_p = 1/2(.831^2+.0379^2)^{1/2} = .416 \text{ or } 41.6\% \quad (121)$$

The solution (49) is then

$$\sigma_{W_N}/W_N = (.416^2 + (.0078)^2 + (7.70E\text{-}4)^2)^{1/2} \quad (122)$$

or

$$\sigma_{W_N}/W_N = .416 \text{ or } 41.6\% \quad (123)$$

1158 248

This is the total propagation error for the large liquid-break test. Again note (as for Case 1) that the final answer is determined by σ_x/x or Equation (115) and (116).

Case 4: $X_p = 1.0$, $h_p = h_{gp}$, $V_p = V_{gp}$, $A_p = 201.89$,

$A_T = 63.65$, $H_T = 24.0$, $V_T = 5.29$, $\sigma_{H_T} = .5$

$$\sigma_x/x = \frac{.419+11.17+.25/778.76^2}{1194.1-1142.5-24/778.26}^{1/2} = \frac{3.40}{51.57} = .066 \quad (124)$$

Next

$$\sigma_y = 2\left[5.85^2*5.84E\text{-}4+22.1^2*1.196E\text{-}4 + 10.3^2*2.70E\text{-}4+70.1^2*2.36E\text{-}7\right]^{1/2} \quad (125)$$

and

$$\sigma_y = 6.81E\text{-}2 \quad .332 \quad 1.269 \quad (126)$$

and

$$y = 29.98 \quad (127)$$

then

$$\sigma_y/y = .011 \quad (128)$$

Solving for (48) yields

$$\sigma_{U_p}/U_p = 1/2 \quad .066^2+(.011)^2 \quad ^{1/2} = .067 \text{ or } 6.7\% \quad (129)$$

The final solution for (49) becomes

$$\sigma_{W_N}/W_N = (.067^2+.0078^2+2.90E\text{-}4)^{1/2} = 6.95E\text{-}2 \text{ or } 6.95\% \quad (130)$$

This is the total error propagation value for Case 4.

5.8.2.2 Steam Vessel Differential Flowrate

Equation (50) is the only one needed for steam vessel differential flowrate error propagation. Equation (50) uses data from Table 9 and Table 10. To solve (50) the following must be solved first:

$$\sigma_{A_v} = 4777.92*.0128=61.16 \quad \sigma_{A_v}{}^2=3740.022 \quad (131)$$

The ΔP readings have an instrumental error of ± 0.64% so that

$$\sigma_{\Delta P_2} = \Delta P_2*\pm.0064=5*.0064=.032, \quad \sigma_{\Delta P_2}^2 = .0010 \quad (132)$$

$$\sigma_{\Delta P_1} = \Delta P_1*.0004=10*.0064=,.064 \quad \sigma_{\Delta P_1}^2 = .0041 \quad (133)$$

Now for Equation (50)

$$\sigma_{W_v}/W_v = \frac{\left[(5-10)^2 3740.02 + 22.82*10^6 (.001+.0041)\right]^{1/2}}{4777.92(5-10)} \quad (134)$$

$$= -\frac{458.13}{23889.6} = -.0192 \text{ or } -1.92\% \quad (135)$$

5.8.2.3 Annubar Differential Ventline Flowrate

Equations (51)-(60) give the necessary relations for this section. Equations (51)-(54) need the following intermediate results. The Precise Sensor pressure values have an instrumental error of 0.77%.

$$\sigma_{P_{vj}}/P_{vj} = .0077, \ \sigma_{P_{vj}} = .27, \ \sigma_{P_{vj}}^2 = .0726 \quad (136)$$

$$\sigma_{T_{vj}}/T_{vj} = .0094, \ \sigma_{T_{vj}} = 2.350, \ \sigma_{T_{vj}}^2 = 5.523 \quad (137)$$

Using (135) and (136) the solution of (51) is

$$\sigma_{\rho_{1j}}/\rho_{1j} = \left[(.0077)^2 + (2.35/(250+460))^2\right]^{1/2} = .0084 \text{ or } 0.84\% \quad (138)$$

Next, the result for (53) is:

$$\sigma_{\rho_{2j}}/\rho_{2j} = \frac{\left[(1.9*10^{-3}+5.6*10^{-7})(.27)\right]}{5.79*10^{-2}+1.9*10^{-3}(35)+2.8*10^{-7}(35)^2} = .0041 \text{ or } 0.41\% \quad (139)$$

The result for (54) is (since $D_1 = D_2 = 0$)

$$\sigma_{k_{2j}}/k_{2j} = 0.0 \quad (140)$$

For Equations (55-59), i = 1 or 2, which means the results from (137) or (138) must be used. First some intermediate results are required.

$$\sigma_{Cj}/C_j = .02, \ \sigma_{Cj} = 18.36, \ \sigma_{Cj}^2 = 336.97 \quad (141)$$

$$\sigma_{\Delta P_{vj}}/\Delta P_{vj} = .0077, \sigma_{\Delta P_{vj}} = .0015, \ \sigma_{\Delta P_{vj}}^2 = 2.37*10^{-6} \quad (142)$$

$$\sigma_{Avj}/A_{vj} = .0107, \ \sigma_{Avj} = 18.413, \ \sigma_{Avj}^2 = 339.02 \quad (143)$$

$$\gamma_{ij} = (k_{11}-1)/k_{11} = .2857 \quad (144)$$

$$C1_{1j} = (917.84)\left[\frac{(1.8*35)0.2}{(250+460)}\right]^{1/2} = 122.271 \quad (145)$$

$$C1_{2j} = (917.84)\left[(5.79*10^{-2} + 1.9*10^{-3}(35) + 2.8*10^{-7}(35)^2)0.2\right]^{1/2} = 144.974 \quad (146)$$

$$C2_{1j} = 1/(288(32.17)\left[\frac{1.8*35}{250+460}\right]2.96*10^{6}*35) = 1.174*10^{-11} \quad (147)$$

$$C2_{2j} = 1/\left[288(32.17)(5.79*10^{-2} + 1.9*10^{-3}(35) + 2.8*10^{-7}(35)^2)(2.96*10^{6})*35\right] = 8.352*10^{-12} \quad (148)$$

The results for the two cases are as follows, Case 1 for i = 1:

First obtain the results for (55)

$$\sigma_{C1_{1j}}/C1_{1j} = \left[.02^2+(.0084/2)^2+(.0077/2)^2\right]^{1/2} = .0208 \quad (149)$$

and

$$\sigma_{C1_{1j}} = 2.543 \quad (150)$$

Next for (56,

$$\sigma_{C2_{1j}}/C2_{1j} = \left[.0084^2+4*.0107^2+.0077^2\right]^{1/2} = .0242 \quad (151)$$

and

$$\sigma_{C2_{1j}} = 2.83*10^{-13} \quad (152)$$

$$\sigma_y/y = \frac{(122.271)(-.7143)\left[\frac{(122.27)^2}{4}*(2.83*10^{-13})^2+(1.17\times10^{-11})^2(2.543)^2\right]^{1/2}}{1-.5(.7143)1.17*10^{-11}*(122.271)^2} \quad (153)$$

or

$$\sigma y/y = \frac{-3.006*10^{-9}}{1.000} = -3.006*10^{-9} \quad (154)$$

Finally, the result for (60) is

$$\sigma_{W_{1j}}/W_{1j} = \left[.0208^2+(-3.01*10^{-9})^2\right]^{1/2} = .0208 \text{ or } 2.08\% \quad (155)$$

This is the total propagation error for W_{1j}.

1158 251

For i = 2, the results are:

$$\sigma_{Cl_{2j}}/Cl_{2j} = \left[.02^2 + (.0041/2)^2 + (.0077/2)^2\right]^{1/2} = .0205 \quad (156)$$

and

$$Cl_{2j} = 6.646 \quad (157)$$

$$\sigma_{C2_{2j}}/C2_{2j} = \left[.0041^2 + 4*.0107^2 + .0077^2\right]^{1/2} = .0231 \quad (158)$$

and

$$\sigma_{C2_{2j}} = 1.93*10^{-13} \quad (159)$$

$$\sigma_y/y = \frac{(144.974)(-.7143)\left[\frac{(144.97)^2}{4}*(1.9*10^{-13})^2 + (8.3\times10^{-12})^2(6.646)^2\right]^{1/2}}{1-.5(.7143)(8.35*10^{-12})*(324.17)^2} \quad (160)$$

$$\sigma_y/y = \frac{-5.886*10^{-9}}{1.000} = -.5.886*10^{-9} \quad (161)$$

Finally, the result for (60) is:

$$\sigma_{W_{2j}}/W_{2j} = \left[.0205^2 + (5.886*10^{-9})^2\right]^{1/2} = .0205 \text{ or } 2.05\% \quad (162)$$

This is the total propagation error for W_{2j}.

5.8.3 Numerical Results Summary

The various propagation errors for the flowrate equations are summarized in Table 13. Only the errors for the final numerical values are shown since these are the final results needed for the flowrate.

6.0 SUMMARY AND COMMENTS

The instrumental and propagation errors for the entire data acquisition system hardware and software have been evaluated in the previous sections. In general, the errors are quite small indicating a clean overall system. Two exceptions are the strain gage thermal drift error and the nozzle flowrate propagation errors under certain specific conditions.

The large propagation errors for Case 1 and Case 3 of the nozzle flowrate equations are a function of the two pressures P_p = 150 psia and P_T = 79 psia.

Table B-13

GE EQUATIONS NUMERICAL RESULTS SUMMARY

Flow Nozzle Flowrate Propagation Errors

Case 1: σ_{W_N}/W_N = 35.5%

Case 2: σ_{W_N}/W_N = 4.71%

Case 3: σ_{W_N}/W_N = 35.5%

Case 4: σ_{W_N}/W_N = 6.95%

Steam Vessel Differential Flowrate Propagation Error

σ_{W_v}/W_v = -1.92%

Annubar Differential Flowrate Propagation Errors

Case 1: $\sigma_{W_{1j}}/W_{1j}$ = 2.08%

Case 2: $\sigma_{W_{2j}}/W_{2j}$ = 2.05%

The large propagation errors for cases 1 and 3 (small and large liquid) of the nozzle flowrate equations are primarily a result of the small enthalpy difference in the denominator of equation (99). The enthalpy difference for steam is appreciably larger and accordingly does not significantly jeopardize the nozzle flowrate data. The error for both steam and water calculations are affected by the enthalpy difference in equation (99). At high pressures the difference in enthalpies is greater and the calculation error is reduced. Low pressures decrease the enthalpy difference and increase the error. The calculated errors are considered as the worst-case error propagation. However, the blowdown nozzle flowrate calculation may be compared with inventory change calculations of the steam supply vessel. The inventory change is determined by differential pressure measurements and serves as an independent check on the accuracy of the blowdown nozzle flowrate. As is discussed and shown in Appendix C, this comparison shows agreement for the liquid flow, which is at worst 20%. Therefore, it is likely that the calculated nozzle flowrates for liquid breaks have a better uncertainty value than that calculated via error propagation relations.

Aside from the error sources already accounted in the error analysis, certain assumptions were made. The nozzle calculations assume that the upsteam conditions were either saturated steam or saturated liquid. This assumption is not entirely valid for the short periods where liquid carryover is suspected to occur during steam breaks and where vapor carryunder occurs during liquid breaks. These periods have been identified in Appendix C.

APPENDIX C
FSTF SYSTEM PERFORMANCE

C.1 GENERAL

To establish that the initial conditions and test configurations bounded the range of Mark I LOCA conditions for chugging and condensation oscillation, pretest predictions of the system performance were made with the General Electric Pressure Suppression Analytical Model. The following section compares the measured steam vessel performance to the pretest predictions to confirm that the system responded as anticipated and the desired test conditions were obtained. The pretest predictions were not made in order to verify the Pressure Suppression Analytical Model, and these comparisons are not included for that purpose.

C.2 STEAM SUPPLY VESSEL

The steam supply vessel (V1), shown in Figure 3.2-1 and described in paragraph 3.2.1, served as the energy source for the test. The two parameters which best indicate the steam supply vessel performance are a) pressure, and b) blowdown flowrate.

a. Pressure - the steam supply vessel measured and predicted depressurization curves are shown in Figures C-1 to C-5 for the five basic blowdown configurations. These configurations are small liquid, large liquid, small steam, medium steam, and large steam. These comparisons show that the measured depressurization rates agree with the pretest predictions for both the small and large liquid break tests, Figures C-1 and 2. Both of these predictions assumed saturated liquid being discharged from the steam supply vessel until the break opening which is near the bottom of the vessel, was uncovered. After the liquid level dropped below the break opening, a two phase homogeneous mixture was assumed for the rest of the blowdown.

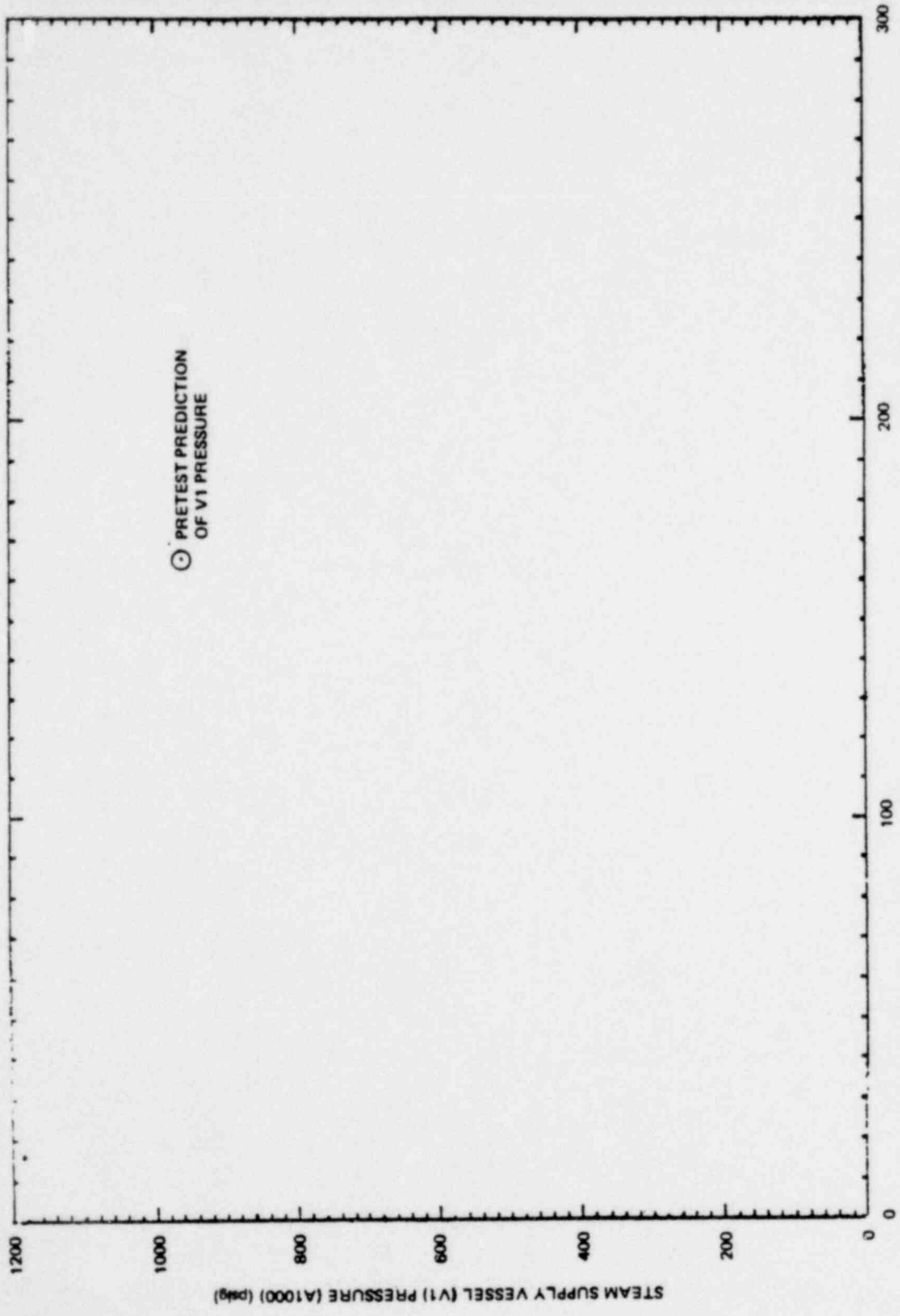

Figure C-1. V1 Pressure Comparison, Small Liquid Break, M3

*Proprietary information deleted

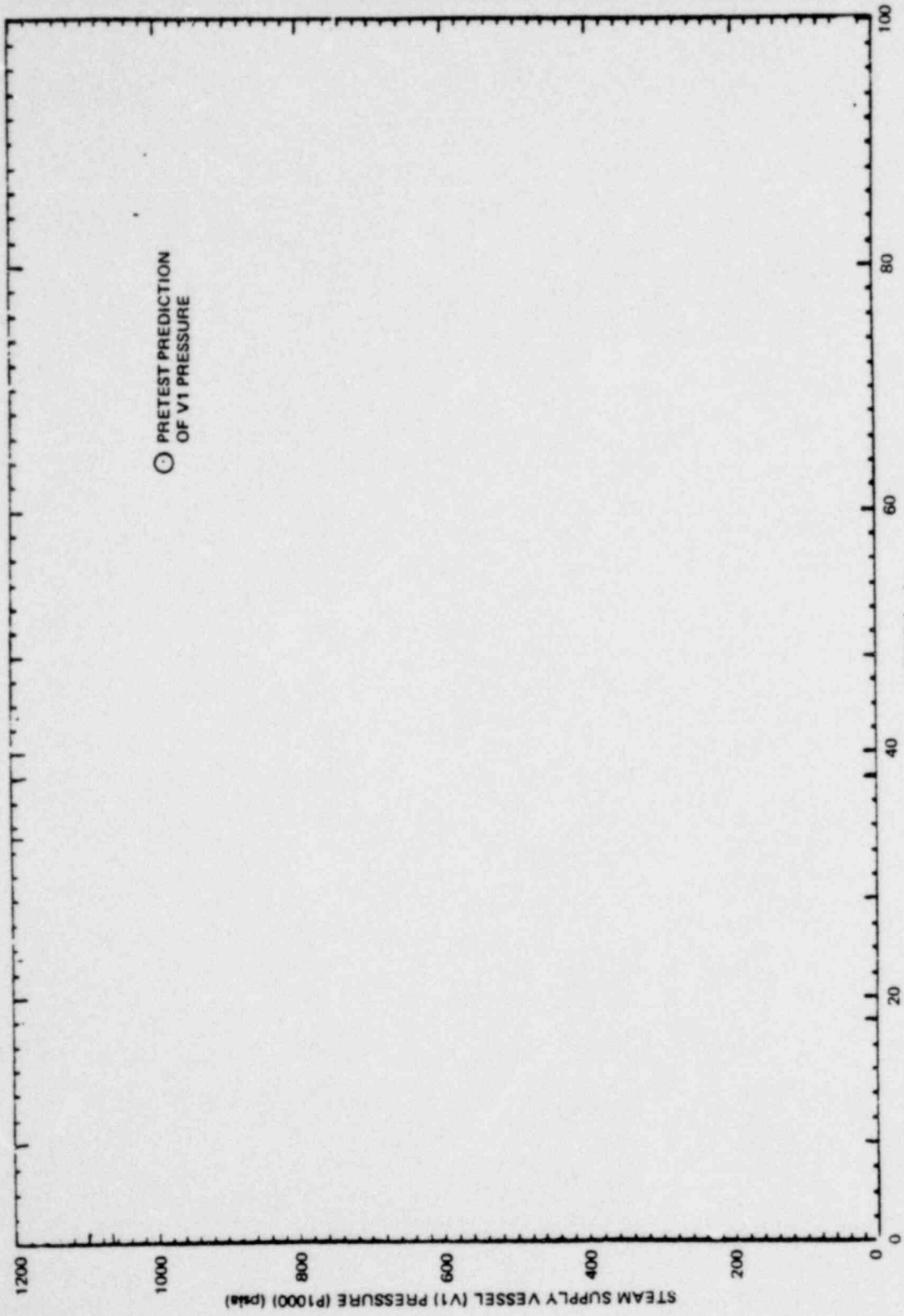

Figure C-2. V1 Pressure Comparison, Large Liquid Break, M8

*Proprietary information deleted

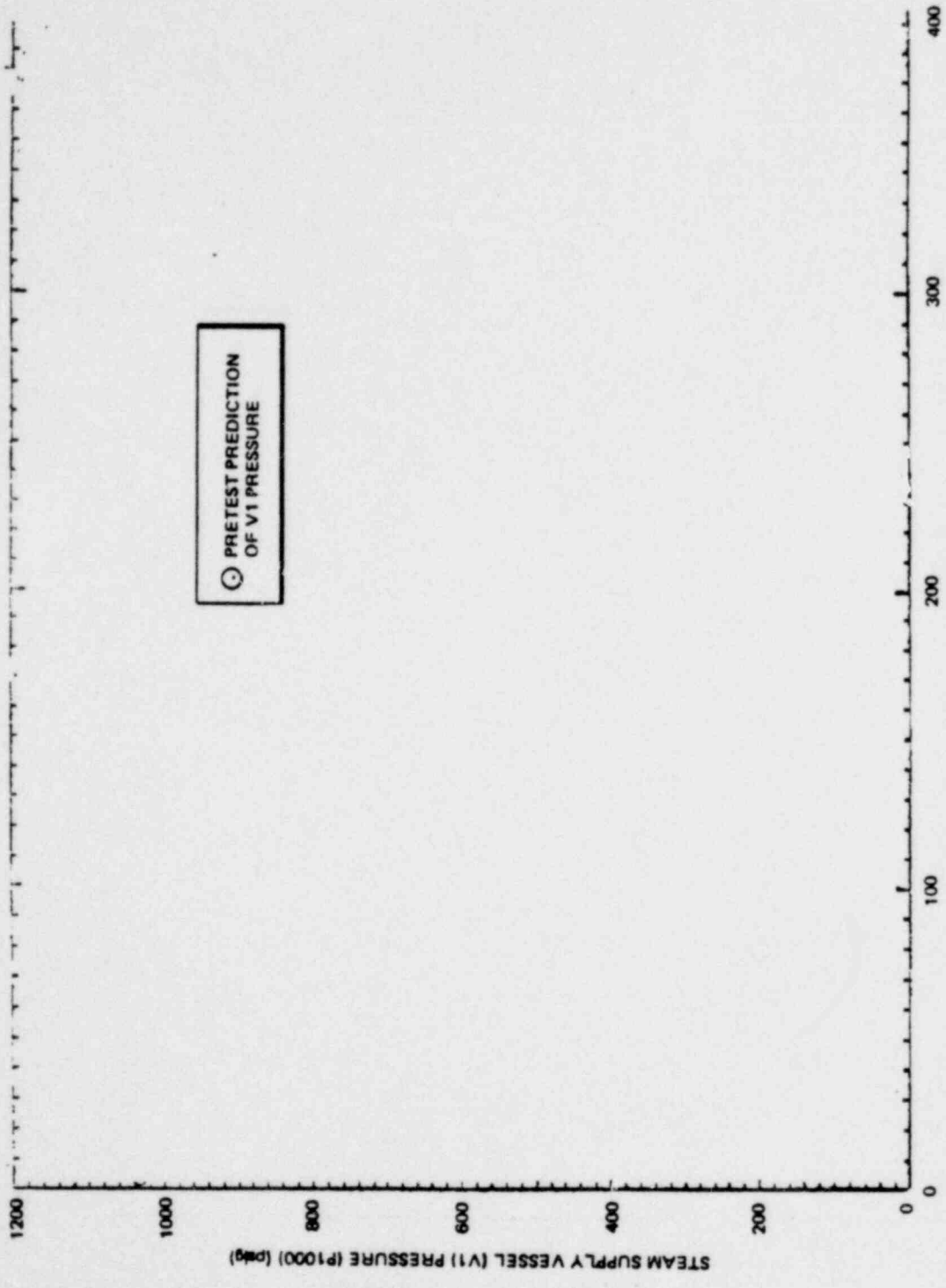

Figure C-3. V1 Pressure Comparison, Small Steam Break, M1

*Proprietary information deleted

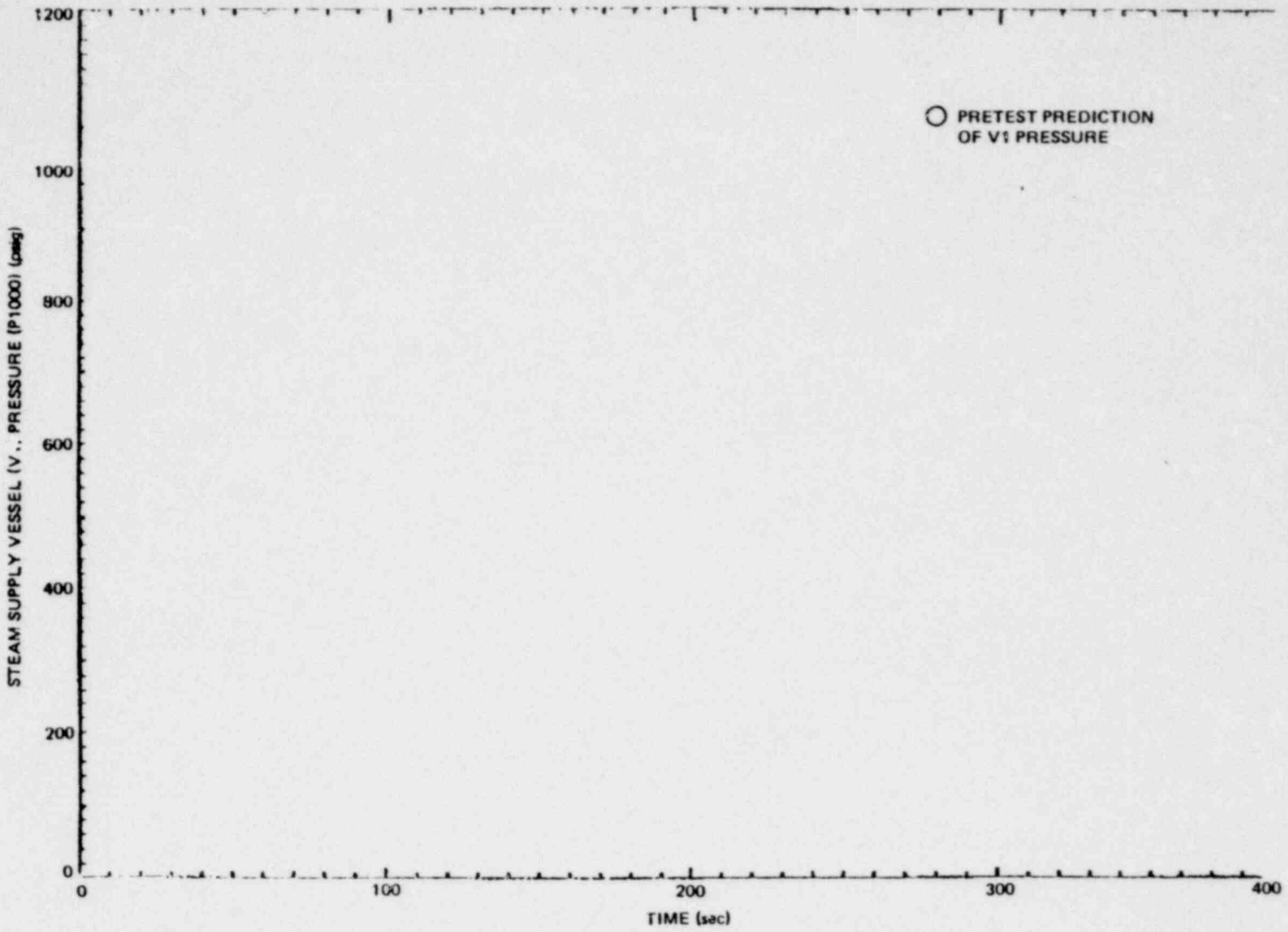

Figure C-4. V1 Pressure Comparison, Medium Steam Break, M2

*Proprietary information deleted

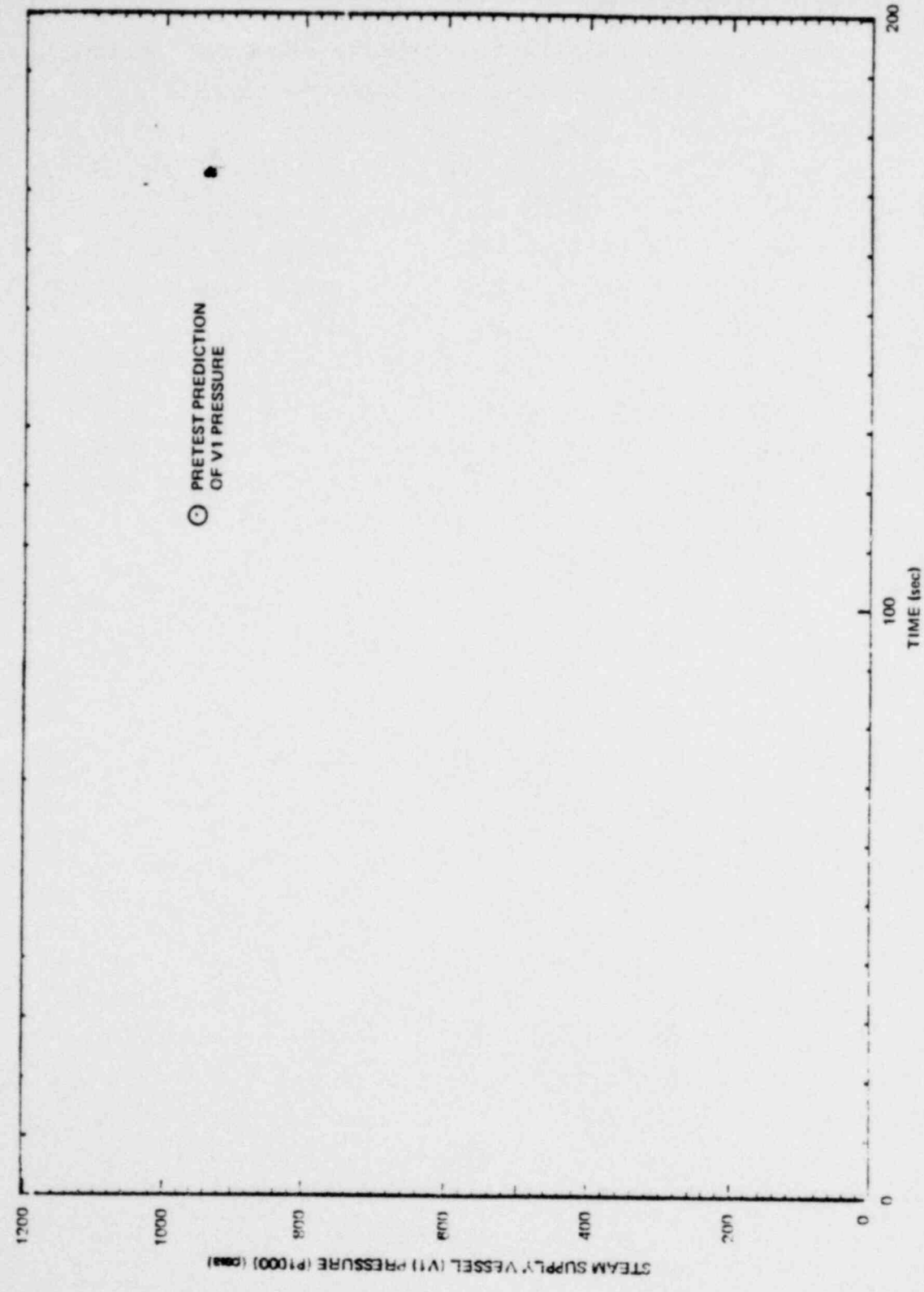

Figure C-5. V1 Pressure Comparison, Large Steam Break, M7

*Proprietary information deleted

Pretest predictions were also made for each of the three different size steam breaks. The steam break predictions assumed saturated steam being discharged from the steam supply vessel during the entire blowdown. Figures C-3, -4 and -5 compare these pretest predictions to the small, medium and large steam break depressurization curves. These results show that the measured steam supply vessel depressurization rates were less than the pretest predictions. This difference in the steam supply vessel measured and predicted depressurization rates results primarily from liquid carryover during the beginning of the steam breaks and the correspondingly higher losses and therefore lower flowrates associated with this initial two phase mixture outflow. This is evident because the large steam break which has the most liquid carryover differs most from the pretest prediction, Figure C-5. The small steam break which has the least liquid carryover differs least from the pretest prediction, Figure C-3. Both of these pretest predictions assumed steam only during the blowdown.

Figure C-6 compares the steam supply depressurization rates for all of the small steam break tests. This comparison shows the blowdowns were repeatable.

b. Blowdown rates - the steam supply vessel blowdown flowrates are shown in Figures C-7 through C-11 for the same five basic blowdown configurations. These figures compare the actual flowrates to the pretest prediction of the blowdown flowrate for each break size and type. The measured flow is calculated from the upstream and throat pressures in the flow nozzle assuming the flow expands isentropically. For liquid breaks, the flow is assumed to be saturated liquid at the nozzle inlet throughout the blowdown. For steam breaks, the flow is assumed to be saturated steam at

Figure C-6. V1 Pressure Comparison, Small Steam Break

*Proprietary information deleted

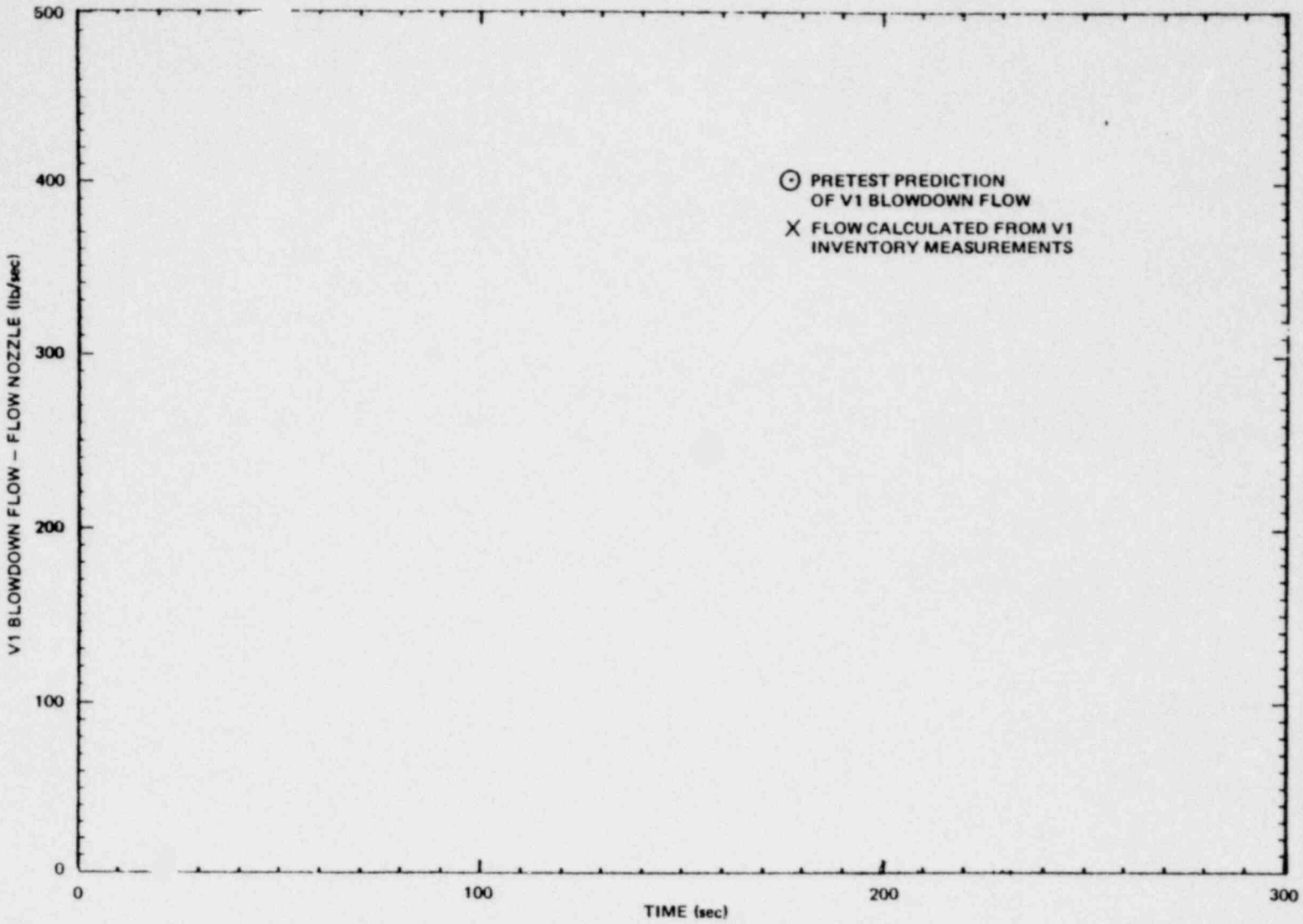

Figure C-7. Blowdown Flow Comparison, Small Liquid Break, M3

*Proprietary information deleted

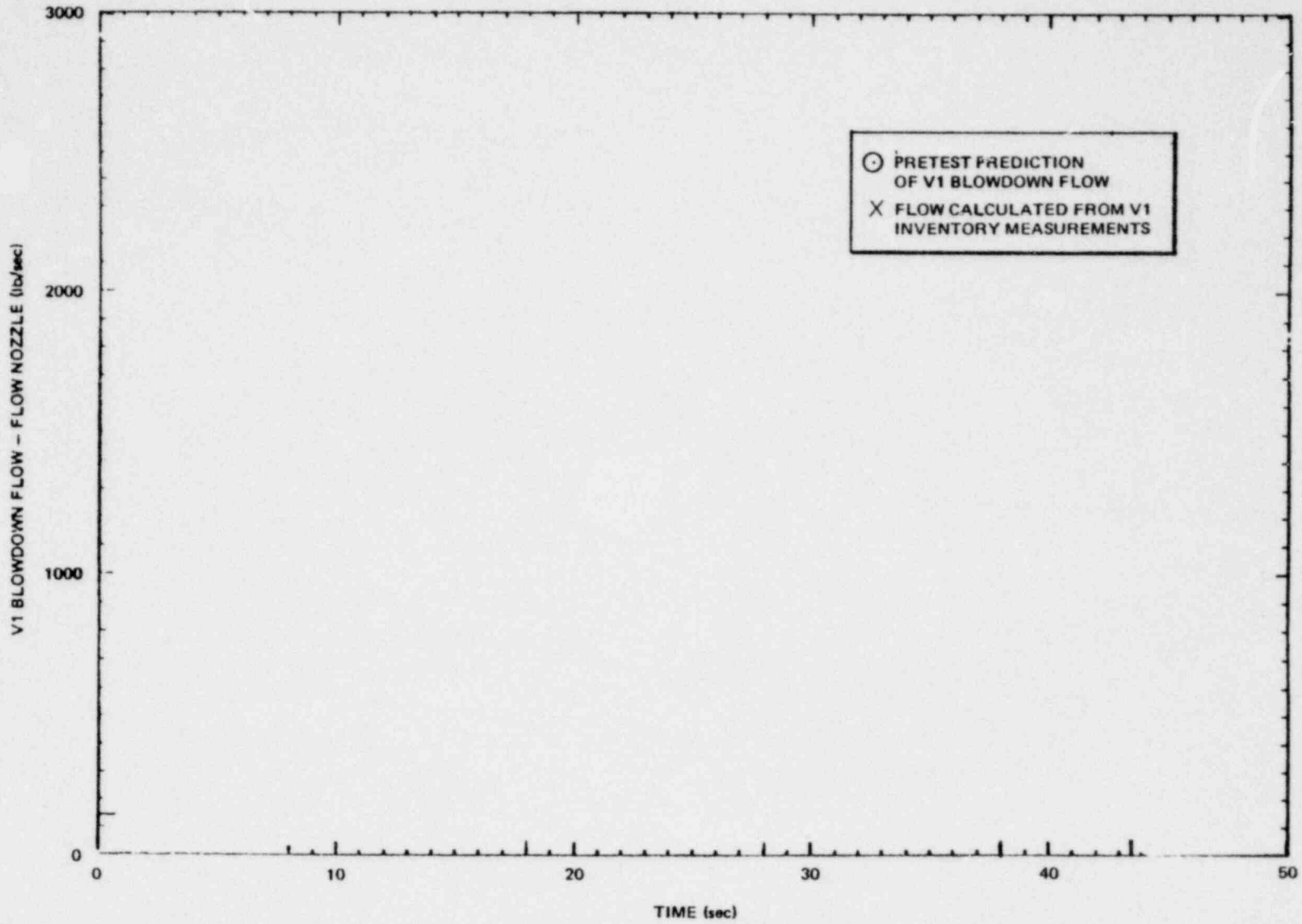

Figure C-8. Blowdown Flow Comparison, Large Liquid Break, M8

*Proprietary information deleted

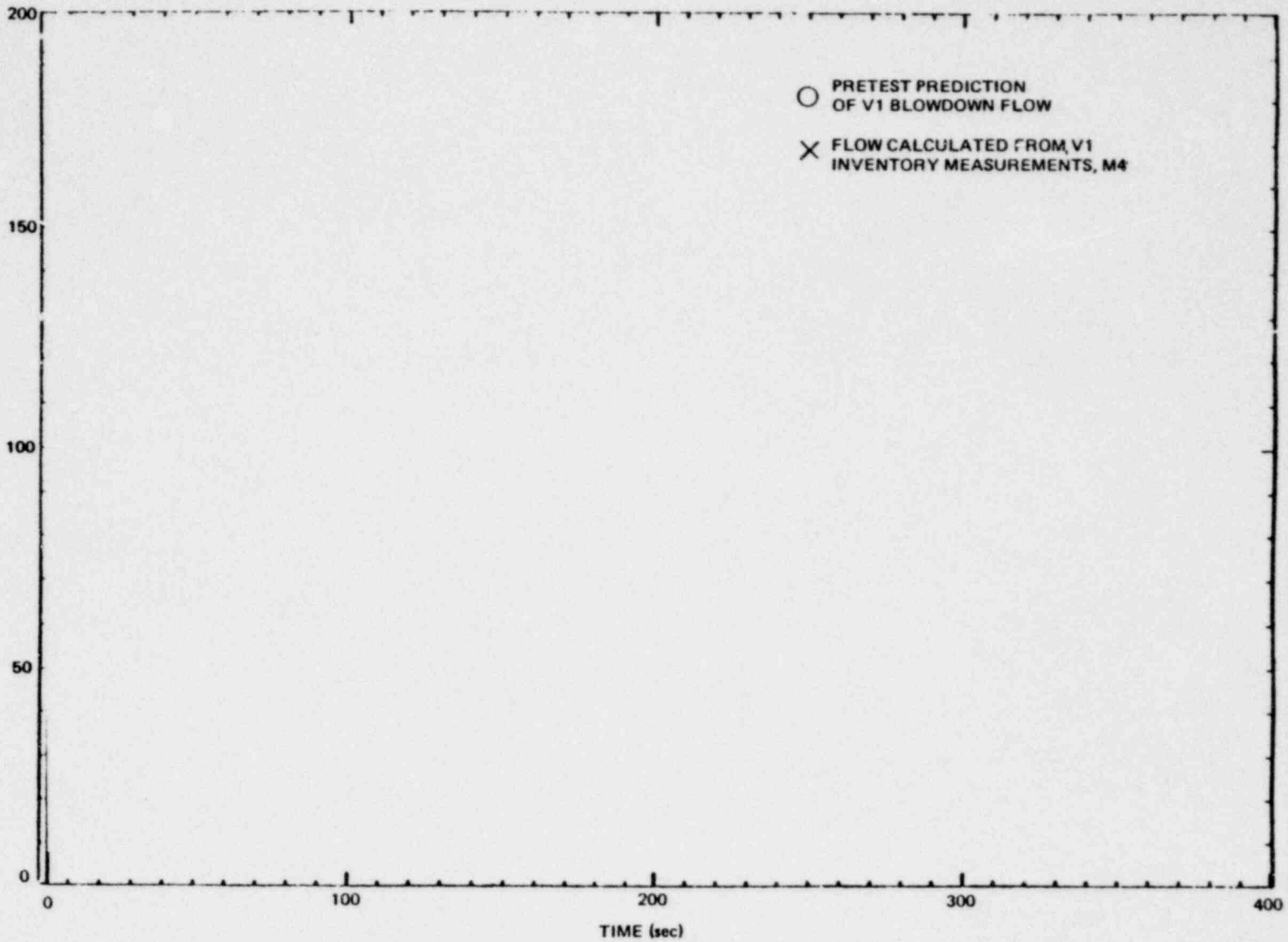

Figure C-9. Blowdown Flow Comparison, Small Steam Break, M1

*Proprietary information deleted

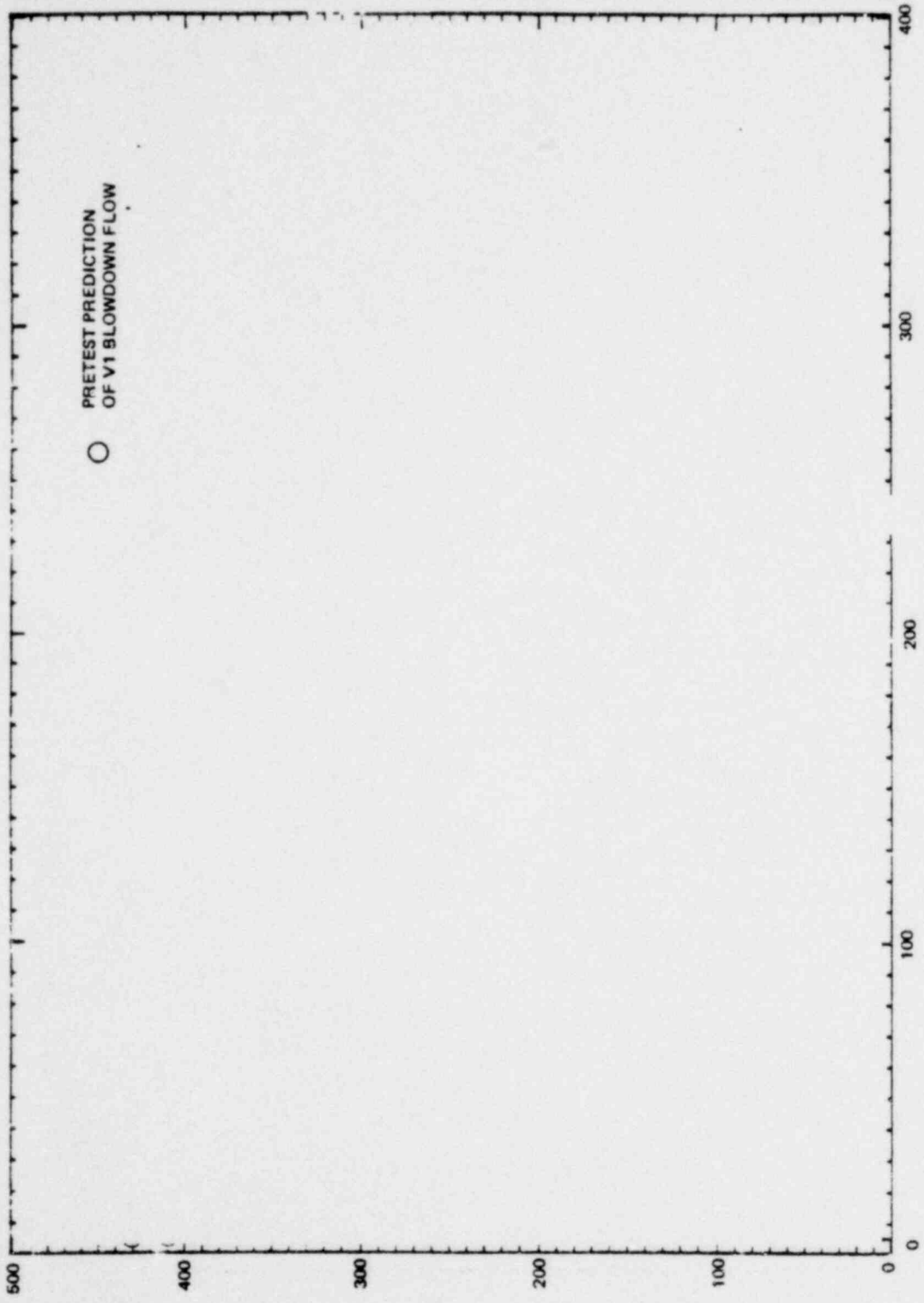

Figure C-10. Blowdown Flow Comparison, Medium Steam Break, M2

*Proprietary information deleted

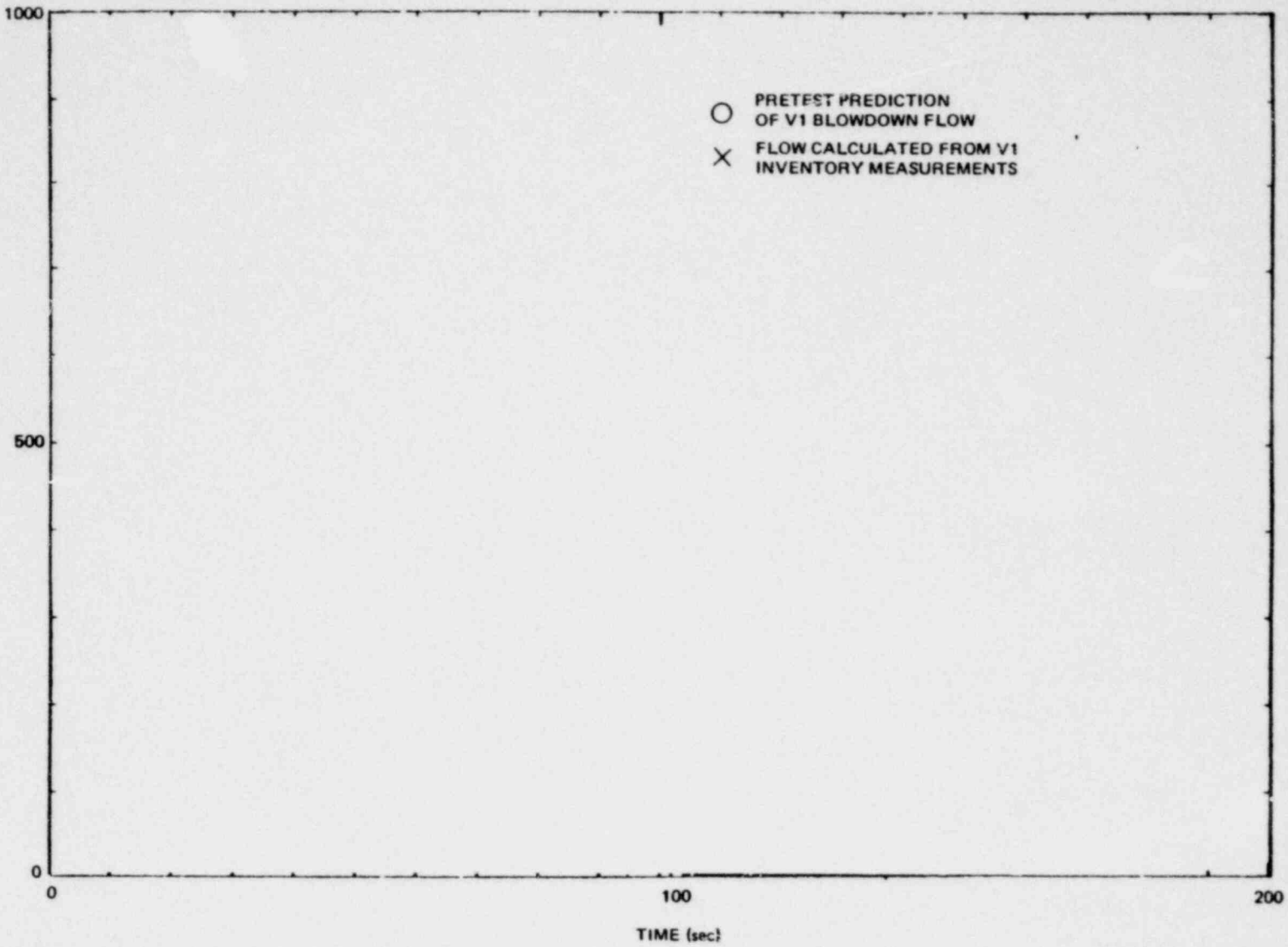

Figure C-11. Blowdown Flow Comparison, Large Steam Break, M7

*Proprietary information deleted

the nozzle inlet throughout the blowdown. As was noted for the steam break depressurization rates the measured steam break flowrate values are higher than pretest predicted values using a steam only assumption.

An additional indication of the blowdown flowrate can be obtained from the steam supply vessel (V1) inventory change determined with differential pressure measurements. Several times during the test were selected for each of the small liquid (M3), the large liquid (M8), large steam (M7), and small steam (M4) tests and the flowrate was calculated from the inventory change measurements at each time selected. They are shown on Figures C-7, C-8, C-9, and C-11. This comparison shows fair agreement for the liquid breaks (Figure C-7 and -8) until the liquid inventory is depleted at which time the flow changes over to steam. This transition from liquid to steam flow is not accounted for in the nozzle flow measurement and the inventory measurement of flow is less than the nozzle measurement as expected. However, for the steam breaks, the difference between the two measurements (flow nozzle vs. inventory) indicate that liquid carryover was occurring during the early part of the steam break blowdowns because the inventory measurements indicate higher flowrates than the nozzle measurements. This comparison also shows that the carryover was greater for the large steam break than for the small steam break. Figure C-12 compares the blowdown flowrates for all of the small steam breaks. It can be seen that the flowrates were very repeatable, and as would be expected, variation of the parameters tested did not significantly affect the blowdown flowrate since the flow is choked at the nozzle through most of the blowdown.

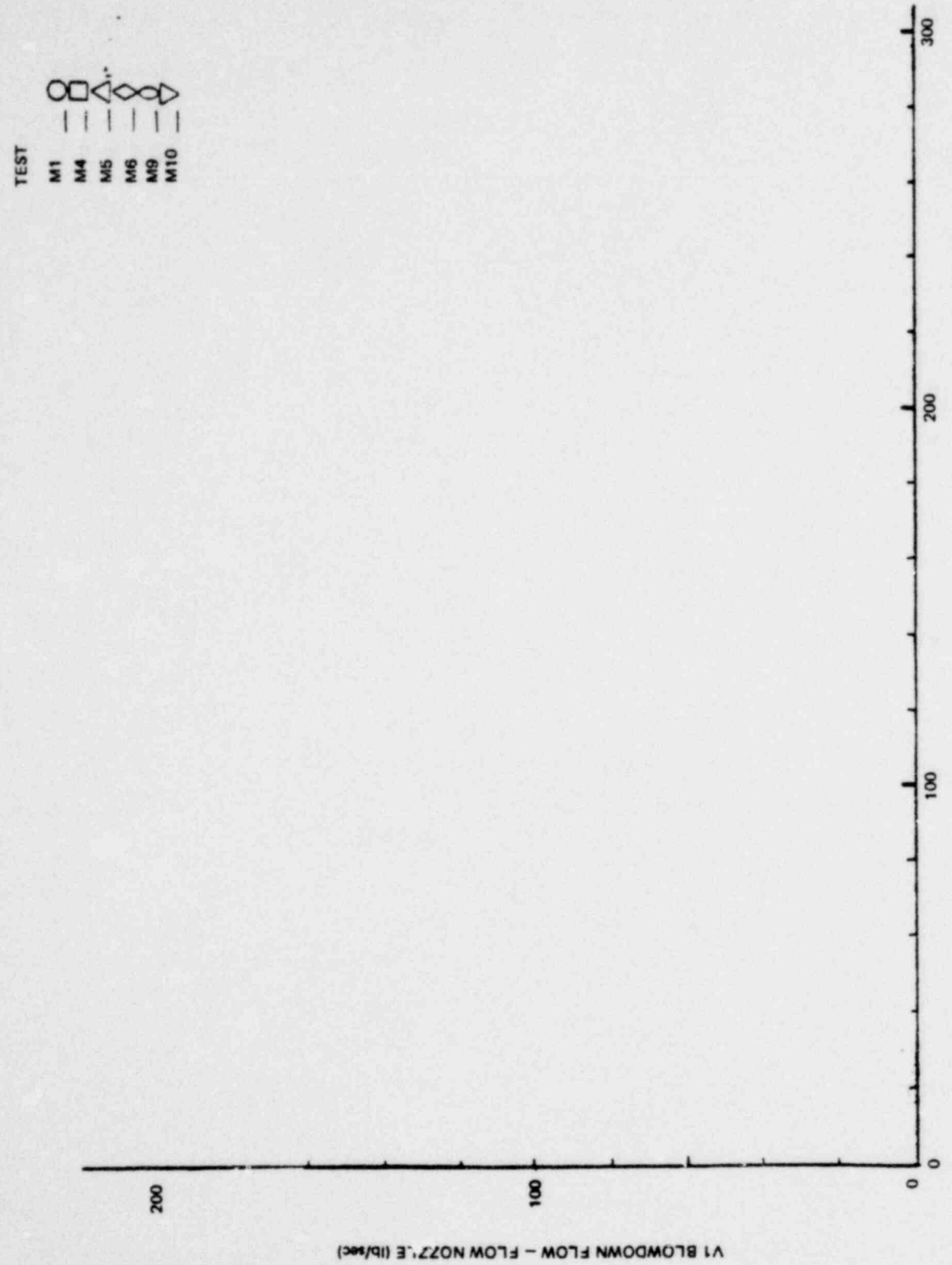

Figure C-12. Blowdown Flow Comparison, Small Steam Break

*Proprietary information deleted

C.3 DRYWELL AND VENT SYSTEM

The drywell vessel (V2) is shown in Figure 3.2-2 and is described in paragraph 3.2.3. One of the vent lines which connects the drywell (V2) to the wetwell (V3) is shown in Figure 3.2-4 and described in paragraph 3.2.4. The system performance of these components is described in the following subsections.

1. Pressure - Table C-1 compares the predicted and calculated values of the pressurization rate of the drywell at test initiation and lists the Figures showing initial pressurization, Figures C-13 to C-17, for the five blowdown configurations. These results show the actual pressurization rates to be within 10% of the calculations. This good agreement of the drywell initial pressurization rate confirms that the expected blowdown energy flowed into the drywell at test initiation. Figures C-18 to C-22 show the actual pressure traces for the five basic blowdown configurations for the entire test duration. Table C-1 tabulates the peak and final drywell pressures. The highest peak drywell pressure of 55 psia occurred during test M8 (large liquid break).

   The maximum drywell pressure oscillations of 5 psi occurred during Test M1 (small steam break) as shown on Figure C-23. These pressure oscillations occurred when large chugs were occurring in the suppression pool.

2. Temperature - Figure C-24 and -25 show a typical drywell and vent line temperature history for a small steam break. The locations of these measurements is given on Figure 3.4-4. As these figures show, the temperatures reach the saturation temperature corresponding to the drywell pressure after test initiation. This is caused by the liquid carryover into the drywell which occurred

Table C-1

DRYWELL PRESSURE AND INITIAL PRESSURIZATION

Fig. No.	Test No.	Blowdown Configuration	Initial $\dot{P}$ Measured (psi/sec)	Initial $\dot{P}$ Calculated (psi/sec)	Maximum Drywell Pressure (psia)	Final Drywell Pressure (psia)
C-13	M1	small steam				
C-14	M3	small liquid				
C-15	M2	medium steam				
C-16	M7	large steam				
C-17	M8	large liquid				

* Could not readily be determined because of high frequency pressure oscillation on pressure signal. The predicted rate is shown for comparison on Figure 6.1-16.

*Proprietary information deleted

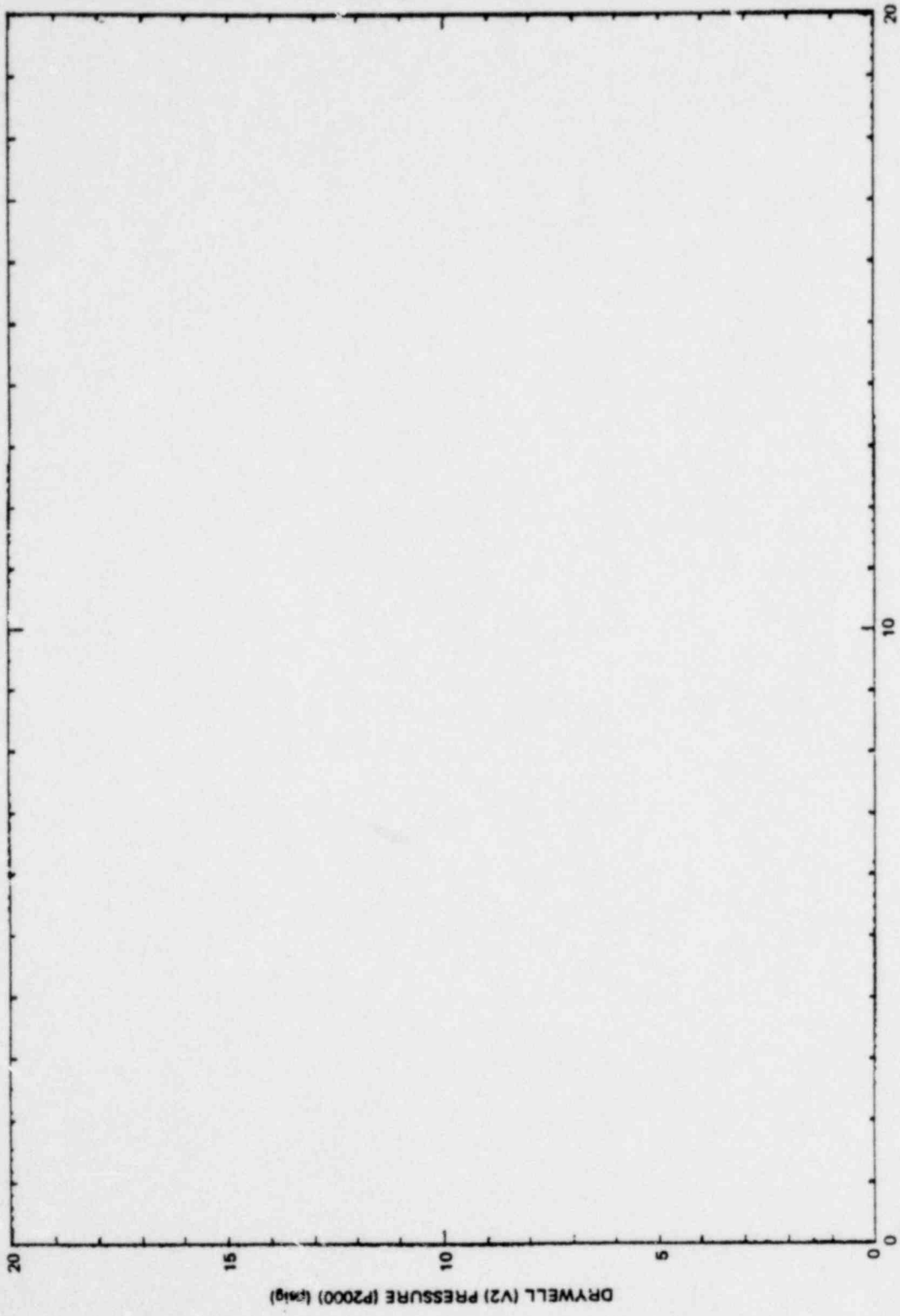

Figure C-13. Drywell Initial P essure, Small Steam Break, Ml

*Proprietary information deleted

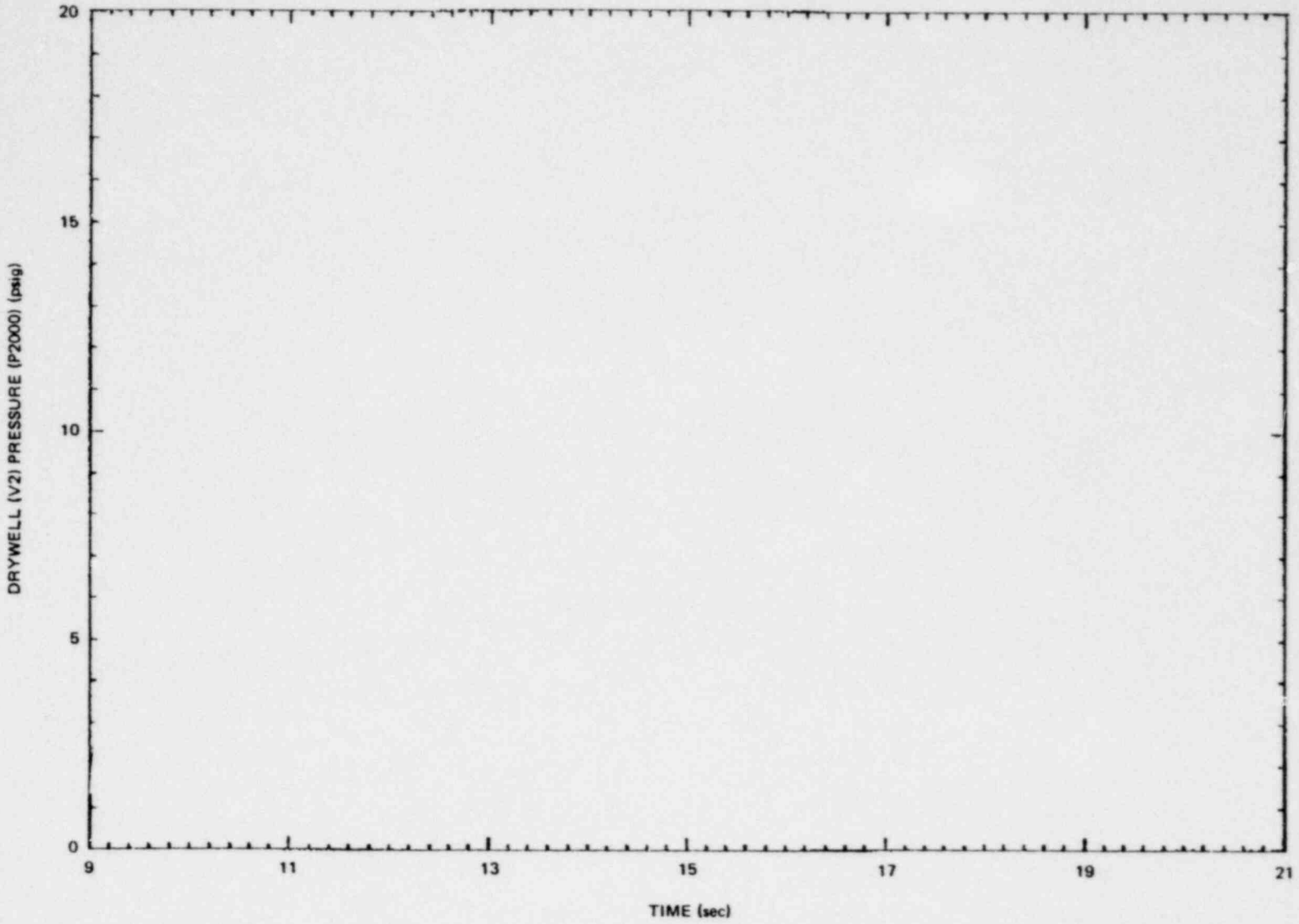

Figure C-14. Drywell Initial Pressure, Small Liquid Break, M3

*Proprietary information deleted

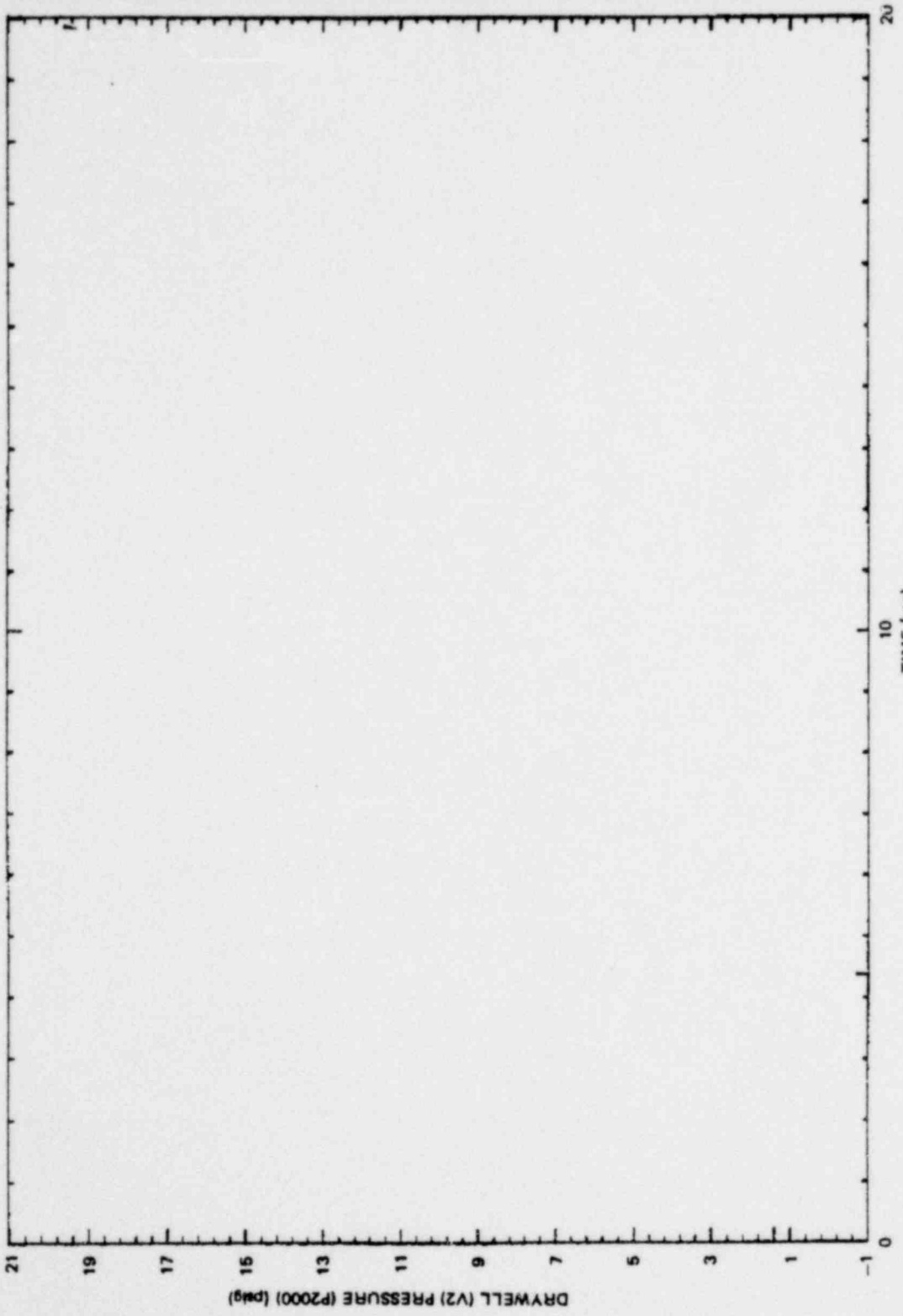

Figure C-15. Drywell Initial Pressure, Medium Steam Break, M2

*Proprietary information deleted

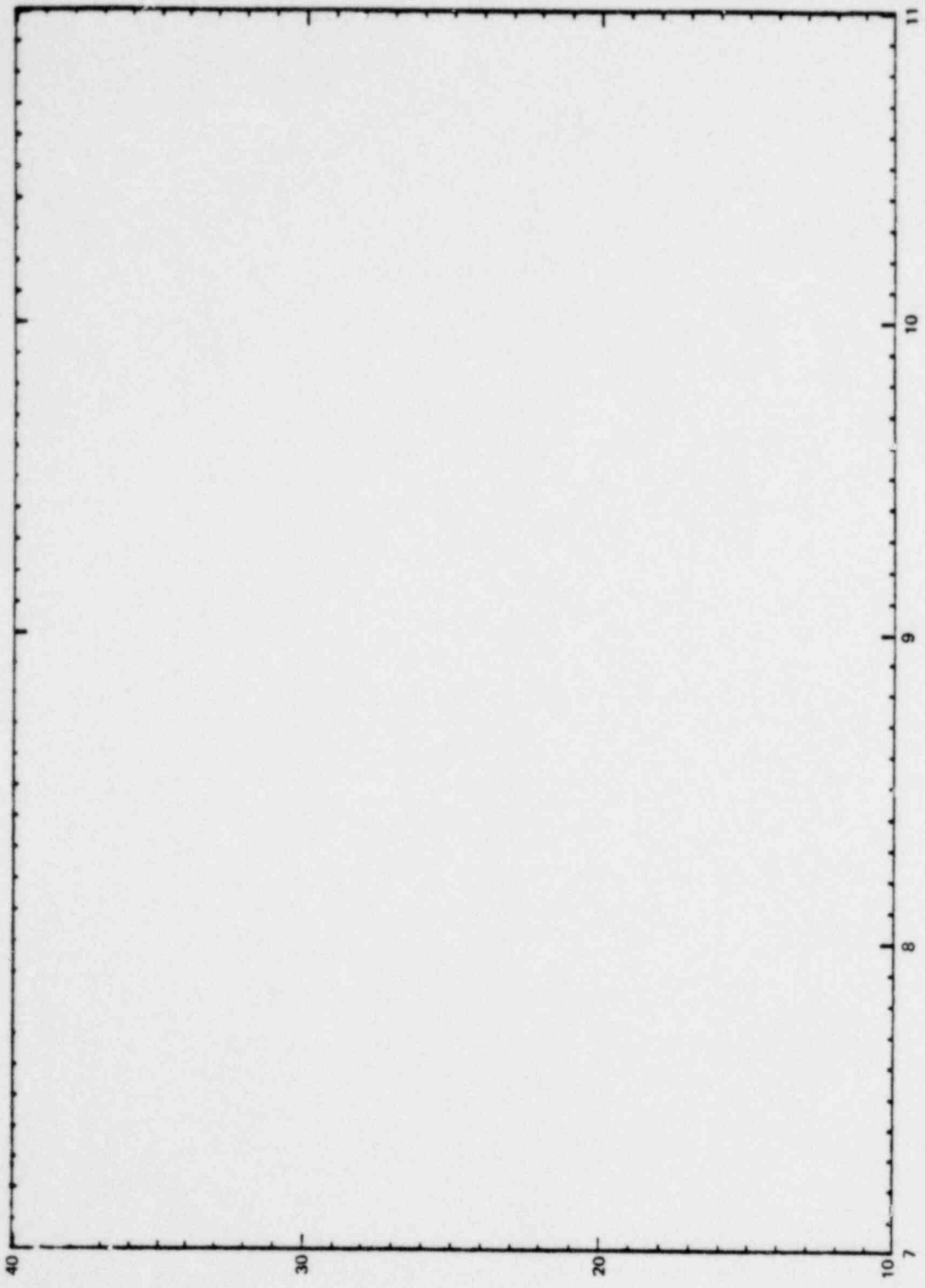

Figure C-16. Drywell Initial Pressure, Large Steam Break, M7

*Proprietary information deleted

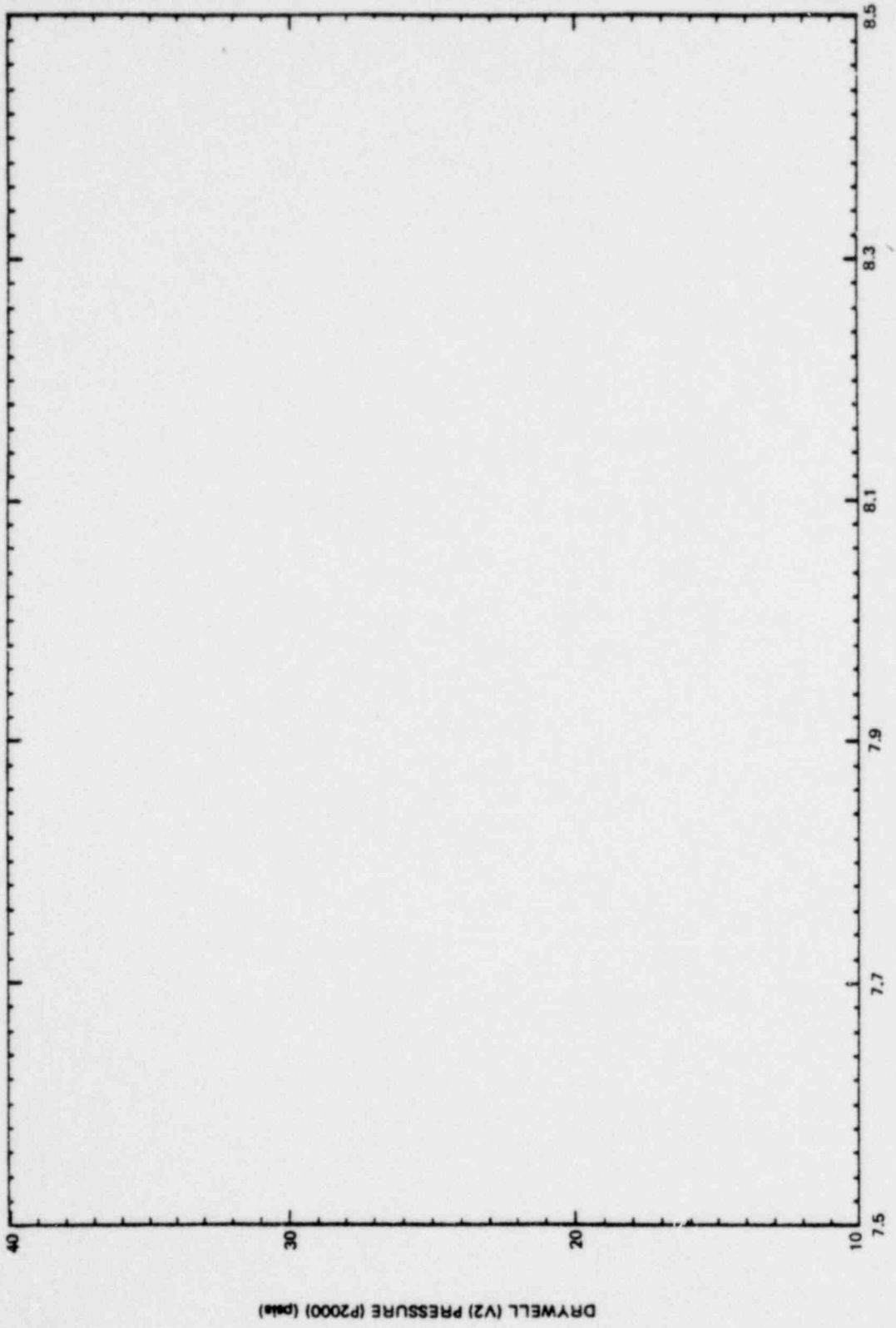

Figure C-17. Drywell Initial Pressure, Large Liquid Break, M8

*Proprietary information deleted

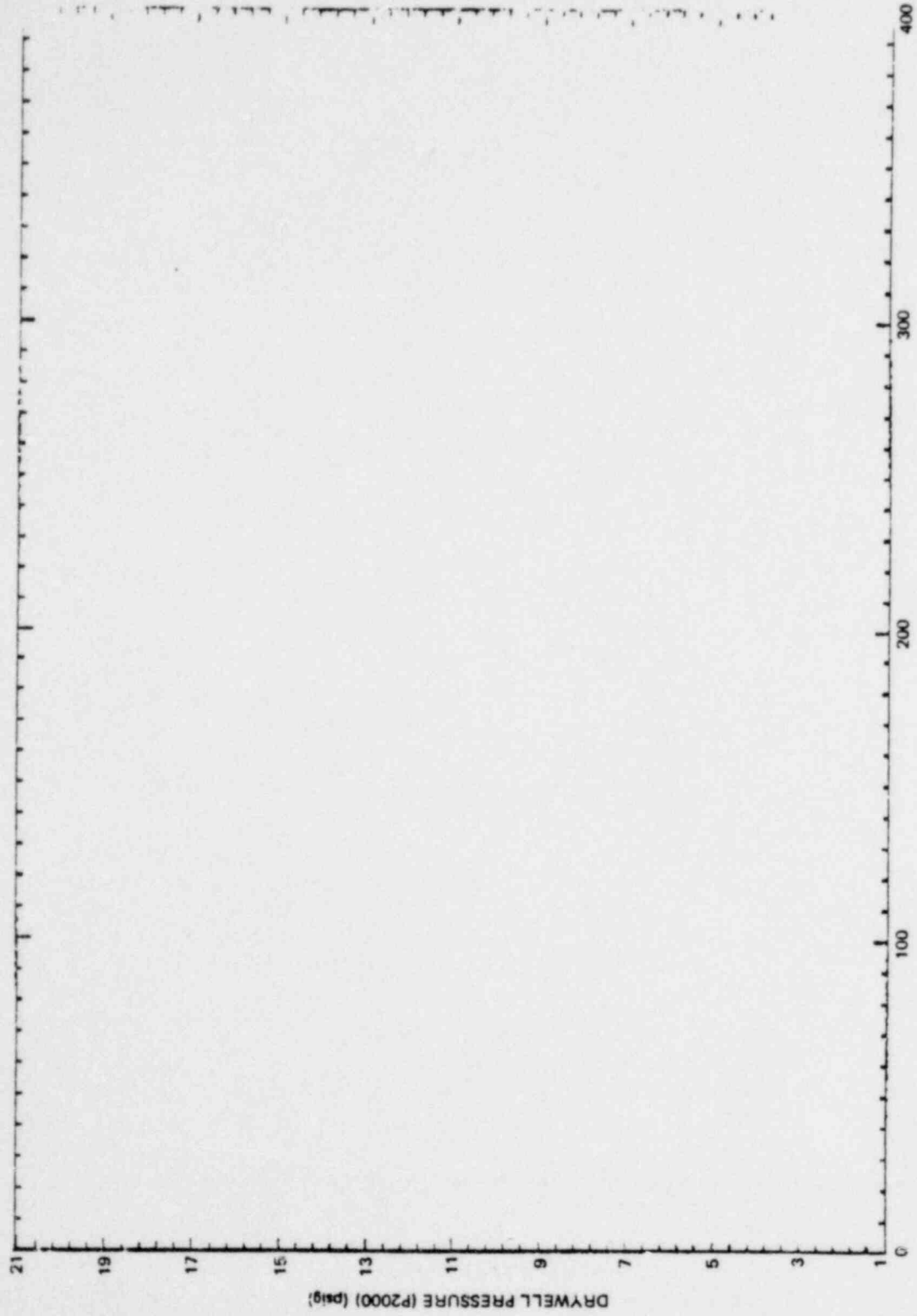

Figure C-18. V2 Pressure, Small Steam Break, M1

*Proprietary information deleted

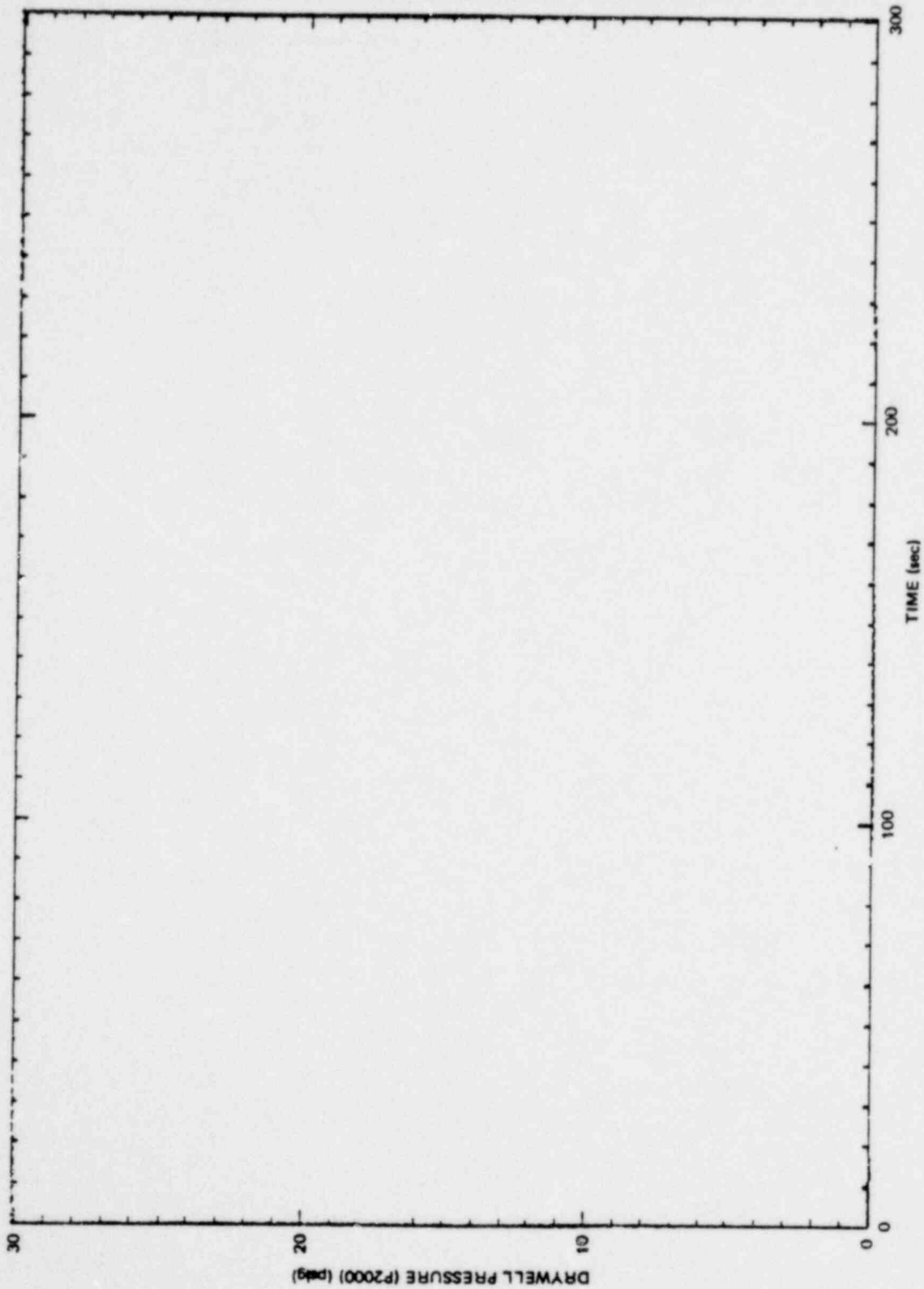

Figure C-19. V2 pressure, Small Liquid Break, M3

*Proprietary information deleted

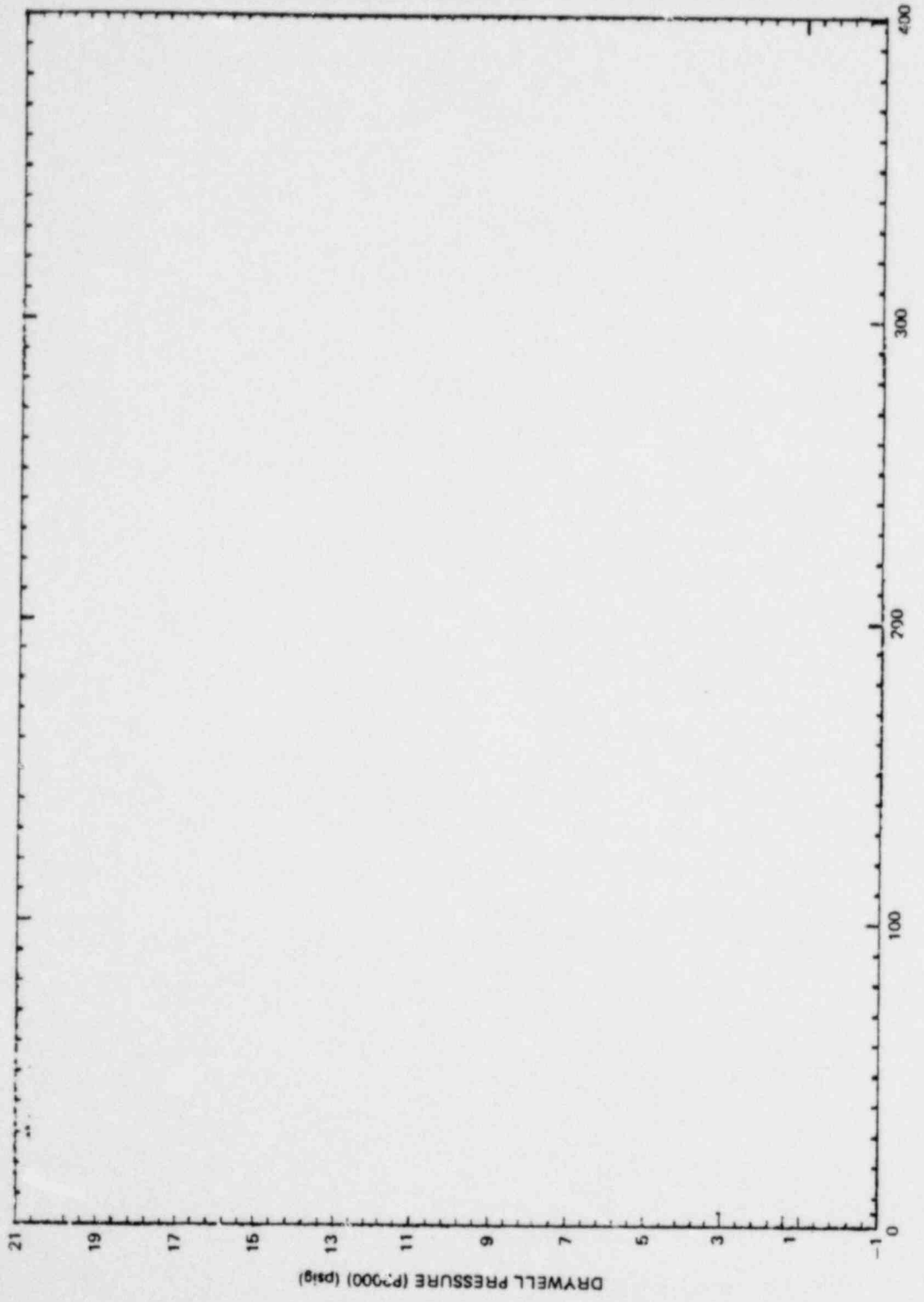

Figure C-20. V2 Pressure, Medium Steam Break, M2

*Proprietary information deleted

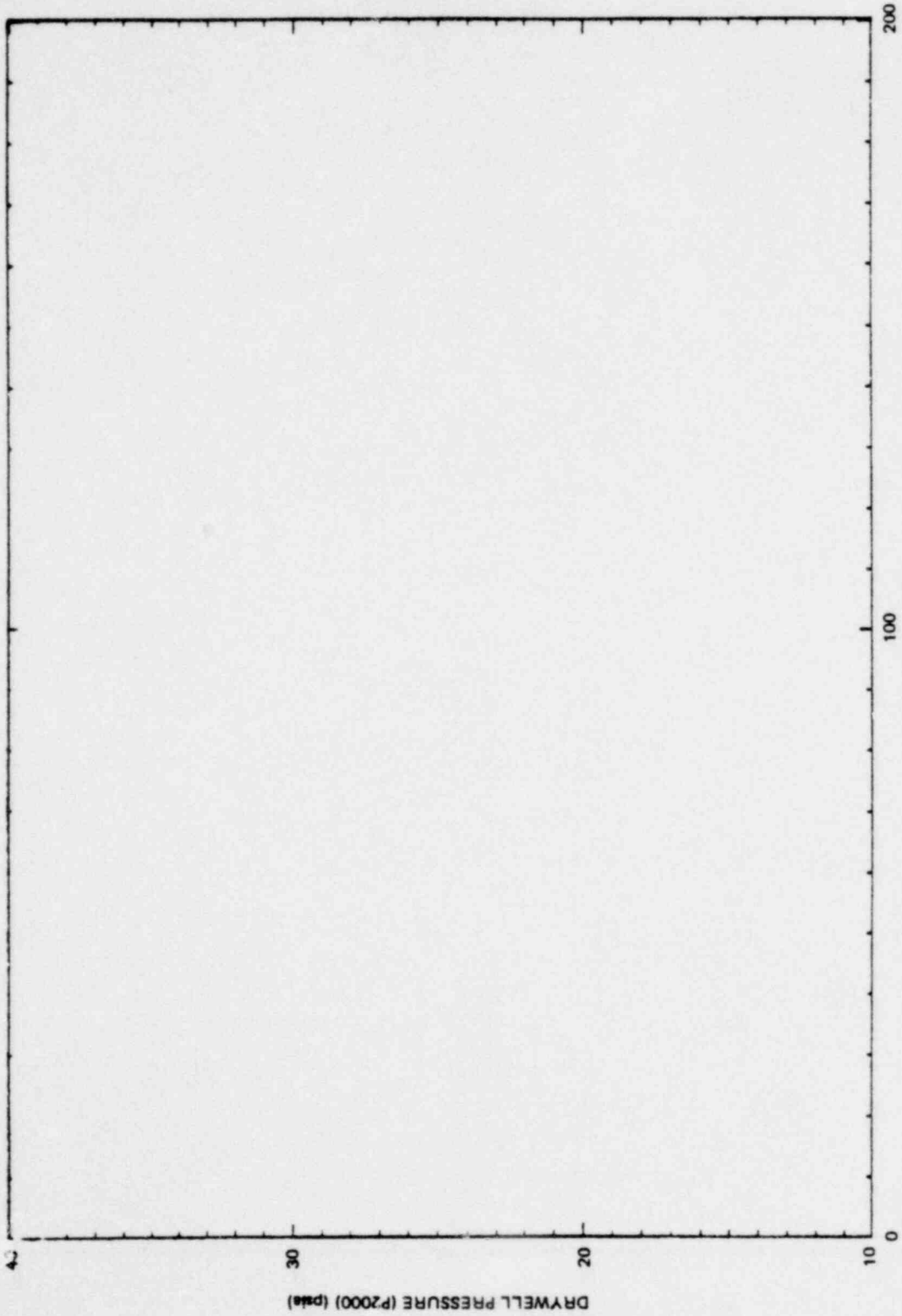

Figure C-21. V2 Pressure, Large Steam Break, M7

*Proprietary information deleted

1158 281

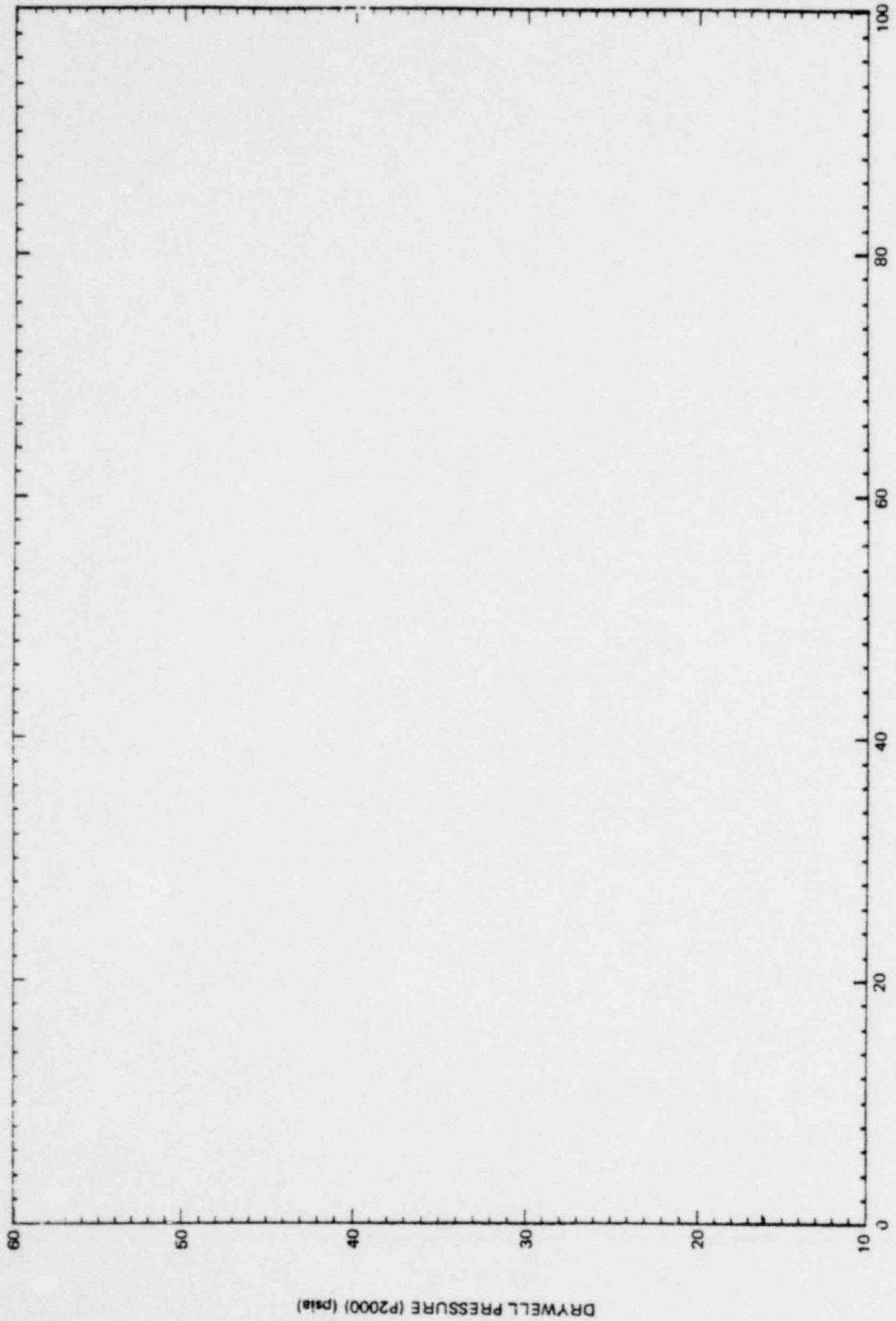

Figure C-22. V2 Pressure, Large Liquid Break, M8

*Proprietary information deleted

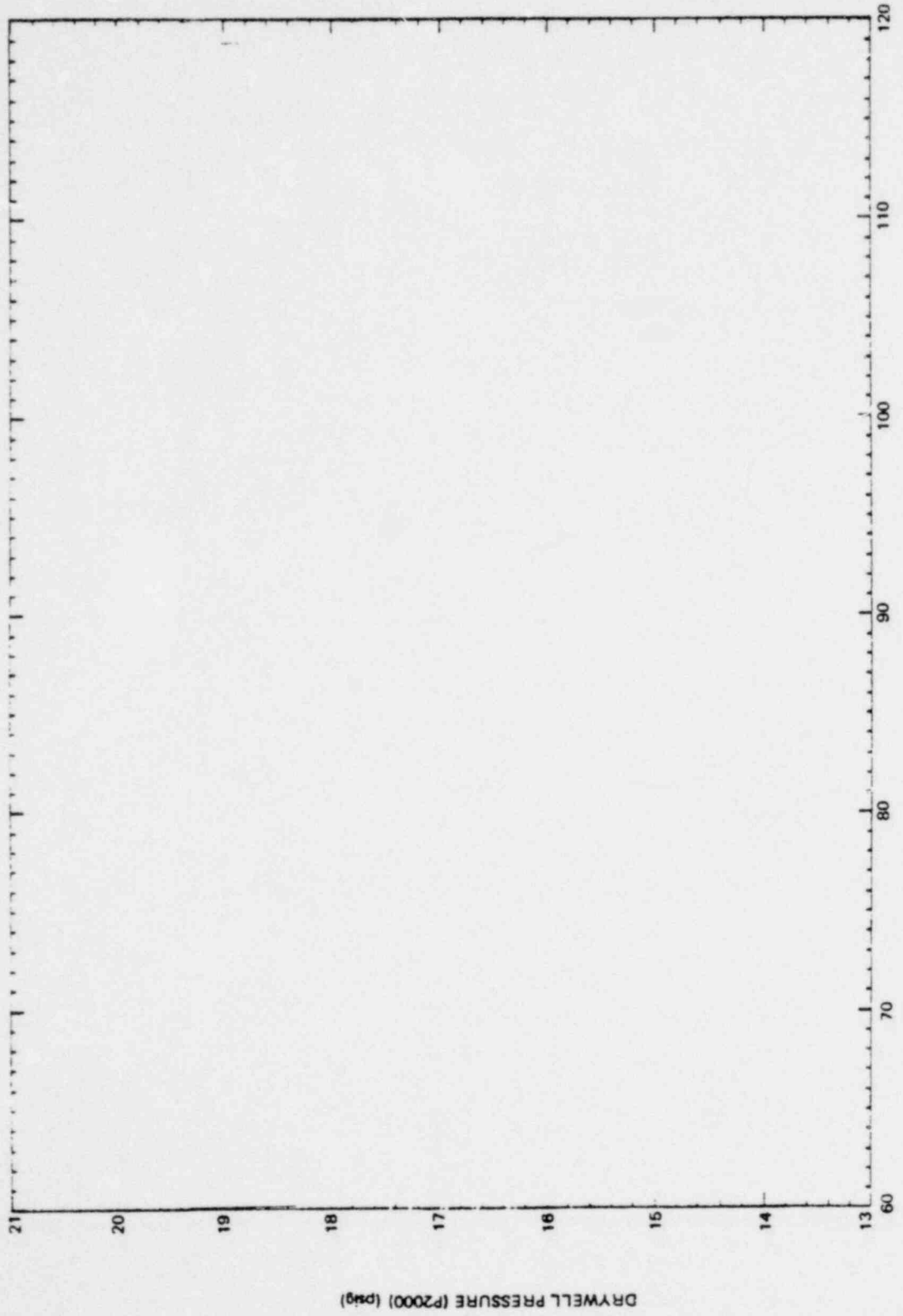

Figure C-23. Expanded Time V2 Pressure, Small Steam Break, M1

*Proprietary information deleted

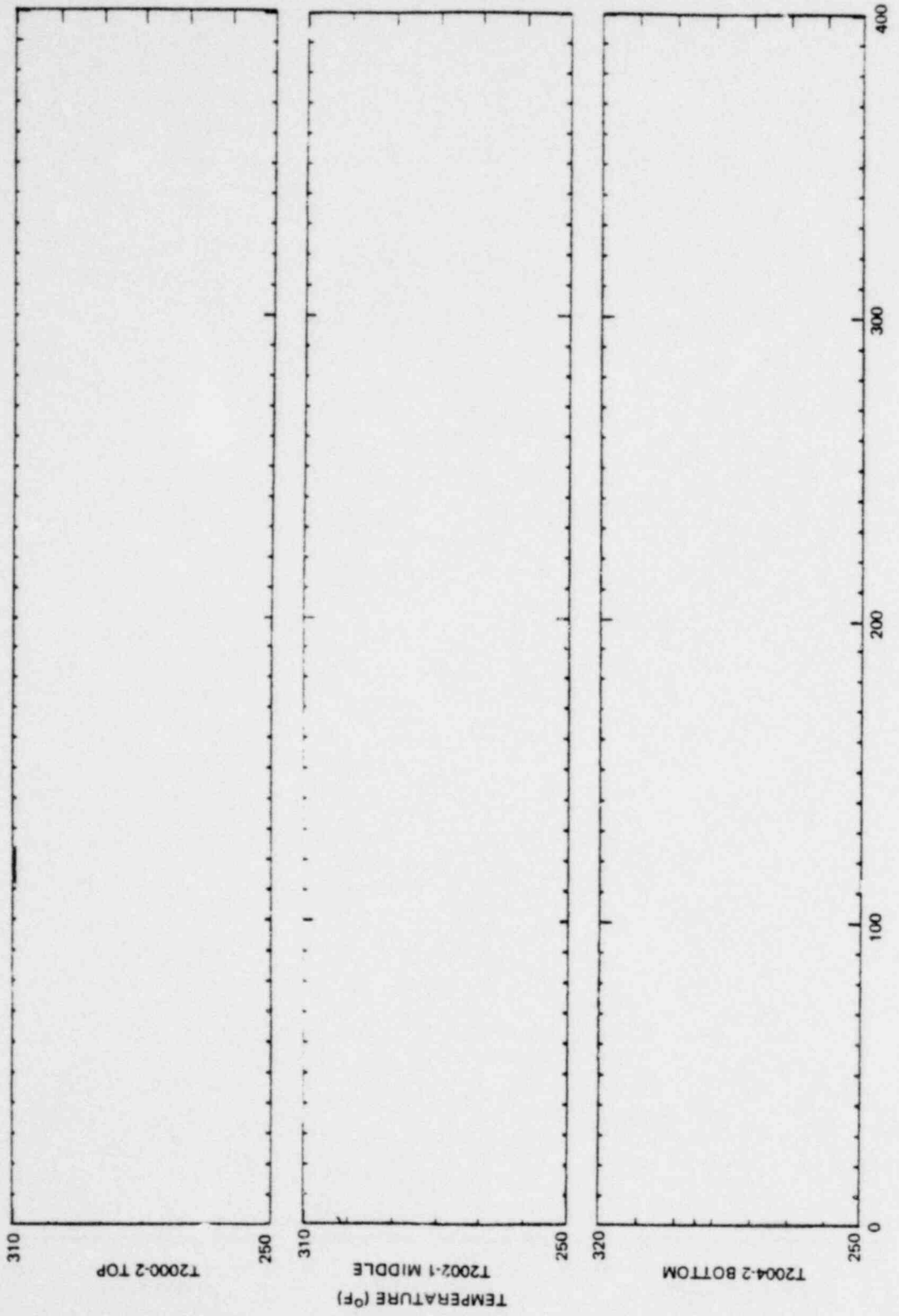

Figure C-24. Drywell Temperatures, Small Steam Break, M9

*Proprietary information deleted

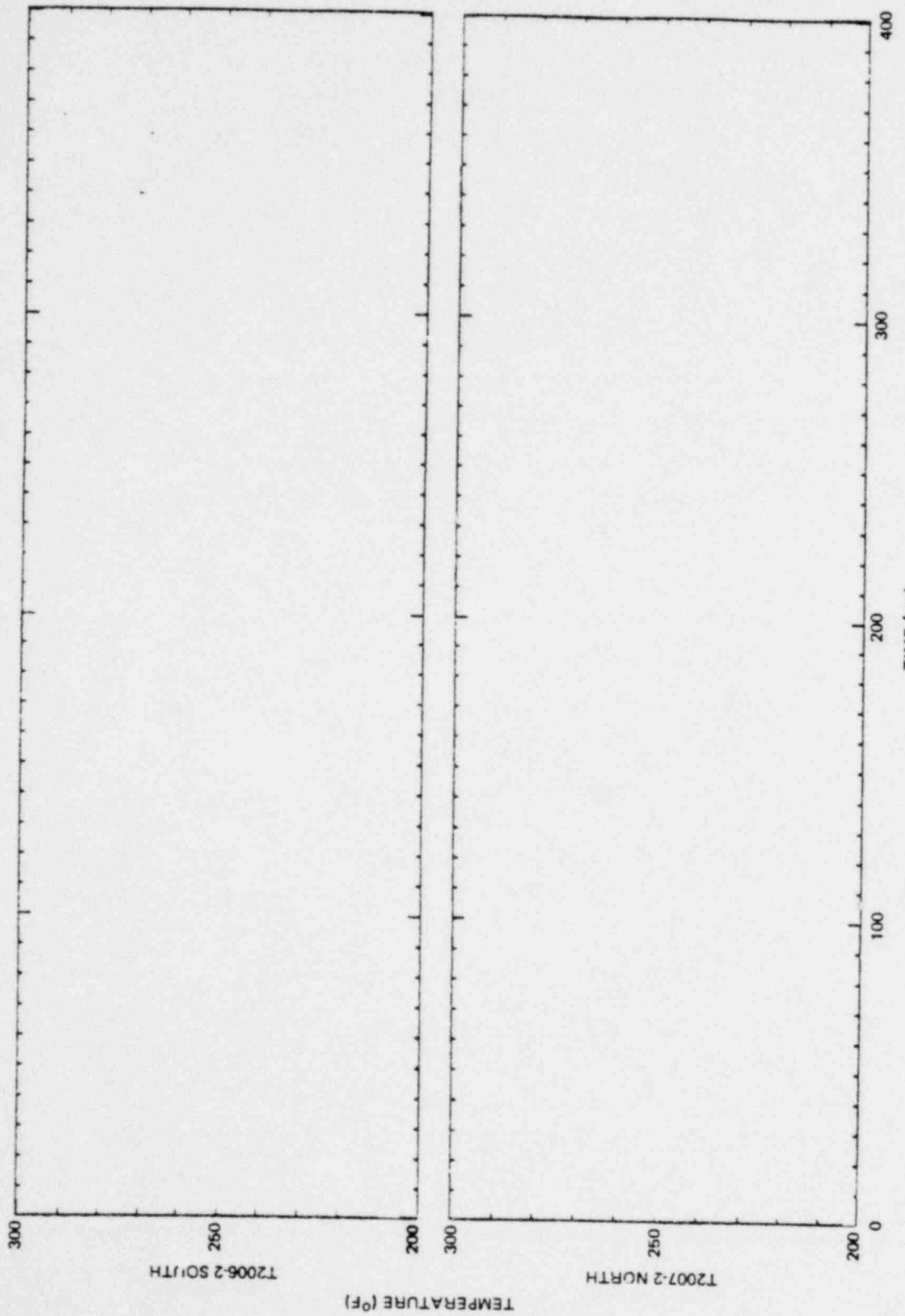

Figure C-25. Vent Line Temperatures, Small Steam Break, M9 *

*Proprietary information deleted

to some extent even for the small steam breaks. Figure C-9 shows that at about 60 seconds, which corresponds to the time at which the temperature traces begin to indicate superheat, liquid carryover was no longer occurring. After the liquid carryover ceased, the drywell contents begin to superheat, first at the top and middle temperature sensors then at the drywell bottom and vent line sensors. Figure C-26 shows the drywell temperature history for the medium steam break. Comparison of these temperature histories, which occurred using the large standpipe in the drywell, to those in Figure C-24, for the small steam break which used the small standpipe in the drywell, show that the temperature histories were similar using the two standpipes. Figure C-28 shows the drywell temperature histories for the large steam break test, M7. Compared to Figure C-27 which shows the medium steam break and also used the large standpipe, it can be seen that the top of the drywell superheated last, indicating that some change occurred in the drywell mixing characteristics for this test. This change was possibly caused by the holes added to the large standpipe in the drywell before test M7. Figure C-29 shows the large liquid break drywell temperature histories. These temperature characteristics were unaffected by the addition of holes in the large drywell standpipe. The drywell temperature for the large liquid break test remained at saturation temperature corresponding to the drywell pressure throughout the test similar to the small liquid break test, shown in Figure C-26.

3. Drywell liquid holdup - The bottom of the drywell was instrumented with a differential pressure transducer (D2000) to measure the drywell liquid holdup (accumulation). This instrumentation installation is shown on Figure 3.4-4. The differential pressure transducer was set up to measure the decrease in differential

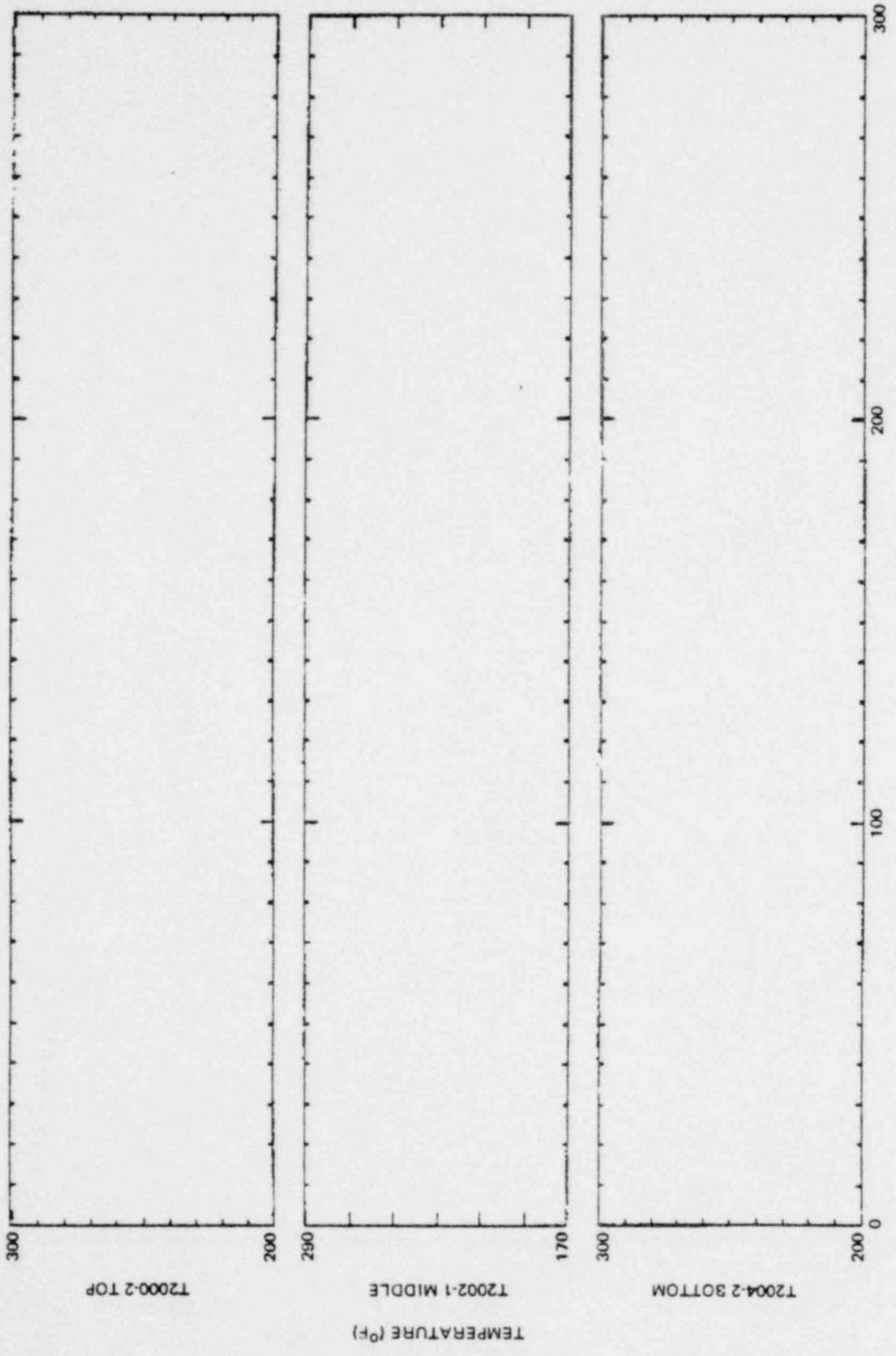

Figure C-26. Drywell Temperature, Small Liquid Break, M3

*Proprietary information deleted

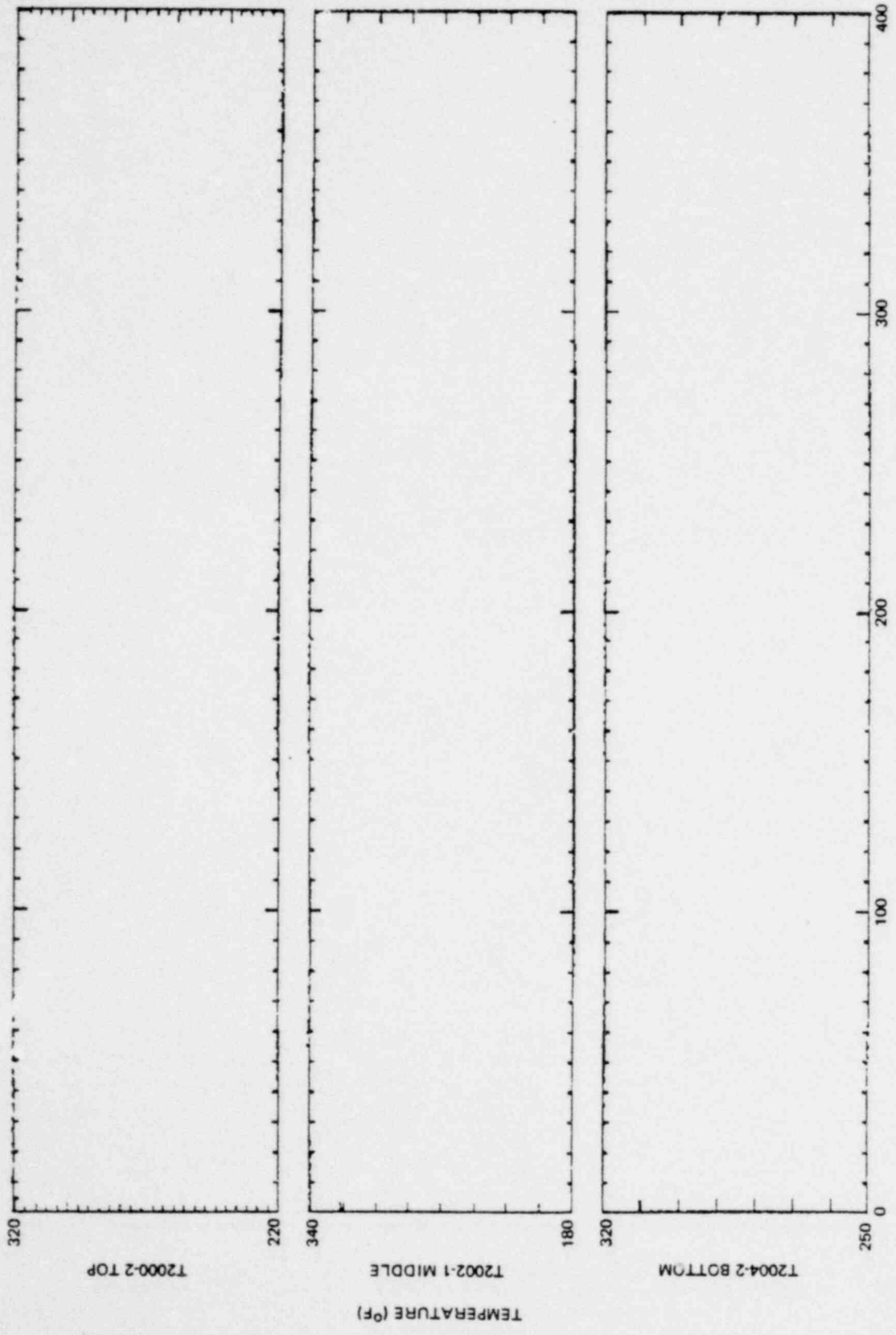

Figure C-27. Drywell Temperature, Medium Steam Break, M2

*Proprietary information deleted

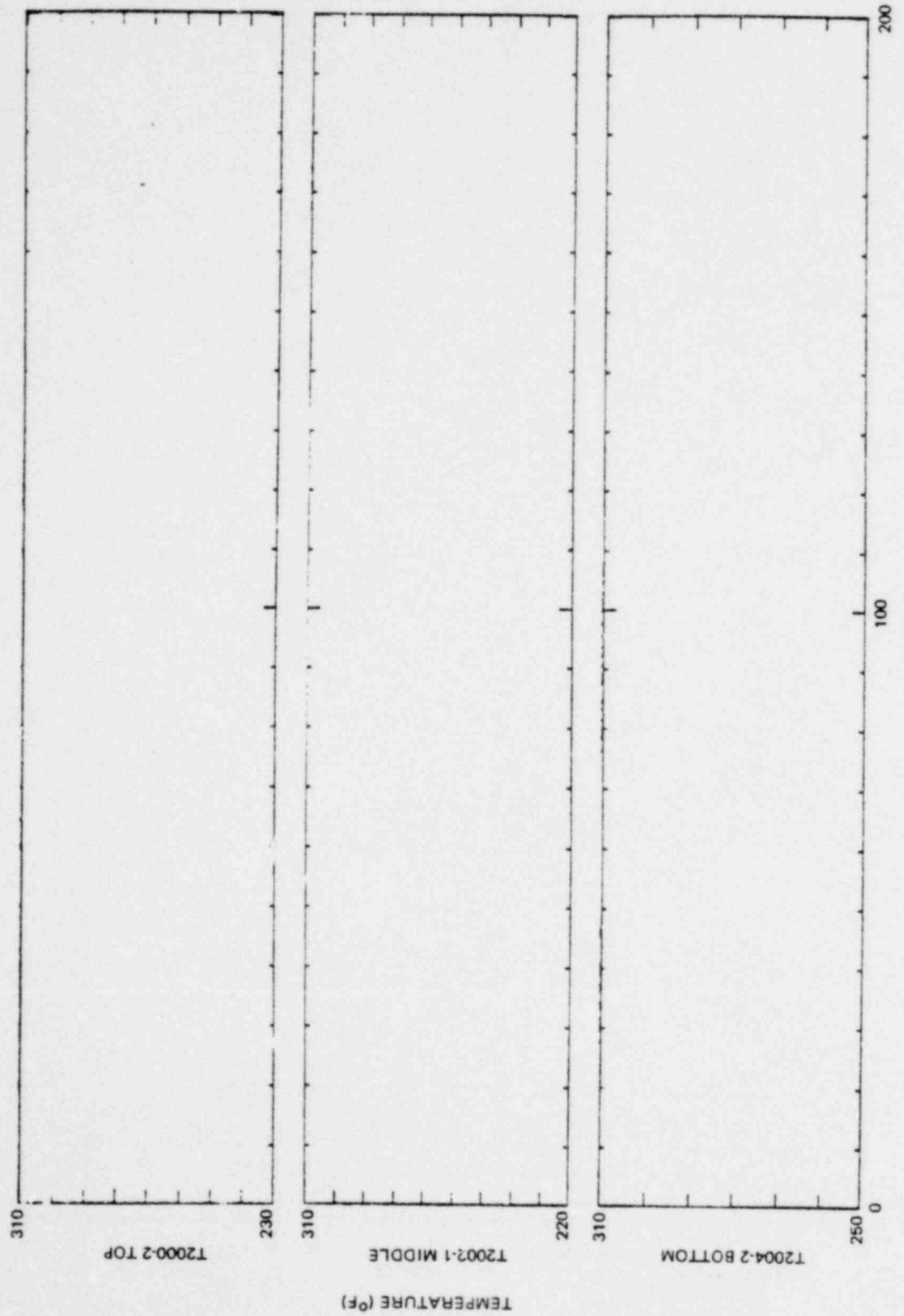

Figure C-28. Drywell Temperature, Large Steam Break, N7

*Proprietary information deleted

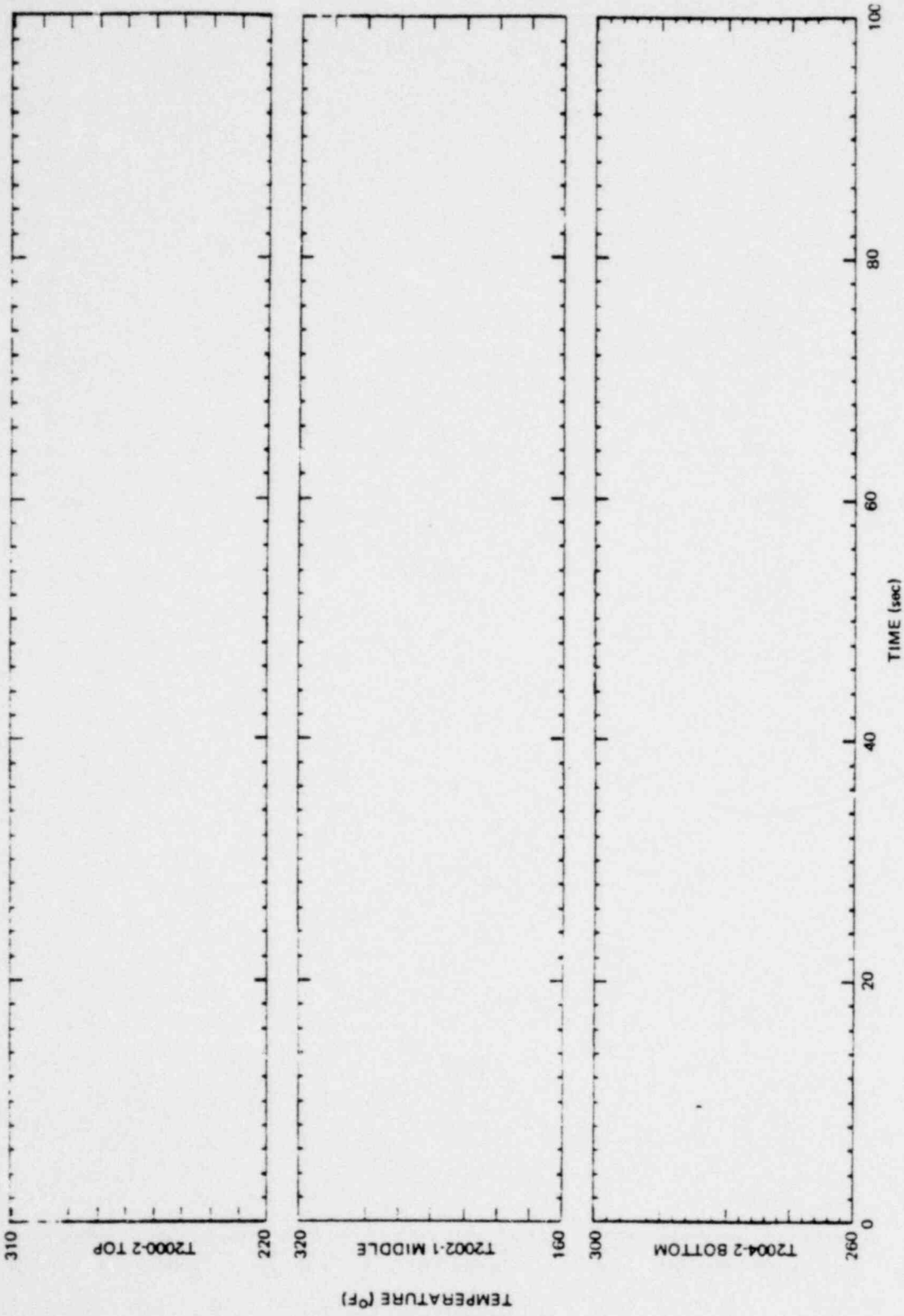

Figure C-29. Drywell Temperature, Large Liquid Break, M8

*Proprietary information deleted

pressure (compared to reference leg) as the liquid accumulated. Data taken during matrix tests M1 (shown on Figure C-30) and M3 (shown on Figure C-31) indicated that no measurable liquid accumulated during these blowdowns. After it had been observed that no liquid had accumulated in the drywell for matrix test M3 (small liquid break, which was most likely to have liquid holdup because of high liquid fraction and low velocity condition), this measurement was discontinued for subsequent tests.

4. Vent air content - Each vent line had an air sampling system installed at the locations shown on Figure 3.4-4. Five samples were taken during the test from each vent line at the specified time periods. Samples 1 to 5 were taken on the South vent line and samples 6 to 10 were taken on the North vent line. Table C-2 shows the sample initiation times and corresponding sample duration times for each of the tests. Figure C-32 compares the small, medium, and large steam breaks. Figure C-33 compares the small and large liquid breaks. It can be seen that increasing break size decreases the air content more quickly. However, both the large steam and large liquid data, after decreasing more rapidly at test initiation, hold a fairly constant value for the rest of the blowdown. This may have been a result of the holes added to the large standpipe in the drywell for these tests. Figure C-34 compares data from all the small steam breaks for which data was available. This shows that all the small steam break tests had similar air clearing characteristics.

5. Vent line flowrate - The vent lines which connect the drywell to the wetwell are described in paragraph 3.2-4 and are shown in Figure 3.2-4. Each vent line had an Annubar flow measuring device installed at the location shwon in Figure 3.4-4. Figures C-35 to -40 show vent line flow information for tests M1 (south

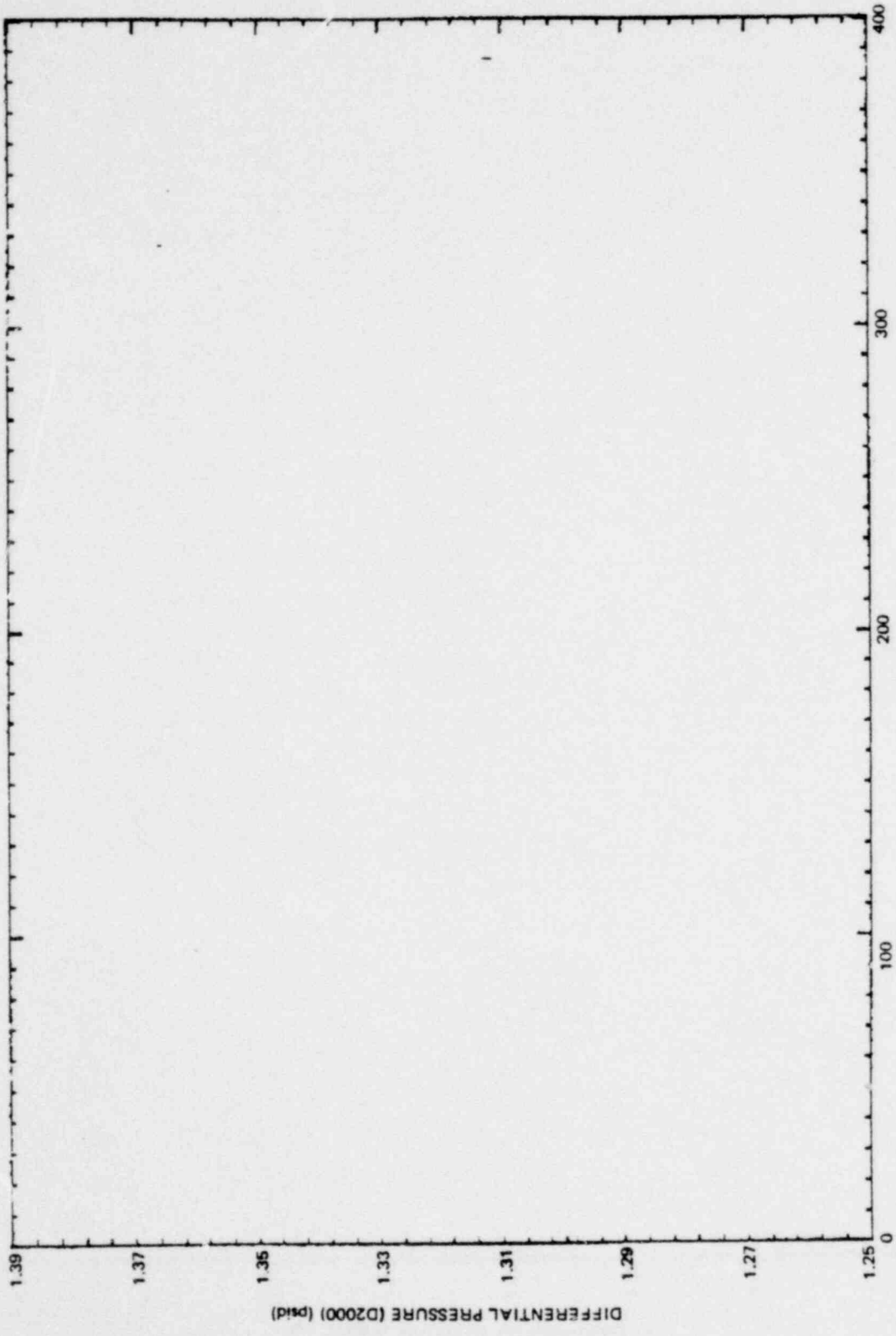

Figure C-30. Drywell Liquid Holdup, Small Steam Break, M1

*Proprietary information deleted

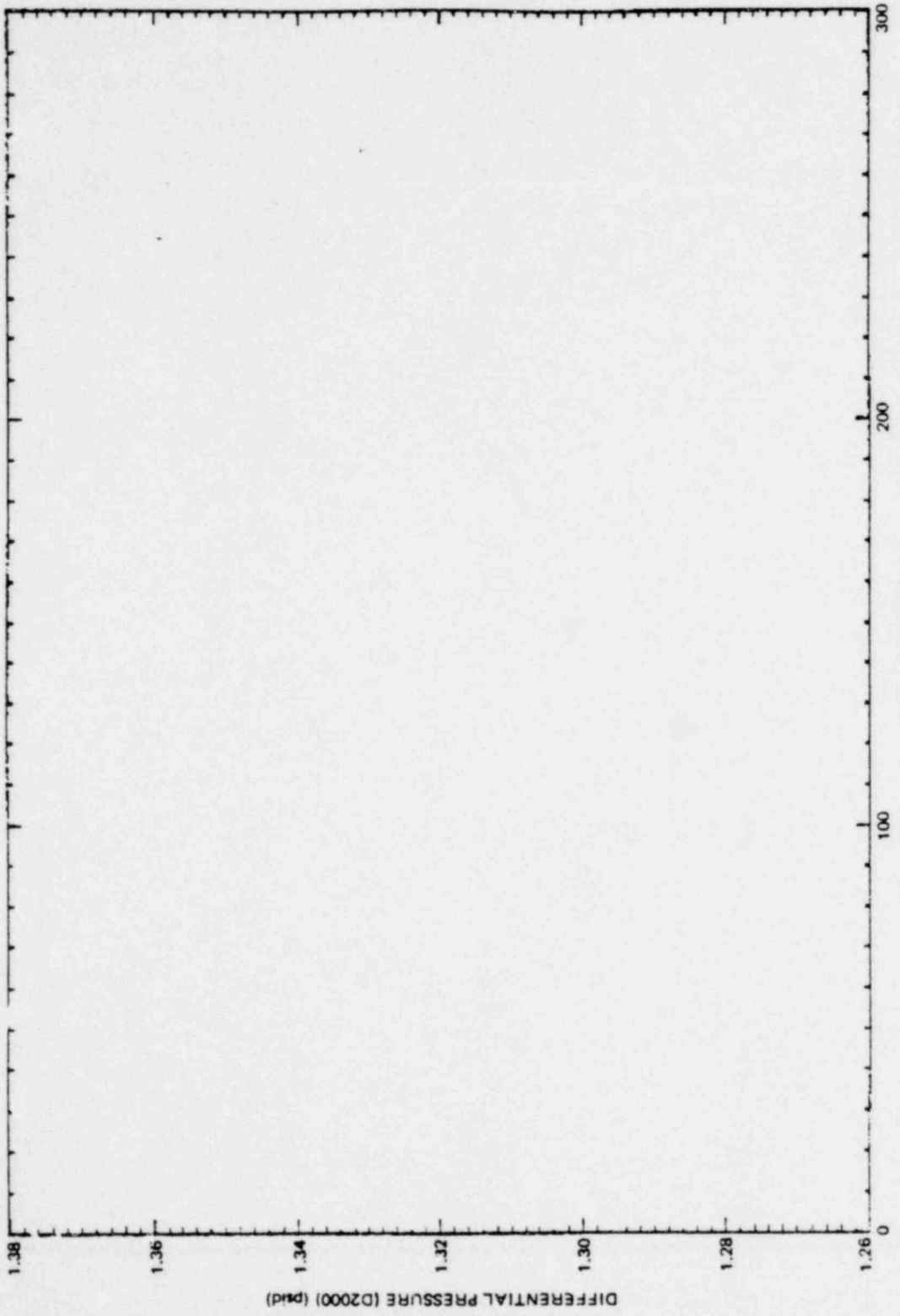

Figure C-31. Drywell Liquid Holdup, Small Liquid Break, M3

*Proprietary information deleted

1158 293

Table C-2

AIR SAMPLE TIMES

Test No.	Initiation Times (sec)	Sample Duration Times (sec)
M1	1, 8, 100, 300, 500	4, 5, 10, 10, 10
M2	1, 5, 30, 65, 100	4, 5, 10, 10, 10
M3	1, 8, 50, 100, 200	4, 5, 10, 10, 10
M4*	1, 8, 50, 100, 250	4, 5, 10, 10, 10
M5*	1, 8, 50, 100, 250	4, 5, 10, 10, 10
M6*	1, 8, 50, 100, 250	4, 5, 10, 10, 10
M9	1, 8, 50, 100, 250	4, 5, 10, 10, 10
M10	1, 8, 50, 100, 250	4, 5, 10, 10, 10
M7	1, 5, 30, 65, 100	4, 5, 10, 10, 10
M8	1, 5, 10, 20, 35	4, 5, 10, 10, 10

* System failed to operate, no data.

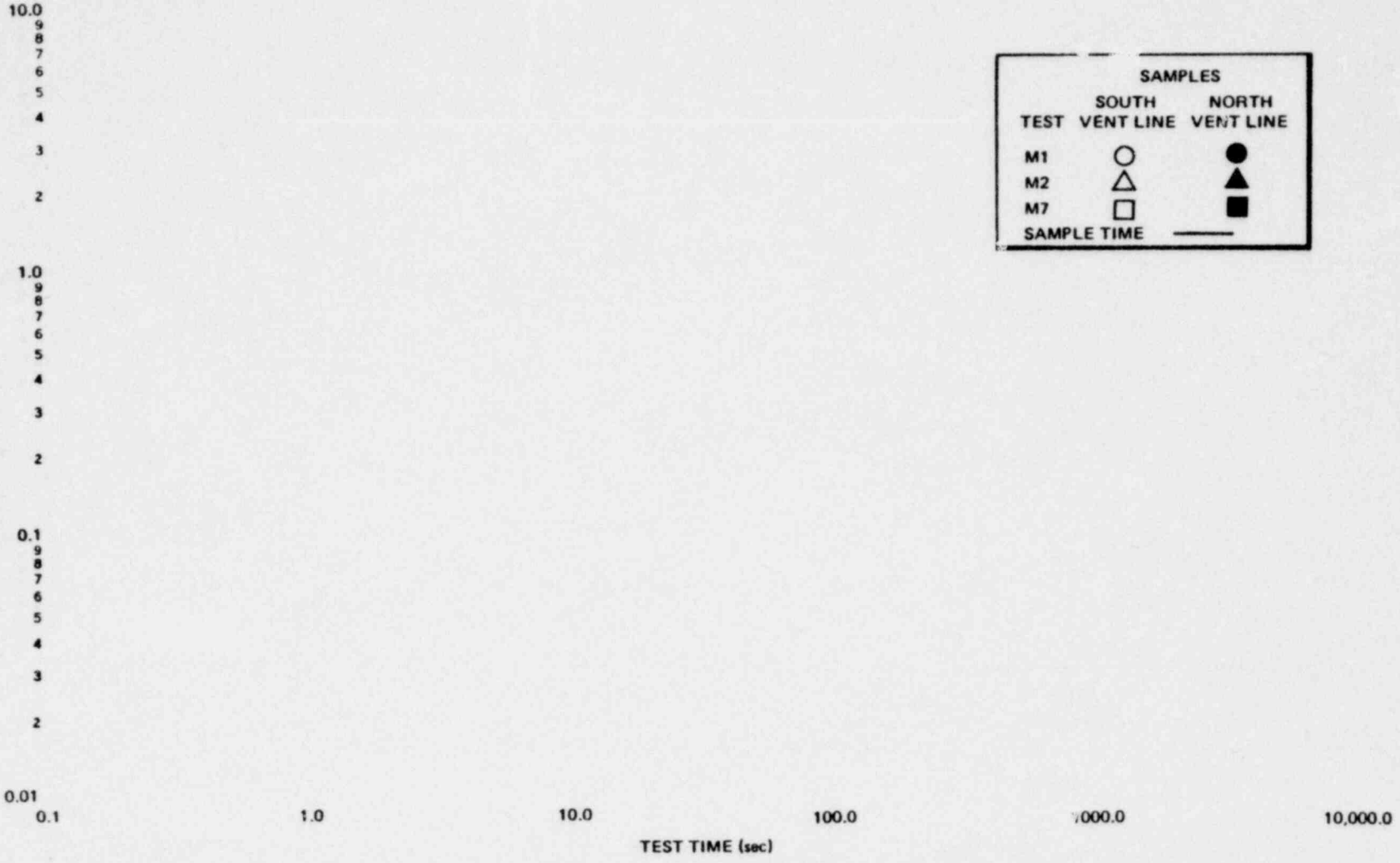

Figure C-32. Vent Line Air Content, Steam Breaks, M1, M2, M7

*Proprietary information deleted

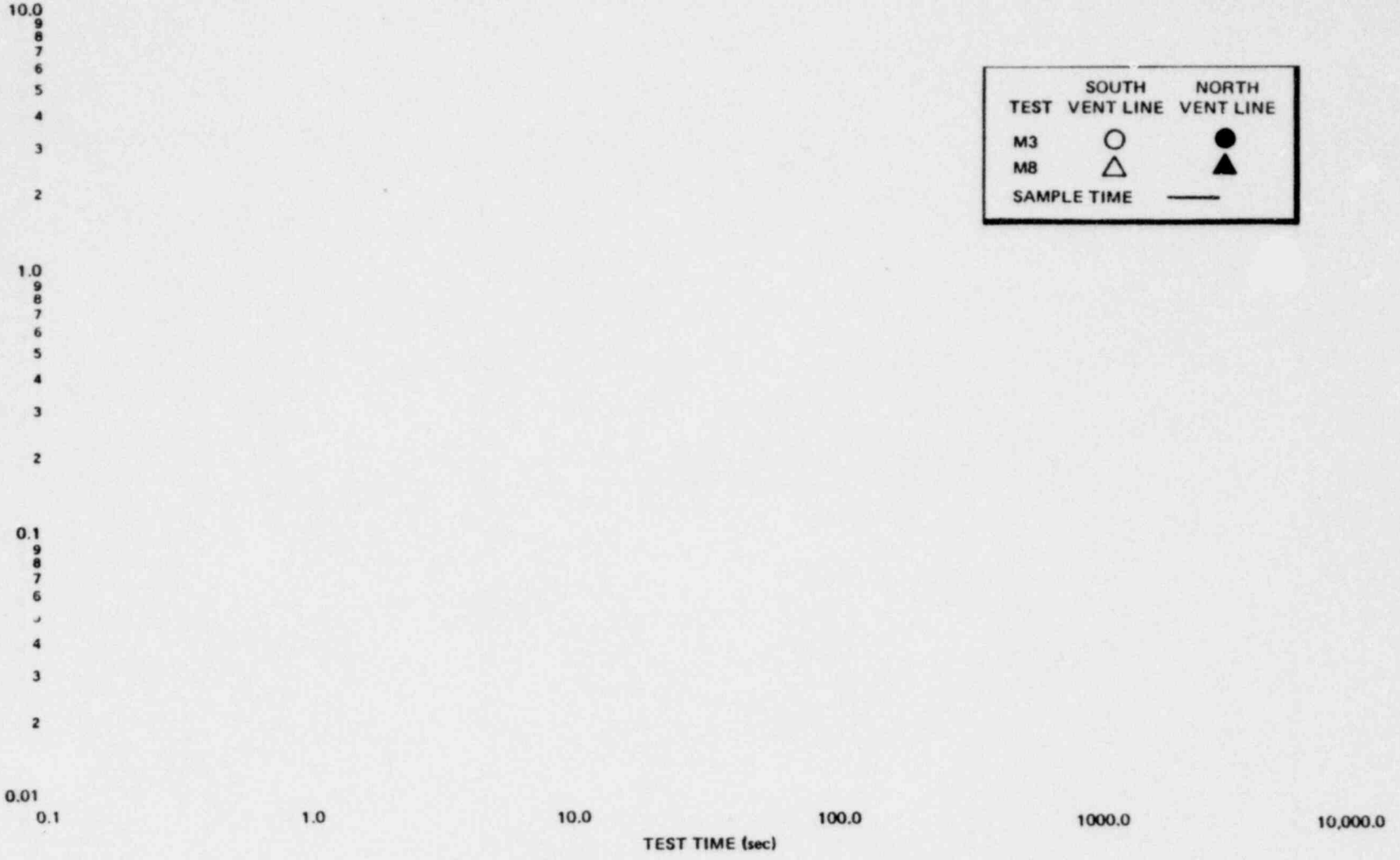

Figure C-33. Vent Line Air Content, Liquid Breaks, M3, M8

*Proprietary information deleted

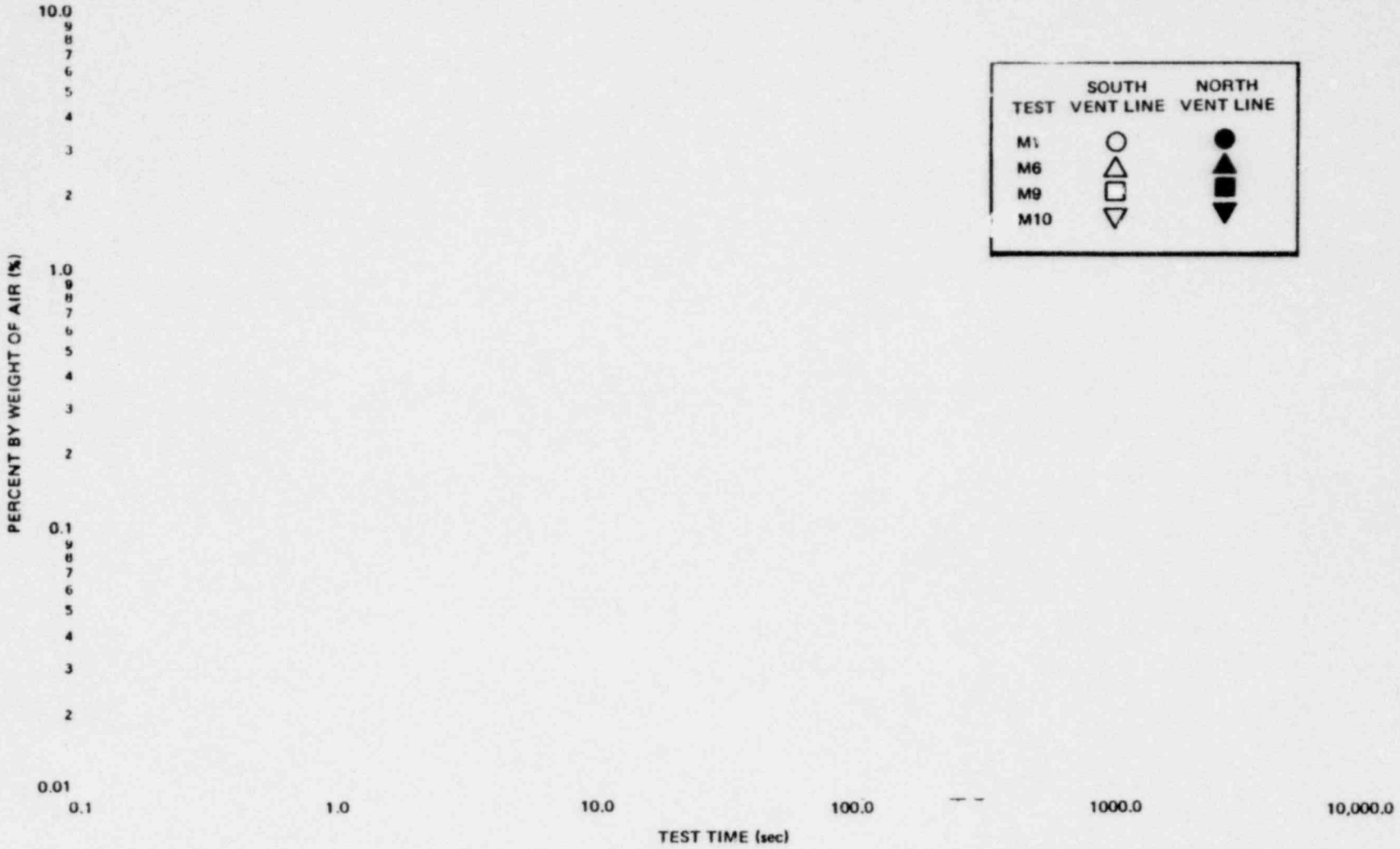

Figure C-34. Comparison of Vent Line Air Content, Small Steam Break

*Proprietary information deleted

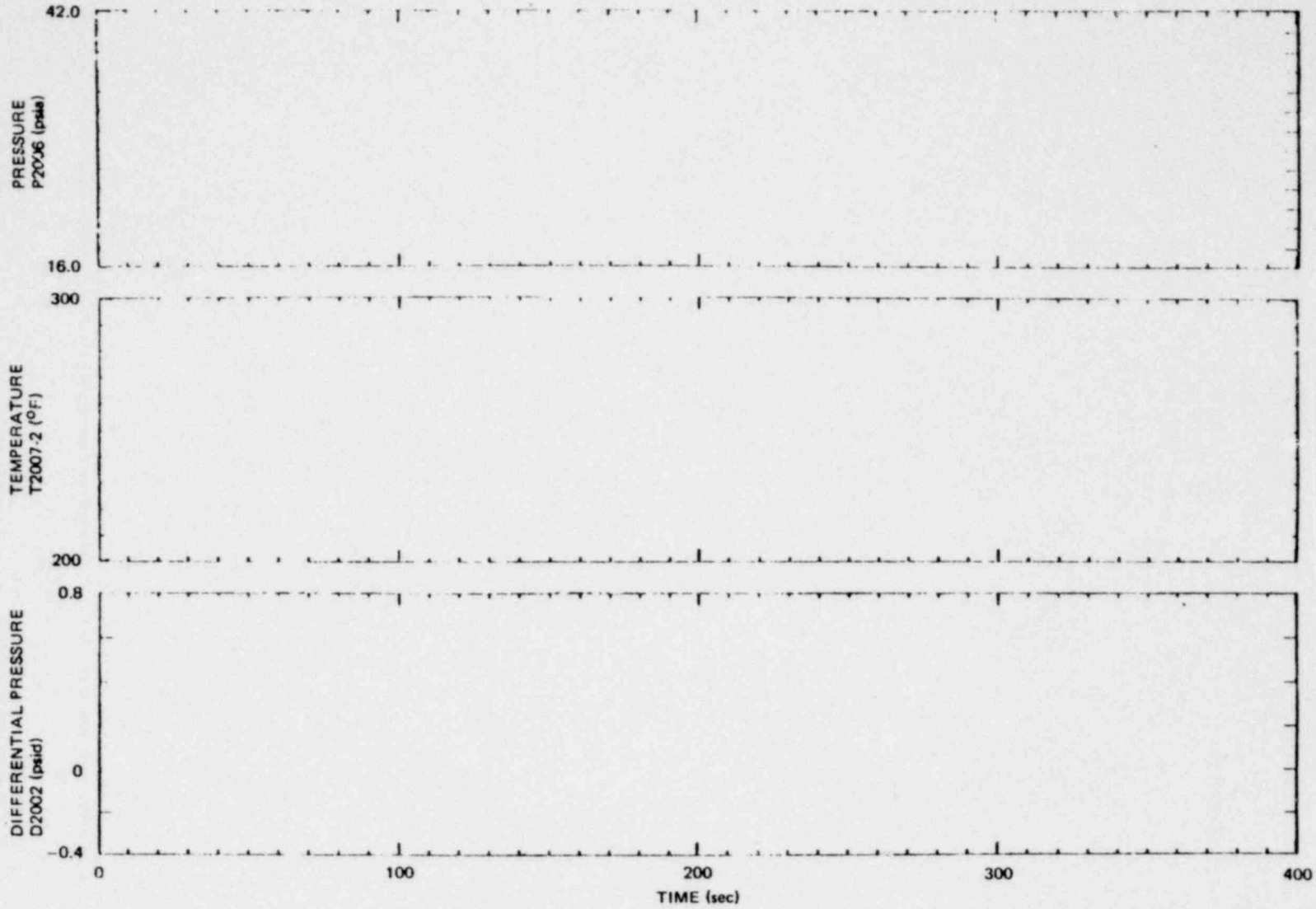

Figure C-35. South Vent Line Parameters, Small Steam Break, M1

*Proprietary information deleted

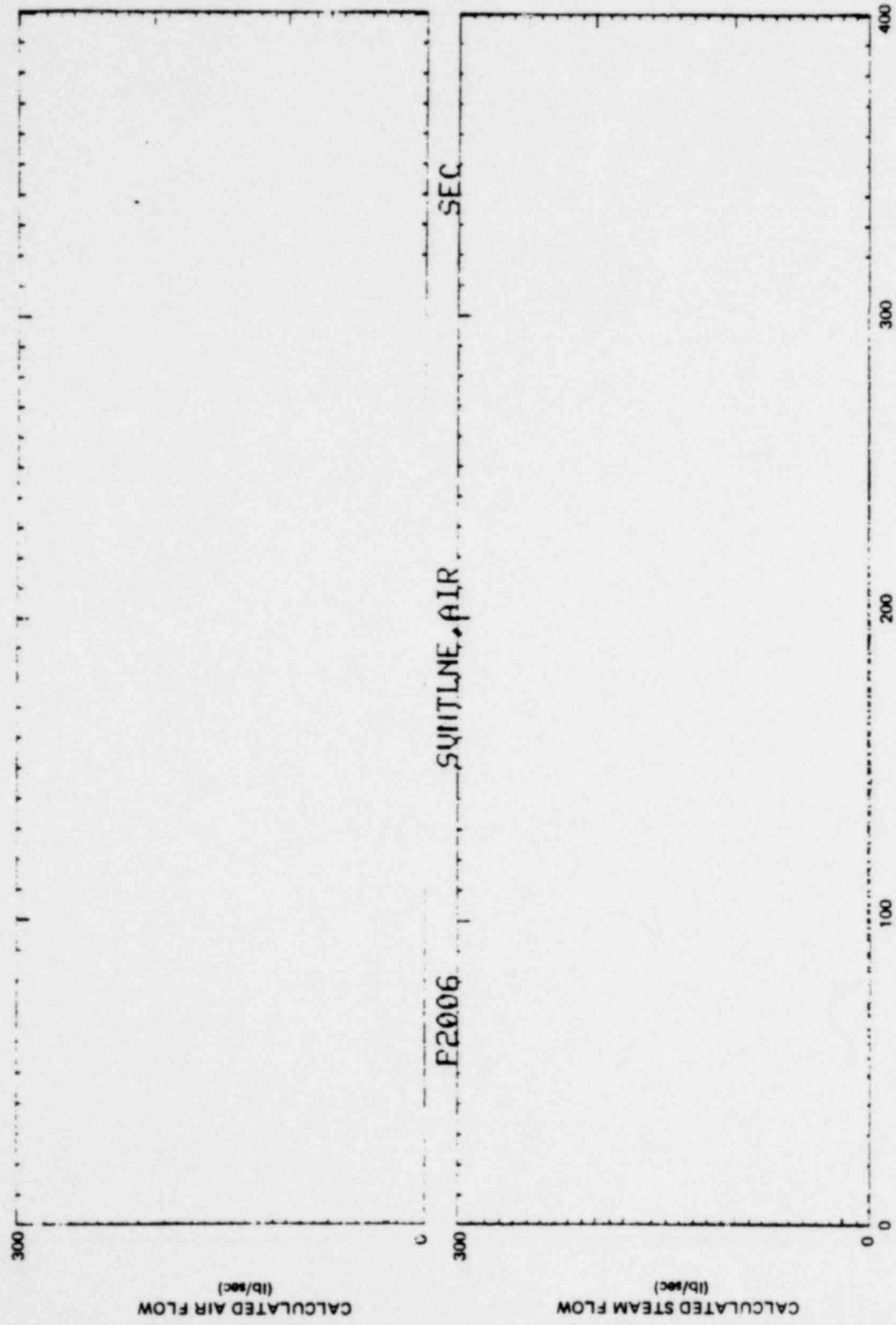

Figure C-36. South Vent Line Flow, Small Steam Break, M1

*Proprietary information deleted

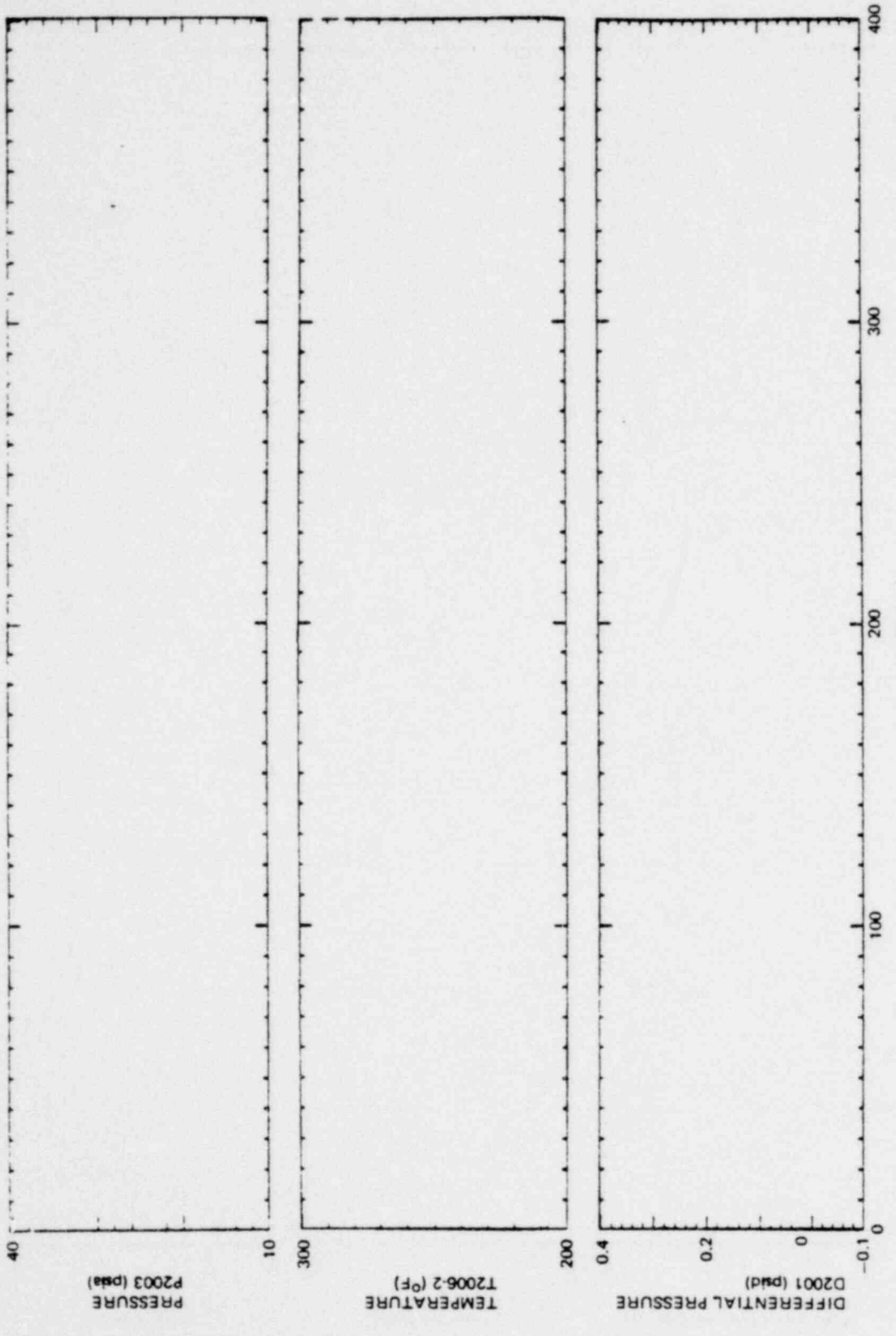

Figure C-37. North Vent Line Parameters, Small Steam Break, M9

*Proprietary information deleted

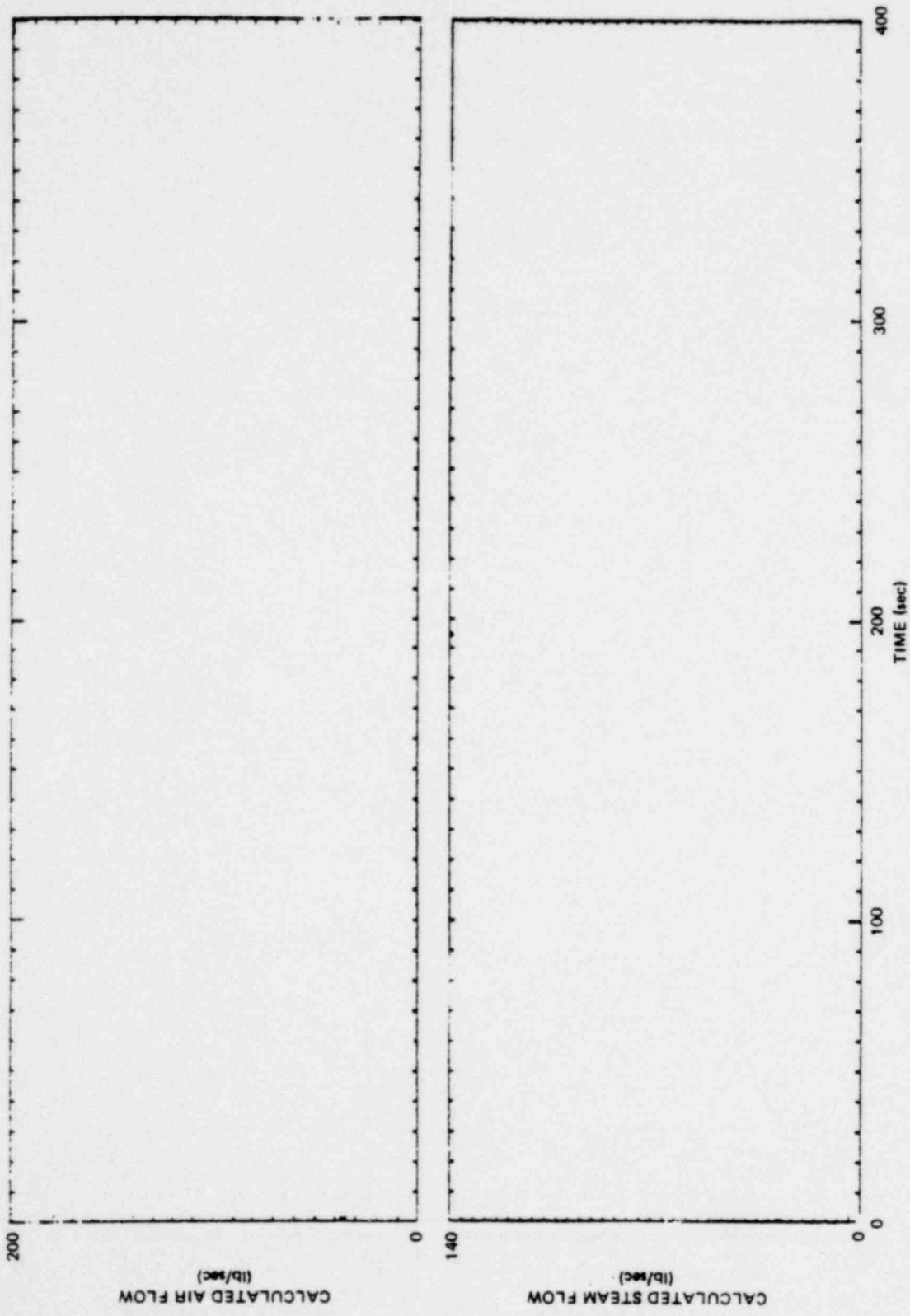

Figure C-38. North Vent Line Flow, Small Steam Break, M9

*Proprietary information deleted

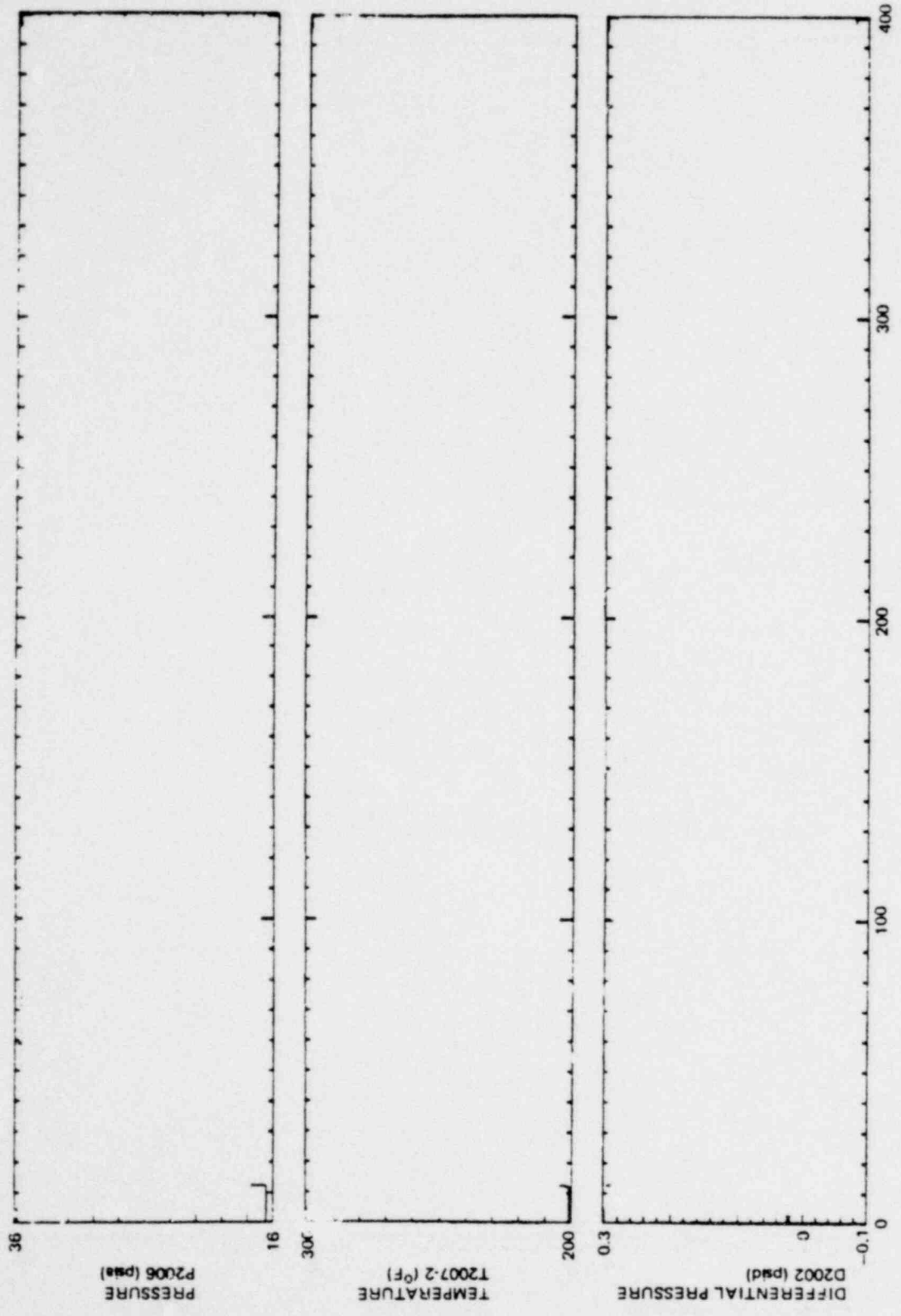

Figure C-39. South Vent Line Parameters, Small Steam Break, M9

*Proprietary information deleted

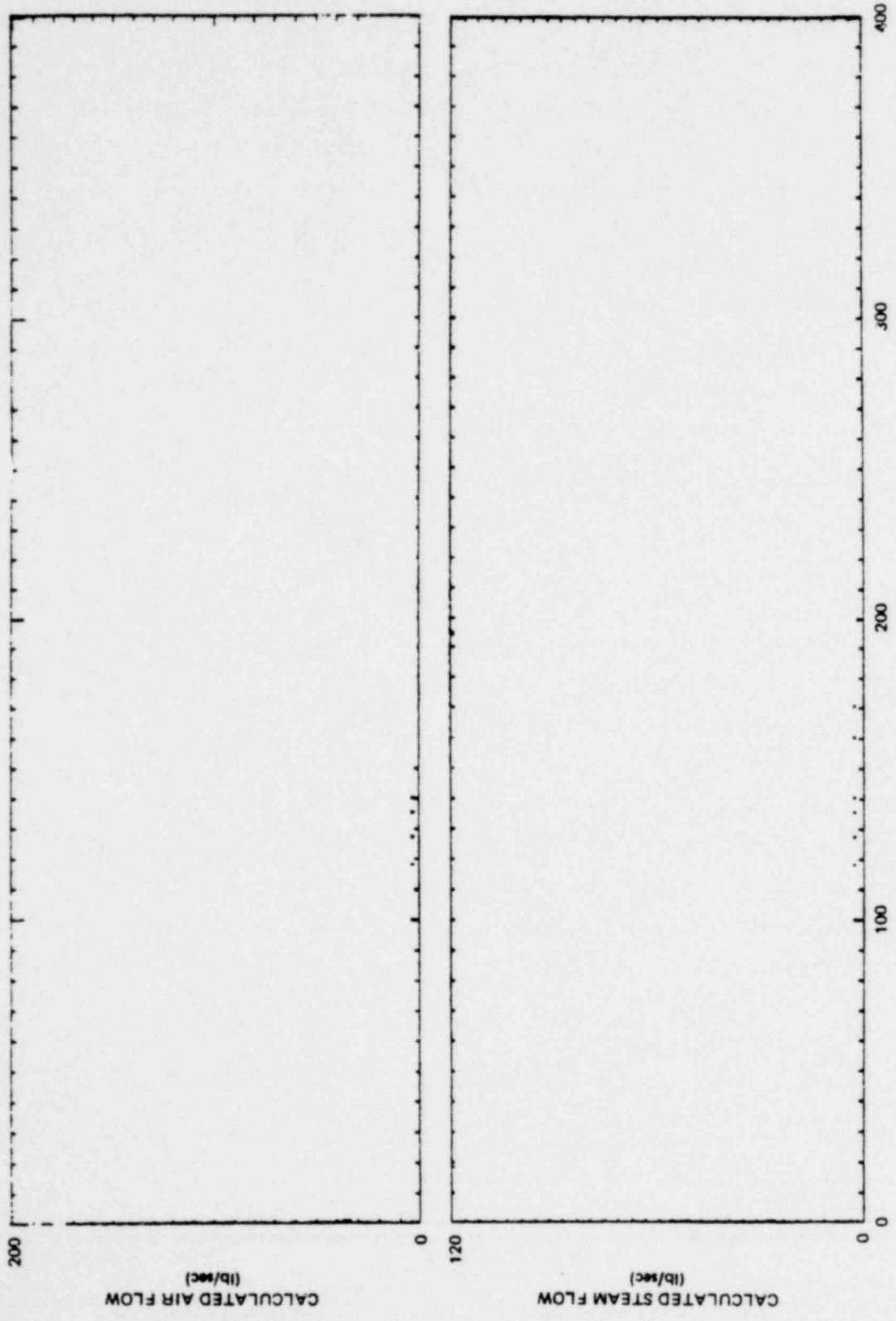

Figure C-40. South Vent Line Flow, Small Steam Break, M9

*Proprietary information deleted

vent line only) and M9 (small steam breaks). For each vent line, the pressure, temperature and differential pressure is shown along with the calculated flowrates assuming either air or steam to be the fluid. By comparing the flowrates on Figures C-36 and -40, it can be seen that the flows were similar from test to test with the small steam break. By comparing the flowrates in Figures C-38 and -40, it can be seen that the flows are similar in both vent lines for the small steam breaks. Figures C-41 to -44 show vent line flows for test M2 (medium steam break) and Figures C-45 to -48 show vent line flows for test M7 (large steam break). As would be expected the vent line flowrates increase as the break size increases.

Figures C-49 to 52 show the vent line flows for test M6 which had elevated initial pool temperature (120°F) and reduced submergence (18 inches). For these initial conditions only, it was observed that the vent line flowrate appeared to increase after approximately 100 seconds, as shown in Figure C-50.

Figures C-53 and -54 show expanded time plots of the vent line flowrates for test M9. Figure C-53 shows North and South vent line steam flows from 50 to 55 seconds which was during condensation oscillation. By closely comparing the two flows it can be seen that they fluctuate in phase. Figure C-54 shows the North and South vent line steam flowrates from 255 to 260 second which was during chugging. Comparison of these flows show that they are not in phase.

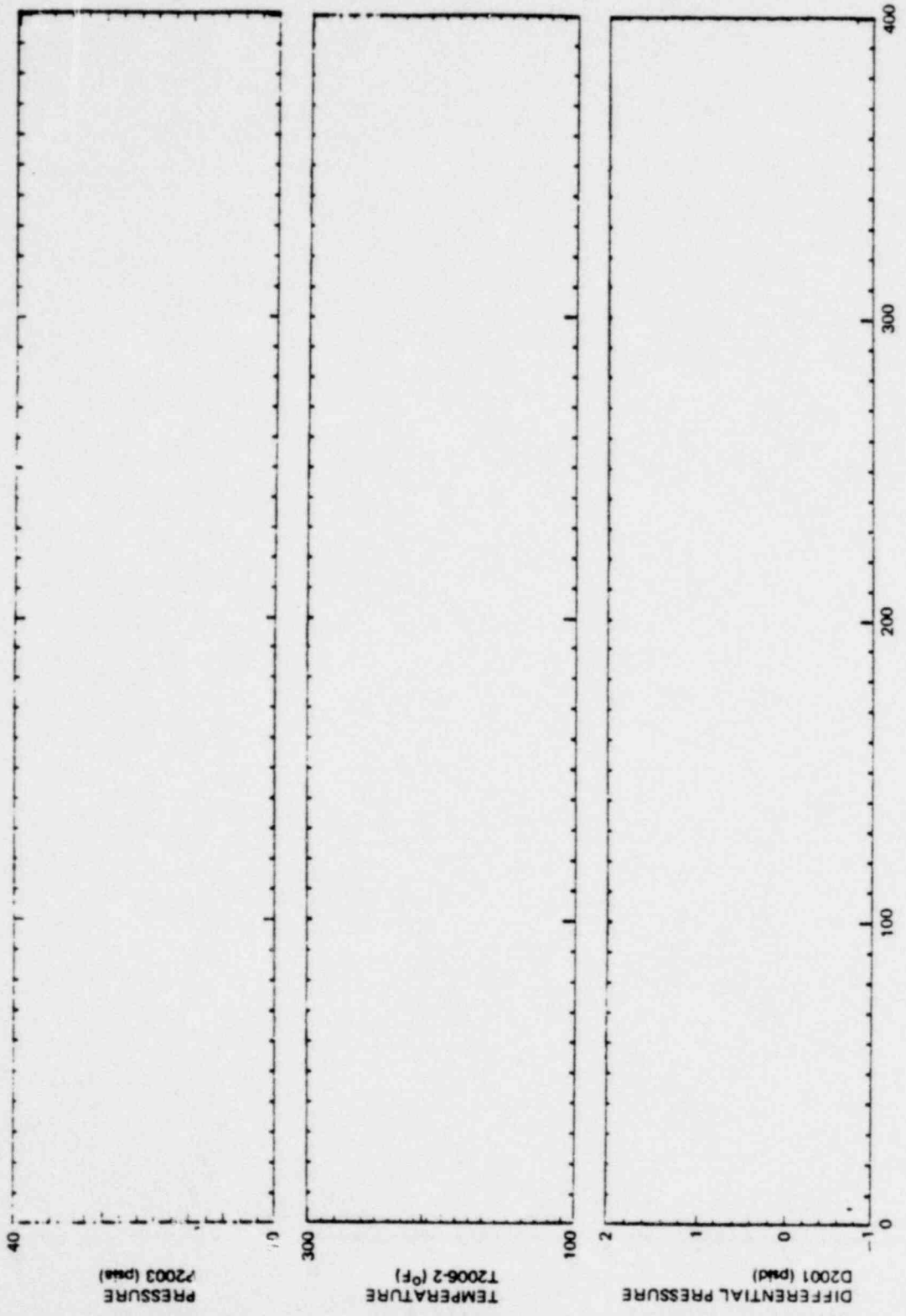

Figure C-41. North Vent Line Parameters, Medium Steam Break, M2

*Proprietary information deleted

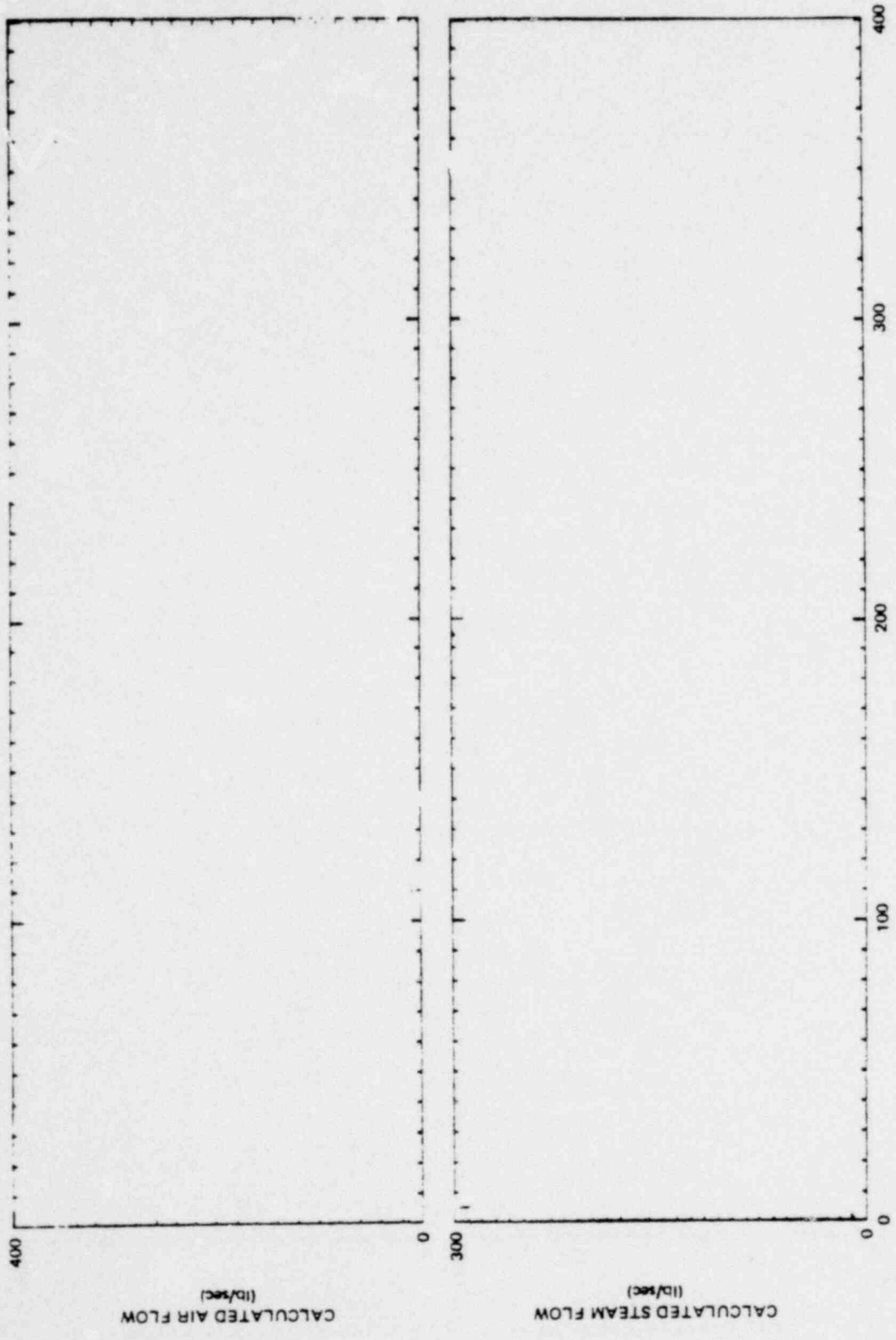

Figure C-42. North Vent Line Flow, Medium Steam Break, M2

*Proprietary information deleted

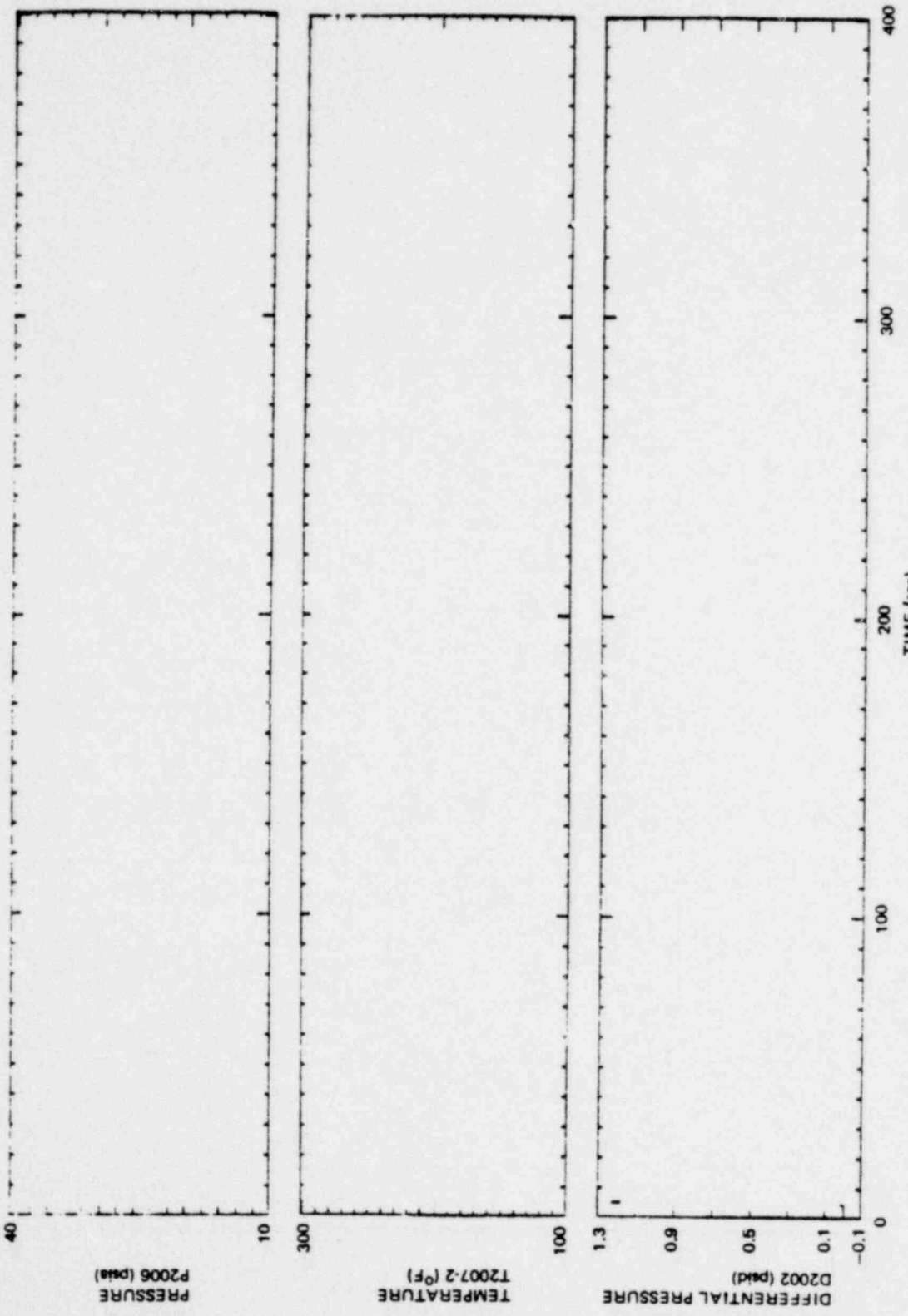

Figure C-43. South Vent Line Parameters, Medium Steam Break, M2

*Proprietary information deleted

Figure C-44. South Vent Line Flow, Medium Steam Break, M2

*Proprietary information deleted

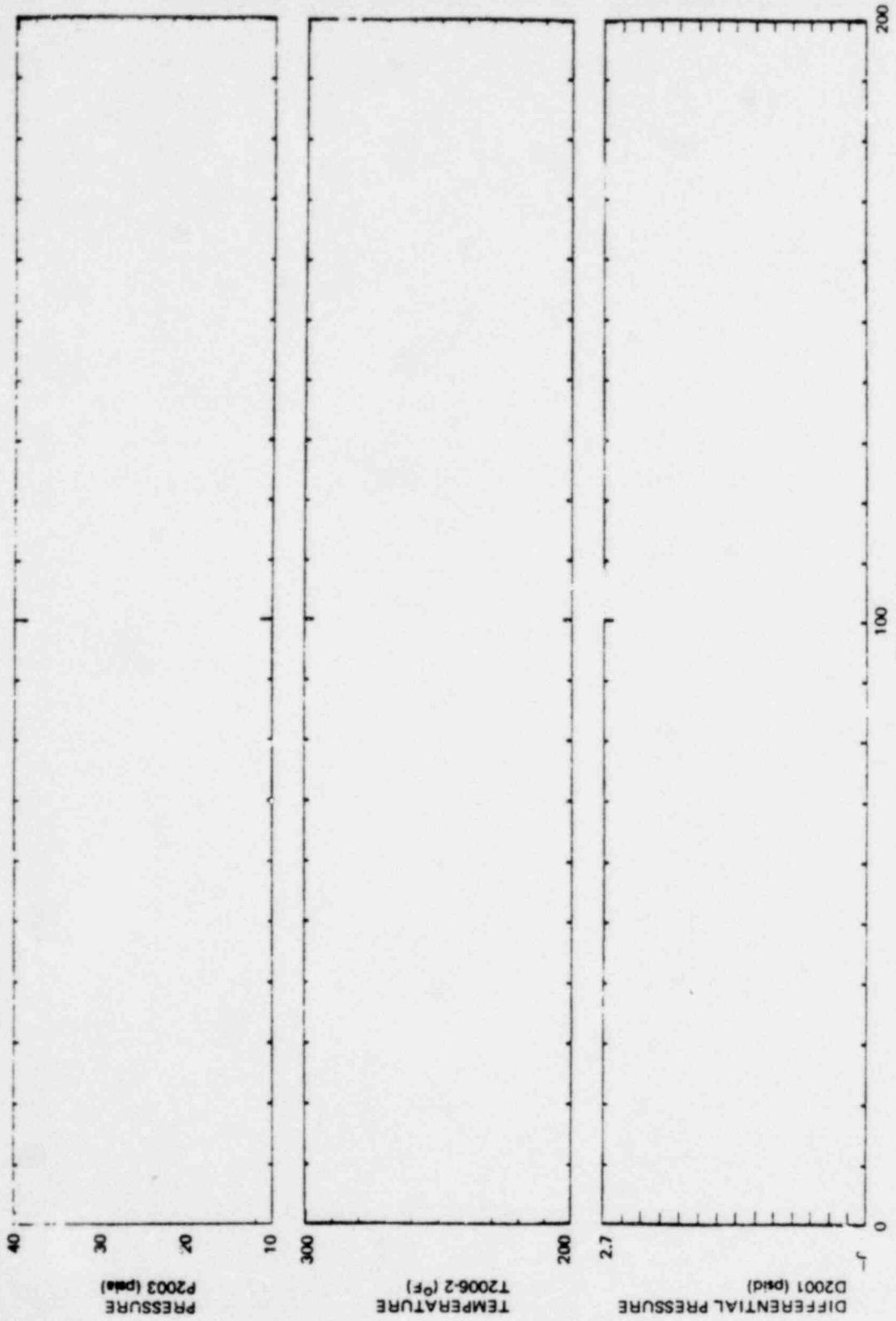

Figure C-45. North Vent Line Parameters, Large Steam Break, M7

*Proprietary information deleted

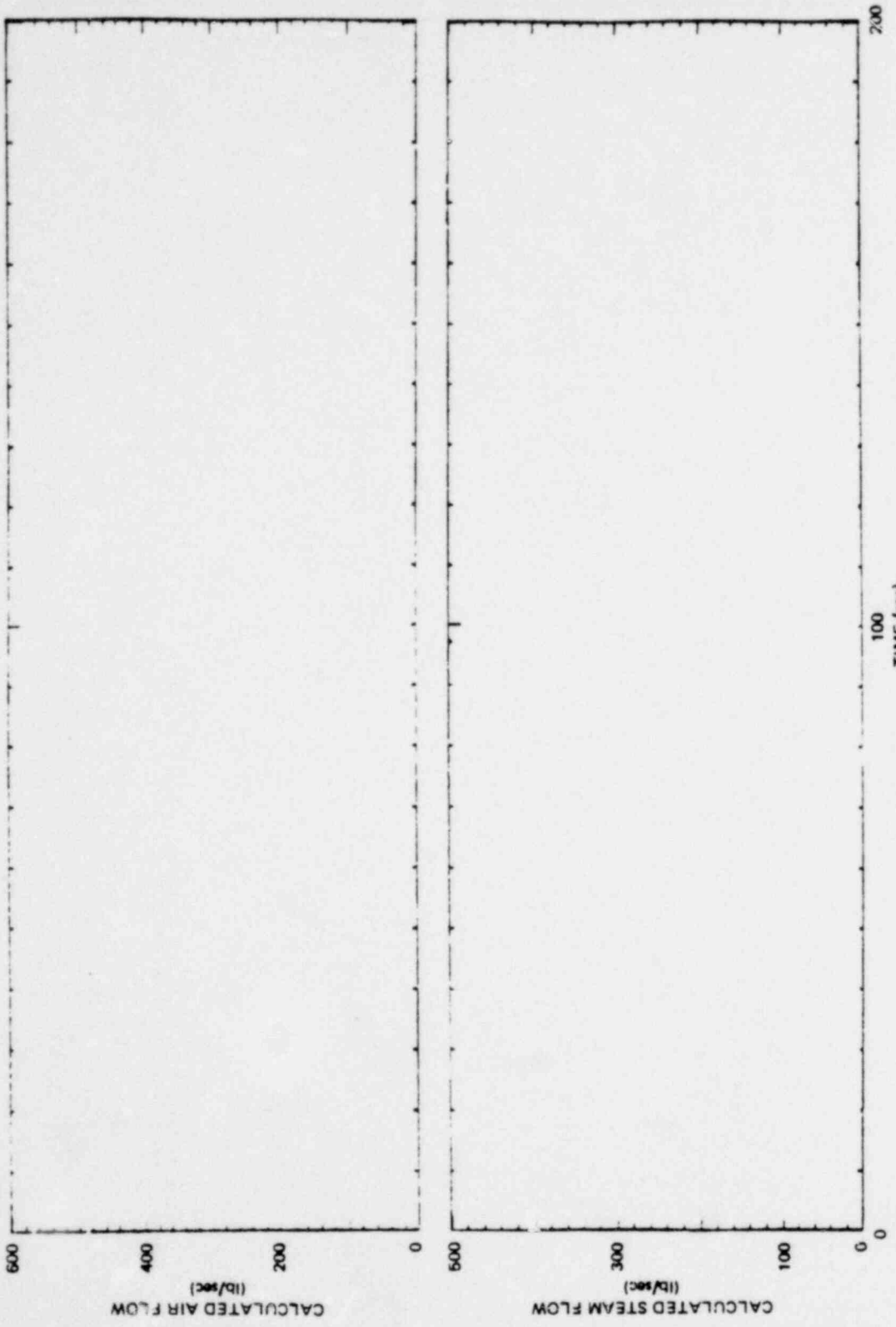

Figure C-46. North Vent Line Flow, Large Steam Break, M7

*Proprietary information deleted

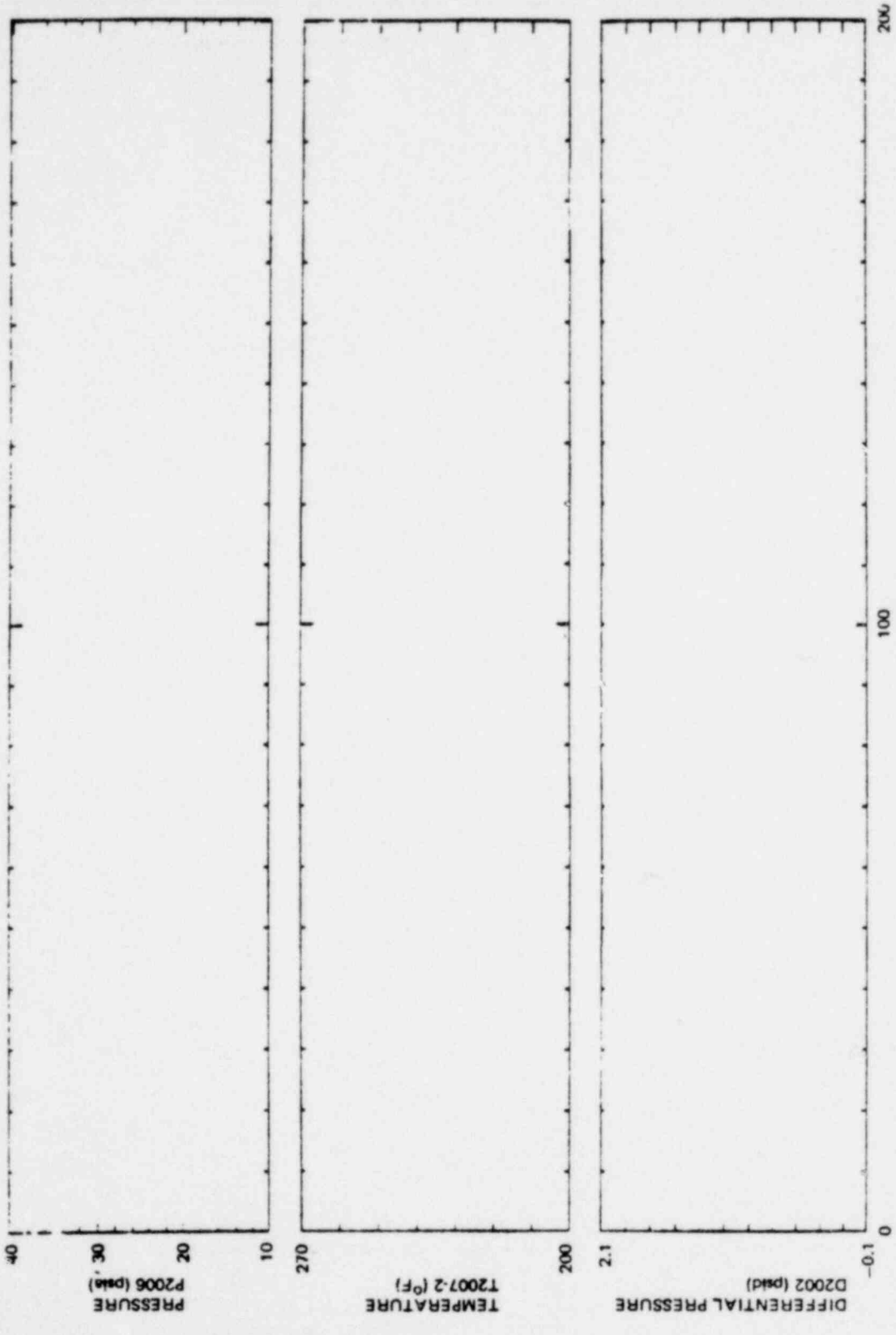

Figure C-47. South Vent Line Parameters, Large Steam Break, M7

*Proprietary information deleted

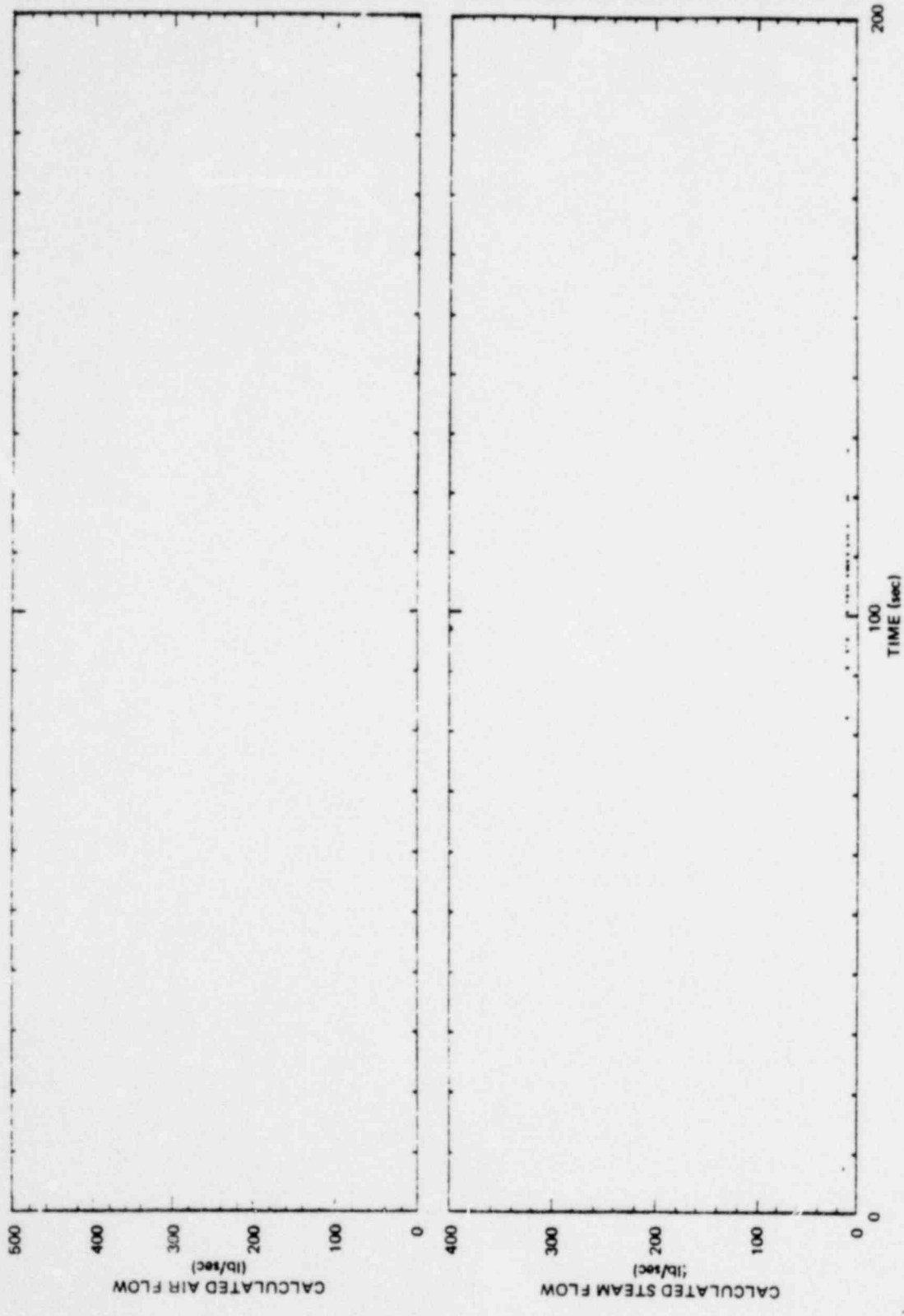

Figure C-46. South Vent Line Flow, Large Steam Break, M7

*Proprietary information deleted

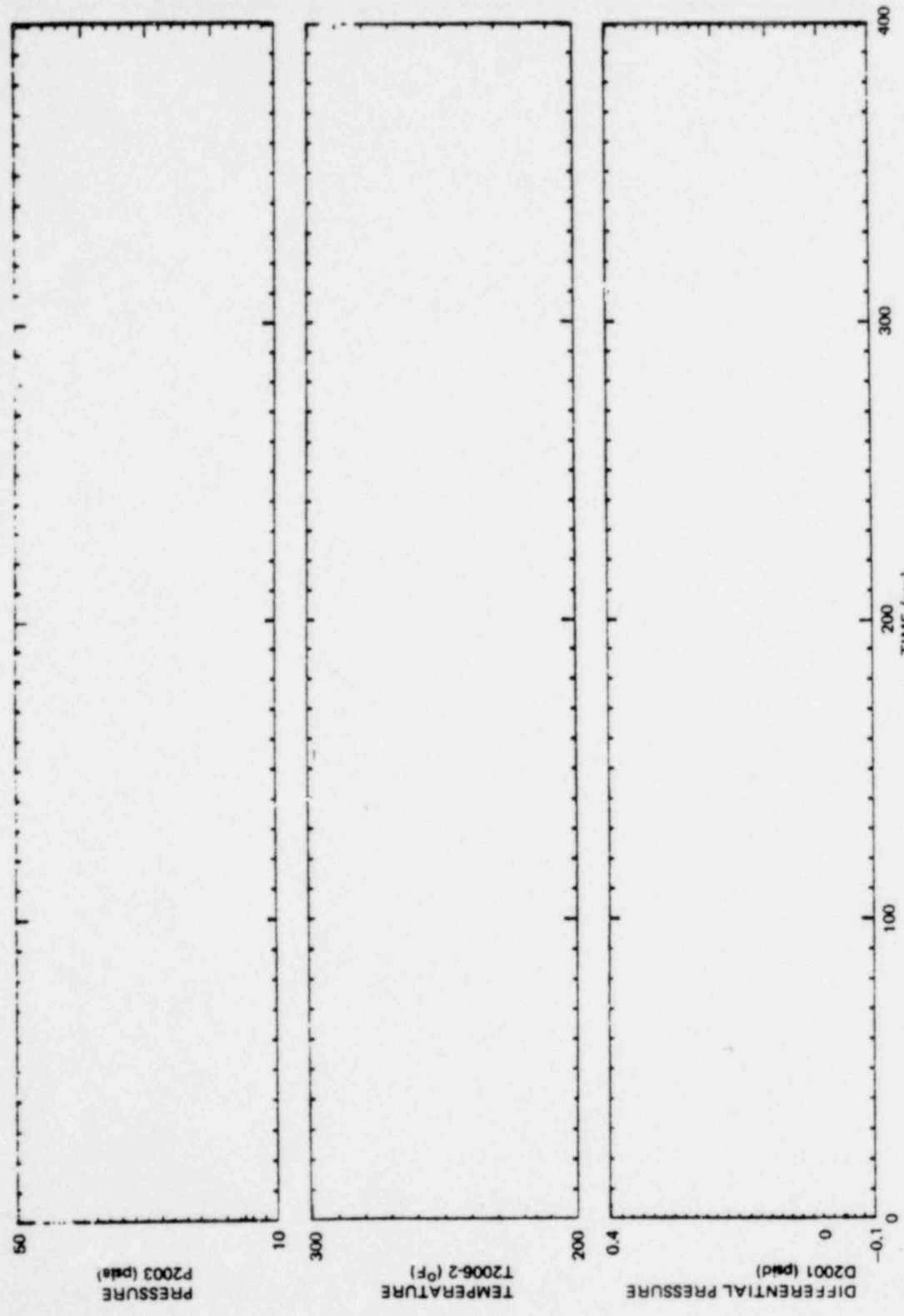

Figure C-49. North Vent Line Parameters, Small Steam Break, M6

*Proprietary information deleted

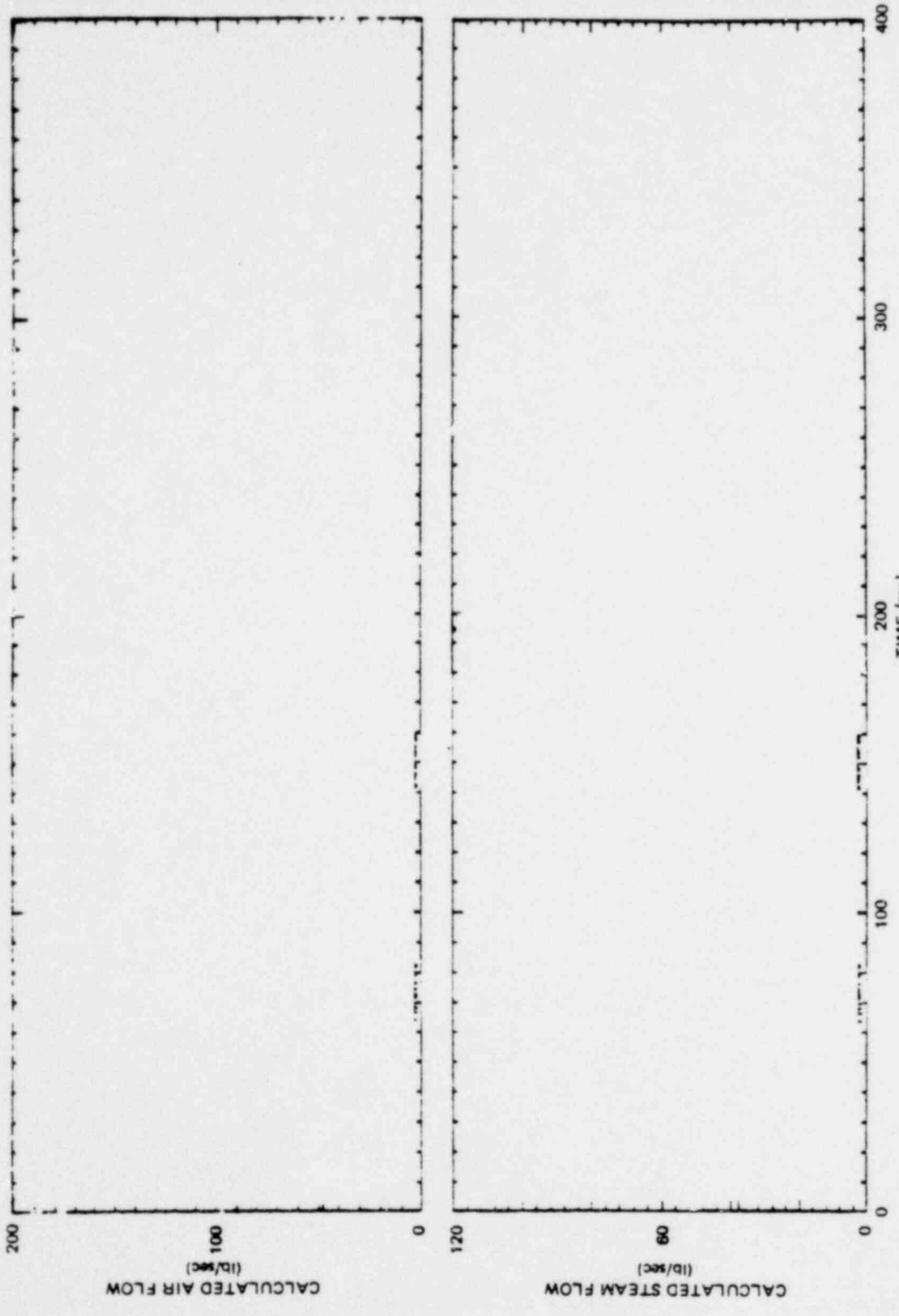

Figure C-50. North Vent Line Flow, Small Steam Break, M6

*Proprietary information deleted

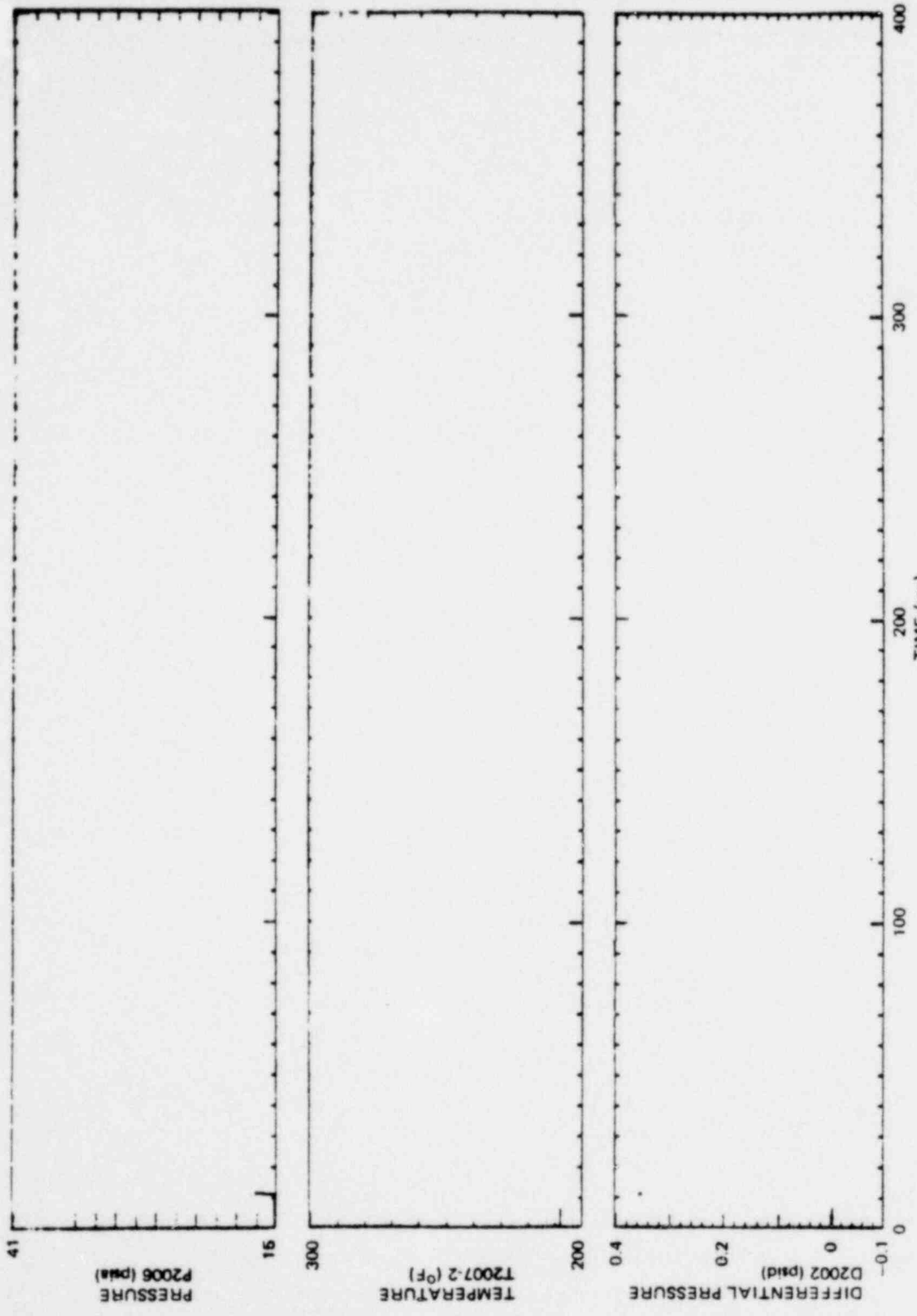

Figure C-51. South Vent Line Parameters, Small Steam Break, M6

*Proprietary information deleted

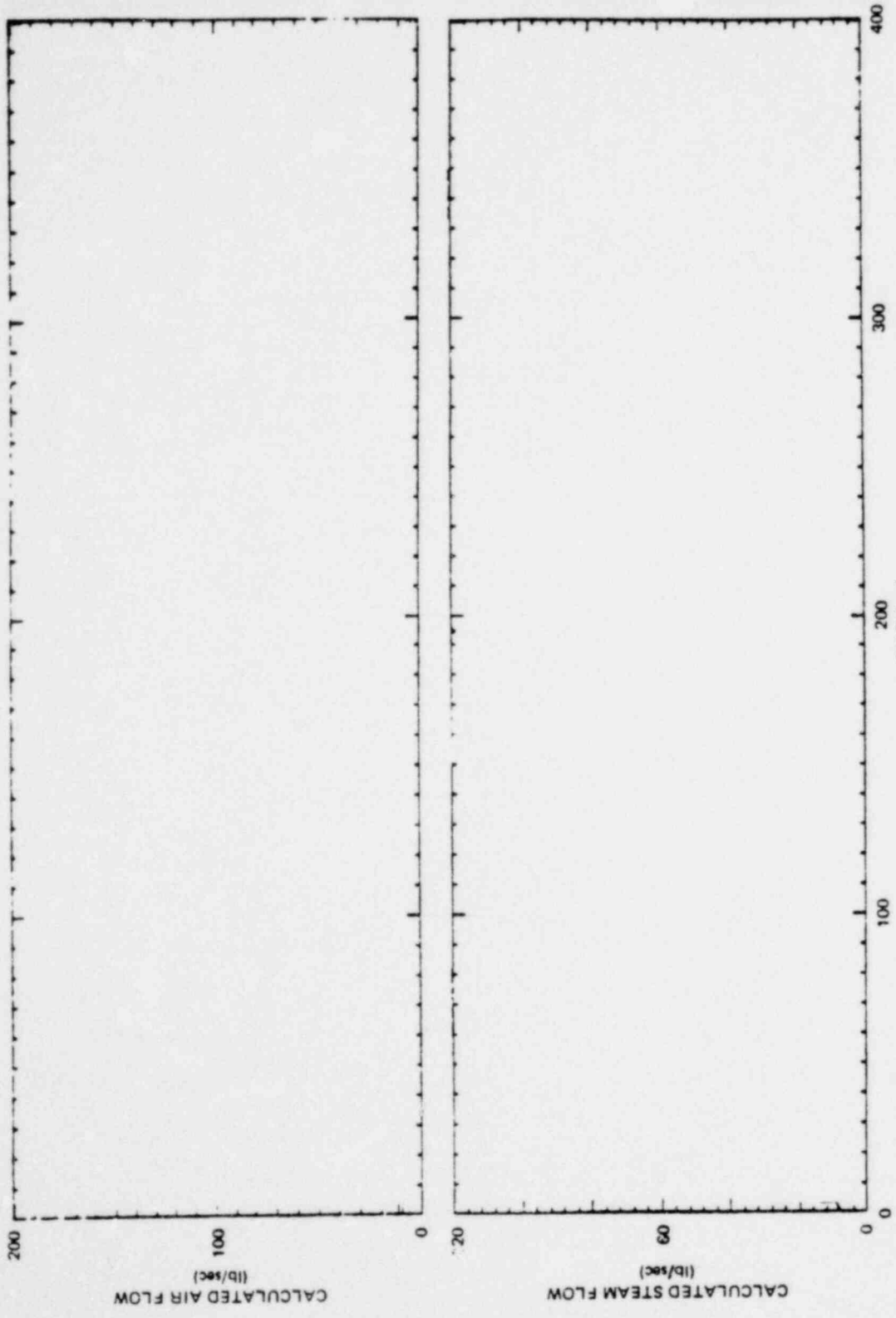

Figure C-52. South Vent Line Flow, Small Steam Break, N6

*Proprietary information deleted

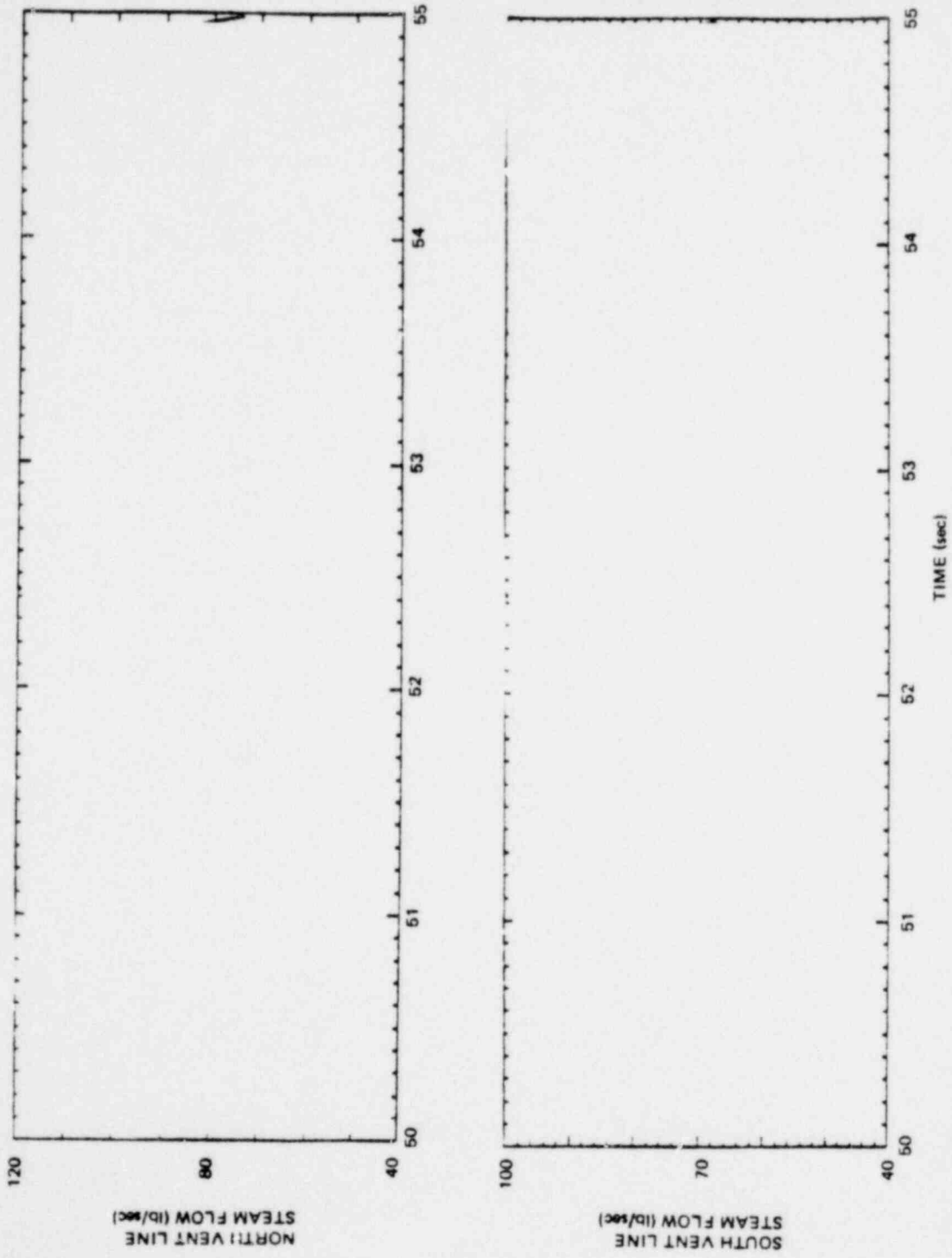

Figure C-53. Comparison of Vent Line Flows During C.O., Small Steam Break, M9

*Proprietary information deleted

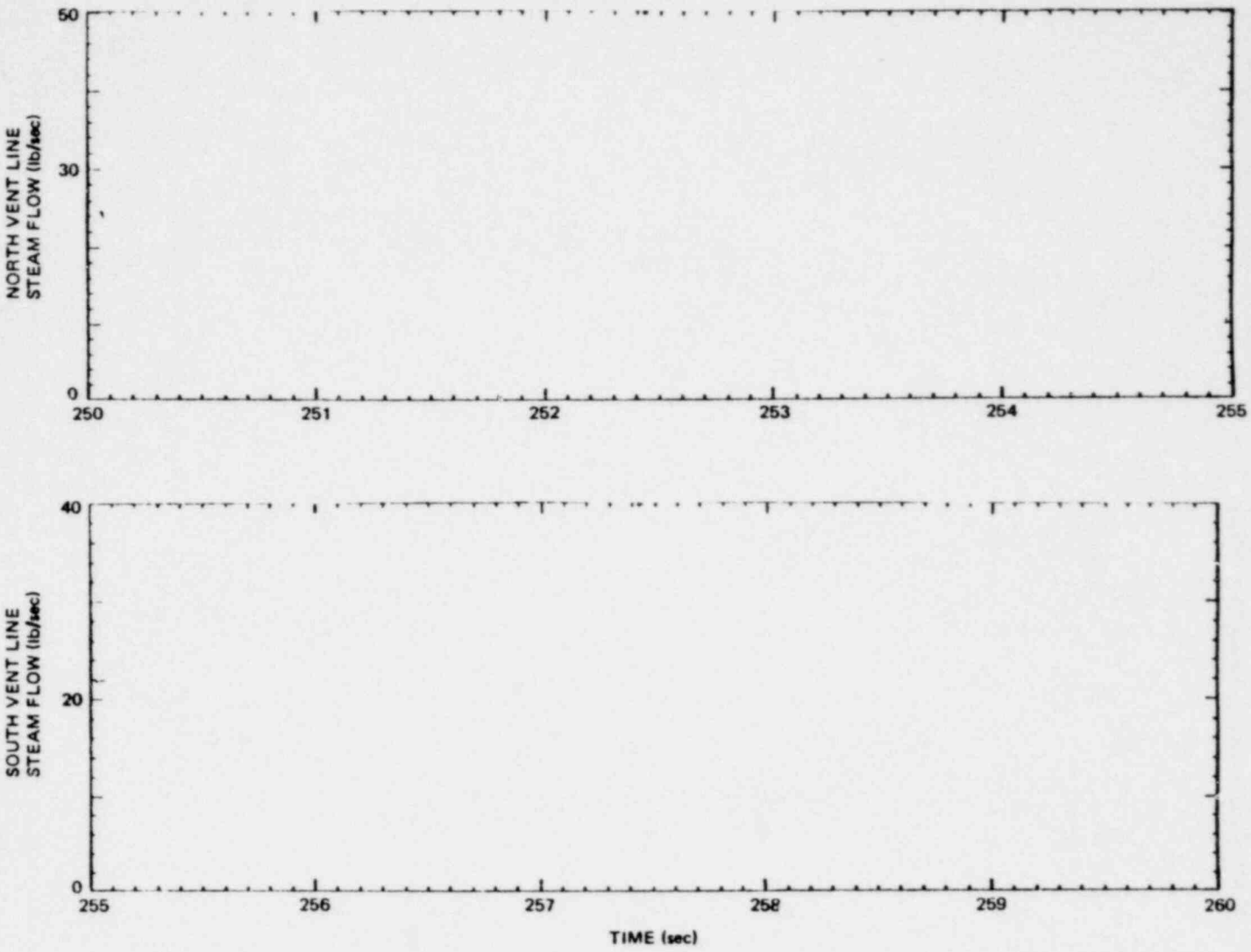

Figure C-54. Comparison of Vent Line Flow During Chugging, Small Steam Break, M9

*Proprietary information deleted

C.4 WETWELL

The wetwell vessel (V3) shown in Figures 3.2-5 and -6 is described in paragraph 3.2.5. The parameters which characterize the system performance of the wetwell are a) the freespace (airspace) pressure and b) the wetwell pool temperatures.

a. Pressure - The wetwell freespace pressure increases as the air is transferred from the drywell and the vent system through the suppression pool to the wetwell airspace. Figures C-55 and -56 compare the wetwell freespace pressures for the steam breaks (M1, M2, M7) and the liquid breaks (M3, M8) respectively. By comparing the two figures it can be seen that the liquid breaks result in higher freespace pressures because of increased mass and energy transfer to the wetwell. Calculations of the final freespace pressures were made for each of the tests in the test matrix using the nominal initial conditions. For one of the tests, matrix test M4, an elevated initial overpressure was used to obtain a final pressure of approximately 30 psig. Table C-3 shows the actual and the calculated final wetwell freespace pressures for each of the tests in the test matrix. Examination of the results shows good agreement between the measured and calculated pressure except for those tests which had either a high predicted final temperature or significant stratification in the suppression pool. Calculations for those tests with higher wetwell pool temperatures (tests M3, M5, M8) are high compared to the final wetwell freespace pressure. These comparisons indicate that the vapor pressure in the airspace is less than the saturation pressure corresponding to the bulk pool temperature as assumed in the predictions.

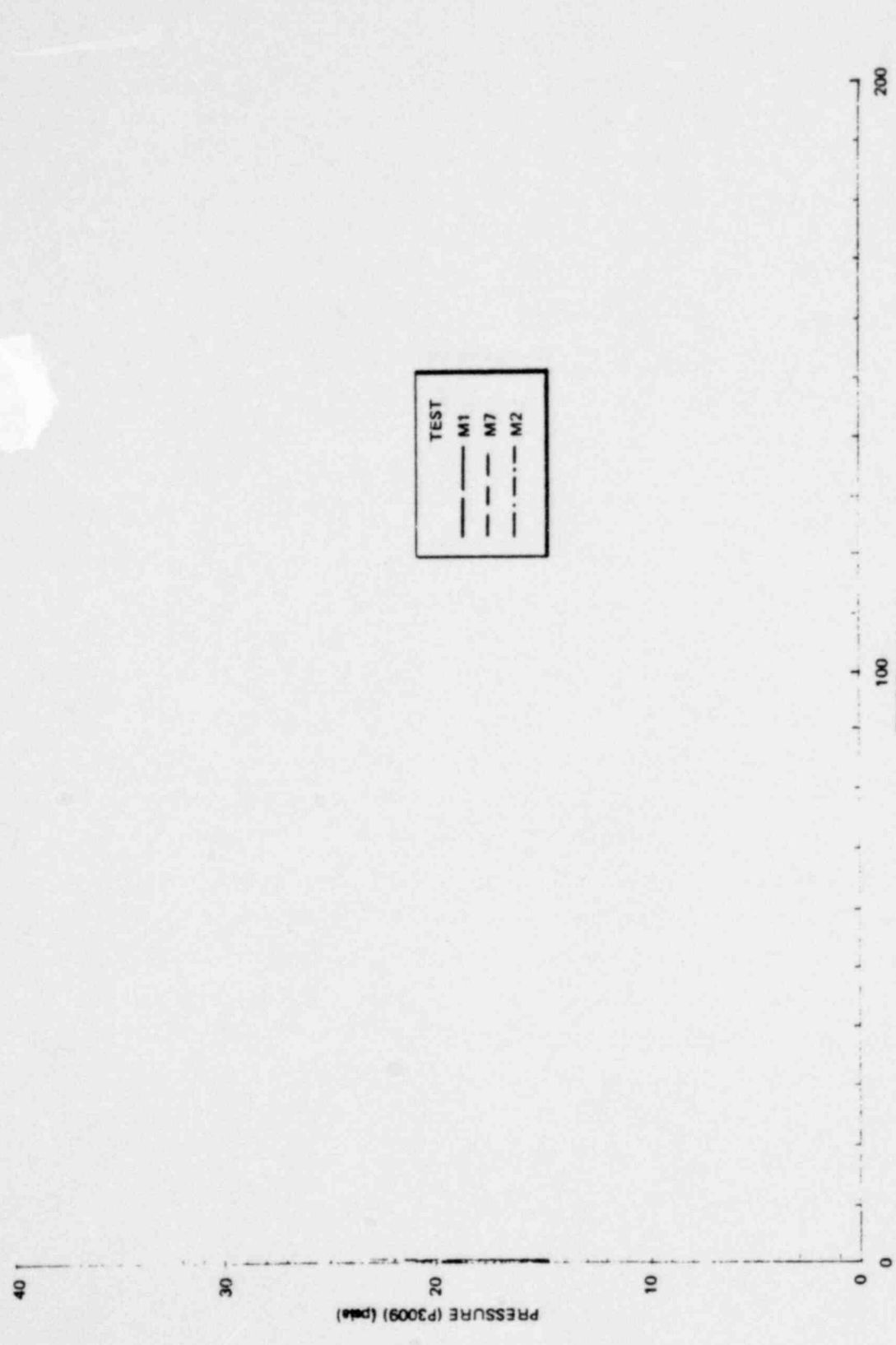

Figure C-55. Comparison of Wetwell Freespace Pressures, Steam Breaks, M1, M2, M7

*Proprietary information deleted

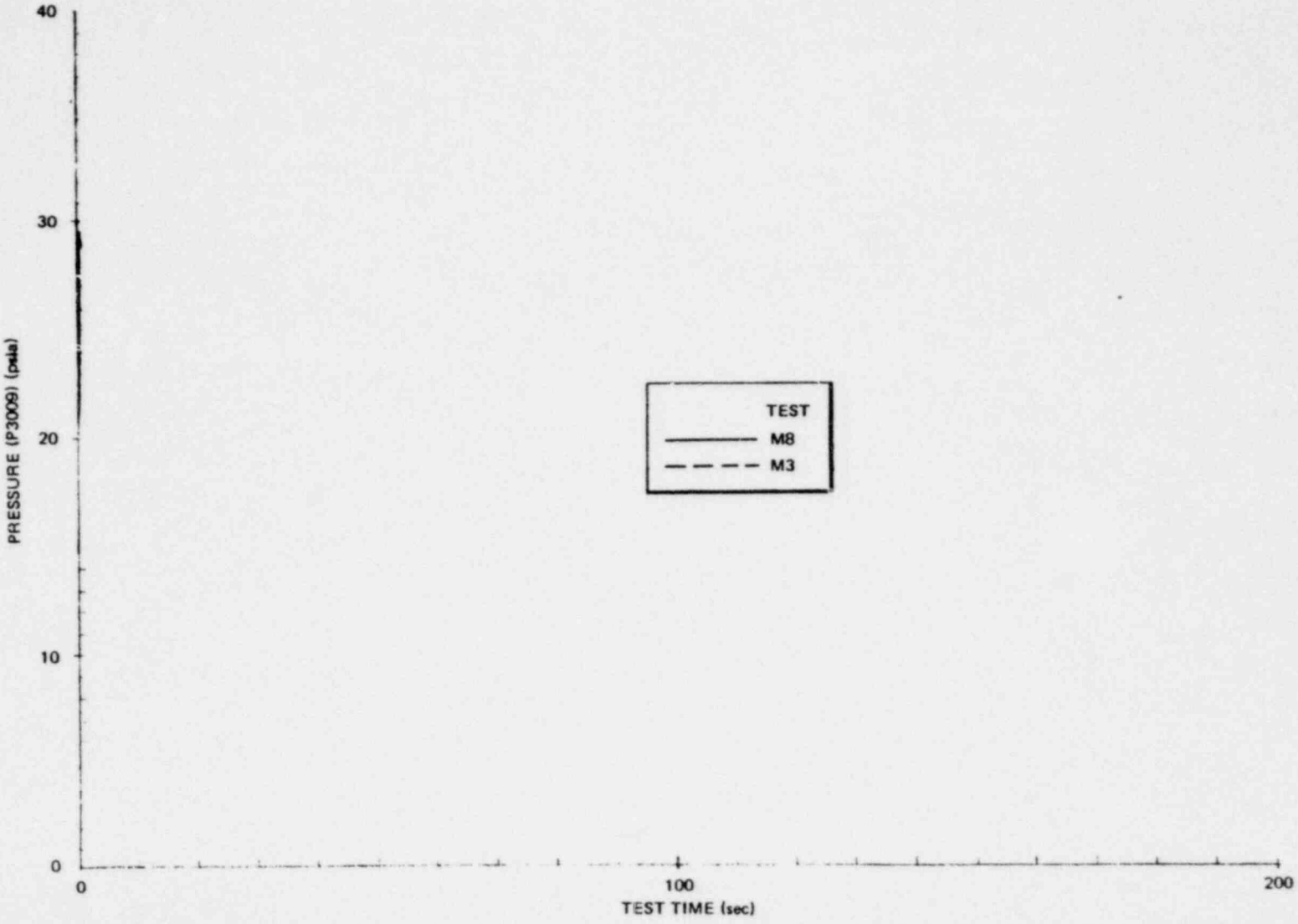

Figure C-56. Comparison of Wetwell Freespace Pressures, Liquid Breaks, M3, M8

*Proprietary information deleted

Table C-3

WETWELL PRESSURES AND TEMPERATURES

Test No.	Test Type	Wetwell Pressure Final (psia)	Wetwell Pressure Calculated (psia)	Wetwell Temperatures Surface (°F)	Wetwell Temperatures Bulk (°F)	ΔT (Surface-Bulk) (°F)
M1	Small Steam					
M2	Medium Steam					
M3	Small Liquid					
M4	Small Steam					
M5	Small Steam					
M6	Small Steam					
M9	Small Steam					
M10	Small Steam					
M7	Large Steam					
M8	Large Liquid					

*Proprietary information deleted

1158 3[illegible]

The freespace pressure history for test M6 was different from the other tests of the test matrix. Figure C-57 shows the pressure history for test M6. Test M6 was performed with a high initial pool temperature (120°F) and reduced submergence (18 inches) to specifically investigate condensation effectiveness under these severe conditions. At approximately 100 seconds, the wetwell pressure starts a second slow increase which continues until the pressure levels off at approximately 28 psig. This final freespace pressure value was high compared to the other steam break tests. Figure C-58 compares measured freespace pressure values with the vapor pressure and with the vapor pressure plus the air pressure (assuming the vapor and air are in thermal equilibrium with the pool surface). In all cases, the vapor pressures is less than the saturation pressure corresponding to the pool surface temperatures. This data also shows that the final freespace pressure is constant for increasing break size (M2, M7), increasing pool initial temperature (M5) and increasing final pool surface temperature.

An additional comparison was made for the pool surface temperature and the freespace air temperature. This comparison is shown in Figure C-59. In all cases, the final wetwell airspace temperature is less than the final pool surface temperature. It can also be seen that the final airspace temperature of test M6 although 25°F lower than the pool surface temperature is higher than would be expected based on the performance of the other steam break tests.

b. Temperature - The water mass in the wetwell serves as the heat sink for the high temperature steam and water in the steam supply vessel. As the energy is transferred to the wetwell, the temperature of the suppression pool increases. Table C-3 compares the pool

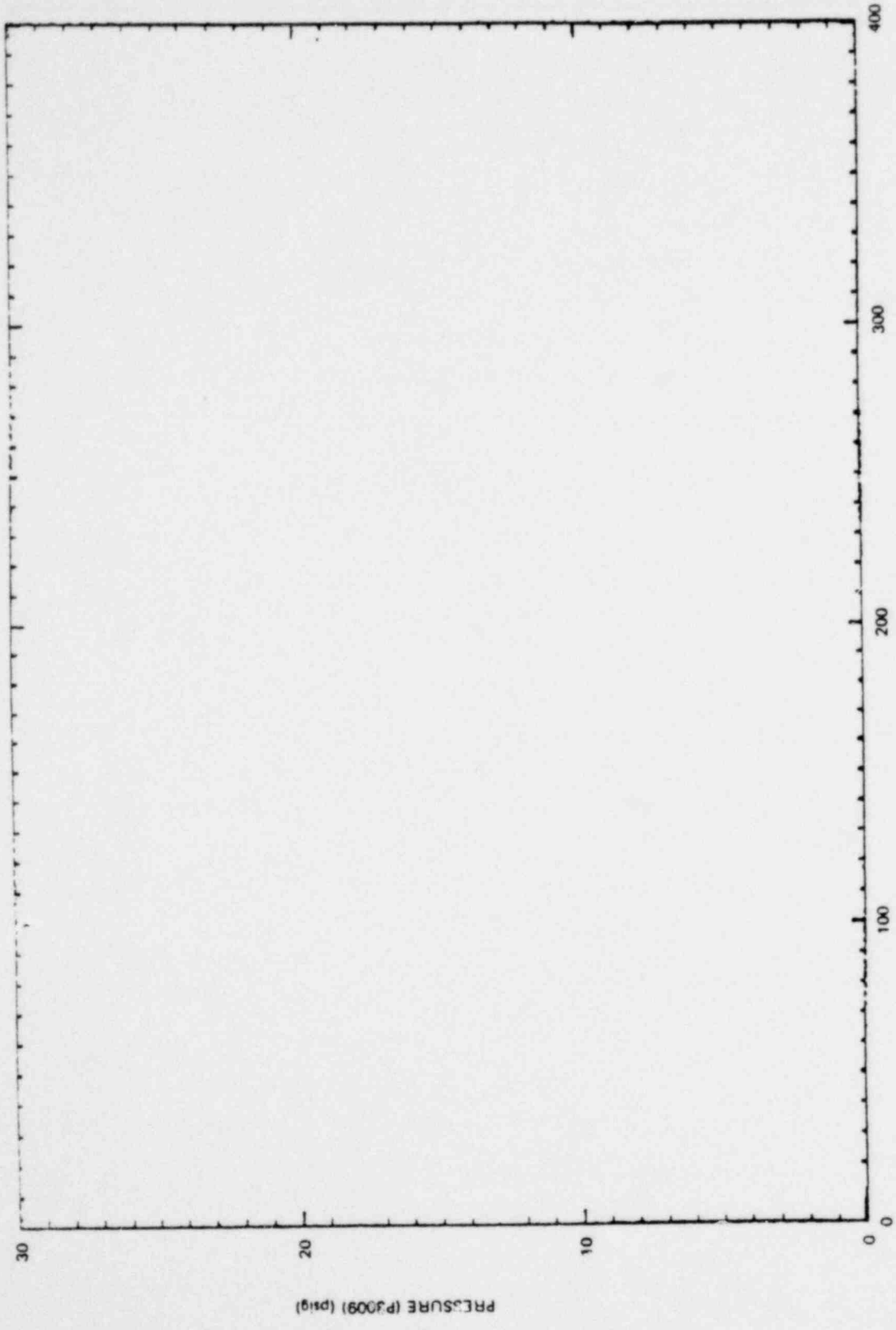

Figure C-57. Wetwell Freespace Pressure, Small Steam Break, M6

*Proprietary information deleted

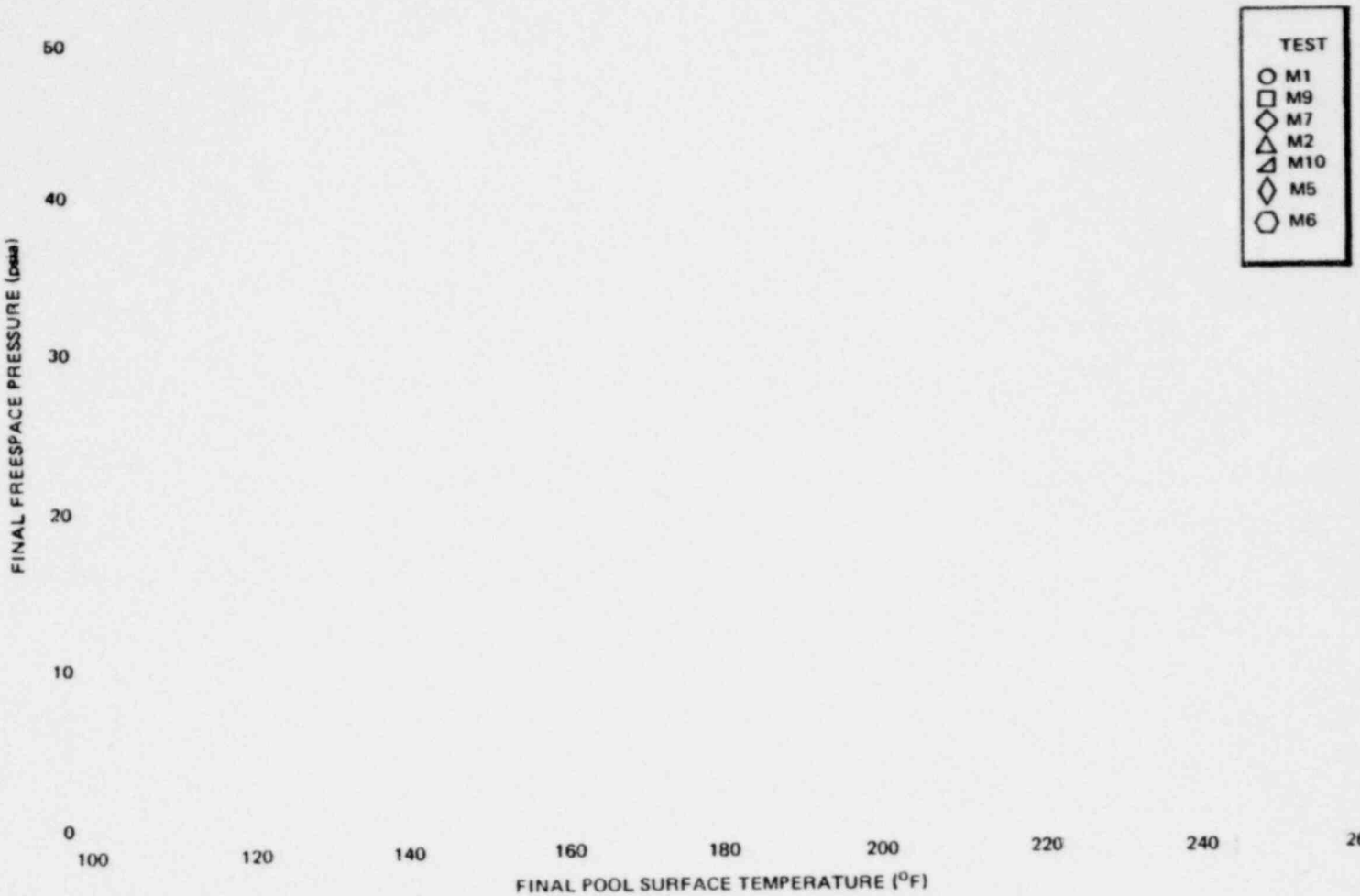

Figure C-58. Comparison of Wetwell Freespace Pressure and Pool Surface Temperatures

*Proprietary information deleted

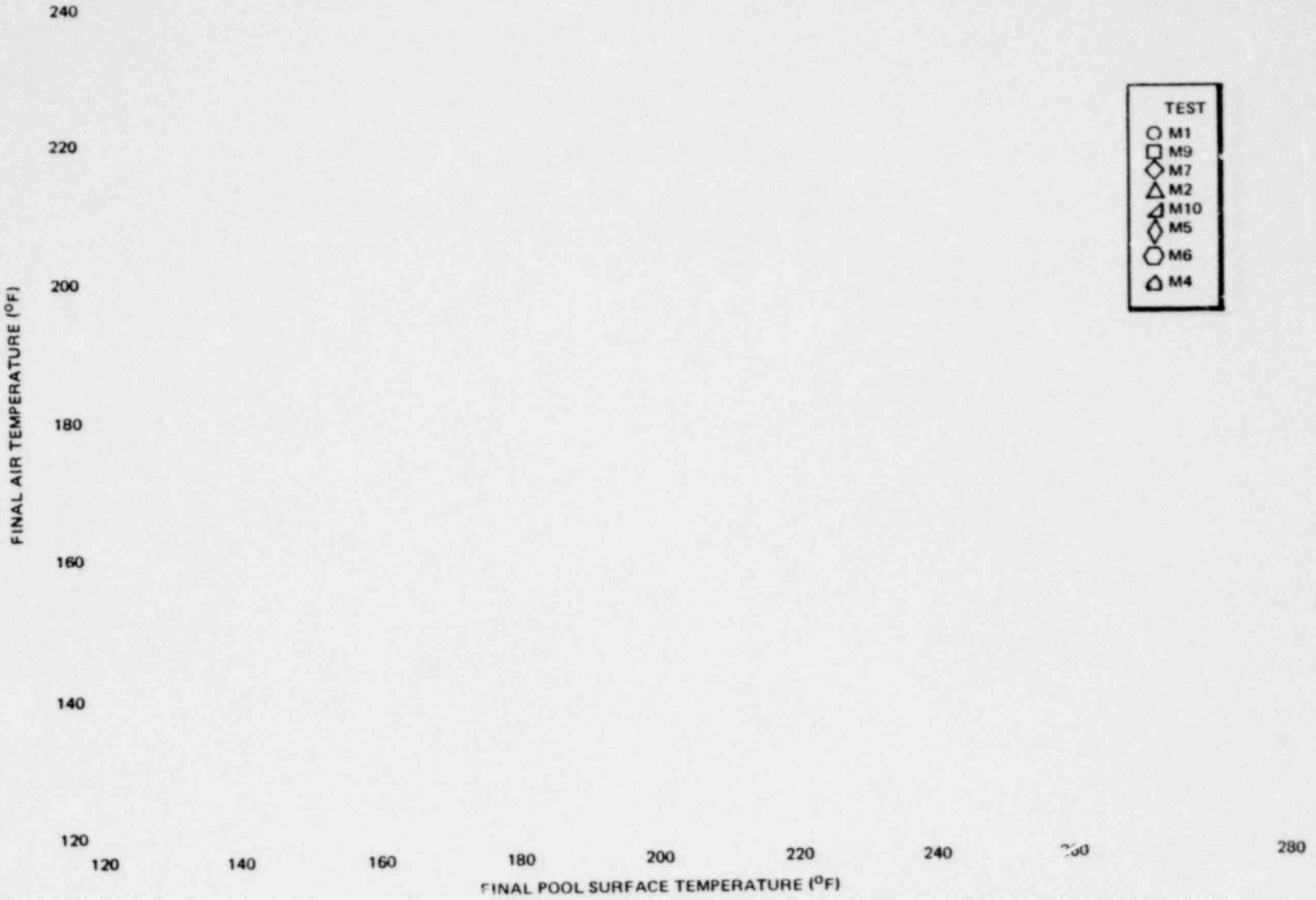

Figure C-59. Comparison of Wetwell Air and Pool Surface Temperatures

*Proprietary information deleted

surface temperature and the bulk temperature for all tests. The bulk temperature does a reasonable job of matching the test results if the wetwell pool is well mixed as was the case for test M1, shown in Figures C-60 to C-64, and test M8, shown in Figures C-65 to C-67. Figure C-61 shows the pool vertical profile for test M1 in which the pool was well mixed after chugging initiated. However if the wetwell pool is not mixed, as was the case for test M6, shown in Figures C-68 to C-70, the energy is concentrated primarily above the exit end of the downcomers shown in Figure C-69. An overall view of the behavior of the wetwell pool can be obtained at the centerline of the pool between downcomers five and six. Figure C-69 shows the vertical temperature profile at this location and clearly shows most of the temperature increase occurring between the bottom of the downcomer and the surface of the pool (refer to Figure 3.4-2 for thermocouple locations).

C.5 VACUUM BREAKER

The vacuum breaker operated during some of the tests. The particular vacuum breaker selected for this test program is described in paragraph 3.2.6. It was installed in the wetwell on the North end of the ring header and was in place for all the tests in the test matrix except for test M10. Table C-4 summarizes the vacuum breaker performance for the matric tests. For test M1, which had the highest initial opening pressure, the pallet hinge was bent and the latching magnet was broken. The position indicator mounted on the pallet shaft failed at 80 seconds, as shown in Figure C-71. During the inspection of the vacuum breaker after test M1, identations were observed in the valve casing which suggest that the pallet opened fully during this test. In some other tests, there was damage which was limited to the pallet sealing gasket. The observed damage had no apparent effect on the wetwell freespace pressure in any test.

Figure C-60. Wetwell Suppression Pool Temperatures, Small Steam Break, M1

*Proprietary information deleted

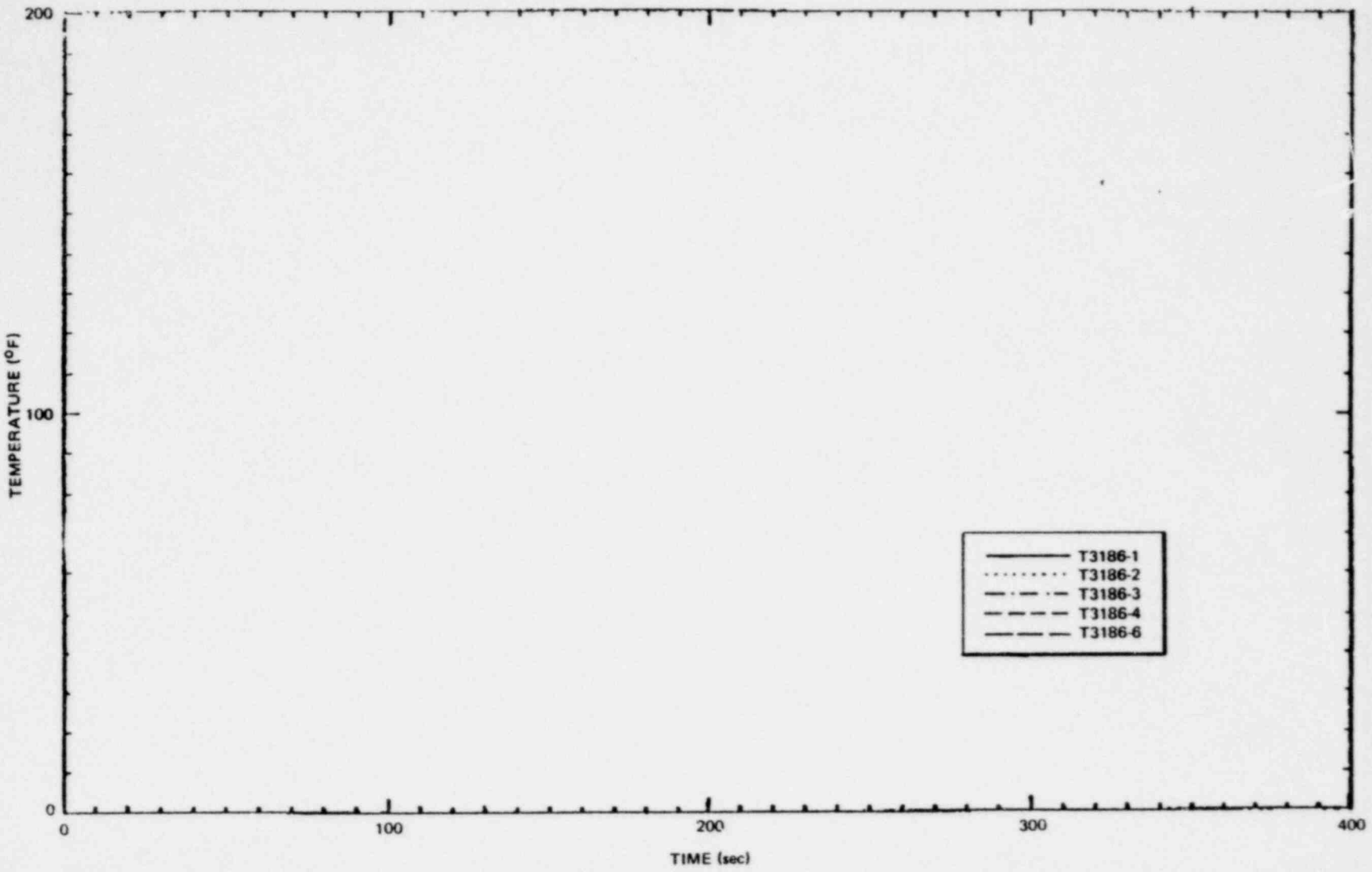

Figure C-61. Comparison of Pool Axial Temperatures, Midbay, Small Steam Break, M1

*Proprietary information deleted

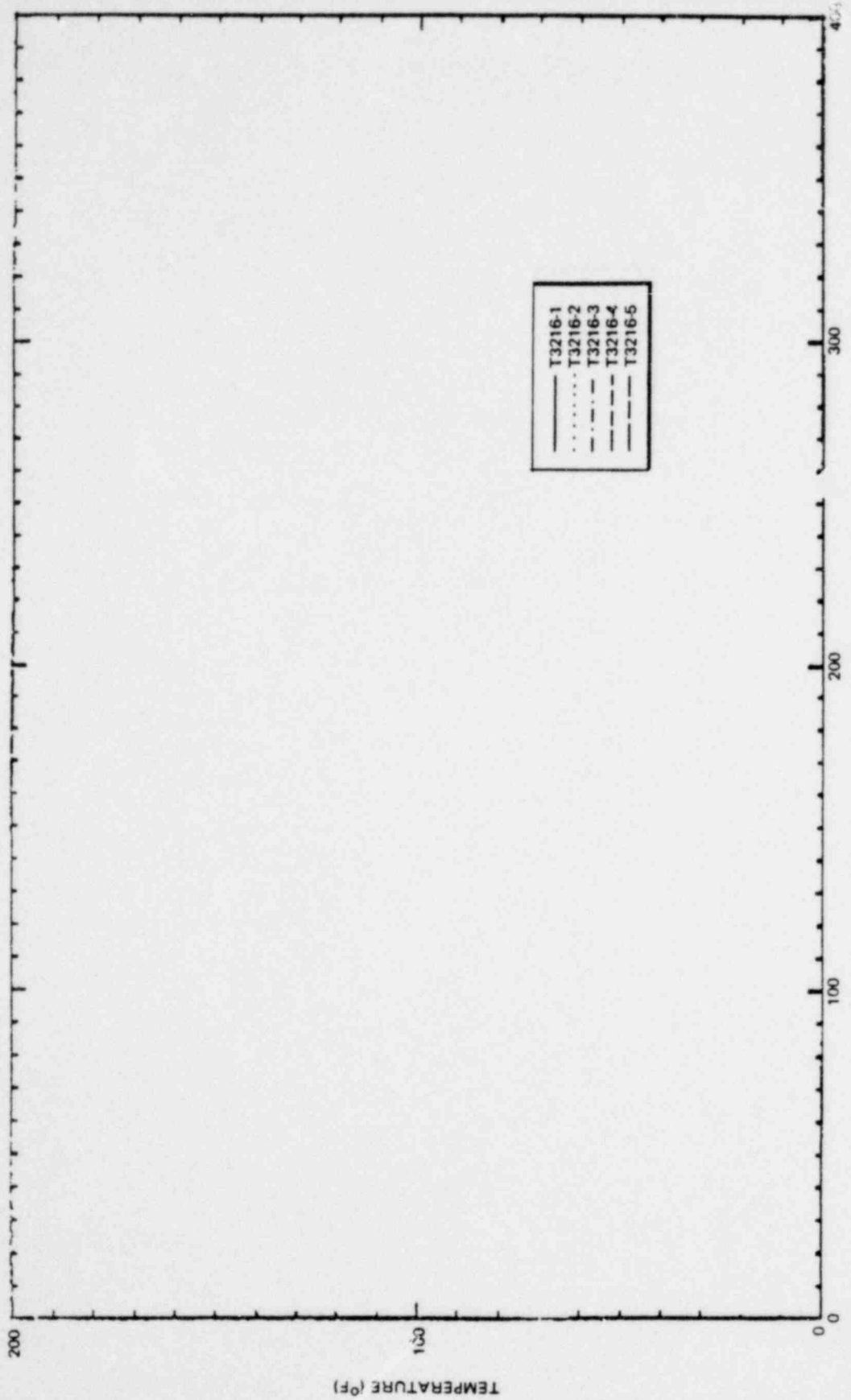

Figure C-62. Comparison of Pool Axial Temperatures, Small Steam Break, M1

*Proprietary information deleted

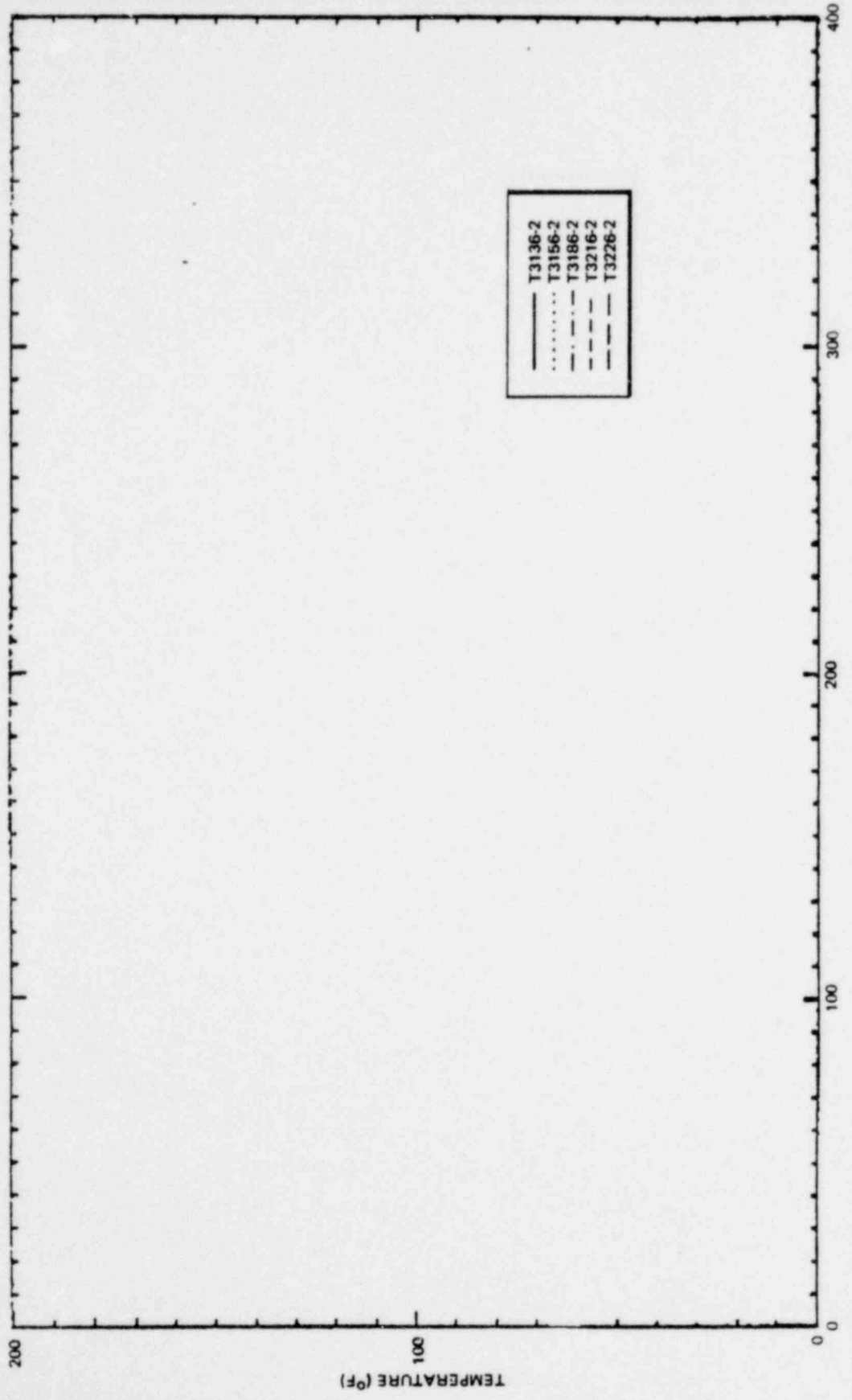

Figure C-63. Comparison of Pool Surface Temperatures, Small Steam Break, M1

*Proprietary information deleted

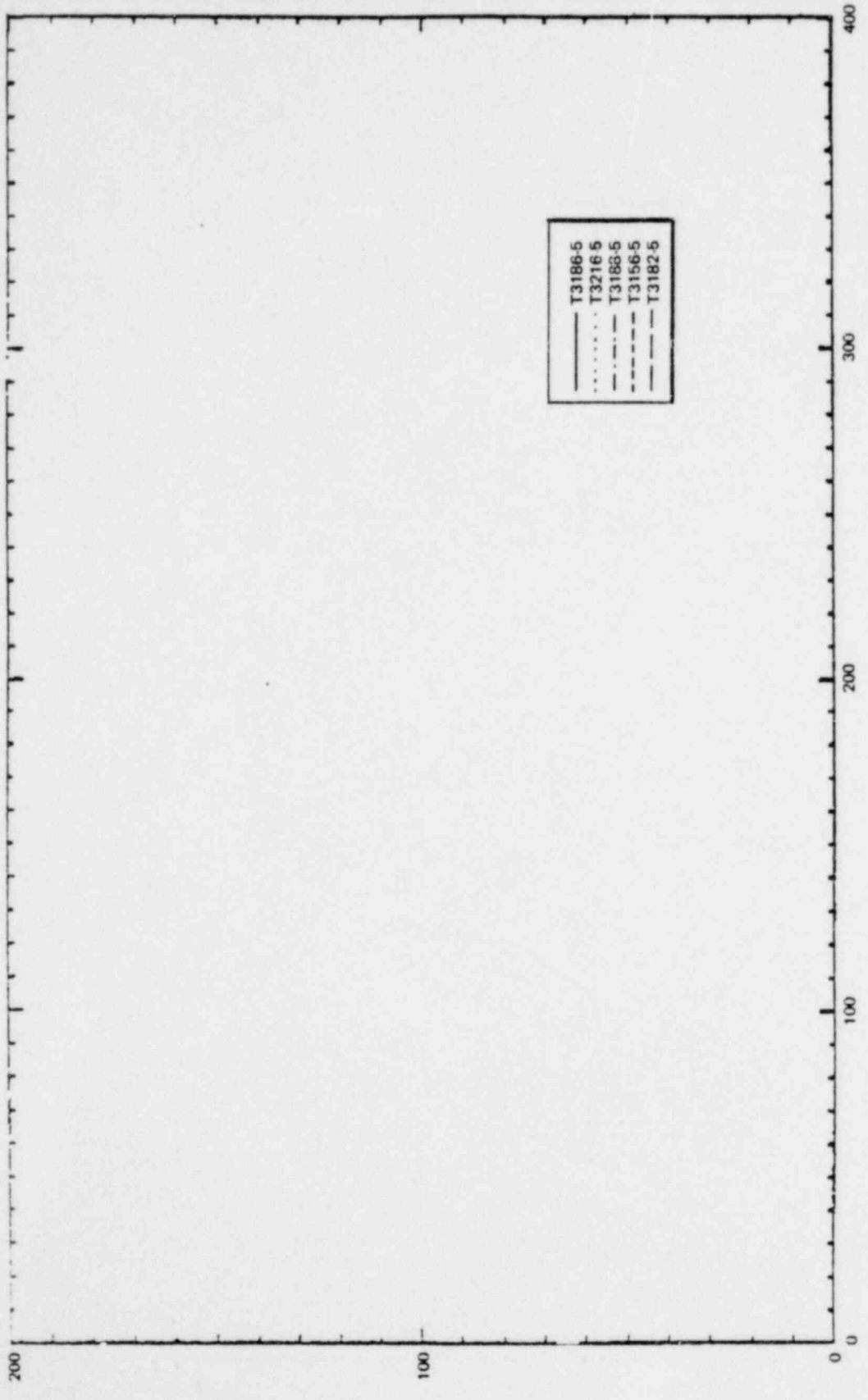

Figure C-64. Comparison of Pool Bottom Temperatures, Small Steam Break, M1

*Proprietary information deleted

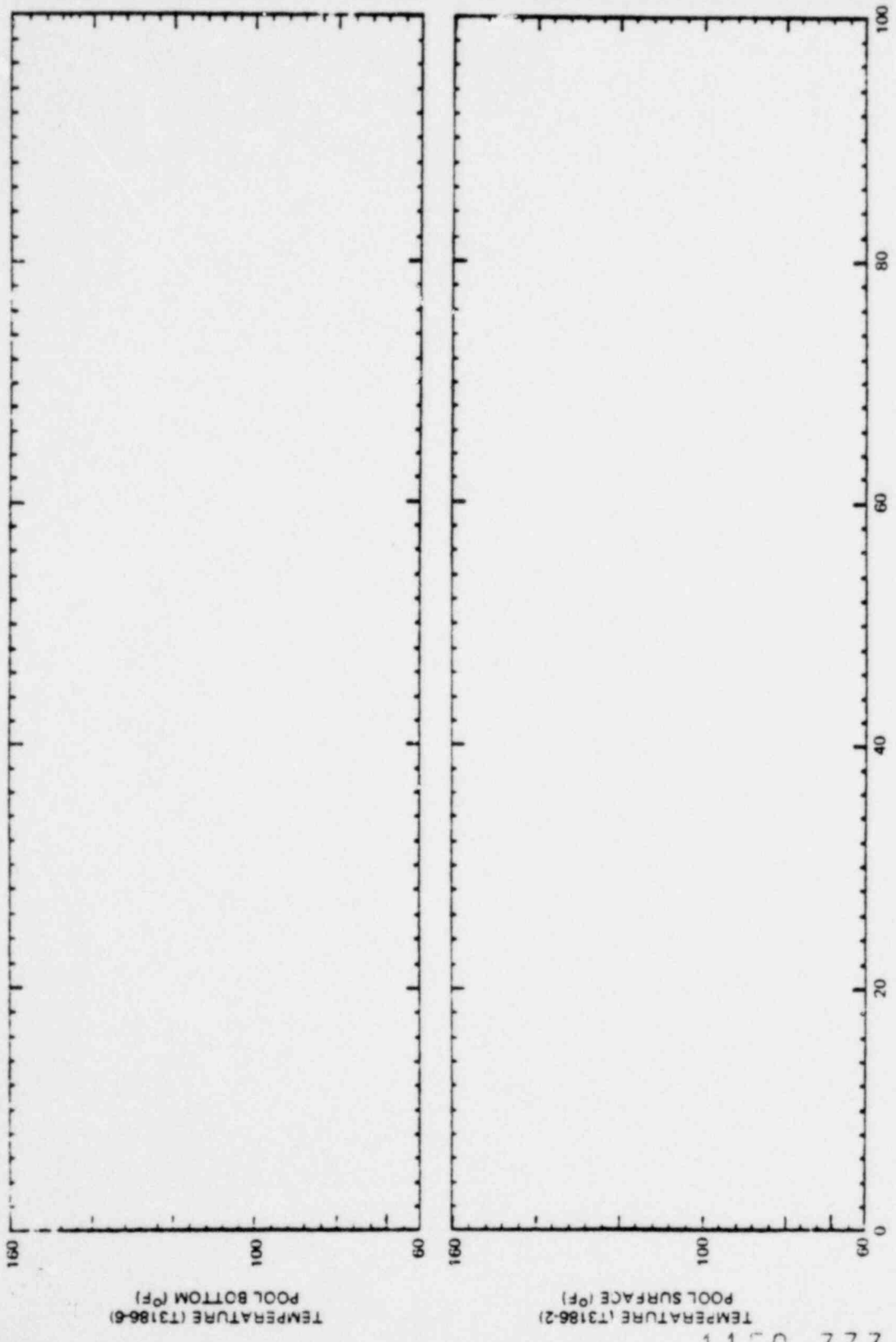

Figure C-65. Wetwell Suppression Pool Temperatures, Large Liquid Break, M8

1158 333

*Proprietary information deleted

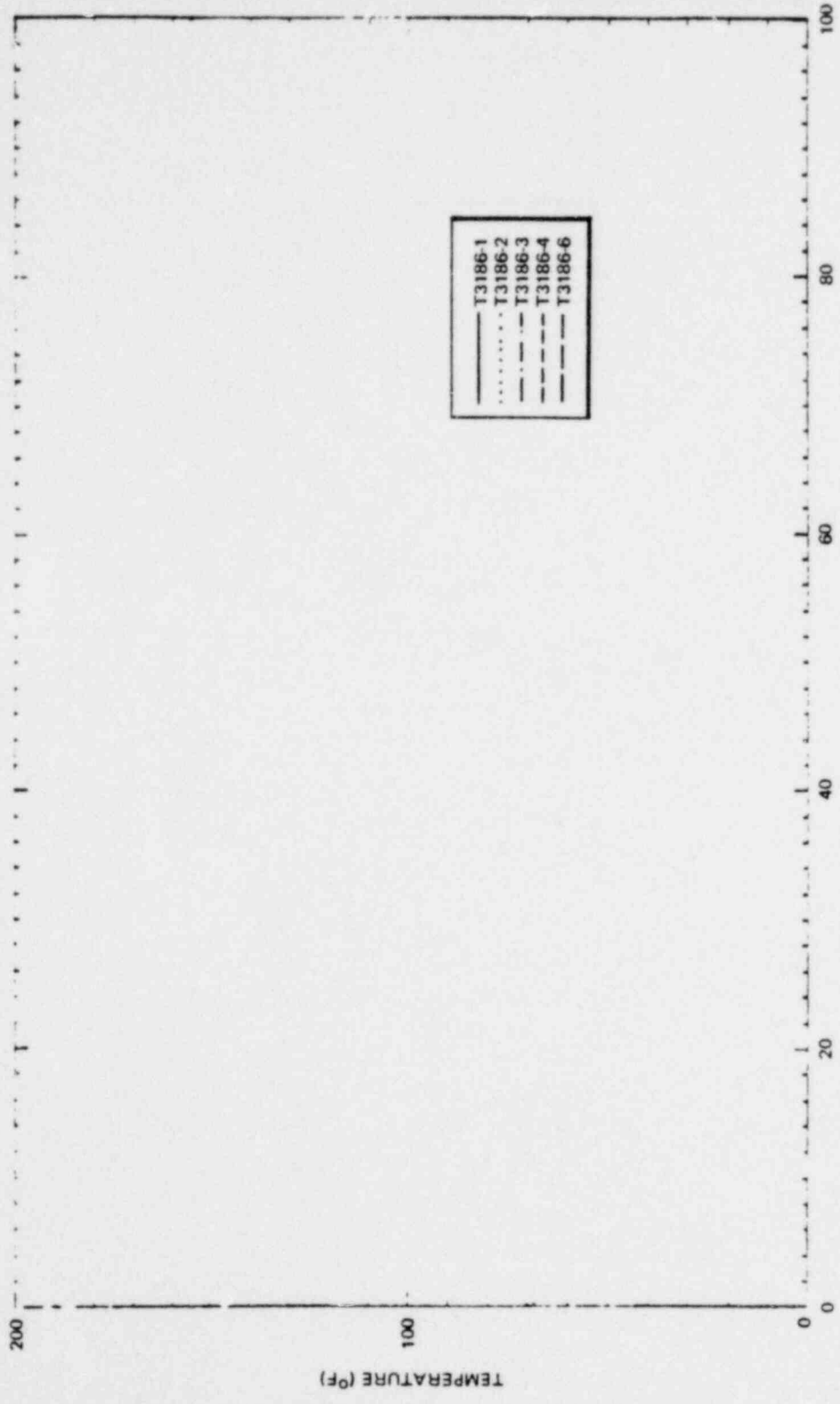

Figure C-66. Comparison of Pool Axial Temperatures, Midbay, Large Liquid Break, M8

*Proprietary information deleted

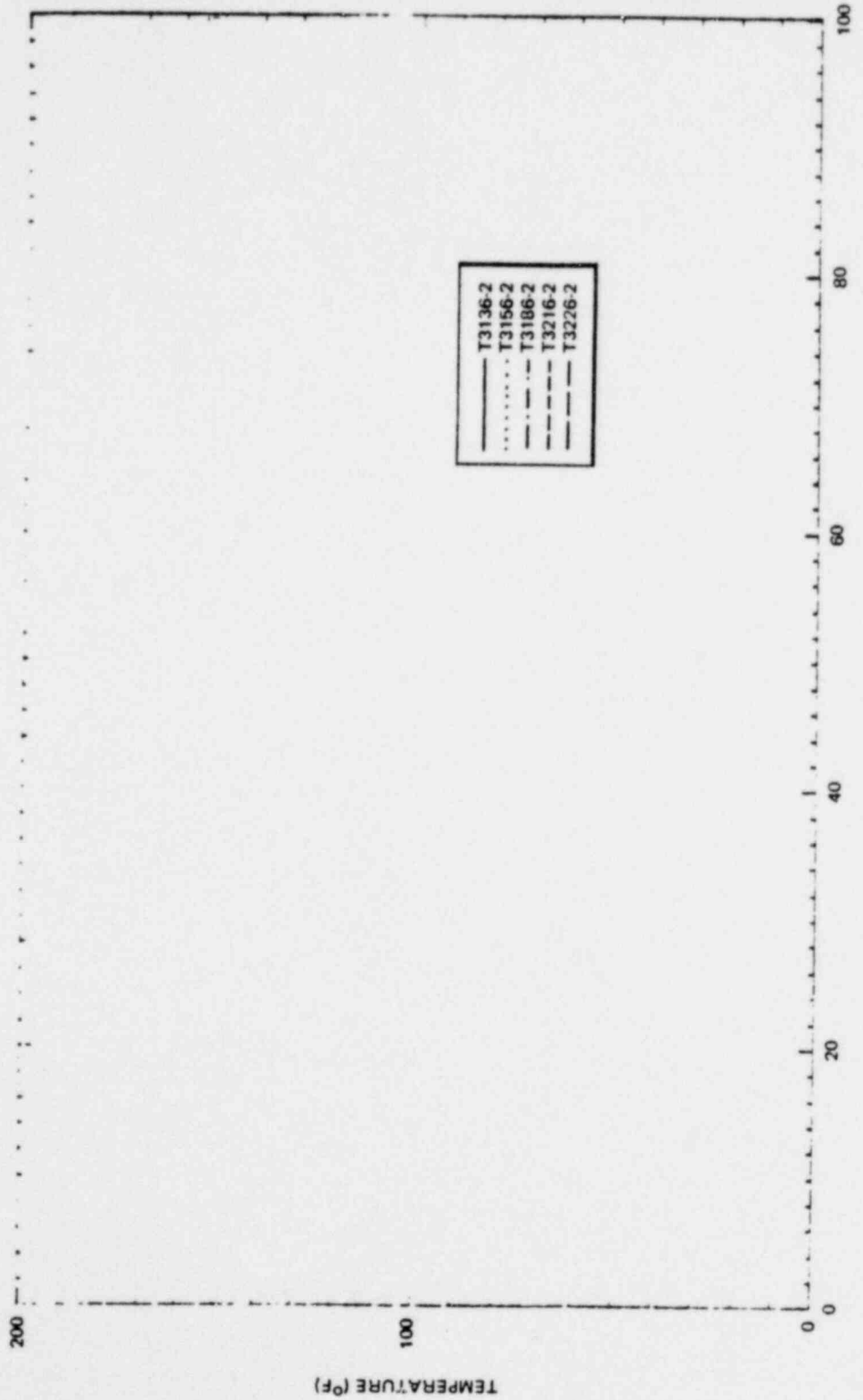

Figure C-67. Comparison of Pool Surface Temperatures, Large Liquid Break, M8

*Proprietary information deleted

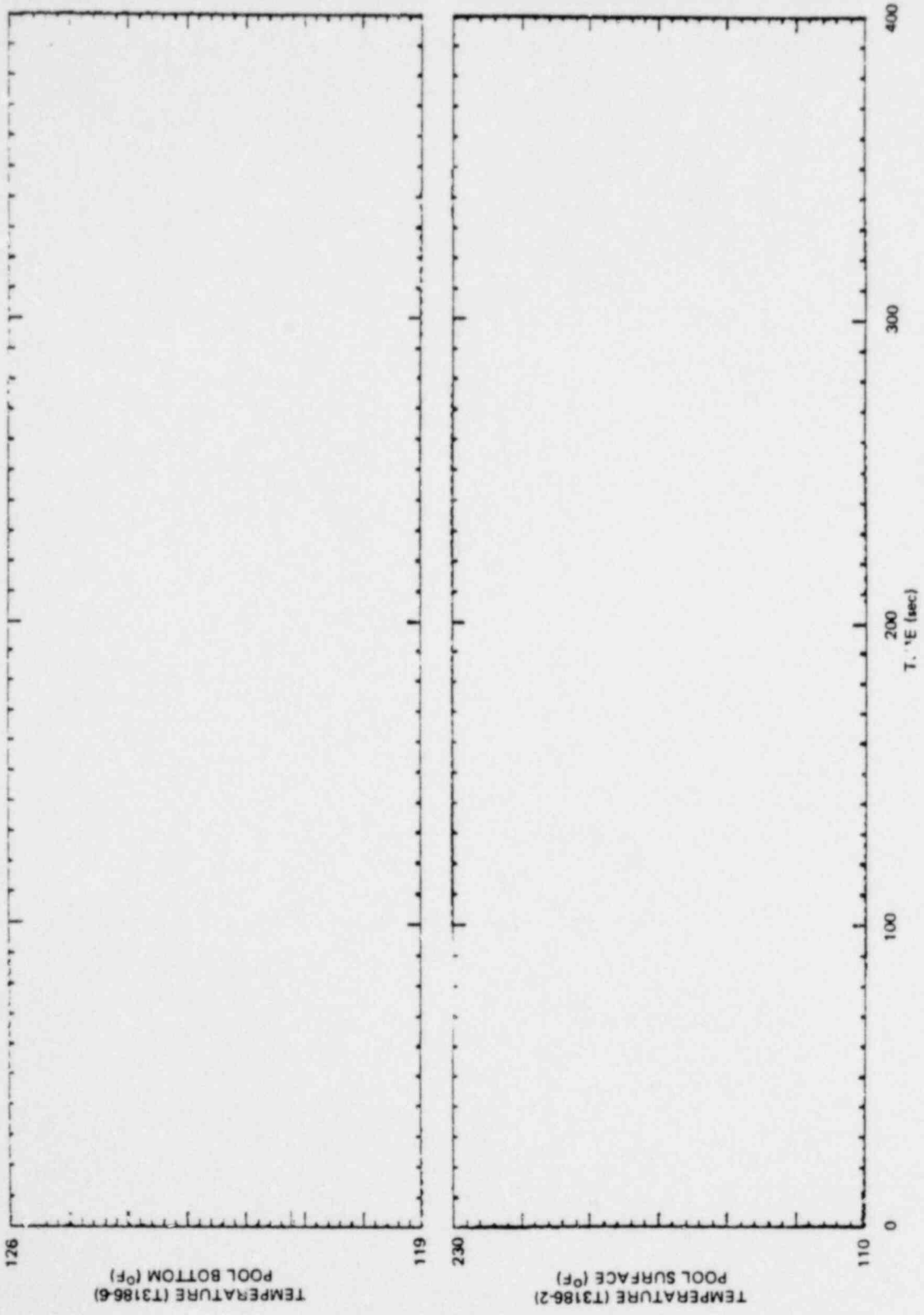

Figure C-68. Wetwell Suppression Pool Temperatures, Small Steam Break, M6

*Proprietary information deleted

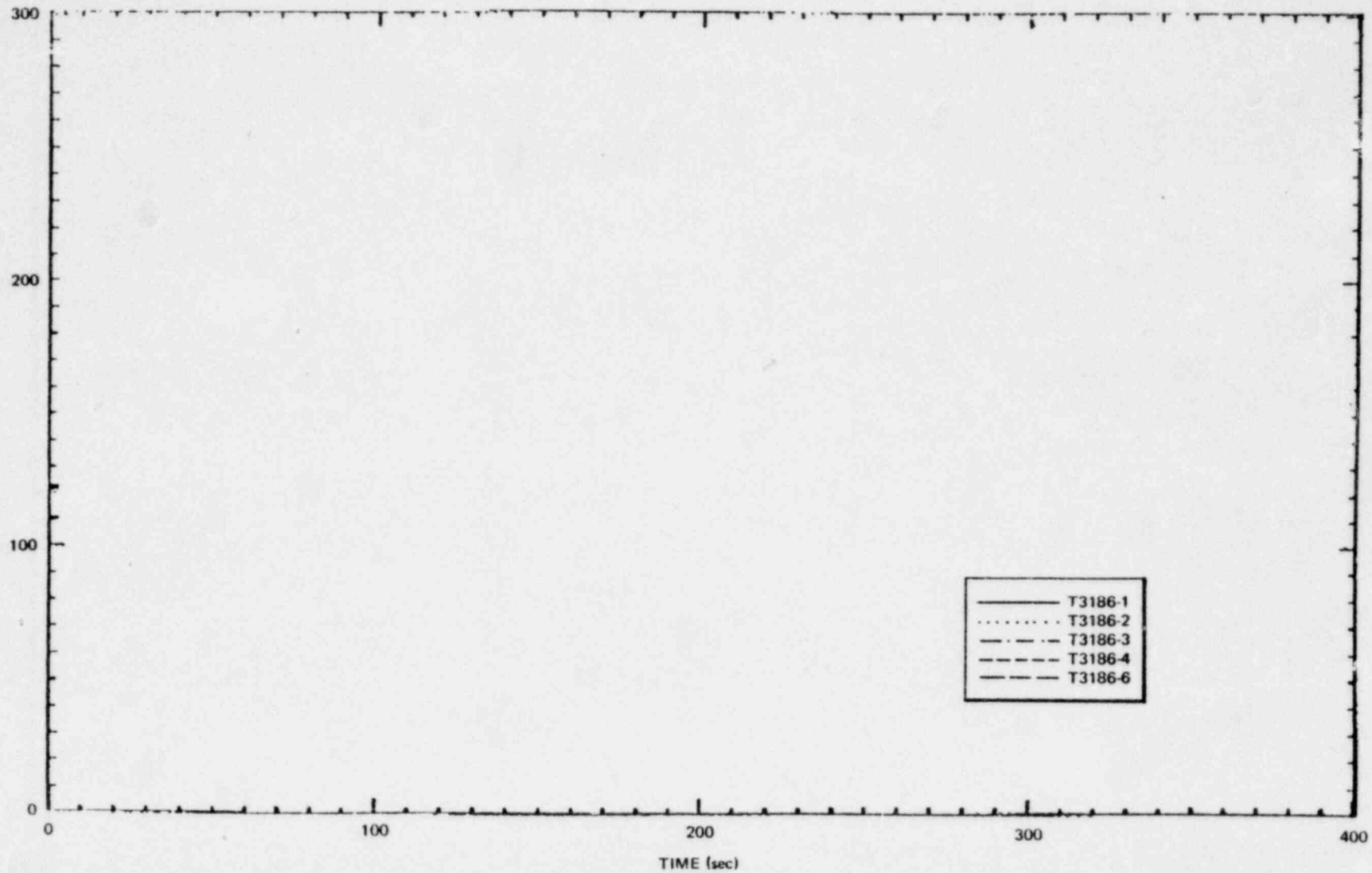

Figure C-69. Comparison of Pool Axial Temperatures, Midbay, Small Steam Break, M6

*Proprietary information deleted

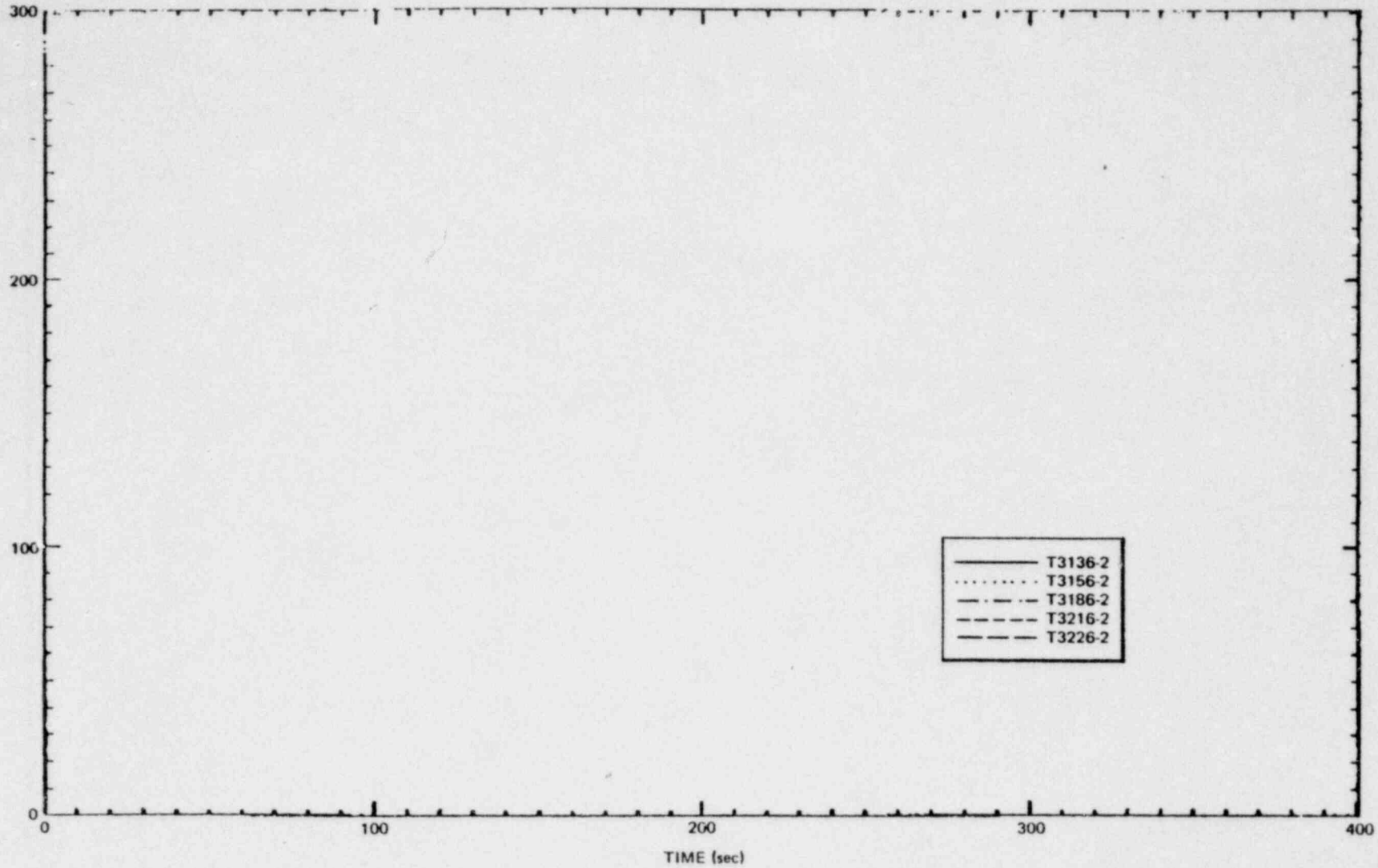

Figure C-70. Comparison of Pool Surface Temperatures, Small Steam Break, M6

*Proprietary information deleted

Table C-4

VACUUM BREAKER PERFORMANCE

Test No.	Number of Times Opened	Test Period When Lifting	Post Test Condition
M1*	>15	Duration of test (probable)	Pallet hinge bent and magnet broken Pallet position indicator failed Gasket damaged
M2	∿15	5 to 66 sec.	Magnet loosened and pallet did not close
M3	1	Immediately after test initiation	No damage
M4	>75	5 to 110 sec.	Gasket damaged (torn at 10 and 1 o'clock) Pallet misaligned
M5	1	Immediately after test initiation	No damage
M6	1	Immediately after test initiation	Gasket indented
M9	∿30	10 to 100 sec. at 210 sec. at 305 sec.	Gasket damaged (torn at 9, 10, and 1 o'clock)
M10		No Vacuum Breaker	
M7	∿20	40 to 70 sec.	No damage
M8	0	---	No damage

* For this test pallet was set to open at 0.2 psid, for all other tests pallet was set to open at 0.1 psid.

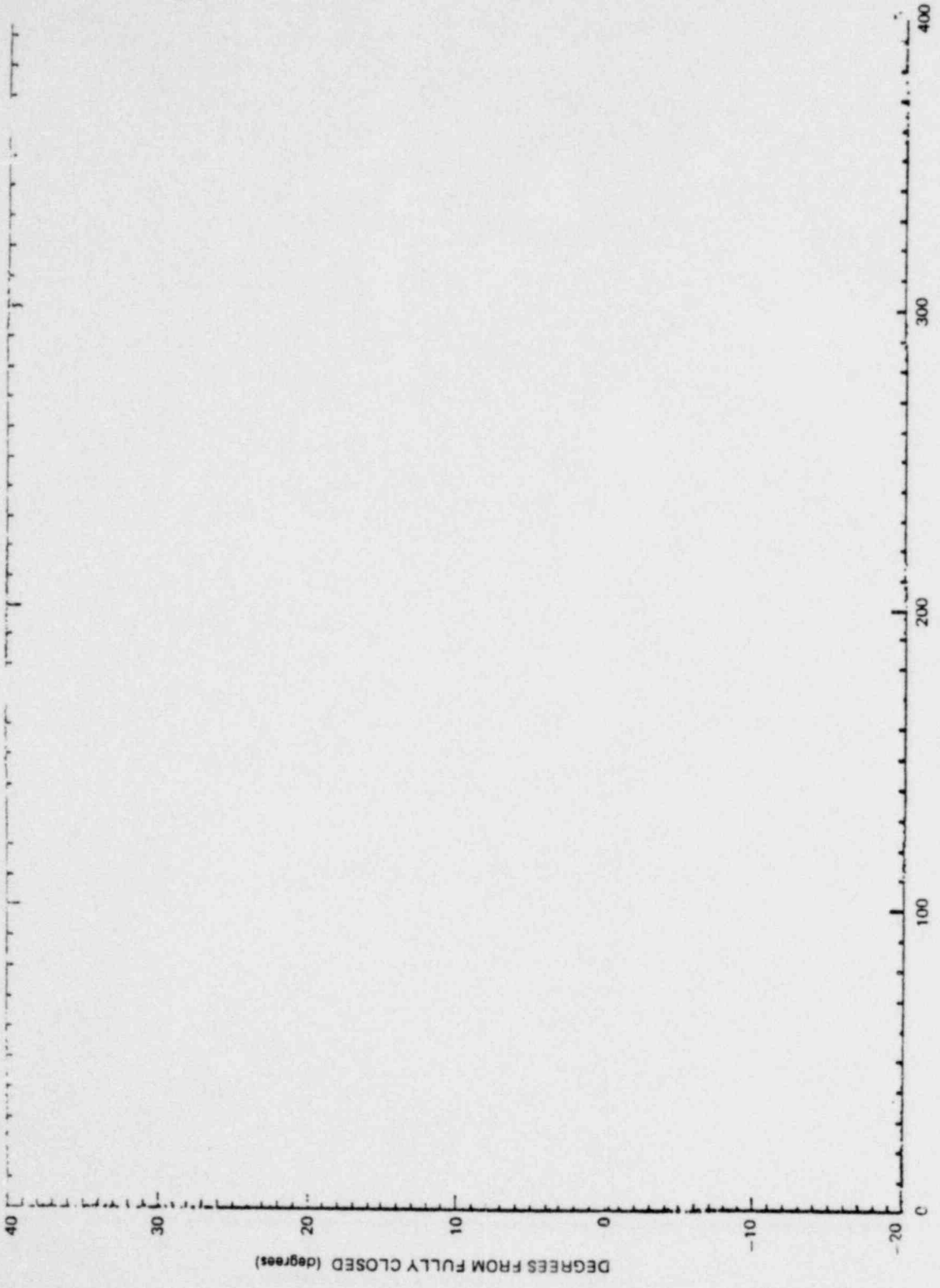

Figure C-71. Vacuum Breaker Pallet Position, Small Steam Break, M1

*Proprietary information deleted

For test M1 the vacuum breaker pallet was instrumented with a continuous indicating potentiometer which would directly indicate the degrees open, as shown in Figure C-71. This figure shows about a 25 degree opening at about 20 seconds and zero shifts in the indicator starting at about 70 seconds. After this time the instrument failed. After this test, because of failure of the potentiometer, position switches were used for more reliable position indication. Figure C-72 shows a typical trace with the pallet lifting once at test initiation. Figure C-73 shows the vacuum breaker position trace for test M4. The vacuum breaker pallet was lifting up to 110 seconds. Figure C-74 shows an expanded time plot over the interval from 30 to 40 seconds for the same test. Figure C-75 also shows an expanded time plot (30 to 40 seconds) of the differential pressure transducer across the vacuum breaker restriction plate for test M4. From Figure C-74, it can be inferred that the vacuum breaker pallet went only slightly past the 3 degree position. From these results, which are typical for all tests other than M1, it is concluded that M1 was the only test in this series which had full open vacuum breaker pallet opening.

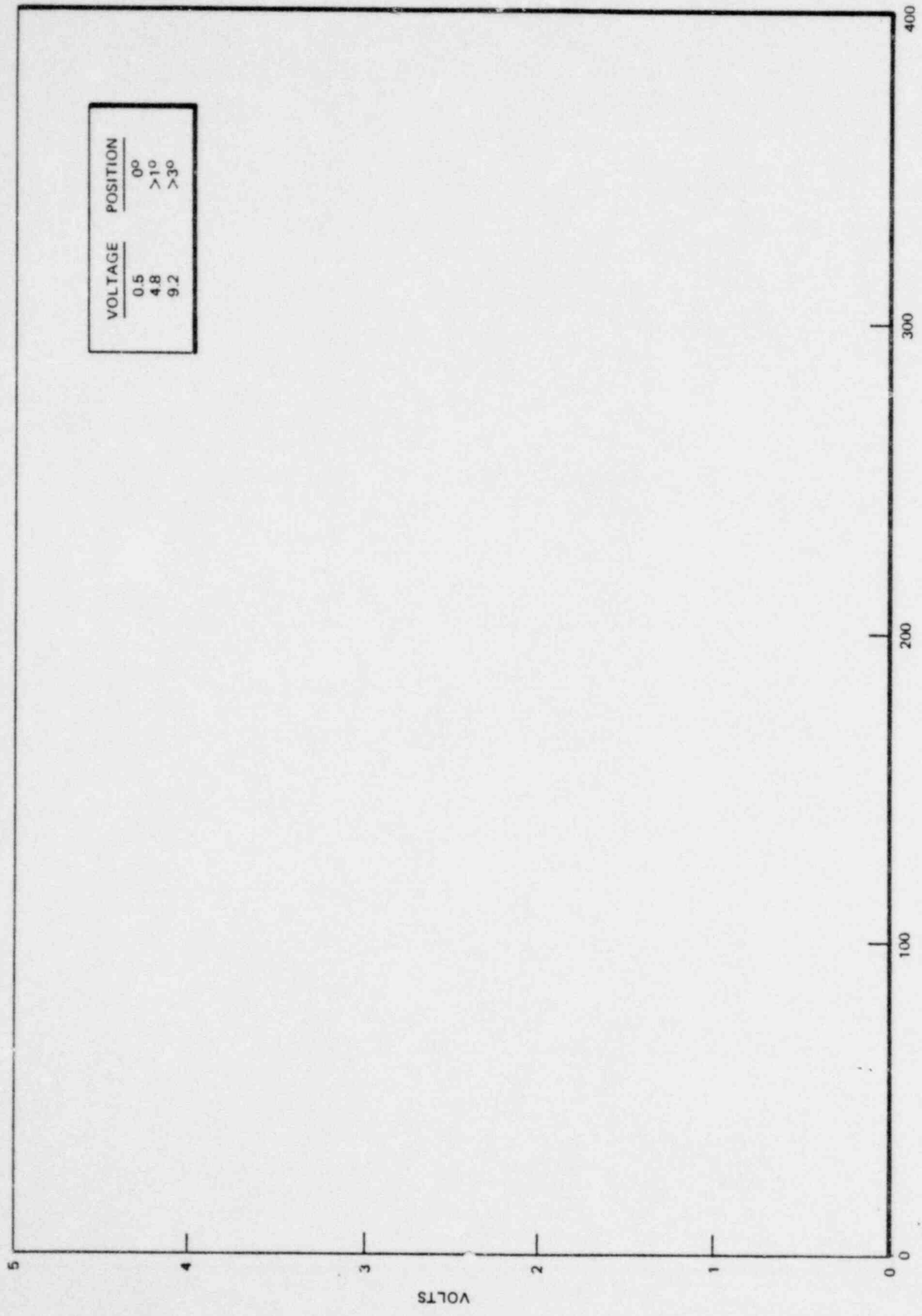

Figure C-72. Vacuum Breaker Pallet Position, Small Steam Break, M6

*Proprietary information deleted

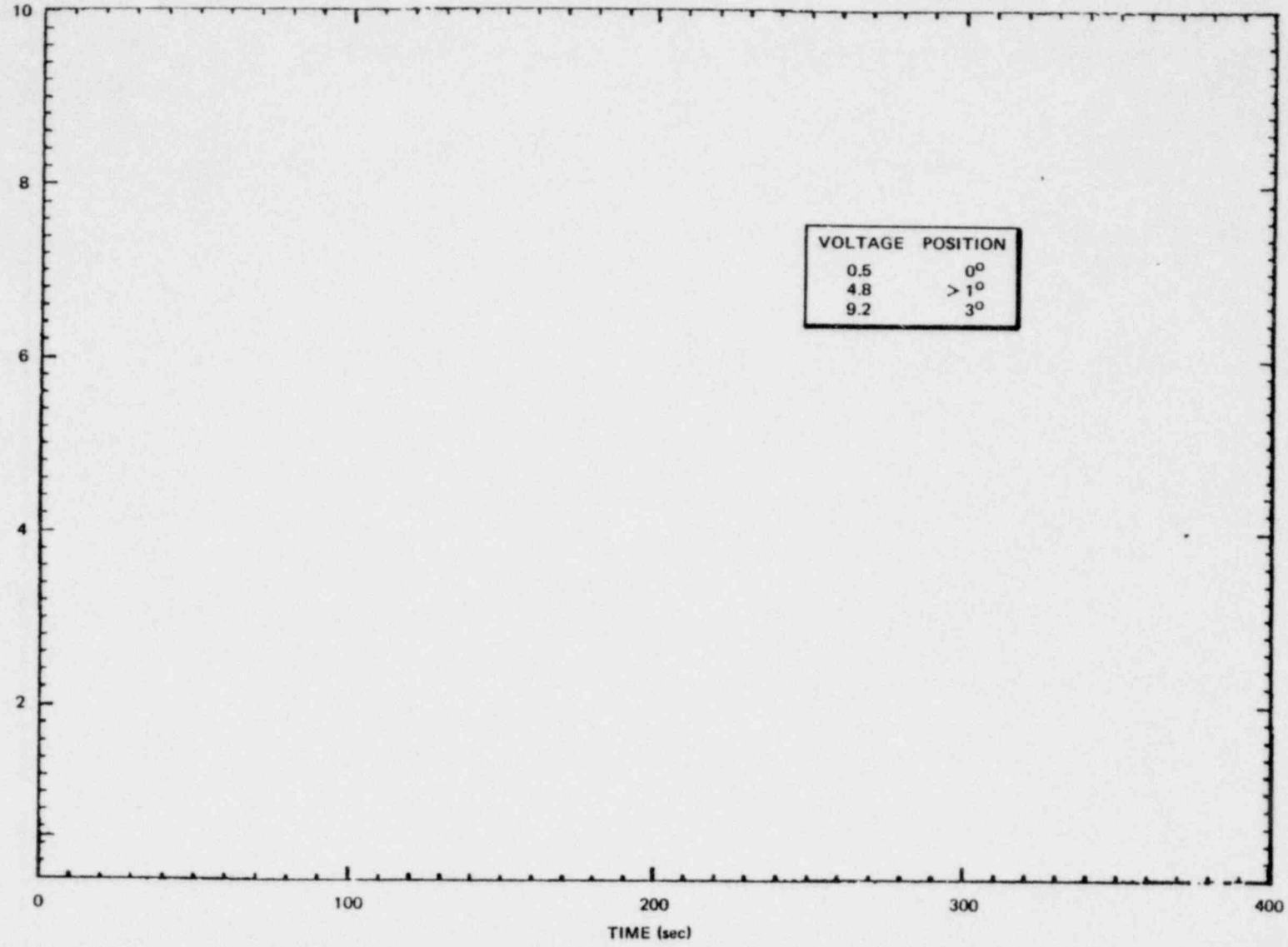

Figure C-73. Vacuum Breaker Pallet Position, Small Steam Break, M4

*Proprietary information deleted

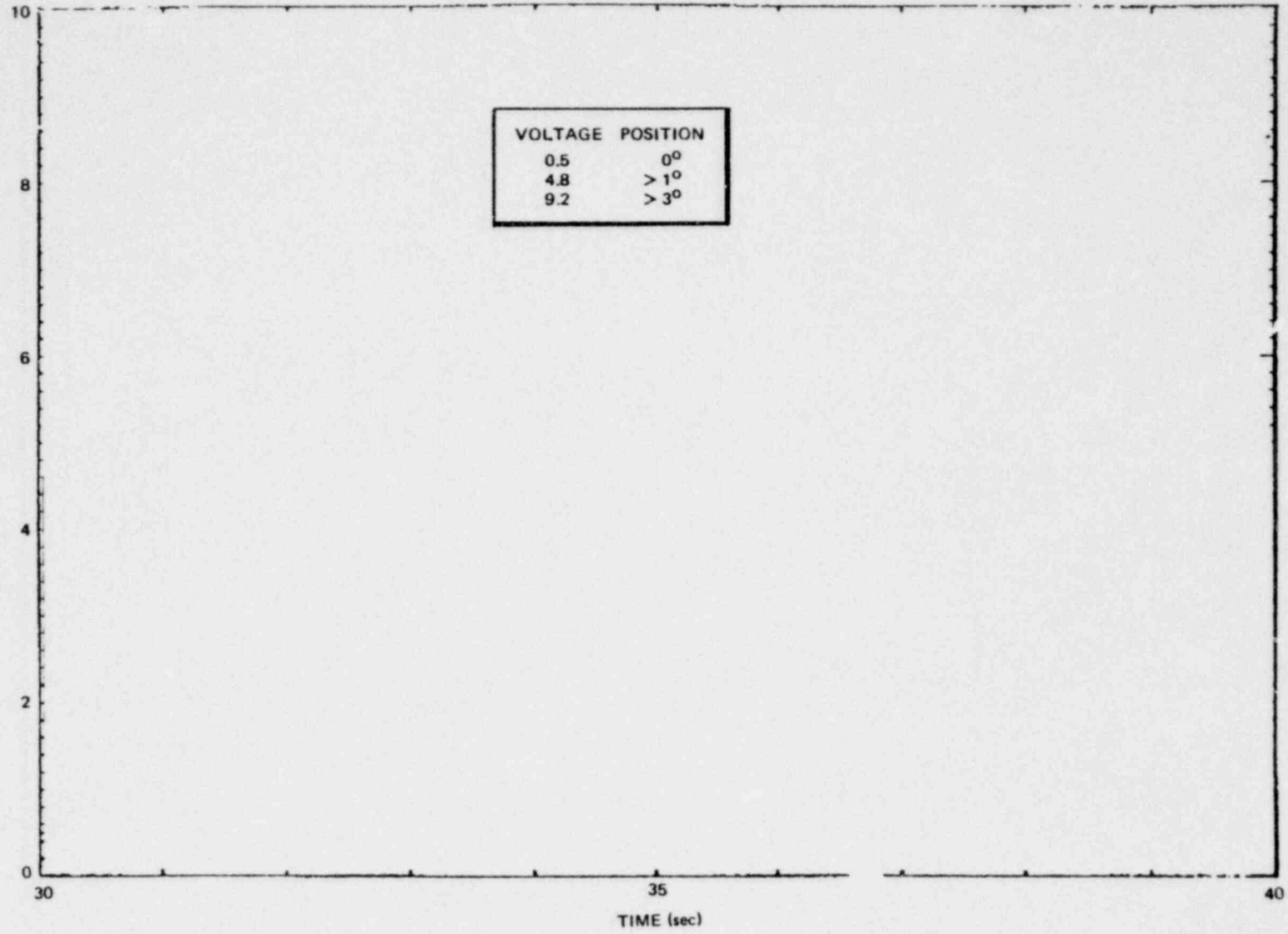

Figure C-74. Vacuum Breaker Pallet Position, Expanded Time Scale, Small Steam Break, M4

*Proprietary information deleted

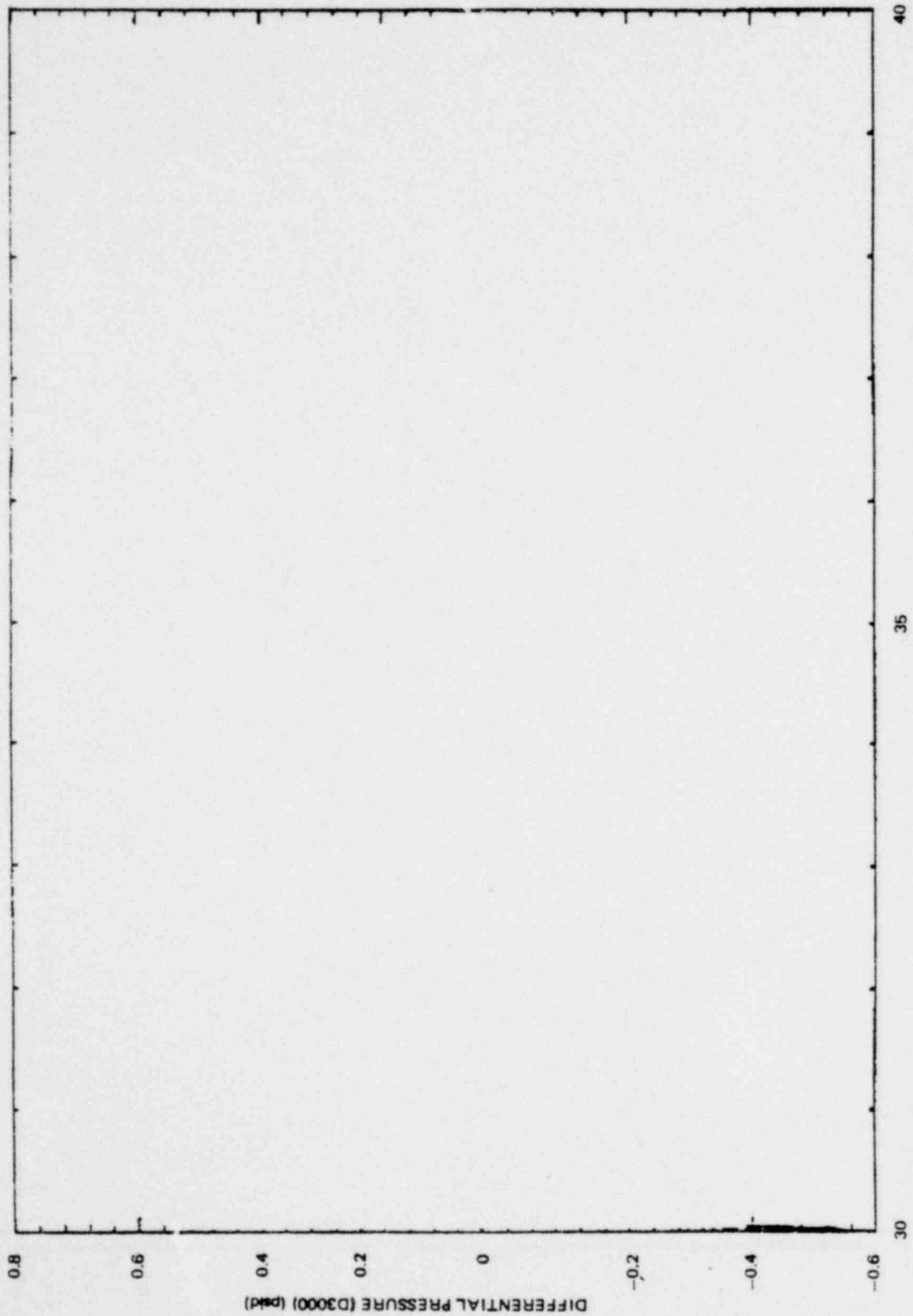

Figure C-75. Vacuum Breaker Restrictor Orifice, ΔP Small Steam Break, M4

*Proprietary information deleted

APPENDIX D
WETWELL STRUCTURAL DYNAMICS TESTS

D.1 DYNAMIC TESTS AND ACQUIRED DATA

Controlled dynamic excitation was applied to the wetwell and the response was measured at several locations on the wetwell.* This section discusses the details of the excitation technique, magnitude and range. The measurement locations are listed. A brief discussion of the data acquisition procedure is included.

Figure D-1 is a schematic of the excitation technique. A hydraulic ram (shaker) driven by a programmable controller attached to location 3185 (bottom, midpoint of wetwell) was used to apply the excitation. The shaker was controlled by a closed loop control system and acceleration, force or displacement was used for feedback. The dynamic frequency sweep range of shaker was between 3 and 30 Hz for these tests. Manual or programmed frequency sweep was performed.

The data acquisition system consisted of 74 transducers (see Table D-1) linked to the FSTF computerized data acquisition system. A sample rate of 900 samples/sec/channel for a period of 600 (or more) seconds was used in a typical frequency sweep run. In case of the steady state dwell tests, the computer acquisition was run for approximately 5 seconds to collect data for that frequency point.

A sweep test was run under automatic sweep generator in the range of 3 to 30 Hz at a rate of 1/2 octave/minute. When the shaker system was stabilized at 3 Hz at the desired displacement or acceleration level, the data acquisition was started. A few seconds later the sweep was started. The total test time for a run was approximately four minutes. When the displacement approached the 0.2" limit, the shaker was controlled by displacement to limit the displacement to 0.2". However, when the displacement was lower, the system was controlled by acceleration. Therefore, in a typical test, the frequency sweep was displacement controlled in the

---

* These tests were conducted with the wetwell filled with water to the nominal value for downcomer submergence.

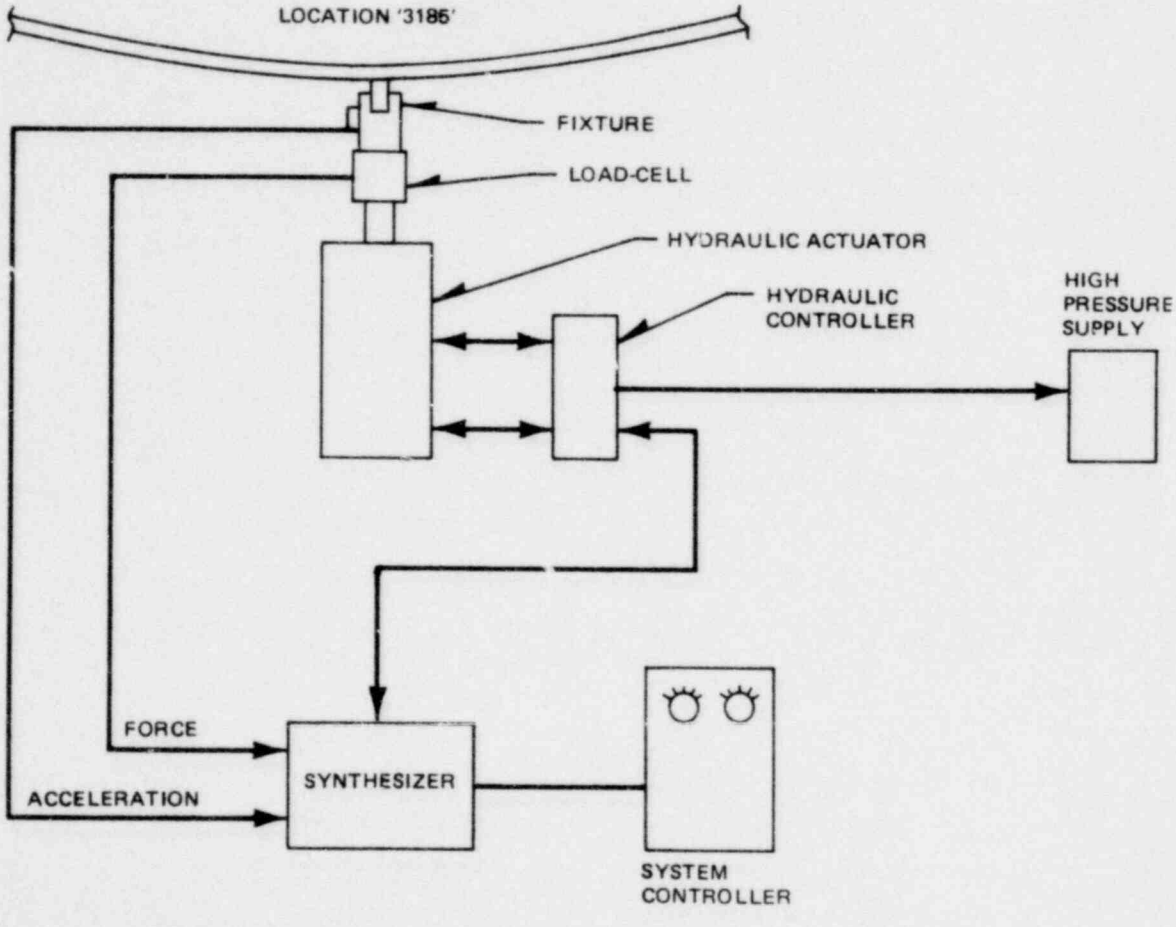

Figure D-1. Shaker Excitation Control System

Table D-1

LIST OF TRANSDUCERS*

1. HYDRAULIC RAM INSTRUMENTATION

Load Cell

Accelerometer

Linear Variable Displacement Transducer

2. WETWELL SHELL INSTRUMENTATION

Accelerometers

G 3005	G 3155	G 3185	G 3215
G 3095	G 3181	G 3187	G 3245
G 3125	G 3183	G 3189	G 3255

Linear Variable Displacement Transducers

X 3005	X 3155		X 3215
X 3095	X 3181	X 3187	X 3245
X 3125	X 3183	X 3189	X 3255

Pressure Transducers

P 3005	P 3155	P 3185	P 3215
P 3095	P 3181	P 3187	P 3245
P 3125	P 3183	P 3189	P 3255

Strain Gages

S 3005-4	S 3185-1	S 3189-1	S 3215-1
S 3005-5	S 3185-2	S 3189-2	S 3215-2
S 3095-4	S 3185-3	S 3189-3	S 3215-3
S 3095-5	S 4185-1	S 4189-1	S 4215-1
S 3125-4	S 4185-2	S 4189-2	S 4215-2
S 3125-5	S 4185-3	S 4189-3	S 4215-3
			S 3245-4
			S 3245-5

* Refer to subsection 3.4 for information on transducer locations.

Table D-1 (Continued)

LIST OF TRANSDUCERS

3. OTHER WETWELL INSTRUMENTATION

Downcomer Pressure Transducers

P 5443

P 5634

P 5644

Water Level Probes

L 3259-3

L 3259-4

L 5607

L 5608

low frequency range; i.e., 3 to 8 Hz, and switched to acceleration in the higher range (8 to 30 Hz). Table D-2 summarizes the various sweep test parameters.

Based upon the review of the sweep tests combined with stress and displacement limits, an acceleration level of 0.5g and a list of frequencies were selected. A review of plots from selected locations on the wetwell combined with forcing function plots indicated resonsnces near 7.5, 9.5, 11.0, 15., 17.5 and 19 Hz.

In the neighborhood of those selected lists of frequencies, steady state test data was collected. The shaker system was set at a selected frequency and data was collected after the system had reached steady state. For a typical frequency of 10 Hz with a model damping ratio of 3 per cent of critical, the steady state would be reached in a few seconds (i.e., in about 2 seconds the transients would be approximately 1%). Then the frequency was shifted to the next value and data was acquired. This procedure was repeated until all frequencies of interest were bracketed. Modal deformation shapes and eigenfrequencies were quantified by these data. Also model damping ratios were estimated from the reduced data.

Stress data was evaluated after each sweep to ensure that stresses did not exceed 15 ksi, nor displacement exceed 0.2 inches. The maximum strain time period was selected and a brief stress analysis was performed. It is inferred from the stress analysis that the stresses did not exceed 15 ksi. Examination of the displacement data for selected locations indicates that the displacement limit of 0.2" was not exceeded.

Table D-2

SUMMARY OF TEST PARAMETERS

Test No.	Frequency Range	Control Value	Comments
1	3 to 5 5 to 30	0.2" 0.1g	Displacement controlled; acceleration controlled at 1 octave/minute
2	3 to 5 5 to 30	0.2" 0.2g	Displacement controlled; acceleration controlled at 1 octave/minute
3	3 to 7 7 to 30	0.2" 0.4g	Displacement controlled; acceleration controlled at 1/2 octave/minute
4	3 to 8 8 to 30	0.2" 0.6g	Displacement controlled; acceleration controlled at 1/2 octave/minute; maximum stresses were approximately 8.5 ksi
5	3 to 20	0.5g	Steady state test; data acquired near selected frequencies only

D.2 EICENPARAMETERS OF WETWELL

This section discusses the dynamic parameters, eigenfrequencies, model deformation shapes and estimated model damping ratios of the wetwell. Based upon the sweep tests it was noted that there were resonances near 7.5, 9.5, 11., 15., 17.5 and 19 Hz. Higher frequency data were not investigated because of the limited scope of test. Therefore, data were acquired near these selected frequencies to quantify the dynamics.

Table D-3 enumerates the dynamic parameters. The eigenfrequency was estimated from the peak response frequency. The model deformation shape for that frequency was computed by normalizing the acceleration at the maximum acceleration point to unity and scaling all other points. The modal damping ratios were estimated using the halfpower bandwidth method. Figures D-2 through D-7 show the estimated mode shapes for the wetwell in the 3 to 20 Hz range. These figures are only intended to illustrate mode shapes and the displacements indicated are not scaled relative to the wetwell diameter.

Table D-3

SUMMARY OF EIGENPARAMETERS*

No.	Frequency Hz	Estimated Damping	Comments
1	7.4	4.2%	First observed mode of wetwell; 5 zero crossings in lower half of shell.
2	9.7	Not Calculated	Six zero crossings in lower half of wetwell
3	11.0	Not Calculated	Shell distortion about 240°
4	15.0	Not Calculated	
5	17.4	Not Calculated	Shell distortion about 120°
6	19.5	2.2%	

* Frequency estimate is ± 0.25 Hz; damping was estimated using half power bandwidth method and is an estimate of modal damping ratio; damping was estimated from G3215 and G3155; all mode shapes are based upon accelerometer data.

1158.354

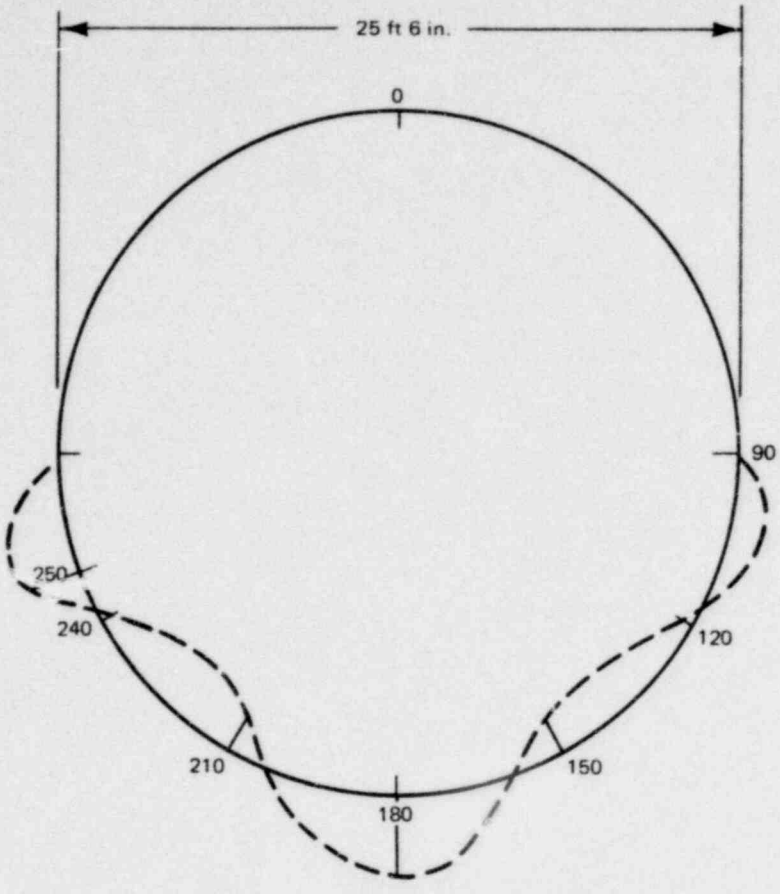

Figure D-2. Wetwell Mode Shape for 7.4 Hz

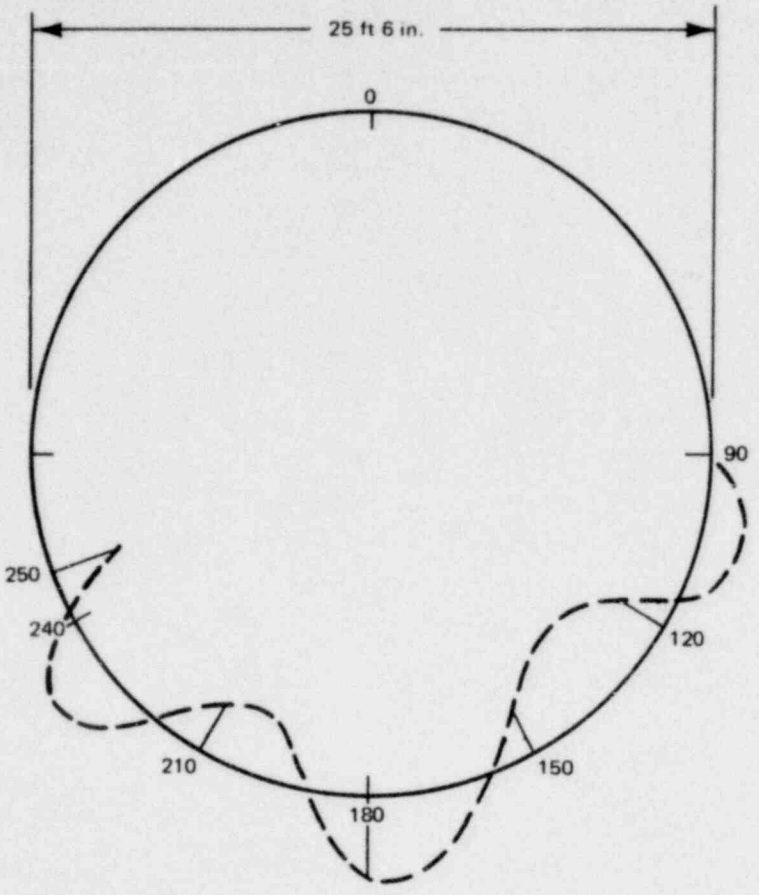

MODE SHAPE AT MIDBAY

MODE SHAPE ALONG WETWELL BOTTOM

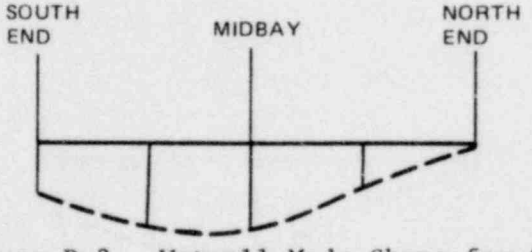

Figure D-3. Wetwell Mode Shape for 9.7 Hz

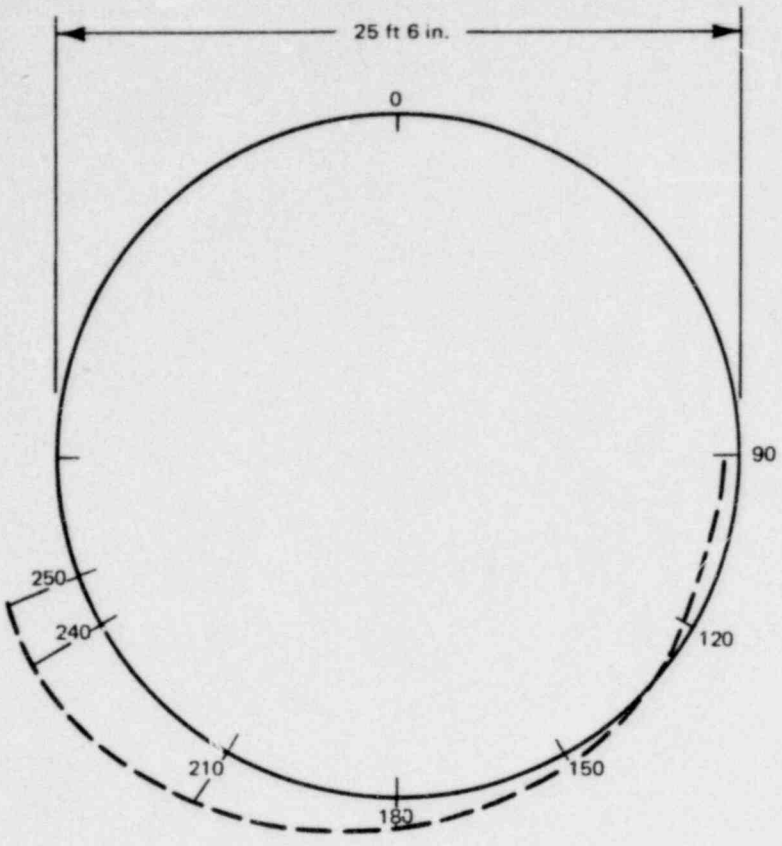

MODE SHAPE AT MIDBAY

MODE SHAPE ALONG WETWELL BOTTOM

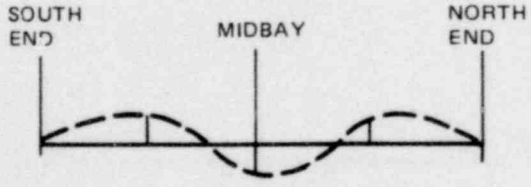

Figure D-4. Wetwell Mode Shape for 11.0 Hz

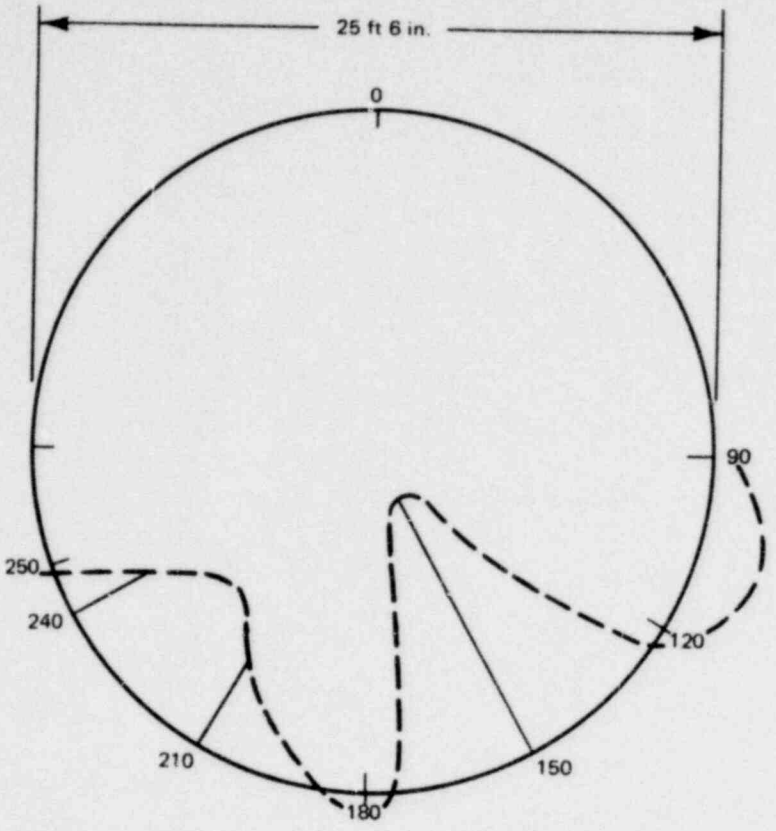

Figure D-5. Wetwell Mode Shape for 15.0 Hz

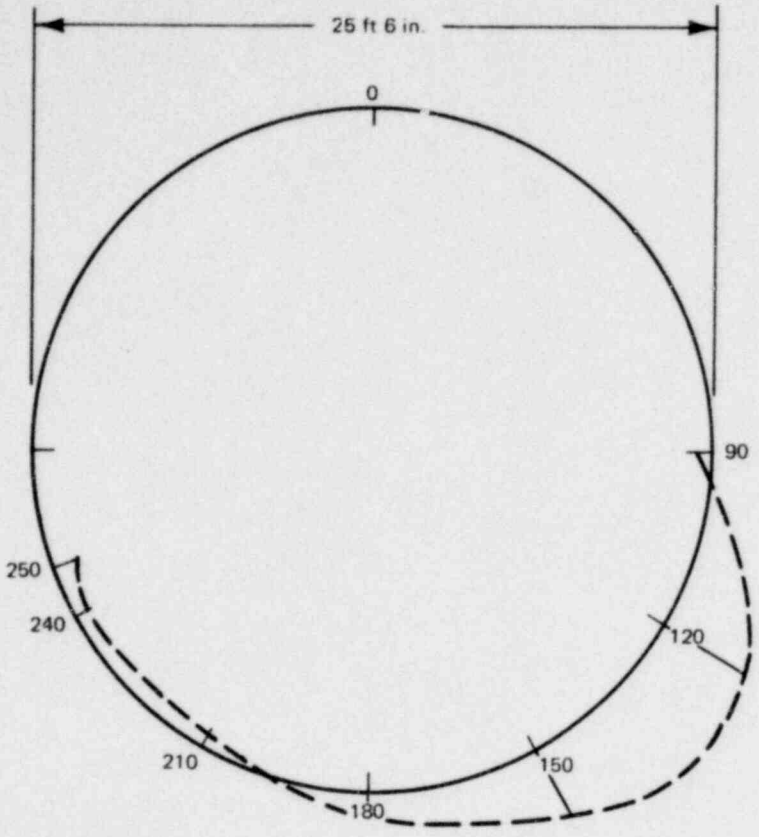

MODE SHAPE AT MIDBAY

MODE SHAPE ALONG WETWELL BOTTOM

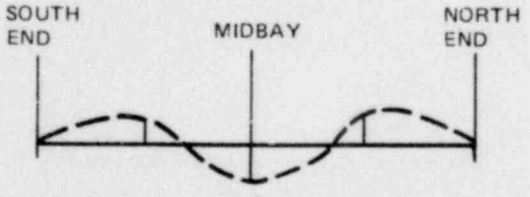

Figure D-6. Wetwell Mode Shape for 17.4 Hz

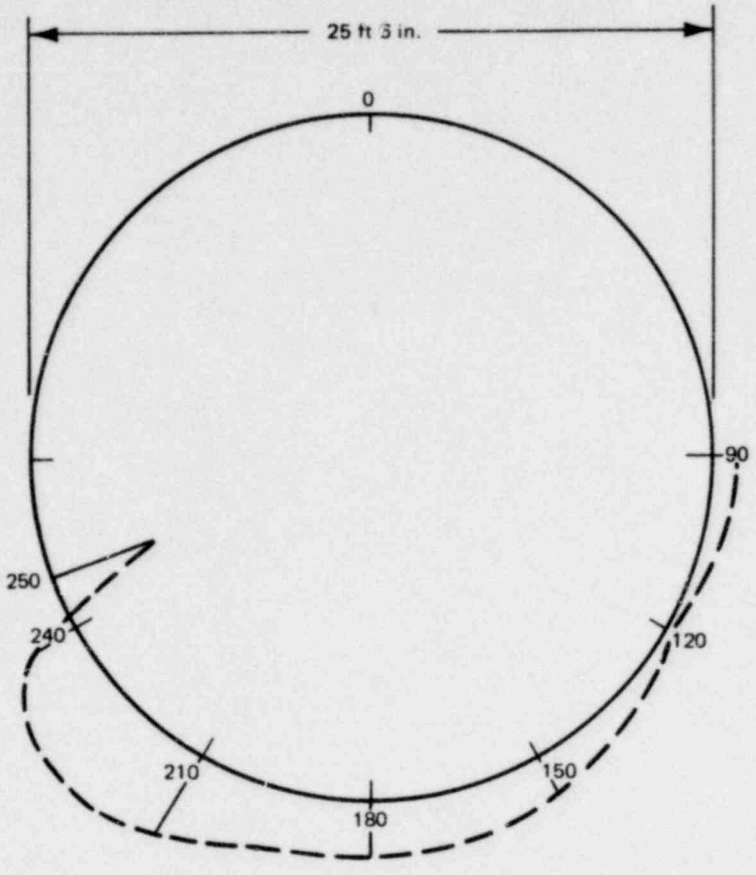

MODE SHAPE AT MIDBAY

MODE SHAPE ALONG WETWELL BOTTOM

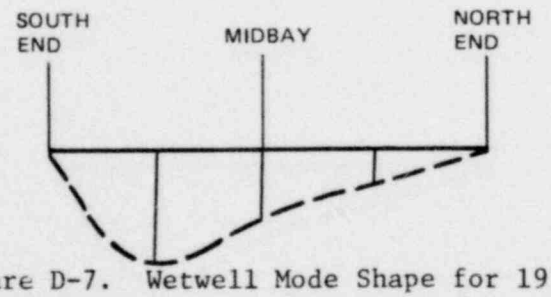

Figure D-7. Wetwell Mode Shape for 19.5 Hz

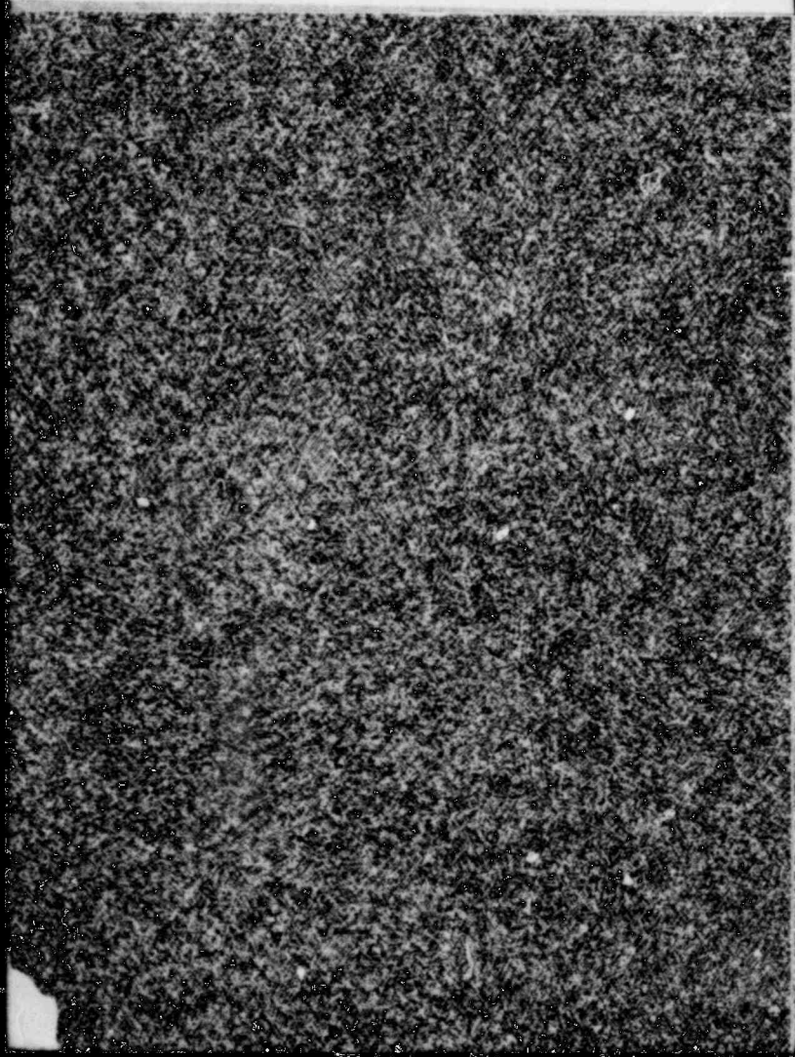

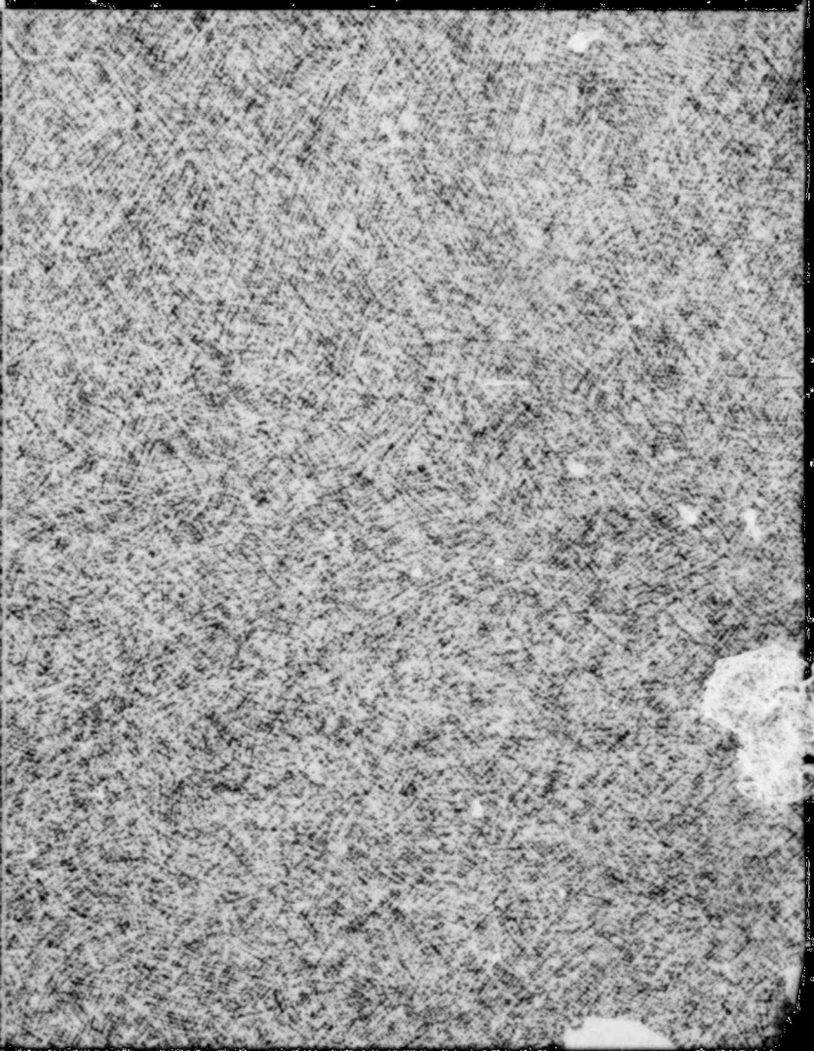

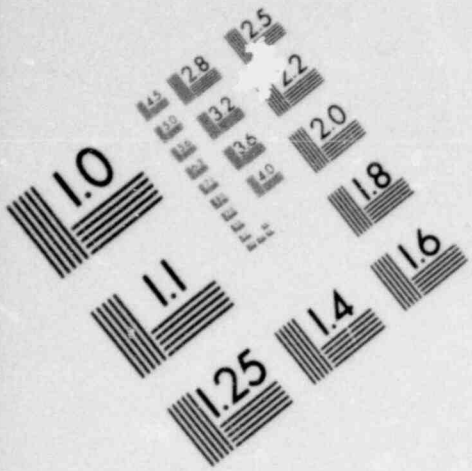

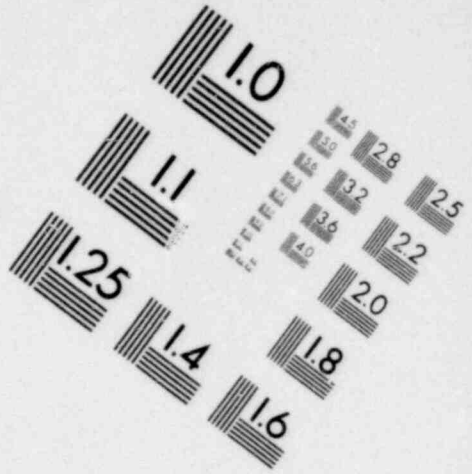

IMAGE EVALUATION TEST TARGET (MT-3)

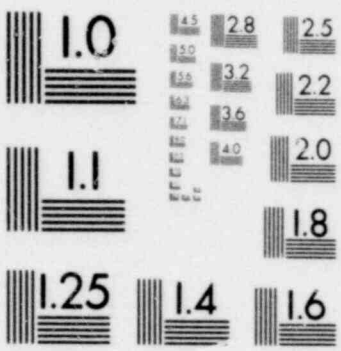

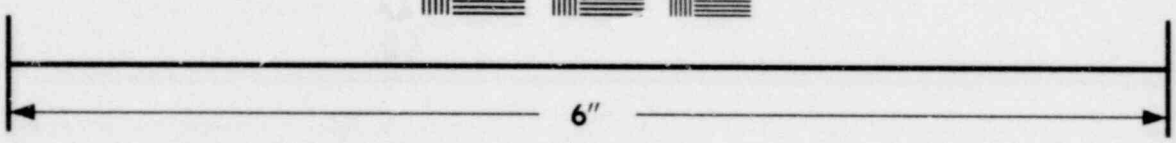

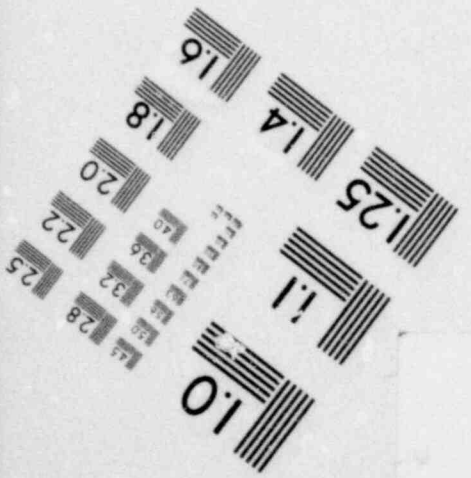

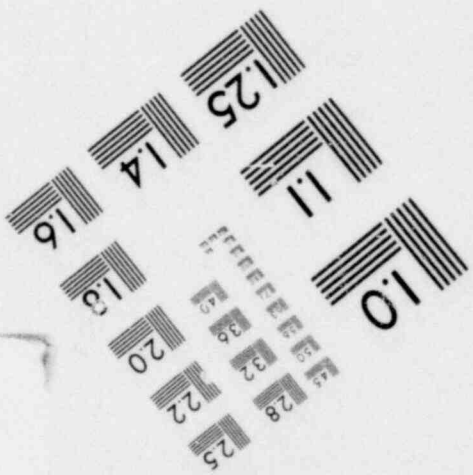

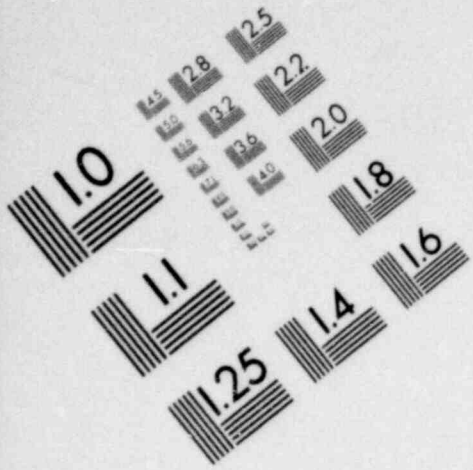

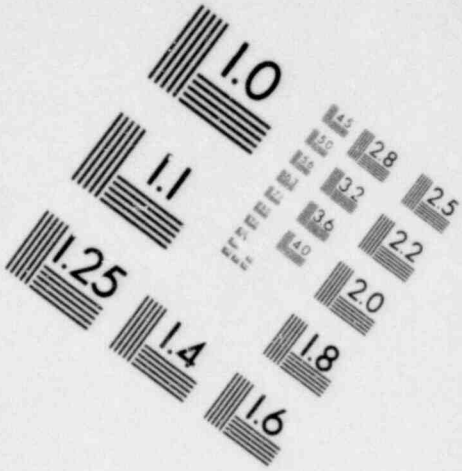

IMAGE EVALUATION TEST TARGET (MT-3)

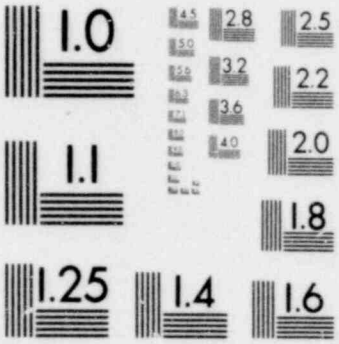

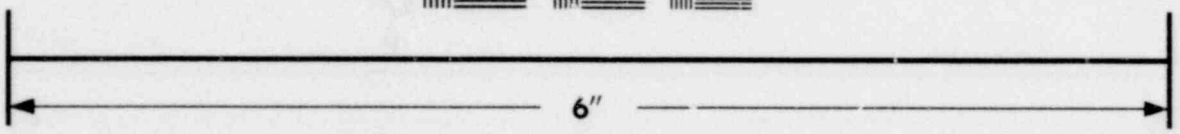

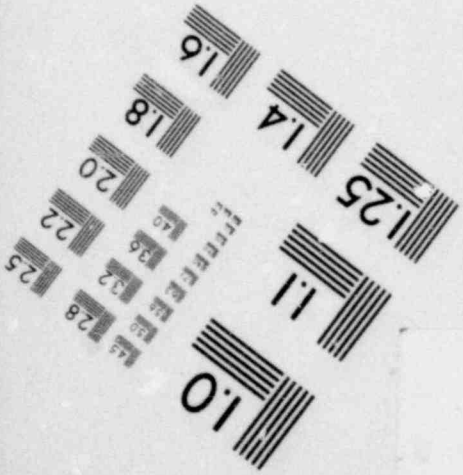

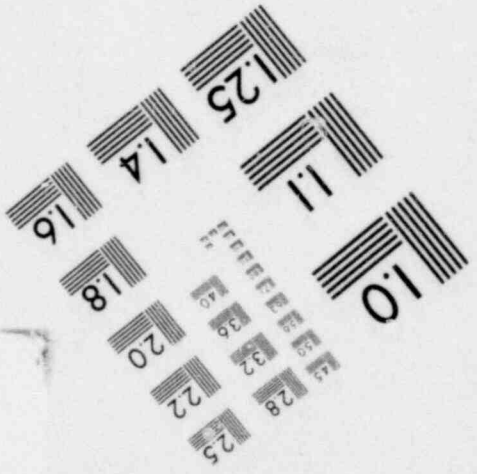

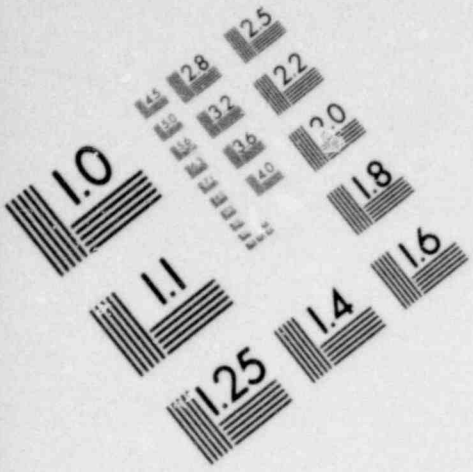

IMAGE EVALUATION TEST TARGET (MT-3)

APPENDIX E

VENT SYSTEM PRESSURE RESPONSE AT TEST INITIATION

APPENDIX E

Vent System Pressure Response at Test Initiation

Pressures in the drywell and vent system rose sharply just after initiation of the medium steam break test. The pressure rises were caused by a shock wave introduced by the rupture disc test initiation scheme and the large blowdown line configuration. The rupture disc assembly, located downstream of the nozzle used to establish the blowdown flow rate, discharges into a long riser pipe. As shown in Section 6.5 of Reference E-1, this test configuration is non-prototypical.

Representative pressure time histories for locations in the drywell, vent arms, vent header and downcomers are shown in Figures E-1 through E-6. The general location for each pressure transducer is indicated in the figures. Precise locations are identified in Subsection 3.4. Note that time zero corresponds to the start of data acquisition, not test initiation time (4.5 seconds based on the drywell pressure). At each location, in the drywell and throughout the vent system, the initial pressure response is characterized by an almost instanteous rise in pressure. It is apparent that this pressure "jump" propagates from the drywell through the vent system. The time delay between when the pressure "jump" occurs in the drywell and when it occurs in the vent header implies an acoustic velocity of about 1,300 ft/sec, which is very near the acoustic velocity for air of 1,320 ft/sec at the drywell initial conditions (atmospheric pressure and 300°F). Hence, the rupturing of the double disc blowdown valve apparently generates a pressure shock that travels through the drywell and vent system.

The pressure shock also propagates through the pool to the wetwell wall, as shown in Figure E-7. This figure shows the wall pressure directly beneath downcomer No. 6 during the time just following initiation of the medium steam break test. Comparison of the magnitudes of the initial pressure peaks observed in downcomer No. 6 and at the wetwell wall beneath downcomer No. 6 suggests that the pressure shock amplitude is attenuated by about 50% at the pool bottom.

Prior to conducting the large steam break test, perforations were drilled in the drywell riser pipe (this pipe is an extension of the large blowdown line which enters the drywell at the bottom and discharges the blowdown flow near the top of the drywell - see Subsection 3.3). These perforations served to reduce the magnitude of the pressure shock. Example drywell and downcomer pressure transients are presented in Figures E-8 and E-9. Comparison of the downcomer pressures for the medium and large steam break tests (Figures E-6 and E-9) indicates that the initial pressure jump is nearly the same for both tests (10 psi). Since the pressure shock strength is a direct function of the break area* and the break area for the large steam break is about twice that for the medium steam break, it can be inferred that the perforations in the riser pipe halved the strength of the pressure shock wave.

The only other test in which a pressure shock wave was observed was the large liquid break test. The drywell riser pipe was perforated for this test also. Although this test had the largest break area, the strength of the pressure shock was less than for the medium and large steam break tests. This can be seen by comparing drywell and downcomer pressures for the medium steam, large steam and large liquid break test. The drywell and downcomer pressure time histories for the large liquid break test are presented in Figures E-10 and E-11, respectively. Note that for the large liquid break test, the initial pressure rise observed in the drywell and downcomers is only about half that observed at the same locations for the medium and large steam break tests. Liquid carryover may account for this result.

*The pressure shock strength is also a function of the back pressure. However, all tests were run with the same vessel pressure so that the pressure shock strength is reduced to being a function of initial mass flow rate.

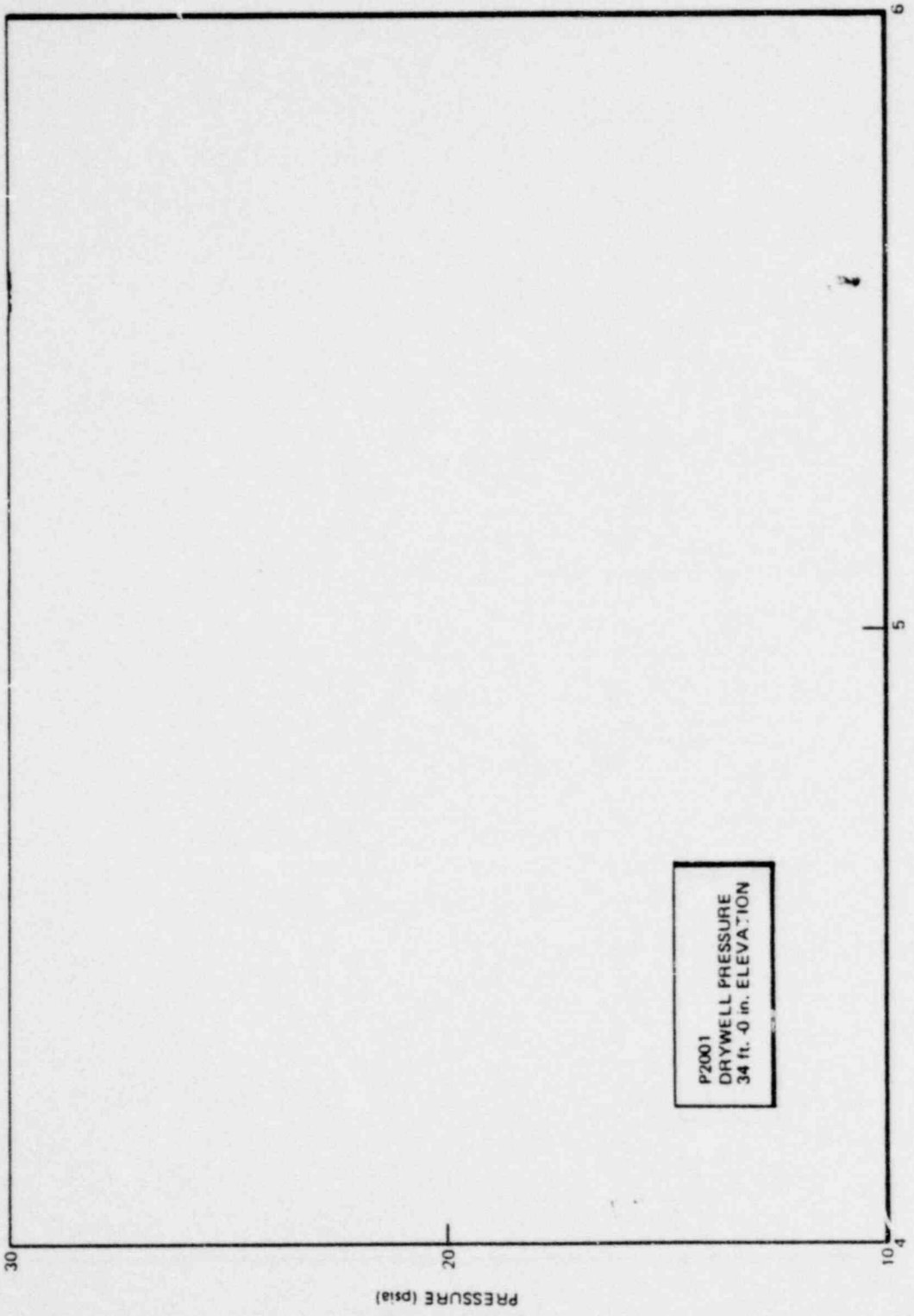

Figure E-1. Pressure Response in the Drywell at Test Initiation (Medium Steam Break Test - M2)

*Proprietary information deleted

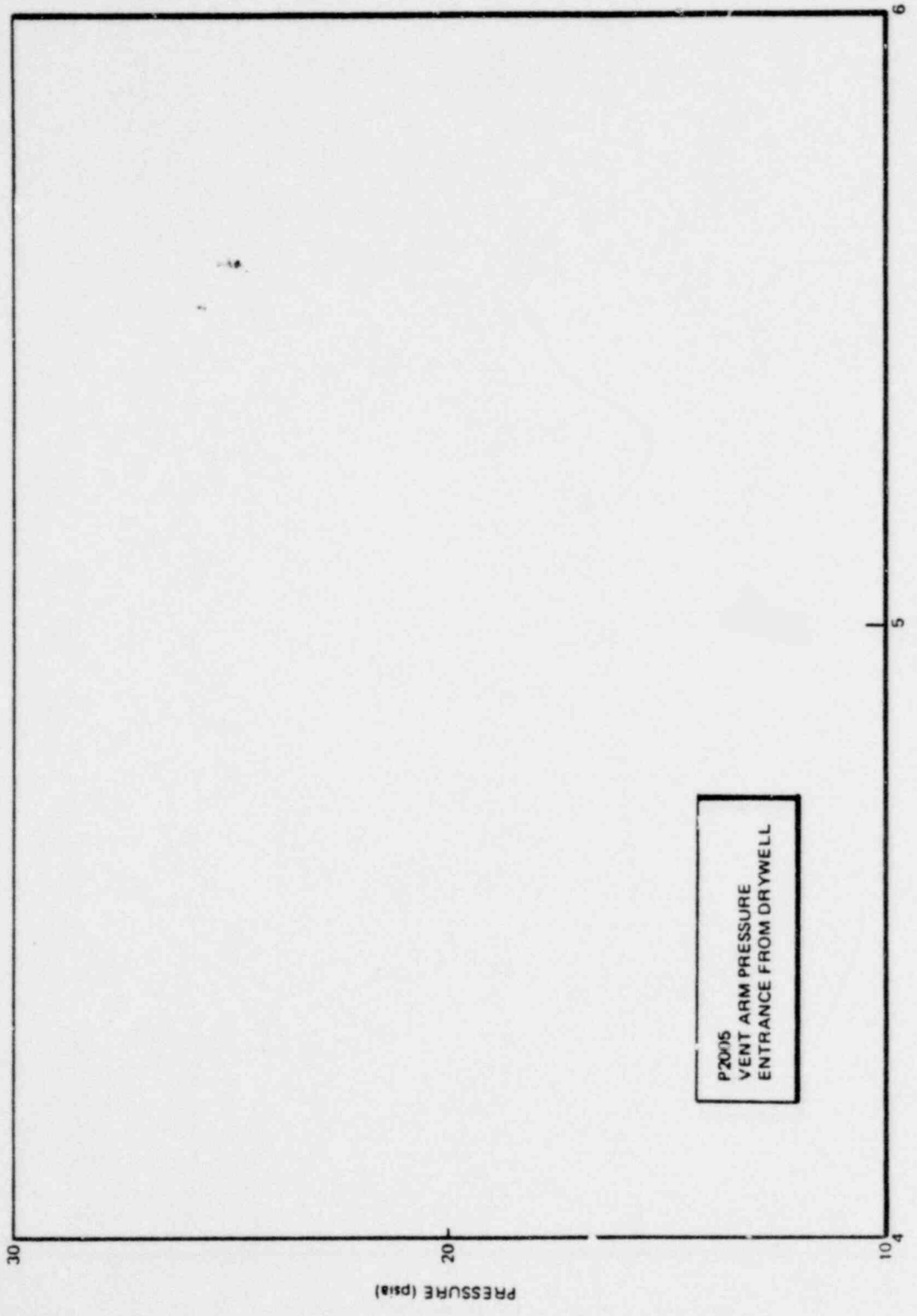

Figure E-2. Pressure Response in the Vent Arms (Entrance) at Test Initiation (Medium Steam Break Test - M2)

*Proprietary information deleted

1159 005

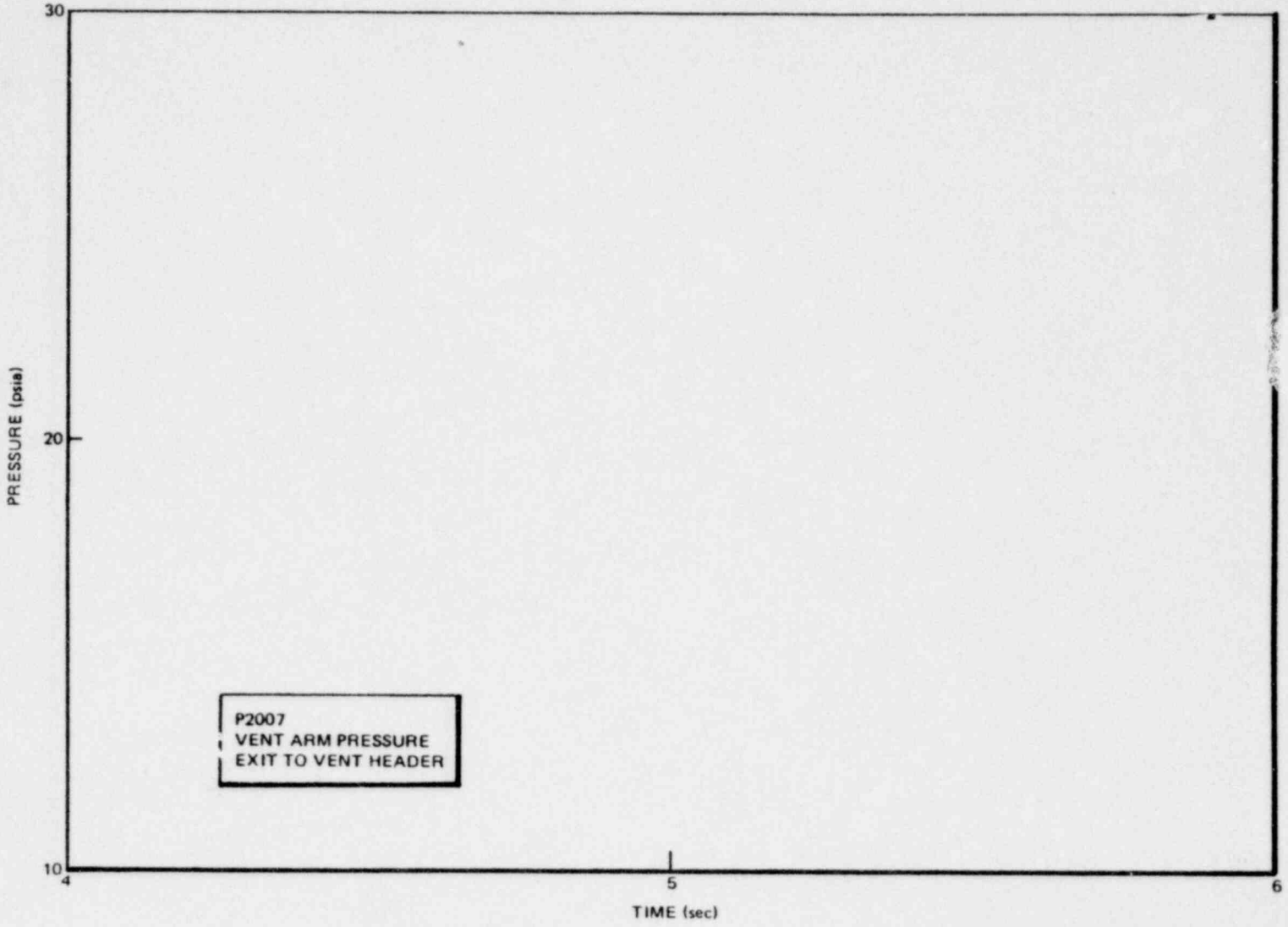

Figure E-3. Pressure Response in the Vent Arms (Exit) at Test Initiation (Medium Steam Break Test - M2)

*Proprietary information deleted

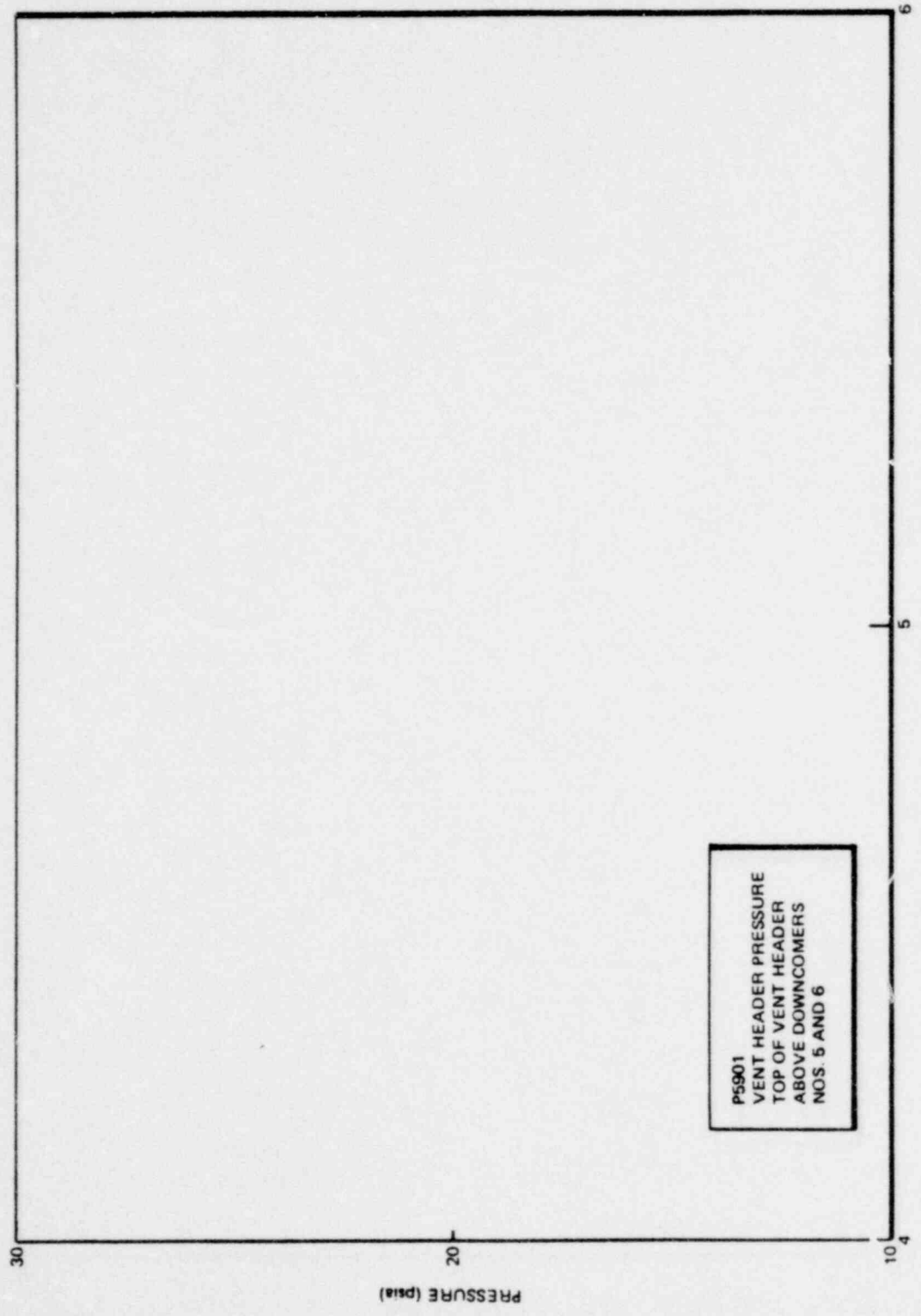

Figure E-4. Pressure Response in the Vent Header at Test Initiation (Medium Steam Break Test - M2)

*Proprietary information deleted

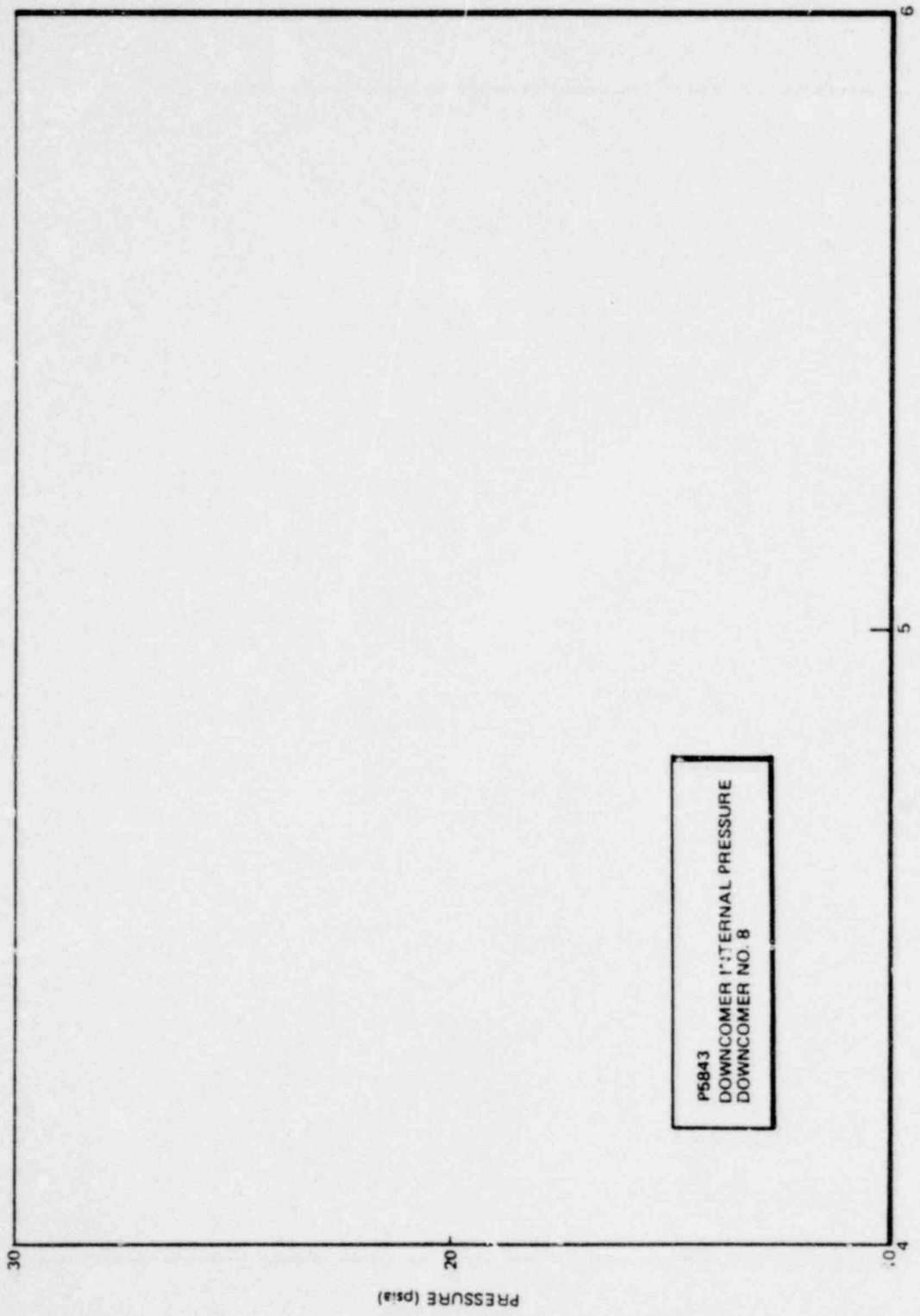

Figure E-5. Pressure Response in Downcomer No. 8 at Test Initiation (Medium Steam Break Test - M2)

*Proprietary information deleted

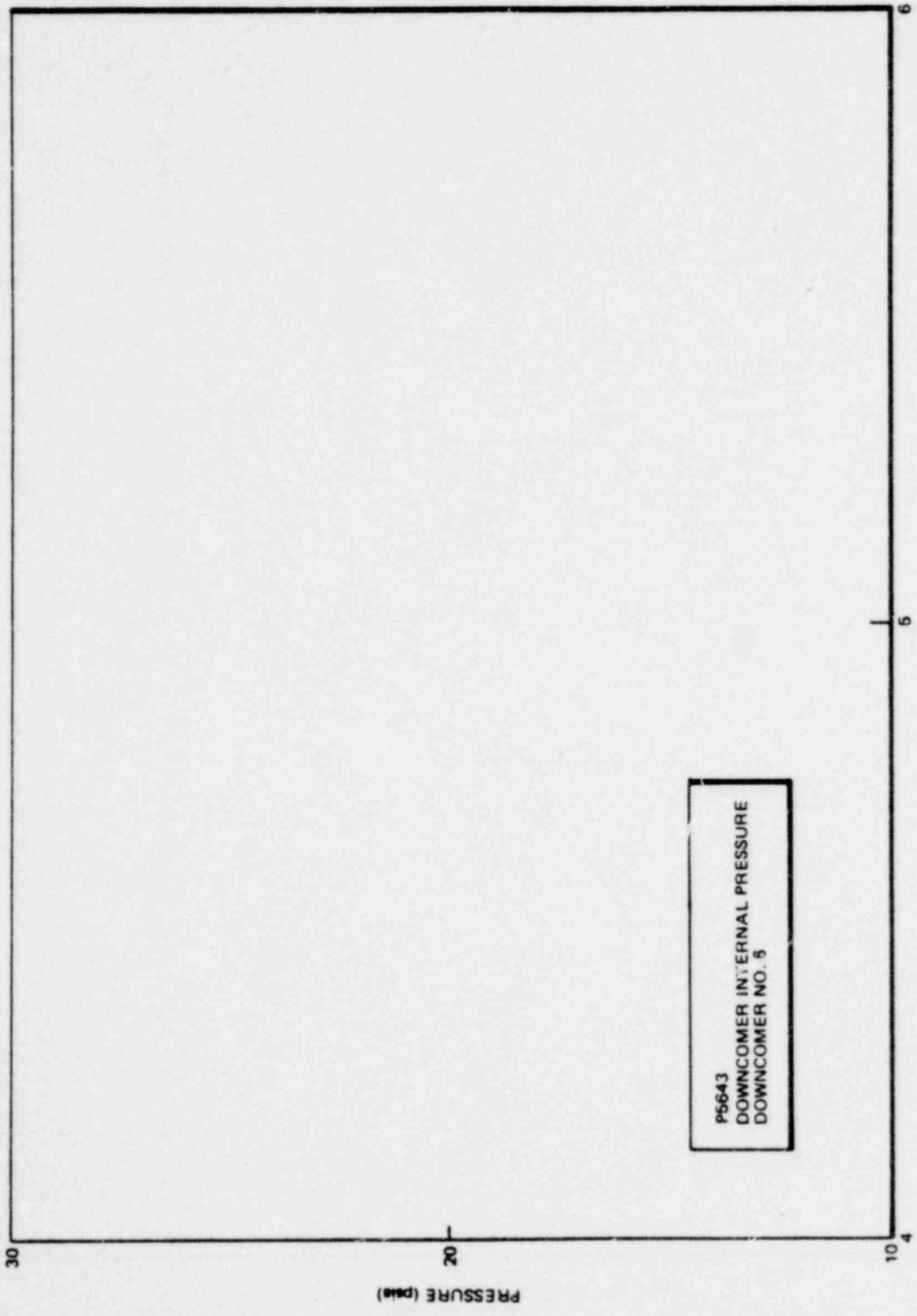

Figure E-6. Pressure Response in Downcomer No. 6 at Test Initiation (Medium Steam Break Test - M2)

*Proprietary information deleted

1159 009

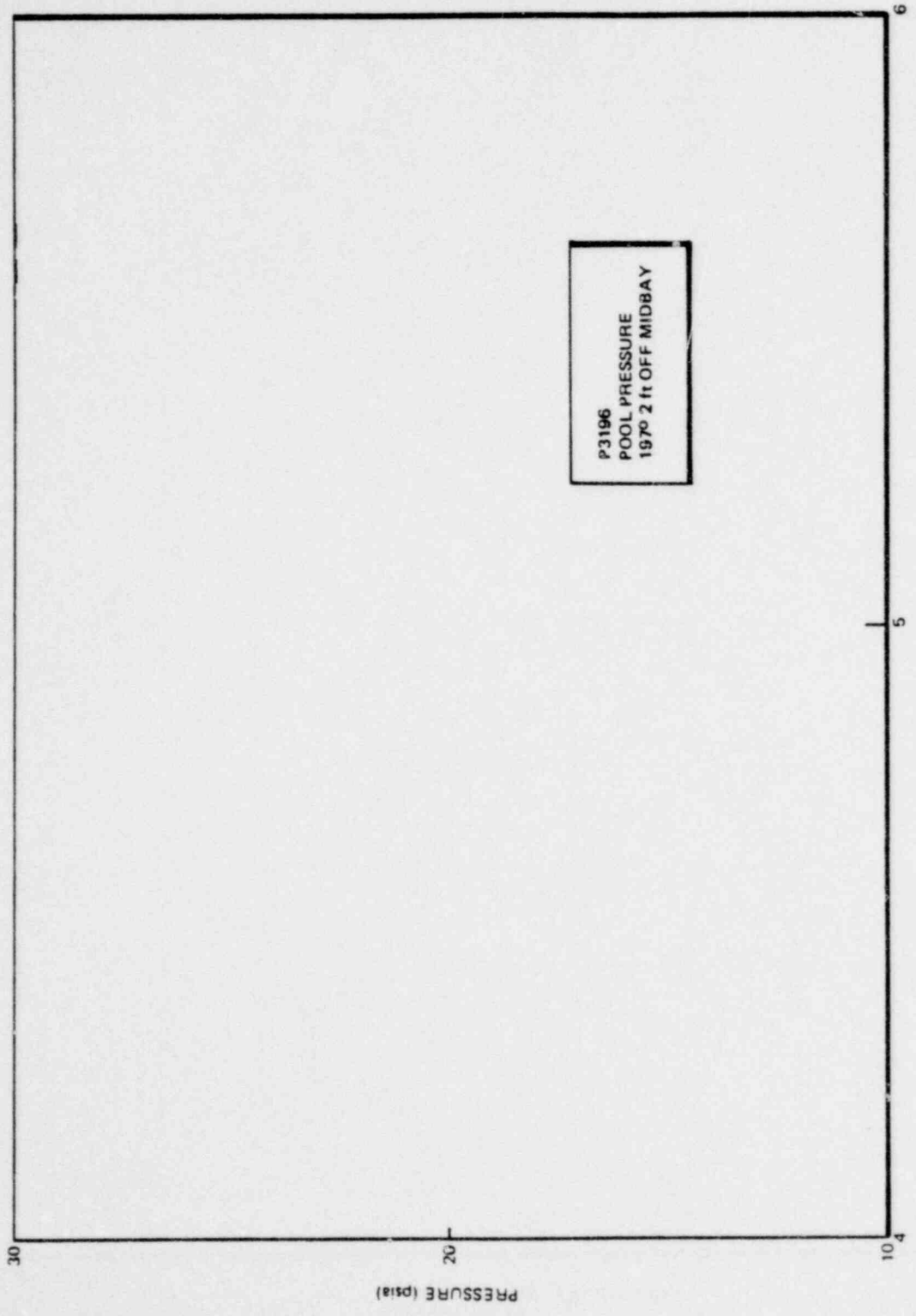

Figure E-7. Pressure Response at Wetwell Wall Beneath Downcomer No. 6 at Test Initiation (Medium Steam Break Test - M2)

*Proprietary information deleted

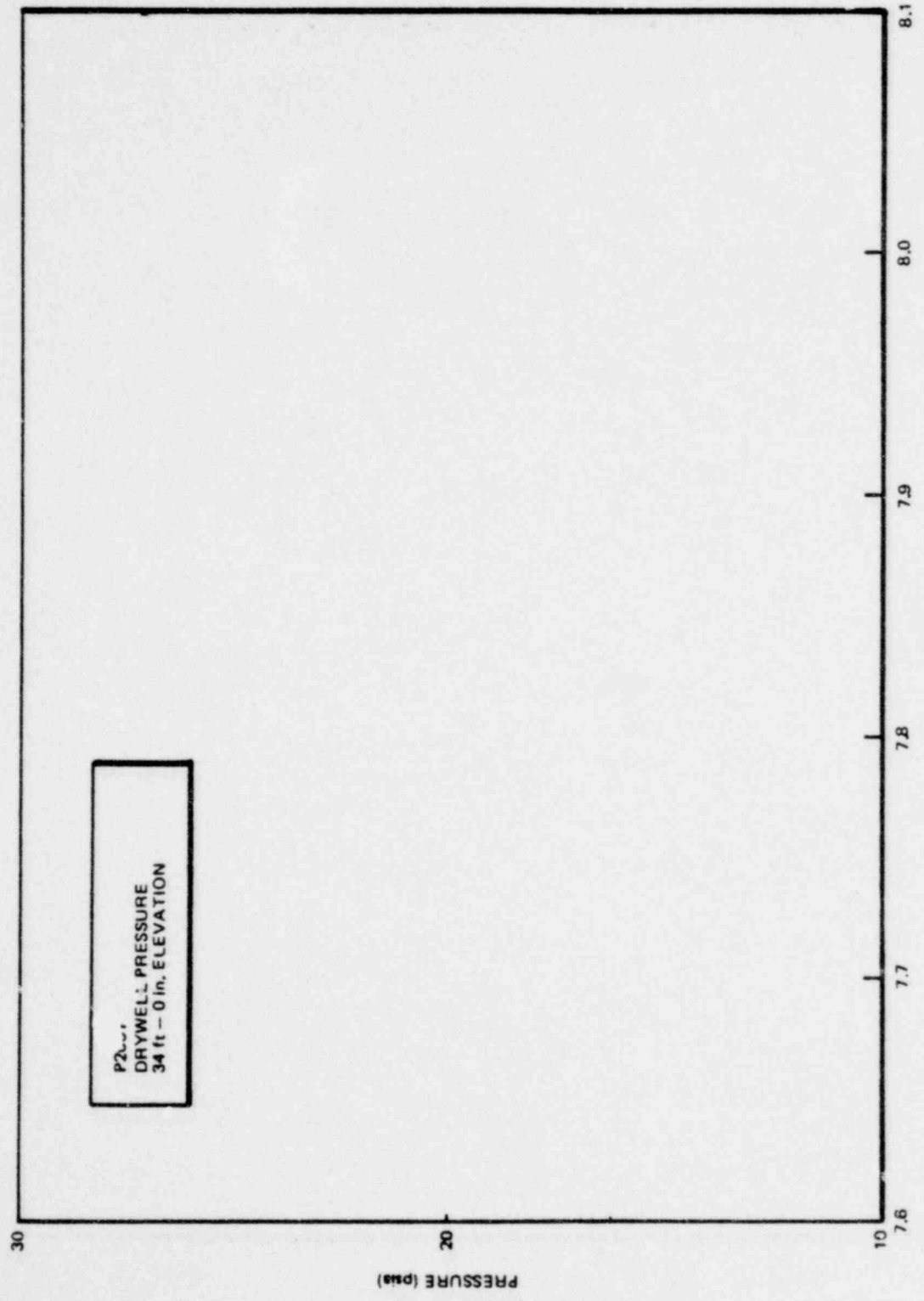

Figure E-8. Pressure Response in the Drywell at Test Initiation (Large Steam Break Test - M7)

*Proprietary information deleted

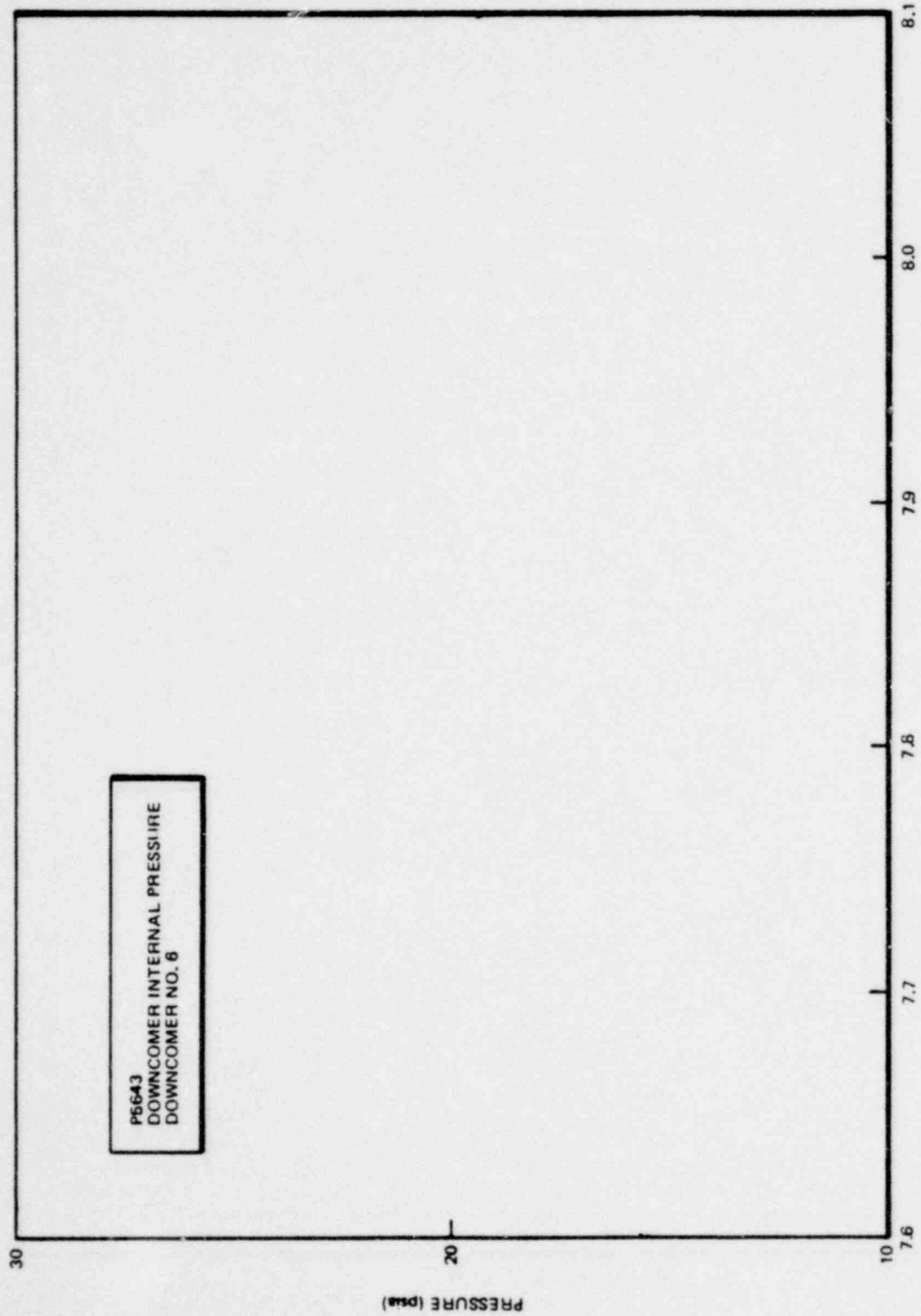

Figure E-9. Pressure Response in Downcomer No. 6 at Test Initiation (Large Steam Break Test - M7)

*Proprietary information deleted

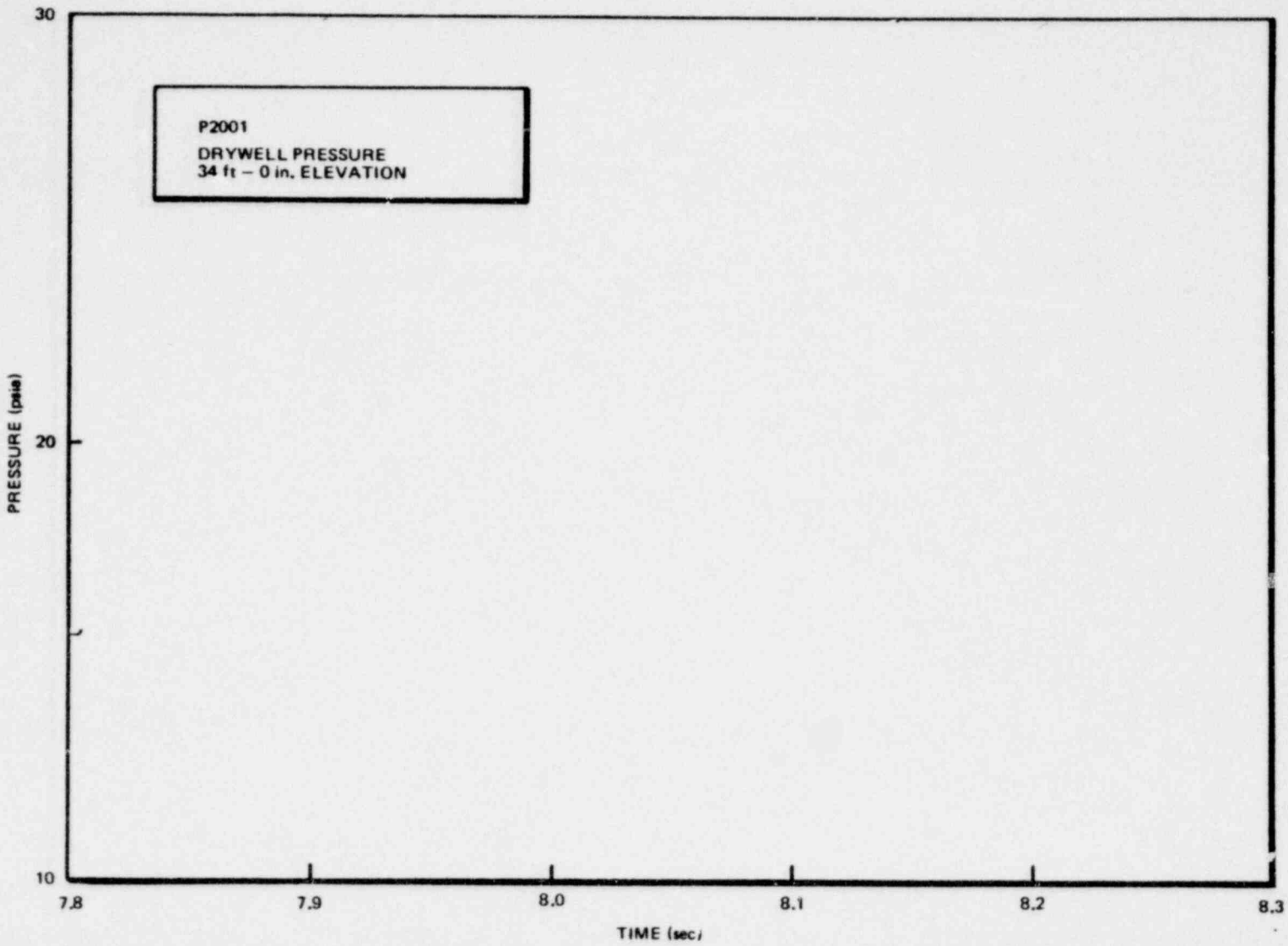

Figure E-10. Pressure Response in the Drywell at Test Initiation (Large Liquid Break Test - M8)

*Proprietary Information deleted

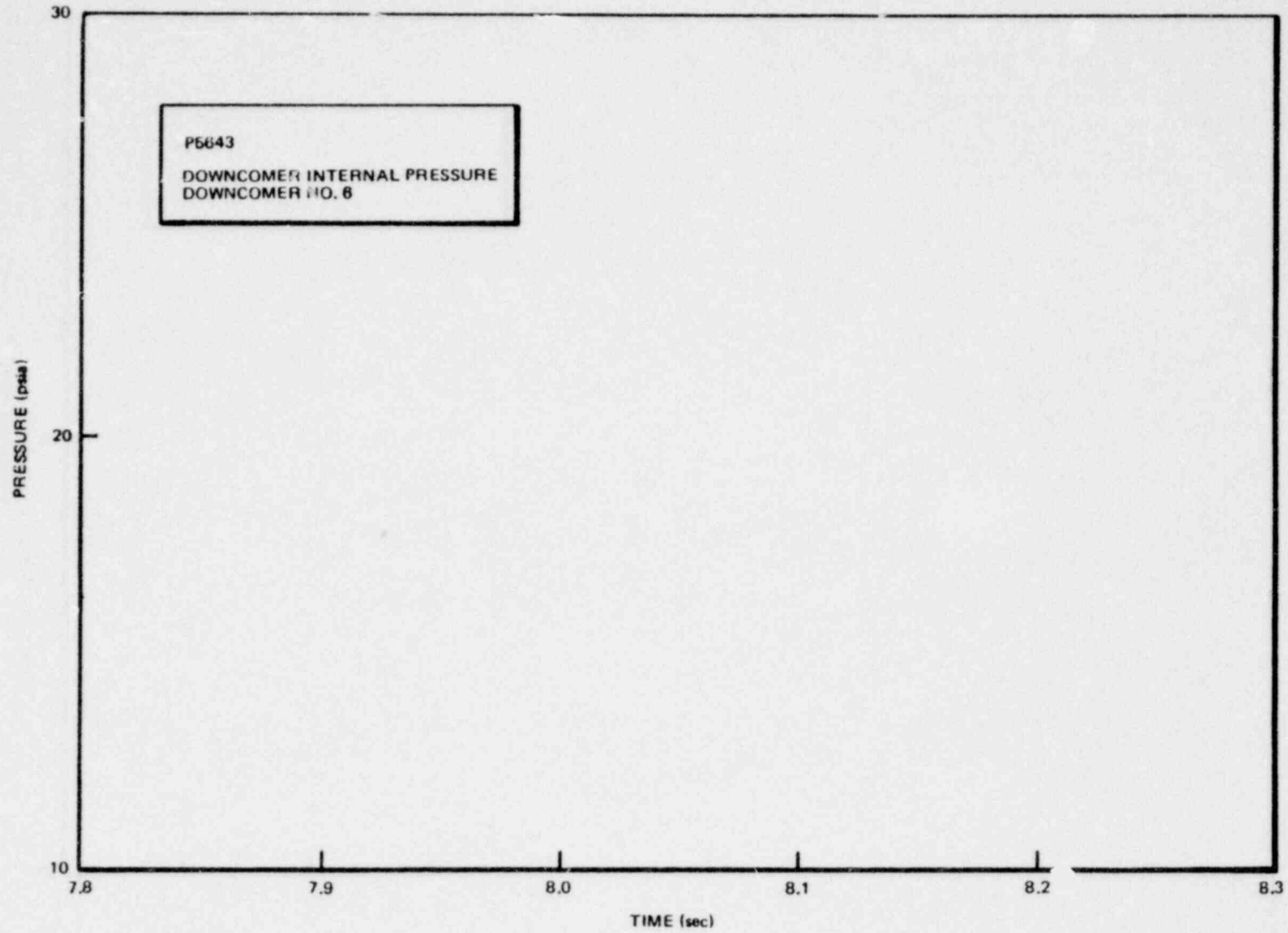

Figure E-11. Pressure Response in Downcomer No. 6 at Jet Initiation (Large Liquid Break Test - M8)

*Proprietary information deleted

REFERENCES

E-1 "Mark I Containment Program: Load Definition Report," General Electric Co., December 1978 (NEDO-21888).

NUCLEAR ENERGY DIVISIONS • GENERAL ELECTRIC COMPANY
SAN JOSE, CALIFORNIA 95125

GENERAL ELECTRIC

TECHNICAL INFORMATION EXCHANGE

TITLE PAGE

AUTHOR G. W. Fitzsimmons et al. SUBJECT 730	TIE NUMBER 79NED84
	DATE April 1979
TITLE Mark I Containment Program Full Scale Test Program Final Report Task Number 5.11	GE CLASS I
	GOVERNMENT CLASS
REPRODUCIBLE COPY FILED AT TECHNICAL SUPPORT SERVICES, R&UO, SAN JOSE, CALIFORNIA 95125 (Mail Code 211)	NUMBER OF PAGES 593

SUMMARY

Test results are reported for a series of ten tests conducted in a full scale mockup of a 22.5° sector of a Mark I containment torus. The test facility included an appropriately-sized drywell and steam vessel to allow simulation of the torus (wetwell) response to a range of LOCA (loss-of-coolant-accident) conditions. Hydrodynamic loads on the wetwell and the structural response of the wetwell shell, downcomer and support columns resulting from the condensation oscillation and chugging regimes were measured. Tests investigating the effects of LOCA break size and type (liquid or steam), downcomer submergence, wetwell freespace pressure, suppression pool temperature, and vent air content were conducted, covering the range of expected Mark I LOCA conditions. This test report includes a description of the test facility, test operation, and a compilation and analysis of the principal test results.

By cutting out this rectangle and folding in half, the above information can be fitted into a standard card file.

DOCUMENT NUMBER NEDO-24539

INFORMATION PREPARED FOR Nuclear Energy Projects Division

SECTION Containment Improvement Programs

BUILDING AND ROOM NUMBER PYD 409 MAIL CODE 905

GENERAL ELECTRIC